

Peter Mulser  
Dieter Bauer

SPRINGER TRACTS IN MODERN PHYSICS 238

# High Power Laser- Matter Interaction

 Springer

# Springer Tracts in Modern Physics

## Volume 238

Managing Editor: G. Höhler, Karlsruhe

Editors: A. Fujimori, Tokyo  
J. Kühn, Karlsruhe  
Th. Müller, Karlsruhe  
F. Steiner, Ulm  
J. Trümper, Garching  
P. Wölfle, Karlsruhe

Available online at  
[SpringerLink.com](#)

Starting with Volume 165, Springer Tracts in Modern Physics is part of the [SpringerLink] service. For all customers with standing orders for Springer Tracts in Modern Physics we offer the full text in electronic form via [SpringerLink] free of charge. Please contact your librarian who can receive a password for free access to the full articles by registration at:

[springerlink.com](#)

If you do not have a standing order you can nevertheless browse online through the table of contents of the volumes and the abstracts of each article and perform a full text search.

There you will also find more information about the series.

# Springer Tracts in Modern Physics

---

Springer Tracts in Modern Physics provides comprehensive and critical reviews of topics of current interest in physics. The following fields are emphasized: elementary particle physics, solid-state physics, complex systems, and fundamental astrophysics.

Suitable reviews of other fields can also be accepted. The editors encourage prospective authors to correspond with them in advance of submitting an article. For reviews of topics belonging to the above mentioned fields, they should address the responsible editor, otherwise the managing editor.

See also [springer.com](http://springer.com)

## Managing Editor

Gerhard Höhler

Institut für Theoretische Teilchenphysik  
Universität Karlsruhe  
Postfach 69 80  
76128 Karlsruhe, Germany  
Phone: +49 (7 21) 6 08 33 75  
Fax: +49 (7 21) 37 07 26  
Email: [gerhard.hoehler@physik.uni-karlsruhe.de](mailto:gerhard.hoehler@physik.uni-karlsruhe.de)  
[www-ttp.physik.uni-karlsruhe.de/](http://www-ttp.physik.uni-karlsruhe.de/)

## Elementary Particle Physics, Editors

Johann H. Kühn

Institut für Theoretische Teilchenphysik  
Universität Karlsruhe  
Postfach 69 80  
76128 Karlsruhe, Germany  
Phone: +49 (7 21) 6 08 33 72  
Fax: +49 (7 21) 37 07 26  
Email: [johann.kuehn@physik.uni-karlsruhe.de](mailto:johann.kuehn@physik.uni-karlsruhe.de)  
[www-ttp.physik.uni-karlsruhe.de/~jk](http://www-ttp.physik.uni-karlsruhe.de/~jk)

Thomas Müller

Institut für Experimentelle Kernphysik  
Fakultät für Physik  
Universität Karlsruhe  
Postfach 69 80  
76128 Karlsruhe, Germany  
Phone: +49 (7 21) 6 08 35 24  
Fax: +49 (7 21) 6 07 26 21  
Email: [thomas.muller@physik.uni-karlsruhe.de](mailto:thomas.muller@physik.uni-karlsruhe.de)  
[www-ekp.physik.uni-karlsruhe.de](http://www-ekp.physik.uni-karlsruhe.de)

## Fundamental Astrophysics, Editor

Joachim Trümper

Max-Planck-Institut für Extraterrestrische Physik  
Postfach 13 12  
85741 Garching, Germany  
Phone: +49 (89) 30 00 35 59  
Fax: +49 (89) 30 00 33 15  
Email: [jtrumper@mpe.mpg.de](mailto:jtrumper@mpe.mpg.de)  
[www.mpe-garching.mpg.de/index.html](http://www.mpe-garching.mpg.de/index.html)

## Solid-State Physics, Editors

Atsushi Fujimori

*Editor for The Pacific Rim*

Department of Physics  
University of Tokyo  
7-3-1 Hongo, Bunkyo-ku  
Tokyo 113-0033, Japan  
Email: [fujimori@wyvern.phys.s.u-tokyo.ac.jp](mailto:fujimori@wyvern.phys.s.u-tokyo.ac.jp)  
[http://wyvern.phys.s.u-tokyo.ac.jp/welcome\\_en.html](http://wyvern.phys.s.u-tokyo.ac.jp/welcome_en.html)

Peter Wölfle

Institut für Theorie der Kondensierten Materie  
Universität Karlsruhe  
Postfach 69 80  
76128 Karlsruhe, Germany  
Phone: +49 (7 21) 6 08 35 90  
Fax: +49 (7 21) 6 08 77 79  
Email: [woelfle@tkm.physik.uni-karlsruhe.de](mailto:woelfle@tkm.physik.uni-karlsruhe.de)  
[www-tkm.physik.uni-karlsruhe.de](http://www-tkm.physik.uni-karlsruhe.de)

## Complex Systems, Editor

Frank Steiner

Institut für Theoretische Physik  
Universität Ulm  
Albert-Einstein-Allee 11  
89069 Ulm, Germany  
Phone: +49 (7 31) 5 02 29 10  
Fax: +49 (7 31) 5 02 29 24  
Email: [frank.steiner@uni-ulm.de](mailto:frank.steiner@uni-ulm.de)  
[www.physik.uni-ulm.de/theo/qc/group.html](http://www.physik.uni-ulm.de/theo/qc/group.html)

Peter Mulser · Dieter Bauer

# High Power Laser–Matter Interaction



Prof. Dr. Peter Mulser  
TU Darmstadt  
Institut für Angewandte Physik (IAP)  
Hochschulstr. 6  
64289 Darmstadt  
Germany  
[Peter.Mulser@physik.tu-darmstadt.de](mailto:Peter.Mulser@physik.tu-darmstadt.de)

Prof. Dr. Dieter Bauer  
Universität Rostock  
Institut für Physik  
AG Quantentheorie u.  
Vielteilchensysteme  
Universitätsplatz 3  
18051 Rostock  
Germany  
[Dieter.Bauer@uni-rostock.de](mailto:Dieter.Bauer@uni-rostock.de)

---

P. Mulser, D. Bauer, *High Power Laser-Matter Interaction*, STMP 238 (Springer, Berlin Heidelberg 2010), DOI 10.1007/978-3-540-46065-7

---

ISSN 0081-3869                            e-ISSN 1615-0430  
ISBN 978-3-540-50669-0                e-ISBN 978-3-540-46065-7  
DOI 10.1007/978-3-540-46065-7  
Springer Heidelberg Dordrecht London New York

Library of Congress Control Number: 2010927139

© Springer-Verlag Berlin Heidelberg 2010

This work is subject to copyright. All rights are reserved, whether the whole or part of the material is concerned, specifically the rights of translation, reprinting, reuse of illustrations, recitation, broadcasting, reproduction on microfilm or in any other way, and storage in data banks. Duplication of this publication or parts thereof is permitted only under the provisions of the German Copyright Law of September 9, 1965, in its current version, and permission for use must always be obtained from Springer. Violations are liable to prosecution under the German Copyright Law.

The use of general descriptive names, registered names, trademarks, etc. in this publication does not imply, even in the absence of a specific statement, that such names are exempt from the relevant protective laws and regulations and therefore free for general use.

*Cover design:* Integra Software Services Pvt. Ltd., Pondicherry

Printed on acid-free paper

Springer is part of Springer Science+Business Media ([www.springer.com](http://www.springer.com))

*This book is dedicated to Professor Gerhard Höhler. Without his continuous encouragement the work would not have been completed.*



# Preface

In the present volume the main aspects of high-power laser–matter interaction in the intensity range  $10^{10}$ – $10^{22}$  W/cm<sup>2</sup> are described. We offer a guide to this topic for scientists and students who have just discovered the field as a new and attractive area of research, and for scientists who have worked in another field and want to join now the subject of laser plasmas. Being aware of the wide differences in the degree of mathematical preparation the individual candidate has acquired we tried to present the subject in an almost self-contained manner. To be more specific, a bachelor degree in physics enables the reader in any case to follow without difficulty. Generally fluid or gas dynamics and its relativistic version is not a part of this education; it is developed in the context where it is needed. Basic knowledge in theoretical mechanics, electrodynamics and quantum physics are the only prerequisites we expect from the reader. Throughout the book the main emphasis is on the various basic phenomena and their underlying physics. Not more mathematics than necessary is introduced. The preference is given to ideas. A good model is the best guide to the adequate mathematics.

There exist already some but not so many, however, good volumes and some monographs on high-power laser interaction with matter. After research in this field has grown over half a century and has ramified into many branches of fundamental studies and applications producing continuously new results, there is no indication of saturation or loss of attraction, rather has excitement increased with the years: “There are no limits; horizons only” (G.A. Mourou). We take this as a motivation for a new attempt of presenting our introduction to the achievements from the beginning up to present. An additional aim was to offer a more unified or more detailed view where this is possible now. Furthermore, the reader may find considerations not encountered in existing volumes on the field, e.g., on ideal fluid dynamics, dimensional analysis, questions of classical optics, instabilities and light pressure. In view of the rapidly growing field of atoms, molecules and clusters exposed to superstrong laser fields we considered it as compulsory to dedicate an entire chapter to laser–atom interaction and to the various modern theoretical approaches related to it. Finally, a consistent model of collisionless absorption is given.

Depending on personal preferences the reader may miss perhaps a section on inertial fusion, on high harmonic generation and on radiation from the plasma, or on traditional atomic and ionic spectroscopy. In view of the specialized literature

already available on the subjects we think the self-imposed restriction is justified. Our referencing practice was guided by indicating material for supplementary studies and establishing a continuity through the decades of research in the field rather than by the aim of completeness. The latter nowadays is easily achievable with the aid of the Internet.

We have tested the text with respect to comprehension and readability. Our first thanks go to Prof. Edith Borie from the Forschungszentrum Karlsruhe. She proof-read great parts of the text very carefully and gave valuable comments. In second place we would like to thank Mrs. Christine Eidmann from Theoretical Quantum Electronics (TQE), TU Darmstadt, for typing in L<sup>A</sup>T<sub>E</sub>X half of the book. We are further indebted to Prof. Rudolf Bock from GSI, Darmstadt, for helpful discussions and precious hints. Further thanks for helpful discussions, critical comments, checking formulas go to Dr. Herbert Schnabl, Prof. Werner Scheid, Dr. Ralf Schneider, Dipl.-Phys. Tatjana Muth, Dr. Steffen Hain, and Dr. Francesco Ceccherini. We want to acknowledge explicitly the continuous effort and support in preparing the final manuscript by Dr. Su-Ming Weng from the Institute of Physics, CAS, China, at present fellow of the Humboldt Foundation at TQE. For his professional input to the section on Brillouin scattering special thanks go to Dr. Stefan Hüller from Ecole Polytechnique in Palaiseau.

Darmstadt, Germany  
Rostock, Germany

*Peter Mulser  
Dieter Bauer*

# Contents

<b>1</b>	<b>Introductory Remarks and Overview</b>	<b>1</b>
<b>2</b>	<b>The Laser Plasma: Basic Phenomena and Laws</b>	<b>5</b>
2.1	Laser–Particle Interaction and Plasma Formation	6
2.1.1	High-Power Laser Fields	6
2.1.2	Single Free Electron in the Laser Field (Nonrelativistic)	9
2.1.3	Collisional Ionization, Plasma Heating, and Quasineutrality	13
2.2	Fluid Description of a Plasma	24
2.2.1	Two-Fluid and One-Fluid Models	24
2.2.2	Linearized Motions	37
2.2.3	Similarity Solutions	44
2.3	Laser Plasma Dynamics	58
2.3.1	Plasma Production with Intense Short Pulses	60
2.3.2	Heating with Long Pulses of Constant Intensity	63
2.3.3	Similarity Considerations	69
2.4	Steady State Ablation	74
2.4.1	The Critical Mach Number in a Stationary Planar Flow	75
2.4.2	Ablative Laser Intensity	78
2.4.3	Ablation Pressure in the Absence of Profile Steepening	82
	References	85
<b>3</b>	<b>Laser Light Propagation and Collisional Absorption</b>	<b>91</b>
3.1	The Optical Approximation	92
3.1.1	Ray Equations	93
3.1.2	WKB Approximation	98
3.1.3	Energy Fluxes	101
3.2	Stokes Equation and its Applications	107
3.2.1	Homogeneous Stokes Equation	107
3.2.2	Reflection-Free Density Profiles	112
3.2.3	Collisional Absorption in Special Density Profiles	113
3.2.4	Inhomogeneous Stokes Equation	115
3.3	Collisional Absorption	118

3.3.1	Collision Frequency of Electrons Drifting at Constant Speed (Oscillator Model) . . . . .	120
3.3.2	Thermal Electrons in a Strong Laser Field . . . . .	129
3.3.3	The Ballistic Model . . . . .	134
3.3.4	Equivalence of Models . . . . .	142
3.3.5	Complementary Remarks . . . . .	143
3.4	Inverse Bremsstrahlung Absorption . . . . .	146
3.5	Ion Beam Stopping . . . . .	149
	References . . . . .	150
<b>4</b>	<b>Resonance Absorption . . . . .</b>	<b>153</b>
4.1	Linear Resonance Absorption . . . . .	154
4.1.1	The Capacitor Model . . . . .	159
4.1.2	Steep Density Gradients and Fresnel Formula . . . . .	160
4.1.3	Comparison with Experiments . . . . .	163
4.2	Nonlinear Resonance Absorption . . . . .	164
4.2.1	High Amplitude Electron Plasma Waves at Moderate Density Gradients . . . . .	165
4.2.2	Resonance Absorption by Nonlinear Electron Plasma Waves . . . . .	168
4.3	Hot Electron Generation . . . . .	172
4.3.1	Acceleration of Electrons by an Intense Smooth Langmuir Wave . . . . .	173
4.3.2	Particle Acceleration by a Discontinuous Langmuir Wave . . . . .	178
4.3.3	Vlasov Simulations and Experiments . . . . .	179
4.4	Wavebreaking . . . . .	182
4.4.1	Hydrodynamic Wavebreaking . . . . .	184
4.4.2	Kinetic Theory of Wavebreaking . . . . .	186
	References . . . . .	191
<b>5</b>	<b>The Ponderomotive Force and Nonresonant Effects . . . . .</b>	<b>193</b>
5.1	Ponderomotive Force on a Single Particle . . . . .	194
5.1.1	Conservation of the Cycle-Averaged Energy . . . . .	195
5.1.2	The Standard Perturbative Derivation of the Force . . . . .	199
5.1.3	Rigorous Relativistic Treatment . . . . .	201
5.2	Collective Ponderomotive Force Density . . . . .	206
5.2.1	Bulk Force . . . . .	206
5.2.2	The Force Originating from Induced Fluctuations . . . . .	206
5.2.3	Global Momentum Conservation . . . . .	209
5.3	Nonresonant Ponderomotive Effects . . . . .	210
5.3.1	Ablation Pressure . . . . .	211
5.3.2	Filamentation and Self-Focusing . . . . .	219
5.3.3	Modulational Instability . . . . .	222
	References . . . . .	225

<b>6 Resonant Ponderomotive Effects</b>	229
6.1 Tools	229
6.1.1 Waves, Energy Densities and Wave Pressure	230
6.1.2 Doppler Shifts	232
6.2 Instabilities Driven by Wave Pressure	238
6.2.1 Resonant Ponderomotive Coupling	238
6.2.2 Unstable Configurations	242
6.2.3 Growth Rates	245
6.3 Parametric Amplification of Pulses	256
6.3.1 Slowly Varying Amplitudes	257
6.3.2 Quasi-Particle Conservation and Manley–Rowe Relations	258
6.3.3 Light Scattering at Relativistic Intensities	259
References	265
<b>7 Intense Laser–Atom Interaction</b>	267
7.1 Atomic Units	267
7.2 Atoms in Strong Static Electric Fields	270
7.2.1 Separation of the Schrödinger Equation	272
7.2.2 Tunneling Ionization	277
7.3 Atoms in Strong Laser Fields	281
7.3.1 Floquet Theory and Dressed States	283
7.3.2 Non-Hermitian Floquet Theory	287
7.3.3 Stabilization	288
7.3.4 Strong Field Approximation	292
7.3.5 Few-Cycle Above-Threshold Ionization	301
7.3.6 Simple Man’s Theory	304
7.3.7 Interference Effects	306
7.3.8 High-Order Harmonic Generation	308
7.3.9 Strong Field Approximation for High-Order Harmonic Generation: the Lewenstein Model	313
7.3.10 Harmonic Generation Selection Rules	315
7.4 Strong Laser–Atom Interaction Beyond the Single Active Electron	319
7.4.1 Nonsequential Ionization	320
References	326
<b>8 Relativistic Laser–Plasma Interaction</b>	331
8.1 Essential Relativity	331
8.1.1 Four Vectors	331
8.1.2 Momentum and Kinetic Energy	336
8.1.3 Scalars, Contravariant and Covariant Quantities	337
8.1.4 Ideal Fluid Dynamics	340
8.1.5 Kinetic Theory	341
8.1.6 Center of Momentum and Mass Frame of Noninteracting Particles	343

8.1.7	Moment Equations . . . . .	344
8.1.8	Covariant Electrodynamics . . . . .	348
8.2	Particle Acceleration in an Intense Laser Field . . . . .	351
8.2.1	Particle Acceleration in Vacuum . . . . .	353
8.2.2	Wakefield and Bubble Acceleration . . . . .	359
8.3	Collisionless Absorption in Overdense Matter and Clusters . . . . .	363
8.3.1	Computer Simulations of Collisionless Laser–Target Interaction . . . . .	364
8.3.2	Search for Collisionless Absorption . . . . .	371
8.3.3	Collisionless Absorption by Anharmonic Resonance . . . . .	378
8.4	Some Relativity of Relevance in Practice . . . . .	392
8.4.1	Overview . . . . .	392
8.4.2	Critical Density Increase for Fast Ignition . . . . .	393
8.4.3	Relativistic Self-Focusing . . . . .	400
	References . . . . .	401
	<b>Index</b> . . . . .	405

# Chapter 1

## Introductory Remarks and Overview

Laser-produced plasmas represent a modern, physically rich topic of electromagnetic interaction with macroscopic matter. The laser intensities extend from the threshold of plasma formation at approximately  $10^{10} \text{ W/cm}^2$  on the nanosecond time scale up to the highest energy flux densities of several  $10^{22} \text{ W/cm}^2$  currently available in the femtosecond domain. The laser is capable of supplying enormous amounts of energy in very short times. The first salient aspect of the laser plasma is its fast dynamics, and in concomitance, its inhomogeneity in density, temperature and flow velocity. As the laser acts preferentially on the light electrons they determine the fast time scale. The interaction itself is characterized by a limiting electron density beyond which no electromagnetic propagation is possible (critical density, cut-off). This property is the main reason for laser plasmas to be very hot and more or less close to ideality, and is responsible for steep density variations in the transition zone from underdense to overdense plasma. The irreversible interaction (absorption, heating of the electrons) is accomplished by friction between electrons and ions due to electron-ion collisions, so-called collisional or inverse bremsstrahlung absorption, and by resonances of the free electrons in the self-generated electrostatic fields. At super-high intensities when the mitigating effect of collisions (and absorption) is almost absent the laser acts more and more as an extremely efficient accelerator of energetic electrons by anharmonic resonance. This collisionless absorption process gives the electron fluid properties far from thermal equilibrium, not to mention the formation of an electron temperature very much exceeding that of the ion fluid. Overdense samples of matter are indirectly heated only by electron heat conduction, fast electron jets, electron plasma waves, plasma radiation and plasma shock waves. On the slow time scale of the ions the electrons are bound to them by quasi-neutrality, one of the fundamental properties of any plasma state.

The dynamics of the laser plasma on the ion time scale is governed by the thermal pressure of the electrons, and to a certain extent, by that of the ions. However, this is only half the truth. Any oscillating force, like that impressed by the laser field, in presence of inhomogeneities gives origin to a secular force on the slow time scale, here in the plasma on the ions. This so-called ponderomotive force, or pressure gradient of light, and more in general, of waves not only does inhibit the tendency towards uniformity in the process of plasma expansion; it does impress

also a whole variety of structures onto the plasma, of resonant character like stimulated Raman and Brillouin scattering as well as various other parametric three-wave interaction phenomena; or of non-resonant character as laser beam filamentation and self-focusing, self-trapping of light, beam self-modulation and ion density profile steepening. The ponderomotive force, although considerably weaker than the direct high-frequency force of the laser beam, determines the plasma dynamics to a decisive degree due to its secular character. It makes the laser plasma inherently unstable.

Under several aspects the laser plasma represents an extreme state of matter far from thermodynamic equilibrium, both on large scale (e.g., spatial gradients of density, temperature, pressure, ionization) and on local scale (e.g., electron and ion temperatures differing from each other, non-equilibrium velocity distribution). In the intense field collisional heating tends towards the generation of super-Gaussian electron distributions in place of a Maxwellian. At resonance electron plasma waves are driven into non-linearities to the extent of breaking, i.e. quenching of modes by self-interaction, and to the already mentioned generation of relativistic electron jets, directly by the action of the laser electric field itself near the critical density or, in the underdense plasma, by the ponderomotive wake behind the laser propagating through the plasma. The Lorentz force governing the electron motion is nonlinear, hence introducing anharmonicities in the high-frequency current densities which as sources for the fields in the Maxwell equations generate high harmonics of the fundamental laser frequency up to some thousandth order. Of particular interest is the interaction of the intense laser field on the atomic and molecular level where, in contrast to standard perturbative external interaction, the main actor is the laser field while the atomic potential represents the perturbation once ionization has occurred. In concomitance, above threshold ionization into the high continuum becomes significant. Effects based on electrons driven back to the ion core by the laser field emerge, such as nonsequential ionization and high-harmonic emission, the latter being particularly relevant for applications, e.g., the generation of attosecond pulses and structural imaging. The dynamics of atoms in strong laser fields have become a rich and fascinating field of modern atomic and plasma physics.

In view of the strong nonlinearities of the basic equations governing the observed phenomena numerical simulation codes have become an indispensable means of accompanying the experiments for analysis and interpretation. Sometimes the simulations themselves need interpretation in the sense that they may not tell at all what the underlying physics producing the results is. An eminent example is collisionless absorption and generation of energetic electrons by anharmonic resonance. Such situations are the moment of truth for simple analytical models.

In the second chapter an introduction to the plasma formation process by intense laser beams is given and the subsequent plasma dynamics is described phenomenologically by the use of a two fluid model. The salient features thereby are quasineutrality and shielding of the plasma. Experience shows that having assimilated these principles may serve as a criterion for the definition of who is a plasma physicist and who is not yet. Another basic concept is laser light absorption by collisions and its equivalence to the inverse bremsstrahlung model. For this reason, in a crude

way it is already introduced in Chap. 2 and then treated extensively in Chap. 3. Generally it is believed that the so-called dielectric approach gives the most satisfactory answer. However, by comparison with the ballistic model we show that under a strong electron drift in the intense laser field the standard dielectric models are inappropriate because of showing very bad convergence and leading to erroneous physical conclusions, for instance on shielding. The root of the difficulties lies in the inappropriate choice of harmonic waves as a basis of description. In other words, describing the hydrogen atom by choosing as a basis the Hermite polynomials of the harmonic oscillator would not lead to enlightenment. The search for an adequate basis is still going on. Chapter 4 is dedicated mainly to the description of linear resonance absorption at the plasma frequency and its mild nonlinearities as well as the self-quenching of the high amplitude electron plasma wave by wave breaking.

Until the first half of the past century light pressure was believed to be a subject of academic interest in the laboratory, only for the equilibrium of stars it played a decisive role, as discovered by A. S. Eddington. In recent years the situation has reversed. We are able to generate pressures by laser light in the laboratory which exceed the gas pressure in the sun easily by a factor of 100. However, already at moderate laser intensities the salient role of light and wave pressure (ponderomotive force) for the plasma dynamics and ablation pressure (profile steepening) as well as for the origin of a whole class of parametric plasma instabilities has become evident. This is shown in detail and under various aspects in Chaps. 5 and 6. At the threshold of laser break down avalanche ionization is by electron impact once a sufficient number of free electrons has been created (first free mysterious electron of Chap. 2). At high laser intensities above  $10^{12} \text{ W/cm}^2$  multiphoton and sequential and non-sequential field ionization start dominating and, in concomitance, lead to a variety of other effects, described altogether in Chap. 7. Finally, Chap. 8 is dedicated to physics induced by relativistic laser beam intensities beyond  $10^{18} \text{ W/cm}^2$ , like electron acceleration, collisionless absorption in simulations and the analysis of the underlying heating mechanism in overdense targets, self-focusing, and applications. Owing to the dominance of relativistic effects a short systematic introduction to relativity and to relativistic kinetic theory is also presented. In general we prefer fluid models to the various kinetic approaches for their physical evidence and simplicity. The hydrodynamic description of plasmas may never be totally correct, on the other hand however, it may be extremely difficult to find situations in which it fails completely. Hydrodynamics is never true and never wrong.

After all, the reader may find some considerations not encountered in existing volumes in the field. Examples may be the topological aspect of ideal fluid dynamics and an elementary introduction to dimensional analysis and similarity in Chap. 2, the oscillator model of dynamical shielding, the nonphysical origin of asymptotic formulas of collisional absorption under strong drift containing the product of two logarithms and a true argument on why the classical Landau length is to be replaced by the reduced de Broglie wavelength in Chap. 3, a thorough discussion of the Fresnel limit of linear resonance absorption in steep density profiles and an attempt to classify the various routes into wave breaking (Chap. 4), alternative derivations of the ponderomotive force density in plasmas and a purely physical proof of the

unstable response of a plasma to this force in Chaps. 5 and 6, the treatment of the ionization dynamics in strong laser fields by a whole variety of modern theoretical approaches (Chap. 7), and finally, the already mentioned solution of the problem of collisionless absorption in overdense matter. As with growing laser intensities the researcher in the field is more and more faced with relativistic phenomena we present a short introduction to essential relativity also.

## Chapter 2

# The Laser Plasma: Basic Phenomena and Laws

High power lasers when focused onto matter lead to extremely rapid ionization by direct photoeffect or, depending on wavelength and material, by multiphoton processes. When a sufficient number of free electrons is created the formation of a dense, highly ionized plasma is more efficiently continued by electron–neutrals and electron–ion impact ionization. In view of many important applications the generation of a homogeneous high density and, at the same time, very hot plasma would be most desirable. Unfortunately, at present high power lasers operate in the near infrared domain. As a consequence, direct interaction of the laser beam with matter is possible only below a limiting density, the so-called critical density which, at nonrelativistic intensities, is typically a hundred times lower than solid density. Only when the oscillatory velocity of the electrons becomes relativistic at laser intensities beyond  $10^{18} \text{ Wcm}^{-2}$  direct interaction with higher densities takes place. It is due to this cut-off that the plasma production process becomes a very dynamic interplay between laser beam stopping and plasma expansion and makes the plasmas created by lasers from overdense matter very inhomogeneous and short-living. Within certain limits efficient energy transfer from the laser to overdense plasma regions is made possible by electron thermal conduction. As there are physical limits inherent in this process also energy transfer to more dense matter is accomplished by shock wave heating and UV and X radiation from the moderately dense plasma.

The dynamics of plasma formation and heating is best understood on the basis of elementary processes induced in atoms and on the electrons by the laser beam. Hence, first, elements of the motion of a single electron in the electromagnetic field and its collisions with atoms and ions are presented. The charged particles lead to collective fields which in turn act back on the single particles. These processes are described in the simplest way by the conservation equations of charge, momentum, and energy of the two-fluid plasma model. Owing to the high mobility of the electrons and ions under intense laser irradiation such a hydrodynamic description in terms of averaged quantities, density, flow velocity, temperature, averaged electric and magnetic fields, can never be the full truth. On the other hand there is its conceptual simplicity which makes of it a very powerful instrument for describing phenomena, even in regions where its validity is questionable. In the following sections of this chapter the basic concepts of collisional heating and quasineutrality are introduced and the basic building blocks of laser-plasma dynamics, linear plasma

waves, thermal waves, shocks and the rarefaction wave are presented and applied to give a first picture of the laser plasma dynamics.

## 2.1 Laser–Particle Interaction and Plasma Formation

It is a common experience that a laser beam when focused in air, generates a spark as soon as the flux density exceeds a well defined, i.e., a reproducible threshold value [1–3]. Such a plasma formation process also occurs in liquids and solids at comparable flux densities. The typical average threshold in insulators is  $I_0 = 10^9 \text{ Wcm}^{-2}$ ; in conducting materials  $I_0$  is lower by orders of magnitude [4, 5]. Thresholds are material- and density-dependent and they are particularly sensitive to impurities and surface quality. As a rule, the thresholds decrease with increasing laser wavelength and pulse duration [6–8].

In this book the interaction of laser radiation with dense matter at flux densities above the threshold for plasma formation is treated. By high power lasers we mean systems for which the intensity exceeds  $I_0$ . Dense matter is characterized by the existence of a critical surface in the plasma, to be defined later. As the plasma rarifies during interaction with the laser beam, many important processes begin to take place in the underdense region in front of the critical surface. Such phenomena may also occur in completely underdense plasmas, in which no critical layer exists.

### 2.1.1 High-Power Laser Fields

Extremely powerful laser systems have been built for various applications, among which inertial confinement fusion (ICF) plays a central role [9–14]. They can be naturally subdivided into two classes: energetic lasers in the ns-ps terawatt (TW) regime and superintense ultrashort lasers, sometimes also called U<sup>3</sup> systems (“Ultrashort, Ultraintense, Ultrapowerful”) or T<sup>3</sup> lasers (“Table-Top TW”) depending on whether operating in the petawatt (PW) or TW sub-ps domain.

The peak of large laser system engineering is currently represented by NIF (“National Ignition Facility”) at Lawrence Livermore National Laboratory (LLNL) and LMJ (“Laser Mega Joule”) in Bordeaux.

At low energies of the order of 1–100 J advances in laser technology have made it possible to generate subpicosecond pulses approaching intensity levels of up to  $10^{23} \text{ Wcm}^{-2}$ , and, nonetheless, containing energy at a level of not more than 1 J. This fact renders the U<sup>3</sup> systems extremely flexible compared to the large ns laser facilities. The use of novel pulse compression techniques leads to pulses as short as 5 fs [15]. In itself the CO<sub>2</sub> laser also represents an interesting and, in contrast to the glass and iodine lasers [16], a highly efficient system. However, owing to its low frequency ( $\omega_{\text{CO}_2} = \omega_{\text{Nd}}/10$ ) collisional coupling to the plasma is reduced, and anomalous interaction with matter intensifies via undesirable parametric and collective processes [17]. For these reasons the high power Antares laser at Los Alamos National Laboratory (LANL) (40 kJ in  $\tau \simeq 2$  ns) was shut down.

Studying high power laser-matter interaction at present means that the power density to be covered ranges from  $I = 10^{10}$  to approximately  $10^{23} \text{ Wcm}^{-2}$  for wavelengths having  $\lambda \lesssim \lambda_{\text{Nd}}$ , i.e., from the near IR to the near UV with  $\lambda \gtrsim \lambda_{\text{KrF}}$ , over times  $\tau$  from tens of nanoseconds down to a few femtoseconds. One should remember that a high power laser pulse with  $\tau = 1 \text{ ns}$  is an energy packet of length  $l = 30 \text{ cm}$ ; at  $\tau = 100 \text{ fs}$  this length shrinks to  $l = 30 \mu\text{m} = 0.03 \text{ mm}$ ! For meaningful laser-matter interaction studies a well defined short rise time and the absence of an undefined prepulse, even of relatively low intensity, is an absolute necessity.

In most cases a clean pulse is composed of many modes characterized by a wavevector  $\mathbf{k}$  and polarization  $\sigma$  so that its total electric field  $\mathbf{E}(\mathbf{x}, t)$  is the sum of the single components  $\mathbf{E}_{k\sigma}(\mathbf{x}, t)$ ,

$$\mathbf{E}(\mathbf{x}, t) = \sum_{k\sigma} \mathbf{E}_{k\sigma}(\mathbf{x}, t), \quad \mathbf{E}_{k\sigma}(\mathbf{x}, t) = \hat{\mathbf{E}}_{k\sigma}(\mathbf{x}, t) e^{i(kx - \omega(k)t)}, \quad (2.1)$$

$\omega(\mathbf{k})$  obeying a proper dispersion relation.  $\hat{\mathbf{E}}_{k\sigma}(\mathbf{x}, t)$  is, in contrast to  $\mathbf{E}_{k\sigma}(\mathbf{x}, t)$ , a slowly varying function of space and time and is called the amplitude of the mode  $k\sigma$ . By choosing  $\hat{\mathbf{E}}_{k\sigma}$  complex, phase differences between modes are automatically taken into account. Since, on the other hand, physical quantities are real, (2.1) reads as  $\Re \mathbf{E} = \sum \Re \mathbf{E}_{k\sigma}$ . When studying nonlinear relations among the  $\mathbf{E}_{k\sigma}$ 's we have to take care of this explicitly. Throughout the book the scalar product of two three vectors  $\mathbf{a}, \mathbf{b}$  is written in the compact form  $\mathbf{ab}$ , and the same convention is used in Chap. 8 for the scalar product of two four vectors  $A$  and  $B$ :  $AB = A^\alpha B_\alpha$ . Possible ambiguities are avoided by the use of brackets, e.g.,  $\mathbf{a} \times (\mathbf{b} \times \mathbf{c}) = (\mathbf{ac})\mathbf{b} - (\mathbf{ab})\mathbf{c}$ ;  $(\mathbf{v}\nabla)\mathbf{v} = (\mathbf{v} \cdot \nabla)\mathbf{v}$ .

One can simplify the radiation field when the interaction process under investigation occurs on a time scale  $T$  of the order of an oscillation period  $2\pi/\omega$  or shorter as is the case for collisional interaction, light propagation, and incoherent scattering. In such and numerous other cases the focused laser beam can be approximated locally by a linearly polarized plane wave of complex amplitude  $\hat{\mathbf{E}}$  (index  $\sigma$  suppressed for compactness),

$$\mathbf{E}(\mathbf{x}, t) = \hat{\mathbf{E}} e^{ikx - i\omega t}, \quad \mathbf{B} = \frac{\mathbf{k}}{\omega} \times \mathbf{E}, \quad (2.2)$$

with the intensity  $I$ , in vacuum, defined by the cycle-averaged modulus of the Poynting vector  $\mathbf{S}$ ,

$$I = |\bar{\mathbf{S}}| = c^2 \epsilon_0 |\overline{\mathbf{E} \times \mathbf{B}}| = \frac{1}{2} c \epsilon_0 \hat{\mathbf{E}} \hat{\mathbf{E}}^*. \quad (2.3)$$

It is in this approximation that the laser energy flux density is identical with an “intensity”  $I$ . For practical purposes the numerical relation between amplitude and intensity is very useful,

**Table 2.1** Wavelength, circular frequency  $\omega$ , photon energy  $\hbar\omega$ , and critical density  $n_c$  of a few high power lasers

Laser	Wavelength, nm	$\omega, \text{ s}^{-1}$	$\hbar\omega, \text{ eV}$	$n_c, \text{ cm}^{-3}$
CO <sub>2</sub>	10,600	$1.78 \times 10^{14}$	0.12	$10^{19}$
I	1315	$1.46 \times 10^{15}$	0.96	$6.5 \times 10^{20}$
Nd	1060	$1.78 \times 10^{15}$	1.17	$10^{21}$
Ti:Sa	800	$2.36 \times 10^{15}$	1.55	$1.8 \times 10^{21}$
KrF	248	$7.59 \times 10^{15}$	4.99	$1.8 \times 10^{22}$

$$\hat{E} [\text{V/cm}] = 27.5 \times \left\{ I [\text{W/cm}^2] \right\}^{1/2}. \quad (2.4)$$

We list wavelengths, frequencies, photon energies, and critical electron density  $n_c = m\varepsilon_0\omega^2/e^2$  [see also (2.94)] for the most common high power lasers in Table 2.1. For the interested reader it should be mentioned that the classical coherent wave (2.2) is an approximation which is only asymptotically reached by the best systems lasing well above threshold. A single mode having a well-defined wavevector  $k_\sigma$  and polarization  $\sigma$  can contain 0, 1, 2, 3, ...,  $n$  photons. Accordingly, the radiation field is in one of the following photon number states (Fock states)  $|0\rangle$  (vacuum),  $|1\rangle$ ,  $|2\rangle$ ,  $|3\rangle$ , ...,  $|n\rangle$ , or a superposition of them. Since the amplitude of these states is sharp,

$$\hat{E} = \left( \frac{2\hbar\omega}{\varepsilon_0 V} \right)^{1/2} \left( n + \frac{1}{2} \right)^{1/2}, \quad (2.5)$$

their phase  $\psi$  is completely uncertain (see, e.g., [18, 19]). Here,  $V$  is the volume of an arbitrary cube containing the mode  $k\sigma$ . The quantum state coming closest to the classical mode (2.2) is the so-called coherent or Glauber state  $|\alpha\rangle$  [18],

$$|\alpha\rangle = \exp \left( -\frac{|\alpha|^2}{2} \right) \sum_{n \geq 0} \frac{\alpha^n}{(n!)^{1/2}} |n\rangle, \quad (2.6)$$

where  $\alpha$  is an arbitrary complex number. Each number state contributes with the probability  $P_n$  of a Poisson distribution,

$$P_n = |\langle n | \alpha \rangle|^2 = \frac{|\alpha|^{2n}}{n!} e^{-|\alpha|^2}.$$

It is easily seen that the average photon number  $n$  and its relative mean square deviation  $\Delta n = \langle n^2 - \langle n \rangle^2 \rangle^{1/2}$  are, by definition,

$$\langle n \rangle = \sum_{n \geq 0} P_n n = |\alpha|^2, \quad \frac{\Delta n}{\langle n \rangle} = \frac{1}{|\alpha|}. \quad (2.7)$$

In high power laser experiments with Ti:Sa wavelength  $\langle n \rangle$  ranges typically from  $10^{10}$  to  $10^{20} \text{ cm}^{-3}$ . The electric field  $\mathbf{E}$  is the expectation value of the field operator

$$\mathbf{E}_{\text{op}} = i(\hbar\omega/2\varepsilon_0 V)^{1/2} \{e^{ikx-i\omega t} a - e^{-ikx+i\omega t} a^\dagger\}, \quad [a, a^\dagger] = 1,$$

$$\mathbf{E}(\mathbf{x}, t) = \langle \alpha | \mathbf{E}_{\text{op}} | \alpha \rangle = -(2\hbar\omega/\varepsilon_0 V)^{1/2} |\alpha| \sin(kx - \omega t + \varphi). \quad (2.8)$$

It differs from the coherent classical wave (2.2) merely by the uncertainty in  $\mathbf{E}$  [18]:

$$\Delta E = \left( \langle \alpha | \mathbf{E}_{\text{op}}^2 | \alpha \rangle - \mathbf{E}^2(\mathbf{x}, t) \right)^{1/2} = (\hbar\omega/2\varepsilon_0 V)^{1/2}. \quad (2.9)$$

This shows that all uncertainty originates from the vacuum state  $|0\rangle$ . It follows from (2.5) to (2.9) that at high intensities and acceptable coherence the classical field (2.2) is an excellent approximation and that quantum field effects do not play a significant role in high power laser matter interaction. However, one must bear in mind that “nonclassical” states of light exist, even at high intensities, for instance photon number states  $|n\rangle$ , the preparation of which is certainly a very difficult task, but nevertheless possible [20, 21]. One of the most striking successes of field quantization is the derivation of the Einstein coefficient  $A$  for spontaneous emission solely from the commutation relations of the photon creation and annihilation operators  $a^\dagger$  and  $a$ .

### 2.1.2 Single Free Electron in the Laser Field (Nonrelativistic)

Above the breakdown threshold, matter is transformed into a dense plasma. The properties of such a fluid are largely determined by the collective motion of free electrons. The electrons themselves move as single particles in the  $\mathbf{E}$ - and  $\mathbf{B}$ -fields which are the superposition of fields  $\mathbf{E}_{\text{ex}}$ ,  $\mathbf{B}_{\text{ex}}$ , imposed from outside, and internal fields  $\mathbf{E}_{\text{in}}$ ,  $\mathbf{B}_{\text{in}}$ , produced by their collective motions. Classically, the dynamics of a free electron of mass  $m$  is governed by the Lorentz force

$$\frac{d}{dt}(m\mathbf{v}) = -e(\mathbf{E} + \mathbf{v} \times \mathbf{B}), \quad (2.10)$$

which in this form with variable mass is correct at any relativistic speed. Throughout the book however all symbols referring to masses  $m$ ,  $m_i$ , etc. indicate their rest masses. Accordingly, the left-hand side of (2.10) is written as  $d(\gamma m\mathbf{v})/dt$  with  $\gamma$  the Lorentz factor. See also the comment on the “relativistic mass increase” following (8.17) in Sect. 8.1.1. A solution  $\mathbf{x}(t)$  is such that the equation is satisfied for given values  $\mathbf{E}(\mathbf{x}(t), t)$  and  $\mathbf{B}(\mathbf{x}(t), t)$  which shows that (2.10) is in general highly nonlinear. However, for a field of the form (2.2) the nonrelativistic solution is easily obtained. To a first approximation,  $\mathbf{B}$  can be disregarded because its magnitude is  $B = E/v_\varphi$ , with the phase velocity  $v_\varphi = \omega/k$ , and  $d/dt$  can be replaced by  $\partial/\partial t$ . One finds for the purely oscillating quantities

$$\mathbf{v} = -i \frac{e}{m\omega} \mathbf{E} = \hat{\mathbf{v}} e^{ikx-i\omega t}; \quad \hat{\mathbf{v}} = -i \frac{e}{m\omega} \hat{\mathbf{E}}, \quad (2.11)$$

$$\boldsymbol{\delta} = \frac{e}{m\omega^2} \mathbf{E} = \hat{\boldsymbol{\delta}} e^{ikx-i\omega t}; \quad \hat{\boldsymbol{\delta}} = \frac{e}{m\omega^2} \hat{\mathbf{E}}. \quad (2.12)$$

$\boldsymbol{\delta}$  is the periodic displacement of the electron;  $\hat{\mathbf{v}}$  and  $\hat{\boldsymbol{\delta}}$  are the amplitudes of  $\mathbf{v}$  and  $\boldsymbol{\delta}$ . For practical purposes it is convenient to normalize their numerical values to the Ti:Sa laser field with intensity  $I$  in  $\text{Wcm}^{-2}$  and  $\lambda_{\text{Ti:Sa}} = 800 \text{ nm}$ ,

$$\hat{\beta} = \frac{\hat{\mathbf{v}}}{c} = 6.8 \times 10^{-10} \frac{\lambda}{\lambda_{\text{Ti:Sa}}} \left\{ I[\text{W/cm}^2] \right\}^{1/2} \quad (2.13)$$

$$\hat{\boldsymbol{\delta}} [\text{nm}] = 8.7 \times 10^{-8} \left( \frac{\lambda}{\lambda_{\text{Ti:Sa}}} \right)^2 \left\{ I[\text{W/cm}^2] \right\}^{1/2}. \quad (2.14)$$

Another expression of interest is the cycle-averaged oscillation energy  $W$ ,

$$W = \frac{1}{4} m \hat{\mathbf{v}}^2 = \frac{e^2}{4m\omega^2} \hat{\mathbf{E}} \hat{\mathbf{E}}^* = \frac{1}{4} e \hat{\boldsymbol{\delta}}^* \hat{\mathbf{E}}; \quad (2.15)$$

$$W [\text{eV}] = 6.0 \times 10^{-14} \left( \frac{\lambda}{\lambda_{\text{Ti:Sa}}} \right)^2 I[\text{W/cm}^2]. \quad (2.16)$$

When the electron oscillation becomes relativistic,

$$W = mc^2 \left\{ \left[ 1 + \frac{1}{2} \left( \frac{e \hat{\mathbf{A}}}{mc} \right)^2 \right]^{1/2} - 1 \right\} \quad (2.17)$$

where  $\hat{\mathbf{A}}$  is the vector potential amplitude. For circular polarization the factors 1/4 in (2.15) and 1/2 in (2.17) have to be multiplied by 2.

The various expressions for  $W$  are given in view of another interpretation later on. In Table 2.2 representative values of  $\hat{\mathbf{E}}$ ,  $\hat{\beta}$ ,  $\hat{\boldsymbol{\delta}}$  and relativistic  $W$  are given for the Nd and KrF laser in the intensity range from  $10^{12}$  to  $10^{20} \text{ Wcm}^{-2}$  and for a monochromatic wave of sun light intensity, all assumed to be concentrated at  $\lambda_{\text{Nd}} = 1060 \text{ nm}$  or at  $\lambda_{\text{KrF}} = 248 \text{ nm}$ , respectively. At  $I = 10^{18} \text{ Wcm}^{-2}$  relativistic effects become noticeable for Nd. The comparison reveals that in normal nonresonant optics the additional motion induced by the light field is completely negligible relative to the internal dynamics of matter and, as a consequence, optics is linear (e.g., the refractive index does not depend on  $\hat{\mathbf{E}}$ ); however this may no longer be true for intense laser fields. It is fortunate for our survival that sunlight is of high frequency, and not coherent over appreciable length scales; otherwise, a voltage difference of 1 kV over 1 m would be generated! Note that at  $10^{11} \text{ Wcm}^{-2}$  and Nd frequency the oscillation amplitude is equal to the Bohr radius.

The nonrelativistic Hamiltonian of the free electron in the Coulomb (or transverse) gauge is

**Table 2.2** Fields and oscillations (relativistic).  $I$  intensity,  $\hat{E}$ ,  $\hat{\beta} = \hat{v}/c$ ,  $\hat{\delta}$  amplitudes of field, relative velocity, and oscillation amplitude, respectively;  $W$  oscillation energy. The last row contains data for sunlight

$I$ [Wcm $^{-2}$ ]	$\hat{E}$ [V cm $^{-1}$ ]	$\lambda_{\text{Nd}} = 1060 \text{ nm}$			$\lambda_{\text{KrF}} = 248 \text{ nm}$		
		$\hat{\beta}$	$\hat{\delta}$ [nm]	$W$ [eV]	$\hat{\beta}$	$\hat{\delta}$ [nm]	$W$ [eV]
$10^{12}$	$3 \times 10^7$	$9 \times 10^{-4}$	0.15	0.1	$2 \times 10^{-4}$	$8 \times 10^{-3}$	$6 \times 10^{-3}$
$10^{13}$	$9 \times 10^7$	$3 \times 10^{-3}$	0.5	1.0	$7 \times 10^{-4}$	$2.6 \times 10^{-2}$	0.06
$10^{14}$	$3 \times 10^8$	$9 \times 10^{-3}$	1.5	10	$2 \times 10^{-3}$	$8.2 \times 10^{-2}$	0.58
$10^{16}$	$3 \times 10^9$	0.09	15.3	1050	0.02	0.82	58
$10^{18}$	$3 \times 10^{10}$	0.68	128.0	96 keV	0.21	8.2	5.7 keV
$10^{20}$	$3 \times 10^{11}$	0.995	235.5	2803	0.91	46.3	410
0.133	10	$3 \times 10^{-10}$	$6 \times 10^{-8}$	$1.4 \times 10^{-14}$	$8 \times 10^{-11}$	$3 \times 10^{-9}$	$8 \times 10^{-16}$

$$H = \frac{1}{2m}(\mathbf{p} + e\mathbf{A})^2. \quad (2.18)$$

$\mathbf{A}(\mathbf{x}, t)$  is the vector potential; it is related to the electric field by  $\mathbf{E} = -\partial_t \mathbf{A}$ . For a monochromatic plane wave  $\mathbf{A} = \mathbf{E}/i\omega$ . The quantity  $\mathbf{p} + e\mathbf{A} = m\mathbf{v}$  is the mechanical momentum. In the dipole approximation  $\mathbf{A}$  does not depend on  $\mathbf{x}$ ,  $\mathbf{A} = \mathbf{A}(t)$ , and the Schrödinger equation (with  $\mathbf{A}$  nonquantized),

$$\frac{1}{2m}[\mathbf{p} + e\mathbf{A}(t)]^2|\psi\rangle = i\hbar \frac{\partial}{\partial t}|\psi\rangle, \quad (2.19)$$

is solvable analytically. In fact, it is easily shown that the Volkov states  $\psi(\mathbf{x}, t) = \langle \mathbf{x} | \psi \rangle$ , (see also Chap. 7),

$$\psi(\mathbf{x}, t) = \exp\left[i\mathbf{k}\mathbf{x} - \frac{i}{2m\hbar} \int^t [\hbar\mathbf{k} + e\mathbf{A}(t')]^2 dt'\right] \quad (2.20)$$

satisfy (2.19). In the absence of the radiation field ( $\mathbf{A} = 0$ ) they reduce to the elementary plane waves  $\psi = \exp(i\mathbf{k}\mathbf{x} - iEt/\hbar)$  of the free electron. The energy expectation values  $E$  are

$$E = i\hbar \langle \psi | \partial_t | \psi \rangle = \langle \psi | H | \psi \rangle = \frac{1}{2m}(\hbar\mathbf{k} + e\mathbf{A})^2.$$

Cycle-averaging leads to

$$\overline{E} = \frac{1}{2m} \overline{(\hbar\mathbf{k} + e\Re \hat{\mathbf{A}} e^{-i\omega t})^2} = \frac{(\hbar\mathbf{k})^2}{2m} + \frac{e^2}{4m} \hat{\mathbf{A}} \hat{\mathbf{A}}^* = E_{\text{kin}} + W, \quad (2.21)$$

in perfect agreement with the classical result for the oscillation energy. Silin and Uryupin [22] used Volkov states to calculate inverse bremsstrahlung absorption in an elegant way in a strong radiation field (see the next chapter).

Expression (2.15) for  $W$  or its quantum mechanical counterpart (2.21) are strictly valid for a plane wave with an amplitude which is constant in space and time. Now imagine that  $\hat{\mathbf{E}}$  varies in space in such a way that  $|(\hat{\delta}\nabla)\hat{\mathbf{E}}|$  is much smaller than  $|\hat{\mathbf{E}}|$ . Such a condition is fulfilled at all nonrelativistic oscillatory speeds, since then  $|\hat{\delta}| \ll \lambda$  holds and, on the other hand the amplitude variation cannot be steeper than  $4|\hat{\mathbf{E}}|/\lambda$  in a standing wave. Consequently,  $W$  given above is also a good approximation in any inhomogeneous monochromatic wave field, for example in a standing wave.  $W$  is a unique function of position only,  $W = W(\mathbf{x})$ , as long as the electron is shifted slowly from one point to another. The question arises as to where the energy change  $\Delta W$  goes. Since a free electron can neither emit nor absorb photons of frequency  $\omega > 0$  (it can only scatter them) the only possible answer to the question of where the change  $\Delta W$  goes to is that the radiation field has done work on the free electron causing the motion of the oscillation center of the electron (velocity  $\mathbf{v}_0$ ,  $E_{\text{kin}} = m\mathbf{v}_0^2/2$ ), according to the energy conservation equation,

$$E_{\text{kin}} + W = \frac{1}{2}m\mathbf{v}_0^2 + \frac{e^2}{4m\omega^2}\hat{\mathbf{E}}\hat{\mathbf{E}}^* = \text{const.}$$

Consequently,  $W$  is effectively a potential and its negative gradient is a force, the so-called ponderomotive force  $f_p$ ,

$$\mathbf{f}_p = -\nabla\Phi_p, \quad \Phi_p = W = \frac{e^2}{4m\omega^2}\hat{\mathbf{E}}\hat{\mathbf{E}}^* = \frac{e^2}{4m}\hat{\mathbf{A}}\hat{\mathbf{A}}^*. \quad (2.22)$$

$\Phi_p$  is called the ponderomotive potential. This interpretation becomes particularly clear when  $W$  is written in the form  $W = \frac{1}{4}e\hat{\delta}^*\hat{\mathbf{E}}$  which is nothing but the time-averaged energy  $-\Re \mathbf{p} \cdot \Re \mathbf{E}/2$  of an oscillating dipole  $\mathbf{p} = -e\hat{\delta}$  in an electric field. It is intuitively clear that the arguments leading to  $\Phi_p$  and  $f_p$  are not limited to monochromatic fields and nonrelativistic motions of free particles, as will be shown in Chap. 5. For laser plasma dynamics and laser-matter interaction  $f_p$  will reveal itself to be a quantity of central importance.

In the radiation field the energy states of an electron change from those of a free electron,  $E = E_{\text{kin}}$ , to  $E_d = E_{\text{kin}} + W$ ; the laser “dresses” the electron,  $E_d$  are the “dressed states” of a free electron. The same holds for a bound electron: the energy states of an atom subject to a radiation field change (known as the dynamic Stark shift); they become dressed states [19]. The energy shift is a function of field amplitude and, consequently, a function of position. Therefore the quantity  $\Delta E =$  Stark shift minus field-induced internal energy [23] may be regarded as the ponderomotive potential  $\Phi_p$  of the bound electron or atom.

### 2.1.3 Collisional Ionization, Plasma Heating, and Quasineutrality

The photon energy of a high power laser is generally too low to ionize matter directly (see Table 2.1). Ionization occurs instead by collisions of fast electrons and by multiphoton and field ionization. In this section a simple model is presented to evaluate the energy absorbed from the laser field by collisions of electrons with atoms and ions. The simplest way to take energy absorption into account is to introduce a frictional force in the nonrelativistic equation of motion of the single electron (Drude model)

$$m \frac{d\mathbf{v}}{dt} + m\nu\mathbf{v} = -e\mathbf{E}. \quad (2.23)$$

$\mathbf{v}$  is the velocity of the single electron relative to the heavy particle and  $\nu$  is the friction coefficient or “collision frequency.”  $\nu$  is a function of the heavy particle density  $n$  (ions, neutrals) and of the electron kinetic energy. When the oscillatory velocity  $\hat{v}$  becomes of the order of the thermal speed

$$v_{\text{th}} = \left( \frac{k_B T_e}{m} \right)^{1/2}, \quad (2.24)$$

$k_B$  Boltzmann constant,  $T_e$  electron temperature,  $\nu$  will also depend on the oscillation energy  $W$ . In the opposite case of  $\hat{v} \ll v_{\text{th}}$  it is convenient to average (2.23) over all relative velocities. Then, under the assumption of an isotropic thermal velocity distribution function  $f(\mathbf{v}) = f_0(v)$  the thermal contributions cancel in the averaging process of the momenta. Equation (2.23) remains valid but now  $\mathbf{v} = \mathbf{v}(\mathbf{x}, t)$  is the velocity of an electron fluid element, i.e., the sum of a drift and the oscillatory speed induced by the field. The average electron collision frequency  $\nu = \langle \nu \rangle$  becomes a function of particle density  $n$  and  $T_e$  only (see Sect. 3.3). The frictional force in (2.23) is a phenomenological ansatz. There are two aspects of it which require justification: (i) that it also makes sense when the electron undergoes several or numerous oscillations between two collisions and (ii) how, physically, field energy dissipation, i.e., absorption, comes about.

Consider the hard sphere model of Fig. 2.1. An electron having a relative speed  $\mathbf{v}_0$  collides with an atom or ion at the time instant  $t_0$ . After the collision its directed velocity is  $\mathbf{v}'_0$ . When no field is applied the incident and reflected angles are equal,  $\alpha' = \alpha$ , and the same holds for  $|\mathbf{v}_0|$  and  $|\mathbf{v}'_0|$ . However, in the presence of an oscillatory field  $\mathbf{E}(\mathbf{x}, t) = \hat{\mathbf{E}} \cos(\mathbf{k}\mathbf{x} - \omega t)$  the magnitude of the sum of velocities,  $\mathbf{v}(t) = \mathbf{v}_0 + \hat{\mathbf{v}} \sin(\mathbf{k}\mathbf{x} - \omega t)$ , is conserved in the collision. That is the origin of irreversibility:  $\mathbf{v}(t)$  now points in an arbitrary direction and  $\alpha'$  is different from  $\alpha$  (“symmetry breaking”). This can be expressed quantitatively as follows. Before the collision the speed of the electron is

$$\mathbf{v}(t) = \mathbf{v}_0 + \hat{\mathbf{v}} \sin(\mathbf{k}\mathbf{x} - \omega t), \quad \hat{\mathbf{v}} = \frac{e}{m\omega} \hat{\mathbf{E}}; \quad t < t_0,$$

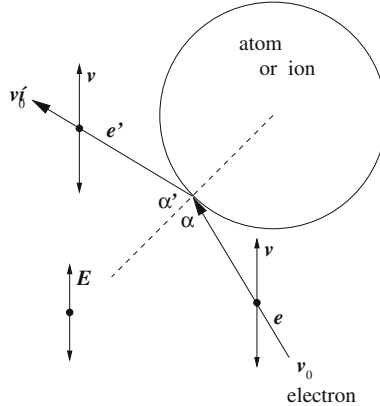


**Fig. 2.1** Elastic collision of an electron with an ion or atom (hard sphere model). A strong  $E$ -field breaks the symmetry of reflection ( $\alpha' \neq \alpha$ )

with  $v_0$  pointing in the direction of the unit vector  $e$ . Due to the collision  $v(t_0)$  is scattered into the direction of  $e'$ , so that the total velocity at  $t' \geq t_0$  is

$$\mathbf{v}(t') = |\mathbf{v}_0 + \hat{\mathbf{v}} \sin(\mathbf{kx} - \omega t_0)| \mathbf{e}' + \hat{\mathbf{v}} \{ \sin(\mathbf{kx} - \omega t') - \sin(\mathbf{kx} - \omega t_0) \}.$$

The energy gain of the electron is  $m_e \{ \mathbf{v}^2(t') - \mathbf{v}^2(t) \}/2$  and, with the help of  $\psi = \mathbf{kx} - \omega t$ ,  $\psi' = \mathbf{kx} - \omega t'$ ,  $\psi_0 = \mathbf{kx} - \omega t_0$  the difference  $\Delta \mathbf{v}^2$  is

$$\begin{aligned} \Delta \mathbf{v}^2 &= \mathbf{v}^2(t') - \mathbf{v}^2(t) = 2\mathbf{v}_0 \hat{\mathbf{v}} (\sin \psi_0 - \sin \psi) + 2\hat{\mathbf{v}}^2 \sin^2 \psi_0 \\ &\quad + 2\mathbf{e}' \hat{\mathbf{v}} |\mathbf{v}_0 + \hat{\mathbf{v}} \sin \psi_0| (\sin \psi' - \sin \psi_0) + \hat{\mathbf{v}}^2 (\sin^2 \psi' - \sin^2 \psi) \\ &\quad - 2\hat{\mathbf{v}}^2 \sin \psi_0 \sin \psi'. \end{aligned} \quad (2.25)$$

The times  $t < t_0$  and  $t_0$  are completely arbitrary with equal probability for a collision to occur at any  $t_0$ . Since the motion is reversible in the interval  $[t, t_0]$ ,  $t$  can be taken arbitrarily close to  $t_0$ ,  $t$  being just before collision, and it can be identified with  $t_0$  in (2.25). Then averaging over one oscillation period  $T$  yields

$$\begin{aligned} \frac{1}{T} \int_{t_0}^{t_0+T} \Delta \mathbf{v}^2 dt_0 &= \hat{\mathbf{v}}^2 + 2\mathbf{e}' \hat{\mathbf{v}} \overline{|\mathbf{v}_0 + \hat{\mathbf{v}} \sin \psi_0|} \sin \psi' + \hat{\mathbf{v}}^2 \sin^2 \psi' - \\ &\quad 2\mathbf{e}' \hat{\mathbf{v}} \overline{|\mathbf{v}_0 + \hat{\mathbf{v}} \sin \psi_0| \sin \psi_0} - \frac{1}{2} \hat{\mathbf{v}}^2 = \Delta \mathbf{v}^2(t'). \end{aligned}$$

This, finally, has to be averaged over  $t'$ :

$$w^2 = \overline{\Delta \mathbf{v}^2(t)} = \hat{\mathbf{v}}^2 - 2\mathbf{e}' \hat{\mathbf{v}} \overline{|\mathbf{v}_0 + \hat{\mathbf{v}} \sin \psi_0| \sin \psi_0}. \quad (2.26)$$

For the two special cases  $e' = -e$  (central collision) and  $e' = e$  (no collision) the intuitive results  $w^2 = 2\hat{v}^2$  and  $w^2 = 0$  are recovered. Equation (2.26) is easily evaluated only for  $|\hat{v}| \ll |v_0|$  (weak electric field or high electron temperature  $T_e$ ):

$$\begin{aligned} |v_0 + \hat{v} \sin \psi_0| &= v_0 \left\{ 1 + 2 \frac{|\hat{v}|}{v_0} \cos(v_0, \hat{v}) \sin \psi_0 \right\}^{1/2} \\ &= v_0 + |\hat{v}| \cos(v_0, \hat{v}) \sin \psi_0 \end{aligned}$$

with  $\cos(v_0, \hat{v})$  being the cosine of the angle between  $v_0$  and  $\hat{v}$ . From this one obtains

$$\overline{|v_0 + \hat{v} \sin \psi_0| \sin \psi_0} = \frac{1}{2} |\hat{v}| \overline{\cos(\hat{v}, v_0)}. \quad (2.27)$$

In the absence of strong electric currents this angular average is zero and the net mean energy gain in one collision is  $m\hat{v}^2/2 = 2W$ , with  $W$  from (2.22).

For hard spheres the differential cross section  $\sigma_\Omega$  is constant and the collision frequency for the single electron is given by  $\nu = n\sigma v_0 = n\pi r^2 v_0$  (with  $n$  the ion density,  $r = r_e + r_i$ , the differential cross section  $\sigma_\Omega = r^2/4$ ,  $\sigma = 4\pi\sigma_\Omega$ , and  $r_e, r_i$  are the collisional radii of the electron and atom or ion). Averaging over a Maxwellian electron distribution

$$f_0 = \left( \frac{\beta}{\pi} \right)^{3/2} e^{-\beta v_0^2}, \quad \beta = m/2k_B T_e = 1/2v_{th}^2. \quad (2.28)$$

yields  $\langle v_0 \rangle = 4\pi \int v_0^3 f_0 dv_0 = (8/\pi)^{1/2} v_{th}$  and the average collision frequency

$$\nu = (8\pi)^{1/2} n r^2 v_{th}. \quad (2.29)$$

Using this, the average energy an electron acquires per unit time is

$$\frac{dE_e}{dt} = \frac{d}{dt} \left( \frac{3}{2} k_B T_e \right) = 2W\nu = n\sigma \left( \frac{8}{\pi} \frac{k_B T_e}{m} \right)^{1/2} \frac{e^2}{m\varepsilon_0 c \omega^2} I = \alpha_e I, \quad (2.30)$$

with the absorption coefficient  $\alpha_e$  per single electron

$$\alpha_e = \left( \frac{8k_B}{\pi} \right)^{1/2} \frac{ne^2}{m^{3/2} \varepsilon_0 c \omega^2} \sigma T_e^{1/2}. \quad (2.31)$$

In passing from  $W$  to  $I$  in (2.30) it has been assumed that the phase and group velocities  $v_\varphi, v_g$  are (approximately) related by  $v_\varphi v_g = c^2$ , and that the refractive index is not far from unity.

As the mean electron energy increases, the excitation and ionization cross sections  $\sigma_{ex}, \sigma_I$  also grow. An avalanche process starts and plasma breakdown occurs when the inequality

$$\frac{dE_e}{dt} = \alpha_e I - \nu_I E_I - \frac{d}{dt} E_{\text{loss}} \geq 0$$

is fulfilled until a significant electron density  $n_e$  has formed. Here,  $\nu_I = n \langle \sigma_I v_0 \rangle$  is the mean ionization frequency,  $E_I$  is the ionization energy and  $E_{\text{loss}}$  comprises all energy losses due to hot electron diffusion (thermal conduction), ion and atom excitation, radiation losses, recombination, and energy loss by expansion of the electron gas. For an approximate breakdown criterion the losses can be disregarded in not too small foci (diameter  $\geq 50\text{--}100 \lambda$ ) and  $\nu_I$  may be determined from the Lotz formula [24, 25],

$$\begin{aligned} \sigma_I &= 2.8\pi a_0^2 \left( \frac{E_H}{E_I} \right)^2 \frac{\ln(u+1)}{u+1}, \quad u = \frac{E_e - E_I}{E_I}, \\ \langle \sigma_I v_0 \rangle [\text{cm}^3 \text{s}^{-1}] &= 6 \times 10^{-8} \left( \frac{E_H}{E_I} \right)^{3/2} \beta_I^{1/2} e^{-\beta_I} \text{Ei}(-\beta_I), \quad \beta_I = \frac{E_I}{k_B T_e} \end{aligned} \quad (2.32)$$

$E_H = 13.6 \text{ eV}$  (hydrogen),  $a_0$  is the Bohr radius,  $E_I$  the ionization energy and  $\text{Ei} = - \int_{\beta_I}^{\infty} e^{-x^2} dx$  is the exponential integral. Breakdown occurs when  $I = I_0$ ,

$$I_0 \simeq \frac{n \langle \sigma_I v_0 \rangle}{\alpha_e} E_I \quad (2.33)$$

is satisfied. Multiphoton or field ionization does not play a role in the breakdown process at low laser intensities  $I \lesssim I_0$ .

### 2.1.3.1 Quasineutrality

Well above threshold  $I_0$ , violent ionization and production of ion-electron pairs occurs. At low electron density  $n_e$  the faster electrons may escape from the volume in which ionization takes place. Due to such a process the volume becomes electrically charged and a macroscopic static electric field builds up which prevents the remaining electrons from escaping. As  $n_e$  increases, the charge imbalance  $Zn_i - n_e$  ( $Z$  is the average ionic charge,  $n_i$  the ion density) is small, i.e.,  $(Zn_i - n_e)/n_e \ll 1$ . We say that the ion-electron fluid is quasineutral and call it a plasma. A criterion for this can be given with the help of the Debye length  $\lambda_D$ . For this purpose consider Fig. 2.2. The surface charge density  $\sigma$  of an infinitely extended plate in vacuum generates a constant electric field of strength  $E = \sigma/2\varepsilon_0$ . When the plate is immersed in a fluid of constant electron and ion temperature  $T = T_e = T_i$  and  $Z\bar{n}_i = \bar{n}_e$ , with  $\bar{n}_e, \bar{n}_i = \text{const}$  in the absence of  $E$ , the free charges rearrange themselves, due to the influence of  $E$  in such a way that equilibrium exists between the pressures  $p_e = n_e k_B T$  and  $p_i = n_i k_B T$ . In a fluid layer of thickness  $dx$

$$dp_e = k_B T dn_e = -en_e Edx, \quad \Rightarrow \frac{1}{n_e} \frac{\partial n_e}{\partial x} = \frac{e}{k_B T} \frac{\partial \Phi}{\partial x}, \quad E = -\frac{\partial \Phi}{\partial x}, \quad (2.34)$$

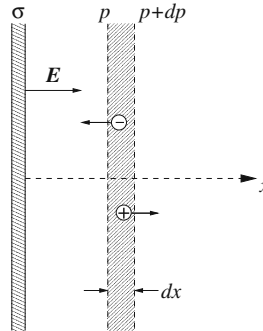


**Fig. 2.2** Screening of an electric charge  $\sigma$  immersed in an isothermal plasma. Potential  $\Phi$  and field  $E$  fall off as  $\exp(-x/\lambda_D)$  with the Debye length  $\lambda_D$ .  $p$  is the thermal pressure

holds and hence,

$$n_e(x) = \bar{n}_e \exp\left(\frac{e\Phi}{k_B T}\right); \quad \bar{n}_e = n_e(x = \infty). \quad (2.35)$$

Analogously, the ion density obeys  $n_i(x) = \bar{n}_i \exp(-Ze\Phi/k_B T)$ . With  $\bar{n}_e = Z\bar{n}_i$  Poisson's law now states

$$\frac{\partial^2}{\partial x^2} \Phi = \frac{e\bar{n}_e}{\varepsilon_0} \left( \exp\left(\frac{e\Phi}{k_B T}\right) - \exp\left(-\frac{Ze\Phi}{k_B T}\right) \right). \quad (2.36)$$

Under the condition  $Ze\Phi/k_B T \ll 1$  this simplifies to

$$\frac{\partial^2}{\partial x^2} \Phi = \frac{\bar{n}_e e^2 (Z + 1)}{\varepsilon_0 k_B T} \Phi \quad \Rightarrow \quad \Phi(x) = \Phi_0 \exp\left(-\frac{x}{\lambda_D}\right),$$

which shows that  $\sigma$  and its field  $E$  are screened by 63% at the distance of a Debye length  $\lambda_D$ ,

$$\begin{aligned} \lambda_D &= \left( \frac{\varepsilon_0 k_B T}{\bar{n}_e e^2 (1 + Z)} \right)^{1/2}, \\ \lambda_D [\text{cm}] &= 6.9 \left( \frac{T [\text{K}]}{(1 + Z)\bar{n}_e [\text{cm}^{-3}]} \right)^{1/2} = 743 \left( \frac{T [\text{eV}]}{(1 + Z)\bar{n}_e [\text{cm}^{-3}]} \right)^{1/2}. \end{aligned} \quad (2.37)$$

A thermal fluid of minimum extension  $d \gg \lambda_D$  is quasineutral. Consequently, a fluid of free charges becomes a plasma when its dimensions exceed  $\lambda_D$  several times.

For  $\lambda_D$  one frequently uses the expression

$$\lambda_D = \left( \frac{\varepsilon_0 k_B T_e}{\bar{n}_e e^2} \right)^{1/2}, \quad \lambda_D [\text{cm}] = 6.9 \left( \frac{T_e[\text{K}]}{\bar{n}_e[\text{cm}^{-3}]} \right)^{1/2}. \quad (2.38)$$

Equation (2.38) is the correct screening length when  $\sigma$  or  $E$  change so rapidly that the ions do not have time to redistribute. For  $Z = 1$  and ions in equilibrium, (2.37) becomes  $\lambda_D [\text{cm}] = 5(T/n_e)^{1/2}$ , if  $\bar{n}_e = n_e$  is used for simplicity. In laser plasmas the following situation may occur:  $n_1$  electrons have temperature  $T_1$  while  $n_2 = n_e - n_1$  have temperature  $T_2$ . Then  $\lambda_D = 6.9 \{T_1 T_2 / [(\xi_1 T_2 + \xi_2 T_1) n_e]\}^{1/2}$ ,  $\xi_{1,2} = n_{1,2}/n_e$ , is the correct screening length of the electrons. If  $\xi_1$  and  $\xi_2$  are of the same order and  $T_1 \ll T_2$  screening is dominated by the cold electrons.

Every point charge in the plasma is subject to the same screening process described above. When in the Poisson equation  $\partial_{xx}^2$  is substituted by  $\nabla^2 = (1/r)\partial_{rr}^2 r$  for spherical symmetry the screened Coulomb potential of a fixed charge  $q$  (i.e.,  $v_q^2 \ll k_B T_e/m$ ) turns out to be the Debye potential

$$\Phi(r) = \frac{q}{4\pi\varepsilon_0 r} \exp\left(-\frac{r}{\lambda_D}\right). \quad (2.39)$$

However, in applying this formula the reader has to make sure in cases of high  $Z$ -values,  $q = Ze$ , that truncating the expansion of  $\exp[-Ze\Phi/(k_B T)]$  after the first order still holds. In dense plasmas the Fermi energy of the free electrons of density  $n_e$ ,

$$E_F = (3\pi^2)^{2/3} \frac{\hbar^2}{2m} n_e^{2/3} = 3.6 \times 10^{-15} (n_e [\text{cm}^{-3}])^{2/3} \text{ eV} \quad (2.40)$$

may exceed  $k_B T_e$ . In such a degenerate plasma screening is determined by the number density of the quantized free electron states. For  $k_B T_e \ll E_F$ , the Debye length is given by

$$\lambda_D = (3\pi^2)^{1/3} \left( \frac{\varepsilon_0}{3m} \right)^{1/2} \frac{\hbar}{e} n_e^{-1/6} = 3.7 \times 10^{-5} (n_e [\text{cm}^{-3}])^{-1/6} \text{ cm}, \quad (2.41)$$

with  $3k_B T_e/2$  replaced by  $E_F$  and  $T_i = 0$ .

A numerical example may illustrate why plasmas are quasineutral. Assume  $n_e = 10^{20} \text{ cm}^{-3}$  and  $Zn_i - n_e = 10^{-6} n_e$ . This charge imbalance creates a voltage  $\Delta V$  over the distance  $d = 0.1 \text{ cm}$  of

$$\Delta V = \frac{e}{2\varepsilon_0} (Zn_i - n_e) d^2 = 9 \times 10^5 \text{ V}.$$

In a thermal plasma an electron temperature of 1 MeV is needed to produce such a potential difference.

Four useful remarks may be added:

*Remark 1* Relation (2.35) is not limited to thermal equilibrium. From the derivation presented here it becomes clear that all that is needed is the knowledge of pressure  $p_e$  (and possibly also  $p_i$ ) and the kinetic temperature  $T_e$  [possibly also  $T_i$ ; for a kinetic definition see (2.83)]. The only change is that  $p_e/n_e$  is no longer connected with  $T_e$  by the factor 2/3 but by another proportionality, generally not differing much from unity.

*Remark 2* In order to decide which particles do the screening in fast processes physical insight into the screening process is useful. The electrons passing close to an ion move along orbits bent towards the ion, in this way coming closer to it. The consequence is that on the average the electron density is increased above its average value  $\bar{n}_e$ . The time needed to establish screening is given by the inverse of the plasma frequency  $\omega_p$ ,  $\tau_s \simeq 2\pi/\omega_p$  [explicitly shown by (3.77) in Sect. 3.3.1]. From the picture follows that in the “standard” case of nearly straight orbits screening begins to weaken when the number of particles in a Debye sphere  $N_D = 4\pi\lambda_D^3\bar{n}_e/3$  drops below  $Z$ .

*Remark 3* Classical screening is due to *free* electrons. In dense, nonideal plasmas bound electrons in Rydberg states may contribute appreciably to screening. In practice such an effect can adequately be taken into account by introducing an effective ion charge number  $Z_{\text{eff}} > Z$ .

*Remark 4* In Poisson’s equation for a point charge (2.35) is used in its linearized version to obtain the Debye potential (2.39). One might argue that  $e\phi/(kT_e) \ll 1$  is violated for small radii  $r$ , and one might try to solve the spherical analogue of (2.36). However, close to the nucleus the Boltzmann factor is incorrect and the Fermi expression has to be used. On the other hand shielding by free or Rydberg electrons is weak for  $r/\lambda_D \ll 1$ , and hence the expression obtained from linearization is an acceptable approximation.

### Charge of a Spherical Cluster

In order to gain additional, more quantitative insight into quasineutrality the net charge  $q'$  of conducting microspheres of radius  $R$  is calculated. The subject is of much interest in the context of laser heated clusters, dust, impurities, aerosols, and small droplets [26]. When a conducting sphere of charge  $q = Ne$  is embedded in an isothermal background plasma it attracts or repels electrons and rearranges the ions in its neighborhood until a new equilibrium charge  $q'$  is reached. If the microsphere is originally uncharged it loses electrons until a new equilibrium of electric and thermal forces is established and a net positive charge of the core results. The equilibrium charge  $q'$  is determined by the Maxwell equation ( $Z = 1$  is assumed)

$$\frac{1}{r^2} \frac{\partial}{\partial r} (r^2 E) = -\frac{e}{\varepsilon_0} (n_e(r) - n_i), \quad n_i = \alpha n_0 = \text{const} \quad (2.42)$$

and the electron pressure balance (2.34)

$$E(r) = -\frac{k_B T_e}{e n_e} \frac{\partial n_e}{\partial r}.$$

Inside the sphere  $\alpha = 1$  and outside  $\alpha < 1$  is set. Substitution of  $E$  in (2.42) and introducing the dimensionless variables  $n = n_e/n_0$  and  $x = r/\lambda_D$ ,  $\lambda_D = [\epsilon_0 k_B T_e/(e^2 n_0)]^{1/2}$ , leads to

$$\frac{1}{x} \frac{d^2}{dx^2}(x \ln n) = n(x) - \alpha. \quad (2.43)$$

This nonlinear equation was solved numerically [26]. The net relative charge  $q'/q$  is obtained from

$$\frac{q'}{q} = \frac{3}{(R/\lambda_D)^3} \int_{R/\lambda_D}^{\infty} x^2 n(x) dx;$$

it is a unique function of the dimensionless parameter  $\xi = R/\lambda_D$ . In Fig. 2.3 results of (a)  $n(x)$  for various parameters  $\xi$  and (b) the relative charge  $q'/q$  as a function of the normalized cluster radius  $\xi$ , embedded in background plasmas of different densities, are presented.

Spheres with radii below  $2\lambda_D$ , when embedded in a background plasma of low density ( $\alpha = 10^{-3}$ ) are fully ionized. At  $R = 10\lambda_D$  the residual charge is  $q' = 0.3q$ . Quasineutrality is guaranteed only from  $R \simeq 30\lambda_D$  on. As expected, with increasing background plasma density, quasineutrality sets in at smaller radii. Contrary to cold Thomas–Fermi theory applied to clusters in the isothermal case no equilibrium exists for a sphere in vacuum ( $\alpha = 0$ ), as may be seen from  $n \rightarrow 0$  with

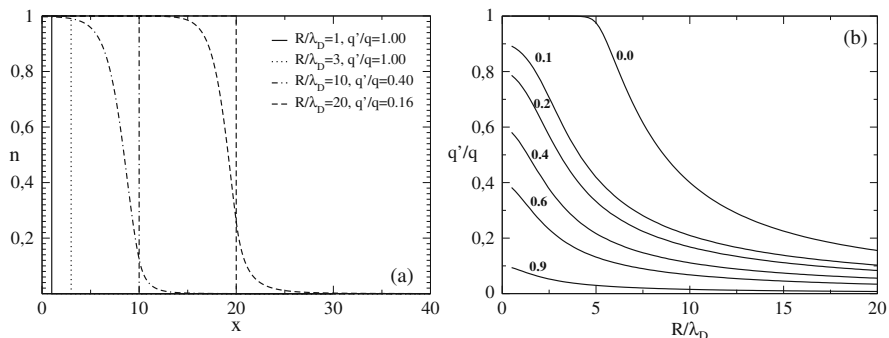


**Fig. 2.3** (a) Equilibrium distribution of electrons of a conducting sphere embedded in an isothermal plasma of relative density  $\alpha = n_i/n_0 = 0.001$ . The spheres of radius smaller than a Debye length  $\lambda_D$  are completely ionized. At  $R = 20\lambda_D$  the residual charge  $q'$  is 16%. (b) Charge fraction  $q'/q$  of a conducting sphere as a function of normalized cluster radius  $R/\lambda_D$  for different values of  $\alpha$ ,  $\alpha = 0.001, 0.1, 0.2, 0.4, 0.6$ , and  $0.9$ .

$r \rightarrow \infty$ . This is analogous to (i) the fact that no isothermal atmosphere can survive on a planet, (ii) the existence of a solar wind from stars, or (iii) the fact that no perfect plasma confinement can be achieved in a ponderomotive trap (see Chap. 5).

### 2.1.3.2 Collision Frequency

The collision frequency  $\nu = n\sigma v_0$  for a single electron and its average  $\nu = n\sigma v_{\text{th}}$  introduced through (2.30) were obtained from an energy consideration under the assumption of  $\hat{v} \ll v_0$ ,  $v_0$  drift velocity, or  $\hat{v} \ll v_{\text{th}}$ , respectively. Strictly speaking,  $\nu$  obtained in this way is the collision frequency for energy transfer. Under the above restriction on  $\hat{v}$  it is the same as the cycle-averaged collision frequency  $\nu$  for momentum transfer, introduced phenomenologically by (2.23). In fact, multiplying the momentum equation by  $\mathbf{v}$  and averaging over one period yields

$$\frac{1}{\tau} \int_{\tau} \frac{d}{dt} \frac{1}{2} m \mathbf{v}^2 dt + \frac{1}{\tau} \nu \int_{\tau} m \mathbf{v}^2 dt = -\frac{1}{\tau} e \int_{\tau} \mathbf{E} \mathbf{v} dt.$$

When  $\hat{\mathbf{E}}(\mathbf{x}, t)$  is slowly varying in time the first term is (nearly) zero; the second is  $2\nu W$  and the term on the right-hand side represents the irreversible work  $dE_e/dt$  done by the laser field on the electron during one cycle; in that case (2.30) is recovered. The finite value of  $\int \mathbf{E} \mathbf{v} dt$  originates from a phase shift of  $\mathbf{v}$  with respect to (2.11) owing to the frictional force  $-m\nu\mathbf{v}$  in (2.23).

Generally, the collision cross section  $\sigma$  is velocity-dependent and the average collision frequency  $\nu$  is obtained from explicitly calculating the average  $\langle \sigma v \rangle$ . An example of strong energy dependence and of particular relevance in plasmas is the differential Coulomb cross section for scattering of an electron with an electron or an ion,

$$\sigma_{\Omega} = \frac{b_{\perp}^2}{4 \sin^4(\vartheta/2)}, \quad \tan \frac{\vartheta}{2} = \frac{b_{\perp}}{b}, \quad b_{\perp} = \frac{Ze^2}{8\pi\varepsilon_0 E_r} = 0.7 \frac{Z}{E_r \text{ [eV]}} \text{ nm.} \quad (2.44)$$

$\vartheta$  is the deflection angle in the center of mass system and  $b_{\perp}$  is the impact parameter for a  $90^\circ$  deflection; it is sometimes referred to as the Landau parameter [27].  $E_r = m_1 m_2 (\mathbf{v}_1 - \mathbf{v}_2)^2 / 2(m_1 + m_2)$  is the reduced energy of the colliding particles (Fig. 2.4). The detailed calculation of  $\sigma(\mathbf{v})$  from (2.44) and folding with the Maxwellian distribution (2.28) for a thermalized plasma leads to the electron-ion collision frequency  $\nu_{ei}$

$$\nu_{ei} = \frac{4}{3} (2\pi)^{1/2} \left( \frac{Ze^2}{4\pi\varepsilon_0 m} \right)^2 \left( \frac{m}{k_B T_e} \right)^{3/2} n_i \ln \Lambda, \quad (2.45)$$

$$\nu_{ei} [\text{s}^{-1}] = 3.6 \times \frac{Z n_e [\text{cm}^{-3}]}{(T_e [\text{K}])^{3/2}} \ln \Lambda$$

where

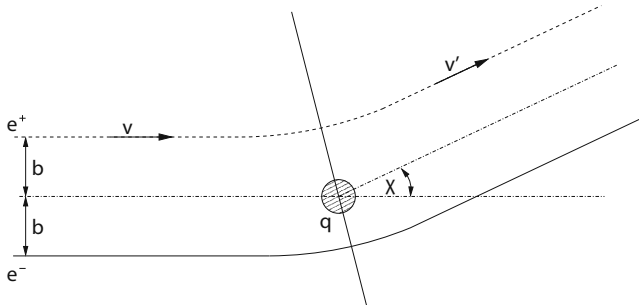


**Fig. 2.4** Deflection of a positive (----) or negative charge  $e$  (—) by a positive ion of charge  $q = Ze$ .  $v = v_e - v_i$  relative velocity,  $b$  impact parameter

$$\Lambda = \lambda_D / b_{\min} \quad (2.46)$$

(see also Sect. 3.3).  $n_i$  is the ion density of charge  $Z$ . In the Coulomb logarithm  $\ln \Lambda$  it is standard to identify  $b_{\min}$  with the maximum of  $b_{\perp}$  and half the reduced thermal de Broglie wavelength  $\bar{\lambda}_B$  for electrons ([28], justified in Sect. 3.3.2),

$$\bar{\lambda}_B = \frac{\hbar}{mv_{\text{th}}}, \quad \bar{\lambda}_B [\text{nm}] = \frac{0.3}{(T_e[\text{eV}])^{1/2}}, \quad v_{\text{th}} = \left( \frac{k_B T_e}{m} \right)^{1/2}. \quad (2.47)$$

Equality  $\bar{\lambda}_B = 2b_{\perp}$  is reached at  $T_e = 25 Z^2 \text{ eV}$ . In the typical laser plasma  $\ln \Lambda \simeq 2\text{--}5$  are reasonable values. Since the knowledge of  $v_{ei}$  is of central importance for understanding collisional laser plasma interaction, the reader should know its value by heart,

$$v_{ei} \simeq (10\text{--}20) \times \frac{Z^2 n_i [\text{cm}^{-3}]}{(T_e [\text{K}])^{3/2}} \text{ s}^{-1} \simeq (1\text{--}2) \times 10^{-5} \frac{Z^2 n_i [\text{cm}^{-3}]}{(T_e [\text{eV}])^{3/2}} \text{ s}^{-1}. \quad (2.48)$$

The majority of Coulomb collisions are small angle deflections; this will be seen in detail in Chap. 3. It follows from (2.23) that  $\tau_{ei} = 1/v$ ,  $v = v_{ei}$ , is the average time for single electron collisions adding up to a  $90^\circ$  deflection. For  $Z = 1$  the electron-electron collision frequency  $\nu_{ee}$  is of the order of  $v_{ei}$ .  $\tau_{ee} = 1/\nu_{ee}$  can be regarded as a measure of the thermalization time of the electron fluid in the sense that in a given time  $\tau$  it is thermalized if  $\tau_{ee} \ll \tau$  holds, and not thermalized by collisions in the opposite case  $\tau_{ee} \gg \tau$ . If  $\tau_{ee} \simeq \tau$  holds, only a more accurate calculation can give the correct answer. The ions thermalize in a characteristic time  $\tau_{ii} \simeq \tau_{ee}(m_i/m)^{1/2}/Z^4$  and  $T_i$  becomes equal to  $T_e$  in about  $\tau_{eq} \simeq \tau_{ee} m_i/(Z^2 m)$  owing to the average energy transfer ratio  $m/m_i$  in a collision. The three times compare with each other in the ratios

$$\tau_{ee} : \tau_{ii} : \tau_{eq} = 1 : \left( \frac{m_i}{m} \right)^{1/2} \frac{1}{Z^4} : \frac{m_i}{m} \frac{1}{Z^2}. \quad (2.49)$$

Isotropization of the electron distribution function is increased by electron–ion collisions, especially when the ions are highly charged. An additional contribution to increase  $v_{ei}$  may originate from inelastic collisions of not fully stripped ions.

### 2.1.3.3 The Mysterious First Free Electron

The electron heating mechanism described by (2.30) and subsequent thermal ionization can work only if a few free electrons in the region of high laser intensity are present. Typical ionization energies  $E_I$  of atoms and molecules range from about 4 to 25 eV (Cs 3.9, H 13.6, He 24.6 eV), and hence none of the high-power lasers of Table 2.1 are capable of directly photo-ionizing them, except Cs by the KrF laser. The only possible mechanism is multiphoton ionization which consists of the “simultaneous” absorption of  $N \geq (E_I + W)/\hbar\omega$  photons. As long as both, photon energy  $\hbar\omega$  and ionization energy  $E_I$ , are large compared to  $W$ , multiphoton ionization can be treated in lowest order perturbation theory (LOPT, see, e.g., [29]). Ionization in stronger laser fields is discussed in Chap. 7.

The ionization cross sections depend sensitively on the individual matrix elements between virtual states and may change by orders of magnitude when the laser frequency or a multiple of it approaches a transition frequency  $\omega_{ij} = (E_i - E_j)/\hbar$  of two virtual energy levels [29, 30]. Fortunately, as the photon number  $N$  needed for ionization increases, the  $\omega$ -dependence greatly decreases and approaches a non-resonant behavior, and the ionization probability  $P_N$  assumes the structure

$$P_N \simeq \sigma_N I^N \quad (2.50)$$

in a wide range of intensities. It can be shown by several independent arguments that the  $N$ th root of the generalized cross section  $\sigma_N$  for multiphoton ionization – with the contributions from higher order diagrams included –  $\sigma_N^{1/N}$  is almost a constant [31], and therefore  $\ln P_N$  plotted as a function of  $\ln I$  is a straight line, as was confirmed by numerous experiments [32–35]. Deviations from this behavior only occur at resonances, close to saturation (when  $P_N \rightarrow 1$ ), or when nonsequential ionization is important (see Chap. 7).

The calculated and measured thresholds for appreciable multiphoton ionization lie all above  $10^{12} \text{ Wcm}^{-2}$  or an order of magnitude higher and there is no doubt that in very pure atomic gases (and probably very pure liquid or solid dielectrics with extremely clean surfaces) these are the thresholds for plasma formation by focused laser beams [36]. On the other hand, it is known that normally breakdown occurs at much lower intensities, sometimes as low as  $10^9 \text{ Wcm}^{-2}$  [37]. From this discrepancy the question arises where the “first” electron comes from. Although in general this is an unsolved question, many reasons for the presence of a few free electrons can be given: ionization by UV light from outside or from the flash lamps of the laser, aerosols or dust particles carrying very weakly bound electrons, negative surface charges on solids. Densely spaced energy levels in molecules may facilitate multiphoton ionization, or two-step ionization-dissociation processes which, for instance in Cs, require much lower laser intensity. Hence, no general answer to

the question is to be expected, nor would one be of much interest. Rather the search for further individual well-defined effects which may lead to breakdown threshold lowering in the actual case under consideration is needed [38–42].

## 2.2 Fluid Description of a Plasma

### 2.2.1 Two-Fluid and One-Fluid Models

The plasma produced by a high power laser is a mixture of ions of several charge states, free electrons, and neutrals. At laser flux densities as high as  $10^{12} \text{ Wcm}^{-2}$  only a plasma produced from frozen hydrogen is fully ionized and consists of a single ionic fluid, the protons, and the electronic fluid. All other plasmas will be fully ionized two-component fluid mixtures only at considerably higher temperatures or laser intensities. Nevertheless, even in the case of partial ionization the two-fluid model of a fully ionized plasma with an average charge number  $Z$  may be adequate to describe its dynamical behavior. With ns laser pulses usually the collision frequencies are also high enough that the existence of an electron temperature  $T_e$  and of an ion temperature  $T_i$  is guaranteed. Then an electron and an ion thermal energy density  $\varepsilon_e$  and  $\varepsilon_i$  and pressure  $p_e$  and  $p_i$  are also defined. The latter are well described by the equation of state of the classical ideal gas,

$$\varepsilon_e = \frac{3}{2} p_e, \quad p_e = n_e k_B T_e, \quad \varepsilon_i = \frac{3}{2} p_i, \quad p_i = n_i k_B T_i, \quad n_e = Z n_i, \quad (2.51)$$

since  $k_B T_e \gg E_F$  generally holds. At first glance this may be surprising, owing to the Coulomb force interactions among the particles. Deviations from the ideal plasma state are characterized by the plasma parameter  $g = 1/(n_e \lambda_D^3)$ , or in physical terms,

$$g = \frac{e^2}{\varepsilon_0 \lambda_D k_B T_e} = 6\pi \frac{\langle E_{\text{pot}} \rangle}{\langle E_{\text{kin}} \rangle}, \quad n_e = \bar{n}_e, \quad (2.52)$$

or by the number of particles in the Debye sphere  $N_D = 4\pi/(3g) \simeq 4/g$ . With the first order corrections for interaction,  $\varepsilon_e$  and  $p_e$  are given by [43]

$$\varepsilon_e = \frac{3}{2} n_e k_B T_e \left(1 - \frac{g}{12\pi}\right), \quad p_e = n_e k_B T_e \left(1 - \frac{g}{24\pi}\right). \quad (2.53)$$

For example, at  $n_e = 10^{20} \text{ cm}^{-3}$  and  $T_e = 100 \text{ eV}$ ,  $T_i = 0$ , one obtains  $\lambda_D = 7.4 \text{ nm}$ ,  $N_D = 172$ ,  $g = 0.024$ ,  $E_F = 0.08 \text{ eV}$ . In this case the relative corrections to  $\varepsilon_e$  and  $p_e$  are less than  $10^{-3}$ .

The two fluids are characterized by their mass densities  $\rho_e = m n_e$ ,  $\rho_i = m_i n_i$ , flow velocities  $\mathbf{v}_e$ ,  $\mathbf{v}_i$  and by  $T_e$ ,  $T_i$ , with  $T_e > T_i$  in general, since the laser heats the electrons (see (2.30)). Let  $V$  be a fixed but arbitrary volume. Particle or mass

conservation requires that the change of particles of species  $\alpha$ ,  $\alpha = e, i$  in  $V$  equals the flux of matter through its surface  $\Sigma$ ,

$$\frac{d}{dt} \int_V n_\alpha dV = \int_V \frac{\partial}{\partial t} n_\alpha dV = - \int_\Sigma n_\alpha \mathbf{v}_\alpha d\Sigma = - \int_V \nabla(n_\alpha \mathbf{v}_\alpha) dV,$$

(for the divergence  $\nabla$  is used instead of  $\nabla \cdot$  everywhere). Since  $V$  is arbitrary the integrands must be equal; thus

$$\frac{\partial}{\partial t} n_e + \nabla(n_e \mathbf{v}_e) = 0, \quad \frac{\partial}{\partial t} n_i + \nabla(n_i \mathbf{v}_i) = 0. \quad (2.54)$$

This is the equation of mass conservation in the Eulerian picture where all dynamic variables  $n_\alpha$ ,  $\mathbf{v}_\alpha$ , etc. are field quantities which depend on position  $\mathbf{x}$  and time  $t$ :  $n_\alpha = n_\alpha(\mathbf{x}, t)$ ,  $\mathbf{v}_\alpha = \mathbf{v}_\alpha(\mathbf{x}, t)$ , etc.

Often it is useful to choose the Lagrangian fluid picture, for instance to describe the expansion of a laser plasma into vacuum or into a surrounding gas. It consists of looking at fluid flow as a continuous mapping (even as a homeomorphism) of one region in space onto another one (Fig. 2.5): A volume element  $dV_0$ , initially at position  $\mathbf{x}(t=0) = \mathbf{a} = (a_1, a_2, a_3)$ , is found at the point  $\mathbf{x}(t)$  after time  $t$ , i.e.,  $\mathbf{x}(t)$  is the image of  $\mathbf{a}$ . The set of points  $\mathbf{x}(\mathbf{a}, t)$ , with  $\mathbf{a}$  held fixed and  $\mathbf{x}(\mathbf{a}, 0) = \mathbf{a}$ , is the trajectory of the volume element starting from  $\mathbf{a}$ . It carries all dynamical variables  $n_\alpha$ ,  $\mathbf{v}_\alpha$ , etc. which now, in this picture, are uniquely identified by the coordinates  $(\mathbf{a}, t)$ . For instance,  $\rho_e(\mathbf{a}, t)$  means  $\rho_e(\mathbf{x}(\mathbf{a}, t), t) = \rho_e(\mathbf{x}, t)$ . In contrast to the Eulerian picture, in the Lagrangian description each fluid element tells us where it has come from. The latter is perfectly analogous to Newton's formulation of particle mechanics, the only difference being now that  $\mathbf{a}$  is a continuous index,  $\mathbf{x}_i(t) \rightarrow \mathbf{x}_{\mathbf{a}}(t) = \mathbf{x}(\mathbf{a}, t)$ .

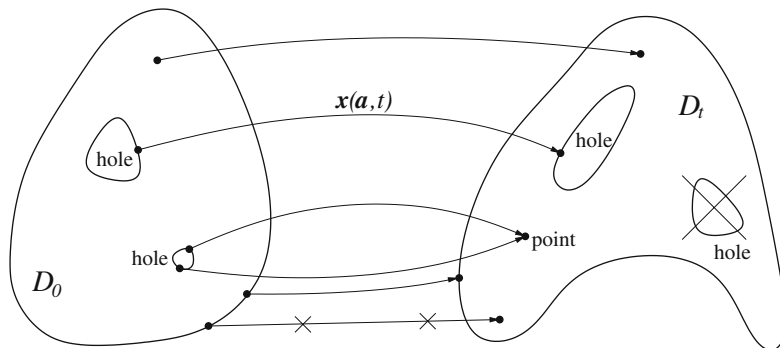


**Fig. 2.5** Formally, fluid flow is a continuous mapping of one domain  $D_0$  onto another domain  $D_t$  characterized by the parameter  $t$  (homeomorphism). In an ideal fluid a hole cannot be closed or opened (but can degenerate to a point) and a point on a boundary is always mapped onto the boundary.  $\mathbf{a}$  initial position,  $\mathbf{x}(\mathbf{a}, t)$  trajectory of a fluid element. The degree of connectivity of a domain is conserved

Mass conservation in the Lagrangian representation is formulated as follows. The arbitrary domains  $D_0, D_t = D(t)$  contain the same number of particles (however, not necessarily the *same* particles). To compare the integrands  $n_\alpha$  as before they have to be transformed to the same domain, say  $D_0$ , with the help of the Jacobian  $J$

$$\int_{D_0} n_\alpha(\mathbf{a}, t=0) dV_0 = \int_{D_t} n_\alpha(\mathbf{x}, t) dV = \int_{D_0} n_\alpha(\mathbf{a}, t) J dV_0, \quad (2.55)$$

$$J(\mathbf{a}, t) = \left| \frac{\partial(\mathbf{x}(\mathbf{a}, t))}{\partial(\mathbf{a})} \right|. \quad (2.56)$$

$D_0$  is arbitrary and hence

$$n_e(\mathbf{a}, 0) = n_e(\mathbf{a}, t) \left| \frac{\partial(\mathbf{x})}{\partial(\mathbf{a})} \right|, \quad n_i(\mathbf{a}, 0) = n_i(\mathbf{a}, t) \left| \frac{\partial(\mathbf{x})}{\partial(\mathbf{a})} \right| \quad (2.57)$$

is the mass conservation (continuity equation) in Lagrangian coordinates. For the infinitesimal time  $t = dt$  and  $\mathbf{x} = \mathbf{a} + \mathbf{v}dt$  one obtains for  $n_e$  (or  $n_i$ ),

$$n_e(\mathbf{a}, 0) = \begin{vmatrix} \frac{\partial}{\partial a_1}(a_1 + v_1 dt) & \frac{\partial}{\partial a_1}(a_2 + v_2 dt) & \frac{\partial}{\partial a_1}(a_3 + v_3 dt) \\ \frac{\partial}{\partial a_2}(a_1 + v_1 dt) & \frac{\partial}{\partial a_2}(a_2 + v_2 dt) & \frac{\partial}{\partial a_2}(a_3 + v_3 dt) \\ \frac{\partial}{\partial a_3}(a_1 + v_1 dt) & \frac{\partial}{\partial a_3}(a_2 + v_2 dt) & \frac{\partial}{\partial a_3}(a_3 + v_3 dt) \end{vmatrix} n_e(\mathbf{a}, dt).$$

The determinant is  $1 + (\partial_{a_1} v_1 + \partial_{a_2} v_2 + \partial_{a_3} v_3)dt = 1 + \nabla_{\mathbf{a}} \mathbf{v} dt$ , plus 15 terms of higher order in  $dt$ . To leading order it follows that  $n_e(\mathbf{a}, dt) - n_e(\mathbf{a}, 0) = -n_e(\mathbf{a}, dt) \nabla_{\mathbf{a}} \mathbf{v} dt$  or, by continuity of  $n_e$  with respect to  $t$ ,

$$\frac{\partial}{\partial t} n_e(\mathbf{a}, 0) = -n_e(\mathbf{a}, 0) \nabla_{\mathbf{a}} \mathbf{v}. \quad (2.58)$$

The temporal derivative is to be taken at constant  $\mathbf{a}$  which means along the trajectory  $\mathbf{x}(\mathbf{a}, t)$ ,

$$\begin{aligned} \frac{\partial}{\partial t} n_e(\mathbf{a}, 0) &= \lim_{\Delta t \rightarrow 0} \frac{n_e(\mathbf{x}(\mathbf{a}, \Delta t), \Delta t) - n_e(\mathbf{a}, 0)}{\Delta t} \\ &= \frac{d}{dt} n_e(\mathbf{x}, t=0) = \left( \frac{\partial}{\partial t} + \mathbf{v} \nabla \right) n_e(\mathbf{x}, 0). \end{aligned} \quad (2.59)$$

Hence, the partial time derivative  $\partial_t$  in the Lagrangian representation is the total (“convective” or “substantial”) time derivative  $d_t = \partial_t + (\mathbf{v} \nabla)$  of the Eulerian picture.  $\partial_t^{\text{Lag.}}$  becomes equal to  $\partial_t^{\text{Eul.}}$  when  $\mathbf{v}$  is zero. In this sense the Lagrangian time derivative is the derivative in the (tangent) inertial system co-moving with the fluid. With the help of (2.59), mass conservation in the Eulerian picture (2.54) follows

immediately from (2.58). In one dimension (2.57) is particularly intuitive and simple. The particles contained in the interval  $da$  at  $t = 0$  will occupy the interval  $dx$  at a later time, i.e.,  $n_e(a, 0)da = n_e(a, t)dx$ , or  $n_e(a, 0) = n_e(a, t)|\partial x/\partial a| = n_e(a, t)J$ . Correspondingly, in 3 dimensions  $J$  is the volume  $\nabla x_1(\nabla x_2 \times \nabla x_3)$  of the parallelepiped formed by the three oblique vectors  $\nabla_a x_i$  in  $a$ -space.

The momentum and energy equations are most easily derived in the Lagrangian picture. For this purpose we assume (for the moment) that the fluid is sufficiently dense so that (i) the extension  $d$  of a volume element  $\Delta V$  in which  $n_\alpha, \mathbf{v}_\alpha$  etc. are reasonably constant is much larger than  $\min\{\lambda, \lambda_D\}$ , ( $\lambda$  is the mean free path), and that (ii) the pressure  $p_\alpha$  is isotropic. Then, as a consequence of (i)  $p_\alpha$  is transmitted to the surface  $\Sigma$  of  $\Delta V$  which contains the mass  $\Delta m_\alpha = \rho_\alpha \Delta V$ . With the additional force density  $\mathbf{f}_\alpha$  (e.g., friction), Newton's second law reads

$$\Delta m_\alpha \frac{d\mathbf{v}_\alpha}{dt} = n_\alpha q_\alpha (\mathbf{E} + \mathbf{v}_\alpha \times \mathbf{B}) \Delta V - \int_{\Sigma} p_\alpha d\Sigma + \mathbf{f}_\alpha \Delta V.$$

With the help of Gauß' theorem the surface integral transforms into the approximate expression  $\int \nabla p_\alpha dV \simeq \nabla p_\alpha \Delta V$ ; dividing by  $\Delta V$  yields

$$\begin{aligned} \rho_e \frac{d\mathbf{v}_e}{dt} &= -n_e e (\mathbf{E} + \mathbf{v}_e \times \mathbf{B}) - \nabla p_e + \mathbf{f}_e, \\ \rho_i \frac{d\mathbf{v}_i}{dt} &= n_i Z e (\mathbf{E} + \mathbf{v}_i \times \mathbf{B}) - \nabla p_i + \mathbf{f}_i. \end{aligned} \quad (2.60)$$

The reader preferring more mathematical rigor may start from a macroscopic volume  $V(t)$  moving with the fluid,

$$\begin{aligned} \frac{d}{dt} \int_{V(t)} \rho_\alpha \mathbf{v}_\alpha dV &= \lim \frac{1}{\Delta t} \left( \int_{V'} \rho'_\alpha \mathbf{v}'_\alpha dV' - \int_V \rho_\alpha \mathbf{v}_\alpha dV \right) \\ &= \lim \frac{1}{\Delta t} \int_V (J' \rho'_\alpha \mathbf{v}'_\alpha - \rho_\alpha \mathbf{v}_\alpha) dV \\ &= \lim \int_V \rho_\alpha(t) \frac{\mathbf{v}_\alpha(t') - \mathbf{v}_\alpha(t)}{\Delta t} dV = \int_V \rho_\alpha \frac{d\mathbf{v}_\alpha}{dt} dV, \end{aligned}$$

with  $t' = t + \Delta t$ , and  $\rho', \mathbf{v}', V', \rho, \mathbf{v}, V$  taken at  $t'$  and  $t$ , respectively. In one of the steps (2.57) has been used. The rest of the calculations leading to (2.60) are standard. However, for omitting the integral signs assumption (i) has to be fulfilled. Alternatively, this result is directly obtained by the substitution  $dm_\alpha = \rho_\alpha dV$  and by observing that  $d dm_\alpha/dt = 0$  and  $M = \int \rho_\alpha dV = \text{const}$ , thus

$$\frac{d}{dt} \int_{V(t)} \rho_\alpha \mathbf{v}_\alpha dV = \frac{d}{dt} \int_M v_\alpha dm_\alpha = \int_M \frac{dv_\alpha}{dt} dm_\alpha = \int_{V(t)} \rho_\alpha \frac{d\mathbf{v}_\alpha}{dt} dV.$$

Energy conservation is expressed by the first law of thermodynamics  $dU = dQ + dW$  in the comoving inertial system. Thereby  $dQ$  is the heat supplied to the mass

$M$  in the volume  $V(t)$ , and  $dW$  is the mechanical compression work done by the pressure  $p_\alpha$ . Recalling (i) and (ii) we have  $dU = d \int \varepsilon_\alpha dV = \int d(\varepsilon_\alpha / \rho_\alpha) dm_\alpha = \int \rho_\alpha d(\varepsilon_\alpha / \rho_\alpha) dV$ ,  $dQ = -dt \int \mathbf{q}_\alpha d\boldsymbol{\Sigma} + dt \int h_\alpha dV$ , with  $\mathbf{q}_\alpha$  the heat flux density and  $h_\alpha$  the heating power density (e.g., the absorbed laser light), and finally  $dW = -dt \int p_\alpha \mathbf{v}_\alpha d\boldsymbol{\Sigma} = -dt \int \nabla(p_\alpha \mathbf{v}_\alpha) dV = -dt \int (p_\alpha \nabla \mathbf{v}_\alpha) dV$  since  $\nabla p$  is zero in the comoving system. As  $V(t)$  is arbitrary equating the integrands requires for the two fluids

$$\begin{aligned} \frac{3}{2} n_e k_B \frac{dT_e}{dt} &= -p_e \nabla \mathbf{v}_e + h_e - \nabla \mathbf{q}_e, \\ \frac{3}{2} n_i k_B \frac{dT_i}{dt} &= -p_i \nabla \mathbf{v}_i + h_i - \nabla \mathbf{q}_i. \end{aligned} \quad (2.61)$$

As long as  $\mathbf{v}_e$ ,  $\mathbf{v}_i$  and the internal energy densities  $\varepsilon_e$ ,  $\varepsilon_i$  are continuous in space and time,  $dQ_\alpha = T_\alpha dS_\alpha = T_\alpha \Delta m_\alpha d\sigma_\alpha$  holds for the entropy  $S_\alpha = \sigma_\alpha \Delta m_\alpha$ , and (2.61) assumes the equivalent form for the specific entropy per unit mass

$$T_e \rho_e \frac{d\sigma_e}{dt} = h_e - \nabla \mathbf{q}_e, \quad T_i \rho_i \frac{d\sigma_i}{dt} = h_i - \nabla \mathbf{q}_i. \quad (2.62)$$

As a special case, when there is no energy deposition by  $h_\alpha$  or  $\mathbf{q}_\alpha$ , all energy change is adiabatic and (2.62) reduces to

$$\frac{d\sigma_e}{dt} = \frac{d\sigma_i}{dt} = 0. \quad (2.63)$$

The main contributions to  $f_e$  and  $f_i$  in (2.60) come from collisions between electrons and ions. According to (2.23)  $f_e = -n_e m_e v_{ei} (\mathbf{v}_e - \mathbf{v}_i) = -f_i$ . For  $v_{ei}$  to be given by (2.45)  $|\mathbf{v}_e - \mathbf{v}_i| \ll v_{\text{th},e}$  has to be fulfilled. Further, there is a continuous exchange of particles of the same fluid between adjacent volume elements  $\Delta V$  and the momentum exchange associated with it gives rise to viscous effects. The viscosity is estimated as follows. Assume the flow component  $v_y$  to have a gradient  $\partial_x v_y$  in  $x$ -direction. By the exchange of two electrons between adjacent volume elements  $\Delta V$ ,  $\Delta V'$  the momentum difference  $m \lambda_x \partial_x v_y$  is transmitted to the slower volume.  $\lambda_x = \lambda v_{\text{th},x} / v_{\text{th}}$  is the mean free path in  $x$ -direction. The total momentum change per unit area is obtained by multiplying with the particle flux  $n_e v_{\text{th},x}$ ; hence, the pressure  $p_e$  is augmented by

$$\Delta p_e = m n_e v_{\text{th},x} \lambda_x \partial_x v_y = m n_e v_{\text{th},x}^2 \partial_x v_y / \nu = (p_e / \nu) \partial_x v_y, \quad \nu = v_{ee} + v_{ei}.$$

$\mu_e = p_e / \nu$  is the approximate shear viscosity coefficient. The same consideration holds for a gradient in the  $y$ -direction leading to a volume viscosity with the same coefficient  $\mu_e$ . The coefficient for the ion fluid is  $\mu_i = p_i / \nu_{ii}$ . Both  $\mu_e$  and  $\mu_i$  are density-independent. Their ratio is

$$\frac{\mu_i}{\mu_e} \simeq \frac{1+Z}{Z^4} \left( \frac{T_i}{T_e} \right)^{5/2} \left( \frac{m_i}{m} \right)^{1/2}.$$

In low- $Z$  laser plasmas the ion viscosity dominates due to the large mass ratio. Numerical estimates in typical low- $Z$  laser plasmas showed only a minor influence on the overall plasma dynamics [44] so that it will be omitted in the momentum and energy equations in the following.

In the energy equations (2.61) electronic heat conduction is of great importance. An analogous consideration for the diffusive energy flux, as before for viscosity, leads to the heat flux density  $\mathbf{q}_e$ ,

$$\mathbf{q}_e = -n_e v_{\text{th,grad}} \lambda_{\text{grad}} \nabla \frac{1}{2} m v_{\text{th}}^2 = -\frac{3 p_e}{2(v_{ee} + v_{ei})} \frac{k_B}{m} \nabla T_e = -\kappa_e \nabla T_e.$$

The index “grad” thereby indicates the projection on the  $\nabla T_e$ -direction. It becomes clear from this formula that electron heat conduction is dominated by the fast electrons in the thermal distribution since  $\kappa_e \sim T_e^{5/2}$ . On the other hand, fast electrons exhibit a much longer mean free path than slower ones; consequently, averaging of single quantities as  $v_{\text{th}}$ ,  $\lambda$ , etc. instead of their products underestimates  $\kappa_e$ . Its true value for  $Z = 1$  is larger by a factor of 3–4 [45],

$$\begin{aligned} \mathbf{q}_e &= -\kappa_e \nabla T_e; \quad \kappa_e = \eta_e \frac{p_e}{v_{ei}} \frac{k_B}{m} = \kappa_0 T_e^{5/2}, \\ \kappa_0 [\text{cgs K}] &= 1.8 \times 10^{-5}, \quad \eta_e = 3.16. \end{aligned} \quad (2.64)$$

As  $Z$  increases  $\eta_e$  increases to  $\eta_e = 13$ .  $\kappa_0$  depends on the charge state as  $\kappa_0 \sim Z^{-1}$ . It is essential for (2.64) to be valid that  $\lambda \ll L = T_e/|\nabla T_e|$  holds everywhere. Another limit on the heat flux  $\mathbf{q}_e$  is imposed by the condition that it can never exceed the energy flux into the half space  $\mathbf{u}_+$ ,  $\mathbf{q}_{\max} = n_e m_e \int \mathbf{u}^2 \mathbf{u} f_e(\mathbf{x}, \mathbf{u}, t) d\mathbf{u}_+/2$  ( $f_e$  electron distribution function, obtained from the Vlasov equation (2.86)). For a Maxwellian distribution  $f_0$  this yields

$$q_{\max} = \left( \frac{2}{\pi} \right)^{1/2} k_B T_e v_{th}; \quad \left( \frac{2}{\pi} \right)^{1/2} = 0.8.$$

The heating function  $h_e$  consists of local laser energy transfer owing to electron–ion collisions (“collisional absorption”) according to  $n_e \alpha_e I = \alpha I$  after (2.30), local damping of resonantly excited electron plasma waves (“resonance absorption”) and local energy transfer from hot electrons accelerated by the laser field and by electron plasma waves (“anomalous heating”). In addition, there is a negative term which is due to cooling of the electron fluid by the colder ions; its magnitude is  $(2m/m_i)v_{ei}n_e(3k_B T_e/2 - 3k_B T_i/2)$ . For the ions only the latter term contributes to  $h_i$ . The two-fluid model is now given by the following system of equations:

$$\frac{\partial n_e}{\partial t} + \nabla n_e \cdot \mathbf{v}_e = 0, \quad \frac{\partial n_i}{\partial t} + \nabla n_i \cdot \mathbf{v}_i = 0; \quad (2.65)$$

$$n_e m \left( \frac{\partial}{\partial t} + \mathbf{v}_e \nabla \right) \mathbf{v}_e = -\nabla p_e - e n_e (\mathbf{E} + \mathbf{v}_e \times \mathbf{B}) \\ - n_e m v_{ei} (\mathbf{v}_e - \mathbf{v}_i), \quad (2.66)$$

$$n_i m_i \left( \frac{\partial}{\partial t} + \mathbf{v}_i \nabla \right) \mathbf{v}_i = -\nabla p_i + e n_e (\mathbf{E} + \mathbf{v}_i \times \mathbf{B}) \\ + n_e m v_{ei} (\mathbf{v}_e - \mathbf{v}_i); \quad (2.67)$$

$$\frac{3}{2} n_e k_B \left( \frac{\partial}{\partial t} + \mathbf{v}_e \nabla \right) T_e = -p_e \nabla \mathbf{v}_e + \frac{2}{7} \kappa_0 \nabla^2 T_e^{7/2} + \alpha I \\ - 3 \frac{m}{m_i} v_{ei} n_e k_B (T_e - T_i), \quad (2.68)$$

$$\frac{3}{2} n_i k_B \left( \frac{\partial}{\partial t} + \mathbf{v}_i \nabla \right) T_i = -p_i \nabla \mathbf{v}_i + 3 \frac{m}{m_i} v_{ei} n_e k_B (T_e - T_i). \quad (2.69)$$

For reasons of simplicity at this point only collisional absorption  $\alpha I$  is taken into account in its simplest form with

$$\alpha = n_e \alpha_e = \frac{e^2 n_e}{\varepsilon_0 m \omega_c^2} v_{ei}, \quad (2.70)$$

$$\alpha [\text{cm}^{-1}] = 6.9 \times 10^{-24} \frac{Z(n_e [\text{cm}^{-3}])^2}{(T_e [\text{K}])^{3/2}} \left( \frac{\omega_{\text{Ti:Sa}}}{\omega} \right)^2 \ln \Lambda.$$

In  $\mathbf{E}$  and  $\mathbf{B}$  all high and low-frequency fields are included. As a consequence of the large mass ratio  $m_i/m$  only the electrons are affected by the high frequency component. This makes it possible to split off the fast motion of the electrons from  $\mathbf{v}_e$ . On the fast time scale the remaining equations are

$$\frac{\partial n_e}{\partial t} + \nabla n_e \cdot \mathbf{v}_e = 0; \quad (2.71)$$

$$n_e m \left( \frac{\partial}{\partial t} + \mathbf{v}_e \nabla \right) \mathbf{v}_e = -\nabla p_e - n_e e (\mathbf{E} + \mathbf{v}_e \times \mathbf{B}) - n_e m v_{ei} \mathbf{v}_e.$$

On the slow, hydrodynamic time scale (index  $s$ ) the momentum equation for the electrons becomes with their slow velocity component  $\mathbf{v}_s = \mathbf{v}_e - \mathbf{v}_{e,\text{fast}}$

$$n_{e,s} m \left( \frac{\partial}{\partial t} + \mathbf{v}_s \nabla \right) \mathbf{v}_s = -\nabla p_{e,s} - n_{e,s} e (\mathbf{E}_s + \mathbf{v}_s \times \mathbf{B}_s) + \boldsymbol{\pi}. \quad (2.72)$$

The quantity  $\boldsymbol{\pi} = n_{e,s} \mathbf{f}_p$  is the ponderomotive force density (see Sect. 2.1.2). If no self-generated dc and external static magnetic fields are considered  $\mathbf{B}_s$  is zero and, as a consequence of quasineutrality,  $\mathbf{v}_s$  becomes equal to  $\mathbf{v}_i$ ,  $\mathbf{v}_s = \mathbf{v}_i = \mathbf{v}$ , so that the separate momentum equations (2.66), (2.67) and (2.72) for the two fluids can be combined into the single-fluid momentum equation

$$\rho \left( \frac{\partial}{\partial t} + \mathbf{v} \nabla \right) \mathbf{v} = -\nabla(p_{e,s} + p_i) + \boldsymbol{\pi}. \quad (2.73)$$

This is a great simplification in numerical calculations. The electron pressure  $p_e$  and the ponderomotive force couple to the ions by a quasistatic electric field  $\mathbf{E}_s$ . The latter is easily determined from (2.72):  $n_{e,s}e\mathbf{E}_s$  is the same term in (2.72), as well as in (2.67), but  $n_{e,s}md\mathbf{v}_s/dt$  is a factor  $Zm/m_i$  smaller than  $n_im_id\mathbf{v}_i/dt$  owing to quasineutrality. From this one has to conclude that the right-hand side terms in (2.72) have to be equal to zero, and hence

$$\mathbf{E}_s = \frac{1}{n_{e,s}e}(\boldsymbol{\pi} - \nabla p_{e,s}) - \mathbf{v}_s \times \mathbf{B}_s, \quad (2.74)$$

i.e., the static field  $\mathbf{E}_s$  is of thermal, magnetic and ponderomotive origin. In the absence of  $\boldsymbol{\pi}$  and  $\mathbf{B}_s$  in an isothermal plasma with  $T_i = 0$ ,

$$\mathbf{E}_s = -\frac{1}{k_B T_e} \frac{\nabla n_e}{n_e} \quad (2.75)$$

holds, and (2.35) follows by integration of (2.75). The model of two coupled fluids is kept solely in the energy equations (2.68), (2.69). For the rest a one-fluid description suffices. At the short time scale imposed by the laser frequency only the electrons react and at the hydrodynamic level the electrons are tied to the ions by the static field  $\mathbf{E}_s$  from (2.74). Radiation effects are important in high- $Z$  targets and can be taken into account in a simple way by introducing a radiation temperature  $T_s$  in addition to  $T_e$  and  $T_i$ . In low- $Z$  underdense plasmas, however, the radiation energy balance plays a minor role and is omitted in this chapter.

In laser generated plasmas situations may occur in which strong dc electric fields  $E_\Omega$  are induced by fast electron jets penetrating across (see Sect. 8.3). As a reaction intense neutralizing return currents of density  $j_r = -en_e v_d$  are driven and lead to Ohmic heating of the background plasma of amount  $j_r E_\Omega$ . If  $E_c = m v_{ei} v_{e,\text{th}}/e$  is the critical field at which the electrons start drifting away (“runaway field”), it has been shown by Fokker–Planck simulations that for  $E_\Omega > 0.1E_c$  (2.68) has to be replaced by two equations, one for  $T_{e\parallel}$  parallel to  $E_\Omega$  containing the heating term  $j_r E_\Omega$  and a second one for  $T_{e\perp}$  perpendicular to  $E_\Omega$ , with coupling coefficients given in [46].

### 2.2.1.1 Conservative Form of the Balance Equations

For theoretical considerations of general nature as well as for numerics it is sometimes useful to formulate all dynamic equations in their canonical form (“conservative” formulation) which states that the temporal change of a conserved physical quantity  $R$  in a fixed volume  $V$  is due to the flux  $\mathbf{S}$  of the quantity across its surface  $\Sigma$ ,

$$\frac{d}{dt} \int_V R dV + \int_{\Sigma(V)} S d\Sigma = 0 \iff \frac{\partial}{\partial t} R + \operatorname{div} S = 0. \quad (2.76)$$

When  $R$  is a tensor of rank  $r$ ,  $S$  is a tensor of rank  $r+1$ . The mass conservation (2.54) is written in this canonical form.  $\rho_\alpha$  and  $n_\alpha$  are scalars ( $r=0$ ) and  $\rho_\alpha \mathbf{v}_\alpha$  are vectors ( $r=1$ ). Next consider (2.73) in the absence of the ponderomotive force  $\boldsymbol{\pi}$ . It is brought into canonical form by multiplying the continuity equation for  $\rho$  by  $\mathbf{v}$  and adding,

$$\frac{\partial}{\partial t} (\rho \mathbf{v}) + \nabla \cdot \{\rho \mathbf{v} \mathbf{v} + (p_e + p_i) \mathbf{I}\} = 0.$$

$\rho \mathbf{v}$  is the momentum density vector and  $\Pi_{ij} = \{\rho \mathbf{v} \mathbf{v} + (p_e + p_i) \mathbf{I}\}_{ij} = \rho v_i v_j + (p_e + p_i) \delta_{ij}$  is the symmetric 2nd rank tensor of momentum density flux. If the pressure is not isotropic the momentum flux density tensor  $\boldsymbol{\Pi}$  reads  $\Pi_{ij} = \{\rho v_i v_j + p_{e,ij} + p_{i,ij}\}$  (see (2.84)). Momentum is neither created nor destroyed; the system is closed. When  $\boldsymbol{\pi}$  does not vanish (2.73) becomes

$$\frac{\partial}{\partial t} (\rho \mathbf{v}) + \nabla \cdot \boldsymbol{\Pi} = \boldsymbol{\pi}. \quad (2.77)$$

The ponderomotive force must appear as a source term because it generates momentum density with the help of the laser radiation field. The source term vanishes only when the latter is included and its momentum density  $\bar{S}/c^2$  ( $\bar{S}$  is the cycle averaged Poynting vector) is added to  $\rho \mathbf{v}$ , since the total momentum  $\int (\rho \mathbf{v} + \bar{S}/c^2) dV$  is conserved (the interested reader may look ahead to Sect. 5.2.3). Similarly  $f_e$  and  $f_i$  and the Lorentz forces appear as source terms in the conservative form of (2.60). Equation (2.77) can also be used as the definition of a force density instead of making recourse to the Eulerian equations (2.60) which are the continuum form of Newton's second law. According to (2.76) or (2.77) a force (density) is the amount of momentum (density) and momentum flux (density) changes that do not sum to zero. There are situations, in particular with the ponderomotive force, in which such a criterion is helpful to find out which is the correct force (density).

To see how an energy balance is brought into canonical form let us first reduce the equations (2.68), (2.69) to obtain the single fluid relation by adding them to yield

$$\frac{3}{2} n k_B \left( \frac{\partial}{\partial t} + \mathbf{v} \nabla \right) T = -p \nabla \cdot \mathbf{v} + \alpha I - \nabla \cdot \mathbf{q}_e. \quad (2.78)$$

Here  $n = n_e + n_i = n_i(1+Z)$  is the total particle density,  $T = (ZT_e + T_i)/(1+Z)$  the average temperature and  $p = p_e + p_i$  the total fluid pressure. Multiplying (2.77) by  $\mathbf{v}$  and mass conservation by  $\mathbf{v}^2$  and adding them to (2.78) leads to

$$\begin{aligned} \frac{\partial}{\partial t} \rho \left( \frac{\mathbf{v}^2}{2} + \frac{3}{2} \frac{Z+1}{m_i} k_B T \right) + \nabla \cdot \left\{ \rho \mathbf{v} \left( \frac{\mathbf{v}^2}{2} + \frac{3}{2} \frac{Z+1}{m_i} k_B T + \frac{p}{\rho} \right) \right\} \\ = \alpha \mathbf{I} - \nabla \cdot \mathbf{q}_e + \boldsymbol{\pi} \cdot \mathbf{v}. \end{aligned} \quad (2.79)$$

Equations (2.77) and (2.79) show that the total flux densities are  $\boldsymbol{\Pi} = \rho \mathbf{v} \mathbf{v} + p \mathbf{I}$  for momentum (viscosity neglected) and  $\mathbf{S} = \rho \mathbf{v} (\mathbf{v}^2/2 + \varepsilon + p/\rho) = \rho \mathbf{v} (\mathbf{v}^2/2 + h)$  for energy, respectively.  $\varepsilon = 3(Z+1)k_B T/2m_i$  is the internal energy per unit mass and  $h = \varepsilon + p/\rho$  the specific enthalpy (not to be confused with the heating functions  $h_e, h_i$ ). Under steady state conditions the time derivatives  $\partial_t$  are zero and the fluxes of mass, momentum and energy are conserved through any section  $\Sigma$  of an arbitrary flux tube,

$$\begin{aligned} \int \rho v d\Sigma = \text{const}, \quad \int (\rho \mathbf{v} \mathbf{v} + p \mathbf{I}) d\Sigma = \text{const}, \\ \int \rho (\mathbf{v}^2/2 + h) (\mathbf{v}/v) d\Sigma = \text{const}, \end{aligned} \quad (2.80)$$

provided the right-hand side terms in (2.77) and (2.79) vanish. As a result, thermal pressure carries momentum and energy. In other words, the reason why  $p$  appears in the energy flux density term in (2.79) whereas it does not in the term for the energy density is that a fluid volume in motion has to do work against the adjacent elements to remove them from where they are presently located.

### 2.2.1.2 Topological Aspects of Fluid Dynamics

When Euler's field equation (2.73),  $\rho d\mathbf{v}/dt = -\nabla p + \boldsymbol{\pi}$ , together with  $d\mathbf{x}/dt = \mathbf{v}$  is solved for all initial positions  $\mathbf{x} = \mathbf{a}$  at  $t = t_0$ , the flow field  $\mathbf{v}(\mathbf{a}, t)$  and the trajectories  $\mathbf{x} = \mathbf{x}(\mathbf{a}, t)$  of all material points  $\mathbf{a}$  in the Lagrangian description are determined [47].  $\mathbf{x}(\mathbf{a}, t)$  can be assumed to be piecewise continuously differentiable with respect to  $\mathbf{a}$  and  $t$ . As long as the fluid density  $\rho$  remains finite, different material points cannot merge into one since mass conservation states that  $\rho(\mathbf{a}, t_0) = \rho(\mathbf{x}, t) J(\mathbf{x}, \mathbf{a}, t)$ . Thus, the Jacobian  $J = |\partial(\mathbf{x})/\partial(\mathbf{a})|$  differs from zero everywhere. Mathematically, this fact is expressed by the property that  $\mathbf{x}(\mathbf{a}, t)$  has to be a continuous one-to-one (biunique) correspondence or, in short,  $\mathbf{x}(\mathbf{a}, t)$  is a topological mapping or a homeomorphism.

A topological mapping and a diffeomorphism in particular, i.e., a continuously differentiable mapping with respect to  $\mathbf{a}$ , have some interesting consequences for an arbitrary fluid volume  $V_0$ , namely:

- (i) A trajectory starting from the interior of  $V_0$  ends in an interior point of  $V_1$ , and a boundary point of  $V_0$  remains a boundary point of  $V_1$ .
- (ii) The degree of connectivity of  $V_1$  is an invariant of fluid motion.

In fact, properties (i) and (ii) are easily shown to be consequences of the continuity of mapping  $\mathbf{x}(\mathbf{a}, t)$ , i.e., open neighborhoods are mapped onto open ones, and the existence of the inverse mapping  $\mathbf{x}^{-1}$  is also guaranteed. The situation of a few cases is illustrated by Fig. 2.5. They have some surprising implications for applied fluid dynamics.

**Example 1.** As a first example a hollow shell of matter is considered which is compressed to a very small diameter. According to property (ii) the hole may shrink to a point; however in ideal fluid dynamics it can never disappear which means that at least at one point inside the shell the density must remain zero. Kidder's analytical solutions [48] for homogeneous pellet compression behave in this way. Prior to the instant of collapse  $t = t_c$  the hole inside the pellet does not fill up with matter to yield  $\rho \neq 0$  everywhere, no matter how small the outer radius  $R$  of the shell has become. Only when  $R$  has reduced to zero at  $t = t_c$  can pellet and void both degenerate to a singularity simultaneously.

**Example 2.** As a second example we consider the problem of foil acceleration and its impact on a solid wall [49]. A mathematically equivalent problem is the following version of the historical Gay-Lussac experiment (Fig. 2.6): A box is subdivided into two chambers one of which is filled with a compressible fluid and the other of which is empty. When the fluid is released by instantaneously removing the separating wall, a rarefaction wave develops, and matter is accelerated into the vacuum. When the fluid arrives at the opposite wall it is stopped; a strong shock then originates from the wall and propagates backward into the counter-streaming fluid [50]. Again a singular point exists; this time it is located at the solid wall. If the rarefaction wave is such that at its front both the density and the sound speed drop to zero,  $\rho$  will remain zero for all times at the wall, the reason being exactly the same as in the former case of pellet compression. To recognize this it is sufficient to mirror the Gay-Lussac (or the foil impact) experiment in the plane of the solid wall. Then a hole of the shape of an infinite slit results which is topologically equivalent to the spherical case. In numerical calculations such a behavior is reproduced only approximately as a result of numerical diffusion. However, the hole is clearly seen. It is useful to know in this context that it is not a numerical artifact but a topological necessity [51].

### 2.2.1.3 The Particle Aspect of the Plasma Fluid

Mass, momentum and energy conservation as derived above are valid for dense fluids in which the lifetime of a fluid element  $\Delta V$  is approximately  $\tau = (\Delta V)^{2/3}/4D$ , with the diffusion constant  $D = \langle v_{\text{th}} \lambda \rangle / 3$ ,  $\lambda$  mean free path. For instance in air under standard conditions  $\tau = 1.5$  ms for a volume element  $\Delta V = (100 \lambda)^3 = (10^{-3})^3 \text{ cm}^3$ . As a fluid becomes more and more rarefied  $\tau$  decreases and collisions are so infrequent that the lifetime  $\tau$  of a volume element ("mass point") becomes equal to the mean volume-crossing time,  $\tau = (\Delta V)^{1/3}/v_{\text{th}}$ . On the other hand, the smallest dimension of plasma structures is given by  $l = \min\{\lambda, \lambda_D\}$ .  $l$  represents the lower limit of the fluid picture for any meaningful subdivision of the plasma.

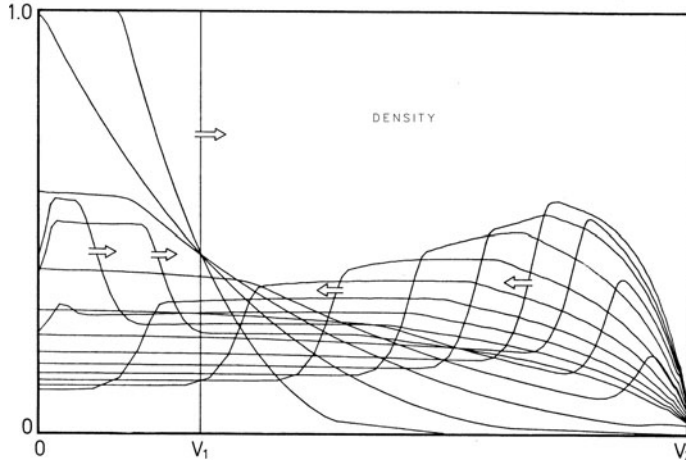


**Fig. 2.6** Foil impact or Gay-Lussac experiment. An ideal gas initially fills volume  $V_1$ . After the gas expands through volume  $V_2$  and reaches the solid wall, a strong back-running shock forms [50]. The density remains zero for all times, and the temperature diverges, just at the wall. Here, in the figure, the finite density is due to numerical diffusion

From the conservation equations solutions are obtained for the orbits  $\mathbf{x}(\mathbf{a}, t)$  of volume elements, for  $\rho(\mathbf{a}, t)$ ,  $\mathbf{v}(\mathbf{a}, t)$ , etc., in the dense as well as in the very rarefied plasma. In the latter case, however, the question of the physical meaning of the orbits arises. For example, does  $\rho(\mathbf{a}, t)$  really represent the matter density at  $\mathbf{x}(\mathbf{a}, t)$  at the time  $t$ ? It becomes immediately clear that the derivation of (2.54) remains valid as long as the macroscopic quantities  $\rho$ ,  $\mathbf{v}$ ,  $T$  etc. can be defined in a meaningful way. In the case of the derivations given above for momentum and energy balance the answer is not at all so clear when looking at the Lagrangian picture. All we know is their validity in the canonical or reduced form in the case of a dense fluid. In the canonical form momentum and energy conservation are deduced exactly in the same way as mass or particle conservation (2.54). All quantities can be defined kinetically and no reference is made to collisions; hence, one deduces that (2.65)–(2.80) are also valid in collisionless fluids, provided momentum and energy fluxes are defined as presented above for collision-dominated fluids. However, now, since  $l > (\Delta V)^{1/3}$  holds, the mapping  $\mathbf{x}(\mathbf{a}, t)$  can no longer be visualized as material orbits or center of mass trajectories of volume elements; the only valid information the mapping yields is the direction and magnitude of the velocity of the fluid element which at the time  $t$  is located at position  $\mathbf{x}$ . The real center of mass  $\mathbf{a}$  generally follows a completely different and nearly unpredictable trajectory.

The state of a moderately dense fluid with  $g \ll 1$  is defined by its one-particle distribution function  $f_\alpha(\mathbf{x}, \mathbf{u}, t)$  indicating the number of particles  $\Delta N_\alpha$  in the six-dimensional phase space volume element  $\Delta\tau = \Delta\mathbf{x}\Delta\mathbf{u}$ ,

$$\Delta N_\alpha = f_\alpha(\mathbf{x}, \mathbf{u}, t)\Delta\mathbf{x}\Delta\mathbf{u}. \quad (2.81)$$

From elementary gas-kinetic theory it is known that the macroscopic quantities are defined as follows,

$$n_\alpha(\mathbf{x}, t) = \int f_\alpha(\mathbf{x}, \mathbf{u}, t) d\mathbf{u}, \quad \mathbf{v}_\alpha = \frac{1}{n_\alpha} \int \mathbf{u} f_\alpha(\mathbf{x}, \mathbf{u}, t) d\mathbf{u}, \quad (2.82)$$

$$T_\alpha = \frac{1}{3} \frac{1}{n_\alpha k_B} \int m_\alpha (\mathbf{u} - \mathbf{v}_\alpha)^2 f_\alpha(\mathbf{x}, \mathbf{u}, t) d\mathbf{u}, \quad (2.83)$$

$$p_{\alpha,ij} = \int m_\alpha (u_i - v_{\alpha i})(u_j - v_{\alpha j}) f_\alpha(\mathbf{x}, \mathbf{u}, t) d\mathbf{u}, \quad (2.84)$$

$$\mathbf{q}_\alpha = \frac{1}{2} m_\alpha \int (\mathbf{u} - \mathbf{v}_\alpha)^2 (\mathbf{u} - \mathbf{v}_\alpha) f_\alpha(\mathbf{x}, \mathbf{u}, t) d\mathbf{u}. \quad (2.85)$$

The tensor  $p_\alpha = p_{\alpha,ij}$  is the scalar pressure  $p_\alpha$  plus the viscosity tensor and  $\mathbf{q}_\alpha$  is the heat flux density. As long as the dynamical variables are defined in this way the conservation equations deduced above are valid for arbitrarily diluted fluids. This can be directly verified by starting from the conservation equation of the one-particle distribution function  $f(\mathbf{x}, \mathbf{u}, t)$  (the index  $\alpha$  is omitted for simplicity). Let us first consider a collisionless fluid. By observing that  $f$  is the particle density in the 6-dimensional phase space and its flux density is given by  $f \mathbf{w}$  with the 6-dimensional velocity  $\mathbf{w} = (\mathbf{u}, d\mathbf{u}/dt)$ , particle conservation requires  $\partial_t f + \text{div}(f \mathbf{w}) = 0$ . Liouville's theorem states for noninteracting particles

$$\nabla \mathbf{w} = \nabla_x \mathbf{u} + \nabla_u \mathbf{q}(\mathbf{E} + \mathbf{u} \times \mathbf{B})/m = 0$$

(or  $\Delta\tau = \text{const}$ ) owing to  $\nabla_x \mathbf{u} = \nabla_x(\mathbf{p}/m)$ ,  $\mathbf{p} = m\mathbf{u} + q\mathbf{A}$ ; thus, the conservation equation reads  $\partial_t f + \mathbf{w} \cdot \nabla f = 0$ , or explicitly,

$$\frac{\partial f}{\partial t} + \mathbf{u} \nabla_x f + \frac{q}{m} (\mathbf{E} + \mathbf{u} \times \mathbf{B}) \nabla_u f = 0. \quad (2.86)$$

This is the celebrated Vlasov equation. It will be used in several contexts in the following chapters. In an alternative manner it follows from the fact that the number of particles  $\Delta N$  in the volume  $\Delta\tau$  is conserved,

$$\frac{d}{dt} \Delta N = \frac{d}{dt} (f \Delta\tau) = f \frac{d(\Delta\tau)}{dt} + \Delta\tau \frac{df}{dt} = \Delta\tau \frac{df}{dt} = 0.$$

$df/dt = 0$  is identical to (2.86). The effect of collisions can no longer be described in terms of a single set of coordinates  $(\mathbf{x}, \mathbf{u}, t)$ ; it must contain at least pairs of sets  $(\mathbf{x}, \mathbf{u})$  (binary collisions). Physically this is clear from the fact that owing to collisions particles are lost from  $\Delta\tau$  or scattered into it from outside. Consequently, a source term ("collision term") appears on the right-hand side of (2.86) which cannot be just a function of  $f$  depending only on  $\mathbf{x}, \mathbf{u}, t$ . It is shown in volumes on statistical mechanics that the correct source term is expressed as an integral over the two-particle distribution function  $f_2(\mathbf{x}_1, \mathbf{u}_1, \mathbf{x}_2, \mathbf{u}_2, t)$  for which in turn a new

conservation equation with a source term containing the three particle distribution function is needed. In this way one arrives at the famous BBGKY hierarchy, named after Bogoliubov, Born, Green, Kirkwood and Yvon. Only the latter is equivalent to the complete description of an ensemble of interacting particles by Liouville's equation [43].

The direct derivation of the fluid equations from (2.86) with or without a collision term is accomplished by multiplying it successively with  $|\mathbf{u}|^0 = 1$ ,  $\mathbf{u}$ ,  $\mathbf{u}^2$  and integrating over all  $\mathbf{u}$ -subspace and making use of the definitions (2.82), (2.83), (2.84), and (2.85), see Sect. 8.1.7. The use of the distribution function  $f$  is appropriate for dilute and moderately dense fluids. Nowadays laser plasmas can be created in which the plasma parameter  $g$  is of the order of unity or larger and the potential energy also contributes significantly, e.g., to the pressure, so that the definitions (2.82), (2.83), (2.84), and (2.85) are no longer appropriate. The macroscopic conservation equations, however, still maintain their validity since, for a dense fluid, all dynamic variables can be defined without making use of  $f$ .

## 2.2.2 Linearized Motions

Equations (2.65), (2.66), (2.67), (2.68), and (2.69) or their simplified versions are highly nonlinear and, consequently very few analytical solutions exist. Owing to their relevance for estimates and understanding and interpreting numerical results, those solutions relevant to laser plasma dynamics are treated in this and the following two sections. At moderate laser intensities static magnetic fields are of minor importance and are omitted here.

### 2.2.2.1 Electron Plasma Waves and Linear Landau Damping

The two-component plasma is capable of rapid charge density oscillations. Owing to their large mass the ions can be considered as a uniform background at rest whereas for the electrons (2.71) apply. For short time intervals  $q_e$  and heat flow to the ions need not be considered and in the absence of radiation the energy equation simplifies to

$$\frac{3}{2} \frac{dT_e}{dt} - \frac{T_e}{n_e} \frac{dn_e}{dt} = 0. \quad (2.87)$$

Here  $\nabla \mathbf{v}_e$  has been replaced by  $-(d_t n_e)/n_e$  from mass conservation. Equation (2.87) can be integrated immediately to yield the familiar adiabatic behavior

$$T_e n_e^{-(\gamma_e - 1)} = \text{const}, \quad p_e n_e^{-\gamma_e} = \text{const}; \quad \gamma_e = \frac{5}{3}. \quad (2.88)$$

However, it must be pointed out that the adiabatic coefficient  $\gamma_e = 5/3$  is correct only under the assumption that there are enough collisions during a change

of  $n_e$  to redistribute the compression work isotropically. In contrast, in a fast one-dimensional compression occurring during a time shorter than the collision time  $\tau_{ee}$  the compression (or expansion) work acts only on one of  $r$  degrees of freedom so that  $r/2 = 3/2$  in (2.87) has to be replaced by  $r/2 = 1/2$  and the adiabatic coefficient becomes  $\gamma_e = (r + 2)/r = 3$  in (2.88), in agreement with the kinetic result from (2.86).

Under the above assumptions the electronic fluid decouples from the ions and its dynamics is determined by the equations

$$\begin{aligned} \frac{\partial n_e}{\partial t} + \nabla(n_e \mathbf{v}_e) &= 0, \quad n_e \left( \frac{\partial}{\partial t} + \mathbf{v}_e \nabla \right) \mathbf{v}_e = -\frac{1}{m} \nabla p_e - n_e \frac{e}{m} \mathbf{E} - n_e v_{ei} \mathbf{v}_e, \\ \nabla \mathbf{E} &= -\frac{e}{\epsilon_0} (n_e - Zn_0), \quad p_e n_e^{-\gamma_e} = \text{const.} \end{aligned} \quad (2.89)$$

In general this system is still “intractable” [52]. However, it becomes solvable in the case of small disturbances  $n_1 = n_e - Zn_0$  from equilibrium  $n_{e0} = n_e - n_1 = Zn_0 = \text{const}$ ,  $\mathbf{v}_{e0} = 0$ ,  $T_{e0} = T_e - T_1 = \text{const}$ ,  $|n_1| \ll n_e$ . In this case the system can be linearized by omitting all higher order terms,

$$\begin{aligned} \frac{\partial n_1}{\partial t} + n_{e0} \nabla \mathbf{v}_e &= 0, \quad n_{e0} \frac{\partial \mathbf{v}_e}{\partial t} = -s_e^2 \nabla n_1 - n_{e0} \frac{e}{m} \mathbf{E} - n_{e0} v_{ei} \mathbf{v}_e; \\ s_e^2 &= \gamma_e \frac{k_B T_{e0}}{m}. \end{aligned}$$

The quantities  $\mathbf{v}_e$  and  $\mathbf{E}$  are removed by differentiating the first equation with respect to time and taking the divergence of the second one, and then using Poisson’s equation. The straightforward result is

$$\frac{\partial^2}{\partial t^2} n_1 + v_{ei} \frac{\partial}{\partial t} n_1 + (\omega_p^2 - s_e^2 \nabla^2) n_1 = 0 \quad (2.90)$$

with

$$\omega_p^2 = \frac{n_{e0} e^2}{\epsilon_0 m}. \quad (2.91)$$

The (electron) plasma frequency  $\omega_p$  is a fundamental quantity in plasma physics. Keeping  $\mathbf{v}_e$ ,  $\mathbf{E}$  or  $T_1$  instead of  $n_1$  leads to an equation in which  $n_1$  is merely to be replaced by  $\mathbf{v}_e$ ,  $\mathbf{E}$  or  $T_1$ , respectively. The plane electron plasma waves (or Langmuir, or electrostatic waves)

$$n_1(\mathbf{x}, t) = \hat{n} e^{i(k_e \mathbf{x} - \omega t)}$$

form a complete orthonormal set of solutions of (2.90) if  $\omega$  satisfies the Bohm-Gross dispersion relation

$$\omega^2 = \omega_p^2 + s_e^2 \mathbf{k}_e^2 - i v_{ei} \omega. \quad (2.92)$$

If we set  $v_{ei} = 0$ , this has the remarkable property of the phase and group velocities  $v_\varphi = \omega/k$  and  $v_g = \partial\omega/\partial k$  satisfying  $v_\varphi v_g = s_e^2$ . The connection of  $n_1$  with  $T_1$ ,  $v_e$ ,  $E$  and the potential  $\Phi$  in a harmonic wave is

$$\begin{aligned} T_1 &= (\gamma_e - 1) T_{e0} \frac{n_1}{n_{e0}}, \quad v_e = v_\varphi \frac{n_1}{n_{e0}}, \quad E = i \frac{e}{\varepsilon_0 k_e} n_1, \\ \Phi &= i \frac{E}{k_e} = - \frac{e}{\varepsilon_0 k_e^2} n_1. \end{aligned} \quad (2.93)$$

In the cold plasma ( $T_e = 0$ ) the restoring force is entirely of electrostatic nature and an arbitrary, small charge distribution oscillates at the plasma frequency  $\omega_p$  given by the expression (2.91), and  $v_g$  is zero. In the warm plasma ( $T_e > 0$ ) there is the additional thermal contribution  $s_e^2 \mathbf{k}_e^2$  to the eigenfrequency of the electrostatic wave and  $v_g$  is finite;  $\omega_p$  is the lower limit (“cut-off”) of  $\omega$  for the wavelength  $\lambda$  tending to infinity. Formally, for  $\lambda$  tending to zero  $\omega$  approaches the other asymptote  $\omega = s_e k_e$  and  $v_\varphi = v_g = s_e$ . For this reason  $s_e$  is called the electron sound velocity. However, such a wave does not exist since its wavelength  $\lambda$  would be much smaller than  $\lambda_D = v_{th,e}/\omega_p$ . This cannot occur because in the collisionless plasma there is no way to transmit the electron pressure to a neighboring volume element much closer than  $\lambda_D$  via the space charge field alone. The electron density for which a given frequency  $\omega$  equals  $\omega_p$  is called the “critical density  $n_c$ ”,

$$n_c = \frac{\varepsilon_0 m}{e^2} \omega^2 = 1.75 \times 10^{21} \left( \frac{\omega}{\omega_{Ti:Sa}} \right)^2 \text{ cm}^{-3}. \quad (2.94)$$

The critical density  $n_c$  is one of the fundamental quantities characterizing the interaction of the laser with dense matter. According to (2.92) a Langmuir wave of frequency  $\omega$  cannot propagate into an “overdense region” with  $n_{e0} > n_c$ . The same holds for electromagnetic waves; they are cut off at  $n_c$  (see Chap. 3).

Collisional damping, with  $\Im\omega = -v_{ei}/2$ , is generally small; for example  $v_{ei}/\omega_{Nd} = 3 \times 10^{-5} Z$  at  $n_{e0} = 10^{20} \text{ cm}^{-3}$  and  $T_e = 1 \text{ keV}$ . However, for  $k_e$  approaching the order of magnitude of  $k_D = 1/\lambda_D$  the particle nature of the electron fluid manifests itself through the phenomenon of Landau damping. Assume a small harmonic electron density disturbance in a field-free plasma at rest with equilibrium distribution function  $f_0(\mathbf{v})$ . By setting

$$f(\mathbf{x}, \mathbf{v}, t) = f_0(\mathbf{v}) + f_1(\mathbf{v}) e^{i(\mathbf{k}_e \mathbf{x} - \omega t)}$$

and linearizing (2.86) in  $f_1$  with  $\mathbf{B} = 0$ , a more general dispersion relation than (2.92) is obtained for the frequency which, although no collisions are considered, is complex:  $\omega \rightarrow \omega + i\gamma$  (see any volume of plasma physics). Under the assumptions (i)  $\gamma \ll \omega$  and (ii)  $(k_e \lambda_D)^2 \ll 1$  the dispersion relation reduces to the algebraic relations

$$\omega^2 = \omega_p^2(1 + 3k_e^2\lambda_D^2 + \dots) = \omega_p^2 + s_e^2k_e^2 + \dots, \quad s_e^2 = 3v_{\text{th}}^2,$$

$$\gamma = \frac{\pi}{2} \frac{\omega\omega_p^2}{k_e^2} \left. \frac{\partial f_0}{\partial v} \right|_{v=v_\varphi}; \quad f_0 = \left( \frac{\beta}{\pi} \right)^{1/2} e^{-\beta v^2}. \quad (2.95)$$

The first line is the Bohm–Gross dispersion relation with  $\gamma_e = 3$ , in accordance with the number of degrees of freedom  $r = 1$  activated by a plane wave in a collisionless plasma. The expression for  $\gamma$  is negative for an equilibrium distribution function  $f_0$  with negative slope and the wave is damped, as is the case for a Maxwellian plasma. For the latter,  $\gamma$  becomes under assumption (i)

$$\begin{aligned} \gamma &= -\left(\frac{\pi}{8}\right)^{1/2} \frac{\omega_p}{(k_e\lambda_D)^3} \exp\left(-\frac{1}{2(k_e\lambda_D)^2} - \frac{3}{2}\right) \\ &= -0.14 \frac{\omega_p}{(k_e\lambda_D)^3} \exp\left(-\frac{1}{2(k_e\lambda_D)^2}\right). \end{aligned} \quad (2.96)$$

For instance, at  $(k_e\lambda_D)^2 = 1/6$ , where (2.95) still holds,  $\lambda = 15\lambda_D$ ,  $\omega = 1.2\omega_p$  and the damping is given by  $|\gamma/\omega| = 0.08$ , i.e., the mean lifetime of the wave is  $N = \Delta t/\tau = \omega/2\pi|\gamma| = 2$  periods. In contrast, at twice the wavelength,  $\lambda = 30\lambda_D$ , the wave undergoes nearly 1000 oscillations until its amplitude reduces to 1/e. If, for some reason,  $f_0$  is flat at  $v_\varphi = \omega/k$  linear Landau damping does not occur as long as (i) and (ii) hold. It is also seen from (2.95) that a weak electron beam when superposed on  $f_0$  with a suitable velocity such as to produce a positive slope at  $v_\varphi$ , excites the Langmuir wave instead of reducing its amplitude (“electron beam instability”). In a Maxwellian plasma, frequencies considerably higher than  $\omega_p$  do not occur, unless the waves are strongly driven. As  $\lambda$  approaches  $\lambda_D$ , Langmuir waves are heavily damped.

Generally electron plasma waves are excited in a limited region from which they are emitted as free-running waves. In laser plasmas such waves are most effectively excited at the critical point in a very narrow region. The situation is very similar to Langmuir wave excitation by an antenna. In both cases one has to look for complex roots of  $k_e$  as functions of real values of  $\omega$ . For a Maxwellian electron fluid the dispersion relation is

$$k_e^2 = k_n^2 = \frac{1}{2\sqrt{\pi}\lambda_D^2} \frac{d}{d\xi} \int_{-\infty}^{+\infty} \frac{e^{-z^2}}{z - \xi} dz, \quad \xi = \frac{1}{\sqrt{2}v_{\text{th}}} \frac{\omega}{k_n}. \quad (2.97)$$

The wave vector has now been assigned an index  $n$  because there is an infinite sequence of roots  $k_n$  for a fixed  $\omega$ . To give a feeling for the strength of damping, in Table 2.3 the first 3 roots of  $k_e$  are calculated as functions of  $\omega/\omega_p$ . For  $\lambda/\lambda_D \gg 1$  higher Landau modes are much more strongly damped than the fundamental mode. As  $k_e$  increases, also the fundamental mode becomes heavily Landau-damped; e.g., at  $\lambda_1 = 5\lambda_D$  the amplitude has reduced by a factor of  $e = 2.718$  after  $\Delta x_1 = 0.21\lambda_1 \simeq \lambda_D$ . From the table also results that for  $\omega \geq 1.1\omega_p$ ,  $k_1$  no longer follows

the Bohm-Gross dispersion relation.  $\Re k_1$  and  $\Im k_1$  from (2.97) and Table 2.3 were found to be in excellent agreement with experiments [53].

Landau damping is not easy to explain in physical terms. The standard argument starts from a single particle in the periodic wave potential given in (2.93). An electron traveling up the potential hill  $-e\Phi$  at speed slightly faster than  $v_\varphi$  is slowed down in transferring part of its kinetic energy to the wave; an electron traveling down the hill at a slightly lower speed than  $v_\varphi$  gains energy from the wave. If there are more such “resonant” particles with  $v < v_\varphi$  than with  $v > v_\varphi$  there is a net energy flow into the electrons and the wave is damped. The deficiency of this explanation is that the attempt to quantify it to obtain (2.96) becomes more involved than Landau’s derivation [54, 55]. Upon changing to a reference system comoving with the wave,  $\Phi$  becomes static. Then, one could make the objection that on the average an electron neither loses nor gains energy. Therefore we prefer a different point of view. Imagine an initial sinusoidal density perturbation  $n_e = n_{eo} + n_1$  with a Maxwellian velocity distribution everywhere. Such a perturbation exactly fulfills the fluid equations (2.89) and leads to an undamped wave in the absence of collisions, i.e.,  $v_{ei} = 0$ . However, in the wave frame energy conservation requires

$$\frac{1}{2}mu'^2 - e\Phi = E', \quad u' = u - v_\varphi.$$

Those electrons with  $E' < -e\Phi_{\min}$  are stopped and forced to oscillate, each in its potential well; they are “trapped” and travel with the wave. Those with  $E' > -e\Phi_{\min}$  are free. However, owing to the periodic potential the time to move one wavelength further for all free electrons becomes longer than  $|u - v_\varphi|/\lambda$  which is the crossing time in the absence of  $\Phi$ . The closer an electron comes to the separatrix between trapped and untrapped particles the larger is the resulting deviation. Hence, groups of electrons traveling at a constant difference  $\Delta u'$  in the field-free region,  $\Delta u' = \Delta u$ , when entering the wave change their relative speed, and coherence is gradually lost. The trapped electrons oscillate at the so-called bounce frequency  $\omega_B$  [52]. For  $E'_{\text{kin}} \ll -e\Phi_{\min}$  it is easily determined from

$$\frac{d^2x'}{dt^2} + \frac{e}{m}\hat{E} \sin k_e x' \simeq \frac{d^2x'}{dt^2} + \frac{e}{m}k_e \hat{E}x' = 0.$$

**Table 2.3** Landau damping of the first 3 modes.  $\Delta x_n/\lambda_n$  relative distance at which the wave amplitude reduces to  $1/e$

$\omega/\omega_p$	$\lambda_1/\lambda_D$	$\Delta x_1/\lambda_1$	$\lambda_2 = \infty, \Delta x_2/\lambda_D$	$\lambda_3/\lambda_D$	$\Delta x_3/\lambda_3$
1.0	$\infty$	$\infty$	0.64	30.1	0.40
1.1	25.8	23.1	0.62	29.5	0.35
1.5	12.8	0.80	0.55	22.4	0.27
2.0	9.2	0.43	0.48	17.1	0.25
2.5	7.5	0.32	0.43	13.7	0.23
3.0	6.5	0.27	0.40	11.6	0.22
4.0	5.2	0.22	0.33	8.9	0.21

This is a harmonic oscillator with frequency

$$\omega_B = \left( \frac{e k_e \hat{E}}{m} \right)^{1/2}. \quad (2.98)$$

The quantity  $\tau_B = 2\pi/\omega_B$  indicates the order of magnitude of time duration for a particle to be trapped. In resonance absorption particle trapping plays a dominant role for damping and eventual breaking of the highly nonlinear electron plasma wave. Collisionless damping due to trapping is denoted as nonlinear Landau damping. Linear Landau damping does not lead to any entropy increase of the system; its reversibility has been successfully demonstrated by the technique of plasma echoes [52]. The latter are completely analogous to spin echoes [56, 57] and to laser echoes in two-level systems and are best visualized by the vector model of the Bloch equations [58].

### 2.2.2.2 Ion Acoustic Waves

In a formal treatment of the ionic fluid in complete analogy to Langmuir waves the frequencies  $\omega$  and  $\omega_p$  would be reduced by the ratio  $(Zm/m_i)^{1/2}$ . However, in such a slow motion the electrons have time to follow adiabatically and to neutralize any ion disturbance. In other words, the momentum equation for the electron fluid reduces to (2.72) with  $\boldsymbol{\pi} = 0$ ,  $\mathbf{B}_s = 0$ . Neglecting viscosity, (2.73) applies for the ions. For small density disturbances  $n_1 = n_i - n_0$ ,  $n_{e1} = n_e - Zn_0$  it reads as follows,

$$n_0 \frac{\partial \mathbf{v}}{\partial t} = -\frac{1}{m_i} \nabla p_i - \frac{1}{m_i} \nabla p_e = -s_i^2 \nabla n_1 - \frac{m}{m_i} s_e^2 \nabla n_{e1}; \quad s_i^2 = \gamma_i \frac{k_B T_i}{m_i}.$$

For the ions the adiabatic law  $p_i n_i^{-\gamma_i} = \text{const}$  applies in the absence of heating from which  $s_i$  follows as specified. From (2.74) and the Poisson equation,

$$\mathbf{E} = -\frac{m}{n_{e0} e} s_e^2 \nabla n_{e1}, \quad \nabla \mathbf{E} = \frac{e}{\epsilon_0} (Zn_1 - n_{e1}),$$

$n_{e1}$  is determined as a function of  $n_1$  through elimination of  $\mathbf{E}$ ,

$$-s_e^2 \nabla^2 n_{e1} = \omega_p^2 (Zn_1 - n_{e1}) \Rightarrow (1 - \gamma_e \lambda_D^2 \nabla^2) n_{e1} = Zn_1;$$

$\lambda_D$  from (2.38). Eliminating  $\mathbf{v}$  from the linearized momentum equation above with the help of  $\partial_t n_1 + n_0 \nabla \mathbf{v} = 0$  yields

$$\frac{\partial^2 n_1}{\partial t^2} = s_i^2 \nabla^2 n_1 + \frac{m}{m_i} s_e^2 \nabla^2 n_{e1} = \left[ s_i^2 + \frac{Z \frac{m}{m_i} s_e^2}{1 - \frac{1}{n_{e1}} \gamma_e \lambda_D^2 \nabla^2 n_{e1}} \right] \nabla^2 n_1. \quad (2.99)$$

Fourier analysis shows that the plane ion acoustic waves

$$n_1 = \hat{n} e^{i(k_a x - \omega_a t)}$$

form a complete set of solutions to (2.99) if  $\omega_a$  satisfies the dispersion relation

$$\omega_a = sk_a, \quad s^2 = \frac{k_B}{m_i} \left( \gamma_i T_i + \gamma_e \frac{ZT_e}{1 + \gamma_e (k_a \lambda_D)^2} \right). \quad (2.100)$$

Quasineutrality requires that  $n_{e1}$  is modulated with the same  $k_a$ . The quantity  $s$  is the ion sound velocity. It remains finite when  $T_i$  approaches zero owing to the electron pressure which in the ion sound wave is transmitted to the ions by the electrostatic field of type (2.74) rather than by collisions. The condition however for this to happen is  $k_a \lambda_D \ll 1$ . The ion plasma frequency  $\omega_{pi}$  does not appear in (2.100) since the slow ionic charge disturbance is nearly completely screened by the fast electrons. Again, if  $y$  stands for any of the perturbations of particle densities  $n_e, n_i$ , temperatures  $T_e, T_i$ , velocities  $v_e, v_i$ , electric field  $E$  or potential  $\Phi$ , each of them obeys the linear acoustic wave equation

$$\frac{\partial^2}{\partial t^2} y - s^2 \nabla^2 y = 0.$$

They are related by

$$\begin{aligned} T_{\alpha 1} &= (\gamma_\alpha - 1) T_{\alpha 0} \frac{n_{\alpha 1}}{n_{\alpha 0}}, \quad v_\alpha = s \frac{n_{\alpha 1}}{n_{\alpha 0}}, \quad n_{e1} = \frac{Zn_1}{1 + \gamma_e (k_a \lambda_D)^2}, \\ E &= -i \frac{e}{\varepsilon_0} \gamma_e k_a \lambda_D^2 n_{e1}, \quad \Phi = i \frac{E}{k_a}. \end{aligned} \quad (2.101)$$

In the long-wavelength limit  $s$  is nearly a constant owing to nearly perfect screening;  $v_e$  is very close to  $v_i = v$  and frictional damping plays no role. Generally the electrons have time to transmit their compression energy to their neighborhood during an oscillation whereas the ions do not. Hence,  $\gamma_e = 1$ , i.e., the electrons behave isothermally and  $\gamma_i = 3$  holds. If however,  $v_{ii} > \omega/2\pi$  is fulfilled,  $\gamma_i$  has to be set equal to 5/3.

According to the standard interpretation of Landau damping at  $T_e \gg T_i$ ,  $v_\phi = s$  is much greater than  $v_{th,i} = (k_B T_i / m_i)^{1/2}$  and the number of resonant particles is negligibly small. Solving Vlasov's equation for electrons and ions under this condition leads to the Landau damping coefficient

$$\frac{\gamma_a}{\omega} = \left( \frac{m}{m_i} \right)^{1/2} \left( \frac{\pi}{8} \right)^{1/2} \exp \left( -\frac{ZT_e}{T_i} - \frac{3}{2} \right). \quad (2.102)$$

For a hydrogen plasma we obtain  $\gamma_a/\omega_a = 1.5 \times 10^{-2} \exp(-T_e/T_i - 3/2)$ . In the range  $1 \leq ZT_e/T_i \leq 10$  a numerical fit of the kinetic dispersion relation leads to [55]

$$\frac{\gamma_a}{\omega} = 1.1 \left( \frac{ZT_e}{T_i} \right)^{7/4} e^{-(ZT_e/T_i)^2}. \quad (2.103)$$

When  $T_i$  approaches  $ZT_e$ ,  $v_\phi$  becomes comparable to  $v_{\text{th},i}$  and strong Landau damping sets in. It was due to the fact that  $T_e \gg T_i$  in a gas discharge that ion acoustic waves were first detected there. In laser-generated plasmas  $T_e \gg T_i$  may be easily reached. If  $\lambda_D$  is much larger than the wavelength  $\lambda_i$  of a periodic perturbation in  $n_i$  the electrons form a uniform homogeneous negative background in which the ions oscillate according to a dispersion relation of Bohm-Gross structure (2.92) or (2.95) with all electron quantities (index  $e$ ) replaced by those for the ions (index  $i$ ). For the pressure term to be efficient the ion mean free path must be smaller than  $\lambda_i$ .

### 2.2.3 Similarity Solutions

In laser dynamics the diffusion of the absorbed energy by electronic heat conduction and by thermal radiation as well as subsequent expansion of the hot plasma into the vacuum or a surrounding low-density gas and plasma cooling by expansion are of particular interest. The dynamics studied in the laboratory are nonstationary and at best exhibit rotational symmetry around the normal to the target onto which the laser beam is focused. This is a typical case for numerical computation. Only much simpler idealized, so to say, few purely one-dimensional cases, are accessible to an analytical treatment. Such solutions are of great relevance for the laser plasma in plane and spherical geometry.

#### 2.2.3.1 The Buckingham $\pi$ -Theorem and Similarity

Nonlinear similarity solutions play such an important role in fluid dynamics that a brief outline of dimensional analysis and its theoretical basis is justified here. It was pointed out by Lord Rayleigh that sometimes physical laws can be found by dimensional considerations alone. His research in hydrodynamics is a good demonstration for this assertion [59, 60]. In 1914 the so called  $\pi$ -theorem was formulated by Buckingham which yields the formal basis for all dimensional and similarity considerations [61]. Roughly spoken, it states that any physical law must be expressible as an equation among dimensionless variables (so called  $\pi$ -variables). As a simple consequence it follows that a fundamental physical theory cannot be constructed without a minimum number of fundamental constants. However, this was explicitly expressed much later only by Sedov [62].

Any physical law may be put into the form

$$y = f(x_1, x_2, \dots, x_n), \quad n \text{ integer} \quad (2.104)$$

with quantities  $y, x_i$  of certain dimensions. By dimension we mean the following: Given a system of  $k$  units M,L,T, ... (e.g., mass, length, time, ...) one has

**Table 2.4** Dimensional matrix consisting of  $n$  columns

	$x_1$	$x_2$	...	$x_n$
M	$\alpha_1$	$\alpha_2$	...	$\alpha_n$
L	$\beta_1$	$\beta_2$	...	$\beta_n$
T	$\gamma_1$	$\gamma_2$	...	$\gamma_n$
:	:	:		:

$$[y] = M^\alpha L^\beta T^\gamma \dots, \quad [x_i] = M^{\alpha_i} L^{\beta_i} T^{\gamma_i} \dots.$$

The exponents  $\alpha, \beta, \gamma, \dots, \alpha_i, \beta_i, \gamma_i, \dots$  constitute the complete dimensional matrix (Table 2.4). If its rank is indicated by  $r$ , then certainly  $r \leq \min(n, k)$ . If a new system of units is used,  $M = \mu m$ ,  $L = \lambda l$ ,  $T = \tau t, \dots$ , the value of  $y$  transforms into  $\bar{y} = \mu^\alpha \lambda^\beta \tau^\gamma \dots =: Ky$  and correspondingly  $\bar{x}_i = \mu^{\alpha_i} \lambda^{\beta_i} \tau^{\gamma_i} \dots =: K_i x_i$ . For (2.104) to be physically reasonable we postulate the following relations to be valid identically

$$\bar{y} = f(\bar{x}_1, \bar{x}_2, \dots, \bar{x}_n) \text{ or } Kf(x_1, x_2, \dots, x_n) = f(K_1 x_1, K_2 x_2, \dots)$$

respectively. These relations express what we mean by dimensional homogeneity.  $f(x_i)$  must contain at least all variables and constants on which  $y$  depends. For example, if  $y$  is the distance of the earth from the sun,  $f$  must contain the time  $t$ , the masses of earth and sun, total energy, angular momentum and the gravitation constant (the position of the moon has also to be included if  $y$  must be known to a higher precision). With the help of linear algebra the following theorem can be demonstrated:

**Buckingham's  $\pi$ -Theorem.** If  $y = f(x_1, x_2, \dots, x_n)$  is dimensionally homogeneous, (i) there exists a product  $x_1^{s_1} x_2^{s_2} \cdots x_n^{s_n}$  of variables  $x_i$  from  $f$  of the same dimension as  $y$ , i.e.,

$$[y] = [x_1^{s_1} x_2^{s_2} \cdots x_n^{s_n}],$$

and (ii)  $y = f(x_1, \dots, x_n)$  can be put into the form

$$\pi = F(\pi_1, \pi_2, \dots, \pi_{n-r}) \quad (2.105)$$

where  $\pi, \pi_1, \dots, \pi_{n-r}$  are  $n - r$  independent dimensionless variables. The  $\pi_i$ 's are power products of the  $x_i$ 's and  $\pi$  may be taken as  $y/(x_1^{s_1} x_2^{s_2} \cdots x_n^{s_n})$ .

**Corollary 1** *If the rank  $r$  of the dimensional matrix is equal to  $n$ ,  $F$  must be a dimensionless constant. This is the most interesting situation occurring with dimensional analysis since solving the problem under consideration reduces to determining this dimensionless constant from simple physical arguments, from solving an ordinary differential equation, or from a single computer run, or from experiment.*

**Definition 1** If from  $\pi_1^{\sigma_1} \pi_2^{\sigma_2} \cdots \pi_{n-r}^{\sigma_{n-r}} = 1$  follows  $\sigma_1 = \sigma_2 = \cdots = \sigma_{n-r} = 0$  the  $\pi_i$ 's are called *independent*. If in a solution  $y = f(x_1, x_2, \dots, x_n)$  the number  $n$  of independent variables can be reduced at least by one we call it a *similarity solution*.  $f(x_1, x_2, \dots, x_n)$  is a *self-similar solution* if the number of dimensionless variables  $\pi_i$  reduces to a single variable. (In the Soviet literature all similarity solutions are often called self-similar. The authors do not follow this convention because there is effectively no need for it). It may be helpful to illustrate the use of the  $\pi$ -theorem by a few simple examples.

**Example 1 Stokes law** Assume a heavy sphere falling in deep water. What is the asymptotic velocity  $v$  of the sphere? One recognizes that a maximum number of variables is viscosity  $\mu$ , weight  $G$  and radius  $R$ . The dimensional matrix in the cgs system of units is presented in Table 2.5. Since its rank is  $r = 3$ ,  $F$  from (2.105) is a constant,  $F = C$ , and  $v$  is uniquely determined by

$$v = C \frac{G}{\mu R} = C' \frac{R^2 g}{\eta}; \quad \eta = \frac{\mu}{\rho}.$$

This is Stokes' formula with  $C = (6\pi)^{-1}$ . It provides a counter example for the frequently expressed contention that  $C$  is always near unity in a "physical problem". If instead of this choice one takes  $\mu$ ,  $\rho$ ,  $g$  and  $R$  as independent variables the rank of the matrix is still  $r = 3$  so that  $4 - 3 = 1$  dimensionless quantity  $\pi_1 = \rho^2 g R^2 / \mu^2$  can be formed and  $v$  is no longer uniquely determined. The reason is that  $\rho$ ,  $g$ ,  $R$  appear in the problem only in the combinations  $R$  and  $\rho R^3 g = 3G/4\pi$  and not as three independent quantities. The success of dimensional analysis depends crucially on the selection of the most restricted number of variables.

**Example 2 Harmonic oscillator** The motion of the harmonic oscillator  $m\ddot{x} + \kappa x = 0$  is completely determined by the quantity  $\kappa/m$  and the oscillation amplitude  $\hat{x}$ . The dimensions of the two quantities are  $s^{-2}$  and cm, respectively. The oscillation period therefore is independent of  $\hat{x}$  and is  $T = C(m/\kappa)^{1/2}$ . The unknown dimensionless constant  $C$  can be determined as follows. From elementary geometry it is known that by introducing a second oscillator  $m\ddot{y} + \kappa y = 0$  perpendicular to  $x$  with equal amplitude  $\hat{y} = \hat{x}$  but a difference in phase of  $\pi/2$  the trajectory  $x = (x, y)$  is a circle of radius  $R = \hat{x}$ . The only velocity that can be constructed from  $\hat{x}$  and  $\kappa/m$  is  $v = \hat{x}(\kappa/m)^{1/2}$ . This velocity equals  $2\pi R/T$  from which  $T = 2\pi(m/\kappa)^{1/2}$  follows.

**Table 2.5** Dimensional matrix of the falling sphere (left-hand side) and charged sphere (right-hand side) problem. In both cases  $r = 3$

	$\mu$	$G$	$R$	$v$		$q$	$p$	$\epsilon_0$	$R$
g	1	1	0	0	C	1	1	1	0
cm	-1	1	1	1	V	0	1	-1	0
s	-1	-2	0	-1	cm	0	-3	-1	1

All Galileo would have had to do is to verify that the oscillation period of his pendulum becomes independent of amplitude when the excursion is small. Then  $T = 2\pi(\ell/g)^{1/2}$  follows automatically.

**Example 3 Blast wave** How secret can the TNT equivalent of a bomb be kept? Consider a homogeneous atmosphere of mass density  $\rho_0$ . In one very restricted region the energy  $W$  is supplied instantaneously (“point explosion”). As a consequence, a blast wave, i.e., a strong shock propagates out into the surrounding space. Its position  $x_s(t)$  depends, under idealized conditions, on  $W/\rho_0$  and  $t$  only. From  $[W/\rho_0] = \text{cm}^5 \text{s}^{-2}$  and  $[x_s] = \text{cm}$  follows

$$x_s(t) = C \left( \frac{W}{\rho_0} \right)^{1/5} t^{2/5}. \quad (2.106)$$

By taking pictures of the blast wave at different times  $W$  is recovered with good accuracy. Subsequently, corrections may have to be made for radiation losses and amplification of the shock front by absorption of radiation. For the constant  $C$  and variants of the model, for example supply of the energy  $W$  to a vacuum-solid interface see [62, 63]. In the kbar pressure range the time-dependence  $\sim t^{2/5}$  in (2.106) has been confirmed recently in air [64].

**Example 4 Rayleigh–Taylor instability** Consider a fluid of density  $\rho_1$  superposed to a fluid of density  $\rho_2$  in a gravity field of acceleration  $g$ . Assume that the original horizontal interface extending in  $x$ -direction is subject to a vertical sinusoidal displacement  $y = y_0 \sin kx$ ,  $k = 2\pi/\lambda$ . It is known from ocean waves in deep water that the vertical motion decays exponentially over the depth of a wavelength  $\Delta y \simeq \lambda$ . Hence, the mass per unit length involved in the acceleration is  $(\rho_1 + \rho_2)(\lambda/s)$ . The gravity force acting on this mass per unit length is  $(\rho_1 - \rho_2)gy_0$ . This results in the equation of motion

$$\ddot{y}_0 + (s/\lambda)Ag y_0 = 0, \quad A = (\rho_2 - \rho_1)/(\rho_1 + \rho_2). \quad (2.107)$$

$A$  is the Atwood number. The complete analysis yields the dimensionless factor  $s = 2\pi$  for small perturbations  $y_0 \ll \lambda$ . For  $A > 0$  the liquid is stable fulfilling harmonic oscillations around  $y = 0$ . For  $A < 0$  the interface becomes Rayleigh–Taylor unstable,  $y_0(t) = \hat{y}_0 e^{\gamma t}$ , with the linear growth rate

$$\gamma = \sqrt{kAg}, \quad k = 2\pi/\lambda \quad (2.108)$$

[65, 66]. The exponential growth (and the harmonic oscillation) originates from the accelerated mass  $\sim \lambda$ .

**Example 5 Net charge of a cluster** As a last example the net charge  $q'$  of a hot plasma sphere (cluster) of positive charge  $q$  and radius  $R$  is considered. Evidently  $q' = qf(\pi_1, \dots)$ . The dimensionless function  $f$  depends on combinations of the equilibrium pressure  $p$ ,  $[p] = \text{VCcm}^{-3}$ , the dielectric constant  $\varepsilon_0$ ,

$[\varepsilon_0] = \text{CV}^{-1}\text{cm}^{-1}$ , and the radius  $R$ . The dimensional matrix, Table 2.5 (right-hand side), shows that  $q$ ,  $p$ ,  $\varepsilon_0$  must appear in the combination  $\varepsilon_0 p/q^2$  and hence the set of possible  $\pi$  variables is  $\pi_1 = \varepsilon_0 p R^{n+4}/(q^2 R^n)$  with  $n$  real and arbitrary. By choosing  $n = 2$ ,  $\pi_1 \sim \lambda_D^2/R^2$ , i.e.,  $q'/q$  is a function of  $\pi_1^{-1/2} \sim R/\lambda_D$ , in agreement with what was found in Sect. 2.1.3.

### 2.2.3.2 Adiabatic and Isothermal Rarefaction Waves in Plane Geometry

In a first approach the expansion of a laser plasma into vacuum can be modeled as follows: consider a half-space ( $x \leq 0$ ) filled with an ideal gas of uniform density  $\rho_0$ , temperature  $T_0$ , and pressure  $p_0$ . Suppose the surface pressure at  $x = 0$  is suddenly reduced to zero at  $t = 0$ . The subsequent dynamics is then governed by

$$\frac{\partial \rho}{\partial t} + \frac{\partial}{\partial x}(\rho v) = 0, \quad \rho \left( \frac{\partial v}{\partial t} + v \frac{\partial v}{\partial x} \right) = -s_0^2 \left( \frac{\rho}{\rho_0} \right)^{\gamma-1} \frac{\partial \rho}{\partial x}. \quad (2.109)$$

The adiabatic sound velocity is  $s = (\gamma p/\rho)^{1/2} = s_0(\rho/\rho_0)^{(\gamma-1)/2}$ . The isothermal case  $T = \text{const}$  is characterized by infinite thermal conductivity or an infinite number of degrees of freedom with  $\gamma = 1$ . Equations (2.109) show that  $\rho$  and  $v$  depend on  $\rho_0, s_0, x, t$ . From the corresponding dimensional matrix we deduce one dimensionless variable  $\pi = x/(s_0 t)$ . Therefore the system above reduces to ordinary differential equations for  $\rho = \rho_0 P(\pi)$ ,  $v = s_0 V(\pi)$ :

$$P'(V - \pi) + PV' = 0, \quad V' (V - \pi) + P^{\gamma-2} P' = 0,$$

where the prime denotes  $d/d\pi$ . By eliminating  $P'$  one obtains

$$V'(V - \pi)^2 - P^{\gamma-1} V' = 0, \quad \text{or} \quad \left( v - \frac{x}{t} \right)^2 = s^2.$$

Using this relation in one of the dimensionless conservation equations it follows that  $dv = -sd\rho/\rho$  and hence, for  $\gamma \neq 1$  (adiabatic case)

$$\rho(x, t) = \rho_0 \left[ 1 - \frac{\gamma-1}{2} \frac{v}{s_0} \right]^{\frac{2}{\gamma-1}}, \quad v = \frac{2}{\gamma+1} \left( \frac{x}{t} + s_0 \right). \quad (2.110)$$

For  $\gamma$  approaching unity (isothermal case)  $\rho$  becomes

$$\rho(x, t) = \rho_0 \lim_{\gamma \rightarrow 1} \left( 1 - \frac{\gamma-1}{2} \frac{v}{s_0} \right)^{\frac{2}{\gamma-1}} = \rho_0 e^{-\frac{v}{s_0}} = \rho_0 e^{-\left(1 + \frac{x}{s_0 t}\right)}. \quad (2.111)$$

These solutions hold in the interval  $-s_0 t \leq x \leq \frac{2}{\gamma-1} s_0 t$ . The rarefaction wave propagates with the phase velocity  $v_\phi = s_0$  into the undisturbed gas. For any instant  $t > 0$  the front of the rarefaction wave  $x_F$  moves with constant speed

$v_F = 2s_0/(\gamma - 1)$ . For  $\gamma = 5/3$ ,  $v_F = 3s_0$ . For this case the rarefaction wave is shown in Fig. 2.6 before it collides with the wall at  $V_2$ .

It is interesting to calculate the heat flow density  $q(x, t)$  which is needed for maintaining the temperature at the constant value  $T_0$ . From the energy equation

$$\frac{3}{2}nk_B \frac{dT}{dt} = -p \frac{\partial v}{\partial x} - \frac{\partial q}{\partial x} = 0$$

we obtain

$$\begin{aligned} q(x, t) &= - \int_x^\infty p \frac{\partial v}{\partial x} dx = -s_0^3 \rho_0 \int_{v(x)/s_0}^\infty \exp\left(-\frac{v}{s_0}\right) d\left(\frac{v}{s_0}\right) \\ &= s_0^3 \rho = ps_0. \end{aligned} \quad (2.112)$$

This is a useful formula for deducing a criterion for nearly isothermal plasma expansion in regions where the flow is planar. In fact, from (2.64) follows  $ps_0 = \kappa_0 T_e^{5/2} |\partial T_e / \partial x|$ . If the dimension of the plane region is  $L$  and  $\Delta p$  is the pressure difference at its end points, then the fractional temperature difference

$$\frac{\Delta T_e}{T_e} \simeq L \frac{s_0 \Delta p}{\kappa_0 T_e^{7/2}} \quad (2.113)$$

must be much smaller than unity. In the adiabatic rarefaction wave  $q$  is zero and no entropy increase occurs by the expansion into vacuum.

With the discovery of fast ion jets from solid targets produced by intense fs laser pulses ion separation in the accelerating electrostatic field accompanying the plasma rarefaction wave has gained new interest. Electron-ion charge separation, originally studied under idealized conditions by Gurevich et al. [67], as well as maximum ion energy and ion energy spectrum have been investigated in great detail in [68] for isothermal targets filling a halfspace and for isothermal thin targets of finite mass [69]. A self-similar solution of expansion of finite mass targets into vacuum in plane, cylindrical and spherical geometry is presented in [70]. Full account is taken of charge separation effects, and the position of the ion front and the asymptotic energy of accelerated ions are calculated analytically. Generalization to a two-temperature electron system reveals the conditions under which the high-energy tail of accelerated ions is determined solely by the hot-electron population. See also [71] on the acceleration of a test ion in a dynamic planar electron sheath, [72] on high energy proton acceleration by short laser pulses interacting with dense plasma targets, and [73] on efficient generation of quasimonoenergetic ions by Coulomb explosions of optimized nanostructured clusters.

The spherical rarefaction wave cannot be solved by dimensional analysis since the initial radius  $r_0$  of the gas cloud enters as an additional independent variable. Only for  $t = d/s_0$ , corresponding to distances  $d \ll r_0$ , is the expansion planar

and it becomes clear that the front  $r_F$  moves at constant velocity  $v_F$  at all times which is the same as in planar geometry. However, with the aid of an additional assumption the authors of [74] were able to obtain a spherical self-similar solution of nanocluster explosion. Of particular relevance for various applications is a demixing and energy selection process occurring in spherical geometry. Clusters in the Coulomb explosion mode, i.e., when all free electrons have escaped from the cluster (“outer ionization” degree equals unity), are capable of generating monoenergetic beams of fast ions. A mixture of ions of different charge to mass ratio  $\alpha$  is unstable against uniform mixing. Under appropriately chosen mixing ratios the component with higher  $\alpha$  is accelerated to nearly monochromatic energies in the Coulomb field of the heavy ions [74].

### 2.2.3.3 The Nonlinear Heat Wave and Huntley’s Addition

Here we solve the following nonlinear heat conduction problem by dimensional analysis [75]. A quantity of energy per unit area  $Q_0$  is instantaneously released at  $t = 0$  in a plane of a solid, liquid or gas from which it diffuses according to the nonlinear equation into its interior

$$\frac{\partial T}{\partial t} = a \frac{\partial}{\partial x} \left( T^\alpha \frac{\partial T}{\partial x} \right); \quad a = \frac{\kappa_0}{c_V}, \quad (2.114)$$

$c_V$  specific heat. For heat conduction in a fully ionized plasma the exponent has to be taken  $\alpha = \frac{5}{2}$ ; with other appropriate values of  $\alpha$  it describes radiation transport. It is easy to show that for  $\alpha > 0$  the heat front coordinate  $x_T(t)$  is finite. For  $\alpha = 0$  (constant thermal conductivity)  $x_T = \infty$  for all  $t > 0$ . The temperature  $T$  will depend on  $q_0 = Q_0/c_V$ ,  $x$  and  $t$ . This leads to the conclusion that only one dimensionless variable

$$\pi = \frac{x}{(aq_0^\alpha t)^{1/(\alpha+2)}}$$

exists (see Table 2.6) and that  $x_T(t)$  and the maximum temperature  $T_0$  (at  $x = 0$ ) are uniquely determined by

$$x_T(t) = A(aq_0^\alpha t)^{1/(\alpha+2)}, \quad T_0(t) = B \left( \frac{q_0^2}{at} \right)^{1/(\alpha+2)}.$$

With  $BT(x, t) = T_0 f(\pi)$ . Equation (2.114) reduces to the ordinary differential equation

$$(\alpha + 2) \frac{d}{d\pi} \left( f^\alpha \frac{df}{d\pi} \right) + \pi \frac{df}{d\pi} + f = 0. \quad (2.115)$$

**Table 2.6** Dimensional matrix in cgsK units for solving (2.114).  $r = 3$ 

	$q_0$	$a$	$x$	$t$
cm	1	2	1	0
s	0	-1	0	1
K	1	$-\alpha$	0	0

The solution is

$$\begin{aligned}
 T(x, t) &= T_0 \left( 1 - \frac{x^2}{x_T^2} \right)^{\frac{1}{\alpha}}, \quad x_T = A(a q_0^\alpha t)^{1/(\alpha+2)}, \quad \int_0^{x_T} T dx = q_0. \\
 A &= \left[ 2 \frac{\alpha+2}{\alpha} \left( \frac{2\Gamma\left(\frac{3}{2} + \frac{1}{\alpha}\right)}{\Gamma\left(\frac{1}{2}\right)\Gamma\left(\frac{1}{\alpha} + 1\right)} \right)^\alpha \right]^{\frac{1}{\alpha+2}}; \quad \alpha = 5/2 \Rightarrow A = 1.480. \\
 B &= A^{2/\alpha} \left( \frac{\alpha}{2(\alpha+2)} \right)^{1/\alpha} \\
 T_0(t) &= \frac{q_0}{x_T(t)} \frac{2\Gamma\left(\frac{3}{2} + \frac{1}{\alpha}\right)}{\Gamma\left(\frac{1}{2}\right)\Gamma\left(\frac{1}{\alpha} + 1\right)}, \quad \langle T \rangle = \frac{q_0}{x_T(t)}. \tag{2.116}
 \end{aligned}$$

For electron heat conduction  $\alpha = 5/2$ ; for this case,

$$T = T_0 \left( 1 - \frac{x^2}{x_T^2} \right)^{2/5}, \quad x_T = A q_0^{5/9} \left( \frac{\kappa_0}{c_V Z} t \right)^{2/9}, \quad \frac{T_0}{\langle T \rangle} = 1.223. \tag{2.117}$$

As  $\alpha$  increases the temperature assumes a rectangle-like distribution. At the beginning the heat diffusion speed tends to infinity and soon after it slows down drastically (Fig. 2.7).

Another relevant situation is given when the heat applied to the surface is delivered continuously with the power law

$$\Phi = \frac{I}{c_V} = B t^\gamma.$$

If one looks for solutions of the form  $T(x, t) = A(vt^\beta - x)^\delta$  one finds  $\beta = 1$ ,  $\gamma = \delta = 1/\alpha$ . At the boundary  $x = 0$   $\Phi = -aT^\alpha \partial T / \partial x$  must hold. Inserting this in (2.114) yields

$$T(x, t) = \left[ \frac{\alpha v}{a} (vt - x) \right]^{1/\alpha}, \quad v = \dot{x}_T = B^{\alpha/(\alpha+2)} \left( \frac{a}{\alpha} \right)^{1/(\alpha+2)}. \tag{2.118}$$

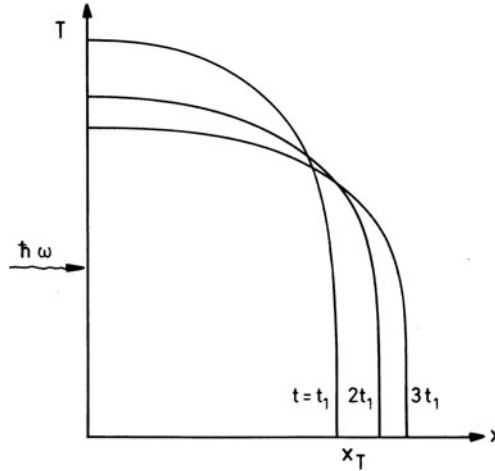


**Fig. 2.7** Nonlinear electron heat wave at three equidistant time intervals  $t_1, 2t_1, 3t_1$  in a medium at rest. The power of  $T$  in the thermal conductivity is  $\alpha = 5/2$ . At  $t = 0$  the diffusion speed is infinite;  $x_T \sim t^{2/9}$

In the frame moving with  $x_T$  this heat wave is stationary. Another exact solution exists for a quantity  $Q = cvq_0$  of heat suddenly released from a point into a half space filled with an isotropic homogeneous medium at rest. Since the procedure is the same as in the plane case only the final result is reported [75]:

$$\begin{aligned}
 T(r, t) &= T_0 \left(1 - \frac{r^2}{r_T^2}\right)^{1/\alpha}, \quad r_T = A'(aq_0^\alpha t)^{1/(3\alpha+2)} \\
 A' &= \left(2 \frac{3\alpha+2}{\alpha\pi^\alpha}\right)^{1/(3\alpha+2)} \left\{ \frac{\Gamma\left(\frac{5}{2} + \frac{1}{\alpha}\right)}{\Gamma\left(1 + \frac{1}{\alpha}\right)\Gamma\left(\frac{3}{2}\right)} \right\}^{\alpha/(3\alpha+2)}, \\
 T_0 &= \frac{4q_0}{\pi^{3/2}r_T^3} \frac{3\alpha+2}{2\alpha} \frac{\Gamma\left(\frac{3\alpha+2}{2\alpha}\right)}{\Gamma\left(\frac{1+\alpha}{\alpha}\right)}. \tag{2.119}
 \end{aligned}$$

In particular with  $\alpha = 5/2$ ,

$$\begin{aligned}
 T &= T_0 \left(1 - \frac{r^2}{r_T^2}\right)^{2/5}, \quad r_T = q_0^{5/19} A' \left(\frac{\kappa_0}{c_V Z} t\right)^{2/19}, \\
 T_0 &= 0.9893 q_0^{4/19} \left(\frac{c_V Z}{\kappa_0 t}\right)^{6/19}, \quad A' = 1.144. \tag{2.120}
 \end{aligned}$$

$r_T$  decreases extremely rapidly with time.

The temperature  $T$  in our treatment has the dimension of Kelvin (K). By assigning such a dimension  $T$  is assumed as a separate physical entity. However, it is equally legitimate to define  $T$  as the ratio of two energies. In this latter case  $T$  is a pure number; the unit K disappears from the dimensional matrix and the rank  $r$  is reduced to  $r = 2$ : the transition from (2.114) to (2.115) is no longer possible in the pure cgs-system of units. The important question arises which system of units should be used in dimensional analysis. The answer was given by H. E. Huntley [76].

**Huntley's addition:** In problems of dimensional analysis take the maximum possible number of independent units. For example, in some cases it is possible to distinguish between masses in the  $x$  and  $y$  directions or between "inertial" and "thermal" masses as separate physical entities. In this way problems were solved successfully by dimensional analysis that were not reducible a priori by the  $\pi$ -theorem. A necessary implication for the success of Huntley's method is that in the process under consideration there is no interaction between the quantities that are given different dimensions.

The interested reader may consult with profit several other volumes on dimensional analysis in addition to Sedov [77–82]. The successful application of dimensional analysis and similarity considerations to continuum mechanics and hydrodynamics sometimes led to the conclusion that dimensional analysis would be appropriate mainly to these disciplines. Only rather recently has it become apparent that the application of Buckingham's  $\pi$ -theorem is not limited to such fields; it should also be important for example in quantum field theory and the theory of phase transitions [83]. Its successful application in biology was demonstrated for example by Günther [84–86].

There are several solutions relevant for laser matter interaction which are not self-similar but become asymptotic solutions of this type. An example is the analytical treatment of homogeneous pellet compression for laser fusion with a behavior in time for  $\rho$ ,  $v$  and  $T$  according to Kidder [48]

$$\rho, v, T \sim \frac{1}{[1 - (t/t_0)^2]^{3/2}} = f(t).$$

For instance,  $\rho(R, t) = \rho_0(R/R_0)^2 f(t)$  is not self-similar. However, for  $t$  approaching the instant of collapse  $t_0$  it comes arbitrarily close to

$$\rho = \frac{\rho_0}{2^{3/2}} \left( \frac{t_0^{1/2} R^{2/3}}{R_0^{2/3} \tau^{1/2}} \right)^3, \quad \tau = t_0 - t,$$

which is self-similar. Kidder's solutions are interesting also from the topological point of view: The void in a spherical shell only closes at  $t = t_0$  when the whole pellet shrinks to a point, as is required from the topological considerations of Sect. 2.2.1.

In connection with converging shocks and compression waves Zeldovich [75] introduced a second “type of self-similar” solutions, a concept which was developed further by Barenblatt [83] with his formulation of intermediate asymptotics. Such a distinction may sometimes be justified from a practical point of view, but from a fundamental point of view no second class of similarity exists. In order to make sense for subdivision into similarities of the first and second kind all similarity problems should belong to these two classes. However, in view of certain solutions [87] a third class of similarity solutions would have to be introduced, and, it is not difficult to imagine that soon a fourth and fifth kind of similarity would have to be invented for other problems. Eventually some further progress beyond Buckingham’s theorem may come from group theoretical methods and the determination of symmetry groups of differential equations [88, 89]. For the diffusion equation (2.114) with  $\alpha = -2$  (e.g., magnetic field diffusion) see in this context Euler et al. [90]. For symmetry properties of Euler-type plasma equations including magnetic fields see [91].

### 2.2.3.4 Plane Shock Wave

The momentum which can be transmitted to a medium by a linear sound wave of intensity  $I$  is given by the wave pressure  $p_w$ ,

$$p_w = \frac{I}{s} (1 + R), \quad (2.121)$$

where  $R$  is the reflection coefficient and  $s$  is the sound speed. A hot plasma expanding from the surface of dense matter, e.g., of a solid, acts like a piston of very high strength. The effect is the generation of a compression wave the intensity of which is far beyond the limit of a linear wave. A compression wave in quasineutral matter steepens until a discontinuity or a steep, narrow transition region has formed. For example, when an ideal gas of density  $\rho_0$ , temperature  $T_0$  and pressure  $p_0$  at rest is compressed by a piston moving at constant speed  $v_1$  a compression wave with spatially constant values  $\rho_1$ ,  $T_1$ ,  $p_1$ ,  $v_1$  builds up which is separated from the undisturbed gas by a transition layer a few mean free path lengths thick. Such a structure is called a shock wave (Fig. 2.8). It propagates with the shock velocity  $v_s$ . For such a discontinuity or transition layer to be stationary  $v_s$  must be supersonic with respect to the undisturbed medium,  $v_s > s_0$ ; otherwise a rarefaction wave would develop at its front.

In a system moving with  $v_s$  the shock wave is stationary and matter flows with velocity  $u_0 = -v_s$  into the discontinuity and streams out of it at the speed  $u_1 = v_1 - v_s$ . The two regions are connected by the continuity of mass, momentum and energy flows. The latter are obtained by integrating the equations of motion in the conservative form across the transition zone and by setting all partial derivatives with respect to time to zero. Then, when  $\pi = 0$ ,  $I = 0$ ,  $\mathbf{q}_e = 0$  the Rankine–Hugoniot relations follow from (2.54), (2.77) and (2.79),

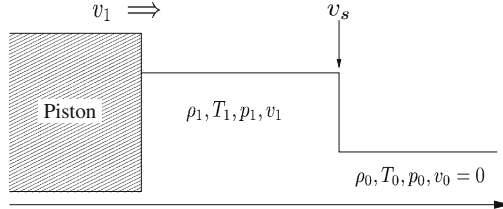


**Fig. 2.8** Shock wave driven by a piston moving at speed  $v_1 = \text{const}$  propagates with phase velocity  $v_s$  into an undisturbed gas at rest of density  $\rho_0$  and temperature  $T_0$

$$\begin{aligned} \rho_1 u_1 &= \rho_0 u_0, \\ p_1 + \rho_1 u_1^2 &= p_0 + \rho_0 u_0^2, \\ \varepsilon_1 + \frac{p_1}{\rho_1} + \frac{1}{2} u_1^2 &= \varepsilon_0 + \frac{p_0}{\rho_0} + \frac{1}{2} u_0^2. \end{aligned} \quad (2.122)$$

$\varepsilon$  is the internal energy per unit mass. On eliminating  $u_0$ ,  $u_1$  from (2.122) one arrives at the Hugoniot equation of state,

$$\varepsilon_1 - \varepsilon_0 = \frac{1}{2} (p_0 + p_1) \left( \frac{1}{\rho_0} - \frac{1}{\rho_1} \right), \quad (2.123)$$

i.e., at the change a volume element undergoes from state  $\rho_0, p_0, \varepsilon_0$  to state  $\rho_1, p_1, \varepsilon_1$  when crossing the shock front.

For an ideal gas, or dilute fully ionized plasma, from (2.122) one calculates the following changes as functions of the Mach number  $M = v_s/s_0$  and  $\gamma = \gamma_e = \gamma_i$  in a straightforward way:

$$\kappa = \frac{\rho_1}{\rho_0} = \frac{(\gamma + 1)M^2}{(\gamma - 1)M^2 + 2}; \quad \frac{T_1}{T_0} = \frac{2\gamma M^2 + 1 - \gamma}{(\gamma + 1)\kappa}. \quad (2.124)$$

For  $M$  or the piston pressure  $p_1$  tending to infinity the compression ratio  $\kappa$  reaches the asymptote  $\kappa = (\gamma + 1)/(\gamma - 1)$ . For a hot plasma this has the value 4. Owing to the violent entropy production in the shock front,  $\kappa$  cannot exceed this limit, in contrast to an adiabatic compression following (2.88) where  $\kappa$  reaches arbitrarily high values. A shock is given the name *strong shock* when  $\kappa$  can be approximated by  $\kappa = (\gamma + 1)/(\gamma - 1)$ . Formally one arrives at this ratio by disregarding  $p_0$  in the Rankine-Hugoniot relations. As long as the width of the shock front is much smaller than its curvature radius equations (2.122), (2.123), (2.124) are equally valid for spherical shocks. This is not true in the center of a converging shock, where much higher values of  $\kappa$  are reached [92, 93]. When a second plane shock is superimposed on the first one the overall compression is  $\kappa = \kappa_1 \kappa_2$ . However, as soon as their two fronts merge a rarefaction wave starts from that point which causes  $\kappa$  to be instantaneously reduced there to a value not exceeding the asymptote  $(\gamma + 1)/(\gamma - 1)$ .

Only in the presence of a cooling mechanism (e.g., ionization, radiation losses; see, e.g., [94]) can a higher  $\kappa$  be reached at the front.

It is useful and physically illuminating to deduce the balance equations (2.122) in the lab frame. The amount of matter compressed per unit time is  $\rho_1(v_s - v_1)$ . The overall force per unit area acting on an arbitrary volume which includes the shock front is  $p_1 - p_0$ . This difference must be equal to the momentum change per unit time  $\Delta mv_1 = \rho_0 v_s v_1$ . In a strong shock this quantity is equated to  $p_1$ . Finally, the work done by two planes including the shock front per unit time and unit area is  $p_1 v_1$ . This leads to a change of kinetic and internal energy  $\rho_0 v_s (\varepsilon_1 - \varepsilon_0 + v_1^2/2)$ . Summarizing one obtains

$$\begin{aligned} \rho_0 v_s &= \rho_1(v_s - v_1), \quad p_1 - p_0 = \rho_0 v_s v_1, \\ p_1 v_1 &= \rho_0 v_s \left( \varepsilon_1 - \varepsilon_0 + \frac{v_1^2}{2} \right). \end{aligned} \quad (2.125)$$

By changing to the relative speeds  $u_0, u_1$  system (2.122) follows. From the first equation the relation between  $v_1, v_s$  and  $\kappa$  is deduced,

$$v_1 = v_s \left( 1 - \frac{1}{\kappa} \right). \quad (2.126)$$

By a properly programmed piston which avoids intermediate shock formation arbitrarily high density values are attainable. For plane geometry the situation is sketched in Fig. 2.9. Infinite density is reached after  $t = \tau$  at position  $x_0$  if the piston (coordinate  $x_p$ ) of Fig. 2.8 moves according to

$$x_p(t) = \frac{x_0}{\gamma - 1} \left\{ \gamma + 1 - 2 \frac{t}{\tau} - (\gamma + 1) \left( 1 - \frac{t}{\tau} \right)^{2/(\gamma+1)} \right\}; \quad t \leq \tau.$$

$x_p$  is obtained from the requirement that all characteristics  $v_1 + s_0$  (straight lines,  $v_1 = \dot{x}_p(t)$ ) converge to the point  $(x_0, \tau)$ . Generally, when a piston is not properly timed some characteristics intersect earlier; from such intersections shock fronts originate and concomitant entropy production opposing the compression sets in.

The plasma produced by laser breakdown at the surface of a solid acts like a semi-transparent, very energetic piston. In Fig. 2.10 the dynamics of crater formation and plasma outflow is simulated [95]. A laser beam of  $10^{15} \text{ Wcm}^{-2}$  peak intensity impinges on a hydrogen target. At the very beginning the target is transparent to the laser light. After breakdown has occurred, the electron density  $n_e$  soon reaches values higher than the critical value  $n_c$ , given by (2.94), at its surface and stops the beam there by metal-like reflection, as well as by collisional and resonance absorption. The electron temperature rises to several keV and the plasma expands, thereby enabling the beam to penetrate to deeper layers of matter which successively undergo the same process of collisional ionization, heating and expansion. The hot plasma acts like a semipermeable piston onto the target. As a consequence, a strong

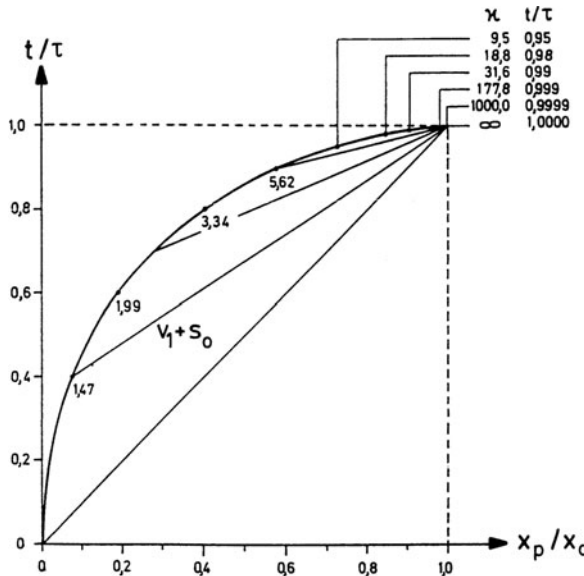


**Fig. 2.9** Fast adiabatic compression in plane geometry. The piston starts from rest and its acceleration is so controlled that all Mach lines  $v + s$  starting from the face of the piston intersect in the point (1,1). The numbers entered along the distance-time curve of the piston represent the compression ratio  $\kappa$  immediately in front of the piston

shock propagates at a typical speed of several  $10^7 \text{ cm/s}$  through the target (dark semicircle in the figure), leaving behind a crater as depicted in Fig. 2.11. Most of the matter removed has escaped by flowing out of the target more or less tangentially to the shock wave, very similar to the fluid flow which originates from the supersonic impact of a projectile on dense matter. Only a small fraction of the matter removed is transformed into hot plasma. The tangential flow component is also responsible for the reduced compression ratio of  $\kappa = 2.8$  in the shock of Fig. 2.10, instead of  $\kappa = 4$ . Only when the diameter of the laser beam is increased by a factor 3–5 is  $\kappa = 4$  reproduced numerically. This is a general phenomenon and occurs also in far more sophisticated numerical codes [14]. The correct value is  $\kappa = 4$  because the one-dimensional Rankine–Hugoniot relations (2.122) apply. Numerics cannot resolve the shock; it averages over an extended domain, in this way producing lower values of compression. By spherically illuminating pellets of several hundreds of  $\mu\text{m}$  in diameter lateral flow is avoided and all ablated matter is transformed into hot plasma. The plasma outflow generates a strong spherically converging compression wave. In this way compressions as high as  $\kappa = 600$  times solid hydrogen density have been achieved with the GEKKO XII laser, with the best result of  $\kappa = 1000$  [97–99]. Recently this value has been reconfirmed in direct drive experiments with the Omega laser system at LLE, Rochester University (oral announcement on IFSA2007, Kobe, Sept. 9–14).

An interesting variant of compression wave is represented by the collisionless shock. At high laser intensity  $I \gtrsim 10^{18} \text{ Wcm}^{-2}$  the light pressure at the target

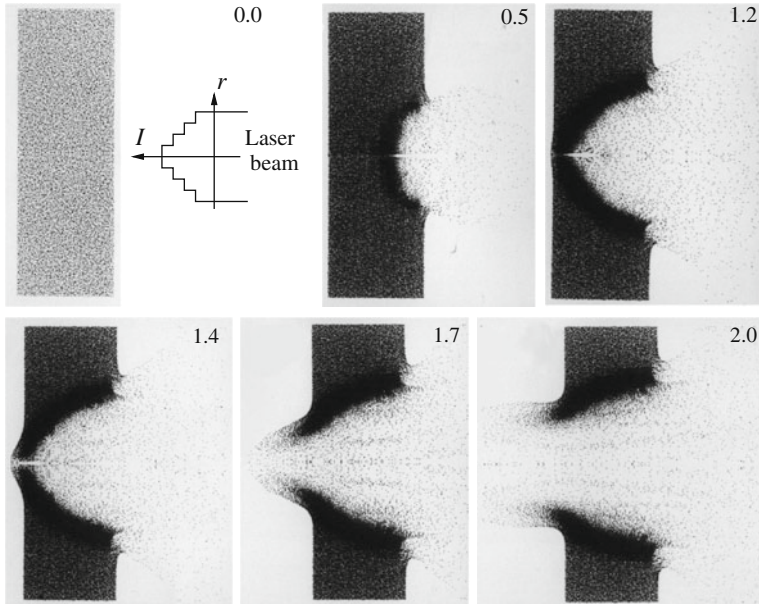


**Fig. 2.10** Laser-solid hydrogen target interaction at  $t = 0, 0.5, 1.2, 1.4, 1.7$  and  $2.0$  ns. Laser intensity  $I = 10^{15} \text{ Wcm}^{-2}$ , beam radius = 4 cells, with intensity distribution as indicated, target size =  $9 \times 30$  cells, critical density  $n_c = n_0/10, n_0 = 5 \times 10^{22} \text{ cm}^{-3}$ . Particle number per cell = 49. The shock width is due to numerical diffusion; in reality it is smaller by orders of magnitude

surface acts like an extremely energetic piston on the electrons into the direction of the laser beam. The electrons are pushed into the dense target until an electrostatic potential  $\Phi$  has built up in the ion layer remaining behind whose strength is capable of fulfilling the steady state momentum equation with  $p_1$  replaced by  $\rho_1 e\Phi/m_i$  in (2.122). Under idealized conditions the internal energy  $\varepsilon$  and the undisturbed pressure  $p_0$  can be neglected so that the motion of the single particles is one-dimensional with  $r = 1$  degree of freedom. Hence  $\gamma = 3$  and the compression becomes  $\kappa = (\gamma + 1)/(\gamma - 1) = 2$ . It reveals once more that in order to reach high compression in a plane shock  $\gamma$  must come as close as possible to unity. However, this is possible only in a system with a high effective number of degrees of freedom  $r$ , as represented by complex molecules and cooling mechanisms (sink of energy like ionization, diffusive and radiative heat conduction). Ponderomotive ion acceleration by relativistic laser pulses is a prominent example of collisionless shock generation [100].

### 2.3 Laser Plasma Dynamics

In this section the dynamics of the hot laser plasma is treated. At moderate laser intensities,  $I \lesssim 10^{14} \text{ Wcm}^{-2}$ , collisional ionization prevails over multiphoton ionization as soon as a modest fraction of electrons has been set free. In the subse-



**Fig. 2.11** Crater produced in copper by a focused Nd laser beam of  $E = 10\text{ J}$ ,  $\tau = 10\text{ ns}$  [96]. Ni-Layer is for protection only

quent heating process a plasma from low  $Z$  material can be considered as fully ionized to a good approximation and the ionization energy can be disregarded in a first approach. The dynamics of the plasma is then well described by the two-fluid equations (2.65), (2.66), (2.67), (2.68) and (2.69), with the absorption coefficient taken from (2.70). The latter relation is only true if, as we assume here, collisional absorption dominates all other heating mechanisms. In simplifying (2.68) and (2.69) one can go one step further by postulating  $T_i = T_e$ , or alternatively  $T_i = 0$  to avoid the solution of the ion energy equation. But even then it is not possible to solve the remaining three balance equations analytically in plane or spherical geometry. The dynamics depends crucially on the time-dependence of the laser pulse. If the laser intensity at the surface of a solid target rises nearly instantaneously, say during a few ps, three different scales in time as well as in space have to be distinguished:

First, due to violent ionization an overdense plasma of solid state density is formed, the thickness of which is of the order of the skin depth  $\delta_s = c/\omega_p \ll \lambda_{\text{Nd}}$ .

Secondly, an electron heat wave propagates into the undisturbed solid with a front coordinate  $x_T(t) = \kappa_0^{2/9} (I^5/c_V^7)^{1/9} t^{7/9}$ . This formula is easily recovered from dimensional considerations in analogy to (2.117). For  $t \rightarrow 0$ ,  $\dot{x}_T$  tends to

infinity which is characteristic of any continuum model of diffusion. From physical considerations it is clear that the real maximum speed is  $\dot{x}_T \lesssim v_{\text{th},e} \simeq s_e$ .

In the third stage the plasma rarefies towards the vacuum with ion sound speed  $s \ll s_e$  and, as the front of the heat wave slows down according to  $\dot{x}_T \sim t^{-2/9}$  a shock wave propagating into the solid builds up as soon as  $\dot{x}_T < \frac{2}{\gamma-1}s$  is fulfilled (see  $v_F$  after (2.111)). From now on a significant amount of the absorbed laser energy originally stored in the electron fluid is transformed into kinetic energy of the plasma, i.e., of the ion fluid.

Owing to the complexity of laser induced plasma dynamics pure cases are of particular interest. Therefore in the following, instantaneous heating by powerful lasers in plane geometry, collisional heating and plasma expansion in plane and spherical geometry with long laser pulses of moderate intensity, similarity solutions as well as steady state plasma production are treated.

### 2.3.1 Plasma Production with Intense Short Pulses

With respect to the achievement of dense, high temperature plasmas the most economic heating is realized when the energy input is so fast that the plasma is heated before any appreciable motion sets in and hence all the absorbed energy is converted into thermal energy. Let us assume that a laser pulse of sub-ns duration  $\tau$  impinges onto the target. Let the absorbed energy per unit area, which is deposited at the surface of the target, be  $q_0 = \int_{-\infty}^{\tau} I_a dt$ ,  $I_a$  absorbed intensity. Then in plane geometry, with  $T_e = T_i = T$  the system (2.65), (2.66), (2.67), (2.68), and (2.69) reduces to the heat diffusion equation (2.114) with  $\alpha = 5/2$ . The specific heat per unit volume is  $c_V = 3n_0(Z + 1)k_B/2$ . The temperature  $T(x, t)$  and its front  $x_T(t)$  are given by (2.117). The value of  $T_0/\langle T \rangle = 1.223$  shows that the temperature profile is roughly approximated by a rectangle. In order to apply these results to heating with ultrashort light pulses and to calculate the amount of heated matter we keep in mind that the lifetime  $\tau_p$  of the solid state density plasma is approximately determined by the rarefaction wave which travels with the isothermal sound velocity  $s = \sqrt{(p_e + p_i)/\rho_0}$  into the heated material. The heat wave stops when the edge of the rarefaction wave reaches the front of the heat wave, i.e., when [101]

$$\int_0^{\tau_p} s dt = x_T(\tau_p).$$

This relation yields the following expressions for the lifetime  $\tau_p$ , thickness of the heated slab  $x_T(\tau_p)$ , and maximum temperature  $T(\tau_p)$  at the instant  $\tau_p$ :

$$\tau_p = \frac{2}{3} \left( \frac{8}{9} \right)^{3/2} A^{9/4} k_B^{-7/4} \kappa_0^{1/2} \frac{m_i^{3/4}}{n_0 Z^{1/2} (Z + 1)^{7/4}} q_0^{1/2}, \quad (2.127)$$

$$x_T(\tau_p) = \frac{2}{3} \left( \frac{8}{9} \right)^{1/3} A^{3/2} k_B^{-7/6} \kappa_0^{1/3} \frac{m_i^{1/6}}{n_0 Z^{1/3} (Z+1)^{7/6}} q_0^{2/3}, \quad (2.128)$$

$$T(\tau_p) = \frac{q_0}{c_V x_T(\tau_p)} = \left( \frac{8}{9} \right)^{1/3} A^{-3/2} k_B^{1/6} \kappa_0^{-1/3} \frac{Z^{1/3} (Z+1)^{1/6}}{m_i^{1/6}} q_0^{1/3}. \quad (2.129)$$

The constant  $A$  is given by (2.116). Note that  $T(\tau_p)$  does not depend on the initial particle density  $n_0$  and depends only weakly on the absorbed energy per unit area  $q_0$ .  $T(\tau_p)$  represents an upper limit for the temperature since at the instant  $\tau_p$  a considerable fraction of the energy is already converted into kinetic energy: if an isothermal rarefaction wave is assumed (worst case) the ratio of kinetic energy to thermal energy at the instant  $\tau_p$  is  $2/3$ .

The above relations are valid for  $T_i = T_e$ . For the other limiting case of cold ions,  $T_i = 0$ , one has merely to substitute  $Z + 1$  by  $Z$  in (2.127), (2.128), and (2.129). In reality the ions are expected to be heated to a certain degree since the electron-ion relaxation time  $\tau_{ei} = m_i/2m_e v_{ei}$  can be shown to be of the same order of magnitude as  $\tau_p$ . In fact, with the relation  $s\tau_p \approx x_F \approx (\kappa_e \tau_p / c_V)^{1/2}$  which follows from (2.127), (2.128) and  $\kappa_e/c_V = \frac{1}{3}\lambda_e v_{th,e}$  one obtains

$$\tau_p \approx \frac{1}{s^2} \frac{\kappa_e}{c_V} = \frac{1}{s^2} \frac{\lambda_e v_{th,e}}{3} \approx \frac{m_i}{kT_e} \frac{v_{th,e}^2}{3v_{ei}} = \frac{m_i}{2m_e} \frac{1}{v_{ei}} = \tau_{ei}.$$

Therefore, when effects are calculated for which the ion temperature enters very sensitively, e.g., neutron production, the ion temperature has to be evaluated accurately [102, 103]. The expansion of the plasma into vacuum for times  $t \leq \tau_p$  and over distances  $\Delta x$  less than the focal radius are approximately described by the plane rarefaction wave (2.110) or (2.111), respectively.

The foregoing model assumes  $\tau \ll \tau_p$ . With long pulses it depends on the rise time of the laser intensity whether or not a thermal or a shock wave develops earlier. If the intensity rises too slowly heat conduction only influences the expanding plasma and not the undisturbed or shocked solid. The problem was solved by Anisimov [104]. Let the absorbed intensity  $I_a(t)$  be such that  $\langle T \rangle$  varies as  $t^\lambda$ . Then

$$\dot{x}_T \simeq \frac{d}{dt} (a T^{5/2} t)^{1/2} \sim t^{(5\lambda-2)/4},$$

whereas the rarefaction wave travels at the speed of sound  $s \sim \langle T \rangle^{1/2} \sim t^{\lambda/2}$ . Comparing the two speeds leads to distinguishing the following situations:

- (a)  $\lambda > \frac{2}{3}$ : For a certain time  $\tau_p$  after the start of irradiation the sound velocity is greater than the penetration velocity of the thermal wave. Thus the process of plasma production at the beginning will be governed by the dynamics of plasma expansion.
- (b)  $\lambda = \frac{2}{3}$ : Both velocities  $\dot{x}_T$  and  $s$  obey the same power law. The dominating energy transport mechanism, either mass flow or heat conduction, is determined

by the coefficients  $A$  and  $B$  of the relations  $v_T = At^{1/3}$  and  $s = Bt^{1/3}$ . If the heat conduction is the dominating process ( $\dot{x}_T > s$ ), one can use the energy equation for a stationary medium without motion to calculate the time variation of the absorbed energy flux density  $\Phi(t)$ . From  $I(t) \propto d[x_T(t)\langle T(t) \rangle]/dt$ , it follows that the dependence is linear,  $I_a(t) \sim t$ .

- (c)  $\lambda < \frac{2}{3}$ : This is just the inverse case to (a). Up to a time  $\tau_p$ , heat conduction is the dominating energy transport mechanism. During this time the absorbed radiation intensity varies as  $t^\alpha$  with  $\alpha < 1$ . The stationary heat wave (2.116) with  $I_a \sim t^{2/9}$  belongs to this class.

The heat wave model was shown to be consistent with experiments performed with 10 ps Nd laser pulses of intensities up to  $3 \times 10^{15} \text{ Wcm}^{-2}$  by Salzmann [105]. The measured electron temperatures in deuterium and carbon targets at 1 J pulse energy were 500 and 200 eV, respectively.

The model presented in this section is based on Spitzer–Braginskii’s thermal conductivity following a power law  $\kappa_e \sim T_e^\alpha$  [see (2.64)]. Subsequent to experiments showing the failure of such a simple local law [106] an avalanche-like enterprise started to investigate experimentally as well as theoretically phenomena of *heat flux inhibition*, nonlocal and anomalous transport. Despite the enormous effort concentrated on electron (and radiative) heat transport the problem is still far from a satisfactory solution. To the reader who wishes a deeper insight in what the current state of the art is may start from the review article by Bell [107] and then consult more recent papers [108–113]. Perhaps only now with the advent of greatly improved multidimensional particle-in-cell (PIC) and Vlasov codes [114–118] is there a chance to come closer to a solution of this complex problem.

### 2.3.1.1 Intense Sub-ps Pulses

At laser intensities of the order of  $10^{17} \text{ Wcm}^{-2}$  and higher collisional absorption is no longer dominating. The interaction with solids and liquids becomes collisionless latest when  $T_e$  exceeds  $10^3 Z^2 \text{ eV}$ ,  $Z$  average ion charge. The plasma formation process is very fast (a few laser cycles) and is a competition between field ionization (Chap. 7) and ionization by collisions. The final state is represented by a highly overdense plasma of solid electron density. Only after 100 fs typical hydrodynamic expansion sets in. According to classical linear optics the plasma should behave like an ideal mirror of 100% reflectivity. General physical intuition tells that such ideal hypotheses have to be handled with care. In fact, early measurements showed that 70–80% “collisionless” absorption and even more is possible [119]. Soon after the experimental finding was qualitatively confirmed by computer simulations [120]. Thus, production of dense, extremely hot plasmas of relativistic electron temperatures is possible with ultrashort superintense laser pulses. However, despite intense search for mechanisms leading to efficient collisionless absorption over more than two decades, a satisfactory explanation of the underlying physical

effects is available only since recently. The physics of these plasmas is the subject of Chap. 8.

### 2.3.2 Heating with Long Pulses of Constant Intensity

In order to get a more detailed picture of the laser target interaction, the system (2.65), (2.66), (2.67), (2.68), and (2.69) has been solved numerically in plane and spherical geometry under the following conditions:

- The target material is solid hydrogen of particle density  $n_0 = 4.5 \times 10^{22}$  and initial temperatures  $T_e = T_i = 0$ ;
- constant laser intensity  $I = I_0$  at Nd wavelength; the absorption is purely collisional;
- total reflection at the critical point;
- heat conduction according to Spitzer–Braginskii, (2.64);
- absence of ponderomotive force,  $\pi = 0$ .

#### 2.3.2.1 Compression Wave

The dynamics of the high-density region in plane geometry is shown in Fig. 2.12 for a  $50\text{ }\mu\text{m}$  thick hydrogen foil irradiated by the laser intensity  $I_0 = 10^{12}\text{ Wcm}^{-2}$  [44]. For simplicity, in this special case  $T_e = T_i = T$  is assumed. Starting from a low initial concentration of free electrons, in less than 0.1 ns a strong absorbing layer forms at the front. Owing to the high plasma pressure a shock builds up which travels at  $2.7 \times 10^6\text{ cm s}^{-1}$  into the foil, reaching the rear surface in less than 2 ns. Since the shock wave has to balance the momentum of the expanding plasma, and the densities in the two regions are very different, only a small fraction of the laser energy is transferred to the shock wave (in the present case 8%). Transfer of a large energy fraction to the compressed phase is possible in gas targets, where the plasma density is comparable to the density in the shocked material. The results of Fig. 2.12 were obtained by assuming the validity of the ideal gas law also for solid hydrogen. This may not be unreasonable because it is a very soft material; at only 40 kbars it is compressed by  $\kappa = 2.7$  [121]. For comparison, to reach a comparable compression ratio of 2.2 in lead, 4 Mbars are needed.

As the amount of energy going into the shock wave is small and we are interested only in the properties of the hot plasma, the solid is treated as incompressible in the following and the interest is concentrated entirely on the plasma properties. Equations (2.65), (2.66), (2.67), (2.68), and (2.69) are solved in plane and spherical geometry. In the spherical case the radius of the pellet is chosen as  $R_0 = 100\text{ }\mu\text{m}$ . In order to make the two cases comparable and to show better the influence of purely geometrical effects,  $R_0$  is kept constant by introducing a self-consistent matter source on the pellet surface which balances the amount of ablated material. The light flux  $F$  in spherical geometry is chosen to produce the intensity  $I_0$  on the original pellet surface, i.e.,  $F = 4\pi R_0^2 I_0$ .

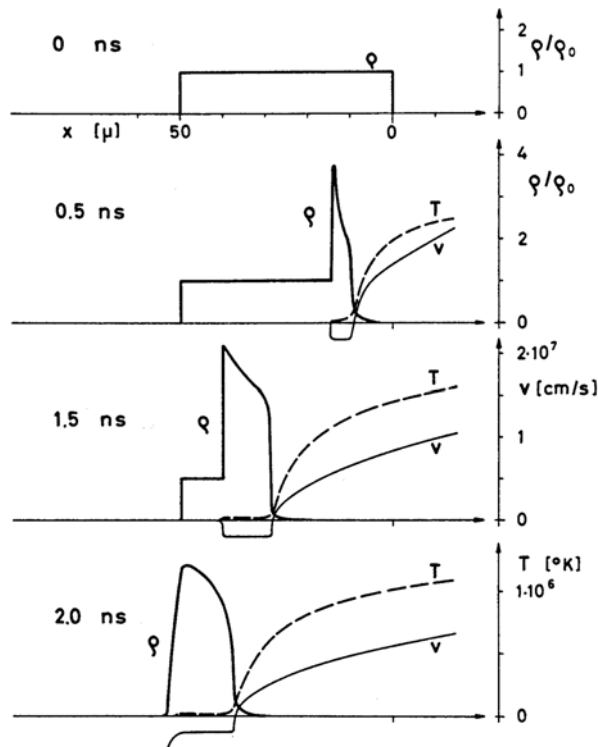


**Fig. 2.12** Plane shock wave in a solid hydrogen foil ( $50 \mu\text{m}$  thickness) at various times for a laser intensity  $I_0 = 10^{12} \text{ Wcm}^{-2}$ . The shock velocity is  $2.7 \times 10^6 \text{ cms}^{-1}$ . Undisturbed foil above, irradiated from the right [44]

### 2.3.2.2 Moderate Laser Intensity

A calculation was performed for solid deuterium with a laser intensity  $I_0 = 5 \times 10^{12} \text{ Wcm}^{-2}$  [122]. Results are shown in Fig. 2.13 for plane (upper figure) and spherical geometry (lower figure) after 5 and 10 ns. The distributions of the dynamical quantities  $n_e (= n_i)$ ,  $T_e$ ,  $T_i$  and of  $I$  and  $F$  are plotted as a function of  $x$  and  $r$ , respectively. Nearer the solid, the particle density drops rapidly and the plasma streams out with velocities of the order of  $10^7 \text{ cm/s}$ . The incoming light and that reflected from the critical point are absorbed according to Beer's law and heat the plasma to considerable electron and ion temperatures. In plane geometry light is absorbed over a large distance on its way forward and backward so that the fraction of reflected light is very low (<2%). In the spherical case the plasma rarefies much more rapidly; accordingly, the absorption length is strongly reduced and the reflection is high (55%). The temperatures are considerably lower in the spherical case and the temperature maxima are shifted towards the target surface. A comparison of the temperature profiles for 5 ns with those for 10 ns and their

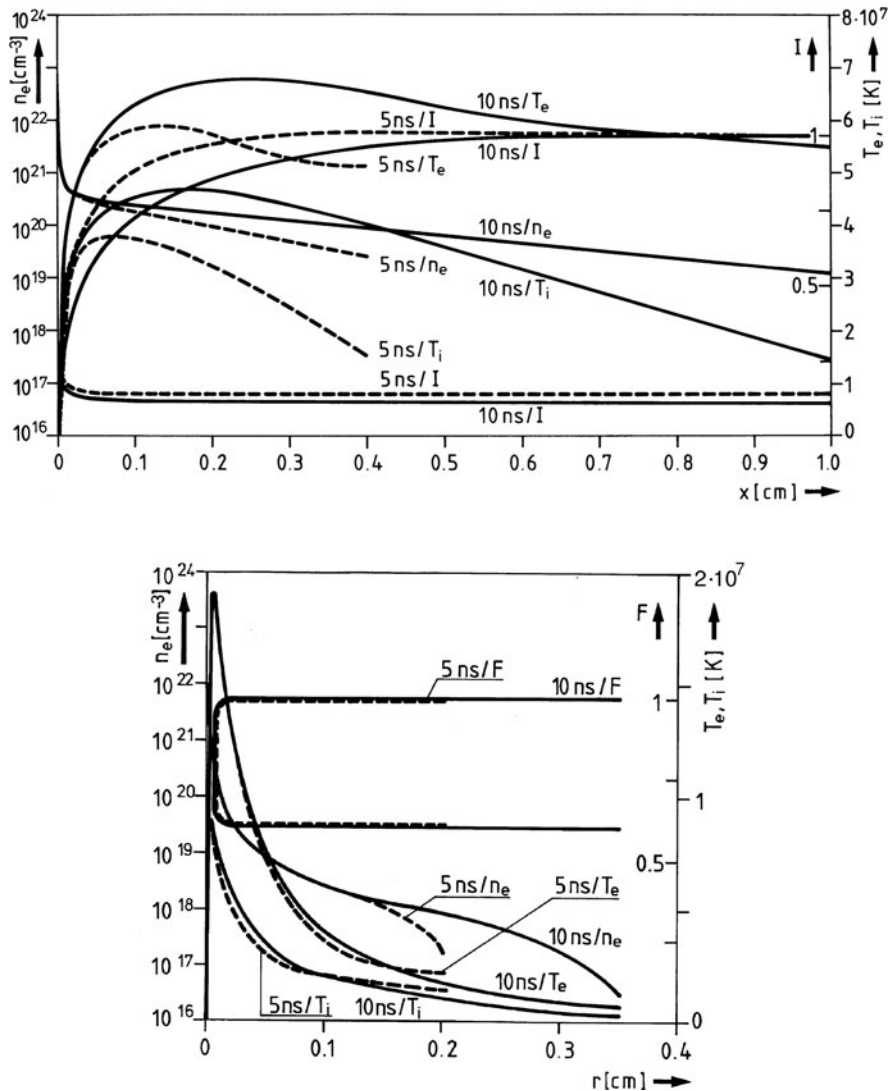


**Fig. 2.13** Plasma production from solid deuterium in plane (upper) and spherical (lower) geometry with a Nd laser intensity  $I_0 = 5 \times 10^{12} \text{ Wcm}^{-2}$  after 5 and 10 ns.  $n_e$  electron density,  $T_e$  electron temperature,  $T_i$  ion temperature,  $I$  laser intensity,  $F = 4\pi r^2 I$  laser flux. Laser pulse impinges from the right. The ratio between thermal ion and electron energies in plane (spherical) geometry is 0.62 (0.47) at 5 ns and 0.66 (0.51) at 10 ns

position as a function of  $r$  shows immediately that in spherical geometry the plasma production process becomes stationary near the target.

The partition of the laser energy into internal and kinetic plasma energy strongly depends on the geometry. In the plane case 43% of the absorbed energy is stored as

thermal energy of the electrons and ions; this ratio remains approximately constant in time. For the pellet a much more unfavorable ratio is expected. In fact, at 5 and 10 ns only 25 and 15%, respectively of the absorbed energy is stored as thermal energy. At the intensity under consideration the influence of heat conduction turned out to be very small. Therefore matter is heated only in regions where light penetrates, and the plasma density – with the exception of a very small region at the target surface – is less than its critical value  $n_c$ .

### 2.3.2.3 Higher Laser Intensity

Corresponding calculations were performed with an intensity of  $I_0 = 10^{15} \text{ Wcm}^{-2}$ . The results are shown in Fig. 2.14 at 2.5 and 5 ns after the start of irradiation. In both geometries the electron temperature is 10 times higher, the ion temperature 4 times higher as compared with the previous case. At high temperatures the plasma production process is determined by light absorption and heat conduction. In contrast to light propagation, thermal diffusion is not limited by any cut-off density, and a large overdense region ( $n_e > 10^{21} \text{ cm}^{-3}$ ) builds up in spherical and especially in plane geometry. Whereas at low intensities its thickness is about one wavelength and its structure is determined by light tunneling at the reflection point, for intensities greater than about  $I_0 = 10^{13} \text{ Wcm}^{-2}$  its extension is given by heat conduction. From the figure in plane geometry one can see that the overdense region is growing in time: at 5 ns two thirds of the plasma produced is heated by thermal diffusion alone. In spherical geometry the heat conduction zone is much smaller and becomes stationary. In the plane case the ratio of thermal to total plasma energy is 47% at 5 ns and increases very slowly with time. Although heat conduction also plays a dominant role in spherical geometry, the partition of thermal and kinetic energy at  $I_0 = 10^{15} \text{ Wcm}^{-2}$  still favors the latter: at 2.5 ns only 23% and at 5 ns not more than 16% of the absorbed radiation appears as thermal energy.

With respect to laser light reflection we note that now, at the higher light intensity, the absorbing region has much larger dimensions; nevertheless the reflection is increased in both geometries as a result of the rise in the electron temperature (16 and 60 % reflection).

Beer's law is a consequence of the WKB or optical approximation; it fails in the vicinity of the reflection point. By solving the wave equation for  $I_0 = 10^{14} \text{ Wcm}^{-2}$  in plane geometry one finds that about 15% of the total absorbed energy goes into the slab where the optical approximation breaks down; in the overdense region only 5% is absorbed. At higher intensities the absorption behind the reflection point is even lower because of the higher electron temperature. Thus the assumption of reflection at the critical density may be considered as approximately correct for calculating the overall dynamic behavior. For considerations in detail see Sect. 3.2.1.

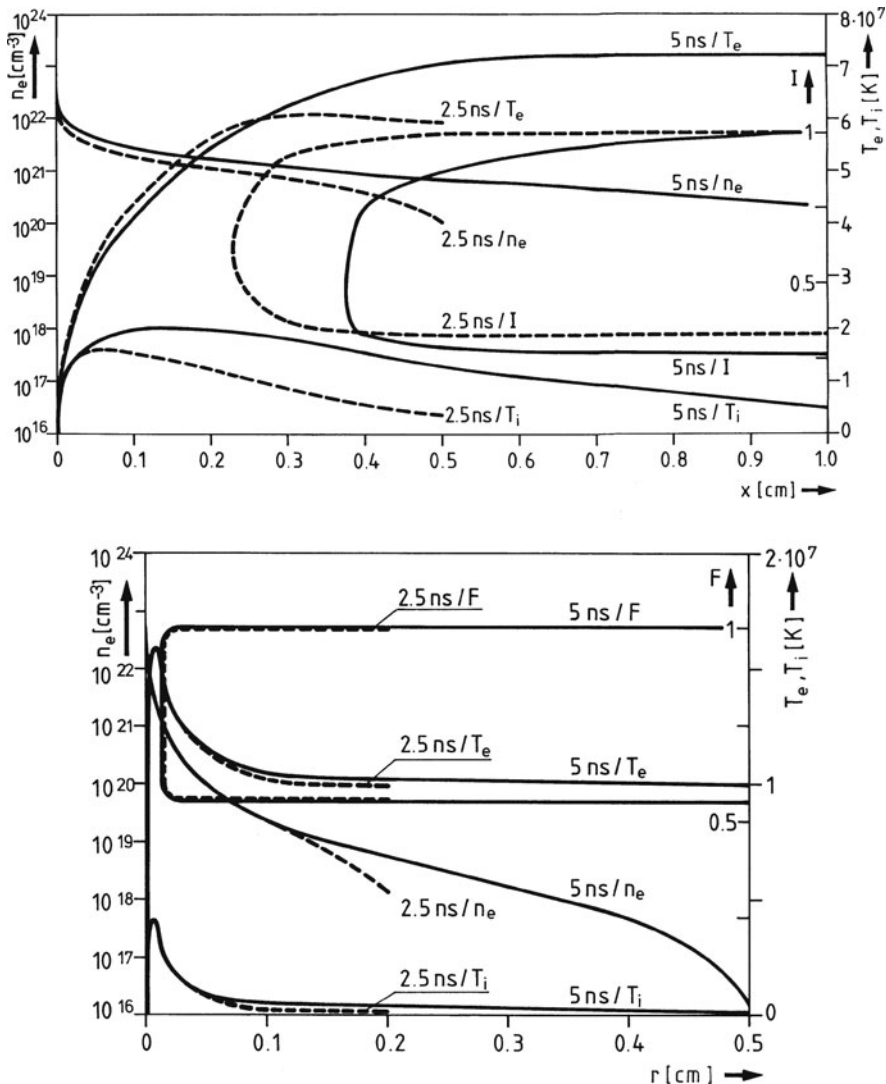


**Fig. 2.14** Plasma production from solid deuterium in plane (upper figure) and spherical (lower figure) geometry with a Nd laser intensity  $I_0 = 5 \times 10^{15} \text{ W cm}^{-2}$  after 2.5 and 5 ns. Symbols as in Fig. 2.13. The ratio between thermal ion and electron energies in plane (spherical) geometry is 0.31 (0.10) at 2.5 ns and 0.32 (0.06) at 5 ns. The target is irradiated from the right

### 2.3.2.4 Multicomponent Plasma

As pointed out earlier, laser plasmas produced from high-Z elements represent mixtures of different ion charge states [123–126]. Such plasmas are of interest as sources of highly stripped ions for accelerators [127]. Optical and mass-spectroscopic investigations of the expanding plasma cloud show that the more highly charged the ions

are the higher is their kinetic energy [128–133]. A first explanation of the energy spectra was based on electrostatic acceleration [67, 129, 134]. In the hot plasma cloud a quasi-static thermoelectric field  $E_s$  builds up according to (2.74) by which the various groups of ions should be accelerated corresponding to their individual charge state  $Z$ . As early as 1971 it was shown that in a fluid model 1% of the actual friction force an ion feels in moving through the plasma cloud is already able to inhibit ion separation [135]. Similar independent theoretical investigations a decade later came to the same conclusion [136]. Meanwhile further investigations indicate that the observed ion separation is presumably a consequence of recombination [126, 137–139]. On such a background Kunz investigated the expansion dynamics of a multicomponent laser plasma numerically by solving coupled rate equations for a whole variety of ionization and recombination processes simultaneously with the expansion process [140]. Independently, similar dynamic calculations were performed in great detail by Granse et al. [141]. Very satisfactory agreement was found with the ion energy spectra most carefully measured by Dinger et al. [131]. Subsequently Rupp and Rohr [142] performed detailed measurements of the recombination dynamics of a plasma as a function of distance from the target. One of the remarkable and basic aspects of these investigations is the important role that reheating of the expanding plasma plays due to recombination: No charged particles would reach the ion collectors if the plasma had cooled down adiabatically. The sensitivity of the ion energies to reheating was shown also by an ingenious analytical investigation [143]. Summarizing, it can be concluded that in the intensity range  $I \simeq 10^{11} - 10^{13} \text{ Wcm}^{-2}$  the experimentally observed ion separation is very likely to be based mainly on the phenomenon of recombination and that electrostatic acceleration has to be excluded as predicted in the early stage of investigations on this subject. Meanwhile detailed measurements exist on the ion velocity distribution and anisotropy of kinetic ion temperature, angular emission distributions of neutrals and ions, and on the effect of recombination processes and ionization states [144, 145]. Binary systems show no directional segregation. The neutrals dominate at low laser intensities ( $I < 10^{12} \text{ Wcm}^{-2}$ ) and large distances from the target: their kinetic energy is generally low and is smaller than that of the singly charged ions. All measurements underline the importance of recombination (e.g. three body recombination) up to distances of 1 m. The expansion dynamics shows also complex structures, i.e., the formation of localized groups of ions propagating at different velocities and densities. In such an environment groups of highly charged ions may also survive [146, 147].

Ion separation is studied more recently with intense short laser pulses in small liquid droplets and clusters. Here, the observed different energies of differently charged ions are generally attributed to thermoelectric acceleration. However, a quantitative proof has not been given yet. So, for instance in analogy to [135], the question of friction between the different ion species would have to be clarified for the new parameters associated with plasmas generated by intense sub ps laser pulses. A kinetic Vlasov treatment of the particle dynamics during the adiabatic expansion of a plasma bunch is presented in [148].

### 2.3.3 Similarity Considerations

From a large number of computer runs with a systematic variation of the parameters the functional dependence of all variables on these parameters can be obtained. Such a procedure is generally time-consuming. Here dimensional analysis is much superior. However, if this method is applied to system (2.65), (2.66), (2.67), (2.68), and (2.69) as it stands, more than one dimensionless variable  $\pi$  is found and the method is not conclusive. If instead  $T_i$  is assumed to be proportional to  $T_e$ ,  $T_i = \xi T_e$ , heat conduction is neglected and the internal energy per unit mass  $\varepsilon = 3k_B(ZT_e + T_i)/2m_i$  is introduced the system reduces in plane geometry to

$$\frac{\partial \rho}{\partial t} + \frac{\partial}{\partial x} \rho v = 0 \quad (2.130)$$

$$\frac{\partial v}{\partial t} + v \frac{\partial v}{\partial x} = -\frac{2}{3\rho} \frac{\partial}{\partial x} \rho \varepsilon \quad (2.131)$$

$$\frac{\partial \varepsilon}{\partial t} + v \frac{\partial \varepsilon}{\partial x} = -\frac{2}{3} \varepsilon \frac{\partial v}{\partial x} + \frac{\alpha}{\rho} I(x) \quad (2.132)$$

$$\alpha = C \frac{\rho^2}{\varepsilon^{3/2}}, \quad I(x) = I_0 \exp\left(-\int_x^\infty \alpha dx\right). \quad (2.133)$$

The initial values are  $I_0 = 0$ ,  $v = 0$ ,  $\varepsilon = 0$ ,  $\rho = \rho_0$  for  $t \leq 0$  and  $I_0 = \text{const} > 0$  for  $t > 0$ . A look at (2.130), (2.131), (2.132), and (2.133) and the boundary/initial conditions reveals that  $\rho$ ,  $v$ ,  $\varepsilon$  depend on  $I_0$ ,  $C$ ,  $x$ ,  $t$  and  $\rho_0$ . However, as long as the average plasma density is much lower than  $\rho_0$ , almost all energy is fed into the plasma, only a small portion being coupled to the solid. The dependence on  $\rho_0$  is weak and hence  $\rho_0 = \infty$  can be set, so that  $\rho_0$  is no longer a free variable [149]. The remaining dimensional matrix is given in Table 2.7. From this the existence of one dimensionless variable  $\pi$  is deduced,

$$\pi = \frac{x}{C^{1/8} I_0^{1/4} t^{9/8}}.$$

It is convenient to express all dimensional variables without using  $x$ ; then they are uniquely determined from the  $\pi$ -theorem as follows,

$$\begin{aligned} \rho &= I_0^{1/4} (Ct)^{-3/8} R(\pi), & v &= I_0^{1/4} (Ct)^{1/8} V(\pi), \\ \varepsilon &= I_0^{1/2} (Ct)^{1/4} E(\pi), & I(x) &= I_0 J(\pi), \end{aligned}$$

and (2.130), (2.131), (2.132), and (2.133) reduces to a system of ordinary differential equations (the prime corresponds to  $d/d\pi$ ),

**Table 2.7** Dimensional matrix of rank  $r = 3$  for (2.130), (2.131), (2.132), and (2.133) with  $\rho_0 = \infty$

	$I_0$	$C$	$x$	$t$
g	1	-2	0	0
cm	0	8	1	0
s	-3	-3	0	1

$$(8V - 9\pi)R' + 8RV' - 3R = 0$$

$$\left(8 - 9\frac{\pi}{V}\right)V' + \frac{16}{3}\frac{(RE)'}{RV} + 1 = 0$$

$$(8V - 9\pi)E' + \frac{16}{3}EV' + 2E - 8\frac{RJ}{E^{3/2}} = 0.$$

Instead of solving this system one can look at quantities not depending on  $x$  such as the mean values  $\langle \rho \rangle$ ,  $\langle v \rangle$ ,  $\langle T_e \rangle \sim \langle \varepsilon_e \rangle$  and the amount of ablated matter per unit area  $\mu(t)$ , or at  $v_{\max}(t)$  and  $T_{e,\max}(t)$ . They cannot depend on  $\pi$  and are therefore uniquely determined up to proportionality constants  $R_0, M_0, T_0$ ,

$$\langle \rho \rangle = R_0 I_0^{1/4} (Ct)^{-3/8}, \quad \mu = M_0 I_0^{1/2} C^{-1/4} t^{3/4},$$

$$\langle T \rangle \sim T_{\max} = T_0 I_0^{1/2} (Ct)^{1/4}. \quad (2.134)$$

These relations representing extremely useful formulae clearly show the power of dimensional analysis. The connection between  $R, V, E$ , etc. and  $R_0, M_0, T_0$ , etc. is found by integration, e.g.

$$\mu(t) = \int_0^\infty \rho dx = I_0^{1/2} C^{-1/4} t^{3/4} \int_0^\infty R(\pi) d\pi \Rightarrow M_0 = \int_0^\infty R d\pi. \quad (2.135)$$

The amount of plasma produced is proportional to  $t^{3/4}$  and hence the process does not become stationary in one dimension. The physical reason is that with increasing  $\mu(t)$  the radiation has to cross more absorbing plasma before reaching the solid. From (2.134) the ratio of thermal to kinetic energy turns out to be time-independent, in good agreement with the numerical results of the foregoing section. The same holds for the coefficient  $R_L$  of the light reflected from the plasma; in fact

$$R_L = 1 - \exp\left(-2 \int_0^\infty \alpha dx\right) = 1 - \exp\left(-2C \int_0^\infty \frac{\rho^2}{\varepsilon^{3/2}} dx\right)$$

$$= 1 - \exp\left(-2 \int_0^\infty \frac{R^2(\pi)}{E^{3/2}(\pi)} d\pi\right) = \text{const.}$$

Under the above conditions of  $q_e = 0$  and  $T_i \sim T_e$  the absorption in one dimension is self-regulating. This was the starting point for Caruso and Gratton [149] who first derived the relations (2.134) by using dimensional analysis. They also determined

the constants  $R_0, M_0, T_0$  with the help of simple physical arguments. To be precise, at finite  $R_L$ ,  $I_0$  has to be replaced by the absorbed intensity  $I_a = (1 - R_L)I_0$ . Considering  $\langle \rho(t) \rangle$  for early times where it exceeds the critical density  $\rho_c$  it becomes clear that  $R_L$  depends also on  $\rho_c$ . A look at Figs. 2.13 and 2.14 tells us that at later times the dependence is weak in plane geometry. The variation may be caused mainly by the missing proportionality between  $T_i$  and  $T_e$ . In order to test (2.134) numerically  $T_i = T_e = T$  was set and absorption was determined from  $dI/dx = -\alpha I$  without taking into account that the beam cannot propagate in the overdense plasma; however, heat conduction was included. For solid hydrogen the comparison is presented in Fig. 2.15 a,b in the quantities  $\mu(t)$  and  $T_{\max}(t)$  in the intensity interval  $I_0 = 10^{11} - 10^{13} \text{ Wcm}^{-2}$  [44]. The agreement is more than satisfactory. The constants  $T_0$  and  $M_0$  can be determined from the figure. Formulas (2.134) hold as long as the distance  $l$  from the plasma-vacuum boundary to the shock front in the solid is less than the focal radius  $r_0$ . For times  $\tau_s \gtrsim r_0/v_{\text{th}}$ ,  $l$  certainly exceeds  $r_0$  and the plasma dynamics becomes stationary. For this case (2.134) transforms into the relations

$$\begin{aligned}\langle \rho \rangle &= R'_0(Cr_0)^{-1/3} I_0^{1/3}, \quad \mu = M'_0 C^{-1/3} r_0^{2/3} I_0^{1/3} t, \\ \langle T \rangle &\sim T_{\max} = T'_0(Cr_0)^{2/9} I_0^{4/9},\end{aligned}\quad (2.136)$$

if  $t$  is replaced by  $r_0/T_{\max}^{1/2}$ . Alternatively one can write down the system (2.130), (2.131), (2.132), and (2.133) in spherical geometry,

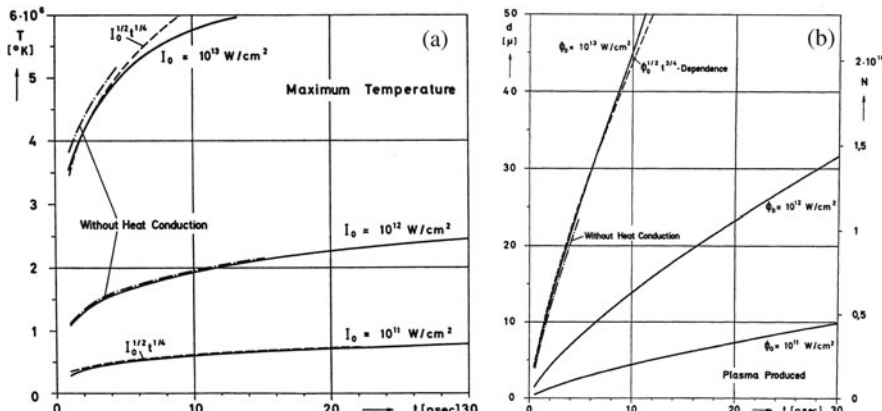


**Fig. 2.15** Comparison of  $T_{\max}$  (a) and  $\mu(t) = \rho_0 d$  (b) from (2.134) (dashed lines) with the numerical solution of (2.130), (2.131), (2.132), and (2.133) for solid hydrogen, completed by heat conduction and ionization energy (solid lines). Missing dashed lines indicate coincidence with numerical results. Deviations in (a) for  $I_0 = 10^{11} \text{ Wcm}^{-2}$  originate from ionization energy

$$\begin{aligned}\frac{\partial \rho}{\partial t} + \frac{1}{r^2} \frac{\partial}{\partial r} (r^2 \rho v) &= 0, \\ \frac{\partial v}{\partial t} + v \frac{\partial v}{\partial r} &= -\frac{2}{3\rho} \frac{\partial}{\partial r} (\rho \varepsilon), \\ \frac{\partial \varepsilon}{\partial t} + v \frac{\partial \varepsilon}{\partial r} &= -\frac{2}{3r^2} \varepsilon \frac{\partial}{\partial r} (r^2 v) + C \frac{\rho}{\varepsilon^{3/2}} I.\end{aligned}$$

The dynamics becomes stationary under the assumption  $\rho_0 = \infty$  in a sphere of initial radius  $r_0$ . In this way the sphere becomes infinitely massive and its size  $r_0$  is not affected by ablation. It is further clear that  $\rho, \varepsilon, v$  depend on  $C$  and  $I_0(r_0)$  separately (with increasing  $C$   $T_{\max}$  rises at constant  $I_0$ ). The dimensional matrix is given in Table 2.8. Its rank is  $r = 3$ .  $I_0, r_0, C$  and  $t$  can be combined to form the dimensionless variable  $\pi_1 = (r_0^8/I_0^2 C)^{1/9} t$  which shows that  $T_{\max}, \langle T \rangle, \langle \rho \rangle$ , etc. are not stationary in a rigorous sense. This is not surprising since the plasma-vacuum interface is continuously increasing in size. Nevertheless it is easily seen in which sense the plasma expansion comes arbitrarily close to a steady state. In fact, far out in the “corona”, say at  $r = R$ , the flow becomes highly supersonic. If a sink is applied there for the plasma such that  $\rho(R) = 0$ , the flow at  $r < R$  is not altered since no signal reaches this region from outside, and for large  $R$  the contribution of the region  $r > R$  to the absorption of laser radiation becomes arbitrarily small. The overall effect of such a measure is that for  $r_0 < r < R$  the flow becomes stationary after the time  $\tau_s \simeq R/v_{\max}$ . Then, combining  $I_0, r_0$  and  $C$  to form the dimensional quantities,  $\langle \rho \rangle, \mu, T_{\max}, \langle T \rangle$  become unique and are given by (2.136). The relations can be tested by the numerical results of Figs. 2.13 and 2.14. First of all the building up of a steady state is well confirmed in spherical geometry; e.g., see the constancy of the maxima of  $T_e, T_i$  and the fluxes  $F$  and the linear increase of  $\mu$  with time. For the ratio of  $T_{\max}$  at  $I_0 = 5 \times 10^{12} \text{ Wcm}^{-2}$  and  $I_0 = 10^{15} \text{ Wcm}^{-2}$  one obtains 9.6 from the similarity model (note that the absorbed intensities  $I_a$  have to be used). In the numerical calculation this ratio amounts to 8.2; hence, there is satisfactory agreement. However,  $\mu(t)$  does not scale according to  $\mu \sim I_a^{1/3}$  since this quantity is very sensitive to heat conduction.

The dependence of the dynamic variables on laser wavelength  $\lambda$  and charge number  $Z$  and ion mass  $m_i$  enter only through the absorption constant  $C$ ,

$$C \sim \lambda^2 Z^3 (Z + \xi)^{3/2} m_i^{-7/2},$$

**Table 2.8** Dimensional matrix for plasma production from a sphere. Possible dimensionless variables are  $\pi_1 = (r_0^8/I_0^2 C)^{1/9} t$ ,  $\pi_2 = r/r_0$

	$I_0$	$r_0$	$C$	$t$
g	1	0	-2	0
cm	0	1	8	0
s	-3	0	-3	1

(see (2.30) and (2.31)). With the approximation  $Z + \xi \simeq Z$  follows in the plane case

$$\langle \rho \rangle \sim \lambda^{-3/4} Z^{-27/16} m_i^{21/16}, \quad \mu \sim \lambda^{-1/2} Z^{-9/8} m_i^{7/8},$$

$$\langle T \rangle \sim \lambda^{1/2} Z^{9/8} m_i^{-7/8}$$

and in the spherical case

$$\langle \rho \rangle \sim \mu \sim \lambda^{-2/3} Z^{-3/2} m_i^{7/6}, \quad \langle T \rangle \sim \lambda^{4/9} Z m_i^{-7/9}. \quad (2.137)$$

For fully stripped ions it may be assumed that  $m_i \sim Z$  and the dependencies reduce to

$$\langle \rho \rangle \sim \lambda^{-3/4} Z^{-3/8}, \quad \mu \sim \lambda^{-1/2} Z^{-1/4}, \quad \langle T \rangle \sim \lambda^{1/2} Z^{1/4} \quad (\text{plane});$$

$$\langle \rho \rangle \sim \mu \sim \lambda^{-2/3} Z^{-1/3}, \quad \langle T \rangle \sim \lambda^{4/9} Z^{2/9} \quad (\text{spherical}). \quad (2.138)$$

Numerical calculations give a detailed picture of the interaction and dynamics of a specific set of parameters. Similarity solutions are much less accurate, but a better overview and physical insight is gained from them. The functional dependencies given here are useful for designing experiments. For a Nd laser their validity range extends from  $I_0 \gtrsim 10^{10} \text{ Wcm}^{-2}$  up to  $I_0 \simeq 10^{14} \text{ Wcm}^{-2}$ . As already seen, for some quantities the intensity interval extends even further. Strong thermal conduction puts a limit on the validity of (2.134) and (2.136). It is a general feature of nonlinear processes that, in contrast to linear ones, each dynamical variable obeys its own range. For some variables, for example ablation pressure or temperature and density distributions in the overdense plasma, more refined models are needed.

From the foregoing considerations the use of the  $\pi$ -theorem might appear more or less mechanical. In situations not involving any approximations or simplifications this is the case. In (2.130), (2.131), (2.132), and (2.133) one could decide for the cgs-Kelvin-system of units and for the particle density  $n = n_i$  and the temperature  $T = (ZT_e + T_i)/(Z + 1)$  instead of  $\rho$  and  $\varepsilon$ . Then one has to deal with

$$\frac{\partial n}{\partial t} + \frac{\partial}{\partial x} nv = 0, \quad \frac{dv}{dt} = -(Z + 1) \frac{k_B}{m_i} \frac{1}{n} \frac{\partial}{\partial x} nT,$$

$$\frac{dT}{dt} = -\frac{2}{3} T \frac{\partial v}{\partial x} + \frac{2}{3} \frac{\alpha}{k_B n(Z + 1)} I,$$

where  $\alpha$  is  $C' Z^2 n^2 / T^{3/2}$ . The independent variables are  $I_0$ ,  $C'/k_B$ ,  $k_B/m_i$ ,  $x$ ,  $t$ ; the rank of the dimensional matrix is  $r = 4$ .  $T_{\max}$  for instance is therefore uniquely determined, i.e.,  $T_{\max} \sim I_0^{1/4} (C'/k_B)^{1/4} (k_B/m_i)^{-3/8} t^{-1/2}$ . This differs from (2.134) and shows the wrong dependence on  $C'$  and  $t$ . Alternatively, the last term in the third equation can equally well be written as  $\sim (\alpha/n)(I_0/k_B)$  and then  $I_0/k_B$ ,  $C'$ ,  $k_B/m_i$ ,  $x$ ,  $t$  appear to be independent variables. Since now no mass unit

appears in  $I_0/k_B$ ,  $C'$  and  $k_B/m_i$  the rank of the matrix is  $r = 3$  and nothing can be concluded on how  $T_{\max}$  depends on  $I_0/k_B$ ,  $C'$ ,  $k_B/m_i$  and  $t$ ; only the contradiction has disappeared. This digression illustrates that the use of the  $\pi$ -theorem generally requires physical intuition and it may stimulate the reader to find out the source of the wrong dependence of  $T_{\max}$  given above.

## 2.4 Steady State Ablation

The knowledge of ablation pressure is important for calculating shock strength in dense matter and investigating equations of state [150], foil acceleration [151] and pellet compression for inertial confinement fusion (ICF) [11, 152, 153], and hole boring in fast ignition [13]. Fast ablation of matter by powerful lasers or particle beams, e.g., light or heavy ions, is one of the methods to create pressures in the Megabar range [154]. Above a certain energy supply in solids and liquids a phase transition occurs to the gaseous state; at even higher energies direct transformation of matter into the plasma state is achieved. Currently the highest pressures in the laboratory are obtained by laser ablation. Already at comparatively low laser pulse energies pressures up to 50 Mbars were measured in shock waves launched in solid foils by direct irradiation [155, 151]. By using ultrashort laser pulses their energy content can be significantly reduced, e.g., a 120 fs pulse of only 30 mJ was able to produce a 3 Mbar shock [156]. Higher pressures were reported in impact experiments using laser-accelerated foils [157, 158]. In numerical simulations of laser-accelerated colliding foils the calculated pressure maxima reached up to 2 Gbar [159], and from experiments the authors concluded that shock pressures over 400 Mbar are achievable [160]. More recently 750 Mbar planar shocks in gold target foils impacted by X-ray driven gold flyer foils were measured by Cauble et al. [161]. Much higher pressures are achievable in converging shocks, as for example 11 Gbar in a laser pellet compression experiment [162]. Intense shock generation represents an extremely significant tool to study equations of state of hot dense matter in radiation physics and astrophysics. For such purposes the shock front has to be planar. The best quality in this respect up to now was obtained by matter ablation induced by thermal radiation from laser heated hohlraums [163, 164]. As the laser beam smoothing technique has gradually improved, shock generation by direct laser drive has gained increasing attention and is now being used with growing success [165–167]. In this way the unavoidable losses of pressure in indirect drive are bypassed. For such reasons and for inertial confinement fusion (ICF) research (pellet compression and spark ignition [168–171]) ablative pressure generation by laser has repeatedly attracted the interest of numerous theoreticians for many years.

The gas dynamic aspect of ablation pressure was studied in great detail in 1D models and with two-dimensional corrections, taking also anomalous heat conduction and fast electron production into account [168]. There are two situations accessible to an analytic treatment: sudden impact heating before hydrodynamic motion

sets in, and the opposite case, i.e., after a steady state has developed. When the flow of the ablated material is quasi-stationary the ablation pressure is easily estimated if the Mach number  $M$  is known at one fixed density value. In laser heating such a natural fixed point is the critical density as soon as collisional absorption in the lower density plasma weakens and resonance absorption starts to dominate. For this reason in a number of papers the problem of the critical Mach number, i.e., the Mach number at this point, was investigated in plane and spherical flows [154, 172–178]. Several arguments were used, in plane and spherical geometry, to show that the Jouget point, that is  $M = 1$ , is located at the critical point or in the overdense region [175]. The analysis of spherical flow is rendered more difficult by the appearance of a characteristic radius as a new parameter. Gitomer et al. [174] solved the problem for high laser flux densities by the guidance of numerical calculations and obtained simple expressions for the ablation pressure. They also showed that in spherical geometry the mass flow at the critical point can be either subsonic or supersonic depending on the limitation of heat flux  $q_e$ .

At the moment there is no universally accepted ablation pressure model. There are contradictions in details between the various models themselves and between the models and the experiments. In some experiments agreement was found more or less with a whole class of simple theoretical pictures but not with those which are believed to be particularly accurate [179]. In the following the basic aspects of steady state laser-matter interaction also for laser intensities at which heat conduction dominates, are elaborated, and a simple model for the ablation pressure is presented. To the reader wishing to go more into detail at moderate laser intensities [151, 168, 177, 180] are particularly recommended. There exists a considerable amount of published material on ablation pressure; nevertheless the degree of apparent contradictions and confusion is very high. In order to contribute to clarification, in the following sections steady state onedimensional models, plane and spherical, are developed. Thereby the effect of heat flow supplied to the expanding corona, hitherto overlooked, is included and the basic gasdynamic relations which hold with certainty once well-defined conditions are fulfilled, are elaborated.

### 2.4.1 The Critical Mach Number in a Stationary Planar Flow

First we study the plane 1D model. When a target with an initially flat surface is heated, the flow of evaporated matter is planar near the solid-gas or solid-plasma interface. As the distance increases the flow pattern becomes more and more divergent creating in this way a zone of a stationary flow field in front of the interface. The temperature increases from a low value in the target, reaches a maximum somewhere in the stationary zone and then decays because of cooling due to expansion (Fig. 2.16). Let us assume that the ablated gas or plasma follows a polytropic equation of state of the form  $p\rho^{-\gamma} = \text{const}$ ,  $\gamma = \text{const}$ , so that the sound velocity  $s$  is given by (2.100) with  $k_a = 0$ . In the isothermal case (infinite heat conduction)

$\gamma_e = \gamma_i = \gamma = 1$ . Mass and momentum flow in the stationary zone are governed by  $\rho v = \text{const}$  and, neglecting ponderomotive forces,

$$\frac{\partial}{\partial x}(\rho v^2 + p) = \rho v \frac{\partial}{\partial x} \left( v + \frac{p}{\rho v} \right) = \rho v \frac{\partial}{\partial x} s \left( M + \frac{1}{\gamma M} \right) = 0. \quad (2.139)$$

The momentum equation tells that

$$P_a = p + \rho v^2 \quad (2.140)$$

is invariant throughout the stationary flow region and represents the true ablation pressure. Differentiating the last expression of (2.139) leads to the relation

$$\left( M + \frac{1}{\gamma M} \right) \frac{1}{s} \frac{\partial s}{\partial x} + \left( M - \frac{1}{\gamma M} \right) \frac{1}{M} \frac{\partial M}{\partial x} = 0. \quad (2.141)$$

From this we conclude that at the position  $x_m$  of the maximum of temperature or sound speed

$$M = \frac{1}{\sqrt{\gamma}} \quad (2.142)$$

holds. The proof is as follows. As one moves from the target to the vacuum  $M$  increases from  $M \ll 1$  to  $M = \infty$ . Let  $x_M$  be the smallest value at which (2.142) holds.  $x_M < x_m$  is not possible because the derivative of  $s$  is positive (for instance, there is no saddle point in  $s$  for  $x < x_m$ ). If  $x_M \geq x_m$  holds,  $\partial s / \partial x$  must again be zero there. This implies either  $x_M = x_m$ , or  $\partial M / \partial x = 0$  at  $x_m$ , respectively. In

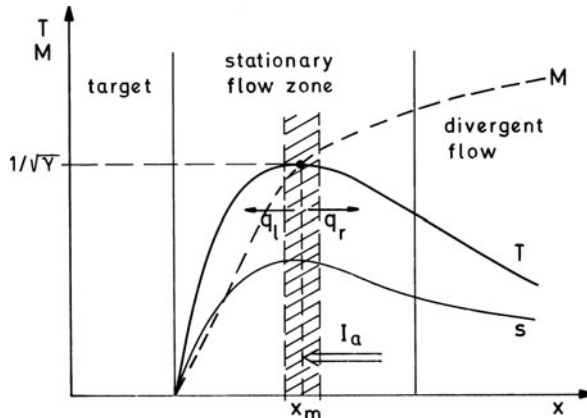


**Fig. 2.16** Steady state 1D model. Distributions of temperature  $T$ , sound speed  $s$  and Mach number  $M = v/s$  in a typical ablation flow into vacuum.  $I_a$  absorbed laser flux,  $q_l, q_r$  heat fluxes; absorption region dashed

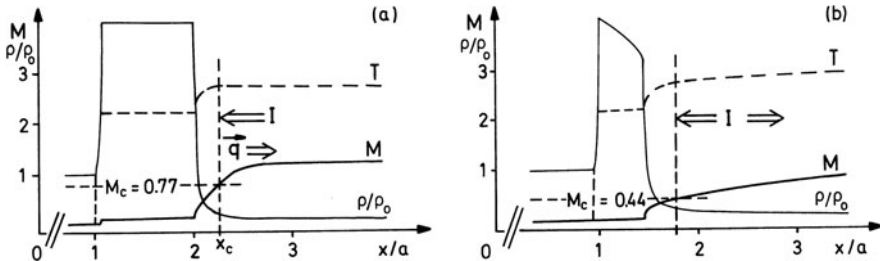


**Fig. 2.17** (a): Steady state plane ablation. Energy input at  $\rho_c/\rho_0 = 0.2$ .  $M_c = \sqrt{1/\gamma}$  is exactly confirmed for  $\gamma = 5/3$ .  $M_c$  does not depend on the value of  $\rho_c$ ; heat conduction according (2.64) is included. (b): Plane nonsteady ablation due to energy deposition at  $x_c$  (50%) as well as in the ablated plasma.  $M_c = 0.44$ . The inhomogeneity of the compressed matter is due to decrease of  $P_a(t)$  (see also Fig. 2.12)

the latter case differentiating (2.139) once more leads to the following relation at  $x = x_m$ ,

$$\left(M + \frac{1}{\gamma M}\right) \frac{1}{s} \frac{\partial^2 s}{\partial x^2} + \frac{s}{M} \left(M - \frac{1}{\gamma M}\right) \frac{\partial^2 M}{\partial x^2} = 0, \quad (2.143)$$

from which owing to  $\partial^2 s / \partial x^2 < 0$  also  $\partial^2 M / \partial x^2 < 0$ , i.e.,  $v = \max$  follows. But this is in contradiction to the physical assumption of the existence of only one maximum in  $T$ . In addition, (2.143) shows that  $x = x_m$  cannot be a saddle point for  $M$ .

$P_a$  can now be calculated from (2.140) if  $s$  and  $\rho$  are known at  $x_m$ . With resonance absorption dominating over collisional absorption (see Chap.3), e.g., at  $I\lambda^2 \gtrsim 10^{13} \text{ Wcm}^{-2}\mu\text{m}^2$ , the energy deposition zone becomes centered around the critical point  $x = x_c$  in a narrow region. Furthermore, in numerous experiments  $q_e$  seemed to be bounded by a limit considerably lower than the classical value (2.64) (“heat flux inhibition” [151, 177]). This situation implies that  $x_m$  lies close to  $x_c$  and that the heat front  $x_T$  is sufficiently close to  $x_m$  to guarantee the flow to be approximately planar in between. To prove numerically whether in this case (2.142) is fulfilled or not the fully time dependent initial value problem of target irradiation by a laser pulse of constant intensity was solved. The energy was deposited in a narrow zone around  $x_c$  and, in order to simulate the divergent flow,  $\rho$  was set equal to zero far out in the supersonic region. As Fig. 2.17a shows, the relation  $M_c = 1/\sqrt{\gamma} = \sqrt{3/5} = 0.774$  is extremely well fulfilled. This is even more surprising if one takes into account that the maximum in  $T$  is very flat. A completely different picture with  $M_c \ll 1/\sqrt{\gamma}$  is obtained when half of the incoming laser flux is deposited to the right of  $x_c$  (Fig. 2.17b). However,  $M \simeq 1/\sqrt{\gamma}$  is again reached at the maximum of  $T$  which is now located far away from the critical point, outside the picture.

Several arguments have been given in the past to show that  $M_c = 1$  should hold. It is evident from the analysis presented here that the validity of those arguments is

questionable for  $\gamma \neq 1$ . It becomes further clear that a supersonic stationary flow at  $x_c$  [175] can only be due to deviations from plane geometry (e.g., divergence effects) regardless of how strong the heat flux in the overdense region is. In an unsteady flow such a restriction does not hold owing to the presence of additional, i.e., inertial terms.

So far exact relations for  $M$  have been obtained in plane geometry if the flow is of hydrodynamic character. For a gas target this is always the case, even at arbitrarily low energy flux densities, as soon as the mean free path is small compared to the target dimensions, and the Mach number at  $T = T_{\max}$  is  $1/\sqrt{\gamma}$ . The situation changes drastically when the cohesive forces, i.e., the sublimation heat of the target material, become high. There is an energy regime in which the evaporated material is almost collision-free. Then the situation can be described by introducing the potential barrier  $U$  representing the sublimation energy per particle. Inside the solid the probability of the particle energies is given by the canonical distribution. When crossing the barrier  $U$  the molecules or atoms undergo a sufficient number of collisions to become Maxwellian so that just above the surface their distribution function is

$$f(0^+; \mathbf{v}) = \frac{n_0}{2} \left( \frac{\beta}{\pi} \right)^{3/2} \exp \left[ -\beta \left( \frac{2U}{m} + v^2 \right) \right], \quad \beta = m/2k_B T.$$

Therefrom the free streaming velocity  $v = v_x$  results,

$$v_x = \frac{\int v_x f d\mathbf{v}}{\int f d\mathbf{v}} = \left( \frac{\beta}{\pi} \right)^{1/2} \int_0^\infty v_x e^{-\beta v_x^2} dv_x = \left( \frac{k_B T}{2\pi m} \right)^{1/2} \quad (2.144)$$

which is smaller by the factor  $(6\pi)^{1/2} = 4.3$  than the thermal velocity  $v_{\text{th}} = (3k_B T/m)^{1/2}$ . The density undergoes a discontinuous transition from  $n_0$  to  $n_0 e^{-U/k_B T}$ .

### 2.4.2 Ablative Laser Intensity

In general the energy supplied to the target may be deposited over a wide region in space as, for instance, is the case of collisionally absorbed short wavelength radiation. However, the opposite situation of Fig. 2.16 in which the energy absorption zone is centered in a narrow region of density as assumed here, is of particular relevance for heating by strong laser pulses, in some deflagrations, and detonations [181]. In such cases the deposited energy flux density  $I_a$  may be thought of as deposited locally and split into the two heat fluxes  $q_l$  and  $q_r$  to the left and to the right, as indicated in Fig. 2.16. In this model the slope of  $T$  is discontinuous at  $x_m$  in order to satisfy  $q_l = \kappa(\partial T / \partial x)_{x_m}$  and  $q_r = -\kappa(\partial T / \partial x)_{x_m}$ .  $q_l$  covers the convection of enthalpy plus kinetic energy of the ablated material whereas  $q_r$  goes entirely into expansion work of the outflowing matter [173] and does not contribute

to the ablation pressure. The energy balance for the steady state is as follows,

$$q_l = I_a - q_r = \rho v \left( w + \frac{v^2}{2} \right) + q_e + P_a v_1, \quad w = \sigma + \varepsilon + \frac{p}{\rho}. \quad (2.145)$$

$\varepsilon$  is the internal energy per unit mass and  $\sigma$  represents the heat of evaporation and/or ionization. The term  $p/\rho$  provides for the work done by the outflowing matter against the rarefying plasma in front of it. The quantity  $q_e$  is the longitudinal and transversal heat flux into the target which is not converted into steady state plasma outflow;  $P_a v_1$  accounts for the work done by the laser to generate the shock wave traveling into the overdense material at shock speed  $v_s$  and matter velocity  $v_1$ . To evaluate the ablation pressure  $q_r$  is needed. In one-dimensional flow an upper limit for it is given by (2.112),  $q_r = ps|_{x=x_m}$  (isothermal case,  $\gamma = 1$ ). It is a good approximation at high electron temperature over a wide range in space. In the simplest case of  $T_i = 0$ ,  $\varepsilon = 3p/2\rho$ , negligible ionization energy, and  $q_e = 0$ ,  $P_a v_1 = 0$  (moderate laser flux), one has

$$I_a = \rho v \left( \varepsilon + \frac{p}{\rho} + \frac{v^2}{2} \right) \Big|_{x_m} + q_r = 4\rho_m s_m^3, \quad q_l = 3\rho_m s_m^3, \quad (2.146)$$

and hence, the maximum of the ratio of heat fluxes is  $q_r/q_l = 1/3$ . It indicates that  $q_r$ , in contrast to the common practice, should not be neglected.  $q_r$  is zero only when  $\gamma$  is identical with the adiabatic exponent.

The actual divergent flow in the outer corona leading to stationary conditions may be approximated by a spherical isothermal rarefaction wave which is the solution of  $\partial_r \rho r^2 v = 0$  and  $\partial_r v^2/2 = -s^2 \partial_r \rho/\rho$ :

$$\rho = \rho_0 e^{-(v^2 - v_0^2)/2s^2}, \quad r^2 = r_0^2 \frac{v_0}{v} e^{(v^2 - v_0^2)/2s^2}. \quad (2.147)$$

The maximum heat flux density  $q_r$  is calculated analogously to (2.112) with the identifications  $v_0 = s$ ,  $\rho_0 = \rho_m$ ,

$$\begin{aligned} q_r &= \int_{r_m}^{\infty} \frac{p}{r^2} \frac{\partial}{\partial r} (r^2 v) dr = \rho_m s^2 e^{1/2} \int_{v=s}^{\infty} \exp\left(-\left(\frac{v}{s}\right)^2\right) v d \exp\left(\frac{v^2}{2s^2}\right) \\ &= \sqrt{2e} \rho_m s^3 \int_{1/\sqrt{2}}^{\infty} 2u^2 e^{-u^2} du = \sqrt{2e} \rho_m s^3 \left\{ \frac{1}{\sqrt{2e}} + \int_{1/\sqrt{2}}^{\infty} e^{-u^2} du \right\} \\ &= \rho_m s^3 \left\{ 1 + \left(\frac{\pi e}{2}\right)^{1/2} \left[ 1 - \text{erf}\left(\frac{1}{\sqrt{2}}\right) \right] \right\} = 1.65 \rho_m s^3. \end{aligned} \quad (2.148)$$

It is higher by the factor 1.65 than for planar flow.

The choice of the integration constants  $v_0$ ,  $\rho_0$  needs a short explanation. At  $x = x_m$ ,  $v$  is equal to the speed of sound for  $\gamma = 1$ ; however the flow pattern, rather than being radial, looks as sketched in Fig. 2.18a for planar and Fig. 2.18b for

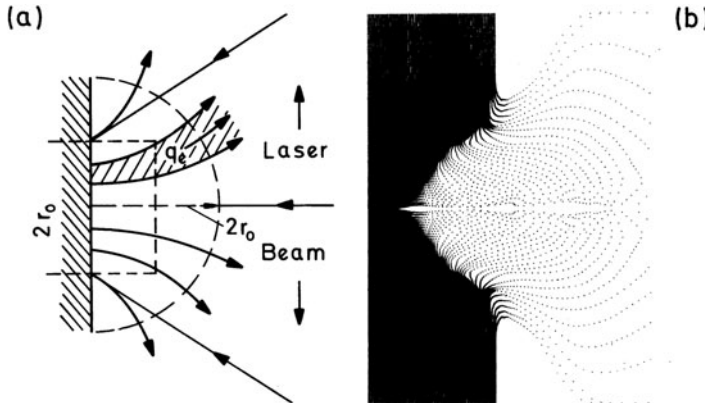


**Fig. 2.18** (a): Streamlines originating from a plane target [182]; (b): PIC calculation with regular injection of particles with the parameters of Fig. 2.10 [95]. Close to the shock streamlines follow the dots of the mass points

concave targets; it is radial only for uniform illumination of spherical targets, e.g. fusion pellets. Nevertheless, the heat flux  $\mathbf{q}_e d\boldsymbol{\Sigma}$  through any surface element  $d\boldsymbol{\Sigma}$  on  $\Sigma(M = 1)$  is the same as for radial flow, provided  $\mathbf{q}_e$  also follows the streamlines. In fact, under the condition  $\rho v d\boldsymbol{\Sigma} = \mu = \text{const.}$  along a streamline, Bernoulli's equation follows from (2.79)

$$\varepsilon + \frac{p}{\rho} + \frac{v^2}{2} + \frac{q_r}{\mu} = \text{const.} \quad (2.149)$$

For  $T = \text{const.}$  it simplifies to

$$\frac{v^2}{2} + \frac{q_r}{\mu} = \text{const}'. \quad (2.150)$$

Since somewhere outside the target the flow becomes spherical this relation shows that  $q_r$  through  $\Sigma(M = 1)$  is the same for all flow patterns owing to  $v^2 = s^2$  there and  $\mu = \text{const.}$  along a flux tube. The assumption  $\mathbf{q}_e \parallel \mathbf{v}$  is reasonable in the vicinity of the axis in many experiments for most of the interaction time. However, strong lateral heat flow would invalidate (2.148). In particle-in-cell (PIC) calculations with  $T_i = T_e = T$ , for instance, the fraction of energy taken by  $q_r$  in the early stage of interaction could amount to 70% of the incident laser energy at  $I = 10^{15} \text{ Wcm}^{-2}$  [95]; at later stages, when a large plasma cloud has formed this fraction reduced to an asymptotic value  $q_r/I_a \simeq 20\text{--}25\%$ . From (2.148) the ratio  $q_r/I_a = 1.65/(3 + 2 + 1/2 + 1.65) = 23\%$  is obtained. At such high laser intensities it is more realistic to assume  $T_i = 0$  (see Fig. 2.13). Then, from (2.148)  $q_r/q_l = 0.55$  follows. This shows once more that  $q_r$  should not be neglected.

The question arises whether the assumption of a steady state is a realistic hypothesis. As far as the overdense (ablative) region is concerned it is reasonable (for a

detailed discussion see the instructive comments in [183, 184] and the references therein). For the underdense corona a more accurate evaluation of  $q_r$  may be based on an interesting discovery by Schmalz and Eidmann ([185] and Fig. 2.19): The isothermal plasma ablation from a sphere of constant radius  $r_0$  fills the surrounding space according to a stationary rarefaction wave (2.147) and then suddenly, at  $t = t_s$  passes over into a time-dependent solution of nearly linear velocity and nearly exponential density distribution in space which is well approximated by the isothermal similarity solution [185, 186]

$$\rho(r, t) = \rho_0 \exp\left(-\sqrt{3} \frac{r - r_0}{s(t - t_0)}\right), \quad v(r, t) = \sqrt{3}s + \frac{r - r_0}{t - t_0}. \quad (2.151)$$

By equating  $v(r)$  of the two distributions with  $t_0 = 0$ ,  $r(t_0) = r_0$ , one obtains

$$t = \frac{s}{v - \sqrt{3}s} \left\{ \left( \frac{v_0}{v} \right)^{1/2} e^{(v^2 - v_0^2)/4s^2} - 1 \right\},$$

or  $v(t)$  which, inserted in (2.147), yields the location of the junction  $r_s$ . The radial heat flux density  $q_r$  is obtained from

$$q_r = \int_{r_m}^{r_s} (p_s/r^2) d(r^2 v_s) + \int_{r_s}^{\infty} (p_u/r^2) d(r^2 v_u),$$

where the indices  $s$  and  $u$  refer to the steady and unsteady state profiles (2.147) and (2.151), respectively. Breaking up of the stationary solution is also observable in the numerical solutions of Figs. 2.13 and 2.14, spherical cases.

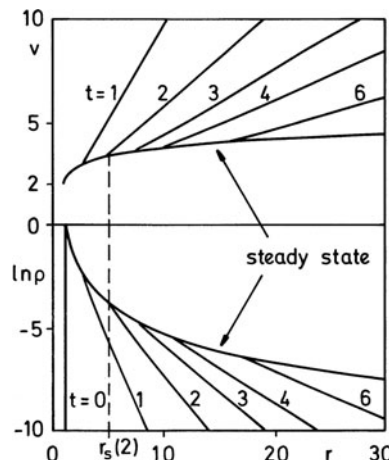


**Fig. 2.19** Numerical solution of stationary spherical isothermal plasma expansion [185]. Normalized velocities and densities over radius  $r$  for different normalized times. The stationary solution changes into a self-similar one at  $r = r_s(t_s)$

### 2.4.3 Ablation Pressure in the Absence of Profile Steepening

The pressure arising from mass ablation  $P_a$  can be determined from (2.140) and (2.145) provided the flow velocity is measured in a reference system in which the ablation region is stationary. In a strict sense this means an inertial frame in which the ablation front stays in a fixed position. For thick targets such a requirement is generally fulfilled to a good approximation. Thin targets undergo an accelerated motion like a rocket as soon as the first shock wave has moved through. Here the correct reference system has to be readjusted at each instant of time; it is a tangent inertial frame. For evaluating  $P_a$ , in principle, an arbitrary point can be chosen in the steady state region. However, since  $v$  is known only at  $x_m$ , this point plays a special role. Neglecting ionization and setting  $q_e = 0$ , (2.145) becomes there

$$q_l = \frac{3\gamma - 1}{2\gamma^{3/2}(\gamma - 1)} \rho_m s_m^3 \quad \text{for } \gamma \neq 1; \quad q_l = 3\rho_m s_m^3 \quad \text{for } \gamma = 1.$$

Elimination of  $s_m$  from these expressions and from (2.145) leads to

$$\begin{aligned} P_a &= 2 \left[ \frac{2(\gamma - 1)}{(3\gamma - 1)} \right]^{2/3} \rho_m^{1/3} (I_a - q_r)^{2/3} \quad \text{for } \gamma \neq 1; \\ P_a &= \frac{2}{3^{2/3}} \rho_m^{1/3} (I_a - q_r)^{2/3} \quad \text{for } \gamma = 1. \end{aligned} \quad (2.152)$$

Specifying for *planar* isothermal heat flow, (2.112) leads to

$$P_a = \frac{2}{4^{2/3}} \rho_m^{1/3} I_a^{2/3} = 0.79 \rho_m^{1/3} I_a^{2/3}; \quad \gamma = 1. \quad (2.153)$$

For the *spherical* case, using (2.148) for  $q_r$ , yields

$$P_a = \frac{2}{4.65^{2/3}} \rho_m^{1/3} I_a^{2/3} = 0.72 \rho_m^{1/3} I_a^{2/3}; \quad \gamma = 1. \quad (2.154)$$

If  $q_r$  is set equal to zero the numerical factor for the isothermal ablation pressure is  $2/3^{2/3} = 0.96$ , i.e., 33% higher.

So far formulas for the ablation pressure have been derived for laser pulses of constant absorbed intensity  $I_a$  (i) under the assumptions of stationary plasma outflow (ii), plane flow in the overdense region (iii), no lateral heat flow in the underdense corona (iv) and narrow absorption region around the critical point (v). If the latter condition is satisfied and ponderomotive effects are very small, i.e.,  $(|\pi|/|\nabla p| \ll 1)$ ,  $\rho_m$  can be identified with the critical density  $\rho_c$ , and hence  $P_a$  scales with the laser wavelength and absorbed intensity as  $P_a \sim (I_a/\lambda)^{2/3}$ .

To compare  $P_a$  deduced here with the experiment for irradiances  $I\lambda^2 \gtrsim 10^{13}$  Wcm $^{-2}$ , ponderomotive effects have to be included. They help to keep the plasma flow one-dimensional in the absorption region owing to density profile steepening [condition (v)] but they also shift the point of critical Mach number  $M = 1/\sqrt{\gamma}$

into the underdense region. Radiation pressure supported and dominated plasma flow will be treated in Chap. 5. It will be shown that profile steepening takes already place at radiation pressures as low as a few percent of  $P_a$ .

At interaction times on the ns time scale crater formation takes place and the steady state overall flow is two-dimensional (2D).  $P_a$  can be calculated in a narrow cylinder on the axis of radius  $r$  and length  $l$ . Due to profile steepening holds  $l \lesssim \lambda$ . Taking radial flow  $v_r$  into account mass conservation requires

$$\nabla(\rho\mathbf{v}) = \frac{\partial}{\partial x}(\rho v) + \frac{1}{r} \frac{\partial}{\partial r}(r\rho v_r) = 0.$$

Regularity of flow on the axis implies  $v_r = \alpha r$ ,  $\alpha = \text{const}$  for  $r/r_0 \ll 1$ ,  $r_0$  radius of the laser beam. Then  $\alpha \simeq v/r_0$  (confirmed by 2D simulations). Thus, the mass flow through a narrow cylinder is one-dimensional, since with  $\lambda/r_0 \ll 1$  holds

$$\pi\rho \left\{ r^2 v + 2r\lambda v_r \right\} \simeq \pi\rho v \left\{ r^2 + 2\frac{\lambda}{r_0}r^2 \right\} \simeq \pi r^2 \rho v,$$

and the foregoing 1D formulas apply. Equation (2.141) is a special form of the generalized Bernoulli equation if  $\partial/\partial x$  is interpreted as derivative along a stream line. In fact, the stationary momentum equation reads

$$\rho(\mathbf{v}\nabla)\mathbf{v} + \nabla p = \rho\nabla \left( \frac{\mathbf{v}^2}{2} + \rho s^2 \right) - \rho\mathbf{v} \times \nabla \times \mathbf{v} = 0.$$

On integrating along a streamline the term containing the curl of  $\mathbf{v}$  vanishes and hence the generalized Bernoulli equation in its differential form results,

$$d\frac{\mathbf{v}^2}{2} + \frac{1}{\rho}d(\rho s^2) = 0.$$

Taken along the axis this is identical with (2.139) and (2.141) under the condition  $\rho v = \text{const}$  since  $d\mathbf{v}^2/2 = \mathbf{v} d\mathbf{v} = \rho^{-1} d\rho \mathbf{v}^2$ .

In the absence of ponderomotive effects the time  $\tau_s$  for  $P_a$  to become stationary is given by the ratio of focal radius  $r_0$  to thermal velocity  $v_{\text{th}}$ ,  $\tau_s \simeq r_0/v_{\text{th}}$ . In the long pulse regime with  $I_0 \simeq 10^{14} \text{ Wcm}^{-2}$  a typical figure would then be  $\tau_s = 5 \times 10^{-3} \text{ cm}/(5 \times 10^7 \text{ cm}^{-1} \text{ s}^{-1}) = 100 \text{ ps}$ . However this is certainly too pessimistic. From  $I_0\lambda^2 \gtrsim 10^{13} \text{ Wcm}^{-2} \mu\text{m}^2$  profile steepening and electronic or radiative heat conduction will be significant and  $r_0$  has to be replaced by the smaller of the two characteristic lengths associated with these phenomena. For profile steepening this is the vacuum laser wavelength  $\lambda$ . The thickness  $d$  of the overdense conduction zone is much harder to determine owing to nonlocal heat transport [107]; however  $d < r_0$  and in most cases even  $d \ll r_0$ , may hold.

The first difficulty with a quantitative comparison of experiments with  $P_a$  given here is that there is no measurement with constant intensity; instead, the laser pulse

can be approximated by a Gaussian time dependence,  $I_a = \hat{I} e^{-(t-t_0)^2/\tau^2}$ . Under the assumption of a quasi-steady state the average ablation pressure  $\bar{P}_a$  measured in the experiments results as

$$\bar{P}_a = a \bar{I}_a^{2/3} = \frac{\hat{I}^{2/3}}{\tau} \int_{-\infty}^{+\infty} \left( e^{-(t-t_0)^2/\tau^2} \right)^{2/3} dt = \left( \frac{3}{2} \right)^{1/2} a (\bar{I}_a)^{2/3}, \quad (2.155)$$

thus showing that the power of  $I_a$  is preserved and only the numerical factor is increased by  $(3/2)^{1/2}$ . In experiments which are believed to be performed under steady state conditions, exponents lower than 2/3 are found, e.g., between 0.5 and 2/3. In a few cases however, a slope of 2/3 was seen (see [187], Fig. 10). The reasons for the discrepancy may be manifold: lateral heat flow, change of irradiation geometry during interaction at high intensities, quasi-steady state not well reached, anomalous transport and nonlocal laser energy deposition. When collisional absorption dominates, the critical density no longer plays its predominant role and the ablation pressure should follow the similarity laws (2.137) or (2.138), respectively, for spherical geometry (see also [188]).

$$P_a \sim \langle \rho k_B T \rangle \sim \langle \rho \rangle \langle T \rangle \sim \lambda^{-2/9} I_a^{7/9} = \lambda^{-0.222} I_a^{0.78}. \quad (2.156)$$

Gupta et al. [189] measured  $\bar{P}_a$  produced by a 2 ns KrF laser pulse in the intensity range  $10^{11} - 10^{13} \text{ W cm}^{-2}$ . Their result of  $\bar{P}_a \sim \bar{I}_a^{(0.66-0.84)}$  confirms the trend indicated by (2.156). A similar scaling, i.e.,  $\bar{P}_a \sim \bar{I}_a^{0.8}$ , was found by Grun et al. [179] with 4 ns Nd laser pulse in the intensity range  $10^{11} - 3 \times 10^{13} \text{ W cm}^{-2}$ .  $\bar{P}_{a,\text{Iodine}}$  agrees well with  $\bar{P}_{a,\text{Nd}}$ , whereas  $\bar{P}_{a,\text{KrF}}$  is 2.5 times as high [49, 151]. For a more detailed discussion see Chap. 5.

An alternative way to generate high pressure which is accessible to an analytical treatment is by impulsive loading. Suppose the laser pulse energy  $E$  is given. In view of the high pressure generation the question of the optimum pulse length is relevant. In general this is a complex problem. A partial answer can be given in the sense that the pressure ratio is between impulsive loading  $P_i$  and the steady state case of  $P_a$ . For this purpose we observe that the shock wave cannot evolve before the heat diffusion speed  $\dot{x}_T$  [see, e.g., (2.117)] has slowed down to the ion sound speed  $s$ . This means that the comparison of pressures has to be made at the time  $\tau_p$  given by (2.127). Then the lowest value of  $P_i$  is determined at the edge of the rarefaction wave where  $v = 0$  holds; hence  $P_i \geq (Z + 1)n_0 k_B T(\tau_p)$ , whereas  $P_a \leq p_m + \rho_m s_m^2$ . On approximating  $\rho_m$  by  $\rho_c$  the inequality  $P_a \leq n_c \left( 1 + \frac{1}{Z} \right) k_B T(\tau_p) \left( 1 + \frac{1}{\sqrt{\gamma}} \right)$  results and hence, the ratio  $P_i/P_a$  fulfills

$$\frac{P_i}{P_a} \geq \frac{\sqrt{\gamma}}{1 + \sqrt{\gamma}} Z \frac{n_0}{n_c}. \quad (2.157)$$

Generally this ratio is much larger than unity.

## References

1. Raizer, Yu.P.: *Laser-Induced Discharge Phenomena*. Consultants Bureau, New York (1977) 6
2. Shen, Y.R.: *The Principles of Nonlinear Optics*, Chap. 27. John Wiley & Sons, New York (1984)
3. Turcu, I.C.E., Gower, M.C., Huntington, P.: *Opt. Comm.* **134**, 66 (1997) 6
4. Evrastov, E.V., et al.: *Sov. J. Quant. Electron.* **18**, 354 (1988) 6
5. Poprawe, R., Beyer, E., Herziger, G.: *Proc. Conf. Gas Flow and Chem. Lasers*, Oxford (1984) 6
6. Rosen, D.I., Weyl, G.: *J. Phys. D: Appl. Phys.* **20**, 1264 (1987) 6
7. Ageev, V.P., Gorbunov, A.A., Danilov, V.P., Konov, V.I., Nikitin, P.I., Prokhorov, A.M.: *Sov. J. Quant. Electron.* **13**, 1595 (1983)
8. Kovalev, A.S., et al.: *Sov. J. Quant. Electron.* **15**, 468 (1985) 6
9. Storm, E.: *J. Fusion Energy* **7**, 131 (1988) 6
10. Storm, E., Lindl, J.D., Campbell, E.M., Bernat, T.P., Coleman, L.W., Emmett, J.L., Hogan, W.J., Hunt, J.T., Krupke, W.F., Lowdermilk, W.H.: *Progress in Laboratory High Gain ICF: Prospects for the Future LLNL Progress Report* (1988), published in *J. Fusion Energy* (1990)
11. Lindl, J.: *Phys. Plasmas* **2**, 3933 (1995) 74
12. Atzeni, S., Meyer-ter-Vehn, J.: *The Physics of Inertial Fusion*. Oxford University Press, Oxford (2004)
13. Tabak, M., Hammer, J., Glinsky, M.E., Kruer, W.L., Wilks, S.C., Woodward, J., Campbell, E.M., Perry, M.D.: *Phys. Plasmas* **1**, 1626 (1994) 74
14. Hain, S., Mulser, P.: *Phys. Rev. Lett.* **86**, 1015 (2001) 6, 57
15. Brabec, T., Krausz, F.: *Rev. Mod. Phys.* **72**, 545 (2000); Wittmann, T., et al.: *Nature Physics* **5**, 357 (2009) 6
16. Brederlow, G., Fill, E., Witte, K.J.: *The High-Power Iodine Laser*. Springer, Berlin (1983) 6
17. Johnson, Th.H.: *Proc. IEEE* **72**, 548 (1984) 6
18. Loudon, R.: *The Quantum Theory of Light*. Clarendon, Oxford (1986) 8, 9
19. Meystre, P., Sargent, M. III: *Elements of Quantum Optics*. Springer, Berlin (1990) 8, 12
20. Varcoe, B.T.H., Brattke, S., Weidinger, M., Walther, H.: *Nature* **403**, 743 (2000) 9
21. Lvovsky, A.I., Hansen, H., Aichele, T., Benson, O., Mlynek, J., Schiller, S.: *Phys. Rev. Lett.* **87**, 050402 (2001) 9
22. Silin, V.P., Uryupin, S.A.: *Zh. Exp. Theor. Fiz.* **81**, 910 (1981); *Sov. Phys. JETP* **54**, 485 (1981) 11
23. Mulser, P., Uryupin, S., Sauerbrey, R., Wellegehausen, B.: *Phys. Rev. A* **48**, 4547 (1993) 12
24. Lotz, W.: *Z. Physik* **216**, 241 (1968); *Z. Physik* **220**, 466 (1969) 16
25. Janev, R.K., Presnyakov, L.P., Shevelko, V.P.: *Physics of Highly Charged Ions*. Springer, Berlin (1985) 16
26. Kanapathipillai, M., Mulser, P., et al.: *Phys. Plasmas* **11**, 3911 (2004) 19, 20
27. Pert, G.J.: *J. Phys. B: At. Mol. Phys.* **12**, 2755 (1979) 21
28. Shkarofsky, I.P., Johnston, T.W., Bachynski, M.P.: *The Particle Kinetics of Plasmas*. Addison-Wesley, Reading, MA (1966) 22
29. Faisal, F.H.M.: *Theory of Multiphoton Processes*. Plenum Press, New York (1987) 23
30. Chin, S.L., Lambropoulos, P.: *Multiphoton Ionisation of Atoms*. Acad. Press, New York (1984) 23
31. Lambropoulos, P., Tang, X.: *J. Opt. Soc. Am. B* **4**, 821 (1987) 23
32. Voronov, G.S., Delone, N.B.: *Sov. Phys. JETP* **23**, 54 (1966) 23
33. Perry, M.D., Szoke, A., Landen, O.L., Campbell, E.M.: *Phys. Rev. Lett.* **60**, 1270 (1988)
34. Yergeau, F., Chin, S.L., Lavigne, P.: *J. Phys. B: At. Mol. Phys.* **20**, 723 (1987)
35. L'Huillier, A., Lompré, L.A., Mainfray, G., Manus, C.: *J. Phys. B: At. Mol. Phys.* **16**, 1363 (1983) 23
36. Poprawe, R., Herziger, G.: *IEEE J. Quant. Electron.* **22**, 590 (1986) 23
37. Beketi, G.: *Principles of Laser Plasmas*. John Wiley & Sons, New York (1976) 23
38. Clarke, P., et al.: *Appl. Phys. A* **69**, 117 (1999) 24

39. Izumida, S., Onishi, K., Saito, M.: Jap. J. Appl. Phys. **1** **37**, 2039 (1997)
40. Koldunov, M.F., Manenkov, A.A., Pokotilo, I.L.: J. Opt. Technol. **63**, 128 (1996)
41. Hosada, M., et al.: Jap. J. Appl. Phys. **1** **38**, 3567 (1999)
42. Fedonov, A.V., et al.: Appl. Surf. Sci. **197**, 45 (2002) 24
43. Balescu, R.: Equilibrium and Nonequilibrium Statistical Mechanics. Wiley-Interscience, New York (1975) 24, 37
44. Mulser, P.: Z. Naturforsch. **25a**, 282 (1970) 29, 63, 64, 71
45. Braginskii, S.I.: Transport Processes in Plasmas. In: Leontovich, M.A. (ed) Reviews of Plasma Physics, Vol. 1. Consultants Bureau, New York (1966) 29
46. Weng, S.M., et al.: Phys. Rev. Lett. **100**, 185001 (2008) 31
47. Chorin, A.J., Marsden, J.E.: A Mathematical Introduction to Fluid Mechanics. Springer, Berlin (1979) 33
48. Kidder, R.E.: Nucl. Fusion **16**, 405 (1976) 34, 53
49. Maaswinkel, A.G.M., Eidmann, K., Sigel, R., Witkowski, S.: Opt. Comm. **51**, 255 (1984) 34, 84
50. Mulser, P., Kärcher, B.: Phys. Lett. A **126**, 383 (1988) 34, 35
51. Mulser, P.: Z. Naturforsch. **42a**, 1147 (1987) 34
52. Davidson, R.C.: Methods in Nonlinear Plasma Theory. Acad. Press, New York (1972) 38, 41, 42
53. Derfler, H., Simonen, T.: J. Appl. Phys. **38**, 5018 (1967) 41
54. Dawson, J.M.: Phys. Fluids **4**, 869 (1961) 41
55. Chen, F.F.: Plasma Physics and Controlled Fusion, Vol. 1. Plenum Press, New York (1984) 41, 43
56. Hahn, E.L.: Phys. Rev. **80**, 580 (1950) 42
57. Carr, H.Y., Purcell, E.M.: Phys. Rev. **94**, 630 (1954) 42
58. Feynman, R.P., Vernon, F.L., Hellwarth, R.W.: J. Appl. Phys. **28**, 49 (1957) 42
59. Rayleigh, L.: Phil. Mag. **34**, 59 (1892); Proc. Royal Soc. **L XIV**, 68 (1899) 44
60. Rayleigh, L.: Nature **95**, 66, 591, 644 (1915) 44
61. Buckingham, E.: Phys. Rev. **4**, 345 (1914) 44
62. Sedov, L.I.: Similarity and Dimensional Methods. Acad. Press, New York (1959) 44, 47
63. De Izarra, C., Caillard, J., Valle, O.: Mod. Phys. Lett. B **16**, 69 (2002) 47
64. Zhi-yuan, Z., et al.: Optoelectronics Lett. **3**, 394 (2007) 47
65. Eliezer, S.: The Interaction of High-Power Lasers with Plasmas, Chap. 11. IOP Publ., Bristol (2002) 47
66. Kull, H.-J.: Phys. Rep. **206**, 197 (1991) 47
67. Gurevich, V.A., Pariiskaya, L.V., Pitaevskii, L.P.: Sov. Phys. JETP **22**, 449 (1966); Gurevich, V.A., Pariiskaya, L.V., Pitaevskii, L.P.: Sov. Phys. JETP **36**, 449 (1973) 49, 68
68. Mora, P.: Phys. Rev. Lett. **90**, 185002 (2003) 49
69. Mora, P.: Phys. Rev. E **72**, 056401 (2005) 49
70. Murakami, M., Basko, M.M.: Phys. Plasmas **13**, 012105 (2006) 49
71. Basko, M.M.: Eur. Phys. J. D **41**, 641 (2007) 49
72. Sentoku, Y., Cowan, T.E., Kemp, A., Ruhl, H.: Phys. Plasmas **10**, 2009 (2003) 49
73. Murakami, M., Mima, K.: Phys. Plasmas **16**, 103108 (2009) 49
74. Murakami, M., Tanaka, M.: Phys. Plasmas **15**, 082702 (2008) 50
75. Zeldovich, Ya.B., Raizer, Yu.P.: Physics of Shock Waves and High-Temperature Hydrodynamic Phenomena. Acad. Press, New York (1967) 50, 52, 54
76. Huntley, H.E.: Dimensional Analysis. McDonald, London (1953) 53
77. Bridgman, P.W.: Dimensional Analysis revised ed. (Yale Univ. Press, New Haven (1931) 53
78. Duncan, W.J.: Physical Similarity and Dimensional Analysis. Arnold, London (1953)
79. Birkhoff, G.: Hydrodynamics; A Study in Logic, Fact and Similitude. Princeton Univ. Press, Princeton, NJ (1960)
80. Langhaar, H.L.: Dimensional Analysis and Theory of Models. John Wiley, New York (1964)
81. Görtler, H.: Dimensionsanalyse. Springer, New York (1975)
82. Spurk, H.J.: Dimensionsanalyse in der Strömungslehre. Springer, Berlin (1992) 53
83. Barenblatt, G.I.: Similarity, Self-Similarity, and Intermediate Asymptotics. Consultants Bureau, New York (1979) 53, 54

84. Günther, B.: Dimensional Analysis and Theory of Biological Similarity, *Physiological Reviews* **55**, 659 (1975) 53
85. Günther, B., Morgado, E.: *Biol. Res.* **36**, 405 (2003)
86. Yates, F.E.: *Am. J. Physiol.* **244**, R589 (1983) 53
87. Wilks, G.: *Dyn. Problems Math. Phys.* **26**, 151 (1983) 54
88. Bluman, G.W., Cole, V.D.: *Similarity Methods for Differential Equations*. Springer, New York (1974) 54
89. Glockner, P.G., Singh, M.C. (ed.): *Symmetry, Similarity and Group Theoretical Methods in Mechanics*. The University of Calgary, Calgary (1974) 54
90. Euler, N., Steeb, W.H., Mulser, P.: *J. Phys. Soc. Japan* **60**, 1132 (1991) 54
91. Ceccherini, F., Cicogna, G., Pegoraro, F.: *J. Phys. A: Math. Gen.* **38**, 4597 (2005) 54
92. Guderley, G.: *Luftfahrtforschung* **19**, 302 (1942) 55
93. Meyer-ter-Vehn, J., Schalk, C.: *Z. Naturforsch.* **37a**, 955 (1982) 55
94. Paul Drake, R.: *High-Energy-Density Physics: Fundamentals, Inertial Fusion and Experimental Astrophysics*. Springer, Heidelberg (2008) 56
95. Lackner-Russo, D., Mulser, P.: A Macroscopic PIC Code for Beam-Target Interaction Studies Garching Report PLF 32 (1980) 56, 80
96. Eidmann, K., Sigel, R.: Backscatter experiments. In: Schwarz, H.J., Hora, H. (eds.) *Laser Interaction and Related Plasma Phenomena*, Vol. 3B. Plenum Press, New York (1974) 59
97. Nakai, S. and the Super-Uniform Implosion Group: ILE Quarterly Progress Report **29**, 9 (1989), ISSN 0289–1549 57
98. Yamanaka, C.: Past, present and future of laser fusion research. In: Nakai, S., Miley, G.M. (eds.) *Laser Interaction*, p. 3. American Institute of Physics, Woodbury (1996)
99. Nakai, S.: Progress of laser fusion at ILE and ICF research in Japan. In: Nakai, S., Miley, G.M. (eds.) *Laser Interaction*, p. 30. American Institute of Physics, Woodbury (1996) 57
100. Badziak, J., et al.: *J. Appl. Phys.* **104**, 063310 (2008) 58
101. Caruso, A., Gratton, R.: *Plasma Phys.* **11**, 839 (1969) 60
102. Shearer, J.W., Barnes, W.S.: *Phys. Rev. Lett.* **24**, 92 (1970) 61
103. Zacharov, S.D., Krokhin, O.N., Kryakov, P.G., Tyurin, E.L.: *JETP Lett.* **12**, 36 (1970) 61
104. Anisimov, S.I.: *JETP Lett.* **12**, 287 (1970) 61
105. Salzmann, H.: *J. Appl. Phys.* **44**, 113 (1973) 62
106. Malone, R.C., McCrory, R.L., Morse, R.L.: *Phys. Rev. Lett.* **34**, 721 (1975) 62
107. Bell, A.R.: Transport in laser-produced plasmas. In: Hooper, M.B. (ed.) *Laser Plasma Interactions 5: Inertial Confinement Fusion*, Proc. 45th Scottish Universities Summer School in Physics, St. Andrews 1994, p. 139. Institute of Physics, Bristol and Philadelphia (1995) 62, 83
108. Tahraoui, A., Bendib, A.: *Phys. Plasmas* **9**, 3089 (2002) 62
109. Batishev, O.V., et al.: *Phys. Plasmas* **9**, 2302 (2002)
110. Santos, J.J., et al.: *Phys. Rev. Lett.* **89**, 025001 (2002)
111. Martinoli, E., et al.: *Las. Part. Beams* **20**, 171 (2002)
112. Jain, N., Das, A., Kaw, P., Sengupta, S.: *Phys. Plasmas* **10**, 29 (2003)
113. Sentoku, Y., Mima, K., Kaw, P., Nishikawa, K.: *Phys. Rev. Lett.* **90**, 155001 (2003) 62
114. Pukhov, A., Meyer-ter-Vehn, J.: *Phys. Rev. Lett.* **76**, 3975 (1996) 62
115. Adam, J.C., Guerin, S., Laval, G., Mora, P., Quesnel, B.: *Phys. Rev. Lett.* **78**, 4765 (1997)
116. Ruhl, H., Sentoku, Y., Mima, K., Tanaka, K.A., Kodama, R.: *Phys. Rev. Lett.* **82**, 743 (1999)
117. Gibbon, P., et al.: *Phys. Plasmas* **6**, 947 (1999)
118. Ruhl, H., Macchi, A., Mulser, P., Cornolti, F., Hain, S.: *Phys. Rev. Lett.* **82**, 2095 (1999) 62
119. Sauerbrey, R., et al.: *Phys. Plasmas* **2**, 1635 (1994) 62
120. Gibbon, P., Bell, A.R.: *Phys. Rev. Lett.* **73**, 664 (1994) 62
121. van Thiel, M., Alder, B.J.: *Mol. Phys.* **10**, 427 (1966) 63
122. Mulser, P., Sigel, R., Witkowski, S.: *Phys. Lett. 6C*, 196 (1973) 64
123. Opower, H., Press, W.: *Z. Naturforsch.* **21a**, 344 (1966) 67
124. Gregg, D.W., Thomas, S.J.: *J. Appl. Phys.* **37**, 4313 (1966)
125. Basov, N.G. at al.: *JETP Lett.* **5**, 141 (1967)

126. Mattioli, M., Veron, D.: *Plasma Phys.* **11**, 684 (1969); Mattioli, M., Veron, D.: *Plasma Phys.* **13**, 19 (1971) 67, 68
127. Irons, F.E., Peacock, N.J.: *J. Phys. B* **7**, 2084 (1974) 67
128. Fenner, N.C.: *Phys. Lett.* **22**, 421 (1966) 68
129. Paton, B.E., Isenor, N.R.: *Can. J. Phys.* **46**, 1237 (1968) 68
130. Demtröder, W., Jantz, W.: *Plasma Phys.* **12**, 691 (1970)
131. Dinger, R., Rohr, K., Weber, H.: *J. Phys. D* **13**, 2301 (1980); Dinger, R., Rohr, K., Weber, H.: *J. Phys. D* **17**, 1707 (1984); *Las. Part. Beams* **4**, 239 (1986); *Las. Part. Beams* **5**, 691 (1987) 68
132. Pitsch, K., Rohr, K., Weber, H.: *J. Phys. D* **14**, L51 (1980)
133. Mann, K., Rohr, K.: *Las. Part. Beams* **10**, 435 (1992) 68
134. Boland, B.C., Irons, F.E., McWhirter, R.W.P.: *J. Phys. B* **1**, 1180 (1968) 68
135. Mulser, P.: *Plasma Phys.* **13**, 1007 (1971) 68
136. Begay, F., Forslund, D.W.: *Phys. Fluids* **25**, 1675 (1982) 68
137. Goforth, R.R., Hammerling, P.: *J. Appl. Phys.* **49**, 3918 (1976) 68
138. Matzen, M.K., Pearlman, J.S.: *Phys. Fluids* **22**, 449 (1979)
139. Latyshev, S.V., Rudskoi, I.V.: *Sov. J. Plasma Phys.* **11**, 669 (1985) 68
140. Kunz, I.: Interpretation of the Ion Energy Spectra in Laser-produced Plasmas Based on the Recombination Model, PhD-Thesis (in German), TH Darmstadt (1990) 68
141. Granse, G., Völlmer, S., Lenk, A., Rupp, A., Rohr, K.: *Appl. Surf. Sci.* **96-98**, 97 (1996) 68
142. Rupp, A., Rohr, K.: *J. Phys. D: Appl. Phys.* **28**, 468 (1995) 68
143. Caruso, A., Gatti, G., Strangio, C.: *Nuovo Cim.* **2**, 1213 (1983) 68
144. Sinha, B.K., Thum-Jäger, A., Rohr, K.P.: *J. Plasma Fusion Res.* **2**, 406 (1999); Sinha, B.K., Thum-Jäger, A., Rohr, K.P.: *J. Plasma Fusion Res.* **410** (1999) 68
145. Thum-Jäger, A., Rohr, K.P.: *J. Phys. D: Appl. Phys.* **32**, 2827 (1999) 68
146. Thum-Jäger, A., Sinha, B.K., Rohr, K.P.: *Phys. Rev. E* **61**, 3063 (2000); Thum-Jäger, A., Sinha, B.K., Rohr, K.P.: *Phys. Rev. E* **61**, 016405 (2001) 68
147. Müller, T., Sinha, B.K., Rohr, K.P.: *Phys. Rev. E* **67**, 026415 (2003) 68
148. Kovalev, V.F., Bychenkov, V.Y., Tikhonchuk, V.T.: *J. Exp. Theor. Phys.* **95**, 226 (2002) 68
149. Caruso, A., Gratton, R.: *Plasma Phys.* **10**, 867 (1968) 69, 70
150. Anisimov, S.I., Prokhorov, A.M., Fortov, V.E.: *Sov. Phys. Usp.* **142**, 395 (1984) 74
151. Eidmann, K., et al.: *Phys. Rev. A* **30**, 2568 (1984) 74, 75, 77, 84
152. Meyer-ter-Vehn, J.: *Nucl. Fusion* **22**, 561 (1982) 74
153. Caruso, A.: *Plasma Phys. Contr. Fusion* **18**, 241 (1976) 74
154. Mulser, P., Hain, S., Cornolti, F.: *Nucl. Instr. Meth. Phys. Res. A* **415**, 165 (1998) 74, 75
155. van Kessel, C.G.M., Sigel, R.: *Phys. Rev. Lett.* **33**, 1020 (1974) 74
156. Evans, R., et al.: *Phys. Rev. Lett.* **77**, 3359 (1996) 74
157. Obenschain, S.P., Grun, J., Ripin, B.H., McLean, E.A.: *Phys. Rev. Lett.* **46**, 1402 (1981) 74
158. Fabbro, R., Faral, B., Virmont, J., Pepin, H., Cottet, F., Romain, J.P.: *Las. Part. Beams* **4**, 413 (1986) 74
159. Fabbro, R., Faral, B., Virmont, J., Cottet, F., Romain, J.P., Pepin, H.: *Phys. Fluids* **B1**, 644 (1989) 74
160. Faral, B., Fabbro, R., Virmont, J., Cottet, F., Romain, J.P.: *Phys. Fluids* **B2**, 371 (1990) 74
161. Cauble, R., Phillion, D.W., Hoover, T.J., Holmes, N.C., Kilkenny, J.D., Lee, R.W.: *Phys. Rev. Lett.* **70**, 2102 (1993) 74
162. Regan, S.P., et al.: *Phys. Rev. Lett.* **89**, 085003 (2002) 74
163. Löwer, T., et al.: *Phys. Rev. Lett.* **72**, 3186 (1994) 74
164. Evans, A.M., et al.: *Las. Part. Beams* **14**, 113 (1996) 74
165. Koenig, M., Faral, F., Boudenne, J.M.: *Phys. Rev. E* **50**, R3314 (1994) 74
166. Benuzzi, A., et al.: *Phys. Rev. E* **54**, 2162 (1996)
167. Batani, D., et al.: *Laser & Part. Beams* **21**, 481 (2003) 74
168. Max, R., Claire, E., McKee, C.F., Mead, W.C.: *Phys. Fluids* **23**, 1620 (1980) 74, 75
169. Ahlborn, B., Key, M.H., Bell, A.R.: *Phys. Fluids* **25**, 541 (1982)
170. Yamanaka, C.: Laser plasma and inertial confinement fusion. In: Rosenbluth, M.N., Sagdeev, R.Z. (eds.) *Handbook of Plasma Physics*, Vol. 3, p. 3. North-Holland, Amsterdam (1991)

171. Richardson, M.C.: Direct drive fusion studies. In: Rosenbluth, M.N., Sagdeev, R.Z. (eds.) *Handbook of Plasma Physics*, Vol. 3, p. 199. North-Holland, Amsterdam (1991) 74
172. Bobin, J.L.: *Phys. Fluids* **14**, 2341 (1971) 75
173. Cojocaru, E., Mulser, P.: *Plasma Phys.* **17**, 393 (1974) 78
174. Gitomer, S.J., Morse, R.L., Newberger, B.S.: *Phys. Fluids* **20**, 234 (1977) 75
175. Matzen, M.K., Morse, R.L.: *Phys. Fluids* **22**, 654 (1979) 75, 78
176. Sanz, J., A. Liñán, Rodriguez, M., Sanmartin, J.R.: *Phys. Fluids* **24**, 2098 (1981)
177. Fabbro, R., Claire, E., Max, R., Fabre, E.: *Phys. Fluids* **28**, 1463 (1985) 75, 77
178. Hain, S., Mulser, P.: *Las. Part. Beams* **15**, 541 (1997) 75
179. Grun, J., et al.: *Phys. Fluids* **26**, 588 (1983) 75, 84
180. Manheimer, W.M., Colombant, D.G.: *Phys. Fluids* **25**, 1644 (1982) 75
181. Pert, G.J.: *J. Plasma Phys.* **29**, 415 (1983) 78
182. Herbst, M.J., Grun, J.: *Phys. Fluids* **24**, 1917 (1981) 80
183. Sammartin, J.R., Montanes, J.L., Barrero, A.: *Phys. Fluids* **26**, 2754 (1983) 81
184. Manheimer, W.M., Colombant, D.G., Gardner, J.H.: *Phys. Fluids* **26**, 2755 (1983) 81
185. Schmalz, R.F., Eidmann, K.: *Phys. Fluids* **29**, 3483 (1986) 81
186. Schmalz, R.F.: *Phys. Fluids* **29**, 1389 (1986) 81
187. Mulser, P.: *Plasma Phys. Contr. Fusion* **28**, 203 (1986) 84
188. Mora, P.: *Phys. Fluids* **25**, 1051 (1982) 84
189. Gupta, P.D., Tsui, Y.Y., Popil, R., Fedosejevs, R., Offenberger, A.A.: *Phys. Fluids* **30**, 179 (1987) 84

# Chapter 3

## Laser Light Propagation and Collisional Absorption

By absorption of electromagnetic radiation we understand the destruction of a certain number of photons and the creation of other forms of energy of the same amount, e.g., plasmons, phonons, accelerated and heated particles. In the language of second quantization the absorption operator reads  $b^+a$  ( $a$  annihilation operator,  $b^+$  creation operator); absorption occurs when its expectation value is nonzero. We call the absorption process collisional or inverse bremsstrahlung if the transformation of photon energy is due to the Coulomb field of single particles, in contrast to collective or collisionless absorption which is due to the resonant interaction with collective fields. There is a clear distinction between collisional and collective: collective interaction depends on one space variable only whereas collisional interaction needs at least two space variables. An example of collisional absorption is the excitation of plasmons by the plasma ions in a cold electron fluid oscillating in an intense laser field and their subsequent damping by breaking, particle acceleration, Landau mechanism and/or collisions.

In the second part of this chapter various models of collisional absorption are presented. First the electron-ion collision frequency is derived from a harmonic oscillator model for a unidirectional particle beam; subsequently the dielectric theory of absorption at finite electron temperature is presented. Here the electrons are treated as a fluid collectively reacting to the electric field of a moving ion. In the ballistic model, introduced next, a friction coefficient is determined from the momentum loss in flow direction due to electron-ion scattering events. The dielectric model is able to describe small angle deflections along nearly straight orbits and screening; the ballistic model adapts equally well to large angle scattering events and bent trajectories. However, screening must be introduced separately. To some extent the two models are complementary to each other. In the weakly coupled plasma they will be shown to lead to identical results.

At a first glance, collisional absorption seems to be the best understood dissipation process. Closer inspection, however, shows that this is not always true for laser plasmas. For instance, there is much uncertainty about screening and the Coulomb logarithm at high electron densities and large laser intensities. The oscillator model provides some insight into the physics of self-consistent cutoffs for the various plasma density domains. Also attention has to be paid to the effect of distortions of a Maxwellian velocity distribution and the role of electron-electron collisions

on  $v$ . Finally the equivalence of inverse bremsstrahlung and collisional absorption is demonstrated as this illustrates an interesting piece of radiation physics at moderate laser intensities ( $I\lambda^2 \leq 10^{16} \text{ Wcm}^{-2}\mu\text{m}^2$ ).

### 3.1 The Optical Approximation

All linear as well as nonlinear optics is governed by Maxwell's equations,

$$\varepsilon_0 c^2 \nabla \times \mathbf{B} = \mathbf{j} + \varepsilon_0 \frac{\partial}{\partial t} \mathbf{E}, \quad \nabla \times \mathbf{E} = -\frac{\partial}{\partial t} \mathbf{B}. \quad (3.1)$$

Classically, the electric current density  $\mathbf{j}$  is given by  $\mathbf{j} = -en_e \mathbf{v}_e + Zen_i \mathbf{v}_i$ ; in quantum plasmas  $\mathbf{v}_e$  and  $\mathbf{v}_i$  have to be substituted by the single-particle momentum operators per unit mass  $\mathbf{p}_e/m$ ,  $\mathbf{p}_i/m_i$ . In both cases the relation between  $\mathbf{j}$  and the polarization  $\mathbf{P}$  is given by [1]

$$\mathbf{j} = \frac{\partial}{\partial t} \mathbf{P} + \nabla \times \left( \mathbf{P} \times \frac{\mathbf{p}}{\rho} \right), \quad \mathbf{p} = \mathbf{p}_e + \mathbf{p}_i. \quad (3.2)$$

This relation can be regarded either as the definition of  $\mathbf{j}$  or of  $\mathbf{P}$ . Traditionally, for plasmas, one prefers to represent all free and dielectric currents by  $\mathbf{j}$ , instead of using  $\mathbf{P}$ ; but this of course is a pure convention. By eliminating  $\mathbf{B}$ , (3.1) reduces to the wave equation

$$\nabla \times \nabla \times \mathbf{E} + \frac{1}{c^2} \frac{\partial^2}{\partial t^2} \mathbf{E} = -\frac{1}{\varepsilon_0 c^2} \frac{\partial \mathbf{j}}{\partial t}. \quad (3.3)$$

In the following all considerations are limited to the classical expression for  $\mathbf{j}$ . For high frequency oscillations it reduces to  $\mathbf{j} = -en_e \mathbf{v}_e$  since in this case the ion motion can be neglected. In an unmagnetized plasma of equilibrium density  $n_0$  the current density may be obtained from the momentum equation of the electronic fluid of system (2.65), (2.66), (2.67), (2.68), and (2.69) in a straightforward manner:

$$\begin{aligned} \frac{\partial \mathbf{j}}{\partial t} &= \varepsilon_0 \omega_p^2 \mathbf{E} - \varepsilon_0 s_e^2 \nabla(\nabla \cdot \mathbf{E}) - v \mathbf{j} - \\ &\quad \frac{e}{m} \mathbf{j} \times \mathbf{B} + \frac{e^2}{m} (n_e - n_0) \mathbf{E} - (\mathbf{j} \nabla) \mathbf{v}_e - \mathbf{v}_e (\nabla \mathbf{j}). \end{aligned} \quad (3.4)$$

$v$  is a linear collisional or noncollisional damping coefficient. Under the additional constraint of the oscillation amplitudes  $\hat{\delta}_e$  being small compared with the wavelength  $\lambda$ , as well as compared with the plasma density scale length  $L = n_0/|\nabla n_0|$ , i.e.,  $|\hat{\delta}_e| \ll L, \lambda$ , a plasma frequency  $\omega_p = (n_0 e^2 / \varepsilon_0 m)^{1/2}$  is defined locally and no higher harmonics of the laser frequency  $\omega$  have to be considered in (3.4). Thus, if the flow velocity is  $\mathbf{v}_0(\mathbf{x})$  and  $\mathbf{j} = \mathbf{j}_{\text{os}} = -en_0(\mathbf{v}_e - \mathbf{v}_0)$  Ohm's law can be written as follows:

$$\frac{\partial \mathbf{j}}{\partial t} = \varepsilon_0 \omega_p^2 (\mathbf{E} + \mathbf{v}_0 \times \mathbf{B}) - \varepsilon_0 s_e^2 \nabla(\nabla \mathbf{E}) - \nu \mathbf{j} - (\mathbf{j} \nabla) \mathbf{v}_0 - \mathbf{v}_0(\nabla \mathbf{j}). \quad (3.5)$$

With the help of the quantities  $k_0 = \omega/c$ ,  $\beta = s_e/c$ ,  $v_\varphi v_g = c^2$  for phase and group velocities of the electromagnetic and  $v_\varphi v_g = s_e^2$  for the electrostatic wave one easily estimates

$$\begin{aligned} \left| \frac{s_e^2 \nabla(\nabla \mathbf{E})}{\omega_p^2 \mathbf{E}} \right| &= \gamma_e (\lambda_D k_e)^2, \quad \left| \frac{(\mathbf{j} \nabla) \mathbf{v}_0}{\varepsilon_0 s_e^2 \nabla(\nabla \mathbf{E})} \right| \leq \frac{\nu_0}{c} \frac{\beta^2}{k_0 L (k \lambda_D)^2}, \\ \left| \frac{\mathbf{v}_0(\nabla \mathbf{j})}{\varepsilon_0 s_e^2 \nabla(\nabla \mathbf{E})} \right| &\leq \frac{\nu_0}{v_g}. \end{aligned} \quad (3.6)$$

As a consequence, plasma flow is generally irrelevant in laser plasma optics and one may set  $\mathbf{v}_0 = 0$ . Then, for a wave of frequency  $\omega$ , (3.3) reduces to the wave equation of linear optics,

$$\nabla \times \nabla \times \mathbf{E} - k_0^2 \eta^2 \mathbf{E} = \beta^2 \nabla(\nabla \mathbf{E}), \quad (3.7)$$

where the refractive index  $\eta$  is given by

$$\eta^2 = 1 - \frac{\omega_p^2}{\omega^2} \frac{1}{1 + v^2/\omega^2} + i \frac{\nu}{\omega} \frac{\omega_p^2}{\omega^2} \frac{1}{1 + v^2/\omega^2}. \quad (3.8)$$

$\mathbf{E} + \mathbf{v}_0 \times \mathbf{B}$  is the electric field seen by an observer comoving nonrelativistically with the plasma. The nonlinear terms of (3.4) which are dropped in (3.7) give rise to the ponderomotive force and most of nonlinear optics phenomena encountered in laser plasmas (see Chaps. 5 and 6).

### 3.1.1 Ray Equations

For moderate density inhomogeneities the local wavelength  $\lambda(\mathbf{x})$  satisfies the inequality  $\lambda(\mathbf{x}) \ll L(\mathbf{x})$  nearly everywhere and the electric field is expressed by the eikonal approximation

$$\mathbf{E}(\mathbf{x}, t) = \hat{\mathbf{E}}(\mathbf{x}, t) e^{i\psi(\mathbf{x}, t)}, \quad (3.9)$$

in which  $\hat{\mathbf{E}}(\mathbf{x}, t)$  and  $\nabla\psi(\mathbf{x}, t)$  are slowly varying functions of space and time (see for instance Sect. 7.7 in [2]).  $\hat{\mathbf{E}}$  and  $\psi$  are called the amplitude and phase of the wave. The local wave vector and frequency are defined as

$$\mathbf{k} = \nabla\psi, \quad \omega = -\frac{\partial}{\partial t}\psi. \quad (3.10)$$

Starting from (3.3) and (3.5) with  $v_0 = 0$ , and keeping only the leading terms in the derivatives of  $\mathbf{E}(\mathbf{x}, t)$  and  $\mathbf{j}(\mathbf{x}, t)$  one arrives again at (3.7) and from there at

$$(\nabla\psi)^2 \mathbf{E} - \nabla\psi(\mathbf{E}\nabla\psi) + \beta^2\nabla\psi(\mathbf{E}\nabla\psi) = k_0^2\eta^2 \mathbf{E}$$

in a straightforward way. By splitting  $\mathbf{E}$  into  $\mathbf{E}_\perp + \mathbf{E}_\parallel$  with respect to the wave vector  $\mathbf{k} = \nabla\psi$ , the two eikonal and dispersion relations follow for the electromagnetic and the electrostatic components,

$$\begin{aligned} \mathbf{E}_\perp : \quad & (\nabla\psi)^2 = k_0^2\eta^2, \quad \omega^2 = \omega_p^2 + c^2k^2, \quad k_0 = \frac{\omega}{c}, \quad k = k_0\eta, \\ \mathbf{E}_\parallel : \quad & (\nabla\psi)^2 = k^2\beta^{-2}; \quad \omega^2 = \omega_p^2 + s_e^2k_e^2; \quad k_e = k\beta^{-1}. \end{aligned} \quad (3.11)$$

Here and in the rest of this section we take  $v = 0$ . Then, the refractive index  $\eta = c/v_{\varphi,\text{em}}$  or  $\eta = s_e/v_{\varphi,\text{es}}$ , respectively, is the same for both waves and, in an isothermal plasma, both propagate along identical trajectories. These trajectories or rays are orthogonal to the surfaces of constant phase,  $\psi(\mathbf{x}, t) = \text{const}$  (Fig. 3.1). In a stationary plasma the phase difference between two points  $P_1, P_2$  at a given time is uniquely determined by

$$\psi(P_2) - \psi(P_1) = \int_{P_1}^{P_2} |\mathbf{k}| ds$$

along a ray segment  $C$ . Along an arbitrary path  $C'$  from  $P_1$  to  $P_2$  one has

$$\psi(P_2) - \psi(P_1) = \int_{C'} \mathbf{k} ds \leq \int_{C'} k ds.$$

This expresses Fermat's principle [3].

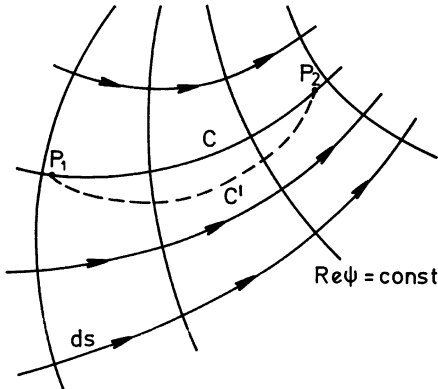


**Fig. 3.1** The rays form a manifold of curves which are perpendicular to the surfaces of constant phase at  $t$  fixed,  $\psi(\mathbf{x}, t) = \text{const}$

From

$$\frac{d}{ds}(\mathbf{k}_0\eta) = \frac{1}{k_0\eta}(\mathbf{k}_0\eta\nabla)(\mathbf{k}_0\eta) = \frac{1}{2k_0\eta}\nabla(\mathbf{k}_0\eta)^2 - \frac{\mathbf{k}_0}{k_0} \times \nabla \times \mathbf{k}_0\eta,$$

$$\nabla \times \mathbf{k}_0\eta = \nabla \times (\nabla\psi) = 0$$

the widely used ray equation

$$\frac{d}{ds}(\mathbf{k}_0\eta) = k_0\nabla\eta \quad (3.12)$$

follows immediately, if use is made of the vector identity  $\mathbf{a} \times (\nabla \times \mathbf{a}) = \nabla(\mathbf{a}^2/2) - (\mathbf{a}\nabla)\mathbf{a}$ . Equation (3.12) is the basis for raytracing. From it  $\eta$  is again recognized as the refractive index. In the fully ionized plasma it is the same for Langmuir waves as for electromagnetic waves. For the electron plasma wave  $s_e$  plays the same role as the speed of light  $c$  does for the laser wave. In general, (3.12) has to be solved numerically. Only in plane and spherical geometry (“stratified” or “layered” medium) is it easily integrated. With the constant vector  $\mathbf{n} = \nabla\eta/|\nabla\eta|$  in plane geometry one has:

$$\frac{d}{ds}(\mathbf{n} \times \mathbf{k}_0\eta) = \mathbf{n} \times \frac{d}{ds}(\mathbf{k}_0\eta) = \mathbf{n} \times k_0\nabla\eta = 0.$$

Similarly, in spherical geometry one finds for a vector  $\mathbf{r}$  having its origin in the center of symmetry of  $\eta(r)$ ,

$$\frac{d}{ds}(\mathbf{r} \times \mathbf{k}_0\eta) = \frac{\mathbf{k}_0}{k_0} \times \mathbf{k}_0\eta + \mathbf{r} \times \frac{d}{ds}(\mathbf{k}_0\eta) = \mathbf{r} \times k_0\nabla\eta = 0,$$

since  $\nabla\eta$  is parallel to  $\mathbf{r}$ . If  $\alpha$  is the angle  $\alpha$  between the local wave vector and  $\nabla\eta$ , the two relations can be expressed in integrated form

$$\eta(x)\sin\alpha = \text{const} \quad (\text{plane}), \quad r\eta(r)\sin\alpha = \text{const} \quad (\text{spherical}). \quad (3.13)$$

Two examples of ray distributions for plane and spherical geometry are sketched in Fig. 3.2. In the plane stratified medium the ray directions are such that the  $y$ -component of  $\mathbf{k}_0\eta$  is conserved. In spherical geometry the momentum  $\mathbf{r} \times \mathbf{k}_0\eta$  relative to the center of symmetry remains constant. It follows from (3.11) that Langmuir and electromagnetic waves cannot propagate beyond the critical density given by (2.94). At oblique or nonradial incidence from the vacuum at the angle  $\alpha_0$  or distance  $b$  from the radius, respectively, the turning point of a ray is located at

$$\eta(x) = \sin\alpha_0 \quad (\text{plane}), \quad r\eta(r) = b \quad (\text{spherical}). \quad (3.14)$$

The phase  $\psi$  is a function of  $\mathbf{x}$  and  $t$ . From the definition (3.10) of the wave vector it is clear that  $\mathbf{k} = \mathbf{k}(\mathbf{x}, t)$ ; hence, owing to the dispersion relations (3.11), the functional dependence of the frequency is  $\omega = \omega(\mathbf{k}, \mathbf{x}, t)$ . The explicit dependence

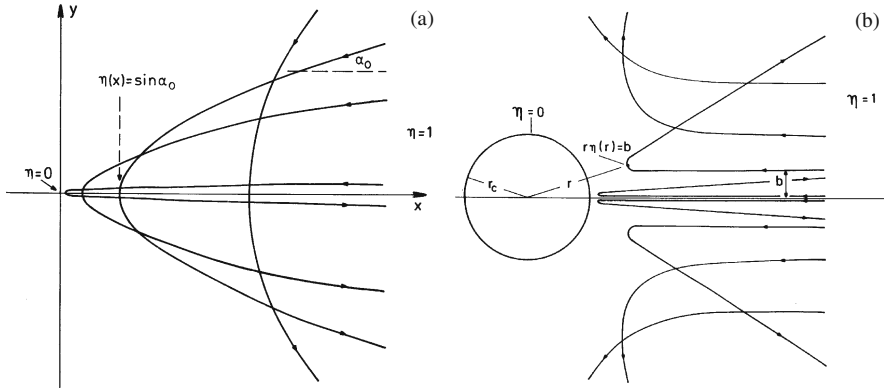


**Fig. 3.2** Raytracing. (a): Plane layered medium. A ray incident from vacuum at the angle  $\alpha_0$  has its turning point at  $\eta(x) = \sin \alpha_0$ . The y-component  $\hbar k_y = \hbar k_0 \eta \cos \alpha = \hbar k_0 \cos \alpha_0$  of the photon momentum is conserved in the stationary medium. (b): Deflection of a parallel beam by a spherical plasma cloud. In the stationary medium the angular momenta  $\hbar k_0 \eta r \sin \alpha = \hbar k_0 b$  of the photons are conserved along their trajectories

on  $\mathbf{x}$  enters through  $\omega_p^2(\mathbf{x}, t)$  and  $s_e^2(\mathbf{x}, t)$ . From (3.10) and  $\nabla \times \mathbf{k} = \nabla \times \nabla \psi = 0$  it follows that

$$\frac{\partial k_i}{\partial t} + \left( \frac{d\omega}{dx_i} \right)_{t=\text{const}} = 0, \quad \frac{\partial k_i}{\partial x_j} = \frac{\partial k_j}{\partial x_i}.$$

With the help of the second relation the first transforms into

$$\begin{aligned} \frac{\partial k_i}{\partial t} + \frac{\partial \omega}{\partial k_j} \frac{\partial k_j}{\partial x_i} + \frac{\partial \omega}{\partial x_i} &= \frac{\partial k_i}{\partial t} + \frac{\partial \omega}{\partial k_j} \frac{\partial k_i}{\partial x_j} + \frac{\partial \omega}{\partial x_i} = \\ \left( \frac{\partial}{\partial t} + \frac{\partial \omega}{\partial k_j} \frac{\partial}{\partial x_j} \right) k_i + \frac{\partial \omega}{\partial x_i} &= 0; \quad \Leftrightarrow \left( \frac{\partial}{\partial t} + \mathbf{v}_g \nabla \right) k_i = -\frac{\partial \omega}{\partial x_i}. \end{aligned}$$

Hence, the set of equations governing an electromagnetic or electrostatic wave, i.e.,

$$\frac{d\mathbf{x}}{dt} = \frac{\partial \omega}{\partial \mathbf{k}}, \quad \frac{d\mathbf{k}}{dt} = -\frac{\partial \omega}{\partial \mathbf{x}}, \quad \frac{d\omega}{dt} = \frac{\partial \omega}{\partial t} \quad (3.15)$$

are Hamilton's canonical equations if we take  $H(\mathbf{p}, \mathbf{q}, t) = \omega(\mathbf{k}, \mathbf{x}, t)$  with  $p_i = k_i$ ,  $q_i = x_i$ . We observe that  $\partial \omega / \partial \mathbf{k}$ , generally defined as the “group velocity” of a wave packet, appears to be the transport velocity of the  $\mathbf{k}$  vector under consideration. The last of (3.15) is a consequence of the preceding canonical equations of motion. From (3.10) follows also the Hamilton–Jacobi equation:

$$\frac{\partial \psi}{\partial t} + \omega \left( \frac{\partial \psi}{\partial \mathbf{x}}, \mathbf{x}, t \right) = 0, \quad (3.16)$$

thus showing that the phase  $\psi$  is an action variable.

A wave vector  $\mathbf{k}$  from (3.10) is given the name photon, plasmon, phonon by definition, in agreement with quantum theory where  $\hbar\mathbf{k}$  is its momentum. The domain of validity of the particle concept in both cases, classical and quantum mechanical, is exactly the same. From the Hamiltonian structure of (3.15) follows that the phase volume  $\Delta\mathbf{x}\Delta\mathbf{k}$  is conserved (Liouville's theorem). Introducing the phase space occupation density  $f(\mathbf{x}, \mathbf{k}, t)$  for photons, plasmons or phonons, respectively, just in the same way as with the one-particle distribution function for material particles in (2.81) along a characteristic the number  $\Delta N = f(\mathbf{x}, \mathbf{k}, t) \Delta\mathbf{x} \Delta\mathbf{k}$  changes in accordance with the source terms for particle generation (emission)  $\lambda(\mathbf{x}, \mathbf{k}, t)$  and particle destruction (absorption)  $-\alpha(\mathbf{x}, \mathbf{k}, t)f$ , i.e.,  $dN/dt = \Delta\mathbf{x} \Delta\mathbf{k} df/dt = \Delta\mathbf{x} \Delta\mathbf{k} (\lambda - \alpha f)$ . In explicit form it reads with the help of (3.15)

$$\frac{\partial f}{\partial t} + \frac{\partial \omega}{\partial \mathbf{k}} \frac{\partial f}{\partial \mathbf{x}} - \frac{\partial \omega}{\partial \mathbf{x}} \frac{\partial f}{\partial \mathbf{k}} = \lambda(\mathbf{x}, \mathbf{k}, t) - \alpha(\mathbf{x}, \mathbf{k}, t)f. \quad (3.17)$$

For fixed  $(\mathbf{x}, t)$  the term  $-\alpha f$  expresses the fact that there is an equal probability to be absorbed for all photons  $\mathbf{k}$ . Equation (3.17) is the basic equation for radiation transport for photons, plasmons, and phonons. In the case of the refractive index  $\eta = 1$  for photons it reduces to the familiar relation

$$\frac{\partial f}{\partial t} + \mathbf{c} \frac{\partial f}{\partial \mathbf{x}} = \lambda(\mathbf{x}, \mathbf{k}, t) - \alpha(\mathbf{x}, \mathbf{k}, t)f, \quad (3.18)$$

which is valid for short wavelength radiation. From (3.17) it is easily seen how it modifies for a homogeneous medium with  $\eta = \text{const}$ . With the help of the Poisson brackets the left hand side of (3.17) can be written as  $\partial f / \partial t + \{\omega, f\}$ .

Two remarks are in order. At first glance the ray equation (3.12) seems to contradict the momentum equation of motion for  $\mathbf{k}$  from (3.15). This is not the case since the refractive index is a function of  $\mathbf{x}$  and  $t$  only whereas  $\omega$  depends on the triple  $\mathbf{k}, \mathbf{x}, t$ . If  $f$  is chosen to represent the photon density the quantity

$$f \frac{\partial \omega}{\partial \mathbf{k}} = \frac{1}{2} \frac{\varepsilon_0}{\hbar} \frac{\hat{\mathbf{E}} \hat{\mathbf{E}}^*}{\omega} \mathbf{v}_g \quad (3.19)$$

is the photon flux density per unit angle and unit wavelength enclosed within a narrow bundle of rays with no lateral losses through its surface. Therefore the spatial losses in the narrow tube are expressible by the gradient, i.e., the variation of flux along a single ray. In Poynting's theorem the flux balance is taken in a volume of arbitrary shape, with no restriction to an unit angle, and as a consequence also lateral losses appear in general, expressible by the operator of divergence on the flux density  $S$  (see Sect. 3.1.3).

From (3.19) and (3.18) follows that in the absence of sources the action density  $(\varepsilon_0/2)\hat{\mathbf{E}} \hat{\mathbf{E}}^*/\omega$  is conserved rather than the energy density  $(\varepsilon_0/2)\hat{\mathbf{E}} \hat{\mathbf{E}}^*$ . In the neighborhood of a critical point the optical approximation  $\lambda(\mathbf{x}) = 2\pi/k_0\eta \ll L$  is never fulfilled and the eikonal approach with its consequences (3.12), (3.13), (3.14),

(3.15), (3.16), (3.17), and (3.18) becomes meaningless. In general, this is also true at the turning points. To see this in the important case of a plane layered medium, the exact wave equation (3.7) may be split into its components. In the coordinate system of Fig. 3.2a the fact that  $\eta$  is independent of  $y$  and  $z$ , a Fourier decomposition in the planes  $x = \text{const}$  is convenient, with  $k_y$  not depending on  $x$ . This is in agreement with the ray equation (3.13),  $k_y = k_0\eta \sin \alpha = k_0 \sin \alpha_0 = \text{const}$ , and means that the momentum of a photon perpendicular to the density gradient is conserved along its geometrical path. Hence,

$$\mathbf{E}(\mathbf{x}, t) = \{E_x(x), E_y(x), E_z(x)\} e^{ik_y y - i\omega t}. \quad (3.20)$$

The individual components obey the three equations (' =  $d/dx$ )

$$E''_x + \frac{k_0^2}{\beta^2}(\eta^2 - \sin^2 \alpha_0)E_x = i \frac{k_0}{\beta^2}(1 - \beta^2) \sin \alpha_0 E'_y, \quad (3.21)$$

$$E''_y + k_0^2(\eta^2 - \beta^2 \sin^2 \alpha_0)E_y = ik_0(1 - \beta^2) \sin \alpha_0 E'_x, \quad (3.22)$$

$$E''_z + k_0^2(\eta^2 - \sin^2 \alpha_0)E_z = 0. \quad (3.23)$$

Hence,  $E_z$  (s-polarized light) decouples from  $E_x$  and  $E_y$ , and is of purely electromagnetic nature. At its turning point  $k_x = k_0(\eta^2 - \sin^2 \alpha_0)^{1/2}$  vanishes and the approximations leading to the dispersion relations (3.11) are no longer justified. For the LHS of (3.21) to be resonantly excited by its RHS ‘‘driver’’, which in laser irradiation is an electromagnetic wave, in addition to  $\omega_{es} = \omega_{em}$ , both terms must have the same spatial dependence. Outside the turning point region, (3.11) holds with  $k_{x,em}$  very different from  $k_{x,es} = k_{x,em}/\beta$  for nonrelativistic temperatures. As a consequence, there, the transverse and longitudinal components decouple and propagate without affecting each other. At the turning points resonant coupling is possible and generally very effective (see the next chapter).

A serious difficulty arises with the expressions (3.12) and (3.15) in an absorbing medium, in particular when the absorption is strong, since then the imaginary parts of  $\mathbf{k}$  and  $\mathbf{v}_g$  can no longer be ignored. Several solutions have been proposed to overcome this difficulty. We remark that an interesting reinterpretation of the group velocity in terms of a time-dependent combination of  $\Re(\partial\omega/\partial\mathbf{k})$  and  $\Im(\partial\omega/\partial\mathbf{k})$  was presented and appropriate ray-tracing equations were derived in [4]. For more recent developments on this subject the interested reader may consult [5] and [6].

### 3.1.2 WKB Approximation

From (3.10) and (3.11) the phase  $\psi$  is obtained by integrating  $d\psi$  along a characteristic  $\mathbf{x} = \mathbf{x}(t) = \int \mathbf{v}_\varphi dt$  or any other path in  $\mathbb{R}^4$ ,

$$\psi(\mathbf{x}, t) = \pm \int^x k_0 \eta(\mathbf{x}', t') d\mathbf{x}' - \int^t \omega(\mathbf{k}; \mathbf{x}', t') dt'. \quad (3.24)$$

Since  $\nabla \times \mathbf{E} = i\nabla\psi \times \mathbf{E}$  and  $\partial_t \mathbf{B} = i\mathbf{B}\partial_t\psi = -i\omega\mathbf{B}$ , (2.2) remains valid for  $\mathbf{B}$  and, in a weakly absorbing medium, the Poynting vector  $\mathbf{S}$  is parallel to  $\mathbf{k}$ . Hence, the energy flows along the characteristics and propagates with the group velocity (Sect. 11.7 in [2]). Now, let the medium be stationary, i.e.,  $\partial_t\eta = 0$ ,  $\eta = \eta(\mathbf{x})$ . Then the characteristics  $\mathbf{x}(t)$  coincide with the rays and (3.24) reduces to the familiar expression  $\psi(\mathbf{x}, t) = \pm k_0 \int \eta ds - \omega t$ . By designating the local cross section of a narrow ray bundle by  $Q(s)$ , in the eikonal region  $\mathbf{x} = \mathbf{x}(s)$  the solutions of (3.7) for  $\mathbf{E} = \mathbf{E}_\perp$  are

$$\mathbf{E}(s) = \left( \frac{Q(s_0)}{\eta(s)Q(s)} \right)^{1/2} \left\{ \hat{\mathbf{E}}_+ e^{ik_0 \int \eta ds} + \hat{\mathbf{E}}_- e^{-ik_0 \int \eta ds} \right\} e^{-i\omega t}. \quad (3.25)$$

These are the WKB solutions with  $\eta(s_0) = 1$ . They simply express the fact that the energy flows with the group velocity along the rays without being attenuated by gradual reflection. The propagating wave  $\mathbf{E}_+$  and counterpropagating wave  $\mathbf{E}_-$  are normal to the rays and do not interact with each other. Specializing for a plane layered medium results in

$$\begin{aligned} \mathbf{E} &= \frac{\hat{\mathbf{E}}_+}{(\eta^2 - \sin^2 \alpha_0)^{1/4}} e^{ik_0 \int \eta dx - i\omega t} + \frac{\hat{\mathbf{E}}_-}{(\eta^2 - \sin^2 \alpha_0)^{1/4}} e^{-ik_0 \int \eta dx - i\omega t}, \\ |\hat{\mathbf{E}}_+| &= \text{const}, \quad |\hat{\mathbf{E}}_-| = \text{const}. \end{aligned} \quad (3.26)$$

At normal incidence the swelling factor of the amplitudes is  $\eta^{-1/2}$ . In the case of  $v \neq 0$  and  $\eta$  complex [and if one does not want to follow [4], for simplicity] the concept of rays still makes sense provided  $\Im\eta \ll \Re\eta$ . Then it does not matter much whether in the ray equation (3.12) and in (3.25) and (3.26)  $\eta$  is substituted by  $\eta_r = \Re\eta$  or by  $|\eta| = (\eta_r^2 + \eta_i^2)^{1/2} \simeq \eta_r(1 + \eta_i^2/2\eta_r^2) \simeq \eta_r$ , ( $\eta_i = \Im\eta$ ). If it is again postulated that the energy flow is along the rays, i.e.,  $\overline{\mathbf{S}} \parallel ds$ , then  $\eta$  is to be replaced by  $\eta_r$  in these equations. This is also in accordance with Ginzburg's proposition (see [7], p. 249).

In regions of finite  $\eta$  steep density gradients are needed in order to cause appreciable reflection. To illustrate this point quantitatively an Epstein transition layer of the following form is considered [8]

$$\eta^2(x) = 1 + P \frac{\exp(kx/s)}{1 + \exp(kx/s)}, \quad (3.27)$$

where  $P$  and  $s$  are free parameters. In Fig. 3.3  $\eta^2(x)$ , with  $P = -3/4$ , is sketched. The transition width  $\Delta$  is determined through  $s$  in the following way:

$$\Delta = \frac{4s}{k}, \quad k = 2\pi/\lambda.$$

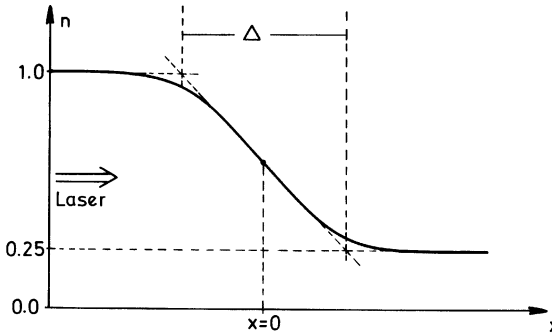


**Fig. 3.3** Epstein transition layer of width  $\Delta$  for the square of refractive index. The wave is incident from the left. Parameter  $P = -3/4$  is assumed

For a light beam normally incident from the left-hand side the reflection coefficient  $R$  is given by [8]

$$R = \frac{\sinh^2[\pi s(1 - \sqrt{1 + P})]}{\sinh^2[\pi s(1 + \sqrt{1 + P})]}.$$

In Table 3.1  $R$  normalized to the Fresnel value of the reflection coefficient  $R_0 = (\eta - 1)^2/(\eta + 1)^2$  for a refractive index step,  $r = R/R_0$ , is shown for  $P = \pm 3/4$  and different values of  $s$ . It may be surprising how fast reflection drops from its Fresnel value  $r = 1$  as soon as  $\Delta$  becomes larger than  $\lambda/4$ ; at  $P < -1$  total reflection occurs for all values of  $s$  [8]. As soon as a WKB condition is fulfilled, local reflection becomes extremely low, and the radiation field can be uniquely split into incident and reflected waves. When the optical approximation fails, a local reflection coefficient  $R(x)$  is no longer uniquely determined.

In the overdense region well beyond the turning point,

$$\kappa = k_0 \Im(\eta^2 - \sin^2 \alpha_0)^{1/2} \gg L^{-1}$$

may be fulfilled so that the eikonal approximation applies again and the amplitude of  $E_z$  from (3.23) decays exponentially (normal skin effect),

$$E_z(x) = E_{z0} \exp\left(-\int \kappa dx - ik_0 \int \Re(\eta^2 - \sin^2 \alpha_0)^{1/2} dx - i\omega t\right). \quad (3.28)$$

**Table 3.1** Normalized reflection coefficient  $r$  for the layer of Fig. 3.3 ( $P = -3/4$ ) and  $P = +3/4$  as a function of the transition width  $\Delta$

$s$	2	1	1/2	1/4	1/8	1/16
$\Delta/\lambda$	1.27	0.64	0.32	0.16	0.08	0.04
$P = +3/4$	$6.1 \times 10^{-10}$	$1.36 \times 10^{-4}$	$3.92 \times 10^{-2}$	0.37	0.77	0.93
$P = -3/4$	$3.1 \times 10^{-5}$	$1.5 \times 10^{-2}$	0.25	0.78	0.91	0.98

When dissipation is absent ( $\nu = 0$ ),  $\Re(\eta^2 - \sin^2 \alpha_0)^{1/2}$  is zero and the wave is evanescent with no energy transport ( $S = 0$ ) in the skin layer.

All considerations in this section hold for longitudinal plasma waves as well. In the formulas  $k_0$  has merely to be replaced by  $k_0/\beta$  ( $\beta = s_e/c$ ) and  $\mathbf{B}$  has to be set equal to zero.

### 3.1.3 Energy Fluxes

Energy conservation is expressed by Poynting's theorem,

$$\frac{1}{2}\varepsilon_0 \frac{\partial}{\partial t}(\mathbf{E}^2 + c^2 \mathbf{B}^2) + \nabla S = -\mathbf{j} \cdot \mathbf{E}. \quad (3.29)$$

The term in parentheses contains the energy density of purely electromagnetic nature. It can vary in time by irradiation, expressed by the divergence of the Poynting vector  $S$ , and by doing mechanical work on matter through the  $\mathbf{j} \cdot \mathbf{E}$  term. To interpret this source and sink term Ohm's law (3.5) in a frame comoving with the plasma may again be used, with  $(\mathbf{j} \nabla) \mathbf{v}_0$  set equal to zero,

$$\mathbf{E} = \frac{1}{\varepsilon_0 \omega_p^2} \left( \frac{\partial \mathbf{j}}{\partial t} + \nu \mathbf{j} + \varepsilon_0 s_e^2 \nabla (\nabla \cdot \mathbf{E}) \right).$$

Now let  $\mathbf{E}$  be purely transverse,  $\mathbf{E} = \mathbf{E}_\perp$ . Multiplying by  $\mathbf{j}$  and averaging over one period leads to  $\Re(\mathbf{j} \cdot \mathbf{E}) = \partial_t(n_e W) + 2\nu n_e W$ , where  $W$  is the mean oscillation energy of the electron. Hence, the cycle-averaged relation (3.29) can be written as

$$\frac{\partial}{\partial t} \left\{ \frac{\varepsilon_0}{4} \hat{\mathbf{E}} \hat{\mathbf{E}}^* + \frac{\varepsilon_0 c^2}{4} \hat{\mathbf{B}} \hat{\mathbf{B}}^* + \frac{1}{2} n_e W \right\} + \nabla \bar{S} = -2\nu n_e W. \quad (3.30)$$

If there is no dissipation ( $\nu = 0$ ) the only energy “absorption”  $\nabla \bar{S} < 0$  is accomplished by increasing the electric, magnetic or kinetic energy densities; they are reversible. When the wave field as well as the plasma density are both stationary,  $\nabla \bar{S} = 0$  must hold. As the wave penetrates a fully ionized plasma with an electron density slowly varying in space the magnetic energy density decreases according to  $\varepsilon_0 c^2 \hat{\mathbf{B}} \hat{\mathbf{B}}^*/4 = \eta^2 \varepsilon_0 \hat{\mathbf{E}} \hat{\mathbf{E}}^*/4$ , whereas the kinetic energy density increases by the same amount. In fact, the total density  $\mathcal{E}$  is

$$\begin{aligned} \mathcal{E} &= \frac{\varepsilon_0}{4} (\hat{\mathbf{E}} \hat{\mathbf{E}}^* + c^2 \hat{\mathbf{B}} \hat{\mathbf{B}}^*) + \frac{1}{2} n_e W \\ &= \frac{\varepsilon_0}{4} \hat{\mathbf{E}} \hat{\mathbf{E}}^* \left( 1 + \eta^2 + \frac{\omega_p^2}{\omega^2} \right) = \frac{\varepsilon_0}{2} \hat{\mathbf{E}} \hat{\mathbf{E}}^*, \end{aligned} \quad (3.31)$$

thus revealing that the magnetic energy gradually transforms into oscillation energy. At the critical point  $B = \eta E/c \sim \eta^{1/2}$  tends to zero and the oscillation energy is

exactly equal to the electric energy. Equations (3.30) and (3.31) are in perfect agreement with the WKB solution (3.25). It is interesting to note that, without dissipation, (3.30) yields with the aid of (2.2) and (3.31)

$$\frac{\partial}{\partial t} \mathcal{E} + \nabla \bar{S} = \frac{\partial}{\partial t} \mathcal{E} + \nabla \left( \frac{\varepsilon_0}{2} c \eta \hat{E} \hat{E}^* \right) = \frac{\partial}{\partial t} \mathcal{E} + \nabla (\mathbf{v}_g \mathcal{E}) = 0$$

for the fully ionized plasma. In a general dispersive medium the last version of energy conservation also holds, but its derivation is more subtle. In the presence of dissipation ( $\nu > 0$ ) the pure absorptive case with  $\partial \mathcal{E} / \partial t = 0$  is of greatest relevance,

$$\nabla \bar{S} = -2\nu n_e W, \quad n_e W = \frac{1}{2} \left( 1 - \Re \eta^2 \right) \mathcal{E}. \quad (3.32)$$

From this the attenuation of a light beam is immediately determined to be governed by

$$\frac{dI}{ds} = \nabla \bar{S} = -\frac{\nu}{c \eta_r} \frac{\omega_p^2}{\omega^2 + \nu^2} I = -\alpha I \Leftrightarrow I(s) = I(s_0) e^{-\int_{s_0}^s \alpha ds}. \quad (3.33)$$

The integrated version is recognized as Beer's law. Alternatively,  $I = |\bar{S}|$  may be calculated directly from (3.25) with the undamped local amplitude  $\hat{E}(s) = \hat{E}_+(Q(s_0)/\eta(s)Q(s))^{1/2}$ ,

$$I(s) = \varepsilon_0 c^2 |\bar{E} \times \bar{B}| = \frac{1}{2} \varepsilon_0 c \eta_r \hat{E} \hat{E}^* e^{-2k_0 \int_s^s \Im \eta ds} = I(s_0) e^{-\int_{s_0}^s \alpha ds}; \\ \alpha = 2k_0 \Im \eta. \quad (3.34)$$

From  $A = \Re \eta^2$  and  $B = \Im \eta^2$  in (3.8) one deduces

$$\eta_r = \Re \eta = \left\{ \frac{1}{2} \left( \sqrt{A^2 + B^2} + A \right) \right\}^{1/2}, \\ \eta_i = \Im \eta = \left\{ \frac{1}{2} \left( \sqrt{A^2 + B^2} - A \right) \right\}^{1/2}. \quad (3.35)$$

Expanding  $\eta$  for  $B^2 \ll A^2$  leads to

$$\eta_r = \left( 1 - \frac{\omega_p^2}{\omega^2 + \nu^2} \right)^{1/2}, \quad \eta_i = \frac{B}{2\eta_r}, \quad \alpha = 2k_0 \Im \eta = \frac{\nu}{c \eta_r} \frac{\omega_p^2}{\omega^2 + \nu^2}, \quad (3.36)$$

i.e., the absorption coefficients from (3.33) and (3.34) become identical, as expected. The refractive index  $\eta_r$  in the denominator is due to the increase of  $\bar{E}$  and  $W$  with

increasing plasma density. If the eikonal approximation is no longer valid, no simple relation exists between  $\mathcal{E}$  and  $\bar{\mathcal{S}}$  and the absorption has to be calculated from (3.30) and the wave equation (3.7) or a simplified version of it, e.g.,  $\Delta \mathbf{E} + k_0^2 \eta^2 \mathbf{E} = 0$ .

For the longitudinal component  $\mathbf{E} = \mathbf{E}_{\parallel}$ ,  $S = 0$  holds and the energy is carried by the thermal motion of the electrons. On the other hand, one would argue that dispersion relations of identical structures lead to energy conservation equations of the same structure. Hence, in the dissipation-free case,  $\partial_t \mathcal{E} + \nabla(\mathbf{v}_g \mathcal{E}) = 0$  should hold again with  $\mathcal{E} = f \varepsilon_0 \hat{\mathbf{E}}_{\parallel} \hat{\mathbf{E}}_{\parallel}^*/2$ , where  $f$  is an eventual proportionality constant and  $v_g = s_e^2/v_{\varphi}$ .

To see whether such an argument holds in the general case one may start from the linearized momentum equations of Sect. 2.2.2 for electrons and ions without dissipation,

$$\begin{aligned} m n_{e0} \partial_t \mathbf{v}_e &= -m s_e^2 \nabla n_{e1} - n_{e0} e \mathbf{E}, \\ m_i n_0 \partial_t \mathbf{v}_i &= -m_i s^2 \nabla n_{i1} + n_0 Z e \mathbf{E}. \end{aligned}$$

Multiplying the first equation by  $\mathbf{v}_e$  and the second one by  $\mathbf{v}_i$  and adding them yields

$$\begin{aligned} \partial_t \left( \frac{1}{2} n_{e0} m \mathbf{v}_e^2 + \frac{1}{2} n_0 m_i \mathbf{v}_i^2 \right) - \mathbf{j} \mathbf{E} &= -m s_e^2 \mathbf{v}_e \nabla n_{e1} - m_i s^2 \mathbf{v}_i \nabla n_{i1} \\ &= -m s_e^2 (\nabla(n_{e1} \mathbf{v}_e) - n_{e1} \nabla \mathbf{v}_e) - m_i s^2 (\nabla(n_{i1} \mathbf{v}_i) - n_{i1} \nabla \mathbf{v}_i). \end{aligned}$$

The linearized mass conservation equations imply

$$n_{\alpha 1} \nabla \mathbf{v}_{\alpha} = \frac{n_{\alpha 1}}{n_{\alpha 0}} \nabla n_{\alpha 0} \mathbf{v}_{\alpha} = -\frac{n_{\alpha 1}}{n_{\alpha 0}} \partial_t n_{\alpha 1} = -\frac{1}{2} n_{\alpha 0} \partial_t \left( \frac{n_{\alpha 1}}{n_{\alpha 0}} \right)^2, \quad \alpha = e, i,$$

and, when substituted in the foregoing equation,

$$\begin{aligned} \partial_t \left( \frac{1}{2} n_{e0} m \mathbf{v}_e^2 + \frac{1}{2} n_0 m_i \mathbf{v}_i^2 \right) + \partial_t \left[ \frac{1}{2} n_{e0} m s_e^2 \left( \frac{n_{e1}}{n_{e0}} \right)^2 + \frac{1}{2} n_0 m_i s^2 \left( \frac{n_{i1}}{n_0} \right)^2 \right] \\ + 2 \nabla \left( \frac{1}{2} \mathbf{v}_{g,e} n_{e0} m \mathbf{v}_e^2 + \frac{1}{2} \mathbf{v}_{g,i} n_0 m_i \mathbf{v}_i^2 \right) - \mathbf{j} \mathbf{E} = 0 \end{aligned} \quad (3.37)$$

is obtained, or

$$\frac{\partial}{\partial t} (\mathcal{E}_{e,\text{kin}} + \mathcal{E}_{i,\text{kin}} + \mathcal{E}_{e,\text{pot}} + \mathcal{E}_{i,\text{pot}}) + 2 \nabla (\mathbf{v}_{g,e} \mathcal{E}_{e,\text{kin}} + \mathbf{v}_{g,i} \mathcal{E}_{i,\text{kin}}) - \mathbf{j} \mathbf{E} = 0,$$

$v_{g,\alpha}$  group velocity. The divergence term was obtained with the help of  $\mathbf{v}_{\alpha} = \mathbf{v}_{\varphi,\alpha} n_{\alpha 1} / n_{\alpha 0}$  from (2.93) and (2.101). When  $\mathbf{j} \mathbf{E}$  is substituted from (3.29) at every time instant the wave energy balance is given by

$$\begin{aligned} \frac{\partial}{\partial t} (\mathcal{E}_e + \mathcal{E}_{e,\text{kin}} + \mathcal{E}_{i,\text{kin}} + \mathcal{E}_{e,\text{pot}} + \mathcal{E}_{i,\text{pot}}) + \nabla \cdot (S + 2S_{e,\text{kin}} + 2S_{i,\text{kin}}) &= 0; \\ S_{e,\text{kin}} &= \frac{1}{2} \frac{s_e^2}{v_\varphi^2} n_{e0} m_e \mathbf{v}_e^2; \quad S_{i,\text{kin}} = \frac{1}{2} s n_0 m_i \mathbf{v}_i^2. \end{aligned} \quad (3.38)$$

Specializing to a monochromatic electron-plasma wave we have, with the help of (2.93) and after cycle-averaging,

$$\begin{aligned} \bar{\mathcal{E}}_{e,\text{kin}} + \bar{\mathcal{E}}_{e,\text{pot}} &= \frac{1}{2} m n_{e0} \left( 1 + \frac{s_e^2}{v_\varphi^2} \right) \bar{\mathbf{v}}_e^2 = \frac{\epsilon_0}{4} \frac{\omega^2 + s_e^2 k_e^2}{\omega_p^2} \hat{\mathbf{E}} \hat{\mathbf{E}}^*, \\ \bar{S}_{e,\text{kin}} &= \frac{\epsilon_0}{4} v_g \frac{\omega^2}{\omega_p^2} \hat{\mathbf{E}} \hat{\mathbf{E}}^*. \end{aligned}$$

Hence, the total cycle-averaged energy density  $\mathcal{E}_s$  and flux density  $I = 2\bar{S}_{e,\text{kin}}$  are

$$\mathcal{E}_s = \mathcal{E}_e + \mathcal{E}_{e,\text{kin}} + \mathcal{E}_{e,\text{pot}} = \frac{\epsilon_0}{2} \frac{\omega^2}{\omega_p^2} \hat{\mathbf{E}} \hat{\mathbf{E}}^*, \quad I = v_g \mathcal{E}_s. \quad (3.39)$$

This shows that the idea based on the dispersion relations was correct with  $f = \omega^2/\omega_p^2$ . When an electron-plasma wave is resonantly excited by the laser,  $\omega = \omega_p$ ,  $f = 1$  holds, since  $k_e = 0$  at resonance (see Chap. 4). Energy conservation (3.38) becomes simplest for the ion acoustic wave,

$$\begin{aligned} \partial_t \mathcal{E}_i + \nabla \cdot \mathbf{I}_i &= 0; \\ \mathcal{E}_i = \bar{\mathcal{E}}_{i,\text{kin}} + \bar{\mathcal{E}}_{i,\text{pot}} &= 2\bar{\mathcal{E}}_{i,\text{kin}} = \frac{1}{2} n_0 m_i \hat{\mathbf{v}}_i^2, \quad I_i = 2\bar{S}_{i,\text{kin}} = s \mathcal{E}_i. \end{aligned} \quad (3.40)$$

The derivation of a relation analogous to (3.38) for dielectric media is more involved.

It is interesting to note that the group velocity enters in the energy flux density only when the total energy density  $\mathcal{E}$  is considered. If, instead, one includes in  $\mathcal{E}$  solely the energy density  $\mathcal{E}_c$  which is carried by the wave and transmitted from point to point  $v_g$  has to be replaced by another speed. Thus, for instance, for an electromagnetic wave in the plasma  $\mathcal{E}_c = \mathcal{E}_e - \mathcal{E}_{e,\text{kin}} = \epsilon_0 \eta^2 \hat{\mathbf{E}} \hat{\mathbf{E}}^* / 4$ , as pointed out in an enlightening article by Johnson [9], and the energy conservation  $\partial_t \mathcal{E} + \nabla \cdot (\mathbf{v}_g \mathcal{E}) = 0$  is replaced by the equivalent expression

$$\partial_t \mathcal{E}_c + \nabla \cdot \bar{\mathbf{S}} = \partial_t \mathcal{E}_c + \nabla \cdot (\mathbf{v}_\varphi \mathcal{E}_c) = 0;$$

$\mathcal{E}_c$  is always carried at the phase velocity  $v_\varphi = c/\eta$ .

The energy balance presented above is strictly valid for waves of infinitesimal amplitude in a homogeneous plasma. Its applicability to nonstationary inhomogeneous plasmas is guaranteed as long as  $\lambda/L \ll 1$  and  $2\pi/\omega T \ll 1$ , with  $L$  and  $T$  the

characteristic length and time scales, respectively, are fulfilled. More precisely, the validity of the above analysis is intimately connected with the adiabatic behavior of an action integral. Therefore, in the following subsection we make use of the principle of least action to derive energy conservation. The less theoretically oriented reader may skip it.

### 3.1.3.1 Variational Treatment

Lagrangian Mechanics is the most general and powerful formalism for solving problems of point dynamics, once the Lagrangian  $L = L(q_i, \dot{q}_i, t)$  of generalized point coordinates  $q_i$  and their time derivatives  $\dot{q}_i$  is known. The familiar equations of motion  $d_t L \dot{q}_i - L_{q_i} = 0$  follow from the principle of least action,

$$\delta \int_{t_1}^{t_2} L(q_i, \dot{q}_i, t) dt = 0.$$

When passing from discrete mass points ( $\delta$ -functions) to the continuous distribution of fields the number of degrees of freedom becomes infinite and the coordinates  $q_i, \dot{q}_i$  become continuous variables  $q(\mathbf{x}, t)$  of the field densities and their derivatives  $\dot{q} = \partial_t q + (\mathbf{v} \nabla) q = f(q_t, q_x)$ . Depending on the problem,  $q$  may represent a matter density  $\rho(\mathbf{x}, t)$ , a velocity field  $\mathbf{v}(\mathbf{x}, t)$  or, as in this section, an electric (or magnetic) field. With  $q = \mathbf{E}(\mathbf{x}, t)$  the principle of least action reads

$$\delta \int_{t_1}^{t_2} \int_R L(E_i, \partial E_i / \partial t, \partial E_i / \partial x_j, t) dt d\mathbf{x} = 0; \quad i = 1, 2, 3. \quad (3.41)$$

By introducing the arbitrary variations  $h_i(\mathbf{x}, t)$  for

$$E_i(\mathbf{x}, t) = E_{i0}(\mathbf{x}, t) + h_i(\mathbf{x}, t),$$

and after integrating by parts to eliminate  $\partial_t h_i$  and  $\partial_j h_i = \partial h_i / \partial x_j$ , the Lagrange equations of motion

$$\frac{\partial}{\partial t} L_{E_{it}} + \frac{\partial}{\partial x_j} L_{E_{ij}} - L_{E_i} = 0; \quad L_{E_{it}} = \frac{\partial L}{\partial E_{it}}, \quad E_{it} = \frac{\partial E_i}{\partial t}, \text{etc,} \quad (3.42)$$

are obtained in the standard way (see, e.g., [2], p. 391). It is seen by inspection that all Lagrangians proportional to

$$\begin{aligned} L_{\perp} &= \frac{1}{2} \left\{ \frac{\omega_p^2}{c^2} E_i^2 + \sum_j (\partial_j E_i)^2 - \frac{1}{c^2} (\partial_t E_i)^2 \right\} \text{ for } \mathbf{E}_{\perp}, \quad i = 1, 2, 3, \\ L_{\parallel} &= \frac{1}{2} \left\{ \frac{\omega_p^2}{c^2} E_i^2 + \beta^2 \sum_j (\partial_i E_j)^2 - \frac{1}{c^2} (\partial_t E_i)^2 \right\} \text{ for } \mathbf{E}_{\parallel}, \quad i = 1, 2, 3, \end{aligned} \quad (3.43)$$

reproduce the wave equation (3.3) with  $\partial_t \mathbf{j} = \varepsilon_0 \omega_p^2 \mathbf{E} - \varepsilon_0 \omega_p^2 \nabla(\nabla \cdot \mathbf{E})$ . For  $\mathbf{E}_\perp$  and  $\mathbf{E}_\parallel$  separately, these become

$$\begin{aligned}\nabla^2 \mathbf{E}_\perp - \frac{1}{c^2} \frac{\partial^2}{\partial t^2} \mathbf{E}_\perp - \frac{\omega_p^2}{c^2} \mathbf{E}_\perp &= 0, \\ \beta^2 \nabla(\nabla \cdot \mathbf{E}_\parallel) - \frac{1}{c^2} \frac{\partial^2}{\partial t^2} \mathbf{E}_\parallel - \frac{\omega_p^2}{c^2} \mathbf{E}_\parallel &= 0.\end{aligned}\quad (3.44)$$

Under the assumption that  $\mathbf{E}$ , longitudinal or transverse, is described by the eikonal approximation, i.e.,  $\mathbf{E} = \hat{\mathbf{E}}(\mathbf{x}, t) \exp(i\psi(\mathbf{x}, t))$ , with  $\hat{\mathbf{E}}$  and  $\mathbf{k} = \nabla\psi$  changing slowly in space and time, (3.41) transforms into equations containing only  $\hat{\mathbf{E}}$ ,  $\psi_t = -\omega$ ,  $\psi_{x_j} = k_j$ , which are all slowly varying variables. Therefore, instead of using  $L = L(\mathbf{E}, \omega, \mathbf{k}, \mathbf{x}, t)$  it is appropriate to introduce the phase-averaged Lagrangian  $\mathcal{L} = \mathcal{L}(\hat{\mathbf{E}}, \omega, \mathbf{k}, \mathbf{x}, t)$ ,

$$\mathcal{L}(\hat{\mathbf{E}}, \omega, \mathbf{k}, \mathbf{x}, t) = \frac{1}{2\pi} \int L(\mathbf{E}, \omega, \mathbf{k}, \mathbf{x}, t) d\psi, \quad (3.45)$$

which no longer exhibits any fast dependence on  $\mathbf{x}$  and  $t$ . By observing that the averaging procedure is interchangeable with the  $\mathbf{x}$  and  $t$ -integration up to higher orders in the phase averaged  $h_i(\mathbf{x}, t)$ ,

$$\delta \int \mathcal{L}(\hat{\mathbf{E}}, \omega, \mathbf{k}, \mathbf{x}, t) dt d\mathbf{x} = \frac{1}{2\pi} \int d\psi \left( \delta \int L(\mathbf{E}, \omega, \mathbf{k}, \mathbf{x}, t) dt d\mathbf{x} \right),$$

the “averaged” principle of least action ([2], Chap. 14),

$$\delta \int \mathcal{L}(\hat{\mathbf{E}}, \omega, \mathbf{k}, \mathbf{x}, t) dt d\mathbf{x} = 0 \quad (3.46)$$

results. Varying in  $\hat{\mathbf{E}}, \omega, \mathbf{k}$  as before leads to

$$\mathcal{L}_{\hat{\mathbf{E}}} = 0, \quad \frac{\partial}{\partial t} \mathcal{L}_\omega - \frac{\partial}{\partial \mathbf{x}} \mathcal{L}_\mathbf{k} = 0; \quad (\mathcal{L}_\omega = -\mathcal{L}_{\psi_t}). \quad (3.47)$$

In the WKB approximation the Lagrangians (3.43) transform into

$$\mathcal{L}_\perp = \frac{1}{4} \left\{ \frac{\omega_p^2}{c^2} + \mathbf{k}^2 - \frac{\omega^2}{c^2} \right\} \hat{\mathbf{E}}_\perp^2; \quad \mathcal{L}_\parallel = \frac{1}{4} \left\{ \frac{\omega_p^2}{c^2} + \beta^2 \mathbf{k}^2 - \frac{\omega^2}{c^2} \right\} \hat{\mathbf{E}}_\parallel^2. \quad (3.48)$$

$\mathcal{L}_{\hat{\mathbf{E}}} = 0$  is proportional to the dispersion relation  $D(\omega, \mathbf{k}) = 0$ ; thus  $\mathcal{L} = \hat{\mathbf{E}}^2 D(\omega, \mathbf{k})$ ,  $\hat{\mathbf{E}} = \hat{\mathbf{E}}_\perp$  or  $\hat{\mathbf{E}}_\parallel$ . With this, the second of (3.43) can be written as

$$\frac{\partial}{\partial t} \left( D_\omega \hat{\mathbf{E}}^2 \right) - \frac{\partial}{\partial \mathbf{x}} \left( \hat{\mathbf{E}}^2 D_\mathbf{k} \right) = 0.$$

From  $D = 0$  follows with  $\omega = \omega(\mathbf{k}, \mathbf{x}, t)$  and

$$D_\omega \mathbf{v}_g + D_{\mathbf{k}} = 0 \quad \Rightarrow \quad \mathbf{v}_g = -\frac{D_{\mathbf{k}}}{D_\omega} = -\frac{\mathbf{f}(\mathbf{k}, \mathbf{x}, t)}{g(\mathbf{k}, \mathbf{x}, t)}, \quad D_{\mathbf{k}} = -g(\mathbf{k}, \mathbf{x}, t)\mathbf{v}_g.$$

Assume now that there is no explicit time dependence. Then, replacing  $D_\omega$  and  $D_{\mathbf{k}}$  by  $g(\mathbf{k}, \mathbf{x})$  and  $g(\mathbf{k}, \mathbf{x})\mathbf{v}_g$  in the above equation leads to

$$\frac{\partial}{\partial t} \left( g(\mathbf{k}, \mathbf{x}) \hat{\mathbf{E}}^2 \right) + \frac{\partial}{\partial \mathbf{x}} \left( g(\mathbf{k}, \mathbf{x}) \mathbf{v}_g \hat{\mathbf{E}}^2 \right) = g(\mathbf{k}, \mathbf{x}) \left\{ \frac{\partial}{\partial t} \hat{\mathbf{E}}^2 + \nabla \left( \mathbf{v}_g \hat{\mathbf{E}}^2 \right) \right\} = 0.$$

In the last step  $\nabla \times \mathbf{k} = 0$  has been used. This proves that dispersion relations of the same structure lead to analogous energy conservation relations. In addition, it shows that the total energy density in linear dielectrics also propagates with the group velocity.

## 3.2 Stokes Equation and its Applications

No general solutions or asymptotic approximations exist for the steady state wave equation (3.7) once the WKB approximation begins to fail as is the case at the turning points of the rays or when the gradient length  $L$  of  $\eta^2$  becomes appreciably less than  $\lambda$ . In practice, in such regions  $\eta^2(\mathbf{x})$  may be approximated by a linear function if the curvature of  $\eta^2$  is not too large. In this way (3.21) and (3.23) can be reduced to the homogeneous and inhomogeneous Stokes or Stokes-Airy equations. In view of their relevance for determining field structures and mode conversion they are treated here briefly.

### 3.2.1 Homogeneous Stokes Equation

In (3.21), (3.22), and (3.23) let  $\eta^2$  be a linear function of the spatial coordinate  $x$ ,

$$\eta^2(x) = q(x - x_c). \quad (3.49)$$

With the new coordinate  $\xi$ ,

$$\xi = (k_0^2 q)^{1/3} (x - x_0), \quad x_0 = x_c + \frac{\sin^2 \alpha_0}{q}, \quad (3.50)$$

where  $x_0$  is the turning point, and  $y = E_z$ , (3.23) transforms into the homogeneous Stokes equation,

$$y'' + \xi y = 0. \quad (3.51)$$

A solution is found by Fourier-transforming  $y$ ,

$$-k^2\varphi(k) + i \frac{d\varphi}{dk} = 0 \quad \Rightarrow \quad \varphi(k) = e^{-ik^3/3}$$

and inverting  $\varphi$  along a suitable contour  $C$ ,

$$y(\xi) = y_0 \int_C \exp i \left( k\xi - \frac{k^3}{3} \right) dk. \quad (3.52)$$

$\Re y$  and  $\Im y$  represent two linearly independent solutions of (3.51). When a light beam is incident from the right the solution must become evanescent in the over-dense halfspace  $\xi < 0$ . This is accomplished by combining  $\Re y$  and  $\Im y$  in a suitable way; the resulting solution is the Airy function  $\text{Ai}(\xi)$ , if  $y_0 = 1/(2\pi)$ :

$$\begin{aligned} \text{Ai}(\xi) &= \frac{f(\xi)}{3^{2/3}\Gamma(2/3)} - \frac{g(\xi)}{3^{1/3}\Gamma(1/3)}; \\ f(\xi) &= 1 - \frac{1}{3!}\xi^3 + \frac{1 \cdot 4}{6!}\xi^6 - \frac{1 \cdot 4 \cdot 7}{9!}\xi^9 + \frac{1 \cdot 4 \cdot 7 \cdot 10}{12!}\xi^{12} \mp \dots, \\ g(\xi) &= -\xi + \frac{2}{4!}\xi^4 - \frac{2 \cdot 5}{7!}\xi^7 + \frac{2 \cdot 5 \cdot 8}{10!}\xi^{10} \mp \dots \end{aligned} \quad (3.53)$$

([10], §10.4 with  $\xi = -z$ ). The second, linearly independent solution is chosen such that it diverges monotonically,

$$\text{Bi}(\xi) = \frac{f(\xi)}{3^{1/6}\Gamma(2/3)} + \frac{g(\xi)}{3^{-1/6}\Gamma(1/3)}.$$

$\text{Ai}$  and  $\text{Bi}$  are shown in Fig. 3.4a. The power series representation is suitable for small values of  $|\xi|$ . For large  $|\xi|$ ,  $\text{Ai}(\xi)$  is expected to be well approximated by its asymptotic forms. With  $\zeta = \int_0^\xi \eta d\xi \sim \int_0^\xi \xi^{1/2} d\xi = \frac{2}{3}\xi^{3/2}$  and  $\arg \xi^{3/2} = \frac{3}{2} \arg \xi$ ,  $\arg \xi^{1/4} = \frac{1}{4} \arg \xi$  they are

$$\begin{aligned} \text{Ai}(\xi) &= \text{Ai}_1(\xi) = \frac{1}{2\sqrt{\pi}\xi^{1/4}} e^{-i\zeta}, \quad \text{for } \frac{\pi}{3} \leq \arg \xi \leq \frac{5}{3}\pi \\ \text{Ai}(\xi) &= \text{Ai}_2(\xi) = \frac{1}{2\sqrt{\pi}\xi^{1/4}} \left\{ \exp i \left( \zeta - \frac{\pi}{4} \right) + \exp \left[ -i \left( \zeta - \frac{\pi}{4} \right) \right] \right\}, \\ &\text{for } -\frac{\pi}{3} \leq \arg \xi \leq \frac{\pi}{3}. \end{aligned} \quad (3.54)$$

The rays emanating from the origin under the angles  $\delta = \pm\pi/3$ ,  $-\pi$  are the so-called anti-Stokes lines. They play an important role for the determination of the correct WKB solutions connecting different regions in the complex  $\xi$ -plane (see, e.g., [11], Sect. 1–4). In Fig. 3.4b a comparison is made between  $|\text{Ai}|^2$  and its asymptotic expansion  $|\text{Ai}_2|^2$  for real  $\xi$ . As soon as  $|\xi| \geq 1.3$  the relative error

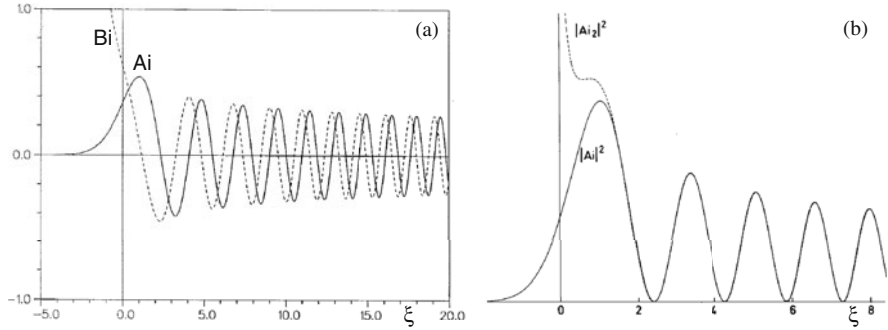


**Fig. 3.4** (a): Airy functions  $Ai$  (solid line) and  $Bi$  (dashed line) as functions of the dimensionless coordinate  $\xi$  from (3.50). (b): Comparison of the asymptotic expansion  $Ai_2 \cdot Ai_2^*$  (dashed line) with the Airy function  $Ai \cdot Ai^*$ .  $\xi$  is taken real (no absorption). For  $|\xi| \geq 1.5$  the relative error  $|Ai|^2 - |Ai_2|^2$  is less than 1%; at  $|\xi|$  equal to unity it amounts to 4%. The standing wave pattern is generated by total reflection in the critical region around  $\xi = 0$

$|Ai - Ai_2|/|Ai|$  becomes less than 1.5%. Even at the maximum of  $Ai$  which lies at  $\xi = 1.045$  the deviation is only 4%. The deviation starts to become exponentially large when  $|\xi|$  is less than 0.5. It is typical for the WKB approximation in general that even the maximum  $E$ -field and its location are approximately reproduced. The accuracy of (3.54) can be estimated analytically by casting the exact solution into the form

$$y(\xi) = C_+ W_+ + C_- W_-; \quad W_{\pm} = \xi^{-1/4} \exp(\pm i \zeta), \quad \xi > 0.$$

The deviations of  $C_{\pm}$  from unity are a suitable measure of the accuracy of  $W_{\pm}$ . In general (see, e.g., [11], Eq. (1-106))

$$|\Delta C_{\pm}| \lesssim \frac{5}{48|\xi|}. \quad (3.55)$$

For large  $|\xi|$  the WKB form becomes extremely precise.

Absorption and reflection coefficients can be calculated for arbitrary, smooth density profiles by bridging the critical point with the help of Stokes' equation. To this end let us assume a wave of unit amplitude incident from vacuum and let the amplitude of the reflected wave be  $s$ . Then from the requirement that the electric field must be continuous one obtains at  $x$ , with the associated  $|\xi|$  lying in the WKB region,

$$\begin{aligned} & \eta^{-1/2} \exp\left(-ik_0 \int_x^\infty \eta dx\right) + s \eta^{-1/2} \exp\left(ik_0 \int_x^\infty \eta dx\right) \\ &= C \xi^{-1/4} \left( e^{i(\xi-\pi/4)} + e^{-i(\xi-\pi/4)} \right). \end{aligned} \quad (3.56)$$

In order to satisfy this relation the incident wave at the RHS must be equal to the incident wave at the LHS, and the same must be true for the reflected wave since, within the limit of the WKB approximation the two waves do not interact. By eliminating the factor  $C$  one obtains for the amplitude ratio  $s$

$$s = \exp \left[ -2i \left( k_0 \int_x^\infty \eta dx - \zeta + \pi/4 \right) \right].$$

The reflection coefficient  $R$  for the intensity is given by

$$R = ss^* \exp \left[ -4 \left( \Im \zeta + k_0 \int_x^\infty |\Im \eta| dx \right) \right]. \quad (3.57)$$

The position  $x$  is somewhat arbitrary. On the one hand  $\Delta x = x - x_c$  must not be too small for the validity of the WKB approximation; on the other hand it should not be too large in order to keep the difference between  $\eta^2$  and its linear approximation small. This difference can be evaluated by taking into account the quadratic term in the expansion of  $\eta^2$ . The coefficient  $s$  would be independent of  $x$  if the WKB solution were exact. In order to be a good approximation,  $|(1/s)(ds/dx)|\Delta x \ll 1$  has to be fulfilled. Straightforward algebra yields

$$\left| \frac{1}{s} \frac{ds}{dx} \right| \Delta x < \left| \frac{1}{s} \frac{ds}{dx} \right| (x - x_0) = \frac{1}{2} \left| \frac{q'}{(k_0 q^2)^{2/3} \xi^{5/2}} \right| \ll 1; \quad q' = \frac{dq}{dx} \Big|_{x_0}. \quad (3.58)$$

The inequality is certainly fulfilled if  $|q'/(k_0 q^2)^{2/3}| \ll 1$  holds.

The formula (3.57) for determining  $R$  is rather general and can be cast into the more convenient form

$$R = \exp \left( -4k_0 \int_{x_0}^\infty |\Im \eta| dx \right) = \exp \left( -2 \int_{x_0}^\infty \alpha dx \right), \quad (3.59)$$

provided that

- (i) in the region around the turning point  $x_0$ ,  $\eta$  can be approximated by a linear function and
- (ii) the position  $\xi$  connecting the linear function with the smooth but otherwise arbitrary function  $\eta^2(x)$  lies in the Stokes region of  $Ai_2$ .

In this form for  $R$  all direct evidence of use of Stokes' equation has disappeared; it merely served to fix the correct lower limit of integration  $x_0$ . Collisional absorption occurring in the overdense (tunneling) region is already included when starting the integration in (3.59) from the turning point  $x_0$ . The factor 4 comes from  $\alpha = 2k_0|\Im \eta|$  in (3.36) and from the fact that the fraction of attenuation of the laser beam is the same on its way into the plasma and out of it after reflection around  $x_0$ .

The homogeneous Stokes equation applies equally well to spherical geometry and normal incidence. Here  $\nabla^2 E = \partial_r(r^2 \partial_r E)/r^2 = \partial_{rr}(rE)/r$ . Hence, by setting  $y = rE$  the stationary electromagnetic wave equation reads

$$\frac{\partial^2}{\partial r^2}y + k_0^2 \eta^2 y = 0, \quad (3.60)$$

of which (3.51) is the special case for linear  $\eta^2$ . There is an important topological difference between solutions of (3.60) for longitudinal and transverse waves. If  $y$  is polarized along  $r$  (e.g., acoustic or electron plasma wave) spherically symmetric solutions of the form  $y = Ce^{i\phi}/r$ ,  $C = \text{const}$ , exist with infinite amplitude at the origin. No such solution exists for a transverse wave. In the latter case  $C$  is always a function of the polar angles  $\varphi$  and  $\vartheta$  as well; the wave shows diffraction at the origin and the amplitude remains finite [12]. It is not possible to uniformly illuminate a sphere by a monochromatic light wave. However, as long as the typical scale length  $L_\perp$  for the intensity variation across the beam is much smaller than  $\lambda$ , (3.60) is a good approximation for a focused laser beam. In the case of small scale beam filamentation [13, 14] it may fail.

### 3.2.1.1 Maximum Electric Field Amplitude

Near the critical or turning point the electric field amplitude may increase considerably. The factor  $f$  by which this happens is the ratio between the maximum  $E$ -field in the plasma  $\hat{\mathbf{E}}_P$  and the vacuum field amplitude  $\hat{\mathbf{E}}_V$  at the same position,

$$f = \frac{|\hat{\mathbf{E}}_P|}{|\hat{\mathbf{E}}_V|} = \frac{|y_P|}{|y_V|}.$$

Let the incident wave have an amplitude of unity. Then at a suitable position  $x$  or  $r$ , (3.56) holds, from which the scaling factor  $C$  is determined,

$$|C| = \frac{\xi_r^{1/4}}{\eta_r^{1/2}} \exp\left[-\left(\Im\xi + k_0 \int_x^\infty |\Im\eta| dx\right)\right] = \left(\frac{k_0}{|q|}\right)^{1/6} R^{1/4}.$$

Keeping in mind that

$$f = |\hat{\mathbf{E}}_P| = 2\sqrt{\pi}|C||\text{Ai}|_{\max},$$

one obtains for the field increase

$$f = 2 \times 0.54\sqrt{\pi}|k_0 q^{-1}|^{1/6} R^{1/4} = 1.90(k_0 L)^{1/6} R^{1/4}. \quad (3.61)$$

This formula is valid for an arbitrary smooth electron density distribution. Its limitation consists only in the approximation of (3.23) and (3.60) by the Stokes

equation (3.51) around the turning point, the validity of which is guaranteed by condition (3.58). In the case of considerable density profile distortions or when the maximum lies in front of the linear region the formula fails. The dependence of  $f$  on  $R$  is very weak. It reflects the experience that in numerical calculations, even with considerable absorption, the field still increases towards the reflection point. In fact, when, for example, 90% of light is absorbed ( $R = 0.1$ ),  $f$  reduces by a factor of only about 2 with respect to the nonabsorbing case. The knowledge of the  $f$  factor is useful for calculating threshold intensities of parametric instabilities or local light pressure effects.

### 3.2.2 Reflection-Free Density Profiles

Instead of starting from the energy flux conservation to derive the WKB solution (3.26) one can alternatively look for an approximate solution to the stationary wave equation (3.23) which, for simplicity, is used now for normal incidence only (the extension to  $\alpha_0 \neq 0$  is straightforward),

$$E'' + k_0^2 \eta^2(x) E = 0. \quad (3.62)$$

Differentiating twice the eikonal expression  $E = C_1 \exp(\pm ik_0 \int \eta dx)$  yields

$$E'' = -k_0^2 E + \{\pm ik_0(\eta' C_1 + 2\eta C'_1) + C''_1\} \exp\left(\pm ik_0 \int \eta dx\right).$$

Inserting this in (3.62) and dropping  $C''_1$  results in the constraint  $\eta'/\eta + 2C'_1/C_1 = 0$ , or when integrated,  $C_1 = \text{const}/\eta^{1/2}$  in agreement with (3.26). Setting  $C_1 = C_2(x)/\eta^{1/2}$  and repeating the previous procedure generates the second correction, etc. However, it is a general experience that if the first order correction, generally named *the* WKB expression, is not sufficiently accurate, inclusion of the next higher orders does not substantially alter the situation. The first approximation with  $C_2 = \text{const}$  is an exact solution of (3.62) for a medium with the refractive index  $n$  given by

$$n^2 = \eta^2 + \frac{1}{4k_0^2} \left\{ 2\frac{\eta''}{\eta} - 3\left(\frac{\eta'}{\eta}\right)^2 \right\} = \eta^2 + \eta_1^2, \quad (3.63)$$

as one may verify by differentiating it twice. The general solution of (3.60) with  $n^2$  for the refractive index squared and  $y = E$  (plane case) is the sum of two noninteracting terms,

$$E = C_+ \eta^{-1/2} e^{+ik_0 \int \eta dx} + C_- \eta^{-1/2} e^{-ik_0 \int \eta dx} = E_+ + E_-.$$

Consequently,  $E = E_+$  with  $C_- = 0$  is also an exact solution. This leads to an interesting conclusion [15]: Any refractive index profile  $n$  constructed according to

(3.63) on an arbitrary twice differentiable function  $\eta(x)$  is *reflection-free*. The  $\eta_1^2$  term acts in such a way that the reflected wave is canceled by interference with the incident wave. For the WKB approximation to hold  $\eta_1^2$  must be small in comparison with  $\eta^2$ . When the collision frequency is high and  $\eta^2$  very smooth  $\eta_1^2 \ll \eta^2$  may hold even at  $x_c$ . Consequently the overall reflection coefficient  $R$  is low, in agreement with one would expect since in such a case the density scale length  $L$  is large and the laser beam is nearly absorbed before reaching  $x_c$ . In the opposite case of  $\nu_{ei}$  small and/or high density gradient around  $x_c$ ,  $\eta_1^2$  is large and no longer monotonic; hence, (3.59) no longer applies to such *resonant* (reflection-free) profiles and no conflict arises. For  $\nu_{ei} = 0$  a reflection-free profile around  $x_c$  does not exist.

### 3.2.3 Collisional Absorption in Special Density Profiles

For practical purposes it is very useful to present explicit formulas for the reflectivity  $R$  and absorption  $A = 1 - R$  for special isothermal density profiles in layered plasmas.

#### 3.2.3.1 Linear Density Profile

As long as  $\nu_{ei}^2/\omega^2 \ll 1$  the refractive index can be approximated by

$$\eta^2 = 1 - \frac{n_e}{n_c} + i \frac{\nu_{ei}}{\omega} \frac{n_e}{n_c} = 1 - \frac{n_e}{n_c} + i \mu \frac{n_e^2}{n_c^2}; \quad \mu = \frac{\nu_{ei,c}}{\omega}.$$

By  $\nu_{ei,c}$  the collision frequency at the critical point is meant. With  $n_e/n_c = 1 - x/L = 1 - u$ ,  $L$  profile length, and  $\eta_i$  approximated by (3.36),

$$\eta_i \simeq \frac{\mu}{2} u^{-1/2} (1 - u)^2,$$

the integral in (3.59) becomes

$$\begin{aligned} \int_{u=0}^1 |\Im \eta| dx &= \frac{\mu L}{2} \int_{u=u_0>0}^1 u^{-1/2} (1 - u)^2 du \\ &= \frac{\mu L}{2} \left( \frac{16}{15} - 2u_0^{1/2} + \frac{4}{3}u_0^{3/2} - \frac{2}{5}u_0^{5/2} \right). \end{aligned} \quad (3.64)$$

The Taylor expansion of  $\eta_i$  overestimates its true value (3.35) around the critical point (it even diverges there); therefore the exact value is obtained when the lower limit of the integration is taken to be some positive  $u_0$  instead of zero. Since, on the other hand the expansion is satisfactory from  $u = 2\mu(1 - u)^2 \simeq 2\mu$  upwards, the relative deviation from the leading term is of the order of  $2.5\mu^{1/2}$ . Hence, with  $\mu \ll 1$ , the reflection coefficient for a linear profile becomes

$$R = R_L \simeq \exp\left(-\frac{32}{15}k_0L\mu\right); \quad \mu = \frac{v_{ei,c}}{\omega} \ll 1. \quad (3.65)$$

For high collision frequencies a more accurate value is obtained from (3.64) by determining  $u_0$  or integrating (3.59) numerically.

The Profile  $n_e = n_c(x_c/x)$

$$\int_0^\infty \eta_i dx = \frac{\mu x_c}{2} \int_{u=0}^1 \frac{du}{(1-u)^{1/2}} = \mu x_c; \quad u = x_c/x. \\ R = R_1 = e^{-4k_0x_c\mu}; \quad \mu \ll 1. \quad (3.66)$$

The Profile  $n_e = n_c(x_c/x)^2$

$$\int_0^\infty \eta_i dx = \frac{\mu x_c}{2} \int_{u=0}^1 \frac{u^2 du}{(1-u^2)^{1/2}} = \frac{\mu x_c}{4} \arcsin 1 = \frac{\mu x_c \pi}{4}. \\ R = R_2 = \exp\left(-\frac{\pi}{2}k_0x_c\mu\right); \quad \mu \ll 1. \quad (3.67)$$

This profile is a satisfactory approximation of a spherical isothermal rarefaction wave.

The Profile  $n_e = n_c(x_c/x)^3$

The integral is evaluated with the help of the gamma function,

$$\frac{2}{x_c\mu} \int_{x>x_c}^\infty \eta_i dx = \int_0^1 \frac{u^4 du}{(1-u^3)^{1/2}} \simeq \frac{4^{2/3} \cdot 3^{1/2}}{7\pi} \Gamma^2(2/3); \quad \mu \ll 1. \\ R = R_3 = \exp\left(-\frac{2}{7\pi} \cdot 4^{2/3} \cdot 3^{1/2} \Gamma^2(2/3) k_0 x_c \mu\right) = \exp(-0.73k_0x_c\mu). \quad (3.68)$$

This profile represents an asymptotically spherical rarefaction wave.

Owing to (3.60) formulas (3.66), (3.67), and (3.68) are equally valid for spherical targets with  $x$  and  $x_c$  substituted by the radii  $r$  and  $r_c$ . The scale length  $L$  of a profile of the form  $n_e = n_c(r_c/r)^\alpha$  is connected with  $r_c$  by  $L = L_\alpha = r_c/\alpha$  and the above reflection formulas read as follows,

$$R_L = \exp\left(-\frac{32}{15}k_0L\mu\right), \quad R_1 = \exp(-4k_0L_1\mu), \quad R_2 = \exp(-\pi k_0L_2\mu), \\ R_3 = \exp(-2.2k_0L_3\mu). \quad (3.69)$$

If the absorption is low, i.e.,  $k_0r_c\mu$  is small, all four formulas give reasonably accurate results. In the case of strong absorption the formulas show that the form

of the density profile very much influences the result. The parameter characterizing absorption is the product  $k_0 r_c \mu$ . From this expression the wavelength dependence can easily be studied under various conditions. If, for example, the critical radius is kept constant the absorption is independent of  $\lambda$  for a given density profile. In fact  $k_0$  varies as  $1/\lambda$  and  $\mu = v_{ei,c}/\omega$  is proportional to  $\lambda$ . On the other hand, from (3.69) a very strong dependence of  $R$  on the ion charge number  $Z$  should be expected. Since  $A \sim Z$  holds for the atomic mass  $A$ , under otherwise identical conditions, the reflection coefficients for deuterium and a high- $Z$  material are related by the power law

$$R_Z = R_{D_2}^Z.$$

If heat conduction plays a role this relation is drastically modified [16].

### 3.2.4 Inhomogeneous Stokes Equation

In contrast to  $E_z$  which propagates freely according to (3.23) the  $E_x$  component in (3.21) appears as a wave driven by the electromagnetic field component  $E_y$ . If there is no incident  $E_z$ -wave from the vacuum,  $E_z$  remains zero everywhere in the layered medium. It decouples from the other field components. This is not the case for  $E_x$ . Under oblique incidence  $E_y$  is different from zero and produces an  $E_x$ -field through (3.21). To see more clearly the structure of this field it is convenient to transform the driver with the help of Faraday's law,

$$(\nabla \times \nabla \times \mathbf{E})_x = ik_y E'_y + k_y^2 E_x = i\omega (\nabla \times \mathbf{B})_x = -k_0 k_y c B_z$$

to obtain Piliya's equation [17], with  $B$  for  $B_z$ ,

$$E''_x + \frac{k_0^2}{\beta^2} (\eta^2 - \beta^2 \sin^2 \alpha_0) E_x = -\frac{k_0 k_y c}{\beta^2} (1 - \beta^2) B(x).$$

At nonrelativistic temperatures  $\beta^2 \ll 1$  and  $k^2/\beta^2 \gg k_0^2$  holds and this equation further simplifies to

$$E''_x + \frac{k_0^2}{\beta^2} (\eta^2 - \beta^2 \sin^2 \alpha_0) E_x = -\frac{k_0 k_y c}{\beta^2} B(x). \quad (3.70)$$

This shows that the magnetic field or, equivalently, the  $E_x$ -component forces the electrons to oscillate along the density gradient and hence, produces a coherent charge separation or electron plasma wave. The mechanism of excitation is sketched in Fig. 3.5. Its longitudinal character is revealed by the local wave number  $k/\beta = k_0 \eta / \beta$  in (3.70) which is identical to that given in (3.11). Under the assumption of a linear density profile, with  $\eta_i = 0$  and setting

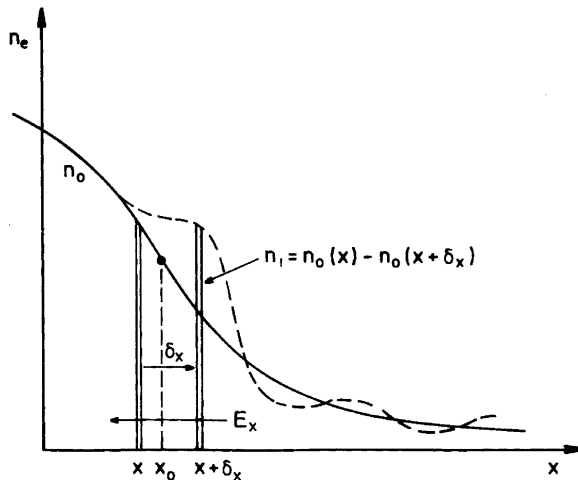


**Fig. 3.5** Excitation of an electron plasma wave along a plasma density gradient. Electrons with equilibrium density  $n_0(x) = Zn_i$  are shifted to  $x + \delta_x$  by the electromagnetic  $E_x$ -field component. Since there the density of the nearly immobile ions is  $n_i(x + \delta_x)$  a charge density imbalance  $\rho_{\text{el}} = e(n_0(x + \delta_x) - n_0(x))$ , oscillating at frequency  $\omega$ , is produced

$$\xi = \left( \frac{k_0^2}{\beta^2 L} \right)^{1/3} (x - x_0), \quad x_0 = L\beta^2 \sin^2 \alpha_0,$$

$$w = \left( \frac{\beta}{k_0 L} \right)^{2/3} \frac{E_x}{cB(0) \sin \alpha_0}, \quad b = -\frac{B(x)}{B(0)}$$

(3.70) transforms into the dimensionless inhomogeneous Stokes-Airy equation

$$w'' + \xi w = b(\xi). \quad (3.71)$$

As already mentioned at the end of Sect. 3.1.1, effective excitation of an electron plasma wave puts certain constraints on the spatial structure of the driver  $b$ . Resonant coupling at frequency  $\omega$  can occur over an extended region when the driver wavelength matches the local electrostatic wavelength; otherwise resonance is limited to a space region that is narrow compared with  $\lambda$ . The latter situation is most easily realized at the turning point owing to the reduction of  $k_e = k_0 \eta / \beta$  there. In Fig. 3.6 numerical solutions of (3.71) are shown for a driver of Gaussian structure acting at the turning point of the electron plasma wave,  $b = \exp(-\xi^2/\delta^2)$ , with  $\delta^2 = 2, 8.33, 20$  and  $\infty$ . It is clearly seen that the maximum amplitude of the wave no longer increases much as soon as the driver halfwidth reaches half a local wavelength  $\lambda_e$  (compare (b)-(d)). The reason for this saturation lies in the constructive and destructive spatial interferences, alternating and nearly canceling each other when the driver is extended and smooth. As a consequence the electron plasma wave amplitude becomes modulated (see Fig. 3.6d).

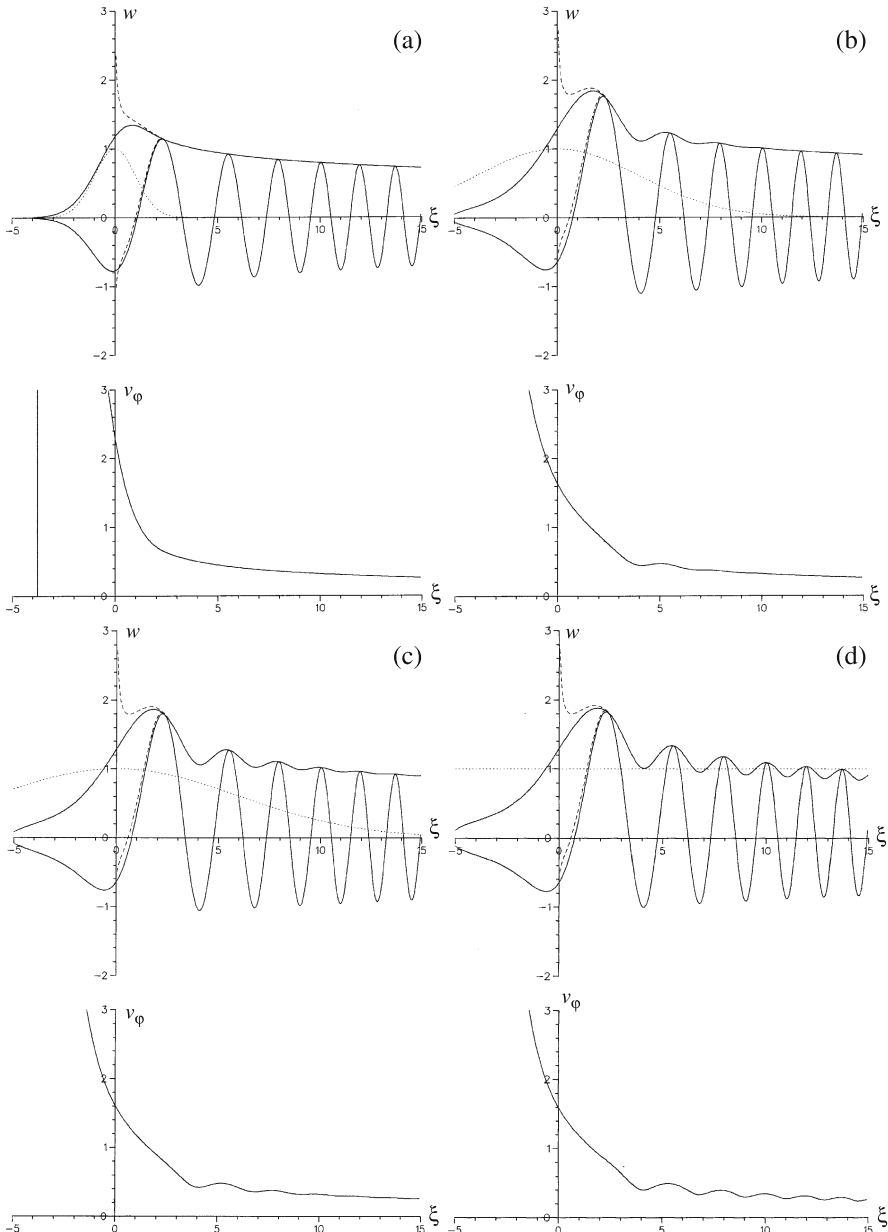


**Fig. 3.6** Solution of the inhomogeneous Stokes equation  $w'' + \xi w = -\exp(-\xi^2/\delta^2)$  for  $\delta^2 = 2$  (a), 8.33 (b), 20 (c), and  $\infty$  (d). Solid lines: numerical results of normalized field  $w$  and its amplitude  $\hat{w}$  (upper curves), and phase velocity  $v_\phi$  of the electron plasma wave (lower curves); dashed lines: WKB approximation of  $w$  and  $\hat{w}$ ; dotted lines: driver  $\exp(-\xi^2/\delta^2)$ . For  $\xi < 0$ ,  $w$  and  $\hat{w}$  decay exponentially

Starting from  $\text{Ai}(\xi)$  and  $\text{Bi}(\xi)$  the general solution of (3.71) is constructed in the familiar way, i.e., using the Green's function for (3.71)

$$w(\xi) = C_1 \text{Ai}(\xi) + C_2 \text{Bi}(\xi) + \int_{-\infty}^{\xi} b(z) \frac{\text{Ai}(z)\text{Bi}(\xi) - \text{Ai}(\xi)\text{Bi}(z)}{W} dz, \quad (3.72)$$

with the Wronskian  $W = \text{Ai}\text{Bi}' - \text{Ai}'\text{Bi} = 1/\pi$ . For a spatially constant driver,  $b = -1$ , the inhomogeneous solution becomes the special function  $\text{Hi}(\xi) = 2\text{Bi}(\xi)/3$ . The correct, purely outgoing electron plasma wave is found from the asymptotic representation of  $\text{Ai}$ ,  $\text{Bi}$  and  $\text{Hi}$  and its evanescent behavior for  $\xi < 0$ ,

$$w = \pi(\text{Hi} - \text{Bi} - i\text{Ai}) = \hat{w} e^{i\Theta}. \quad (3.73)$$

Here  $\hat{w}$  is the amplitude of  $w$ , and  $\Theta$  the phase. Around the saddle point  $\xi = 0$  the square of the amplitude  $\hat{w}^2$  has the power series expansion

$$\begin{aligned} \hat{w}^2(\xi) = & 1.658 + 1.209\xi + 0.238\xi^2 - 0.0839\xi^3 \\ & - 0.0523\xi^4 - 7.40 \times 10^{-3}\xi^5 + \dots \end{aligned}$$

The maximum of  $\hat{w} = 1.88$  occurs at  $\xi_m = 1.8$ . Figure 3.6 also shows that the WKB solution of (3.71) deviates very little from the exact solutions for  $\xi > \xi_m$ . The decay of  $\hat{w}$  is slowest for  $b = 1$  and behaves like  $1/\xi^{1/4}$  for  $\xi \gtrsim \xi_m$ . On the other hand, since saturation of  $\hat{w}_{\max}$  occurs approximately for drivers of halfwidth  $\xi_m$ ,  $\xi_m$  is the correct measure of the width of the resonance  $x_m - x_0$ . It increases as  $L^{1/3}$ . The lower curves in Fig. 3.6 indicate the phase velocity  $v_\varphi$  at which a point  $\xi$  satisfying  $w(\xi, t) = 0$  propagates. In contrast to the Bohm-Gross expression the true  $v_\varphi$  does not diverge at the turning point.

### 3.3 Collisional Absorption

The physical mechanism of collisional absorption was analyzed in Sect. 2.1.3 under the assumption that electrons and ions are elastic hard spheres. This model explains how irreversibility, i.e., heating, and anisotropy of the electron distribution function come about. It was also shown that all that is required of particle kinetics to determine absorption is the knowledge of the electron-ion (and, eventually, the electron-electron) collision frequency, provided the model of a fully ionized plasma is valid. As long as the thermal electron speed is nonrelativistic all electrons have a mass close to their rest mass  $m$  and “see” nearly the same electric field  $\mathbf{E}(\mathbf{x}, t)$  with a frequency  $\omega'$  close to  $\omega$  so that they all oscillate locally at nearly identical  $\mathbf{v}_{os}$ . Hence, the momentum exchange in electron-electron collisions, occurring with frequency  $\nu_{ee}$ , only leads to isotropization of the distribution function  $f(\mathbf{x}, \mathbf{v}_e, t)$  and to thermalization, i.e., Maxwellization, at later times. In the reference system

comoving at  $v_{os}(t)$  an electron-electron collision looks the same as in the absence of the laser field. Thus, they do not directly contribute to inverse bremsstrahlung absorption.

In plasmas produced by high intensity lasers the electron temperatures are generally such that the model of a two-component fully ionized plasma is valid. The frictional force, introduced phenomenologically by (2.23), originates, under most conditions, from long-range, small-angle electron-ion collisions. As a consequence, the collision frequency  $\nu_{ei}$  becomes highly dependent on the energy of the colliding electrons and, under standard conditions, it is the result of thousands of *simultaneous* collisions rather than of single binary events (see Fig. 3.7). Expression (2.45) for  $\nu_{ei}$  was derived for a Maxwellian velocity distribution,  $v_{os} \ll v_{th,e}$ , and  $\ln \Lambda$  appreciably larger than unity. Since in laser plasmas each of these conditions may be violated, a more general derivation of  $\nu_{ei}$  is needed. Large radiation field effects were considered first by Silin [18] on the basis of a classical analysis. Early quantum mechanical treatments were given in [19] and [20]. A similar treatment for dense plasmas, in particular for  $\lambda_B > \lambda_D$ , has only very recently been undertaken [21, 22]. In strong heating by lasers, the relaxation of slow electrons is faster than that of more energetic ones. As a consequence the electron velocity distribution may become non-Maxwellian [23] and nonisotropic [24].

In the following, the main physical effects determining collisional absorption are described by introducing appropriate models in the test particle approximation. First,  $\nu_{ei}$  is calculated for a monoenergetic unidirectional electron beam in the oscillator model approximation. This model turns out to be particularly useful for explaining dynamical screening of the ion charges and for determining the various cut-offs in a self-consistent way and the validity of the impact approximation used by Pert [25–27]. The oscillator model is relevant for ion beam stopping and, to a certain degree, for absorption of superintense laser beams in dense targets.

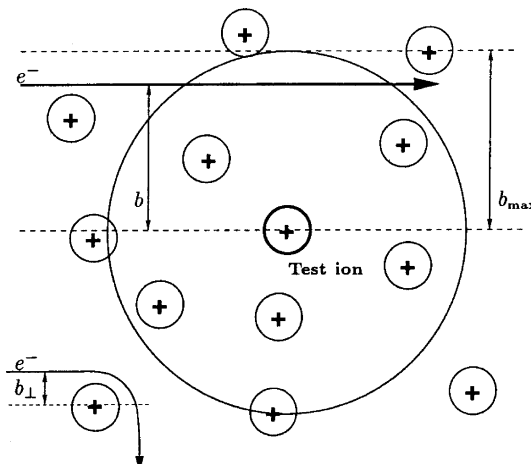


**Fig. 3.7** In the weak coupling case (standard plasma) an electron collides simultaneously with many ions; small angle deflections dominate

### 3.3.1 Collision Frequency of Electrons Drifting at Constant Speed (Oscillator Model)

Let us assume a homogeneous electron plasma streaming at constant velocity  $\mathbf{v}_0$  and a single ion of charge  $q = Ze$  at rest immersed in the electronic fluid (Fig. 3.8). The electrons are assumed to be held at equilibrium density  $n_0$  by a uniform noninteracting ion background (test particle model). During the passage, the electrons are attracted by the ion (and released after passage). Due to the passage of the charge  $q$  an electron at equilibrium position  $\mathbf{x}' = -\mathbf{v}_0 t$  in the comoving frame will be shifted by the amount  $\delta(\mathbf{x}, t) = \delta_{\parallel} + \delta_{\perp}$  parallel and perpendicular to  $\mathbf{v}_0$ . As long as  $b_{\perp} \ll n_0^{-1/3}$ , the deflection angle  $\chi$  is very small for almost all impact parameters  $b$  and the electron trajectories can be approximated by straight lines  $\mathbf{x} = \mathbf{v}_0 t$ . It is this assumption which enables one to reduce multiple simultaneous Coulomb interactions to binary encounters. The disturbance in the electron density  $n_e(\mathbf{x}, t)$  induced by the passing ion is small for almost all impact parameters  $b$  so that particle conservation is expressible in its linearized form,

$$0 = \frac{\partial}{\partial t} n_1 + \nabla \left( n_e \frac{d\delta}{dt} \right) \simeq \frac{\partial}{\partial t} n_1 + \nabla \left( n_0 \frac{\partial}{\partial t} \delta \right).$$

Integration in time leads to

$$n_1(\mathbf{x}, t) = -\nabla(n_0 \delta). \quad (3.74)$$

In the following  $n_0$  is assumed to be constant in space and hence  $n_1 = -n_0 \nabla \delta$ . Combining this with Poisson's law one arrives at an expression for the electric field,

$$\mathbf{E} = \frac{en_0}{\epsilon_0} \delta + \frac{q}{4\pi\epsilon_0 r^3} \mathbf{r}, \quad (3.75)$$

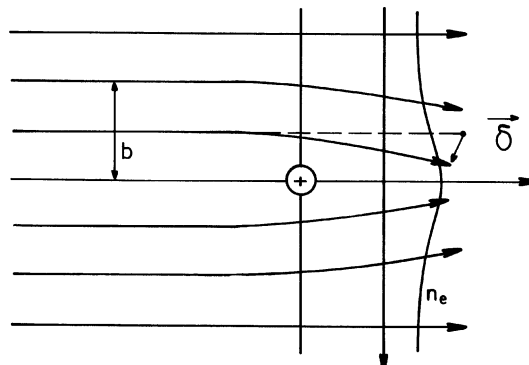


**Fig. 3.8** Oscillator model: A parallel monoenergetic beam of electrons is attracted by an ion at rest. As a consequence, the single orbits deviate by the vector  $\delta(t)$  from straight lines and the electron density  $n_e$  increases towards the symmetry axis. This nonuniformity of  $n_e$  leads to a restoring force acting back on the electrons

since  $\nabla(r/r^3) = 4\pi\delta(\mathbf{r})$ . Magnetic fields can be neglected. From the approximation of straight trajectories one obtains as a function of the collision parameter  $b$

$$\begin{aligned} E_{\parallel} &= \frac{en_0}{\varepsilon_0}\delta_{\parallel} + \frac{\kappa v_0 t}{(b^2 + v_0^2 t^2)^{3/2}}, & E_{\perp} &= \frac{en_0}{\varepsilon_0}\delta_{\perp} + \frac{\kappa b}{(b^2 + v_0^2 t^2)^{3/2}}; \\ \kappa &= \frac{q}{4\pi\varepsilon_0}. \end{aligned} \quad (3.76)$$

By linearizing the momentum equation,  $\partial_{tt}\delta = -(e/\mu)\mathbf{E}$  ( $\mu \simeq m$  is the reduced mass) one ends up with two equations for forced harmonic oscillators with eigenfrequency  $\omega_p$ ,

$$\ddot{\delta}_{\parallel} + \omega_p^2\delta_{\parallel} = -\frac{e}{\mu}\kappa \frac{x}{(b^2 + x^2)^{3/2}}, \quad \ddot{\delta}_{\perp} + \omega_p^2\delta_{\perp} = -\frac{e}{\mu}\kappa \frac{b}{(b^2 + x^2)^{3/2}}, \quad (3.77)$$

with  $x = v_0 t$  [28]. The restoring force has its origin in the induced space charge (see  $n_e$  in Fig. 3.8) which screens the electrons from feeling the force of the bare charge  $q = Ze$  of the ion. Ignoring screening corresponds to setting  $\omega_p = 0$  and leads to the well-known divergence in the total Coulomb cross section.

For its usefulness we remember in this place that a particular solution of the inhomogeneous linear differential equation  $y'' + a(x)y = f(x)$  is given by [29]

$$y(x) = h(x) \int^x \frac{g(\zeta)f(\zeta)}{W(\zeta)} d\zeta - g(x) \int^x \frac{h(\zeta)f(\zeta)}{W(\zeta)} d\zeta \quad (3.78)$$

with  $W = gh' - g'h$  and where  $g$  and  $h$  are solutions of the homogeneous differential equation.

Equations (3.77) have to be solved with appropriate initial conditions. To find them we observe that the solutions of the homogeneous equations are  $\delta = \hat{\delta} \exp(\pm i\omega_p t)$ , when switched on adiabatically at  $t = -\infty$ . Hence,  $\delta(-\infty) = \dot{\delta}(-\infty) = 0$  and, after introducing the *dynamic Debye length*  $\lambda_0$ ,

$$\lambda_0 = \frac{v_0}{\omega_p}, \quad (3.79)$$

and the dimensionless variables  $\xi = x/\lambda_0$ ,  $\beta = b/\lambda_0$  the solutions are

$$\begin{aligned} \delta_{\parallel}(\xi) &= \frac{b_{\perp}}{\beta} \left\{ \sin \beta\xi \int_{-\infty}^{\xi} \frac{u \cos(\beta u) du}{(1+u^2)^{3/2}} - \cos \beta\xi \int_{-\infty}^{\xi} \frac{u \sin(\beta u) du}{(1+u^2)^{3/2}} \right\}, \\ \delta_{\perp}(\xi) &= \frac{b_{\perp}}{\beta} \left\{ \sin \beta\xi \int_{-\infty}^{\xi} \frac{\cos(\beta u) du}{(1+u^2)^{3/2}} - \cos \beta\xi \int_{-\infty}^{\xi} \frac{\sin(\beta u) du}{(1+u^2)^{3/2}} \right\}. \end{aligned}$$

In this model the cold electron plasma oscillations at  $\omega = \omega_p$  persist indefinitely. In reality, owing to finite wave-wave and wave-particle interactions they slowly decay, thereby converting their kinetic and potential energies into thermal energy of the

plasma. Their damping is mainly due to profile steepening and cold wavebreaking (see Sect. 4.4). The relevant amplitudes of  $\delta_{\perp}$ ,  $\delta_{\parallel}$  occur at  $\xi = \infty$  and since integrals of the odd functions vanish, they are given by

$$\hat{\delta}_{\parallel} = \frac{b_{\perp}}{\beta} \int_{-\infty}^{+\infty} \frac{u \sin(\beta u) du}{(1+u^2)^{3/2}} = b_{\perp} \int_{-\infty}^{+\infty} \frac{\cos(\beta u) du}{(1+u^2)^{1/2}} = 2b_{\perp} K_0(\beta), \quad (3.80)$$

$$\hat{\delta}_{\perp} = \frac{b_{\perp}}{\beta} \int_{-\infty}^{+\infty} \frac{\cos(\beta u) du}{(1+u^2)^{3/2}} = \frac{\pi^{1/2}}{\Gamma(3/2)} b_{\perp} K_1(\beta) = 2b_{\perp} K_1(\beta). \quad (3.81)$$

Expression (3.80) is obtained from a partial integration.  $K_0$  and  $K_1$  are modified Bessel functions ([10], Sect. 9.6). For small values of  $\beta$  their expansions are, with  $\gamma = 0.57722$ ,

$$\begin{aligned} K_0(\beta) &= -\left(\ln \frac{\beta}{2} + \gamma\right) + \left(\frac{\beta}{2}\right)^2 \left(1 - \ln \frac{\beta}{2} - \gamma\right) + \dots \\ K_1(\beta) &= \frac{1}{\beta} + \left(\frac{\beta}{2}\right) \left(\ln \frac{\beta}{2} + \gamma - \frac{1}{2}\right) + \dots \end{aligned} \quad (3.82)$$

For  $\beta = 1$  these expansions for  $K_0$  and  $K_1$  differ by 1 and 7% from the true values. For large values of  $\beta$  the corresponding asymptotic expansions are

$$\begin{aligned} K_0(\beta) &= \left(\frac{\pi}{2\beta}\right)^{1/2} e^{-\beta} \left\{1 - \frac{1}{8\beta} + \frac{9}{128\beta^2} \mp \dots\right\}, \\ K_1(\beta) &= \left(\frac{\pi}{2\beta}\right)^{1/2} e^{-\beta} \left\{1 + \frac{3}{8\beta} + \frac{15}{128\beta^2} \pm \dots\right\}. \end{aligned}$$

Both amplitudes diverge for  $\beta \rightarrow 0$  (see Fig. 3.9.), since

$$K_0(\beta \rightarrow 0) \sim -\ln \beta, \quad K_1(\beta \rightarrow 0) \sim \frac{1}{\beta}.$$

The energy irradiated per unit time into plasma waves by a single ion through a plane orthogonal to  $v_0$  and at a fixed distance  $x \rightarrow +\infty$  is given by

$$\dot{W} = \frac{1}{2} \mu \omega_p^2 n_0 v_0 \lambda_0^2 \int_{\beta_0}^{\infty} 2\pi \beta \left(\hat{\delta}_{\parallel}^2 + \hat{\delta}_{\perp}^2\right) d\beta + v_0 D(\beta_0). \quad (3.83)$$

This gives rise to a frictional force  $f$  on the ion,  $\dot{W} = f v_0$ . The lower cutoff is introduced to avoid the divergence occurring at  $b \rightarrow 0$ ; it is a consequence of the straight orbit approximation for the deflected electrons and is removed by taking into account the finite deflection angles  $\vartheta$  in close encounters. Their contribution to  $\dot{W}$  is indicated by  $v_0 D(\beta_0)$ . To calculate  $D$  it has to be mentioned first that strongly bent trajectories, e.g., with  $b \lesssim b_{\perp}$ , owing to widely varying curvatures intersect

each other in such a way that almost no electron density disturbance  $n_1$  is produced, i.e., they do not contribute to screening as long as  $b_\perp \ll \lambda_0$  is fulfilled. As a consequence, (3.77) hold for impact parameters  $b \geq b_0 = \alpha b_\perp$ , with  $\alpha$  not far from unity and to be determined later. The frictional force  $D(\beta_0)$  that the unscreened ion feels from the electrons undergoing deflections from  $\vartheta = \pi$  to a  $\vartheta_0$  (corresponding to  $b = 0$  and  $b = b_0$ ) is determined by the momentum change in the  $x$ -direction per unit time,

$$\begin{aligned} D(\beta_0) &= n_0 v_0 \int_{\vartheta_0}^{\pi} \mu v_0 (1 - \cos \vartheta) \sigma_\Omega d\Omega \\ &= 2\pi \mu n_0 v_0^2 b_\perp^2 \int_{\vartheta_0}^{\pi} \frac{1 - \cos \vartheta}{4 \sin^4(\vartheta/2)} \sin \vartheta d\vartheta \\ &= 4\pi \mu n_0 v_0^2 b_\perp^2 \int_{\vartheta_0}^{\pi} \frac{d \sin(\vartheta/2)}{\sin(\vartheta/2)} = Z \mu \omega_p^2 b_\perp \ln \frac{1}{\sin(\vartheta_0/2)}. \end{aligned} \quad (3.84)$$

Equation (3.83) can be rewritten with the help of (3.84) and (2.44) as

$$\dot{W} = Z \mu \omega_p^2 v_0 b_\perp \left\{ \beta_0 K_0(\beta_0) K_1(\beta_0) + \frac{1}{2} \ln \left( 1 + \frac{b_0^2}{b_\perp^2} \right) \right\}$$

since  $d(\beta K_0 K_1)/d\beta = -\beta(K_0^2 + K_1^2)$  (see [10], Sect. 9.6.26). Hence,

$$\begin{aligned} \dot{W} &= Z \mu \omega_p^2 v_0 b_\perp \left\{ -\ln \frac{\beta_0}{2} - \gamma + \frac{\beta_0^2}{4} - \frac{\beta_0^2}{2} \left( \ln \frac{\beta_0}{2} + \gamma \right)^2 + \frac{1}{2} \ln \left( 1 + \frac{b_0^2}{b_\perp^2} \right) \right\} \\ &= Z \mu \omega_p^2 v_0 b_\perp \left\{ \ln \left[ \frac{\lambda_0}{b_\perp} \left( 1 + \frac{b_\perp^2}{b_0^2} \right)^{1/2} \right] + \ln 2 - \gamma \right. \\ &\quad \left. + \frac{\beta_0^2}{4} \left[ 1 - 2 \left( \ln \frac{\beta_0}{2} + \gamma \right)^2 \right] \right\}. \end{aligned} \quad (3.85)$$

The connection between the electron-ion collision frequency and  $\dot{W}$  is obtained from (2.23) by multiplying by  $v_0$ ,

$$\dot{W} = Z \mu v_0^2 \nu_{ei}. \quad (3.86)$$

Thus, the collision frequency becomes:

$$\begin{aligned} \nu_{ei} &= \frac{\omega_p^2 b_\perp}{v_0} \left\{ \ln \left[ \frac{\lambda_0}{b_\perp} \left( 1 + \frac{b_\perp^2}{b_0^2} \right)^{1/2} \right] + 0.116 \right. \\ &\quad \left. + \frac{\beta_0^2}{4} \left[ 1 - 2 \left( \ln \frac{\beta_0}{2} + 0.58 \right)^2 \right] \right\}. \end{aligned} \quad (3.87)$$

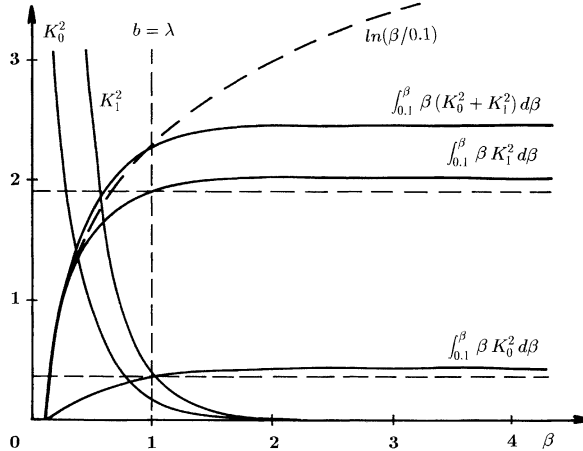


**Fig. 3.9** Modified Bessel functions squared,  $K_0^2$  and  $K_1^2$ , their weighted integrals,  $\int_{0.1}^{\beta} \beta K_0^2 d\beta$ ,  $\int_{0.1}^{\beta} \beta K_1^2 d\beta$  and their sum, as functions of the normalized collision parameter  $\beta = b\omega_p/v_0$ . The dotted curve is the Coulomb logarithm  $\ln(\lambda_0/b_\perp)$ , with  $\beta = \beta_\perp = 0.1$ . Hence, when  $b = \lambda_0$ ,  $\ln \Lambda = 2.3$ .

The integrals  $\int \beta K_0^2 d\beta$  and  $\int \beta K_1^2 d\beta$  are shown in Fig. 3.9 for the lower limit of integration  $\beta = \beta_l = 0.1$ . For  $\beta_l$  approaching zero the first integral remains finite whereas the second diverges logarithmically. When  $\lambda_0 \gg \max(b_\perp, \lambda_B)$  (weakly coupled plasma)  $b_0$  can be chosen such that  $b_\perp \ll b_0 \ll \lambda_0$  holds. The term in the curly bracket then shrinks to the standard Coulomb logarithm  $\ln \Lambda_0 = \ln(\lambda_0/b_\perp)$  and is insensitive to a particular choice of  $b_0$  which discriminates between “straight” and bent orbits. The parameter  $b_\perp$  enters in (3.87) in a natural way and is to be considered merely as a convenient abbreviation for a combination of atomic and kinematic quantities. There is no need to introduce additional concepts as, for example, a “parameter of closest approach,” frequently encountered in text books. The closest approach is  $b = 0$  and not  $b = b_\perp$  or  $b = \lambda_B$ . In order to study the limits of validity of  $\ln \Lambda_0$  for small ratios  $\Lambda_0 = \lambda_0/b_\perp$  it is convenient to choose  $b_0 = (b_\perp \lambda_0)^{1/2}$ . Then  $v_{ei}$  becomes

$$v_{ei} = \frac{\omega_p^2 b_\perp}{v_0} \{ \ln \Lambda_0 + B + C \}, \quad (3.88)$$

$$B = \ln \left( 1 + \frac{1}{\Lambda_0} \right)^{1/2}, \quad C = 0.116 + \frac{1}{4\Lambda_0} \left[ 1 + \frac{1}{2}(0.23 + \ln \Lambda_0)^2 \right].$$

In evaluating  $v_{ei}$  from (3.87),  $\beta_0$  as small as  $\beta_0 = 2\beta_\perp$ , or  $\alpha = 2$ , is tolerable since  $\cos(\vartheta_0/2) = 0.89$  is still sufficiently close to unity, and the factor  $(1 + b_\perp^2/b_0^2)^{1/2}$  contributes only by  $\ln \sqrt{1.25} = 0.11$ . In Table 3.2 typical values of  $\ln \Lambda_0$  and the two corrections  $B$  and  $C$  are given. For  $\ln \Lambda_0 \geq 3$  the standard Coulomb logarithm is an acceptable approximation in the oscillator model. At  $\Lambda_0 = 2$ ,  $\ln \Lambda_0$  deviates from the more exact value  $\ln \Lambda_0 + B + C$  already by 40%. In high-density and/or

**Table 3.2** Behavior of  $\ln \Lambda_0$  and its corrections  $B$  and  $C$  from (3.88) for small values of  $\Lambda_0 = \lambda_0/b_{\perp}$ 

$\Lambda_0$	100	10	5	3	2	1.5	1
$\ln \Lambda_0$	4.6	2.3	1.6	1.1	0.7	0.4	0.0
$B$	0.005	0.05	0.09	0.14	0.2	0.25	0.35
$C$	0.15	0.22	0.25	0.27	0.29	0.32	0.37

high- $Z$  plasmas  $\lambda_0$  may become comparable to or even smaller than  $b_{\perp}$ . In such a case (3.87) has to be modified for several reasons. One is immediately seen from Fig. 3.9, since then  $\beta_0$  is in the interval  $\beta > 1$  where  $\ln(\beta/0.1)$  starts deviating considerably from  $\int \beta(K_0^2 + K_1^2)d\beta$  and hence  $v_{ei}$  depends sensitively on the choice of  $\alpha$ . Another criterion to be obeyed is  $4\pi\lambda_0^3 n_0/3 \gtrsim Z$  for effective Debye screening. We come back to these problems in connection with collisional absorption in a thermal plasma.

From the oscillator model the cutoff of the Coulomb potential at the dynamic Debye length  $\lambda_0$  arises self-consistently. Performing all calculations with a bare Coulomb potential corresponds to ignoring the restoring force in (3.77) and leads to the well-known divergent result. The origin of screening and the reason for convergence become clear from the oscillator model (see Fig. 3.8): An electron on the distant orbit with  $b$  larger than a certain  $b_{\max}$  feels a weak attractive Coulomb force over a long time; the oscillators (3.77) are very slowly shifted from their equilibrium position and then slowly released. The whole process occurs adiabatically and all energy the oscillators had acquired is given back after the encounter. At an intermediate  $b$ , the oscillators associated with  $\delta_{\parallel}$ ,  $\delta_{\perp}$  are excited since the driving force changes rapidly enough to produce Fourier components not far from the eigenfrequency  $\omega_p$ . As a result, energy is taken irreversibly from the translational motion and transformed into oscillatory energy. Finally, at very small  $b \simeq b_{\perp}$  the exciting force has frequencies much larger than  $\omega_p$  so that the oscillator behaves like an attracted particle with zero restoring force. It is well-known that the deflection angle  $\vartheta$  of a nearly straight orbit can be calculated exactly if the maximum Coulomb force  $qe/4\pi\epsilon_0 b^2$  is assumed to act over the finite distance of  $2b$  ([30], Sect. 13.1). Consequently, the effective interaction time in such a collision is  $\tau = 2b/v_0$ . A cutoff at  $b_{\max} = \lambda_0$  means that interaction times during which the oscillator undergoes more than

$$\frac{\tau}{2\pi/\omega_p} = \frac{\lambda_0 \omega_p}{\pi v_0} = \frac{1}{\pi} \quad (3.89)$$

oscillations have no irreversible, i.e., collisional effect on the system. It becomes clear from this picture that at zero temperature the parameter which separates collective behavior from single particle events is  $b_0 \simeq 2b_{\perp}$ , and *not* the Debye length  $\lambda_0$ .

The excitation of a plasma wave by an ion moving uniformly through a homogeneous plasma was simulated numerically with a Vlasov code in full generality, i.e., nonlinearities in  $n_e$  and bent electron orbits are included [31, 32]. A typical example

is shown in Fig. 3.10. For moderate ion charges the nonlinearity in  $n_e$  and in the electrostatic potential is small; at high Z-values, however, it is no longer negligible (see Fig. 3.10b) and leads, as a consequence of trapping of free electrons in the ion potential, to a dependence of  $v_{ei}$  on  $n_i$  which is smaller than  $Z^2$  of expressions (3.87) and (3.88).

So far the effect of a single ion on an electron has been calculated. When  $v_{ei}$  produced by the ions of a plasma is considered, one electron feels *simultaneously* the influence of many ions and their collisions overlap since  $\lambda_0 \gg n_0^{-1/3}$  (Fig. 3.7). Under the conditions that (i) the overlapping collisions occur along nearly straight orbits and that (ii) collisions with curved orbits do not overlap ( $b_0 < n_0^{-1/3}$ ) this problem is easily solved. To this end imagine the ions at the locations  $\mathbf{x}_i$ . At the time  $t$  each of them has produced the shift  $\delta_i(t) = \delta_{i\parallel}(t) + \delta_{i\perp}(t)$  according to (3.77). They sum up to a total instantaneous shift  $\delta(t)$  and hence the total oscillatory energy of an electron at position  $\mathbf{x} = (a, b)$  is

$$\frac{1}{2}\mu\hat{\delta}^2(a, b) = \frac{1}{2}\mu\left(\sum_{i=1}^N \hat{\delta}_i(t)\right)^2 = \frac{1}{2}\mu \sum_{i,j=1}^N \hat{\delta}_i \hat{\delta}_j = \frac{1}{2}\mu \sum_{i=1}^N \hat{\delta}_i^2, \quad (3.90)$$

i.e., owing to randomly distributed phases all collisions add up as if they occurred one after another. As a consequence,  $N$  ions radiate  $N\dot{W}$  power by electron plasma waves and (3.86) remains valid for overlapping long-range Coulomb collisions. Expressed differently, in this way the collective part of  $v_{ei}$  is calculated in its first Born approximation (no multiple scattering), since  $v_0$  is kept constant over the duration of the collision with one ion.

In most elementary derivations of  $v_{ei}$  based on the momentum change of a single electron in the forward direction, only  $\delta_\perp$  is taken into consideration. From Fig. 3.9 it is seen that  $\delta_\parallel$  also contributes. Imagine two parallel layers of electrons at a suitable distance from each other. When the first layer has reached the position of the

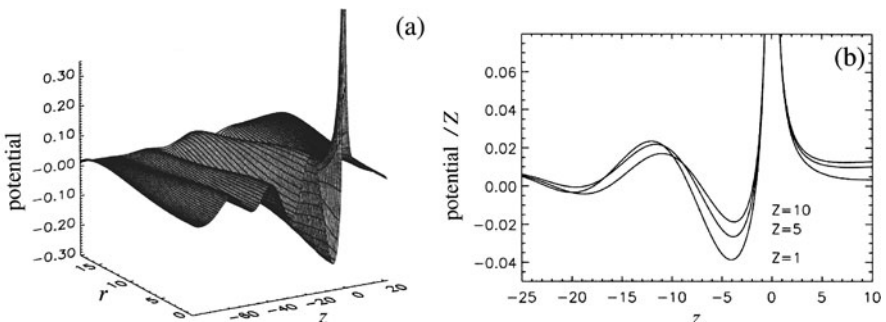


**Fig. 3.10** (a): Excitation of an electron plasma wave by an ion at position  $z = 0$ ,  $r = 0$  of charge  $Z$  (normalized by the number of electrons in the Debye sphere) in a plasma streaming from right to left at speed  $v_0/v_{th} = 4$  (from [31]). (b): Electrostatic potential/Z on the  $z$  axis as a function of the normalized charge  $Z$  (from [31]). In the linear theory the three curves coincide

ion it has its maximum velocity  $v_0 + \varepsilon$  by attraction whereas the layer behind has not yet. This difference in speed leads to a charge nonuniformity oscillating in the direction of  $\mathbf{v}_0$ . Its relative importance increases with decreasing Coulomb logarithm  $\ln(\lambda_0/b_\perp)$ . In fact, for  $\mathbf{v}_0 = \text{const}$  the ratio of the two contributions to the absorption coefficient  $\alpha_\perp + \alpha_\parallel$  for  $\ln \Lambda_0 \gtrsim 2$  is given by

$$\frac{\alpha_\parallel}{\alpha_\perp} = \frac{1}{2 \ln \Lambda_0}. \quad (3.91)$$

In a harmonic laser field the electrons oscillate with the oscillation velocity  $\mathbf{v}_{\text{os}}(t)$  and the displacement  $\mathbf{p}(t)$ ,

$$\mathbf{v}_{\text{os}}(t) = \hat{\mathbf{v}}_{\text{os}} e^{-i\omega t}, \quad \hat{\mathbf{v}}_{\text{os}} = -i \frac{e}{m\omega} \hat{\mathbf{E}}, \quad \mathbf{p}(t) = \hat{\mathbf{p}} e^{-i\omega t}, \quad \hat{\mathbf{p}} = \frac{e}{m\omega^2} \hat{\mathbf{E}}.$$

As a consequence the collision frequency becomes time-dependent,  $\nu_{ei} = \nu_{ei}(t)$ . The portion of energy irreversibly transferred to the electrons per unit time under steady state conditions is obtained from the cycle-averaged quantity  $\bar{\mathbf{j}}\bar{\mathbf{E}}$ . With the help of (2.23) a meaningful definition of the cycle-averaged collision frequency  $\bar{\nu}_{ei}$  is given by

$$\bar{\mathbf{j}}\bar{\mathbf{E}} = \overline{\nu_{ei} n_e m \mathbf{v}^2} = 2\bar{\nu}_{ei} n_{e0} \bar{\mathcal{E}}_{\text{os}}, \quad n_{e0} = \overline{n_e(t)}, \quad \bar{\mathcal{E}}_{\text{os}} = \frac{1}{2} m \bar{\mathbf{v}}^2. \quad (3.92)$$

With  $\nu_{ei}$  replaced by  $\overline{\nu_{ei}(t)}$  in the foregoing sections all absorption formulas remain valid.

The determination of the time-averaged collision frequency  $\bar{\nu}_{ei}$  for vanishing electron temperature represents a nearly exactly solvable problem. It may serve as a bench mark result for critically analyzing the various approximate results in the literature. However, even under the limitation  $T_e = 0$  the analysis is of considerable complexity [33]. In (3.75) the former  $\mathbf{r} = \mathbf{b} + \mathbf{v}_0 t$  is replaced by  $\mathbf{r} = \mathbf{b} + \mathbf{p}(t)$ . Under the assumption of steady state and no memory effect extending over more than one oscillation, with the help of the Anger functions of index  $\sigma = \omega_p/\omega$  [34],

$$J_\sigma(x) = \frac{1}{\pi} \int_0^\pi \cos(\sigma\xi - x \sin \xi) d\xi,$$

one arrives (making use of trigonometric identities) at the collective part of the collision frequency  $\bar{\nu}_c$ ,

$$\bar{\nu}_c = 2 \frac{\hat{b}_\perp \omega_p^2}{\hat{v}_{\text{os}}} \int_{-\infty}^{\infty} \frac{b_0}{\hat{p}} |x| K_0(b_0|x|/\hat{p}) K_1(b_0|x|/\hat{p}) J_\sigma^2(x) dx; \quad (3.93)$$

$$\hat{b}_\perp = \frac{\kappa e}{m \hat{v}_{\text{os}}^2}, \quad \hat{p} = |\hat{\mathbf{p}}|. \quad (3.94)$$

The total collision frequency  $\bar{v}_{ei}$  is the sum of  $\bar{v}_c$  and the contribution from the bent orbits with  $b < b_0$ . In Fig. 3.11 the integral of expression (3.93) is evaluated numerically as a function of  $\sigma$  for  $p/b_0 = 20, 40, 60, 80$ . It shows weak local maxima in the neighborhood of even integer values of  $\sigma$ . The integral is highest for  $\omega_p = 0$ . This case corresponds to suppressing the restoring force, i.e., dynamical shielding, in (3.75). As pointed out, with a constant electron velocity  $v_0$ , for  $b \rightarrow \infty$  a logarithmically diverging expression for  $\bar{v}_{ei} = v_{ei}$  is obtained. In contrast, with a periodically oscillating electron velocity  $v_{os}(t)$ ,  $\bar{v}_{ei}$  no longer diverges at  $b = \infty$ . The reason for this behavior is that now the bare Coulomb cross section is modified by the presence of the laser field, or, in other words, it is “dressed” by the laser photons. The contribution of collisional absorption by excitations of plasmons parallel to  $\hat{\mathbf{E}}$  is shown in Fig. 3.11b. For the parameters used here it is at most 15% of the total value.

For  $\sigma = \omega_p/\omega = n$ ,  $n$  integer, an asymptotic expansion of (3.93) can be given as follows,

$$\begin{aligned}\bar{v}_c = \frac{2}{\pi} \frac{\omega_p^2 \hat{b}_\perp}{\hat{v}_{os}} & \left[ \ln^2(p/b_0) + (8 \ln 2 - 4\lambda(n)) \ln(p/b_0) + 16 \ln^2 2 - \frac{\pi^2}{12} \right. \\ & \left. - 16\lambda(n) \ln 2 + 4\lambda^2(n) \right] + O\left(\frac{\ln^3(p/b_0)}{(p/b_0)^2}\right),\end{aligned}\quad (3.95)$$

$$n = \frac{\omega_p}{\omega} = 0, 1, 2, \dots, \quad \lambda(n) = \sum_{k=1}^n \frac{1}{2k-1}, \quad \text{i.e.,} \quad \lambda(0) = 0, \quad \lambda(1) = 1, \dots$$

It becomes evident from Fig. 3.11a that for  $\omega_p < \omega/5$  screening is no longer relevant. Therefore the collision frequency is given by setting  $\sigma = n = 0$  in (3.95),

$$\bar{v}_c = \frac{2}{\pi} \frac{\omega_p^2 \hat{b}_\perp}{\hat{v}_{os}} \left[ \ln^2(p/b_0) + 5.5 \ln(p/b_0) + 6.86 \right], \quad \omega_p \lesssim \omega/5. \quad (3.96)$$

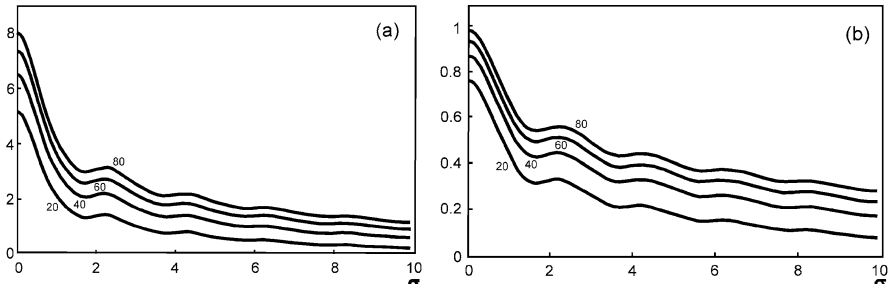


**Fig. 3.11** (a) Evaluation of the integral (3.93) as a function of  $\sigma = \omega_p/\omega$  for  $p/b_0 = 20, 40, 60, 80$ ; (b) contribution of  $\delta_\parallel$  to the integral for the same parameters. Main contribution to absorption originates from plasmon excitation perpendicular to  $v_{os}$

A detailed analysis of (3.93) shows that for  $\sigma = 0$  the integrand decays exponentially from  $x = p/b_0$  on. This means that screening acts as if the bare Coulomb potential is cut off at  $b_{\max} = p = \hat{v}_{\text{os}}/\omega$ . If  $\sigma > 0$ ,  $J_\sigma^2(x < \sigma) \simeq 0$  holds and the corresponding cut off is  $b_{\max} = \hat{v}_{\text{os}}/\omega_p$ .

### 3.3.2 Thermal Electrons in a Strong Laser Field

The random motion of the plasma electrons in the mean field approximation may be described by a classical one particle distribution function  $f(\mathbf{x}, \mathbf{v}_e, t)$  when its kinetic temperature  $T_e$  is much higher than the Fermi temperature  $T_F = E_F/k_B$ . In the presence of the laser field a drift velocity is superposed and hence the distribution function  $g(\mathbf{x}', \mathbf{v}', t)$  in the lab frame is

$$g(\mathbf{x}', \mathbf{v}', t) = f(\mathbf{x}, \mathbf{v}_e, t), \quad \mathbf{x}' = \mathbf{x} + \mathbf{p}(t), \quad \mathbf{v}' = \mathbf{v}_e + \mathbf{v}_{\text{os}}(t). \quad (3.97)$$

As a consequence of the attraction by an ion an electric field  $\mathbf{E}_{\text{in}}$  is induced by thermal and dynamical shielding. In the case that the screening length  $\lambda$  is much larger than  $b_\perp$  and  $\lambda_B$  the majority of the particle orbits is nearly straight and again a collision parameter  $b_0$ ,  $\max(b_\perp, \lambda_B) \ll b_0 \ll \lambda$ , can be introduced which separates close encounters from remote ones. The electrons with  $b > b_0$  behave fluid-like and are adequately described by the linearized dielectric Vlasov model.

The Vlasov equation (2.86) with a test ion of charge  $q = Ze$  reads in the oscillatory frame  $\mathbf{x} = \mathbf{x}' - \mathbf{p}(t)$

$$\begin{aligned} \frac{\partial f}{\partial t} + \mathbf{v}_e \frac{\partial f}{\partial \mathbf{x}} + \frac{e}{m} \nabla \Phi \frac{\partial f}{\partial \mathbf{v}_e} &= 0, \\ \Phi = \Phi_C + \Phi_{\text{in}}, \quad \Phi_C &= \frac{\kappa}{|\mathbf{x}'|}, \quad \nabla \Phi_{\text{in}} = -\mathbf{E}_{\text{in}}. \end{aligned} \quad (3.98)$$

$\Phi_{\text{in}}$  is the induced screening potential. The Coulomb potential  $\Phi_C$  of the ion oscillates around its position in the lab frame  $\mathbf{x}' = 0$  according to  $\mathbf{x} = \mathbf{x}' - \mathbf{p}(t)$ . By setting  $f = f_0(\mathbf{v}_e) + f_1(\mathbf{x}, \mathbf{v}_e, t)$ , with  $f_1$  the disturbance introduced by the test charge, and linearizing around  $f_0$  yields

$$\frac{\partial f_1}{\partial t} + \mathbf{v}_e \frac{\partial f_1}{\partial \mathbf{x}} + \frac{e}{m} \nabla (\Phi_C + \Phi_{\text{in}}) \frac{\partial f_0}{\partial \mathbf{v}_e} + \frac{e}{m} \nabla \Phi_C \frac{\partial f_1}{\partial \mathbf{v}_e} = 0. \quad (3.99)$$

Poisson's equation requires

$$\nabla^2 \Phi_{\text{in}} = \frac{n_0 e}{\epsilon_0} \int f_1 d\mathbf{v}_e, \quad \nabla^2 \Phi_C = -\frac{q}{\epsilon_0} \delta(\mathbf{x} + \mathbf{p}(t)). \quad (3.100)$$

It is standard to omit the last term in (3.99) although it is of first order. By its neglect strong ion field effects (close encounters, bent orbits) are excluded.

The  $\nabla$  operators are removed by a Fourier transform in space,  $\tilde{\Phi}(\mathbf{k}, \Omega) = (2\pi)^{-2} \int \Phi(\mathbf{x}, t) \exp(-i\mathbf{k}\mathbf{x} + i\Omega t) d\mathbf{x} dt$ , etc., and (3.99), (3.100) reduce to algebraic relations. Equations (3.100) transform into

$$\tilde{\Phi}_{\text{in}}(\mathbf{k}, \Omega) = -\frac{n_0 e}{\epsilon_0 \mathbf{k}^2} \int \tilde{f}_1(\mathbf{k}, \Omega, \mathbf{v}_e) d\mathbf{v}_e, \quad (3.101)$$

$$\begin{aligned} \tilde{\Phi}_{\text{C}}(\mathbf{k}, \Omega) &= \frac{q}{(2\pi)^2 \epsilon_0 \mathbf{k}^2} \int \delta(\mathbf{x} + \mathbf{p}(t)) e^{-i\mathbf{k}\mathbf{x} + i\Omega t} d\mathbf{x} dt \\ &= \frac{q}{(2\pi)^2 \epsilon_0 \mathbf{k}^2} \int e^{i(\Omega t + \mathbf{k}\hat{\mathbf{p}} \cos \omega t)} dt \\ &= \frac{q}{2\pi \epsilon_0 \mathbf{k}^2} \sum_{n=-\infty}^{\infty} i^n \delta(\Omega + n\omega) J_n(\mathbf{k}\hat{\mathbf{p}}) \end{aligned} \quad (3.102)$$

where the identities

$$e^{\pm iz \cos \zeta} = \sum_{n=-\infty}^{\infty} (\pm i)^n J_n(z) e^{\pm in\zeta}, \quad \delta(z) = (2\pi)^{-1} \int e^{ikz} dk$$

for the Bessel functions of integer order  $J_n$  and for the delta function have been used. The Fourier transform of (3.99) yields

$$(\Omega - \mathbf{k}\mathbf{v}_e) \tilde{f}_1(\mathbf{k}, \Omega) = \frac{e}{m} (\tilde{\Phi}_{\text{C}} + \tilde{\Phi}_{\text{in}}) \mathbf{k} \frac{\partial f_0}{\partial \mathbf{v}_e}. \quad (3.103)$$

In a static linear homogeneous medium the dielectric constant  $\epsilon$  connects the external, induced, and total electric fields  $\mathbf{E}_{\text{ex}}$ ,  $\mathbf{E}_{\text{in}}$ ,  $\mathbf{E}$  with the polarization  $\mathbf{P}$  in the following way,

$$\epsilon \mathbf{E} = \epsilon (\mathbf{E}_{\text{ex}} + \mathbf{E}_{\text{in}}) = \mathbf{E} + \frac{1}{\epsilon_0} \mathbf{P}.$$

By means of Poisson's equation and  $\nabla \mathbf{P} = -\rho_{\text{in}}$  this translates into

$$\epsilon \rho = (\rho - \rho_{\text{in}}) = \rho_{\text{ex}}, \quad \epsilon \Phi = (\Phi - \Phi_{\text{in}}) = \Phi_{\text{ex}} \quad (3.104)$$

for the total, external, and induced charge densities  $\rho$ ,  $\rho_{\text{ex}}$ ,  $\rho_{\text{in}}$  and potentials  $\Phi$ ,  $\Phi_{\text{ex}}$ ,  $\Phi_{\text{in}}$ . Thus,  $\rho = \rho_{\text{ex}}/\epsilon$ ,  $\mathbf{E} = \mathbf{E}_{\text{ex}}/\epsilon$ ,  $\Phi = \Phi_{\text{ex}}/\epsilon$ .

Introducing the dielectric function  $\epsilon = \epsilon(\mathbf{k}, \Omega)$ , within the validity of linear response these relations hold for a single Fourier component in fields varying in space and time. Substituting  $\tilde{f}_1$  from (3.103) in  $\tilde{\Phi}_{\text{in}}$  in (3.101) yields

$$\tilde{\Phi}_{\text{C}} = \tilde{\Phi} - \tilde{\Phi}_{\text{in}} = \tilde{\Phi} \left\{ 1 + \frac{n_0 e^2}{\epsilon_0 \mathbf{k}^2 m} \int \frac{\mathbf{k} \partial f_0 / \partial \mathbf{v}_e}{\Omega - \mathbf{k}\mathbf{v}_e} d\mathbf{v}_e \right\}.$$

Hence, owing to  $\Phi_C = \Phi_{\text{ex}}$ ,  $\rho_C = \rho_{\text{ex}}$ , and  $\tilde{\Phi}_C = \tilde{\Phi}_{\text{ex}}$ ,  $\tilde{\rho}_C = \tilde{\rho}_{\text{ex}}$

$$\epsilon(\mathbf{k}, \Omega) = \frac{\tilde{\Phi}_C}{\tilde{\Phi}} = 1 + \frac{\omega_p^2}{k^2} \int \frac{k \partial f_0 / \partial \mathbf{v}_e}{\Omega - k \mathbf{v}_e} d\mathbf{v}_e. \quad (3.105)$$

It is analytic in the entire half plane  $\Im \Omega > 0$ . For a real quantity  $h(\mathbf{x}, t)$  the relation  $\tilde{h}^*(\mathbf{k}, \Omega) = \tilde{h}(-\mathbf{k}^*, -\Omega^*)$  holds and, consequently,  $\epsilon^*(\mathbf{k}, \Omega) = \epsilon(-\mathbf{k}^*, -\Omega^*)$ . The total potential  $\Phi(\mathbf{x}, t) = \Phi_C(\mathbf{x}, t) + \Phi_{\text{in}}(\mathbf{x}, t)$  reads now in the frame moving with  $\mathbf{v}_{\text{os}}(t)$

$$\Phi(\mathbf{x}, t) = \frac{1}{(2\pi)^3} \frac{q}{\epsilon_0} \sum_{n=-\infty}^{\infty} \int \frac{i^n}{k^2 \epsilon(\mathbf{k}, -n\omega)} J_n(\mathbf{k} \hat{\mathbf{p}}) e^{ikx + in\omega t} d\mathbf{k}. \quad (3.106)$$

The force  $f_q$  acting on the ion at position  $\mathbf{x}(t) = -\hat{\mathbf{p}} \cos \omega t$  is

$$\begin{aligned} f_q &= -q \nabla \Phi(-\hat{\mathbf{p}} \cos \omega t, t) \\ &= -\frac{1}{(2\pi)^3} \frac{q^2}{\epsilon_0} \sum_{n=-\infty}^{\infty} \int \frac{i^{n+1} \mathbf{k} J_n(\mathbf{k} \hat{\mathbf{p}})}{k^2 \epsilon(\mathbf{k}, -n\omega)} e^{-ik \hat{\mathbf{p}} \cos \omega t + in\omega t} d\mathbf{k} \\ &= -\frac{1}{(2\pi)^3} \frac{q^2}{\epsilon_0} \sum_{l,n=-\infty}^{\infty} \int \frac{i^{n+1-l} \mathbf{k}}{k^2 \epsilon(\mathbf{k}, -n\omega)} J_l(\mathbf{k} \hat{\mathbf{p}}) J_n(\mathbf{k} \hat{\mathbf{p}}) e^{i(n-l)\omega t} d\mathbf{k}. \end{aligned}$$

The cycle-averaged energy absorbed per unit volume and unit time is

$$\begin{aligned} \overline{jE} &= -\frac{n_0}{Z} \overline{f_q v_{\text{os}}(t)} = -i \frac{n_0}{Z} \frac{1}{2m\omega} \hat{E} f_q (e^{i\omega t} - e^{-i\omega t}) \\ &= \frac{n_0 e^2 q}{2m\omega \epsilon_0} \frac{\hat{E}}{(2\pi)^3} \sum_{n=-\infty}^{\infty} \int \frac{i \mathbf{k} d\mathbf{k}}{k^2 \epsilon(\mathbf{k}, -n\omega)} \\ &\quad \times \{J_{n-1}(\mathbf{k} \hat{\mathbf{p}}) J_n(\mathbf{k} \hat{\mathbf{p}}) + J_n(\mathbf{k} \hat{\mathbf{p}}) J_{n+1}(\mathbf{k} \hat{\mathbf{p}})\} \\ &= \frac{1}{(2\pi)^3} \frac{\omega_p^2}{\omega} q \hat{E} \sum_{n=-\infty}^{\infty} \int \frac{i \mathbf{k} d\mathbf{k}}{k^2 \epsilon(\mathbf{k}, -n\omega)} J_n^2(\mathbf{k} \hat{\mathbf{p}}) \frac{n}{k \hat{\mathbf{p}}}. \end{aligned}$$

In the last step the property  $J_{n-1}(x) + J_{n+1}(x) = 2n J_n(x)/x$  was used.  $\hat{E}$  is the real laser field amplitude. Owing to the cylindrical symmetry the integration over  $\mathbf{k} \perp \hat{\mathbf{p}}$  can be performed easily in polar coordinates,

$$\begin{aligned} \overline{jE} &= \frac{1}{(2\pi)^3} \frac{\omega_p^2}{\omega} q \hat{E} \sum_{n=-\infty}^{\infty} \int_0^\infty \frac{i dk}{\epsilon(k, -n\omega)} \frac{2\pi}{\hat{\mathbf{p}}} \int_{-1}^1 n J_n^2(k \hat{\mathbf{p}} \cos \vartheta) d \cos \vartheta \\ &= m \hat{v}_{\text{os}} Z \frac{\omega_p^2}{\pi^2 \hat{\mathbf{p}}^2} \sum_{n=1}^{\infty} n \int_0^\infty \frac{dk}{k} \Im \frac{1}{\epsilon(k, -n\omega)} \int_0^{k \hat{\mathbf{p}}} J_n^2(\xi) d\xi. \end{aligned} \quad (3.107)$$

In the last passage the properties  $J_{-n}(\xi) = (-1)^n J_n(\xi)$ ,  $J_n^2(-\xi) = J_n^2(\xi)$ ,  $\epsilon(\mathbf{k}, -\Omega^*) = \epsilon^*(\mathbf{k}, \Omega)$  for  $\mathbf{k}$  real and  $\Omega = -n\omega$ , and  $\hat{v}_{os} = e\hat{\mathbf{E}}/m\omega$  were used. The electron distribution function  $f_0(\mathbf{v}_e)$  is to be used in a system of reference in which no net drift results, i.e.,  $\int \mathbf{v}_e f_0(\mathbf{v}_e) d\mathbf{v}_e = 0$ ; all drift is in the ions. The time-averaged collision frequency  $\bar{v}_{ei}$  follows from (3.92).

For a Maxwellian distribution function  $f_e$  (3.105) reads

$$\epsilon(k, \omega) = 1 + \frac{k_D^2}{k^2} \left( 1 - 2\eta e^{-\eta^2} \int_0^\eta e^{x^2} dx + i\sqrt{\pi}\eta e^{-\eta^2} \right), \quad \eta = \frac{\omega}{\sqrt{2}kv_{th}}. \quad (3.108)$$

The electron thermal velocity is  $v_{th} = (k_B T_e/m)^{1/2}$  and  $k_D = 1/\lambda_D$ , with  $\lambda_D = v_{th}/\omega_p$  the familiar electron Debye length. Simple expressions of  $\overline{\mathbf{j}\mathbf{E}}$  are attainable for  $\hat{v}_{os} < v_{th}$  and  $v_{os} \gg v_{th}$ ; for intermediate ratios of  $v_{os}/v_{th}$  (3.107) must be evaluated numerically. A comparison of the classical expression for the differential Coulomb cross section  $\sigma_\Omega$  in terms of the impact parameter  $b$  (2.44) with its identical quantum expression formulated in terms of plane waves of wave vector  $\mathbf{k}$  (see [35], p. 387),  $b$  and  $|\mathbf{k}|$  are related by  $k = |\mathbf{k}| = 1/b$  and, correspondingly,  $k_\perp = 1/b_\perp$  and  $k_B = 1/\lambda_B$ . If  $b$  is a few times larger than  $\lambda_B$  it is the center of a narrow wave packet around  $k = 1/b$ . Hence, for  $\omega \gtrsim \omega_p$  the relevant  $k$ -interval in (3.108) is  $k > k_D$  or, equivalently,  $\omega_p/kv_{th} \lesssim \sqrt{2}\eta < 1$ . It yields

$$\Im\left(\frac{1}{\epsilon}\right) \simeq -\left(\frac{\pi}{2}\right)^{1/2} \frac{k_D^2}{k^3} \frac{\omega}{v_{th}} \frac{e^{-\frac{\omega^2}{2k^2v_{th}^2}}}{(1+k_D^2/k^2)^2}. \quad (3.109)$$

Let us take for the moment  $\hat{v}_{os} \ll v_{th}$  to arrive at  $k\hat{p} \ll 1$  and  $J_1(\xi) = \xi/2$  as the leading term owing to  $J_n(\xi \ll 1) \simeq (\xi/2)^n/n!$ . Hence, in the weak laser field approximation (3.107) simplifies to

$$\overline{\mathbf{j}\mathbf{E}} = \frac{4}{3} \left(\frac{\pi}{2}\right)^{1/2} Z \left(\frac{n_e e^2}{4\pi \varepsilon_0 m}\right)^2 \frac{m\hat{v}_{os}^2}{v_{th}^3} \int_0^{(\infty)} \frac{k^3}{(k^2 + k_D^2)^2} dk. \quad (3.110)$$

The indefinite integral is  $[\ln(k^2 + k_D^2) + k_D^2/(k^2 + k_D^2)]/2$ . It diverges for  $k \rightarrow \infty$ . This is a consequence of linearization and omission of the last term in (3.99) or, equivalently, of the straight orbit approximation. In perfect analogy to the treatment of close encounters by  $D(\beta_0)$  in (3.84)ff  $k_0 = 1/b_0$  has to be introduced, with  $b_0$  dividing straight orbits from bent trajectories. After folding with a Maxwellian and averaging  $v_{os}(t)\langle D(\beta_0) \rangle$  over one laser cycle the resulting quantity has to be added to (3.110). We do not continue further here because the subject is treated more adequately in the next subsection dedicated to the ballistic collision model. We conclude by observing that the classical dielectric model yields a lower self-consistent cut-off at  $k = k_D$ , but it diverges for large  $k$ -values related to close electron-ion encounters. The divergence at large  $k$ -values is avoided in a quantum

treatment, e.g., following a Kadanoff-Baym [36, 21] or a quantum Vlasov treatment [37]. A complementary derivation in some respect, based on a generalized linear response theory, is given in [38]. The authors arrive at the same expression (3.107) in which now the classical expression of  $\epsilon(k, \omega)$  is replaced by its quantum counterpart  $\epsilon_q(k, \omega)$  [39],

$$\begin{aligned}\epsilon_q(k, \omega) = & 1 + \frac{k_D^2}{\sqrt{2}k^2} \frac{k_B}{k} \left[ D\left(\eta + \frac{k}{\sqrt{2}k_B}\right) - D\left(\eta - \frac{k}{\sqrt{2}k_B}\right) \right] \\ & + i\left(\frac{\pi}{2}\right)^{1/2} \frac{k_D^2}{\sqrt{2}k^2} \frac{k_B}{k} e^{-\eta^2} e^{-\frac{1}{2}(k/k_B)^2} \sinh(\sqrt{2}\eta),\end{aligned}\quad (3.111)$$

with  $\eta$  as before and  $D(y) = e^{-y^2} \int_0^y e^{x^2} dx$ . The evaluation of (3.107) with  $\epsilon = \epsilon_q$  is complicated. Following again [39] one arrives at

$$\begin{aligned}\overline{jE} &= \frac{Zm\omega_p^4}{\pi^2 \hat{v}_{os}} \int_0^\infty \frac{dk}{k} F\left(\frac{k}{k_D}, \frac{\omega}{\omega_p}, \frac{\hat{v}_{os}}{v_{th}}\right), \\ F &= \left(\frac{\omega}{\omega_p}\right)^2 \sum_{l=1}^{\infty} l \frac{\Im \epsilon_q(k, il\omega)}{|\epsilon_q(k, il\omega)|^2} \int_0^{k\hat{v}_{os}/\omega} d\xi J_l^2(\xi), \quad \bar{v}_{ei} = \frac{\overline{jE}}{2n_e E_{os}}\end{aligned}\quad (3.112)$$

for all ratios  $\hat{v}_{os}/v_{th}$ . In many applications holds  $\lambda_D \gg b_0 > \tilde{\lambda}_B \gtrsim 2b_\perp$ . Then, for  $\hat{v}_{os} \ll v_{th}$  with  $\epsilon_q$  used in (3.107) follows the upper cut-off  $k = k_{\max} = \sqrt{2}k_B$ . The validity of (3.110) extends, strictly speaking, only up to  $k = 1/b_0$ . However, when adding the cycle-averaged contribution of the close encounters  $v_{os}(t)\langle D(\beta_0) \rangle$  the sum of both is obtained by extending the interval up to  $k_{\max}$  and is insensitive to the special choice of the cut  $b_0$  over an adequate range. Hence, the integral yields  $\ln(\lambda_D/\tilde{\lambda}_B) + 0.06$  which is nearly identical with the familiar Coulomb logarithm  $\ln \Lambda$ ,  $\Lambda = \lambda_D/\tilde{\lambda}_B$ , and  $v_{ei}$  becomes identical to the Spitzer–Braginskii collision frequency (2.45) for a Maxwellian plasma. It should be stressed that although electron trajectories with  $b = \tilde{\lambda}_B$  are generally bent and invalidate any Born approximation or linearization (3.99), under the limitations above the correct result for  $v_{ei}$  is obtained through the cut-off at  $b_{\min} = \tilde{\lambda}_B/2$ . The collision frequency for  $\hat{v}_{os} \gg v_{th}$  is also obtained by making use of  $\epsilon_q(k, \omega)$  and the asymptotic forms of  $J_n(\xi)$  for large arguments. We list the results of [19, 20, 37], all derived for  $\omega^2 \gg \omega_p^2$ ,

$$\begin{aligned}\text{Shima–Yatom : } v_{ei} &= C \ln \frac{2\hat{v}_{os}}{v_{th}} \left( \ln \frac{v_{th}/\omega}{\tilde{\lambda}_B} + \ln \frac{2\hat{v}_{os}}{v_{th}} \right) \\ \text{Silin : } v_{ei} &= 2C \left( 1 + \ln \frac{\hat{v}_{os}}{2v_{th}} \right) \ln \frac{v_{th}/\omega}{\tilde{\lambda}_B} \\ \text{Kull–Plagne : } v_{ei} &= 2C \ln \frac{\hat{v}_{os}}{v_{th}} \ln \left[ \sqrt{2} \frac{v_{th}/\omega}{\tilde{\lambda}_B} \left( \frac{\hat{v}_{os}}{v_{th}} \right)^{1/2} \right]\end{aligned}\quad (3.113)$$

(“double Coulomb logarithm”) where  $C = m_e \omega_p^4 / (n_e \hat{v}_{\text{os}}^3)$ . The most careful asymptotic analysis is undertaken in [37]. In connection with the expressions (3.113) in particular and with the dielectric model in general, several remarks are to be made. (i) Expressions (3.113) for the same physical quantity differ from each other. Evidently there is no unique asymptote. However, the validity of each expression may be best for some interval of  $\hat{v}_{\text{os}}/v_{\text{th}}$ . Do they hold for all ratios  $\omega_p/\omega > (1 \sim 3)$ ? (ii) The evaluation of (3.107) in full generality is of considerable complexity and does exclude close encounters. At ratios  $\hat{v}_{\text{os}}/v_{\text{th}} \gg 1$  up to  $10^3$  Bessel terms may have to be added to achieve convergence. (iii) To remove the differential operators  $\partial/\partial t$  and  $\nabla$  from (3.99) transformation to Fourier space is done which, as a consequence necessitates the decomposition of the anharmonic time dependence  $\exp(i \cos \omega t)$  to a complete set of Bessel functions. Great loss of a physical picture is the consequence. For example, what is the physics behind a function like

$$\ln \left[ \left( \sqrt{2} \frac{v_{\text{th}}/\omega}{\lambda_B} \left( \frac{\hat{v}_{\text{os}}}{v_{\text{th}}} \right)^{1/2} \right)^{\ln \hat{v}_{\text{os}}/v_{\text{th}}} \right]$$

from (3.113)? (iv) In its nature a collision is short in comparison to the laser plasma period  $2\pi/\omega$ , it resembles a narrow Gaussian, if not even a  $\delta$ -type interaction. To decompose it into functions of  $\mathbf{kx}$  of constant amplitude is counterintuitive (e.g., like treating the hydrogen atom in the basis of the Hermite polynomials of the harmonic oscillator in  $\mathbb{R}^3$ ). In transport theory time-dependent quantities are of interest, e.g., the heating function  $\mathbf{j}(t)\mathbf{E}(t)$  at low frequency  $\omega$ . It is a hopeless enterprise to evaluate it in the framework of the standard dielectric theory (see the double sum of products  $J_l J_n$ ). Searching for a more appropriate description, i.e., a more adequate basis, may represent a challenging problem of mathematical physics. With the introduction of the ballistic model for collisions a first step may be done in the right direction.

### 3.3.3 The Ballistic Model

Collisions of individual electrons with a fixed ion of charge number  $Z$  are considered. The momentum loss along the original electron trajectory due to deflection is calculated and the result is averaged over all impact parameters  $b$  and all velocities  $\mathbf{v}(t) = \mathbf{v}_{\text{os}}(t) + \mathbf{v}_e$ ,  $\mathbf{v}_e$  taken from  $f(\mathbf{x}, \mathbf{v}_e, t)$  in the oscillating frame as before in (3.97). As a result the time-dependent collision frequency  $\nu_{ei}(t)$  is obtained. Finally, cycle averaging yields  $\bar{\nu}_{ei}$ . For simplicity the distribution function  $f$  is assumed to be homogeneous and locally isotropic; hence  $f(\mathbf{x}, \mathbf{v}_e, t) = f(\mathbf{v}_e, t)$ . The momentum loss  $\Delta p$  in a Coulomb collision along  $\mathbf{v}(t)$  follows from the differential Coulomb cross section  $\sigma_\Omega$  in (2.44) by integration over  $b$ , with  $\sigma = \pi b_{\text{max}}^2$  the total cross section,

$$\begin{aligned}\Delta \mathbf{p} &= m\mathbf{v} \frac{b_\perp^2}{\sigma} \int_{\vartheta=\varepsilon}^{\pi} \frac{(1 - \cos \vartheta) \sin \vartheta}{4 \sin^4 \frac{\vartheta}{2}} d\vartheta d\varphi = 4\pi m\mathbf{v} \frac{b_\perp^2}{\sigma} \int_{\vartheta=\varepsilon}^{\pi} \frac{d \sin \frac{\vartheta}{2}}{\sin^2 \frac{\vartheta}{2}} \\ &= 4\pi m\mathbf{v} \frac{b_\perp^2}{\sigma} \ln \frac{(b_\perp^2 + b_{\max}^2)^{1/2}}{b_\perp}.\end{aligned}\quad (3.114)$$

The Coulomb logarithm  $\ln \Lambda = \ln[(b_\perp^2 + b_{\max}^2)^{1/2}/b_\perp]$  is discussed later. The momentum loss per unit time is  $\dot{\mathbf{p}} = \sigma n_i |\mathbf{v}| \Delta \mathbf{p}$ ,

$$\dot{\mathbf{p}} = -m v_{ei}(\mathbf{v}) \mathbf{v} = -\frac{K}{v^3} \mathbf{v} \ln \Lambda, \quad K = \frac{Z^2 e^4 n_i}{4\pi \varepsilon_0^2 m}. \quad (3.115)$$

By the first equality the collision frequency  $v_{ei}(\mathbf{v})$  for the momentum loss  $\mathbf{p} = m\mathbf{v}$  is defined. Equation (3.115) implies that simultaneous collisions are reduced to a sequence of successive encounters since small angle deflections obey the relations  $\langle \Delta \mathbf{v} \rangle = \mathbf{v} \langle [1 - \cos \vartheta(t)] \rangle = \mathbf{v} \langle \vartheta^2(t) \rangle / 2 = \mathbf{v} \sum_{i=1}^N \vartheta_i^2(t) / 2 = \mathbf{v} / v^2 \sum \delta_i^2(t) / 2$ , in perfect analogy to (3.90). To obtain the ensemble-averaged momentum loss  $\langle \dot{\mathbf{p}} \rangle$  averaging has to be done on  $\mathbf{v}/v^3$  over the thermal velocities  $\mathbf{v}_e$ . For an isotropic distribution function  $f(v_e)$  the velocity  $\mathbf{v}$  consists of all vector sums as sketched in Fig. 3.12. The quantity  $\dot{\mathbf{p}}$  is parallel to  $\mathbf{v}$ , whereas  $\langle \dot{\mathbf{p}} \rangle$  is directed along  $\mathbf{v}_{os}$ . With the angle  $\chi$  as indicated in the figure we find

$$\langle \dot{\mathbf{p}} \rangle = m v_{ei}(t) \mathbf{v}_{os} = -K \int_0^\infty \int_0^\pi \frac{\mathbf{v}}{v^3} 2\pi v_e^2 \sin \chi f(v_e) \ln \Lambda d\chi dv_e. \quad (3.116)$$

The combined velocity is  $v = |\mathbf{v}| = (\mathbf{v}_{os}^2 + \mathbf{v}_e^2 + 2\mathbf{v}_{os}\mathbf{v}_e)^{1/2}$ . The collision frequencies  $v_{ei}(t)$  and  $\bar{v}_{ei}$  follow as

$$v_{ei}(t) = 2\pi \frac{K}{m v_{os}(t)} \int_0^\infty \int_{-1}^1 \frac{\cos \alpha v_e^2 f(v_e) \ln \Lambda}{v_{os}^2 + v_e^2 + 2v_{os}v_e \cos \chi} d\cos \chi dv_e, \quad (3.117)$$

$$\bar{v}_{ei} = 4\pi \frac{K}{m \hat{v}_{os}^2} \overline{\int_0^\infty \int_{-1}^1 \frac{\mathbf{v}_{os} \mathbf{v}}{v^3} v_e^2 f(v_e) \ln \Lambda d\cos \chi dv_e}. \quad (3.118)$$

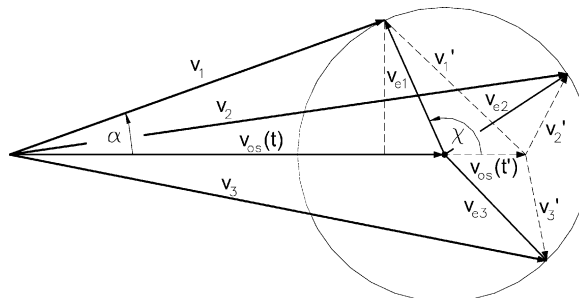


**Fig. 3.12**  $\mathbf{v}_i = \mathbf{v}_{e,i} + \mathbf{v}_{os}(t)$ ,  $\mathbf{v}_{os}(t)$  quiver motion

These expressions are much simpler than (3.107), however they do not handle collective resonances around  $\omega = \omega_p$ . The integration over  $b$  in the Coulomb logarithm runs from  $b = 0$  to  $b = b_{\max}$ . No lower cut-off appears, only  $b_{\max}$  must be determined.

### 3.3.3.1 Cut-offs

Let us assume that  $b_{\perp}$  and  $\lambda_B$  are well separated from  $b_{\max}$  and  $\lambda_D$ . In addition  $b_{\max} \gg b_0$ ,  $b_0$  separating straight from bent orbits, is assumed to be valid as is the case in the weakly coupled plasma. First  $b_{\max}$  is fixed. Under the current conditions Jackson's model applies [see paragraph containing (3.89)]. For  $\hat{v}_{\text{os}}/v_{\text{th}} \gtrsim 3$  the time-averaged speed is, owing to  $v^2 \sim \sin^2 \omega t$ ,  $\bar{v} = v/\sqrt{2}$ . From  $\tau_{\text{int}} = 2b/\bar{v} \leq \tau_{\text{laser}}/3$  follows

$$\frac{2b_{\max}}{v/\sqrt{2}} = \frac{1}{3} \frac{2\pi}{\omega} \implies b_{\max} = \frac{v}{\sqrt{2}\omega}. \quad (3.119)$$

The accuracy of this cut-off can be checked by comparing (3.118) with (3.112). The outcome will result very satisfactory, as shown in the following.

In the literature  $b = b_{\perp}$  or  $b = \lambda_B$  is generally referred to as a “lower cut-off”  $b_{\min}$ . This is unfortunate and totally misleading. Finally, to make the confusion complete,  $b_{\min} = b_{\perp}$  is given the name of “closest approach” [Sect. 3.3.1, e.g. (3.84), (3.85)]. A standard argument for choosing  $\lambda_B$  as a lower cut-off is that a higher degree of localization of encounters  $b < \lambda_B$  is meaningless because of the uncertainty principle. As seen in Sect. 3.3.1 in classical Coulomb scattering  $b_{\perp}$  results from an exact integration starting from  $b = 0$ . Perpendicular deflection plays no special role from the point of physics, it is merely a compact mathematical symbol. We want to stress further that the classical Rutherford cross section  $\sigma_Q$  for the Coulomb potential is identical with the corresponding exact quantum mechanical expression and with its first Born approximation [35]. In a quantum calculation integration is also done over all scattering angles, corresponding classically to all values  $b > 0$  [see (2.44)]. However, owing to screening the cross section of a charged particle in the plasma falls off more rapidly than  $1/b^4$ . That is the reason why in transport theory  $\lambda_D$  appears. Let us first consider the quasi-static screening at  $\hat{v}_{\text{os}} \ll v_{\text{th}}$  given by the Debye potential (2.39) in the weak coupling limit. Its differential cross section  $\sigma_D(\vartheta)$  in first Born approximation is given by [35]

$$\sigma_D(\vartheta) = \frac{b_{\perp}^2}{4[\sin^2(\vartheta/2) + (\lambda/2\lambda_D)^2]^2}, \quad \lambda_B = \frac{\hbar}{mv}. \quad (3.120)$$

Replacing  $\sigma_D(\vartheta)$  in  $\Delta p$  from (3.114) leads to  $L_C$  in place of  $\ln \Lambda$ ,

$$L_C = \frac{1}{2} \ln \left( \frac{1}{\rho^2} + 1 \right) - \frac{1}{1 + \rho^2} \simeq \frac{1}{2} \left( \ln \frac{1}{\rho^2} - 1 \right) = \ln \frac{\lambda_D}{\lambda_B} + 0.2, \quad \rho = \frac{\lambda_B}{2\lambda_D}. \quad (3.121)$$

It shows that, taken the first Born approximation for granted, in (3.114)  $b_\perp$  should always be replaced by  $\tilde{\lambda}_B$ . This is in clear contradiction to the rule that  $b_{\min}$  (which is not a lower cut-off) in  $\Lambda = b_{\max}/b_{\min} = b_{\max}/\tilde{\lambda}_B$  goes over into  $\Lambda = b_{\max}/b_\perp$  as soon as  $\tilde{\lambda}_B \lesssim (1 \sim 2)b_\perp$  ([40] p. 262). The contradiction arises for  $\lambda_D \rightarrow \infty$ . Scattering of a plane wave is an acceptable concept for potentials falling off rapidly, e.g., a Debye potential, but not for  $V \sim 1/r$  which is of infinite extension and gives contributions to scattering up to  $b = \infty$ . When scattering of finite wave packets is considered the contradiction disappears. However, the pertinent published literature is not very clear and often merely formal (see for instance [41] and [42], to name just two). Here we present a physically correct and more lucid explanation.

By setting  $k_0^2 = 2mE/\hbar^2 = 1/\tilde{\lambda}_B^2$  and  $\eta^2 = 1 - V(\mathbf{r})/E$  the stationary one-particle Schrödinger equation assumes the structure of (3.7) when  $\nabla E = 0$  is set. Under WKB conditions  $\eta$  obeys the ray equation (3.12). In the domain of validity of it the scattering angle  $\vartheta$  is the deflection angle of the trajectory (“ray”) associated with the collision parameter  $b$ . According to (2.44)  $\vartheta$  and  $b$  are related by  $\sin^2 \vartheta/2 = b_\perp^2/(b_\perp^2 + b^2)$ . Let be  $\tilde{\lambda}_B = rb_\perp$  and  $b_0 = s\tilde{\lambda}_B$ , where  $r$  and  $s$  are of order unity. By definition  $b_0$  subdivides the scattering potential into two regions,  $b > b_0$  and  $b \leq b_0$ . In the outer region WKB holds (“straight” orbits,  $b_0 \gg b_\perp$ ). By setting for instance  $r = s = 2$  follows  $\vartheta(b_0) = \vartheta_0 = 28^\circ$ ,  $\cos \vartheta_0 = 0.88 \simeq 1$ , and hence the first Born approximation (3.120) for  $\sigma_D(\vartheta)$  is also valid there. Owing to  $b_0 \ll b_{\max}$  screening in the inner domain  $b \leq b_0$  is irrelevant and scattering is calculated to an excellent approximation from the unscreened Coulomb potential. With the help of (3.114) the total momentum loss  $\Delta \mathbf{p}$  is

$$\Delta \mathbf{p} = 4\pi m v \frac{b_\perp^2}{\sigma} \left[ \ln \frac{b_\perp^2 + b_0^2}{b_\perp^2} + \ln(x^2 + \rho^2) \Big|_0^{x_0} - \frac{x^2}{x^2 + \rho^2} \Big|_0^{x_0} \right] \quad (3.122)$$

where  $x = \sin \vartheta/2$ ,  $x_0 = \sin \vartheta_0/2$ ,  $\rho = \tilde{\lambda}_B/2\lambda_D$ . If in the inner region  $\sigma_D(\vartheta)$  is used instead of  $\sigma_\Omega$ , from the second and third terms in (3.122) taken within the limits  $x = x_0$  and  $x = 1$  follows

$$\begin{aligned} \ln \frac{1 + \rho^2}{x_0^2 + \rho^2} - \frac{1}{1 + \rho^2} + \frac{x_0^2}{x_0^2 + \rho^2} &\simeq \ln \frac{1}{x_0^2 + \rho^2} \simeq \\ - \ln \left[ \frac{b_\perp^2}{b_\perp^2 + b_0^2} + \frac{b_\perp^2}{\lambda_D^2} \right] &\simeq \ln \frac{b_\perp^2 + b_0^2}{b_\perp^2}. \end{aligned}$$

Thus, the Debye potential can be used in the entire region  $0 \leq b < \infty$  if  $(\lambda_D/b_0)^2$  is considerably larger than  $(b_\perp^2 + b_0^2)/b_\perp^2$ , and the Coulomb logarithm reads as given by  $L_C$  in (3.121).

The situation is more complicated for  $\tilde{\lambda}_B < b_\perp$ . In evaluating (3.122) the condition  $b_0 \gg b_\perp$  must hold to guarantee the validity of WKB and the first Born approximation in the outer region. At the same time the use of the unscreened Coulomb potential in the inner region requires again  $b_0 \ll \lambda_D$ . In general the

frequently encountered simple rule of replacing  $\bar{\lambda}_B$  by  $b_\perp$  in the Coulomb logarithm represents an improvement. However, it is not exact; the correct cut-off results in a more complicated expression obtained from (3.122). In laser plasmas generally  $\bar{\lambda}_B \gg b_\perp$  holds and the opposite situation is not of great relevance.

In the following we limit ourselves to  $\bar{\lambda}_B > b_\perp$ . Guided by the structure of  $\sigma_D(\vartheta)$  in (3.120) which contains  $(\bar{\lambda}_B/2)^2/\lambda_D^2$  we redefine  $b_{\min} = \bar{\lambda}_B/2 = \hbar/2mv$ . The formal justification for it may come from the kinetic formulation in terms of Wigner distribution functions and is therefore to be considered of universal character not bound to the special Debye potential of scattering [39]. In practice the model of a coherent plane wave is not applicable to lateral extensions larger than  $\simeq \bar{\lambda}_D$ . Under the condition  $\hat{v}_{os} \ll v_{th}$  the quiver motion induces only small periodic oscillations of the screening Debye sphere. The much faster thermal motion compensates small deformations. This is expected to hold to an acceptable approximation up to  $\hat{v}_{os} \lesssim v_{th}$ . In the Coulomb logarithm, however,  $\lambda_D = v_{th}/\omega_p$  has to be replaced by  $v_{th}/\omega$  if  $\omega > \omega_p$  holds, as outlined at the beginning of this subsection for arbitrary velocity  $v$ . In case of  $\omega < \omega_p$  the plasma frequency as the faster oscillation frequency takes the role of the limiting interaction time for a collision, in agreement with the oscillator model of Sect. 3.3.1. In summary, the Coulomb logarithm to be used in the ballistic model for the individual velocity  $v$  is

$$\ln \Lambda = \ln \frac{b_{\max}}{b_{\min}}, \quad b_{\max} = \frac{v}{\sqrt{2 \max(\omega, \omega_p)}}, \quad b_{\min} = \frac{\bar{\lambda}_B}{2} = \frac{\hbar}{2mv}. \quad (3.123)$$

This expression for  $\ln \Lambda$  is used now in evaluating (3.116) and (3.117), (3.118).

### 3.3.3.2 Collision Frequencies in the Ballistic Model

The evaluation is done for a Maxwellian  $f(v_e) = f_M(v_e)$  as a representative case in many occasions. For a rough estimate of  $v_{ei}(t)$  in (3.117)  $\ln \Lambda$  may be averaged over the angle  $\chi$  and treated as a constant [43],

$$\langle \ln \Lambda \rangle \simeq \ln \langle \Lambda \rangle = \ln \frac{\sqrt{2m}\langle v^2 \rangle}{\hbar\omega_m} = \ln \left[ \frac{\sqrt{2m}}{\hbar\omega_m} (v_{os}^2 + v_{th}^2) \right], \quad \omega_m = \max(\omega, \omega_p). \quad (3.124)$$

When the further approximation  $\cos \alpha = 1$  is introduced the integral reduces to a simple expression assuming the structure of the gravitational force of a spherical mass distribution on a single mass point, and  $v_{ei}(t)$  reads

$$v_{ei}(t) = \frac{K \ln \langle \Lambda \rangle}{mv_{os}^3(t)} \int_0^{v_{os}(t)} 4\pi v_e^2 f_M(v_e) dv_e. \quad (3.125)$$

For  $\hat{v}_{os} \ll v_{th}$  it becomes time-independent and agrees with Spitzer-Silin [44] for  $\omega < \omega_p$ . By cycle-averaging  $v_{ei}(t)$  it turns out that  $\overline{\ln \langle \Lambda \rangle}$  is best approximated by

$$\overline{\ln \langle \Lambda \rangle} = \ln \overline{\langle \Lambda \rangle} = \ln \left[ \frac{\sqrt{2m}}{\hbar \omega_m} (\hat{v}_{os}^2 / 4 + v_{th}^2) \right]. \quad (3.126)$$

The collision frequency  $\bar{v}_{ei}$  becomes

$$\bar{v}_{ei} = \frac{K \ln \overline{\langle \Lambda \rangle}}{m \hat{v}_{os}^2} \frac{1}{v_{os}(t)} \int_0^{v_{os}(t)} 4\pi v_e^2 f_M(v_e) dv_e. \quad (3.127)$$

Explicit expressions of (3.125) and (3.127) for various cases may be found in [43]. The approximations introduced here,  $\ln \overline{\langle \Lambda \rangle} = \overline{\ln \Lambda}$  and  $\cos \alpha = 1$ , are not very accurate. Their main advantage is simplicity of evaluation which can be done analytically with  $f(v_e) = f_M(v_e)$ . A thorough evaluation of (3.116), (3.117), and (3.118) has to be done numerically integrating over  $f(v_e)$ ,  $(v_{os} v)/v^3$  and  $\ln \Lambda$  from (3.123) at the same time [45]. Expression (3.118) has been determined in Fig. 3.13(a) for  $T_e = 100$  eV and a density  $n_e = n_i = 10^{21} \text{ cm}^{-3}$  as a function of  $\hat{v}_{os}/v_{th}$  and the frequency ratios  $\omega/\omega_p = 0.5$  (black dots), 1.5 (gray rhombs), and 5.0 (gray triangles). Comparison is made with the dielectric expression (3.112), see black and gray continuum lines. The Coulomb logarithm shown on the ordinate is the cycle-averaged multiple integral of (3.112). It may be regarded as the true effective Coulomb logarithm  $\ln \Lambda_{eff} = \overline{\ln \Lambda}$ . For  $T_e = 1$  keV the same quantities as before are shown in Fig. 3.13(b). The agreement between the two models is excellent. The dashed lines result from the approximation (3.127). They show an increase above the correct quantities by 20–30%. On the other hand (3.127) is useful for its simplicity.

It has been stressed that evaluating (3.107) in the so-called “long wavelength limit”  $k p \ll 1$  may lead to inexact values of absorption, for instance to  $\ln \Lambda$  with  $b_{max} = \langle v \rangle / \omega_p$  instead of  $\langle v \rangle / \max(\omega, \omega_p)$  and concomitant incorrect evaluation of  $\sum J_n^2(\xi)$ . In other words, the long wavelength approximation seems to be appropriate for low laser intensities only (see (3.110)). However, this limitation has its

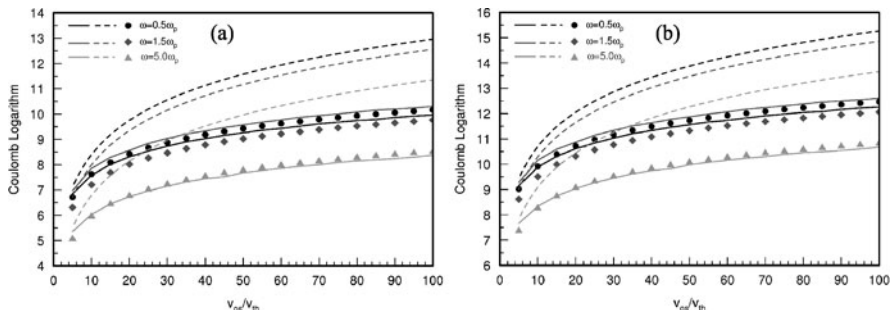


**Fig. 3.13** Cycle- and velocity-averaged effective Coulomb logarithm  $\ln \Lambda_{eff} = \overline{\ln \Lambda}$  as a function of  $\hat{v}_{os}/v_{th}$  for  $\omega/\omega_p = 0.5$  (dots), 1.5 (rhombs), and 5.0 (triangles). **(a)**:  $T_e = 100$  eV; **(b)**:  $T_e = 1$  keV, and  $n_e = n_i = 10^{21} \text{ cm}^{-3}$ ; ballistic model, continuous black and gray lines: dielectric model; dashed lines: (3.126) and (3.127)

origin in the decomposition of  $\exp(i\mathbf{k}\hat{\mathbf{p}} \cos \omega t)$  into Bessel functions, see (3.102). The ballistic model does not make use of the decomposition into Bessel functions and the problem does not appear although it makes also use of the “long wavelength approximation” in another place [see  $v_{os}(t)$  and  $\mathbf{p}(t)$  in (3.97) not depending on  $\mathbf{x}$ ]. In terms of physics the long wavelength approximation is correct for all wavelengths of interest, including the soft X-ray domain, and for intensities at least up to  $I\lambda^2 = 10^{18} \text{ Wcm}^{-2} \mu\text{m}^2$ .

Far from  $\omega/\omega_p = 1$  the dielectric values of  $\bar{v}_{ei}$  are slightly lower than those from the ballistic model. Exception is made at  $\omega/\omega_p = 1.5$  where the situation is inverted (see rhombs and gray continuous line). The reason becomes clear from Fig. 3.14 where  $\ln \Lambda_{\text{eff}}$  is reported as a function of  $\omega/\omega_p$ . It is clearly seen that there is a resonant increase around  $\omega = \omega_p$  in the dielectric model which the ballistic model is unable to reproduce (at least in the form given here). Such resonances have been reported, in a simplified approximation, for the first time by Dawson and Oberman [46]; in the context see also [47]. In [48] the domain  $\omega = \omega_p$  was investigated with more care which led to a qualitative agreement with Fig. 3.14 (maximum at  $\omega = 1.2\omega_p$  and a plateau for  $\omega < \omega_p$ ). Figure 3.14 shows in a convincing way the validity of the choice  $\omega_m = \max(\omega, \omega_p)$  in  $b_{\max}$  of (3.123), (3.124) for  $\omega \neq \omega_p$ . At  $\omega \simeq \omega_p$  the plasma is parametrically unstable (see Chap. 6), and resonant excitation of high-amplitude Langmuir waves may occur (Chap. 4), with the consequence that the dielectric model becomes invalid here also.

As a last point we have to discuss the asymptotic expressions (3.113) and to understand where the double logarithm comes from and why in the Coulomb logarithm appears  $v_{th}$  and not an expression like (3.126). To this aim an exact averaged effective Coulomb logarithm  $L_g(\hat{v}_{os}/v_{th}) = \overline{\ln \Lambda}$  is determined in such a way as to make the two quantities (3.118) and (3.127) equal in magnitude [39],

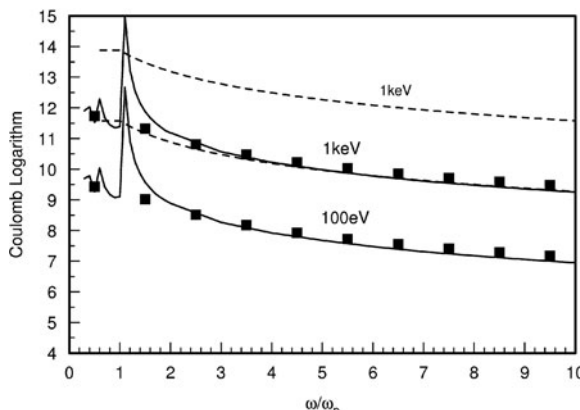


**Fig. 3.14**  $\ln \Lambda_{\text{eff}}$  as a function of  $\omega/\omega_p$  for  $n_e = n_i = 10^{21} \text{ cm}^{-3}$  and  $T_e = 100 \text{ eV}$  and  $1 \text{ keV}$ . Black squares: ballistic model, continuous lines: dielectric model, dashed lines: approximation (3.126)

$$\begin{aligned}\bar{v}_{ei} &= 4\pi \frac{K}{m\hat{v}_{os}^2} \int \frac{\mathbf{v}_{os}\mathbf{v}}{v^3} \ln \Lambda v_e^2 f(v_e) dv_e \\ &= 4\pi \frac{K}{m\hat{v}_{os}^2} L_g \left( \frac{\hat{v}_{os}}{v_{th}} \right) \overline{\frac{1}{v_{os}(t)} \int_0^{v_{os}(t)} v_e^2 f(v_e) dv_e}. \quad (3.128)\end{aligned}$$

For a Maxwellian the resulting function  $G(\hat{v}_{os}/v_{th}) = L_g / \ln \Lambda_S$  is now presented. The Coulomb logarithm  $\ln \Lambda_S$  (index S indicating Spitzer or Silin) is taken from Kull-Plagne in (3.113) with  $n_e = n_i = 10^{21} \text{ cm}^{-3}$  and  $T_e = 100 \text{ eV}$ .  $G$  is a universal function of the single variable  $\hat{v}_{os}/v_{th}$ . The two asymptotes proportional to  $(\hat{v}_{os}/v_{th})^2$  for  $\hat{v}_{os} < v_{th}$  and  $\ln(\hat{v}_{os}/v_{th} + 1)/(\hat{v}_{os}/v_{th})$  for  $\hat{v}_{os}/v_{th} \gtrsim 3$  reproduce the standard Spitzer–Silin formula in the limit of vanishing  $\hat{v}_{os}/v_{th}$  [see (3.125)] and lie between Silin and Kull-Plagne for  $\hat{v}_{os}$  exceeding  $v_{th}$ . We deduce that, in agreement with physical intuition, quiver velocities below  $v_{th}$  lead to a weak reduction of  $\bar{v}_{ei}$  only. On the other hand, in the domain  $\hat{v}_{os}/v_{th} > 1$  there is no unique best fit. The special choice depends on the interval to be fitted. For example, the interval  $1 < \hat{v}_{os}/v_{th} \leq 5$  is not fitted well by any formula from (3.113). Finally, Fig. 3.15 shows that there is no physical content in the paradoxical formula  $\ln \Lambda_S$  and no physics in the product of two logarithms in (3.113). They are merely originating from the use of Bessel functions in solving the problem of collisional absorption in one special way. A possible factor  $\ln(\hat{v}_{os}/v_{th})$  is purely kinetic and not due to shielding. The branch  $G(\hat{v}_{os}/v_{th} \geq 5)$  of Fig. 3.15 can be easily fitted by a single parabola instead of a double logarithm.

The ballistic model offers great advantages in comparison to the various dielectric approaches: direct physical insight, no slowly converging summations over oscillating functions, easy extension to moderately nonideal plasmas. For example, overlapping collisions do not alter  $v_{ei}$  as long as they do not superpose for collision parameters  $b < b_0$ , with  $\vartheta(b_0) \lesssim 30^\circ$ . A clear advantage of the dielectric approach is that it does not need an upper cut-off for  $b$  (lower cut off for  $k$ ) and can handle,

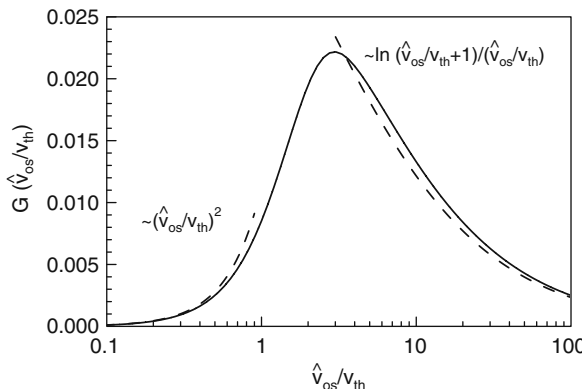


**Fig. 3.15** The function  $G(\hat{v}_{os}/v_{th})$  and two asymptotic fits for  $\hat{v}_{os}/v_{th} \rightarrow 0$  and  $\hat{v}_{os}/v_{th} \rightarrow \infty$

to a limited extent, plasma resonances in a straightforward manner (in this context see [45]).

So far we have not specified  $v_{os}(t)$ . From the kinetic derivation of the first moment conservation equation it becomes clear that in (2.23) and in the Drude model  $\mathbf{v}$  is the velocity of a fluid element and not that of a single electron. As long as  $v_{ei} \ll \omega$  holds it makes very little difference whether  $v_{os}(t)$  is identified with the oscillatory velocity of an individual electron or the drift velocity of an oscillating fluid element. However, in the opposite case of  $v_{ei} \gg \omega$  a consistency problem may arise because the single particle drift from which  $v_{ei}$  is calculated and the fluid drift may differ from each other. Some reasoning shows that at least for Coulomb logarithms somewhat larger than unity they still coincide since most of the orbits contributing to  $v_{ei}$  are straight. Hence,  $v_{os}(t)$  has to be calculated from (2.23) with  $v_{ei}$  included. At  $\hat{v}_{os}/v_{th} > 1$  the electron-ion collision frequency  $\nu_{ei}$  from (3.117) shows a strong time-dependence. As an immediate consequence higher harmonics appear in  $v_{os}$  and, in concomitance, in the current density  $\mathbf{j}_e$ , in  $\mathbf{E}$  and  $\mathbf{B}$ . The anharmonicity is expected to be particularly strong in a dense plasma when  $T_e$  is low and  $\hat{v}_{os} \gg v_{th}$ .

### 3.3.4 Equivalence of Models

#### 3.3.4.1 Boltzmann Model

Boltzmann's kinetic equation,

$$\frac{\partial f}{\partial t} + \mathbf{v} \frac{\partial f}{\partial \mathbf{x}} - \frac{e}{m} \mathbf{E} \frac{\partial f}{\partial \mathbf{v}} = \int (f' f'_i - f f_i) \sigma_{\Omega} |\mathbf{v}_{ei}| d\Omega d\mathbf{v}_i \quad (3.129)$$

is linearized,  $f = f_0 + f_1$ ,  $f_i$  ion distribution function, to obtain the current induced by the laser field,  $\mathbf{j} = -en_e \int \mathbf{v} f_1 d\mathbf{v}$ . Silin calculated this expression to obtain the cycle-averaged absorption from  $\bar{\mathbf{j}} \bar{\mathbf{E}}$  [18]. To show the equivalence of the two models the ions may be assumed immobile owing to  $|\mathbf{v}_i| \ll |\mathbf{v}_e|$ . Then by taking the first moment of (3.129) and observing the identity  $\int \mathbf{v}' f(\mathbf{v}) \sigma(\vartheta) |\mathbf{v}| d\mathbf{v}' = \int \mathbf{v} f(\mathbf{v}') \sigma(\vartheta) |\mathbf{v}| d\mathbf{v}'$  one obtains the momentum equation

$$\frac{d\mathbf{u}}{dt} + \frac{e}{m} \mathbf{E} = -n_i \int (\mathbf{v} - \mathbf{v}') f(\mathbf{v}) \cdot 2\pi \sigma(\vartheta) |\mathbf{v}| d\mathbf{v} d\vartheta = -\nu_{ei} \mathbf{u}. \quad (3.130)$$

Remembering that  $\mathbf{j} = -en_e \int \mathbf{v} f(\mathbf{v}) d\mathbf{v} = -en_e \mathbf{u}$ , from Drude's ansatz (2.23) results  $\bar{\mathbf{j}} \bar{\mathbf{E}} = 2\nu_{ei} \bar{\mathcal{E}}_{os}$ . This is identical with the Boltzmann result. The identity is most easily seen if  $f$  is expressed in the frame moving with velocity  $\mathbf{u}$  since there  $\mathbf{j}$  stems entirely from  $f_1 = f - f_0$ . It is essential to use  $\sigma(\vartheta)$  of the self-consistently screened Coulomb potential.

### 3.3.4.2 Drude vs Dielectric Model

In order to establish the equivalence of the models one has to show that  $\mathbf{E}_{\text{in}} = m v_{ei} \mathbf{u} / e$ . The correctness of this relation is recognized by intuition:

- (i) The force on the test ion by all plasma electrons balances the  $Z$ -fold force of all plasma ions on one electron (actio = reactio, owing to suppression of retardation effects);
- (ii) under the assumption that the collision time  $\tau$  is the shortest time scale [which is fulfilled, see (3.89)], the momentum change per unit time of an electron due to collisions is just the instantaneous force of all ions on a single electron.

The formal proof is most conveniently done by calculating the first moment of (3.129) for the relative velocity  $\mathbf{u}_r$ ,

$$\frac{d\mathbf{u}_r}{dt} - v_{ei} \mathbf{u}_r - \frac{e}{m} \nabla \phi = 0; \quad \mathbf{u}_r = \int \mathbf{v}_e f_1 d\mathbf{v}_e.$$

Summing this over all electrons in the same way as in Sect. 3.3.2 and making use of (i) above, the assertion follows since  $\langle d\mathbf{u}_r/dt \rangle = 0$  holds by definition. All treatments of inverse Bremsstrahlung presented so far are equivalent to each other in the weak coupling limit and  $\hbar\omega/kT_e \ll 1$ .

### 3.3.5 Complementary Remarks

#### 3.3.5.1 Non-Maxwellian Distribution Function

A serious impact of a large  $\hat{v}$  on absorption is seen in the distribution function [23]. By comparing the time  $\tau_h$  of heating the electrons up to the temperature  $T_e$ ,

$$\tau_h = \frac{3}{2} n_e k T_e / \langle \mathbf{j} \cdot \mathbf{E} \rangle = 3\tau_{ei} \left( \frac{v_{\text{th}}}{\hat{v}} \right)^2, \quad \tau_{ei} = v_{ei}^{-1},$$

one finds that  $\tau_h$  becomes shorter than the electron-electron collision time  $\tau_{ee}$  as soon as

$$Z \hat{v}^2 \gtrsim 3 v_{\text{th}}^2$$

holds. After one electron-ion or electron-electron collision  $f(\mathbf{v})$  becomes nearly isotropic for moderate  $v_{\text{os}}/v_{\text{th}}$ -ratios. However, when driven at constant  $\mathbf{E}$ -field strength,  $f(\mathbf{v})$  evolves into a self-similar distribution of the form (Fig. 3.16),

$$f(\mathbf{v}) = \kappa e^{-v^5/5u^5}, \quad u^5 = \frac{10\pi n_i Z^2 e^4 \ln \Lambda}{6m^2} \hat{v}^2 t. \quad (3.131)$$

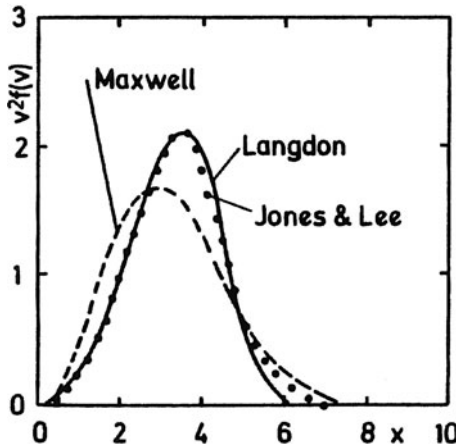


**Fig. 3.16** Effect of the laser field on the electron distribution function  $v^2 f(v)$  for  $\hat{v}_{\text{os}}^2/v_{\text{th}}^2 = 2.25$  ([24]: dotted, and [23]: solid)

The tendency towards the evolution of a super-Gaussian (broadened Maxwellian) has been confirmed in [49] for  $\hat{v}_{\text{os}}/v_{\text{th}} = 2$  and plasma parameter  $g = 0.1$ , in agreement with molecular dynamics simulations for  $\hat{v}_{\text{os}}/v_{\text{th}} \leq 1$  [50]. In a more recent treatment which includes electron-electron collisions self-consistently and allows for an anisotropic part of the distribution function it has been found that  $f(v)$  consists of a super-Gaussian of slow electrons and a Maxwellian tail of energetic electrons [51]. The systematic study of the evolution of  $f(v)$  by Fokker–Planck simulations in [52] reveals a departure from a Maxwellian when  $\hat{v}_{\text{os}}/v_{\text{th}} \simeq 1$  and a final returning to a Maxwellian at  $\hat{v}_{\text{os}}/v_{\text{th}} \gg 1$  due to the inefficiency of absorption. This behavior is easily understood if one bears in mind that with increasing drift motion the electron-ion interaction time decreases whereas the electron–electron collisions are not affected by a drift that is common to all electrons. Finally, significant and surprising enough, at  $\hat{v}_{\text{os}}/v_{\text{th}} = 10$  and  $g = 0.1$  the authors of [49] observed a so far unexplained distribution function narrowing of the respective Maxwellian. They showed that the effect originates from electron–ion collisions.

### 3.3.5.2 Coulomb Focusing

From the classical collision scheme Fig. 2.1 it follows that, depending on the scattering angle, under the influence of a strong laser field an electron can gain an appreciable amount of energy in a single collision. The gain is highest in the back scatter configuration from an attractive potential and less significant from a potential that is repulsive. The distinction between positive and negative charge scattering from a Coulomb center clearly contrasts with pure Coulomb scattering for which  $\sigma_{\Omega}$  is indifferent with respect to charge conjugation. Additionally, in presence of the laser field an electron can be captured temporarily by the ion fulfilling several cycles for a while before being ejected again. In the quantum scattering process

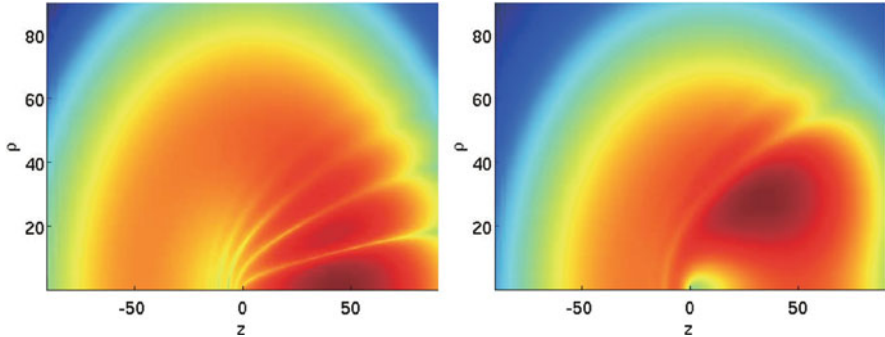


**Fig. 3.17** Spatial probability density of a Gaussian wavepacket with momentum  $\hbar k_0 = 0.005 m_e c$  scattered by an attractive (left graph) and a repulsive (right graph) Coulomb potential. The interference maxima indicate Coulomb focusing in the attractive and defocusing in the repulsive case [53]

interference occurs between the plane incoming and the spherical outgoing wave and, as a consequence, charge accumulation (attractive potential) and rarefaction (repulsive) behind the ion can be observed in the direction of the laser field (Fig. 3.17). This so-called Coulomb focusing phenomenon can lead to strongly enhanced scattering [53]. In a refined ballistic model it should be taken into account.

### 3.3.5.3 Giant Ions

Strong enhancement of collisional absorption can occur due to the coherent superposition of collisions in clusters. The absorption coefficient  $\alpha$  due to collisions in a plasma is proportional to the ion density  $n_i$  and the square of the ion charge,  $\alpha \sim Z_i^2 n_i$ . When  $N$  ions cluster together the density of the scatterers  $n_C$  decreases by  $N$  but their charge increases by  $Z_i N$ , resulting in an increase of  $\alpha \sim N$ . In order to obtain realistic amplification factors of collisional absorption due to clustering  $g = \alpha_C / \alpha$ ,  $\alpha_C$  absorption coefficient of the cluster medium, the fraction  $\xi$  of ions forming clusters, their “outer ionization” degree  $\eta_C$ , i.e., the net charge of the cluster, and the collision frequency  $v_{eC}$  of an electron with the cluster gas in the presence of the intense laser field need to be known. It holds [54]

$$v_{eC} = \xi \eta_C^2 \frac{Z_C}{Z_i} \frac{L_C}{\ln \Lambda_{ei}} v_{ei}, \quad \alpha_C = \frac{v_{eC}}{c} \frac{\omega_p^2}{\omega^2}. \quad (3.132)$$

In  $\Lambda_{ei}$  is the Coulomb logarithm of the plasma ions and  $L_C$  is the generalized Coulomb logarithm of the cluster of radius  $R$ , both to be determined. The Coulomb scattering angle  $\chi$  is a function of the impact parameter  $b$ . For  $b > b_c = R(1 + 2b_\perp/R)^{1/2}$ ,  $\chi(b = b_\perp) = \pi/2$ , it coincides with the Rutherford scattering angle. For orbits crossing the cluster it is determined numerically. For a uniform charge distribution inside the cluster  $\chi$  is shown in Fig. 3.18 for  $b_\perp = 2.5R$  and  $b_\perp = 0.5R$ .  $L_C$  is

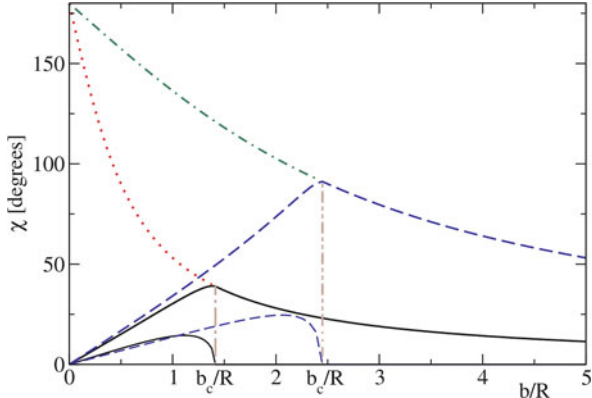


**Fig. 3.18** Scattering angle  $\chi$  as a function of the impact parameter  $b$  for a uniform charged spherical cluster. *Bold dashed curve* for  $b_{\perp} = 2.5R$ , and *solid curve* for  $b_{\perp} = 0.5R$ ,  $R$  cluster radius. The corresponding deflections inside the cluster are indicated by the thin dashed and solid lines ending at their respective  $b = b_c$  points. The dotted-dashed and the dotted lines starting from  $\chi = 180^\circ$  refer to Coulomb scattering from a point charge  $q$

$$L_C = \frac{1}{2} \int_0^{b_c} \frac{(1 - \cos \chi) b \, db}{R^2} + \frac{1}{2} \ln \left[ \frac{b_{\perp}^2 + b_{\max}^2}{b_{\perp}^2 + b_c^2} \right]. \quad (3.133)$$

Multiplication factors of order  $10^3$ – $10^4$  are achievable for realistic cluster parameters. Coherent amplification of collisional absorption is relevant for dusty plasmas, aerosols, sprays, perhaps foams, and small droplets of liquids, all of them with  $R \ll \lambda$ .

### 3.4 Inverse Bremsstrahlung Absorption

To illustrate the physics of absorption of radiation by collisions from a different point of view in this section the absorption coefficient  $\alpha$  is deduced from the emission of bremsstrahlung radiation of an optically thin plasma in the weak laser field limit.

The total power  $P$  emitted by an accelerated nonrelativistic electron is given by ([30], Sect. 14.2)

$$P = \frac{2}{3} \frac{e^2}{4\pi\epsilon_0 c^3} \dot{v}^2(t). \quad (3.134)$$

In a nearly thermal plasma velocity changes  $\dot{v}(t)$  are mainly produced by electron-ion and electron-electron collisions. An electron-ion pair constitutes a dipole system to a very good approximation as long as the maximum impact parameter  $b_{\max}$  is small compared to the wavelength emitted. For laser plasmas in the intensity

range  $v_{\text{os}} < v_{\text{th}}$  and frequencies of  $\omega \simeq \omega_{\text{Nd}}$  this is always the case because of  $\lambda_{\text{Nd}} \gg \lambda_D \simeq b_{\max}$ . On the other hand, a colliding electron–electron system represents a quadrupole which at nonrelativistic speeds and under the above conditions gives negligible contribution to radiation emission. The colliding electron–electron pair can also be viewed as two electric dipoles of relative phase difference  $\pi$ . As a consequence, their dipole emission cancels. Since the principle of detailed balance applies, absorption of radiation does not occur in electron–electron encounters either.

The total spectral intensity  $I_\omega$  emitted by  $n_e$  electrons into the unit solid angle is obtained by Fourier-transforming Larmor's formula (3.134), and averaging over all impact parameters  $b$  and the corresponding velocity distribution  $f(\mathbf{v})$ . In this way, for a Maxwellian velocity distribution

$$I_\omega = \frac{d^2 P}{d\Omega d\omega} = \frac{\Re(\eta)\omega_p^2}{4\sqrt{3}\pi^2 c^3} v_{ei} k T_e \frac{\sigma(\omega, T_e)}{\ln \Lambda} e^{-\hbar\omega/kT_e} \quad (3.135)$$

is obtained with  $v_{ei}$  from (2.45) [55].  $\sigma(\omega, T_e)$  is the Gaunt factor which provides for the necessary quantum corrections in different  $(\omega, T_e)$  regions. For  $\omega_{\text{Nd}}$  and moderate harmonics  $\hbar\omega \ll kT_e$  holds and the ratio between the thermal de Broglie wavelength  $\lambda_B$  and  $b_\perp$ ,

$$\lambda_B/b_\perp = \frac{4\pi\varepsilon_0}{Ze^2} \left( \frac{kT_e}{m} \right)^{1/2} \hbar = 0.18(T_e[\text{eV}])^{1/2}/Z, \quad (3.136)$$

in laser plasmas is such that the Born–Elwert expression for  $\sigma(\omega, T_e)$  applies since  $(\lambda_B/b_\perp)^2 \gg 1$  holds ([40], Chap. 8):

$$\sigma(\omega, T_e) = \frac{\sqrt{3}}{\pi} \ln \left( \frac{4}{G} \frac{kT_e}{\hbar\omega} \right) = 0.55 \left[ 0.81 + \ln \frac{kT_e}{\hbar\omega} \right]; \quad G = 1.781. \quad (3.137)$$

For instance, for  $kT_e/\hbar\omega = 10^3$ ,  $\sigma = 4.2$  results. The absorption coefficient  $\alpha_\omega$  can now be determined from Kirchhoff's law. Bremsstrahlung radiation from an optically thin plasma generally represents such a small energy loss that (i) the plasma can be in thermal equilibrium kinetically even though thermal radiative equilibrium is not established and (ii) the spectral radiation intensity  $I_\omega(T_e)$  is entirely determined – to a high degree of accuracy – by the kinetic electron distribution. Therefore, the relation

$$\frac{I_\omega}{\alpha_\omega} = I_{\text{Planck}} = \frac{\hbar\omega^3}{4\pi^3 c^2} \frac{[\Re(\eta)]^2}{\exp\left(\frac{\hbar\omega}{kT_e}\right) - 1} \quad (3.138)$$

holds. Consequently, the absorption coefficient becomes

$$\alpha_\omega = \left(1 - \exp\left(-\frac{\hbar\omega}{kT_e}\right)\right) \frac{kT_e}{\hbar\omega} \frac{1}{c} \left(\frac{\omega_p}{\omega}\right)^2 \frac{v_{ei}}{\Re(\eta)} \frac{\ln\left(\frac{4}{G} \frac{kT_e}{\hbar\omega}\right)}{\ln\Lambda}. \quad (3.139)$$

From  $\hbar\omega/kT \ll 1$  the factor  $\left(1 - \exp(-\frac{\hbar\omega}{kT_e})\right) kT_e/\hbar\omega$  becomes unity. Comparison with (3.36) yields

$$\frac{\alpha_\omega}{\alpha} = \frac{1}{\ln\Lambda} \ln\left(\frac{4}{G} \frac{kT_e}{\hbar\omega}\right).$$

To give a numerical example, for  $\hbar\omega/kT_e = 10^{-3}$  the ratio becomes  $\alpha_\omega/\alpha = 7.7/\ln\Lambda$ ; for  $\ln\Lambda = 7.7$  the spectral absorption coefficient  $\alpha_\omega$  becomes equal to  $\alpha$ . In any case these considerations show that

- (a)  $\alpha_\omega$  is, within the uncertainty of  $\ln\Lambda$ , practically the same as  $\alpha$ , in this way justifying the identification of “inverse bremsstrahlung absorption” with “collisional absorption”;
- (b) the bremsstrahlung intensity  $I_\omega(T_e)$  represents the spontaneously emitted amount of radiation, whereas in the absorption coefficient  $\alpha$  stimulated re-emission of radiation is also included;
- (c) at very low temperatures or higher photon energies (e.g.,  $\hbar\omega/kT_e \simeq 1$ ) a purely classical calculation of  $\alpha$  begins to fail because then  $1 - e^{-\hbar\omega/kT} \neq \hbar\omega/kT$ .

Observation (b) needs two further comments. There are several ways of formulating the principle of detailed balance and Kirchhoff’s law. It is convenient to use it in the form of (3.138) where the emitted power density per unit solid angle is indicated by  $I_\omega$ . This is because experimentally  $I_\omega$  can be uniquely determined only when the surrounding radiation field is zero; as a consequence  $I_\omega$  represents the *spontaneously* emitted radiation. On the other hand, in a measurement of  $\alpha_\omega$  the “true” or effective absorption coefficient is determined which is the difference between absorption and stimulated re-emission of radiation between two energy levels  $E_1$  and  $E_2$  ( $E_2 - E_1 = \hbar\omega$ ). With their populations  $n_1$  and  $n_2$ , the Einstein coefficients  $B_{12} = B_{21}$  for stimulated emission, and  $\rho_\omega$  the spectral radiant energy density,  $\rho_\omega = 4\pi I_\omega/c$ ,  $\alpha_\omega$  is determined by

$$\alpha_\omega I_\omega = (n_1 B_{21} - n_2 B_{12}) \rho_\omega = \frac{4\pi}{c} B_{12}(n_1 - n_2) I_\omega. \quad (3.140)$$

The refractive index  $\eta$  and degeneracy are assumed to be unity. If  $\kappa_\omega$  refers to level excitation by absorption,

$$\kappa_\omega = \frac{4\pi}{c} B_{12} n_1,$$

and the levels are in thermodynamic equilibrium (for instance, because of collisions; Maxwellian distribution in the case of continuous energy spectrum), hence  $n_2 = n_1 e^{(-\hbar\omega/kT_e)}$ , one obtains

$$\alpha_\omega = \kappa_\omega [1 - \exp(-\hbar\omega/kT_e)]. \quad (3.141)$$

$\kappa_\omega$  is often used in theoretical work, however, it is not accessible to direct observation. For correctness it has to be mentioned that the rate equation (3.140) holds as soon as the shortest time of interest is much longer than the transverse relaxation (or phase memory) time  $T_2$  [56]. In conclusion, when Kirchhoff's law is written in the form  $I_\omega/\alpha_\omega = I_\omega^{\text{Planck}}$ ,  $I_\omega$  is the spontaneously emitted radiation and  $\alpha_\omega$  is the net absorption coefficient. Both  $I_\omega$  and  $\alpha_\omega$  are directly observable quantities.

### 3.5 Ion Beam Stopping

In a fully ionized plasma an ion projectile p of mass  $m_p$ , charge  $Z_p e$  and velocity  $\mathbf{v}_0$  is slowed down by collisions with the plasma electrons and its ions of charge  $Z e$ . For  $\ln \Lambda \gtrsim 1$  small angle deflections prevail and the energy transfer to an electron is by  $m_i/Zm$  larger than to a plasma ion. At the same time the p-e and p-i collision rates are related to each other by  $n_e \sigma_e \simeq n_e \sigma_i / Z$ . This implies that the projectile moves straight, except rare p-i events, and the energy loss of the projectile is nearly all to the electrons. In the following p-i collisions are neglected. The energy loss of the projectile ion per unit length  $dE/dx$ , the so-called stopping power is given by [compare (3.117)]

$$\frac{dE}{dx} = -2\pi K Z_p \int_0^\infty \int_{-1}^1 \frac{\mathbf{v}_0 \mathbf{v}}{v^3} \ln \Lambda v_e^2 f(v_e) d \cos \chi dv_e \quad (3.142)$$

with  $\ln \Lambda$  from (3.124),  $K = Ze^4 n_e / (4\pi \epsilon_0^2 m)$  from (3.115) and  $\mathbf{v} = \mathbf{v}_0 + \mathbf{v}_e$ . For a rough estimate the simplifications leading to (3.126) (see Fig. 3.13) may be introduced to arrive at

$$\frac{dE}{dx} \simeq -4\pi K Z_p \frac{\ln \langle \Lambda \rangle}{v_0} \int_0^{v_0} v_e^2 f(v_e) dv_e. \quad (3.143)$$

For a Maxwellian  $f_e = f_M(v)$  from (3.143) one obtains by multiple partial integration in the domain  $v_0/v_{\text{th}} \lesssim 2$

$$\begin{aligned} \frac{dE}{dx} &\simeq -\frac{1}{3} \sqrt{\frac{2}{\pi}} K Z_p \ln \langle \Lambda \rangle \frac{v_0^2}{v_{\text{th}}^3} e^{-v_0^2/2v_{\text{th}}^2} \\ &\times \left[ 1 + \frac{1}{5} \left( \frac{v_0}{v_{\text{th}}} \right)^2 + \frac{1}{5 \cdot 7} \left( \frac{v_0}{v_{\text{th}}} \right)^4 + \frac{1}{5 \cdot 7 \cdot 9} \left( \frac{v_0}{v_{\text{th}}} \right)^6 + \dots \right]. \end{aligned} \quad (3.144)$$

At  $v_0 = v_{\text{th}}$  the bracket amounts to  $1 + 0.23$ . By the same procedure for  $v_0/v_{\text{th}} \gtrsim 2$  results

$$\frac{dE}{dx} \simeq -K Z_p \ln(\Lambda) \frac{1}{v_0} \left\{ 1 - 2\sqrt{\frac{2}{\pi}} \frac{v_0}{v_{\text{th}}} e^{-v_0^2/2v_{\text{th}}^2} \left[ 1 + \left( \frac{v_{\text{th}}}{v_0} \right)^2 + \left( \frac{v_{\text{th}}}{v_0} \right)^4 \right] \right\}. \quad (3.145)$$

For  $v_{\text{th}} = 0$  and  $Z_p = Z$  this becomes identical with  $-\dot{W}$  in (3.85).

**Barkas effect.** In 1953 F.M. Smith et al. [57] found a minute difference between stopping power in emulsion of positive and negative pions. Subsequently it was verified in countless experiments that the range of a fast particle in matter differs from that of its antiparticle. Generally the difference in stopping of a negative particle from its positive counterpart is called Barkas effect. It clearly indicates that stopping is not just due to pure binary encounters because the Coulomb cross section  $\sigma_{\Omega}$  respects charge conjugation. Hence, the difference must have its origin in the presence of spectators involved in the collision. Theoretical investigations have confirmed this interpretation for stopping in neutral matter [58]. In the plasma screening assumes the role of a spectator and the Barkas effect is present there as well [59]. A theoretical treatment of stopping in dense nonideal plasmas going well beyond the standard analysis ( $Z_b^3$ -term, see [57]) is presented in [60]. There is an asymmetry between the orbits of a positive and a negative point particle in a screened Coulomb potential as becomes clear from short inspection of Fig. 2.4.

## References

1. Penfield, P., Haus, H.A.: Electrodynamics of Moving Media, Chap. 1. MIT Press, Cambridge, MA (1967) 92
2. Whitham, G.B.: Linear and Nonlinear Waves. John Wiley & Sons, New York (1974) 93, 99, 105, 106
3. Born, M., Wolf, E.: Principles of Optics, Sec. 3.3. Pergamon Press, Oxford (1980) 94
4. Muschietti, L., Dum, C.T.: Phys. Fluids B **5**, 1383 (1993) 98, 99
5. Sonnenschein, E., Rutkevich, I., Censor, D.: Phys. Rev. E **57**, 1005 (1998) 98
6. Nordland, B.: Phys. Rev. E **55**, 3647 (1997) 98
7. Ginzburg, V.L.: The Propagation of Electromagnetic Waves in Plasmas. Pergamon Press, Oxford (1964) 99
8. Rawer, K.: Ann. Phys. **35**, 385 (1939); **42**, 294 (1942) 99, 100
9. Johnson, F.S.: Am. J. Phys. **58**, 1044 (1990) 104
10. Abramowitz, M., Stegun, I.A.: Pocketbook of Mathematical Functions. Harri Deutsch, Frankfurt/Main (1984) 108, 122, 123
11. Mathews, J., Walker, R.L.: Mathematical Methods of Physics. Benjamin/Cummings, Menlo Park, CA (1964) 108, 109
12. Mulser, P., van Kessel, C.: J. Phys. D: Appl. Phys. **11**, 1085 (1978) 111
13. Willi, O., Rumsby, P.T.: Opt. Comm. **37**, 45 (1981) 111
14. Jones, R.D., Mead, W.C., Coggeshall, S.V., Aldrich, C.H., Norton, J.L., Pollak, G.D., Wallace, J.M.: Phys. Fluids **31**, 1249 (1988) 111
15. Kofink, W.: Ann. Physik **1**, 119 (1947) 112
16. Cojocaru, E., Mulser, P.: Plasma Phys. **17**, 393 (1974) 115

17. Piliya, A.D.: Sov. Phys. Tech. Phys. **11**, 609 (1966) 115
18. Sulin, V.P.: Zh. Eksp. Teor. Fiz. **47**, 2254 (1964); Sov. Phys. JETP **20**, 1510 (1965) 119, 142
19. Shima, Y., Yatom, H.: Phys. Rev. A **12**, 2106 (1975) 119, 133
20. Sulin, V.P., Uryupin, S.A.: Sov. Phys. JETP **54**, 485 (1981) 119, 133
21. Bornath, Th., Schlanges, M., Hilse, P., Kremp, D., Bonitz, M.: Laser & Part. Beams **18**, 535 (2000) 119, 133
22. Reinholtz, H., Redmer, R., Röpke, G., Wierling, A.: Phys. Rev. E **62**, 5648 (2000) 119
23. Langdon, A.B.: Phys. Rev. Lett. **44**, 575 (1980) 119, 143, 144
24. Jones, R.D., Lee, K.: Phys. Fluids **25**, 2307 (1982) 119, 144
25. Pert, G.J.: J. Phys. B: At. Mol. Phys. **8**, 3069 (1975) 119
26. Pert, G.J.: J. Phys. A: Gen. Phys. **9**, 463 (1976)
27. Pert, G.J.: J. Phys. B: At. Mol. Phys. **12**, 2755 (1979) 119
28. Mulser, P., Niu, K., Arnold, R.C.: Nucl. Inst. Meth. Phys. Res. A **278**, 89 (1989) 121
29. Korn, G.A., Korn, T.M.: Mathematical Handbook. McGraw-Hill, New York (1968) 9.3–3 121
30. Jackson, J.D.: Classical Electrodynamics. John Wiley, New York (1975) 125, 146
31. Boine-Frankenheim, O.: Energieverlust von schweren Ionen in Plasmen, Dissertation, TH Darmstadt (1996) 125, 126
32. Boine-Frankenheim, O.: Phys. Plasmas **3**, 1585 (1996) 125
33. Mulser, P., Saemann, A.: Contrib. Plasma Phys. **37**, 211 (1997) 127
34. Anger, C.T.: Neueste Schriften der Naturforschungs-Gesellschaft in Danzig, pp. 1–29 (1855) 127
35. Sakurai, J.J.: Modern Quantum Mechanics, Sec. 7.13. Benjamin/Cummings, Menlo Park, CA (1985) 132, 136
36. Kremp, D., Bornath, Th., Bonitz, M.: Phys. Rev. E **60**, 4725 (1999) 133
37. Kull, H.-J., Plagne, L.: Phys. Plasmas **8**, 5244 (2001) 133, 134
38. Wierling, A., Th. Millat, Röpke, G., Redmer, R.: Phys. Plasmas **8**, 3810 (2001) 133
39. Schneider, R.: Equivalence and Unification of the Ballistic and the Kinetic Treatment of Collisional Absorption, PhD thesis Tech. Univ. Darmstadt, Darmstadt (2002) 133, 138, 140
40. Shkarofsky, I.P., Johnston, T.W., Bachynski, M.P.: The Particle Kinetics of Plasmas. Addison-Wesley, Reading, MA (1966) 137, 147
41. McDowell, M.R.C.: Phys. Fluids **4**, 1332 (1961) 137
42. de Ferrarii, L., Arista, N.R.: Phys. Rev. A **29**, 2145 (1984) 137
43. Mulser, P., Cornolti, F., Bésuelle, E., Schneider, R.: Phys. Rev. E **63**, 016406 (2001) 138, 139
44. Spitzer, L.: Physics of Fully Ionized Gases, p. 146. Interscience, New York (1967) 138
45. Mulser, P., Schneider, R.: J. Phys. A: Math. Theor. **42**, 214058 (2009) 139, 142
46. Dawson, J.M., Oberman, C.: Phys. Fluids **5**, 517 (1962) 140
47. Decker, C.D., Mori, W.B., Dawson, J.M., Katsouleas, T.: Phys. Plasmas **1**, 4043 (1994) 140
48. Kaw, P.K., Salat, A.: Phys. Fluids **11**, 2223 (1968); Salat, A., Kaw, P.K.: Phys. Fluids **12**, 342 (1969) 140
49. Bornath, Th., et al.: J. Phys.: Conf. Ser. **11**, 180 (2005) 144
50. Pfalzner, S., Gibbon, P.: Phys. Rev. E **57**, 4698 (1998) 144
51. Weng, S.M., Sheng, Z.M., He, M.Q., Wu, H.C., Dong, Q.L., Zhang, J.: Phys. Plasmas **13**, 113302 (2006) 144
52. Weng, S.M., Sheng, Z.M., Zhang, J.: Phys. Rev. E **80**, 056406 (2009) 144
53. Rascol, G., Bachau, H., Tikhonchuk, V.T., Kull, H.-J., Ristow, T.: Phys. Plasmas **13**, 103108 (2006) 145
54. Mulser, P., Kanapathipillai, M., Hoffmann, D.H.H.: Phys. Rev. Lett. **95**, 103401 (2005); last value in Table II must read  $2.3 \times 105$  145
55. Lang, K.R.: Astrophysical Formulae, p. 46. Springer-Verlag, New York (1974) 147
56. Shoemaker, R.L.: Coherent transient infrared spectroscopy. In: Steinfeld, J.I. (ed.) Laser and Coherent Spectroscopy, Sec. 3.3. Plenum Press, New York (1978). 149
57. Smith, F.M., Birnbaum, W., Barkas, W.H.: Phys. Rev. **91**, 765 (1953) 150
58. Sigmund, P., Schinner, A.: Nucl. Instr. and Meth. B **212**, 110 (2003) 150
59. Sayasov, Yu.S.: J. Plasma Phys. **57**, 373 (1997) 150
60. Gericke, D.O., Schlanges, M., Bornath, Th., Kraeft, W.D.: Contrib. Plasma Phys. **41**, 147 (2001) 150

# Chapter 4

## Resonance Absorption

The most familiar absorption process of laser radiation is inverse bremsstrahlung. As the electron temperature increases Coulomb collisions become less effective and, in the absence of other conversion processes, a plasma becomes highly transparent to the laser radiation when the electron density  $n_e$  is below its critical value  $n_c$ ; alternatively, in case an overdense layer exists, i.e.,  $n_e > n_c$ , the laser plasma is highly reflecting. However, at oblique incidence of radiation there is an effective collisionless absorption process which consists of the resonant conversion of laser light into an electron plasma wave of the same frequency  $\omega$ . This phenomenon of resonance absorption was first described by Denisov [1] for a cold and by Piliya [2] for a warm plasma. Only later was its relevance for collisionless laser plasma heating recognized [3, 4]. Subsequently, accurate conversion rates as a function of density scale length  $L$  and angle of incidence  $\alpha_0$  were determined numerically [5]. The most accurate and complete study of the phenomenon in the linear regime was undertaken in [6, 7].

As already discussed in connection with the inhomogeneous Stokes equation in Sect. 3.2.4. the excitation of a Langmuir wave occurring resonantly over a wide region in space requires the simultaneous conservation of the photon (index em or no index) and plasmon (index es) energies and momenta,  $\hbar\omega_{\text{es}} = \hbar\omega_{\text{em}}$ ,  $\hbar\mathbf{k}_{\text{es}} = \hbar\mathbf{k}_{\text{em}}$ . Owing to the dispersion relations (3.11) for the two waves at nonrelativistic temperatures ( $s_e^2 \ll c^2$ ) matching is fulfilled only at the critical points where  $k_{\text{em}} \simeq k_{\text{es}} \simeq 0$  holds, and hence the local plasma frequency equals the laser frequency. It follows from Fig. 3.6 that with a smooth driver, resonance does not extend over more than half a local electrostatic wavelength  $\lambda_{\text{es}}$ . In the laser generated plasma the incident electromagnetic wave acts as a resonant driver for the electron plasma wave propagating down the density gradient and is dependent on the angle of incidence: At normal incidence the laser field has no component along the density gradient; at grazing incidence the field has the right direction; however, the laser beam is reflected from the plasma too far away from the critical point. At an intermediate optimum angle a conversion factor of 0.5 is reached in flat density profiles. In steep plasma profiles as well as at relativistic temperatures the conversion rate and the optimum angle both increase and conversion can rise up to 100% [7]. The excited electron plasma wave is not converted back into electromagnetic waves and is, consequently, absorbed by the plasma. At low temperatures and flat density gradients significant damping can

occur by electron-ion collisions. At intermediate laser intensities there may exist conditions for linear Landau damping to play a more important role [8]. At flux densities above  $10^{14}(\omega/\omega_{\text{Nd}})^2 \text{ Wcm}^{-2}$  the electrostatic wave becomes nonlinear in its amplitude and the electron density modulation assumes a very pronounced spike-like shape due to self-interaction of modes. In the potential wells associated with the wave, effective electron trapping and acceleration occurs and nonlinear Landau damping dominates. At even higher laser fluxes the Langmuir wave becomes aperiodic; wavebreaking occurs. In the following all these phenomena, starting from linear mode conversion, are treated extensively and the conversion rates are calculated.

In recent years intense high contrast laser pulses are available the length of which is such that all interaction takes place before the ionic rarefaction wave starts. The observation of an angular dependence of collisionless absorption very similar to classical resonance absorption under p-polarization raises the question on the nature of the absorption process in this case and on the possible transition from resonant absorption to Fresnel formulas for discontinuous changes of the refractive index. Under certain conditions such a smooth transition from resonance absorption to ordinary linear optics at interfaces can be constructed. Whether such a coincidence has a real physical basis or whether it is purely accidental will also be discussed. The question is of primary interest for a correct interpretation of the collisionless absorption mechanism measured in experiments and confirmed by simulations, however hitherto not understood until recently (see Sect. 3.3).

## 4.1 Linear Resonance Absorption

It is standard to treat linear resonance absorption in the layered medium approximation of Chap. 3. By the method of numerical microparticle simulation more complex plasma density profiles can be chosen. However, realistic 3D simulations in the space and velocity coordinates are feasible since more recent years only, see e.g. [9]. Fortunately all essential aspects of mode conversion and conversion rates can be studied to a satisfactory degree in a plane layered medium. In such a geometry the linear phenomenon is governed by the system of (3.21), (3.22) or (3.70) and (3.22), respectively. If the magnetic field is known the conversion can be determined from (3.70), or Piliya's equation alone. Even for the layered medium a complete solution of the coupled equations for  $E_x$  and  $B$  has only been obtained numerically up to now. A typical solution of  $E_x$  and  $B$  in a linear density profile is shown in Fig. 4.1 at four different times as a function of  $\xi$ , with  $\beta = 0.1$ ,  $q = (k_0 L)^{2/3} \sin^2 \alpha_0 = 0.5$ , and  $\xi$  from Sect. 3.2.4 [6].  $\beta = 0.1$  corresponds to an electron temperature  $T_e = 1.8 \text{ keV}$ . The evolution of the electron wave, its motion to the right and its decoupling from the laser wave are clearly observable. The dotted line indicates the magnetic field  $B = B_z$  and shows the periodicity of the electromagnetic component of  $E_x$ . In the WKB region the electron plasma wave propagates nearly parallel to the density gradient since, as a consequence of

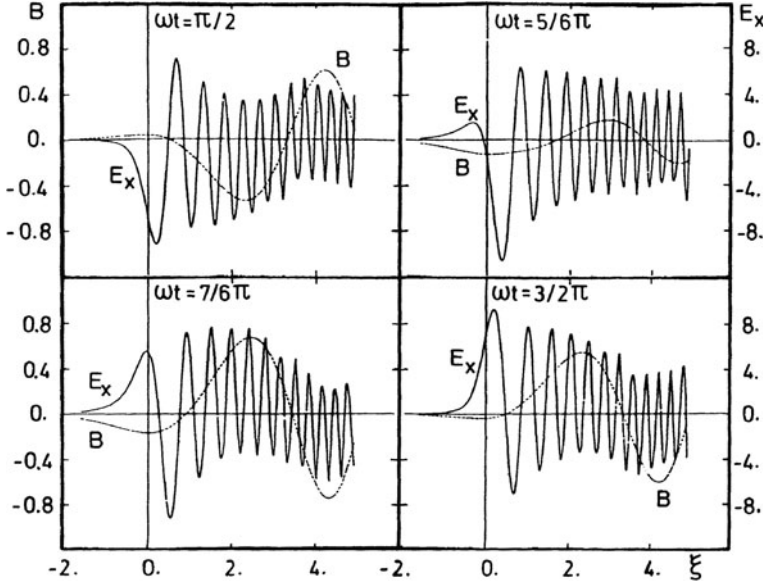


**Fig. 4.1** Resonance absorption in a layered plasma.  $E_x$  and  $B$  evolving in time.  $E_x$  is the superposition of  $E_{x,\text{es}}$  (small wavelength) and  $E_{x,\text{em}}$  (the same wavelength as  $B$ !). Linear density profile. Note that  $B$  is almost spatially constant in the resonance region around  $\xi = 0$ ;  $\xi = (k_0^2/\beta^2 L)^{1/3}(x - x_0)$ ,  $x_0 = L\beta^2 \sin^2 \alpha_0$ ,  $\beta = 0.1$ ,  $q = (k_0 L)^{2/3} \sin^2 \alpha_0 = 0.5$

the ansatz  $\hat{E}(x, y) = \hat{E}(x) \exp(i k_y y)$  (momentum conservation), for its angle  $\alpha_1$  results

$$\sin \alpha_1 = \beta \sin \alpha_0, \quad (4.1)$$

and  $E_{\text{es}} \simeq E_{x,\text{es}}$  holds. In the overdense region  $E_x$  as well as  $E_y$  become evanescent with a decay behavior which is determined by the two periodicities  $k/\beta$  and  $k$  for the electron plasma wave and the electromagnetic mode.

The field distributions are uniquely determined as soon as three independent parameters, e.g.,  $\alpha_0$ ,  $\beta$ , and  $q = (k_0 L)^{2/3} \sin^2 \alpha_0$  are given. In Fig. 4.2 typical distributions of  $|E_x|^2$  and  $|B|^2$  are shown as functions of  $\xi$  for  $q = 0.5$  and  $\beta = 0.1$ ; they represent the envelopes of  $E_x = E_{x,\text{em}} + E_{x,\text{es}}$  and  $B$  of Fig. 4.1. The decrease of  $|B|$  according to the WKB approximation [10],

$$|B(x)| = B_{\text{inc}}(\eta^2 - \sin^2 \alpha_0)^{1/4},$$

its flat local maximum at  $x = 0$ , and the modulation of  $E_{x,\text{es}}$  due to the superposition of  $E_{x,\text{em}}$ , i.e.,  $|E_x|^2 = |E_{x,\text{es}} + E_{x,\text{em}}|^2$  are characteristic of resonance absorption. Owing to the flat maximum, the driver  $B$  exhibits in the resonance region, the inhomogeneous Airy-Stokes equation (3.71) with a constant driver  $b = -1$  yields an excellent approximation to  $E_x$  (see the dashed curve in Fig. 4.2). As

outlined in Sect. 3.2.4 for a spatially constant driver  $B$ , resonance terminates at  $\xi_m$  where  $|E_x|^2$  reaches its maximum; thus the resonance width in dimensionless form is given by  $2\xi_m$ . With  $x_m$  indicating the position of the maximum  $|E_x|^2$  and with  $x_0 = L\beta^2 \sin^2 \alpha_0$  from Sect. 3.2.4 this becomes in real space

$$d = 2x_m = 2 \left( \frac{\beta^2 L}{k_0^2} \right)^{1/3} \xi_m, \quad \xi_m = 1.8, \quad (4.2)$$

provided  $x_0/(x_m - x_0) = (k_0 L \beta^2)^{2/3} \sin^2 \alpha_0 / \xi_m \ll 1$  is fulfilled. With  $\beta = 0.1$  and  $k_0 L \leq 50$  this latter inequality is well obeyed for all angles of incidence  $\alpha_0$  and the resonance curve is nearly symmetric. Then  $d$  scales as  $(k_1 L)^{1/3} / k_1$ ,  $k_1 = k_0 / \beta$ . Although the density profile in Fig. 4.2 is flat,  $d$  is very small (dashed region). As a consequence of the driver not being exactly constant, in the exact solution of the coupled system of (3.21) and (3.22)  $\xi_m = 1.7$  is obtained from Fig. 4.2. When  $L$  is fixed at small angles of incidence the electromagnetic turning point is close to the critical point and much intensity reaches the coupling region, but the driver in (3.70), owing to the factor  $\sin \alpha_0$  in  $k_y$ , is small. As  $\alpha_0$  increases less intensity tunnels to the critical surface; however, this may be overcompensated by the factor  $\sin \alpha_0$ , and resonant excitation of  $E_{es}$  reaches a maximum. As  $\alpha_0$  increases further the exponential decrease of intensity tunneling to the critical point prevails and resonance absorption becomes ineffective. This situation is illustrated in Fig. 4.3. Resonance is strongest for  $q \simeq 0.4$  (3rd picture).

Let us now determine the conversion rate  $A = |S_{x,es}/S_{x,em}|$  for steady state resonance absorption. The electromagnetic and electrostatic flux densities in  $x$ -direction are (with  $I_0$  the vacuum flux density of amplitude  $E_0$ )

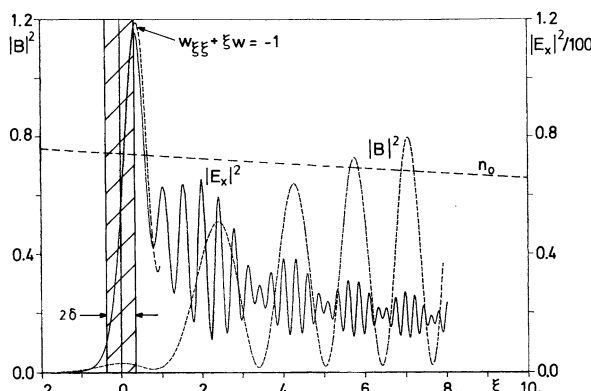


**Fig. 4.2** Resonance absorption: Distribution of  $|E_x|^2$  and  $|B|^2$  over the flat plasma density profile  $n_0$  as a function of  $\xi$ . Dashed region shows the resonance width  $2\xi_m$  ( $\xi_m$  position of maximum  $|E_x|^2$ ). Stokes equation reproduces well resonance behavior (dashed curve close to resonance)

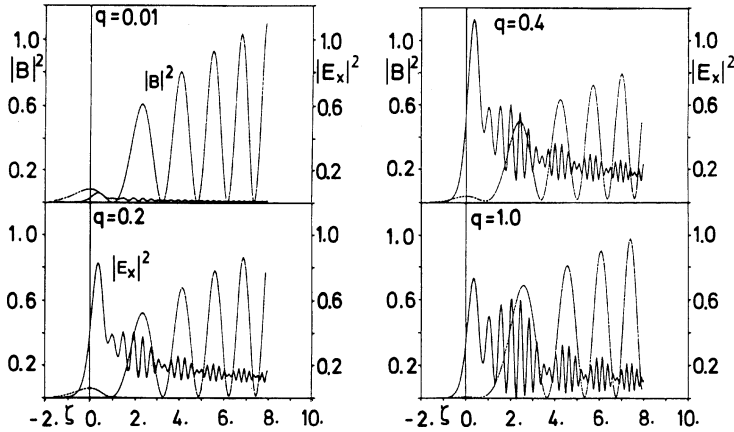


**Fig. 4.3** Resonance absorption. The same distributions as in Fig. 4.2 for different angles of incidence,  $q = (k_0 l)^{2/3} \sin^2 \alpha_0$

$$\begin{aligned} S_{x,\text{em}} &= \frac{1}{2} v_{g,x} \varepsilon_0 |\hat{E}_{\text{em}}(x)|^2 = \frac{1}{2} c \eta (1 - \sin^2 \alpha_0)^{1/2} \varepsilon_0 |\hat{E}_{\text{em}}(x)|^2 \\ &= (1 - \sin^2 \alpha_0)^{1/2} I_0, \\ S_{x,\text{es}} &= \frac{1}{2} v_{g,x} \varepsilon_0 |\hat{E}_{\text{es}}(x)|^2 = \frac{1}{2} s_e \eta (1 - \sin^2 \alpha_1)^{1/2} \varepsilon_0 |\hat{E}_{\text{es}}(x)|^2 \simeq I_{\text{es}}. \end{aligned}$$

By making use of the asymptotic expansion of (3.71) with  $b = -1$  (see [11], p. 162 ff),

$$w = -\frac{\pi^{1/2}}{\xi^{1/4}} \exp i \left( \frac{2}{3} \xi^{3/2} + \frac{\pi}{4} \right); \quad \frac{\eta}{\xi^{1/2}} = \left( \frac{\beta}{kL} \right)^{1/3}.$$

From the definition of  $w$  in Sect. 3.2.4 follows

$$S_{x,\text{es}} = \frac{\pi}{2} c^3 \varepsilon_0 k L |B(0)|^2 \sin^2 \alpha_0. \quad (4.3)$$

Hence, the conversion factor of resonance absorption is

$$A = \pi k_0 L \frac{\sin^2 \alpha_0}{(1 - \sin^2 \alpha_0)^{1/2}} \left| \frac{B(0)}{B_{\text{inc}}} \right|^2. \quad (4.4)$$

As soon as  $A$  is known this relation may be used to determine the “driver”  $B(0)$ . With  $I_0$  in  $\text{W/cm}^2$ ,

$$\begin{aligned}|B(0)| \sin \alpha_0 &= B_{\text{inc}}(1 - \sin^2 \alpha_0)^{1/4} \left(\frac{A}{\pi}\right)^{1/2} (k_0 L)^{-1/2} \\&= 5.16 \times 10^{-6} \left(\frac{A I_0}{k_0 L}\right)^{1/2} (1 - \sin^2 \alpha_0)^{1/4} [\text{Tesla}].\end{aligned}\quad (4.5)$$

Expressions (4.4) and (4.5) are based on the assumption of  $|B| = \text{const}$  over the whole resonance interval; for smooth density distributions with no significant curvature and  $k_0 L \geq 2\pi$  this simplification is justified. In Fig. 4.4 the conversion factor  $A$  is shown as a function of  $q$  for different electron temperatures and  $k_0 L \leq 2\pi$ . As expected from (3.71) there is almost no difference between cold and warm plasma up to temperatures  $T_e = 20 \text{ keV}$  (i.e.,  $\beta^2 = 0.1$ ; [6]). At  $T_e = 0$  the maximum conversion rate is  $A = 0.49$ . For  $\xi < 2$  the local electric field amplitude is given by

$$\left|\frac{\hat{E}_x}{E_0}\right|^2 = (1 - \sin^2 \alpha_0)^{1/2} (k_0 L)^{1/3} \frac{A}{\pi \beta^{4/3}} |w|^2. \quad (4.6)$$

Solving for its maximum value  $|\hat{E}_{x,\max}|$  yields

$$\left|\frac{\hat{E}_{x,\max}}{E_0}\right|^2 = 1.1 (1 - \sin^2 \alpha_0)^{1/2} (k_0 L)^{1/3} A \beta^{-4/3}. \quad (4.7)$$

This may be compared with the maximum amplitude  $E_{z,\max}$  of s-polarized light not exhibiting resonance, (3.61).

For  $T_e = 0$  analytical conversion rates  $A$  have been given by several authors [12–14], for finite  $T_e$  but with  $B = \text{const}$  cf. [15]. Their result is

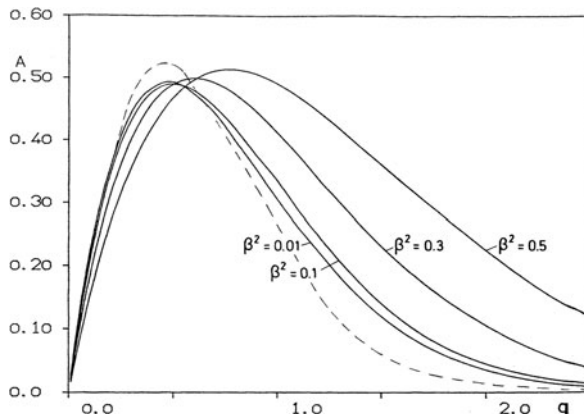


**Fig. 4.4** Temperature dependence of resonance absorption. Conversion factor  $A$  as a function of  $q = (k_0 L)^{2/3} \sin^2 \alpha_0$ . Dashed line: Hinkel-Lipsker [15]

$$A = \frac{(k_0 L)^{2/3} \sin^2 \alpha_0}{|1 - i\pi^2(k_0 L)^{2/3} \Gamma \sin^2 \alpha_0|^2} |2\pi \text{Ai}'|^2; \quad \Gamma = \text{Ai}'(\text{Bi}' + i\text{Ai}'). \quad (4.8)$$

Its numerical evaluation is the dashed line in Fig. 4.4. The deviations from the result in [7] are due to the simplification  $B = \text{const}$ . For  $\beta \leq 0.1$  the power series solution in [12] is much more accurate and practically coincides with the numerical result in [7]. The conversion  $A$  peaks at  $\sin \alpha_0 \simeq (2kL)^{-1/3}$  [16]. As  $T_e$  becomes relativistic and  $s_e$  approaches  $c$  resonant phase matching occurs over a wide range and the conversion factor  $A$  approaches unity at  $q \simeq 0.7 - 0.9$  [7], whereas at low temperatures  $A_{\max} = 0.49$  at  $q = 0.5$ . The shift of the maximum of  $A$  towards higher  $q$ -values is a consequence of  $x_0$  increasing with  $\beta$  in Sect. 3.2.4 and hence favoring resonance in lower density regions.

### 4.1.1 The Capacitor Model

So far, all results were obtained by starting from a rather general wave equation and solving it in an inhomogeneous medium under some simplifying assumptions among which linearity of  $\mathbf{j}$  is the most important one. Additional simplifications were introduced by neglecting  $\beta^2$  in comparison to 1 in (3.21) and (3.70) and taking a spatially constant driver  $B = B(0)$ . Owing to the  $\exp(-i\omega t)$  time dependence of  $E_x$  and  $B$  (3.70) is equivalent to the equation of a resonantly driven electron plasma wave parallel to  $\nabla n_0$ ,

$$\frac{\partial^2}{\partial t^2} E_x - s_e^2 \frac{\partial^2}{\partial x^2} E_x + \omega_p^2 E_x = c\omega^2 B \sin \alpha_0. \quad (4.9)$$

Let  $x_c$  be the position of the critical point and let us integrate (3.22) over an interval enclosing  $x_c$  under the restriction  $\lambda \leq L$ ,

$$ik_{0y} \int_{x < x_c}^{x > x_c} E'_x dx = ik_{0y} E_x(x) = \int_{x < x_c}^{x > x_c} (E''_y + k_0^2 \eta^2 E_y) dx \simeq E'_y(x).$$

The inequality  $\lambda \leq L$  enters in the last step; in steep density gradients  $\eta$  becomes large already in the vicinity of  $x_c$ . From  $E'_y \simeq ik_{0y} E_x$  and  $|E'_y| \simeq k_0 \eta |E_y|/\beta$  in the resonance interval, we have

$$|E_y| \simeq |E_x| \frac{\beta}{\eta} \sin \alpha_0 \ll |E_x|; \quad \beta/\eta \ll 1. \quad (4.10)$$

That is the main result of a more involved estimate [17]. It shows that  $\nabla \mathbf{E} = \partial \mathbf{E}_x / \partial x$  is a good approximation in not too steep density gradients and the displacement  $\delta_e$  of an electronic fluid element is nearly  $\delta_{e,x}$ . The latter is the basic assumption of the so-called capacitor model [4, 10, 18, 19].

When curvature of the ion density profile in the resonance zone does not play a decisive role (this is the case in expanding plasmas produced by smooth laser pulses) the wave number  $k_e^*$  of the electron plasma wave at the edge of resonance is deduced from  $\xi_m = 1.8$  in (4.2),

$$k_e^* = \frac{\omega}{s_e} \left\{ \beta^2 \sin^2 \alpha_0 + \xi_m \left( \frac{\beta}{k_0 L} \right)^{2/3} \right\}^{1/2} \simeq 1.8^{1/2} \left( \frac{k_0^2}{\beta^2 L} \right)^{1/3}. \quad (4.11)$$

The second expression holds when  $x_0$  can be ignored. As the electron plasma wave moves out into the lower density corona,  $k_{es}$  increases and Landau damping sets in; it can also be determined in the framework of the capacitor model [8]. This has to compete with the WKB reduction of  $\hat{E}_{es} \sim \eta^{-1/2}$ . The corresponding dependence of the electron amplitude  $\hat{n}_1 = \hat{n}_e - n_0$ ,  $n_0 = \langle n_e \rangle$ , shows the opposite behavior; thus

$$\hat{E}(x) = \left( \frac{\eta(x_1)}{\eta(x)} \right)^{1/2} \hat{E}(x_1), \quad \hat{n}_1(x) = \left( \frac{\eta(x)}{\eta(x_1)} \right)^{1/2} \hat{n}_1(x_1), \quad (4.12)$$

if  $x_1$  is an arbitrary position out of resonance where the WKB approximation is valid.

#### 4.1.2 Steep Density Gradients and Fresnel Formula

The capacitor model developed here may fail either when the density profile curvatures become significant in the resonance interval or/and when  $L$  becomes of the order of the electron displacement  $\lambda_e$  or less. The latter effect has been studied in the literature by adopting Epstein type density transition layers of the form [7]

$$\eta^2(x) = \frac{1}{2} - \frac{1}{1 + \exp(-x/\Delta)}, \quad L = 4\Delta.$$

It was found, and it is shown in Fig. 4.5 that (i) the conversion  $A$  deviates from the curves of Fig. 4.4 as soon as  $k\Delta$  becomes smaller than 2, (ii) at a given temperature the maximum of  $A$  increases with decreasing transition width  $\Delta$ , and (iii) the local angle  $\alpha$  at the resonant layer at which maximum conversion occurs is shifted towards larger values, in contrast to the vacuum angle  $\alpha_0$  which is reduced. A particularly interesting and clear result is obtained for an infinite plasma density step with  $\Delta \rightarrow 0$ . In this case total mode conversion, i.e.,  $A = 1$ , is found for all temperatures when the electron plasma wave is emitted into the direction of the incident radiation field  $E_0$  [7]. It requires the existence of an underdense plasma shelf in front of the discontinuity, generated for example by a laser prepulse.

Resonance absorption of intense electromagnetic fields at the surface of solid targets plays an important role in the interaction of ultrashort laser pulses with matter

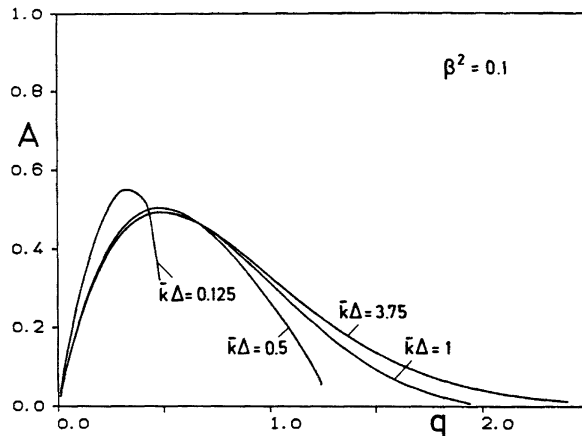


**Fig. 4.5** Conversion curves  $A$  as functions of the optical layer thickness  $\bar{k}\Delta$  and angle of incidence.  $q = (k_0 L)^{2/3} \sin^2 \alpha_0$ ,  $\bar{k} = k_0/2$ ,  $\beta^2 = 0.1$

(i.e.,  $\lesssim 10^{-14}$  s) since during such times almost no rarefaction wave builds up and absorption occurs at a density discontinuity. It has been argued that degenerate resonance absorption takes place here which is characterized by nonresonant, extremely anharmonic forced oscillations of the first electronic layer at the surface [20, 21], and that absorption occurs at rather large angles of incidence. This kind of absorption is treated more extensively in the context of ultrashort laser pulse-matter interaction in Chap. 8 and its correct physical interpretation is given there.

With  $\Delta$  shrinking to zero one could expect the absorption  $A$  to approach Fresnel's formula for p-polarized light shining on a metal under oblique incidence. This is indeed the case for ratios  $v_c/\omega$  of collision frequency  $v_c$  to laser frequency  $\omega$  suitably chosen as shown explicitly in [22] by solving the exact Helmholtz equation in an exponential isothermal density profile of variable scale length  $L$  and in [23, 24] by applying a layered plasma model to various density (e.g., Epstein transition) profiles. These latter authors have found "qualitative" agreement between resonance absorption of 250 fs long pulses in short scale length plasmas and Fresnel optics. The finding may suggest that there is such a correspondence between resonance absorption and classical optics. In particular, the insensitivity of the reflection coefficient  $R$  towards  $v_c/\omega$  over a wide range of values and for  $kL < 1$  [22] is understood from the following simple model for a sharp refractive index transition (see for instance [10], p. 215, [14], p. 42). The dielectric displacement component  $D_x$  is continuous across the transition, i.e.,  $\epsilon E_x = E_{\text{inc}}[1 + \sqrt{R} \exp(i\alpha)]$ ,  $\alpha$  real. In a linear density profile of scale length  $L$  and a damping coefficient  $v$  normalized to  $\omega$ ,  $\epsilon E_x$  translates into  $E_x = E_{\text{inc}}[1 + \sqrt{R} \exp(i\alpha)]/(\xi + iv)$ ,  $\xi = (x_c - x)/L$ ,  $x_c$  critical point. The damping stands either for a collision frequency or a loss due to wave dispersion at finite electron temperature, i.e., energy outflow from the critical region. Then the absorption coefficient  $A = 1 - R$  reads

$$A = \int \langle j_x E_x \rangle dx / E_{\text{inc}} \sim [1 + \sqrt{R} e^{i\alpha}] v \int |E_x|^2 dx \sim [1 + \sqrt{R} e^{i\alpha}] \int \frac{v}{\xi^2 + v^2} d\xi \quad (4.13)$$

For  $v \lesssim 0.3$  the integral can be extended from  $-\infty$  to  $+\infty$  to yield the value  $1/\pi$ . It shows that  $A$  becomes insensitive to damping  $v$  and scale length  $L$ . On the other hand one must keep in mind that the dependence of  $R$  on small damping values is also weak and its value remains close to unity for electron densities of the order of 100 times critical density. In fact, at  $80^\circ$  of incidence and  $L/\lambda < 0.1$  the reflection for  $v = 0.01, 0.1$ , and  $1.0$  is  $R = 0.99, 0.92$ , and  $0.5$ , i.e., the penetrating field is very small and consequently  $A$ , despite the constant value of the integral close to  $1/\pi$ , vanishes for  $L \rightarrow 0$ , except for unrealistically high collision frequencies. There is an additional restriction. In order for the above expression for  $A$  to hold with  $v$  reducing to zero the incident laser field must also reduce to zero to avoid wave breaking owing to  $E_{x,\max} \sim 1/v$ . After all, Fresnel's formulas are restricted to linear optics. From such a requirement one deduces for the limiting intensity  $I_{\max}$  for  $L \rightarrow 0$  [25] [see also (4.15) below]

$$\begin{aligned} I_{\max} &= \frac{1}{2} \left( \frac{4}{3\pi} \right)^{2/3} \left( \frac{m}{e} \right)^2 (c^8 \omega^7)^{1/3} (\epsilon L^{1/3})^2 \\ &\rightarrow I_{\max} [\text{W/cm}^2] = 2.9 \times 10^{18} (\epsilon \times L[\text{m}]^{1/3})^2. \end{aligned} \quad (4.14)$$

The tolerable limit for linearity of the electron plasma wave  $n_1$  is indicated by  $\epsilon = n_1/n_c$ . With  $\epsilon = 0.1$  and  $L = 10 \text{ nm}$  linear resonance absorption is for  $6 \times 10^{13} \text{ W cm}^{-2}$  at its limit. The  $L^{2/3}$ -dependence reflects the property of the resonance width increasing with  $L^{1/3}$ . Particular experimental effort was dedicated to the collisionless absorption of sub-ps laser pulses in short scale length plasmas from solid targets in [22–24, 26]. In [22] it is shown how resonance absorption may be used as an elegant and very reliable diagnostic tool for determining the laser scale length  $L$ . In [26] the reader may find an interesting comparison between fluid models and collisionfree PIC simulations. Both, although fundamentally different from each other, fit well to the experimental results, at a price, however, of introducing an artificial viscosity and, in concomitance, strong artificial damping in the fluid program to avoid wave breaking. In presence of artificial viscosity to check the absorption  $\int \mathbf{j} \cdot \mathbf{E} dx$  over the whole density transition profile is a necessity. Only if  $\int \mathbf{j} \cdot \mathbf{E} dx$  is essentially localized around the critical point and in the evanescent region the result perhaps may be reliable. In this context a short discussion of the correct boundary conditions at a vacuum-matter interface may shed additional light on the question whether resonance absorption for  $\Delta \rightarrow 0$  goes over into the laws of linear optics. Thereby it must be kept in mind that such an analysis, owing to its linear character, is valid only for very low intensities.

Fresnel's reflection formula for  $R = 1 - A$  resembles one aspect of resonance absorption, namely the Brewster minimum of  $R$  which is a consequence of the fact that an oscillating electron does not radiate into its oscillation direction. This makes also Kull's result [7] of total conversion into an electron plasma wave emanating

into the lower density shelf understandable. Fresnel's formula is derived from the conditions that the tangential component of the electric field  $\mathbf{E}_t$  and the normal component of the electric displacement  $\mathbf{D}_n$  are continuous. Now, to obtain Fresnel's situation the transition width  $\Delta$ , together with the density of the lower shelf and the electron temperature  $T_e$  has to reduce to zero. From Maxwell's equation (3.1), when applied to the infinitesimal area  $d\mathbf{F} = \mathbf{e}_y dx dz$ , follows for  $\mathbf{B} = \mathbf{B}_t$ :

$$\epsilon_0 c^2 (\nabla \times \mathbf{B}) d\mathbf{F} = (j_y - i\omega \epsilon_0 E_y) dx dz = (B_{z,\text{vac}} - B_{z,\text{plasma}}) dz.$$

For  $\Delta \rightarrow 0$ ,  $E_y$  and  $j_y$  both diverge logarithmically at  $T_e = 0$ ,  $E_y, j_y \sim \ln(1/\Delta)$ , and hence  $\mathbf{B}_t = B_z \mathbf{e}_z$  is continuous across the vacuum-plasma interface. As a consequence the Poynting vector  $\mathbf{S} = S_x \mathbf{e}_x$  is also continuous across the surface and resonance absorption reduces to zero. Continuity of  $\mathbf{S}$  requires total reflection from the overdense plasma in perfect agreement with Fresnel's result. In order to be in agreement with the foregoing absorption formula  $\sqrt{R} \exp(i\alpha) = -1$  must be set (in this context the reader may consult [27] for a more detailed consideration).

However, this is not the whole story. From  $\mathbf{D}_n$  being continuous a discontinuity of  $\mathbf{E}_n$ , i.e., the induction of an oscillating surface charge follows. The oscillation leads to a delocalization of this charge and to a finite transition width, as considered in [20, 21]. Such an argument led to the boundary condition of  $\mathbf{E}_n$  being also continuous at the interface and with it to a correction of Fresnel's reflection formula for p-polarized light incident onto a metal surface with  $\omega_p > \omega$  [28]. For a quantitative discussion of this situation with a weak incident field the interested reader may consult the monograph of Forstmann and Gerhardt [29].

In conclusion, only within a restricted domain of parameters  $v$ ,  $L$  and laser intensity  $I$  the Fresnel formula for absorption of p-polarized waves may appear as the limiting case of linear resonance absorption. On physical grounds, however, there is no basis for such an identification over the whole range of the density scale length  $L \rightarrow 0$ . For high laser intensities anharmonic resonance, not contained in Fresnel's formula at all, will play a decisive role (see Sect. 8.3.3).

#### 4.1.3 Comparison with Experiments

Resonance absorption with ns laser pulses was experimentally shown to occur by several groups [30–34] and to be in agreement with linear theory at Nd laser intensities up to  $I = 10^{14} \text{ W/cm}^2$ . A clear difference between s- and p-absorption was found at all angles of incidence  $\alpha_0 < 60^\circ$ . The most accurate and complete measurements in the intensity range from  $10^{13}$  to  $10^{14} \text{ W/cm}^2$  were performed in the past in [35] on plexiglass targets with a Nd-YAG laser of 35 ps pulse length. The absorption was detected simultaneously in five parallel channels of observation: reflection of the fundamental wave, second harmonic generation, charge and velocity distribution of the expanding plasma cloud, and relative ablation pressure on the target. All five channels gave equivalent results and the absorption of p-polarization exceeded

that for s-polarization by about a factor of 2 on the average. The excited Langmuir wave can interact nonlinearly with the incident laser light, thus creating the second harmonic,  $2\omega_{\text{Nd}}$  with an intensity proportional to  $A$ . Some characteristic deviations between experiments and theory of resonance absorption may have to be attributed to fluctuations of the plasma density profile. Theoretically the influence of stochastic density oscillations was studied by several authors [36–38] for long pulses. It was found that the excitation level of the Langmuir wave decreases monotonically with increasing amplitude of the density fluctuations.

Resonance absorption by excitation of a plasma wave at twice the laser frequency is possible at normal or nearly normal incidence when the Lorentz force  $-ev_{\text{os}} \times \mathbf{B}$  prevails over the driving force  $-e\mathbf{E}$  at the fundamental frequency.

## 4.2 Nonlinear Resonance Absorption

The theory of resonance absorption exposed in the preceding section is valid as long as the ratio  $\hat{n}_1/n_0$  is small compared to unity in the resonance interval. From (3.74) and from  $\delta$  in (2.12), we have  $n_1 \simeq -in_0k_e eE/m\omega^2$ . At the maximum of  $\hat{E}$ , one must take  $k_e = k_e^*$  from (4.11), and (4.7) may be used to relate the amplitude  $\hat{n}_1$  to the incident laser intensity  $I_0$ . After some transformations the following relation is obtained,

$$\frac{\hat{n}_1}{n_0} = \sqrt{2}\xi_m^{1/2} \frac{e}{m(c\varepsilon_0)^{1/2}} (k_0 L)^{5/6} A^{1/2} \frac{1}{\omega L} \left( \frac{I_0}{\omega^2} \right)^{1/2}. \quad (4.15)$$

At the Nd laser intensity  $I_0 = 10^{14} \text{ W/cm}^2$  and  $L = \lambda_{\text{Nd}}$  one obtains from there

$$\frac{\hat{n}_1}{n_0} = 0.28 A^{1/2}, \quad (4.16)$$

which shows that for these parameters the linear description of the electron plasma wave in the resonance interval is close to its limit. At higher intensities a nonlinear theory of mode conversion must be developed. In general, a complete description of this phenomenon can only be obtained by including Maxwell's equations and employing numerical methods. However, in order to describe essential features of the nonlinear behavior and to make analytical predictions, models of resonant electron plasma wave excitation can be used. The simplest choice is again the capacitor model. In the following it will be used to study some nonlinear resonance absorption characteristics. Vlasov simulations of the capacitor model are then used to test the hydrodynamic approach and to study electron trapping and acceleration. An entirely different model will be introduced in Chap. 8 to study collisionless absorption of ultrashort laser pulses on solid surfaces. The underlying idea is that with a strong driver the resonance frequency becomes a function of the oscillation amplitude, i.e., of driver strength. By this effect an originally nonresonant volume element may

undergo resonance with the laser frequency if the beam intensity is sufficiently high (see Sect. 8.3.3 on anharmonic resonance).

### 4.2.1 High Amplitude Electron Plasma Waves at Moderate Density Gradients

Two models were used to study high amplitude oscillations in a cold plasma, one treating the plasma at rest and describing the nonlinear density fluctuations as the result of superposition of localized linear oscillators [18], the other one by employing the fully nonlinear momentum fluid equation of a streaming plasma [39]. To some extent nonlinear wave excitation in a warm plasma at rest can be reduced to the latter model by choosing an effective flow velocity for the plasma.

In what follows a plasma of finite temperature at rest is assumed. In the capacitor approximation, i.e.,  $\mathbf{E} = (E, 0, 0)$ ,  $\nabla E = \partial E / \partial x$ ,  $\nabla \times \mathbf{B} = (ik_y B, 0, 0)$ , Maxwell's equations and the equation of motion are

$$\begin{aligned}\frac{\partial E}{\partial t} &= ik_y c^2 B + \frac{e}{\varepsilon_0} n_e v_e, \quad \frac{\partial E}{\partial x} = \frac{e}{\varepsilon_0} (n_0 - n_e), \\ \frac{dv_e}{dt} &= -\frac{s_e^2}{n_e} \frac{\partial n_e}{\partial x} - \frac{e}{m} E.\end{aligned}\quad (4.17)$$

Elimination of  $E$  leads to

$$\frac{d^2 v_e}{dt^2} + \frac{d}{dt} \left( s_e^2 \frac{1}{n_e} \frac{\partial n_e}{\partial x} \right) + \omega_p^2 v_e = -i \frac{ec^2}{m} k_y B. \quad (4.18)$$

Advantageously, here  $\omega_p$  contains the ion background density  $n_0/Z$ ,

$$\omega_p^2 = \frac{e^2 n_0(x, t)}{\varepsilon_0 m},$$

rather than the instantaneous electron density  $n_e$ . Replacing  $(x, t)$  by the Lagrangian coordinates  $(a, t)$ , in which  $a$  is the initial position of the electron and ion fluid elements, leads to

$$x_i = a, \quad x_e(a, t) = a + \delta_x(a, t), \quad \delta_x(a, t) = \int_0^t v_e(a, t) dt, \quad n_e = \frac{n_0}{1 + \partial \delta_x / \partial a}. \quad (4.19)$$

In the new coordinates (4.18) becomes

$$\frac{\partial^2}{\partial t^2} v_e + \frac{s_e^2}{\gamma n_0^\gamma} \frac{\partial^2}{\partial t \partial a} \left( \frac{n_0}{1 + \partial \delta_x / \partial a} \right)^\gamma + \omega_p^2(a, t) v_e = \frac{1}{2} \omega^2 v_d e^{-i\omega t} + cc. \quad (4.20)$$

The oscillation center approximation was assumed to obtain the term  $\omega_p^2(a, t)v_e$ . This is justified for inhomogeneity lengths  $L$  and electrostatic wavelength  $\lambda_e$  if  $L > 2\lambda_e$ . The electron fluid is assumed to obey an adiabatic law,  $p_e = \text{const} \times n_e^\gamma$ , the driver  $v_d$  stands for  $v_d = -iec^2k_yB(0)/m\omega^2$ . For  $L > 2\lambda_e$ , one may further transform (4.20),

$$\frac{\partial}{\partial t} \left\{ \frac{\partial^2}{\partial t^2} \delta_x + \frac{s_e^2}{\gamma} \frac{\partial}{\partial a} (1 + \frac{\partial}{\partial a} \delta_x)^{-\gamma} + \omega_p^2 \delta_x \right\} = \frac{1}{2} \omega^2 v_d e^{-i\omega t} + cc.,$$

and integrate it once to obtain

$$\frac{\partial^2}{\partial t^2} \delta_x + \frac{s_e^2}{\gamma} \frac{\partial}{\partial a} (1 + \frac{\partial}{\partial a} \delta_x)^{-\gamma} + \omega_p^2 \delta_x = \frac{i}{2} \omega v_d e^{-i\omega t} + cc. \quad (4.21)$$

For small amplitudes  $(1 + \partial \delta_x / \partial a)^{-\gamma} \simeq 1 - \gamma \partial \delta_x / \partial a$  and, with the help of  $\delta_e = \delta_x$  from (2.12), (4.21) reduces to (4.9), since then  $\partial / \partial a \simeq \partial / \partial x$ . For a cold plasma ( $s_e^2 = 0$ ) it leads to the Koch-Albritton model [18] of uncoupled harmonic oscillators from which, through (4.19) the electron density is recovered. Although there is strong coupling between the single fluid elements,  $v_e$  and  $\delta_x$  are sinusoidal in the cold plasma, but  $n_e$  is not, in contrast to a linear wave which is sinusoidal in all variables that can be used to describe it. By setting

$$\begin{aligned} \delta_x &= \delta_1 + \frac{1}{2} \sum_{\sigma \geq 2} \left\{ \delta_\sigma e^{-i\sigma\omega t} + \delta_\sigma^* e^{i\sigma\omega t} \right\}, \\ g &= 1 + \frac{1}{4} \binom{\gamma+2}{2} k_1^2 |\delta_1|^2 + \frac{1}{8} \binom{\gamma+4}{4} k_1^4 |\delta_1|^4 + \dots \end{aligned}$$

in the warm plasma the amplitude-dependent dispersion relation for the fundamental wave  $\delta_1$ ,

$$\omega^2 = \omega_p^2 \left\{ 1 + g \left( \frac{s_e k_1}{\omega_p} \right)^2 \right\}, \quad (4.22)$$

and the amplitude ratios for the higher harmonics are obtained [40],

$$\begin{aligned} \frac{\hat{\delta}_2}{\hat{\delta}_1} &= \frac{\gamma+1}{2} \frac{\eta^{3/2} g^{-1/2} \omega^2}{3\omega_p^2 g + 4(g-1)\eta^2 \omega^2} \frac{\hat{v}_1}{s_e}, \quad v_1 = \dot{\delta}_1, \\ \frac{\hat{\delta}_3}{\hat{\delta}_1} &= \frac{\gamma+1}{4} \frac{\eta^3 \omega^2}{g^2} \left( \frac{\hat{v}_1}{s_e} \right)^2 \frac{\frac{3(\gamma+1)\omega^2}{3\omega_p^2 g + 4(g-1)\eta^2 \omega^2} + \frac{\gamma+2}{2}\eta}{8\omega_p^2 + 9(g-1)\eta^2 \omega^2}. \end{aligned} \quad (4.23)$$

In the resonance region  $\eta^2 \ll 1$ ,  $(s_e k_1 / \omega_p)^2 \ll 1$ ,  $g = 1$ ,  $\omega_p^2 = \omega^2$  holds and these relations simplify to

$$\frac{\hat{\delta}_2}{\hat{\delta}_1} \simeq \frac{\gamma + 1}{6} \eta^{3/2} \frac{v_1}{s_e}, \quad \frac{\hat{\delta}_3}{\hat{\delta}_1} \simeq \frac{1}{2} \left( \frac{\gamma + 1}{4} \right)^2 \eta^3 \left( \frac{v_1}{s_e} \right)^2, \quad (4.24)$$

showing the interaction of modes: As the excited wave moves away from the resonance region towards lower densities the refractive index  $\eta$  increases from zero to one, thus leading to an increase of higher order modes. The modified dispersion (4.22) is a consequence of self-interaction of the fundamental mode  $\delta_1$ . Due to the excitation of higher harmonics at finite electron temperature  $v_e$  and  $\delta_x$  no longer remain sinusoidal. This behavior is clearly seen in the numerical solution of (4.20) in Fig. 4.6. The maxima of  $v_e$  are more peaked than its minima. As a result,  $\delta_x$  has a tendency to assume a sawtooth shape. The spike-like character is especially pronounced in the electron density  $n_e$ . Such structures of “bubbles and spikes” are very characteristic of large amplitude electrostatic waves and are encountered in the nonlinear evolution of the Rayleigh-Taylor instability (see Chap. 5 in [41]). The main contribution to peaking of  $n_e$  comes from mass conservation of (4.19) and is best understood in the cold plasma case; there

$$\delta_x = \hat{\delta} \cos \omega_p t, \quad n_e = \frac{n_0}{1 + (\partial \hat{\delta} / \partial a) \cos \omega_p t}$$

holds and  $n_e$  oscillates between  $n_0/2$  and  $\infty$ . In the warm plasma  $n_e$  remains above  $n_0/2$  in all situations [42].

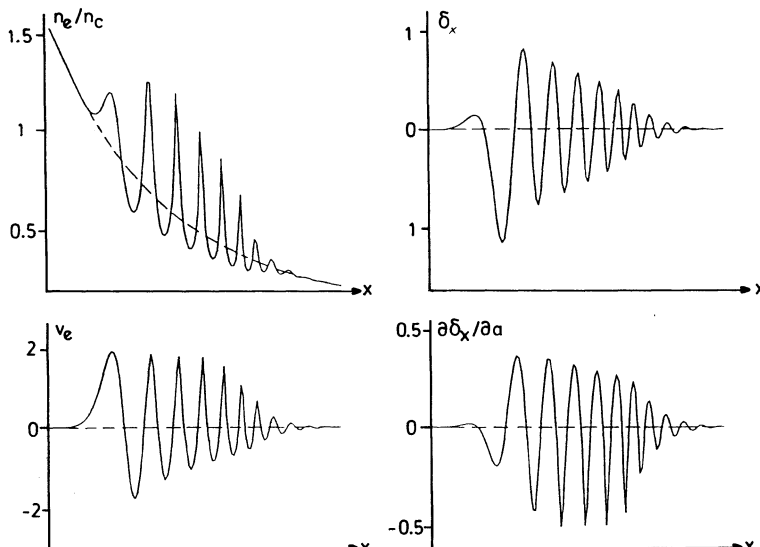


**Fig. 4.6** Nonlinear electron plasma wave. Normalized electron density  $n_e$ , electron quiver velocity  $v_e$ , excursion  $\delta_x = \int v_e dt$  and  $y = \partial \delta_x / \partial a$  as functions of  $x$ . Nearly the same picture results if these quantities are plotted as functions of the Lagrange coordinate  $a$

### 4.2.2 Resonance Absorption by Nonlinear Electron Plasma Waves

With increasing laser intensity or at low electron temperature the electron plasma wave may exceed the linear limit and may even break. Furthermore, particle-in-cell (PIC) simulations have shown that the particle aspect appears more and more as the Langmuir wave potential increases and particle trapping and acceleration dominates [43]. As we shall see in the following these phenomena lead to strong collisionless damping of the Langmuir wave. It is therefore quite natural to extend the traditional, somewhat vague definition of nonlinear Landau damping (see for example [44]) to include such processes. This makes clear that at high intensities a kinetic description of resonance absorption is needed. With particle trapping the following questions arise: What structure does a strongly nonlinear Langmuir wave assume, and to what extent does the much simpler fluid description still give a satisfactory answer? How is the mode conversion efficiency, i.e., the absorption coefficient  $A$ , affected by the nonlinear evolution of the plasma wave? These questions can be answered properly by numerically solving the Vlasov equation.

The evolution of the one-dimensional electron distribution function  $f(x, v, t)$  under the action of an external driver field  $E_d$  and the induced self-consistent field  $E(x, t)$  in such a fixed ion background of charge density  $en_0(x)$  is governed by the Vlasov and Poisson equations,

$$\frac{\partial f}{\partial t} + v \frac{\partial f}{\partial x} - \frac{e}{m} (E + E_d) \frac{\partial f}{\partial v} = 0, \quad \frac{\partial E}{\partial x} = \frac{e}{\varepsilon_0} \left( n_0 - n_c \int_{-\infty}^{\infty} f dv \right). \quad (4.25)$$

This procedure is much more involved than corresponding PIC simulations; however, as a compensation, it generates almost no numerical noise and leads to finer resolution in regions of low density in phase space [45]. Starting with a Maxwellian distribution function

$$f_0(x, v) = \frac{1}{(2\pi)^{1/2} v_{\text{th}}} \exp\left(-\frac{x}{L}\right) \exp\left(-\frac{v^2}{2v_{\text{th}}^2}\right),$$

the result of the Vlasov calculation of the Langmuir wave is compared with hydrodynamic solutions obtained from (4.20) [25]. In Fig. 4.7a the driving field amplitude, measured in units of the thermal electric field  $E_{\text{th}} = k_B T_e / e \lambda_D = (m_e k_B T_e)^{1/2} \omega/e$ , is  $\hat{E}_d = 0.02$ , and in (b)–(d) it is twice as strong,  $\hat{E}_d = 0.04$ . All pictures are taken at the same time  $\omega t = 120\pi$ . The first two, (a) and (b), are the hydrodynamic results and show the characteristic peaking as presented in Fig. 4.6. The analogous Vlasov result is shown in (c). The agreement in the general wave structure is excellent. For comparison, in picture (d) the corresponding result of a PIC calculation with  $6 \cdot 10^4$  particles, applied to a nonlinear density profile with the same gradient  $n_c/L$  at the resonance point, is plotted. The advantage of the 1D Vlasov simulation is evident.

The amount of particles trapped and accelerated (detrapped) by the wave of Fig. 4.7 can be estimated from the distribution function in Fig. 4.8a: trapped particles are recognized by closed loops in the potential wells, detrapped ones form the undu-

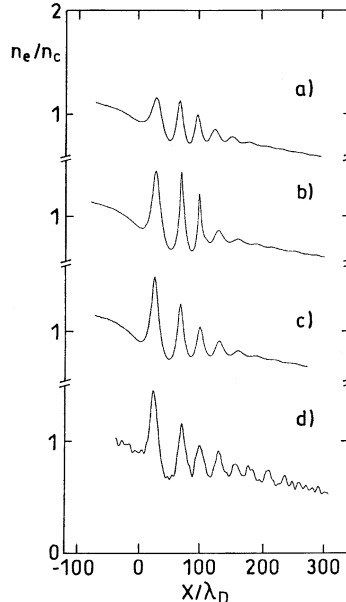


**Fig. 4.7** High-amplitude electron plasma wave in the capacitor model with driving field amplitude (a)  $\hat{E}_d = 0.02$  and (b)–(d)  $\hat{E}_d = 0.04$  and  $L = 600\lambda_D$  at time  $\omega t = 120\pi$ . The critical density is at  $x = 0$ . Normalized electron density  $n_e/n_c$  (a), (b) from the fluid model, (c) from the Vlasov simulation, and (d) from a PIC calculation with  $6 \cdot 10^4$  particles (large numerical noise). Jitter in the phase between (a)–(c) and (d) is due to small time step differences between the different numerical procedures

lating contours leaning to the right. For comparison, in Fig. 4.8b the distribution function from the PIC calculation of the same wave is presented. Here, in contrast to the Vlasov code, the evaluation of the distribution function is not possible in those regions where almost no simulation particles are present. How strongly nonlinear Landau damping exceeds linear Landau damping can be deduced from Fig. 4.9 for the two driver strengths  $\hat{E}_d = 0.04$  and  $\hat{E}_d = 0.08$ . It shows that, except at very low  $\hat{E}_d$ -values, linear Landau damping (dotted curves) is totally dominated by damping due to particle trapping and acceleration (at low driver strength the comparison with linear Landau damping was used to test the accuracy of the numerical procedure employed here). More quantitatively, Vlasov simulations show that linear Landau damping holds up to the following laser intensity limit,

$$I_0 = 2 \times 10^{13} \left( \frac{\omega_{Nd}}{\omega} \right)^2 \left( \frac{300\lambda_D}{L} \right)^{1/3} \text{Wcm}^{-2}. \quad (4.26)$$

The first wave crest is the only resonantly driven maximum. All other maxima which are outside the resonance region stop growing due to nonlinear Landau damping at  $\hat{E}_d \approx 0.04$ ; the additional absorbed energy is transferred to fast electrons. The first field maximum increases with growing driver strength as plotted in Fig. 4.10. For

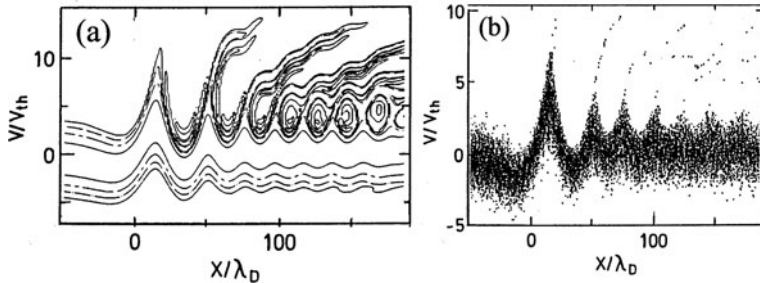


**Fig. 4.8** Electron distribution in the wave in Fig. 4.7b-d after 60 cycles. **(a)** Vlasov simulation: contour lines of the distribution function for  $f = 10^{-4}, 10^{-3}, 10^{-2}$ , and  $10^{-1}$  in phase space. **(b)** Particle simulation with  $v_{\text{th}} = 0.05c$ ; a fraction of the particles are plotted as dots in phase space. Fast electrons escaping to the right are clearly seen

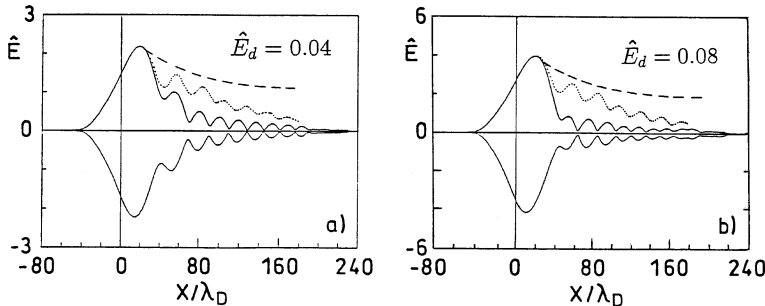


**Fig. 4.9** Envelopes of the electric field for  $L = 300\lambda_D$  and **(a)**  $\hat{E}_d = 0.04$  and **(b)**  $\hat{E}_d = 0.08$ . Dashed curves: amplitude maxima from the fluid theory (no damping,  $\hat{E} = \text{const}/\{1 - \exp[-x/L]\}^{1/2}$ ); dotted curves: linear Landau damping after [8]; solid curves: true nonlinear Landau damping. Amplitude modulations are due to  $\hat{E}_d$  being constant in space

$\hat{E}_d \gtrsim 0.15$ , the Vlasov simulation results deviate substantially from the linear theory result, as indicated by the dots in the figure.

When the driver strength is further increased (e.g., beyond  $\hat{E}_d = 0.18$  for  $L = 100\lambda_D$ ), all maxima except the resonant one start fluctuating due to trapping of entire bunches of electrons, and out of resonance the Langmuir wave completely loses its periodic structure, i.e., it breaks (Sect. 4.4). At the latest, as soon as the highly nonlinear phenomenon of intense phase mixing sets in one would expect strong deviations from the fraction  $A$  of resonantly absorbed laser intensity, as calculated from the linear theory in the foregoing section. However, surprisingly enough, the Vlasov simulations indicate that for moderately steep density profiles ( $k_0 L \gtrsim 2$ ) at least up to  $L\hat{E}_d^2 = 30$  the absorbed power  $\bar{P}_{\text{abs}} = A I_0 \cos \alpha_0$  ( $= \langle \int j E_d dx \rangle_t$  in the capacitor model;  $j$  current density) is given by the linear theory with the maximum  $A(\alpha_0)_{\text{opt}} = 0.49$  (see Fig. 4.11). Converting the  $L\hat{E}_d$ -values for a plasma of  $T_e = 1$  keV into laser intensities  $I_0$  according to (4.4) and (4.5),

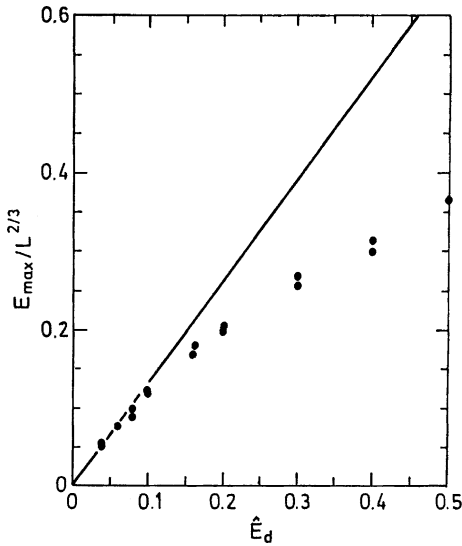


**Fig. 4.10** Comparison of maximum electric-field amplitude from Vlasov simulations (dots) and from the linear theory (straight line). The latter scales as  $\hat{E}_{\max} = 1.28 \cdot (L/\lambda_D)^{2/3} \hat{E}_d$  [8]

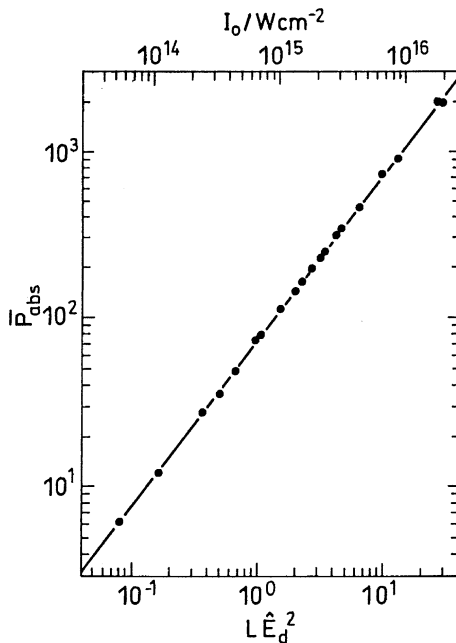


**Fig. 4.11** Validity of linear resonance absorption: mean absorbed power  $\bar{P}_{\text{abs}}$  as a function of the driving field strength  $\hat{E}_d$  (bottom scale) and laser intensity for  $\lambda = 1.06 \mu\text{m}$  and  $T_e = 1 \text{ keV}$  in case of maximum absorption (top scale). Dots: Vlasov simulations; straight line: linear theory

$$\hat{E}_d = \left( \frac{2AI_0 \cos \alpha_0}{\pi \varepsilon_0 \omega L} \right)^{1/2}, \quad (4.27)$$

the intensity scale at the top of Fig. 4.11 is determined. It shows that the absorption  $A$  is correctly calculated from the linear theory at least up to

$$I_0 = 2 \times 10^{16} \text{ Wcm}^{-2}/(\lambda_L/\mu\text{m})^2. \quad (4.28)$$

This is 200 times higher than the limit given by (4.16). It can be explained as follows. In the linear theory wave conversion takes place only within the resonance zone of width  $d$  from (4.2) given above. Outside this region the plasma wave decouples from the driver and becomes a freely propagating wave. Vlasov simulations show that in the nonlinear regime these characteristics still persist and almost no energy is coupled into the Langmuir wave outside the resonance region. In the nonlinear case the most remarkable difference is the generation of fast electrons. However, a large fraction of the energy transferred to the accelerated electrons is taken from the induced electrostatic wave field which is still almost sinusoidal in the resonance zone. Outside this region only thermalization of the plasma waves and fast electrons takes place. In other words, the accelerated electrons or fluid elements, respectively, have already acquired nearly their total energy just in the moment of breaking.

In order to show clearly the structure of the nonlinear plasma wave and its damping, in Figs. 4.7, 4.8, and 4.9 moderately steep density profiles have been chosen. Figs. 4.10 and 4.11 contain data for density profiles with  $L$  as short as  $20\lambda_D$  which in Nd-laser plasmas is typically  $L \approx \lambda/5$ ; this models ponderomotive profile steepening which ranges from  $L \simeq \lambda$  to  $L \approx \lambda/10$  (see Chap. 5). Detailed calculations of the conversion efficiency in linear resonance absorption showed that only for  $k_{\text{em}}L < 1$  the conversion exceeds the value  $A = 0.49$  under special conditions [7].

Caviton and soliton formations with subsequent collapse are, of course, not observed in a model with fixed ions. However, although interesting in themselves [46], in laser plasmas produced by smooth ns and ps pulses from solid targets they are transient phenomena and do not play a major role since the plasma flow has a strong smoothing effect on any eventual ion density fluctuation generated in the resonance region.

### 4.3 Hot Electron Generation

Wave-particle interaction in its weakest form leads to linear Landau damping as treated in Sect. 2.2.2. Below a certain amplitude the traveling potential of an electron plasma wave is not strong enough to trap a significant fraction of the electrons; instead they follow straight orbits. With increasing amplitude, the potential (2.93) becomes sufficiently large to capture first those particles having velocities not far from the phase velocity  $v_\phi$  of the wave. As an electron is trapped in a potential well it oscillates with the bounce frequency  $\omega_B$  around its minimum and is carried into

regions where  $v_\varphi$  and  $n_1$  are increased or decreased. In the first case effective particle acceleration takes place. In the second case an electron may remain trapped and the difference of its kinetic energy is given back to the wave, or it becomes free again and carries away the energy imparted to it by the wave. Such detrapped electrons are seen on the wave crests in Fig. 4.8b. The bounce frequency of an electron oscillating close to the minimum of a wave potential like (2.93) is easily determined. Expansion of  $\Phi$  around its maximum yields

$$\Phi = -\frac{e^2 \hat{n}_1}{\varepsilon_0} \frac{(x - x_0)^2}{2}.$$

Hence, the bounce frequency is

$$\omega_B = \left( \frac{e^2 \hat{n}_1}{\varepsilon_0 m} \right)^{1/2}, \quad (4.29)$$

i.e.,  $\omega_B$  is the plasma frequency of the electron density amplitude. With increasing oscillation amplitude  $\omega_B$  remains behind this formula in a sinusoidal potential, i.e., in a linear electron plasma wave, and it does so owing to the flattening effect of the minima of  $n_e$  according to Fig. 4.6 when the wave amplitude increases.

In laser produced plasmas fast, i.e., superthermal electrons were observed as early as in 1971 [47]. Since their energy distribution was not far from a Maxwellian a *hot temperature*  $T_h$  could be assigned to them, in contrast to the thermal electrons whose temperature  $T_e$  was given the name *cold electrons*  $T_c$  although typical values of  $T_c$  in laser produced plasmas on ns time scales range from 0.5 to 5 keV. In plasmas produced by high-intensity CO<sub>2</sub> lasers considerably higher values of  $T_c$  are reached. The hypothesis that the main sources for hot electron generation in the ns and ps regimes are resonance absorption at the critical density and stimulated Raman scattering as well as two-plasmon decay at a quarter of the critical density (Chap. 6) was successively confirmed by particle simulations [48, 49]. Electron acceleration and, in concomitance, acceleration of ions up to several 10 MeV becomes an important phenomenon when superintense laser pulses interact with gas and solid targets (Chap. 8).

In view of the importance the wave-particle interaction in laser plasmas, an analytical treatment of it and a classification of its main aspects are presented first. Thereby the authors mainly follows [50] (alternatively [40]).

### 4.3.1 Acceleration of Electrons by an Intense Smooth Langmuir Wave

In the analytical treatment a one-dimensional model is used for the wave and the particle motion in it. The electron plasma wave is assumed to propagate in the positive  $x$ -direction, with amplitude  $\hat{E}$  and wavelength  $\lambda = 2\pi/k$  being weakly

space dependent. The electron equation of motion may be written as follows,

$$m\ddot{x} = -e\hat{E}(x) \sin \left( \int_{x_0}^x k(x') dx' - \omega t \right). \quad (4.30)$$

An asymptotic series solution of this equation can be obtained by a method due to Kruskal [51]. In our context it is sufficient to determine only the first term. To leading order the procedure is equivalent to the method of averaging [52], which has been employed in the computation of electron trajectories in a wave with slowly time dependent amplitude [53].

In solving the equation of motion two different cases have to be treated separately: that of a trapped electron bouncing to and fro in a potential trough of the wave, moving on the average with the phase velocity, and that of an untrapped particle going over hill and valley. The solutions are best given in terms of an amplitude variable  $y$  which is taken to be the total particle energy in the wave frame divided by  $\frac{1}{2}mv_\varphi^2$ .

As a result of Kruskal's method one obtains the dependence of the normalized particle energy  $y$  on the wave amplitude  $\hat{E}(x)$ , wave number  $k(x)$  and an eventual static field  $E_0(x)$ . For untrapped particles it is given by [40, 50]

$$\frac{1}{k^2} \left[ 1 + y + \sigma \frac{4}{\pi} (w + y)^{1/2} E(\kappa) \right] - 4\Phi = \text{const}, \quad (4.31)$$

while for trapped particles

$$\frac{1}{k^2} \left( \frac{w}{2} \right)^{1/2} \left[ E \left( \frac{1}{\kappa} \right) + \left( \frac{1}{\kappa^2} - 1 \right) K \left( \frac{1}{\kappa} \right) \right] = \text{const}. \quad (4.32)$$

$w(x)$  is the wave potential amplitude  $e\hat{E}(x)/k(x)$  normalized to  $\frac{1}{2}mv_\varphi^2$ ,

$$w(x) = \frac{2e\hat{E}(x)k(x)}{m\omega^2}. \quad (4.33)$$

The modulus  $\kappa$  of the elliptic integrals of the first and second kind,  $K(\kappa)$  and  $E(\kappa)$ , is defined as

$$\kappa^2 = \frac{2w}{w + y}. \quad (4.34)$$

$\sigma = \pm 1$  is the sign of the particle velocity in the wave frame. Finally,

$$\Phi(x) = -\frac{e}{2m\omega^2} \int_{-\infty}^x E_0(x') dx' \quad (4.35)$$

is, apart from a factor, the potential of the static field.

The corresponding equations for the phase variable  $\phi$  are skipped because these are of no further importance. Relations (4.31) and (4.32) can be derived from an action integral [50]. Thus, they are adiabatic invariants of the motion. The main point of this derivation is that since the equation of motion is not autonomous (and cannot be made so by simply transforming to the wave frame because time then reappears in the amplitude), energy and time have to be considered as an additional pair of canonical variables. These additional variables contribute to the action integral for untrapped particles, while their contribution vanishes in the case of trapped particles.

A difficulty arises from particles being trapped when the wave amplitude increases or being detrapped when it decreases. During such a transition the adiabatic assumption is violated because of the logarithmic divergence of the particle's bounce period  $T$ ,

$$T(\kappa) = 2 \left( \frac{2}{w} \right)^{1/2} \kappa K(\kappa), \quad (4.36)$$

in the vicinity of the transition point where  $\kappa$  approaches unity. Thus, an appreciable change of the adiabatic invariant might occur in a transition; for example, in the limiting case of an electron sitting on a wave top all the time and traveling with phase velocity the change of the adiabatic invariant is of order unity. However, for the vast majority of particle trajectories the adiabatic invariant changes by an amount of order  $\varepsilon = \max |\lambda \partial_x \hat{E} / \hat{E}|$ , as has been explicitly shown [54]. Changes of order unity can only occur if the trajectory crosses the separatrix within a narrow neighborhood of the potential energy maxima. Thus the effect of a nonadiabatic transition on the adiabatic invariant is negligible with respect to the whole ensemble of particle trajectories.

For the following considerations the acceleration of electrons in a wave field of the type shown in Fig. 4.12 is significant. For simplicity  $\lambda$  is taken to be constant and no static electric field is taken into account. Invariant (4.31) then becomes

$$1 + y + \sigma \frac{4}{\pi} (w + y)^{1/2} E(\kappa) = v_i^2, \quad (4.37)$$

where  $v_i$  is the initial particle velocity far outside of the wave field, normalized to the phase velocity  $v_\varphi$ .

Three different groups of particles have to be distinguished:

- A. Particles entering from the right with initial velocity  $v_i < 0$ . In the wave frame, these particles move initially to the left, i.e.,  $\sigma = -1$ , with a normalized energy  $y_0 = (v_i - 1)^2 > 1$  in the wave frame.
- B. Particles entering from the left with  $0 < v_i < 1$ . Initially, in the wave frame, they move to the left,  $\sigma = -1$ , with an energy in the range  $0 < y_0 < 1$ .
- C. Particles entering from the left with  $v_i > 1$ , which corresponds to a positive velocity ( $\sigma = +1$ ) in the wave and  $y_0 > 0$ .

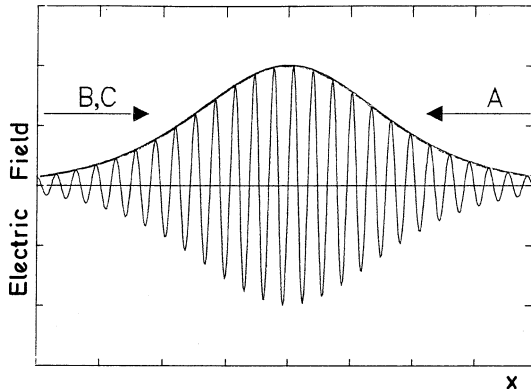


**Fig. 4.12** Electron plasma wave of constant wavelength moving at phase velocity  $v_\varphi$  to the right. Wave amplitude  $\hat{E}(x)$  is fixed in the lab frame: for a comoving observer the wave grows until reaching a maximum and then decays. Velocities of the incoming electrons, A:  $v_i = v_0/v_\varphi < 0$ , B:  $0 < v_i < 1$ , C:  $v_i > 1$

The motion of a particle entering with initial velocity  $v_i$  is characterized in this case by the dependence of the particle energy  $y$  on the wave amplitude  $w$ . This is shown in Fig. 4.13a for  $\sigma = -1$  (particles of group A) and (b) for  $\sigma = +1$  (particles of group C). The upper parts above the straight lines  $y = w$  describe the motion of untrapped particles, whereas the lower parts describe trapped particles. The lower parts of (a) and (b) are identical, since the direction of motion  $\sigma$  oscillates along the trajectory of a trapped particle. When a curve reaches the straight line  $y = w$ , the corresponding particle is trapped or detrapped. As discussed above, there is no discontinuity in the action integrals at the transition point, so that the trajectories of trapped and untrapped particles can be connected there continuously.

If trapping occurs for a given  $v_i$ , the transition point  $y_t = w_t$  can be calculated from (4.37)

$$1 + w_t + \sigma \cdot \frac{4}{\pi} \sqrt{2w_t} = v_i^2. \quad (4.38)$$

After trapping, the particle's trajectory is given by

$$w^{1/2} \left[ E \left( \frac{1}{\kappa} \right) + \left( \frac{1}{\kappa^2} - 1 \right) K \left( \frac{1}{\kappa} \right) \right] = w_t^{1/2}. \quad (4.39)$$

For a wave field with normalized maximum amplitude  $w_0$  (or  $\tilde{w}_0$ ) only those parts of Fig. 4.13a,b with  $w < w_0$  ( $w < \tilde{w}$ ) apply. Particles moving on trajectories which are inside the solid curve in (a) cannot be trapped by the wave, irrespective of the maximum wave amplitude. Within this region, particles are either reflected with final velocity outside the wave  $v_f = -v_i$  (curve c), or cross the wave packet with  $v_f = v_i$  (curves b, d). In both cases no net change of particle energy results. It follows from (4.37) that all particles entering with  $0 < v_i < v_c$  from the left or with

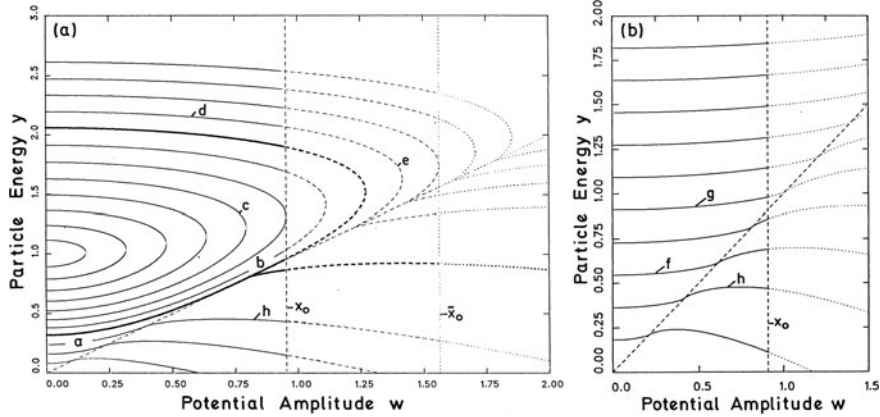


**Fig. 4.13** Particle energy  $y$  in the frame as a function of wave amplitude  $w$  for different initial velocities  $v_i = v_0/v_\varphi$ . (a): particles belonging to group A ( $\sigma = -1$ ), solid curve:  $|v_i| = v_c$  (critical velocity for trapping). (b): particles belonging to group C ( $\sigma = +1$ ). Dashed lines in diagonal direction:  $y = w$

$-v_c < v_i < 0$  from the right pass through or are reflected, depending on the critical velocity

$$v_c = \left[ 1 - \frac{8}{\pi^2} \right]^{1/2} \simeq 0.435, \quad (4.40)$$

Reflection occurs when the maximum wave amplitude  $w_0$  exceeds the value 1.27. Another essential result of (4.37) is that a particle entering a wave of the type of Fig. 4.12 can only gain energy when it becomes temporarily trapped.

In order to check the degree of adiabaticity of (4.37) the exact equation of motion (4.30) was integrated numerically for a large number of different initial values with a symmetric Epstein profile for the wave envelope:

$$w(x) = \frac{4w_0 e^{\gamma kx}}{(1 + e^{\gamma kx})^2}.$$

The theoretical predictions are not affected by the detailed shape of the envelope. In Fig. 4.14 the final velocity is plotted versus the initial velocity for different damping coefficients  $\gamma$ . The branch around the origin represents the reflection regime, the cross shaped structure around  $v_f = v_i = 1$  is the trapping regime; and the remaining two curves are produced by particles which are trapped over a fraction of a bounce period only and scattered back to final velocities  $v_i < -v_c$ . As can be inferred from the figure the adiabatic theory agrees with the numerical results up to rather high values of  $\gamma$  [cases (a), (b)]. For stronger variations significant deviations from adiabaticity occur [cases (c), (d)].

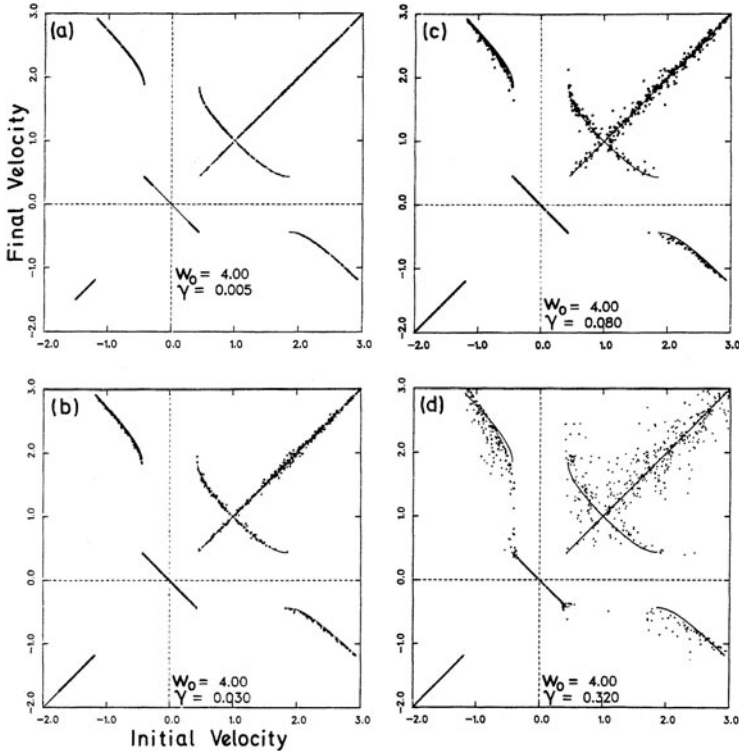


**Fig. 4.14** Spectra of final velocities  $v_f$  as a function of initial velocity  $v_i$  for different coefficients  $\gamma$ . Curves: theoretical spectra, dots: numerical points

### 4.3.2 Particle Acceleration by a Discontinuous Langmuir Wave

A resonantly excited electron plasma wave may be idealized by a suddenly rising wave structure as presented in Fig. 4.15 which results from cutting the wave structure of Fig. 4.12 in the middle. The acceleration achievable in such a wave field can be investigated by the same methods employed before. The main difference from the former case is that particles entering the wave field from the left across the discontinuity start with an initial energy  $y_0$  which in the wave frame is given by

$$y_0 = (v_i - 1)^2 - w_0 \cos \tau_0 . \quad (4.41)$$

Now,  $y_0$  depends not only on the initial velocity  $v_i$ , but also on the phase  $\tau_0$  ( $0 < \tau_0 < 2\pi$ ). Thus, for particles entering with a given value of  $v_i$  there exists a whole spectrum of initial energies  $y_0$ , leading to a corresponding spectrum of final velocities  $v_f$ .

The possible range of final velocities for given  $v_i$  and  $w_0$  is obtained from (4.37) and Fig. 4.13a,b by taking into account all values of  $y_0$  which belong to an interval of width  $2w_0$  around the particle energies  $y = (v_i - 1)^2$ .

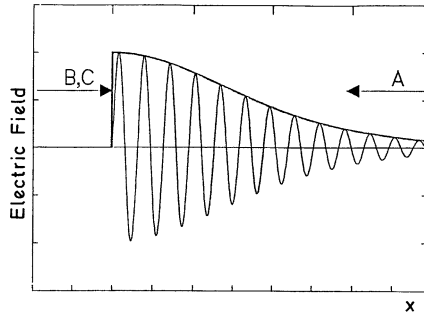


**Fig. 4.15** Electric field of a wave with discontinuously rising envelope

A comparison between theoretical prediction and numerical calculation is shown in Fig. 4.16. According to theory, all  $(v_i, v_f)$ -points have to be within the two spoon-shaped regions (solid curves). Again, there is excellent agreement with the numerical results. Particles entering the field region from the left with initial velocities below the phase velocity can be accelerated to a maximum speed which is independent of  $v_i$ , but which increases with  $w_0$ , i.e., with  $\hat{E}_{\max}$ :

$$v_{\max} = v_\varphi \left( 1 + 2 \frac{\hat{E}_{\max}}{v_\varphi} + \frac{4}{\pi} \left( \frac{2\hat{E}_{\max}}{v_\varphi} \right)^{1/2} \right)^{1/2}. \quad (4.42)$$

This important formula shows that, owing to the time dependence of  $\hat{E}$  in the wave frame, the maximum energy gained by a particle from the wave in the wave frame is *not*  $\Delta\mathcal{E} = 2 \times \frac{1}{2}m(v_i - v_\varphi)^2$ , although this is frequently found in the literature. The latter formula only holds for a single reflection without temporary trapping.

The behavior illustrated by Fig. 4.16 is quite contrary to that of a wave of the type shown in Fig. 4.12 where the maximum  $v_f$  depends on  $v_i$  but not on  $w_0$  as soon as a particle has enough initial energy to undergo trapping. Another important difference is that in a suddenly rising field particles with arbitrarily low initial velocity may be trapped provided that the field strength is sufficiently high and the envelope rises steeply enough, whereas in the case of slowly increasing amplitude no particles with  $v_i < v_c \simeq 0.435$  can be trapped.

### 4.3.3 Vlasov Simulations and Experiments

The energy spectrum of Fig. 4.16 arises from electrons trapped and successively accelerated and detrapped only once. For a given  $v_i$  considerable energy broadening is due to the different phases with respect to the electron plasma wave at which the particles cross the narrow resonance zone. Additional spreading of energy results from folding over a suitable interval of initial velocities by which a starting temper-

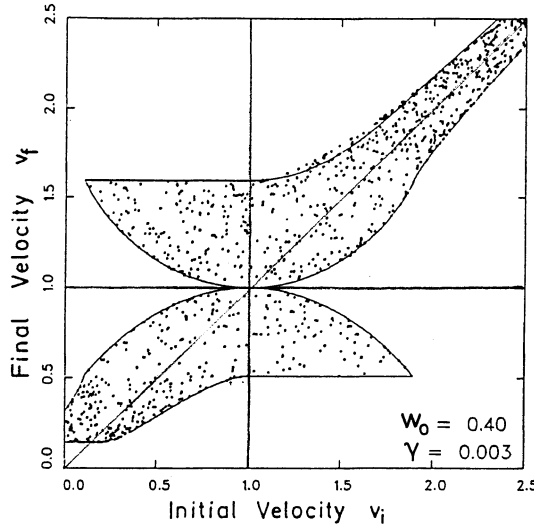


**Fig. 4.16** “Schneider’s spoons”. Spectrum of final velocities  $v_f$  of particles accelerated in a Langmuir wave of suddenly rising amplitude

ature  $T_c$ , always present in a real plasma, is simulated. Finally, only a small fraction of electrons can escape from the plasma after having crossed the wave once, whereas the majority of them are trapped by the electrostatic field and may cross the critical region several times. This mechanism leads to additional heating, if not increased relative energy spreading. To analyze these aspects a kinetic description or particle simulations must be used.

Extensive particle simulations [19, 43, 48, 49, 55–57] have shown that the spectrum of the hot electrons is close to Maxwellian and was sometimes attributed to multiple acceleration by Langmuir waves [43]. More recent calculations based on the Vlasov equation [45] clearly confirm the Maxwellian energy distribution of the trapped electrons and thus the existence of a temperature  $T_h$ . In Fig. 4.17 the space averaged distribution functions  $f(v) = \langle f(x, v) \rangle$  for driver strengths of  $\hat{E}_d = 0.04$  (a) and  $\hat{E}_d = 0.08$  (b) in a fixed ion density profile of  $L_c = 300\lambda_D$  are shown and the values of  $T_h = 16$  and  $36\text{ keV}$  are calculated. In addition to the much reduced noise in the Vlasov simulations the significant result which is found is that the Maxwellian character of  $f(x, v)$  is already established at the right edge of the resonance zone of Fig. 4.2. In a run with  $\hat{E}_d = 0.05$  and  $L_c = 300\lambda_D$  a modest variation of  $f(x, v)$  was only found when  $x$  was varied from  $x = x_m$  (end of resonance) to  $x = L_c$ . There is a maximum velocity  $v_{\max}$  at which the Maxwellian distribution suddenly breaks up. A comparison of these “experimental” values with formulas from the literature can be made, in particular with Schneider’s expression (4.42) and another simple expression, which in normalized quantities reads [58]

$$v_{\max} = \left(8\hat{E}_d L_c\right)^{1/2}.$$

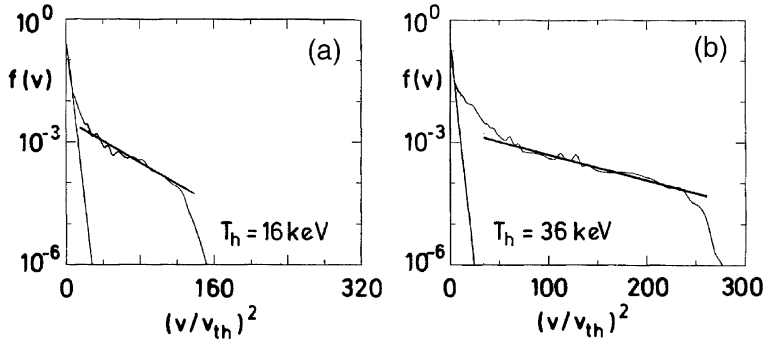


**Fig. 4.17** Electron distribution function averaged over space,  $f(v) = \langle f(x, v) \rangle$  for a normalized driver  $\hat{E}_d = 0.04$  (a) and  $\hat{E}_d = 0.08$  (b). The ion density scale length is  $L_c = 300\lambda_D$  in both cases.  $T_h$  temperature of the fast electrons,  $T_c$  “cold” bulk temperature (steep straight lines)

The result of a comparison with seven Vlasov runs is summarized in Table 4.1. Thereby  $v_\varphi$  was taken at  $x = x_m$ . The agreement with (4.42) is excellent whereas the simpler formula above, though leading to too low values, may serve for a rough estimate. Its agreement with simulations is expected to improve with decreasing scale length  $L_c$ . According to both formulae  $v_{\max}$ , and the corresponding  $T_h$  increase with phase velocity  $v_\varphi$ . This means that more energetic electrons are to be expected from electron plasma waves excited in flat density profiles, e.g., from stimulated Raman scattering and two-plasmon decay; its confirmation by particle simulations and experiments is well established [48, 59–62] (see also Chap. 8). For practical purposes scaling laws for  $T_h$  and the number density  $n_h$  of hot electrons are important. For the construction of such functional dependences from simple models in the ns laser pulse regime the reader may consult the excellent review by Haines [64]. In the long pulse regime all authors seem to agree on a combined  $(I_0\lambda^2)^\delta$ -dependence of  $T_h$ , and most of them (Vlasov simulations included) find  $\delta$ -values not far from 1/3. According to [48],

$$T_h \simeq 14(I_0\lambda^2)^{1/3} T_c^{1/3}, \quad (4.43)$$

when  $T_h$ ,  $T_c$  are measured in keV,  $I_0$  in units of  $10^{16} \text{ Wcm}^{-2}$  and  $\lambda$  in  $\mu\text{m}$ . Their best fit to experiments at  $(I_0\lambda^2) > 10^{15} \text{ W}\mu\text{m}^2\text{cm}^{-2}$  was  $\delta = 0.25$ . In this context the reader interested in a comparison with other simulations may consult [57].

Electron trapping and acceleration is one root of anomalous heat flux density  $\mathbf{q} = \mathbf{q}_e$  out of the critical layer [40, 45, 9]. In Fig. 4.18a the spatial distribution of  $q_e$  from a Vlasov simulation at  $\tau = 60\pi$  (dashed line) and  $\tau = 80\pi$  is presented for  $E_d = 0.04$  and  $L_c = 300\lambda_D$ . The first isolated peak of  $q_e$  reaches its maximum exactly at the border  $x_m$  of the resonance zone. The divergence of  $q_e$  manifests itself in large deviations of single volume elements from adiabatic behavior. In Fig. 4.18b the dependence of the kinetic pressure  $p_e = m \int (v - u_e)^2 f dv$  [see (2.84), relativistic (8.53); here  $u_e$  is the mean fluid velocity] on the electron density

**Table 4.1** Comparison of the maximum electron velocity from a Vlasov simulation of resonance absorption with analytical formulae

$\hat{E}_d$	$L = 100 \lambda_D$			$L = 300 \lambda_D$			
	0.06	0.1	0.2	0.04	0.08	0.12	0.16
Vlasov simulation	$\approx 10$	$\approx 12$	$\approx 15$	$\approx 12$	$\approx 17$	19.5	$\approx 22$
Equation (4.42)	10.7	11.9	14.3	13	17.6	19.5	21.2
$v_{\max} = (8\hat{E}_d L_c)^{1/2}$	6.9	8.9	12.6	9.8	13.9	17	19.6

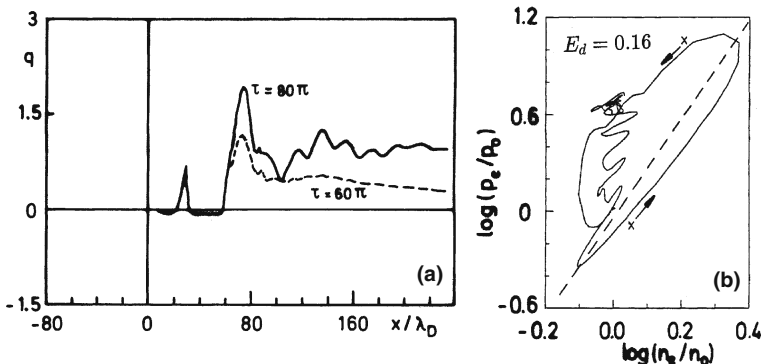


**Fig. 4.18** (a): Anomalous heat current density  $q = (m/2) \int (v - u_e)^3 f dv$  at  $\tau = 60\pi$  (dashed) and  $80\pi$  (solid) for a driver  $E_d = 0.04$ . (b):  $\log n_e$ - $\log p_e$ -plot of an electron fluid element of particle density  $n_e$  and pressure  $p_e$  in the highly nonlinear electron plasma wave. The deviation of the trajectory from the straight line is a measure of the time-integrated divergence of the local heat flow  $q$ . Driver strength is  $E_d = 0.16$

$n_e$  is shown in a log–log plot for a driver  $E_d = 0.16$ . In the absence of heat flow each volume element can move only along the diagonal corresponding to  $\gamma = 3$ . Owing to the heat flux of the fast electrons a single volume element, when compressed in a density spike of the wave, at first remains in the neighborhood of the  $\gamma = 3$  line (see lower arrow), but then, in the valley of the wave, a jet of fast electrons and with them a high value of  $q_e$  have been built up. The latter is responsible for the trajectory in the diagram far above the diagonal (follow upper arrow).

## 4.4 Wavebreaking

The excitation of large amplitude electron plasma waves has attracted great and continuous attention since 1959 when it was shown that cold plasma oscillations break when the oscillatory velocity  $v_{os}$  equals their phase velocity  $v_\phi = \omega/k$  [65]. Later this criterion was extended to warm electron plasma waves and it was

found from the fluid approach that the electron density  $n_e$  of a free harmonic wave in a homogeneous plasma of density  $n_0$  must fulfill the inequality  $n_e/n_0 \leq (v_\varphi/s_e)^{2/(\gamma+1)}$  [66]. When approaching this limit, the electrostatic potential of the wave and its enthalpy are growing so rapidly that a single electron fluid element begins to be reflected from the periodic potential and wavebreaking sets in [42].

These criteria were derived for homogeneous plasmas. In not too steep density gradients where the WKB approximation applies, the Coffey criterion may still be used (see below). In the resonance zone the wave becomes strongly inhomogeneous, the WKB approximation no longer holds and, therefore, breaking at resonance has to be distinguished from breaking off resonance. For the cold plasma ( $T_e = 0$ ) at rest a fluid dynamic breaking criterion was formulated in [18]. From these four papers it becomes clear what wavebreaking means within a fluid approach. On the other hand, as seen in the foregoing section, kinetic phenomena greatly affect the structure of the Langmuir wave and its damping. Hence, two main questions arise: (i) what is a meaningful definition of wavebreaking in the kinetic theory, and (ii) what is the appropriate breaking criterion, if kinetic effects become significant or dominate. For example, one may ask whether such a phenomenon as kinetic wavebreaking occurs at all when one keeps in mind how strongly the Langmuir wave is damped by particle trapping and acceleration. It is amusing – and surprising – that the scientific community has been using the concept of “wavebreaking” in laser-matter interaction for more than 20 years without having been aware of this situation, except [67]: “Thus we see that there is no one-to-one correspondence between hot electron production and wavebreaking as is sometimes suggested”. Only tentative, more or less vague characterizations of wavebreaking have been presented which, at a closer inspection, may not appear very useful. A definition of wavebreaking was given only later [68]. In connection with particle acceleration by superintense lasers the phenomenon of Langmuir-type wavebreaking has been enriched by new fundamental aspects [69–71].

For clarity, wavebreaking in the fluid approach is referred to as “hydrodynamic wavebreaking” here. Since resonance absorption of smooth laser pulses becomes quasi-stationary after very short times (several laser periods) it is appropriate to develop a steady state model for cold wavebreaking in the resonance region [39]. Such a model is interesting in itself and may serve to illustrate the difference of stationary wavebreaking out of resonance. In the following subsection hydrodynamic breaking criteria are derived. A possible solution to general wavebreaking is presented in the subsequent paragraph. Currently we may distinguish five types of wave breaking: geometrical breaking, cold plasma wave breaking, fluid-like breaking in the warm plasma, kinetic wave breaking, and resonant (wave) breaking. The second and third types are also referred to as hydrodynamic breaking.

Geometrical wavebreaking was discovered late although, intuitively, it may appear as the most natural breaking scenario. It was found in 2D and 3D PIC simulations of the wake of an intense ultrahot laser pulse traveling through an underdense plasma. When the wave fronts off axis travel faster than the central part they may collapse and interpenetrate leading to the destruction of the wave [70, 71]. Resonant breaking of regular fluid dynamics, in particular of a wave, is induced by local anharmonic resonance (see Sect. 8.3.3).

#### 4.4.1 Hydrodynamic Wavebreaking

In a cold plasma ( $T_e, s_e = 0$ ) there is no energy transport out of the resonance region unless the plasma is streaming at a finite velocity  $v_0$ . Introducing this in (4.19) by setting  $x_i = a + \int v_0(a, t) dt$  and  $x_e = x_i + \int v_e dt$  one arrives at the harmonic oscillator equation,

$$\frac{\partial^2}{\partial t^2} v_e + \omega_p^2(a, t) v_e = \frac{1}{2} \omega^2 v_d e^{-i\omega t} + \text{c.c.}, \quad (4.44)$$

with resonance frequency  $\omega_p$  varying in time: A volume element starting in the overdense region is off resonance owing to  $\omega_p \gg \omega$ ; it then approaches resonance  $\omega_p = \omega$  and, rarefying further, in the underdense region ( $\omega_p < \omega$ ) it decouples again from the driver. Formally, (4.44) is obtained from (4.21) by setting  $s_e = 0$ . For  $v = v_e - v_0$  a sufficiently accurate solution of (4.44) in our context here is found from (3.78),

$$v = i \frac{\omega^2 v_d}{2\omega_p^{1/2}} e^{-i\varphi} \int_0^t \frac{e^{i(\omega t' - \varphi')}}{\omega_p^{1/2}} dt'; \quad \varphi(a, t) = \int_0^t \omega_p(a, t') dt', \quad (4.45)$$

if the flow velocity obeys the inequality  $v_0 \lesssim L\omega/\pi$ . With  $L$  the density scale length at resonance a self-consistent density profile is  $n_0 = n_c/(1 + a/2L)^2$ . Inserting  $n_0$  in (4.45) yields in the resonance region

$$v(a, t) = i \frac{L^{1/2} \omega^{1/2} v_d e^{i\omega a/v_0 + \sigma^2}}{v_0^{1/2}} \int_{-\infty}^{\sigma} e^{-i\sigma'^2} d\sigma', \quad \sigma = \frac{1}{2} t \left( \frac{\omega v_0}{L} \right)^{1/2}. \quad (4.46)$$

The modulus of  $\int_{-\infty}^{\sigma} e^{-i\sigma'^2} d\sigma'$  is the familiar Cornu spiral. It shows that secular growth of  $|v(a, t)|$  occurs around resonance (Fig. 4.19). From it the resonance width  $\Delta$ , with  $\sigma$  running from  $-\pi/2$  to  $+\pi/2$ , is deduced to be

$$\Delta = 2\pi \left( \frac{v_0 L}{\omega} \right)^{1/2}. \quad (4.47)$$

Wavebreaking occurs when in (4.19)  $\partial\delta_x/\partial a = -1$ . For this to occur at the edge of resonance ( $\sigma = \pi/2$ ).

$$\frac{v_d}{v_0} = \left| \frac{1}{2} + i \frac{\pi}{2} e^{i(\pi/2)^2} \int_{-\infty}^{\pi/2} e^{-i\sigma'^2} d\sigma' \right|^{-1} = 0.36 \quad (4.48)$$

must be fulfilled [39]. At resonance cold wavebreaking is due to the overlapping of two originally distinct volume elements as a result of their different phase shifts in the neighborhood of the resonance point. Due to such shifts a Langmuir wave in a cold streaming plasma may break as soon as  $v_{os} > 0.75 v_\varphi$  is satisfied, i.e., at a

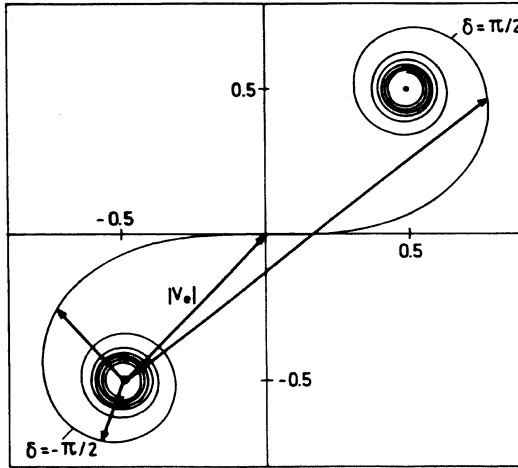


**Fig. 4.19** The value of  $|w| = \left| \int_{-\infty}^{\sigma} e^{-i\sigma'^2} d\sigma' \right|$  is the length of the vector extending from the center of the lower Cornu spiral to a point of the double spiral determined by the parameter  $\sigma$ , which is proportional to the length of the arc, i.e., time. Maximum growth occurs around the resonance  $\sigma = 0$ . The maximum of  $|w| = 2.074$  is reached at  $\sigma = 1.53$  (compare  $\pi/2 = 1.57$ )

slightly lower than the Dawson limit [65]. In order to compare the breaking time  $t_b$  of [18] with (4.48) it is reasonable to set  $t_b = \Delta/v_0$ . In this way the laser intensity causing breaking there differs from ours by a factor of 3.

Off resonance Coffey's criterion applies. Its derivation from (4.17) is as follows. In a reference system moving with local phase velocity  $v_\varphi$

$$u = v - v_\varphi, \quad \frac{\partial}{\partial x} n_e u = 0 \Rightarrow n_e u = n_0 v_\varphi, \quad n_e = \frac{n_0}{1 - v/v_\varphi},$$

$$\frac{1}{2} m_e \frac{\partial u^2}{\partial x} = -m_e \frac{s_0^2}{\gamma - 1} \frac{\partial}{\partial x} \left( \frac{n_e}{n_0} \right)^{\gamma-1} - eE, \quad \gamma \neq 1,$$

holds. By eliminating  $E$  and  $u$  the following relations are obtained for  $\xi = n_e/n_0$ ,

$$\gamma > 1 : \frac{\partial^2}{\partial x^2} \left\{ \xi^{\gamma-1} + \frac{\mu}{\xi^2} \right\} = b(\xi - 1), \quad \mu = \frac{\gamma - 1}{2} \left( \frac{v_\varphi}{s_0} \right)^2,$$

$$b = (\gamma - 1) \frac{\omega_p^2}{s_0^2},$$

$$\gamma = 1 : \frac{\partial^2}{\partial x^2} \left\{ \ln \xi + \frac{\mu}{\xi^2} \right\} = b(\xi - 1), \quad \mu = \frac{1}{2} \left( \frac{v_\varphi}{s_0} \right)^2, \quad b = \frac{\omega_p^2}{s_0^2}.$$

If these equations are integrated once, from a position with  $\xi =$  minimum to an appropriate  $x$ -value,

$$\left( \frac{s_0^2}{v_\varphi^2} \xi^{\gamma-2} - \xi^{-3} \right) \xi' = \frac{b}{2\mu} \int_{x:\xi=\min}^x (\xi - 1) dx, \quad (4.49)$$

it can be seen that the solution  $\xi(x)$  is symmetric with respect to its minima and maxima for

$$\frac{n_e}{n_0} \leq \xi_0 = \left( \frac{v_\varphi}{s_0} \right)^{2/(\gamma+1)}. \quad (4.50)$$

However, there is no permanent wave for  $\xi > \xi_0$ .  $\xi = \xi_0$  is a branch point with a periodic wave of zero radius of curvature in the maxima and an aperiodic solution. (Note that in a periodic wave with  $\xi > \xi_0$  intervals could be found in which the LHS and RHS of (4.49) would have different signs!). The physical reason for the existence of  $\xi_0 < \infty$  is that for  $\xi > \xi_0$  the compression work increases in such a way that the energy balance can no longer be satisfied. In the derivation of the criterion the integration is done over half a wavelength; hence, it is invariant with respect to WKB type inhomogeneities.

#### 4.4.2 Kinetic Theory of Wavebreaking

A kinetic wave description is needed to answer questions (i) and (ii) in a satisfactory manner. It becomes further clear that in the case of  $v_{os} \ll v_{th}$  the answers can hardly be found on the basis of PIC simulations owing to their inherent large noise. Therefore, again the system (4.25) in combination with the capacitor model is used and the driving field  $\hat{E}_d$  is measured in units of the thermal field  $E_{th}$  as in Sect. 4.2.2. The ions are treated as a fixed smooth neutralizing background of inhomogeneity length  $L$ , the latter being chosen as a free parameter. The initial velocity distribution is Maxwellian,  $f_0 = (2\pi)^{-1/2} v_{th}^{-1} \exp(-x/L) \exp(-v^2/2v_{th}^2)$ . Figure 4.20 shows the evolution of  $f$  in terms of contour lines  $f = \text{const}$  after 20, 25 and 40 periods for  $L = 300 \lambda_D$  and  $\hat{E}_d = 0.04$  with  $E_{th} = kT_e/e\lambda_D$  and Debye length at resonance,  $\lambda_D = v_{th}/\omega$ . After a much higher number of cycles  $f$  looks very similar and does not show any new aspects, thus indicating that a quasi-steady state is reached at the times considered here. Short reflection may convince the reader that closed loops in the contour plots refer to trapped particles. The contour lines extending to high velocities and leaning to the right are to be assigned to accelerated and detrapped particles. They are modulated by the periodic wave potential and their inclination increases as is characteristic for free streaming particles. The electron density is plotted in Fig. 4.21. The dashed smooth curve is the Coffey limit (4.50). Owing to strong nonlinear damping the Langmuir wave never reaches this limit, except for the first maximum, even at much higher driver strengths  $\hat{E}_d$ . This behavior is confirmed for three other  $L$ -values in Fig. 4.21. The Coffey criterion does not apply to the first (resonant) density maximum. For instance, in (a) it is clearly higher than the Coffey limit, but there is no indication of breaking (see also the first smooth and regular

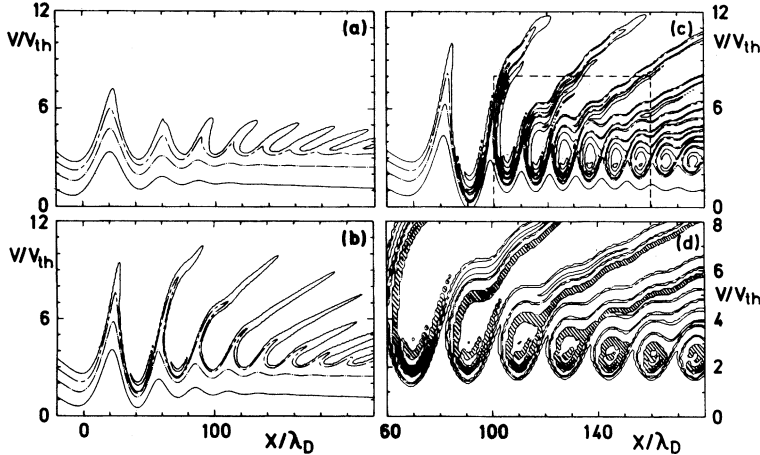


**Fig. 4.20** Distribution function evolving from the initial distribution  $f_0(x, v) = (2\pi)^{-1/2} \exp(-x/L) \exp(-v^2/2v_{th}^2)$  with  $L = 300 \lambda_D$  and  $E_d = 0.04$  after (a) 20, (b) 25, and (c) 40 periods; (d) enlarged plot of area indicated in (c) after 50 periods. The contour lines refer to  $f = 10^{-1}, 10^{-2}, 10^{-3},$  and  $10^{-4}$ , the critical density with  $\omega_p = \omega$  is located at  $x = 0$ . Trapped electrons form closed loops (d); the velocity modulation of the detrapped electrons is due to the periodic electric field of the Langmuir wave.  $\hat{E}_d$  is normalized to  $E_{th} = kT_e/e\lambda_D$ ,  $\lambda_D = v_{th}/\omega$

maximum in Fig. 4.22a,b). For  $\hat{E}_d \geq 0.04$  all maxima of  $n_e$  except the first do not increase further; but the wave remains periodic and smooth. As a first result, we can clearly see that, although fast electrons are generated by trapping, the wave is still regular and periodic in the sense mentioned above. In conclusion, fast electron generation alone does not indicate wavebreaking.

However, above a certain threshold  $\hat{E}_d^*$  the distribution function undergoes a qualitative change: the Langmuir wave becomes irregular, it breaks, as illustrated by Fig. 4.22 for  $n_e$  and  $E$  at  $\hat{E}_d = 0.2$  in a density profile of scale length  $L = 300\lambda_D$ . Inspection of the corresponding evolution of the distribution function (see Fig. 4.23) reveals the reason for such a behavior. The mean oscillatory velocity in the resonance region becomes so large that trapping of whole *bunches* of rather slow electrons occurs. These bunches of coherently moving electrons are partly *coalescing* (see black zones in Fig. 4.23) and remain trapped for at least several wavelengths, thus creating an additional aperiodic macroscopic electric field. From a fluid point of view the phenomenon is similar to what is called intense mixing of volume elements exhibiting different oscillation phases. (A Grassberger–Procaccia analysis of the electric field and the electron density at fixed  $x$  reveals the transition from a quasiperiodic to a chaotic attractor [45]). The electrons in these bunches contribute to the heat conduction, so that the heat flux  $q$  increases suddenly with wavebreaking. For example at  $x = 50\lambda_D$  one obtains ( $\eta$  refractive index,  $q$  electron heat flow density)

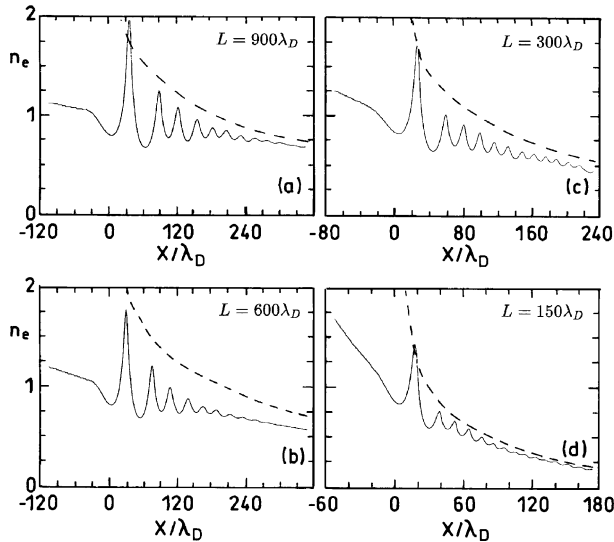


**Fig. 4.21** Resonantly excited electron plasma waves in ion density profiles with different scale lengths  $L$ . Electron density  $n_e$  and breaking limit after Coffey (dashed curves); off resonance this limit is never reached owing to nonlinear Landau damping. (a)  $\hat{E}_d = 0.06$ ,  $\omega t = 120 \pi$ ; (b)  $\hat{E}_d = 0.06$ ,  $\omega t = 80 \pi$ ; (c)  $\hat{E}_d = 0.08$ ,  $\omega t = 100 \pi$ ; (d)  $\hat{E}_d = 0.1$ ,  $\hat{\omega}t = 70 \pi$

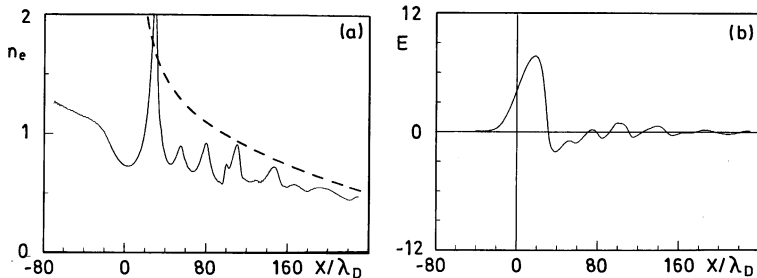


**Fig. 4.22** Langmuir wave excited by driver of strength  $\hat{E}_d = 0.2$  in a plasma of scale length  $L = 300 \lambda_D$ : the irregular shape indicates breaking. (a) Electron density  $n_e$ ; (b) electric field  $E$  as a function of space; dashed curve: Coffey limit

$$\begin{array}{lll} \eta : & 0.06 & 0.09 & 0.12 \\ q : & 0.31 & 0.32 & 0.49 \end{array}$$

In contrast to hot electron generation the bunches are not accelerated to high energies.

As a consequence of these numerical studies, the following definition can be given: Wavebreaking is the loss of periodicity in at least one of the macroscopically observable quantities [68]. This definition extends to both hydrodynamic and kinetic descriptions. In contrast to a linear wave where an irregularity occurs in all variables

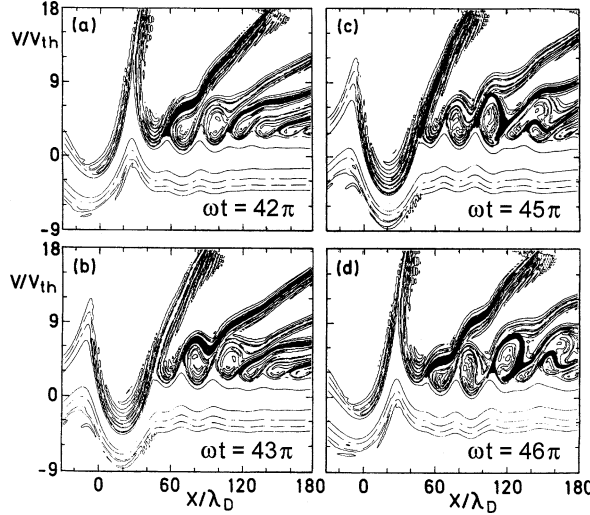


**Fig. 4.23** Route to wavebreaking. The distribution function for  $L = 300 \lambda_D$  and  $\hat{E}_d = 0.2$  after (a) 21, (b) 21.5, (c) 22.5, and (d) 23 periods. Contour lines for  $f = 10^{-1}, 10^{-2}, 10^{-3}$ , and  $10^{-4}$ . Trapping and coalescence of entire electron bunches is evident (see black colored streaks)

simultaneously, breaking may appear to a different degree in the various quantities (e.g.,  $n_e$  and  $E$  in Fig. 4.22). The first, i.e., resonant density maximum may satisfy Coffey's inequality or exceed this limit, even when the wave does not break (cf. Figs. 4.21 and 4.22).

Starting from the breaking condition for the streaming cold plasma, we replace the streaming velocity by the group velocity of the plasma wave, because the latter is now the speed of energy transport (at least approximately in a nonlinear wave). From the fluid theory of resonance absorption we obtain for the group velocity at the end of the resonance zone  $v_g = s_e^2/v_\varphi \approx 2(L/\lambda_D)^{-1/3}v_{th}$ . Inserting this into (4.48) at the place of  $v_0$  yields

$$\hat{E}_d > \hat{E}_d^* = 0.72(L/\lambda_D)^{-1/3}. \quad (4.51)$$

This breaking threshold is in very good agreement with the results of the Vlasov simulations, which are displayed in Fig. 4.24. The reason for the validity of inequality (4.51) at finite electron temperature is that in the resonance region the electronic oscillatory motion  $v_e$  is mainly determined by the total electric field  $E = \hat{E}_d + E_{wave}$ , and is only slightly affected by the much smaller force due to the electron pressure gradient [72].

Next, the threshold intensity for wavebreaking is calculated. Making use of the scaling  $L/\lambda_D \sim I_L^{-1/2}$  from [49], where  $I_L$  is the vacuum laser intensity, (4.51) translates to  $I_L^* = 2 \cdot 10^{15} \text{ W/cm}^2$  for the Nd-laser if a degree of absorption of 25% is assumed.

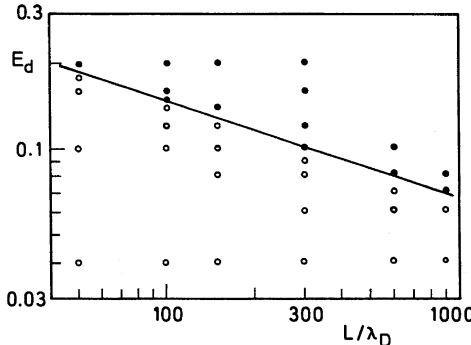


**Fig. 4.24** Driver strength threshold  $\hat{E}_d^*$  for wavebreaking as a function of scale length  $L$ . Straight line: Eqs. (4.48) and (4.51). The circles in the  $(\hat{E}_d, L)$ -plane represent Vlasov simulations with wavebreaking (solid) and without wavebreaking (blank)

Finally it is mentioned that the kinetic analysis of wavebreaking of freely propagating Langmuir waves in a *homogeneous* plasma shows that the same phenomenon also occurs here and that one scenario of breaking (others may also exist) is again trapping of *entire bunches* of electrons. However, the limit at which the wave breaks is much higher than the Coffey criterion would indicate. It must also be mentioned that in the light of recent PIC and Vlasov simulations (for example [71]) it appears doubtful whether the hydrodynamic breaking limit becomes ever relevant because of the sudden increase of collective noise produced by kinetic effects. It is an open question how the two criteria correlate.

We conclude that wavebreaking is a phenomenon on its own, to be distinguished from trapping of more or less uncorrelated electrons. The definition of wavebreaking presented here has a clear meaning and is also applicable to a kinetic description. Further, it has been shown that a criterion for wavebreaking in smooth ion density profiles can be deduced from the model of a cold streaming plasma. In addition, the Coffey criterion is not applicable to resonance absorption.

In general, when adjacent electron fluid elements are driven by a spatially inhomogeneous intense electromagnetic field they easily happen to cross and to mix up together, i.e., the regular motion becomes disordered. In particular this is believed to happen in the so-called Brunel effect at the plasma-vacuum interface [20, 21] and in “ $j \times B$  heating” in the skin layer [73], and in collisionless absorption by collective interaction [74, 75]. In the light of deeper insight into the nature of collisionless absorption at high laser intensities (wave) breaking is a consequence of anharmonic resonance (Chap. 8). Wavebreaking and breaking of flow will lead to an increased plasma fluctuation level, spectral broadening of reflected laser light, temporal pulsations, Maxwellian-like spectra of accelerated particles, and eventually to lower saturation levels of stimulated Raman and Brillouin scattering at high laser intensities. It seems to be a widely accepted belief that wave breaking is an efficient mechanism for electron acceleration (“when the wave breaks electrons become fast”). Closer inspection, in particular analysis of resonant breaking, leads to the conclusion that

rather the opposite is true, i.e., first electrons are accelerated and then breaking sets in. Breaking is an extremely versatile phenomenon, like turbulence, and there may exist as many scenarios for its onset as in the latter.

## References

1. Denisov, N.G.: Sov. Phys. JETP **4**, 544 (1957) 153
2. Piliya, A.D.: Sov. Phys. Tech. Phys. **11**, 609 (1966) 153
3. Godwin, R.P.: Phys. Rev. Lett. **28**, 85 (1972) 153
4. Freidberg, J.P., Mitchell, R.W., Morse, R.L., Rudinski, L.I.: Phys. Rev. Lett. **28**, 795 (1972) 153, 159
5. Forslund, D.W., Kindel, J.M., Lee, K., Lindman, E.L., Morse, R.L.: Phys. Rev. A **11**, 679 (1975) 153
6. Kull, H.-J.: Linear Mode Conversion in Laser Plasmas, Report MPQ 50, Max-Planck-Institute for Quantum Optics, Garching (1981) 153, 154, 158
7. Kull, H.-J.: Phys. Fluids **26**, 1881 (1983) 153, 159, 160, 162, 172
8. Colunga, M., Mora, P., Pellat, R.: Phys. Fluids **28**, 854 (1985) 154, 160, 170, 171
9. Ruhl, H.: Plasma Sources Sci. Technol. **11**(3A), A154 (2002) 154, 181
10. Ginzburg, V.L.: The Propagation of Electromagnetic Waves in Plasmas. Pergamon Press, Oxford (1964) 155, 159, 161
11. Abramowitz, M., Stegun, I.A.: Pocketbook of Mathematical Functions. Harri Deutsch, Frankfurt/Main (1984) 157
12. Pert, G.J.: Plasma Phys. **20**, 175 (1978) 158, 159
13. Speziale, T., Catto, P.J.: Phys. Fluids **22**, 681 (1979)
14. Krueer, W.L.: The Physics of Laser Plasma Interactions, p. 39. Addison-Wesley, Redwood City, CA (1988) 158, 161
15. Hinkel-Lipsker, D.E., Fried, B.D., Morales, G.J.: Phys. Rev. Lett. **62**, 2680 (1989) 158
16. Gildenberg, V.B.: Sov. Phys. JETP **18**, 1359 (1964) 159
17. Speziale, T., Catto, P.J.: Phys. Fluids **20**, 990 (1977) 159
18. Koch, P., Albritton, J.: Phys. Rev. Lett. **32**, 1420 (1974) 159, 165, 166, 183, 185
19. DeGroot, J.S., Tull, J.E.: Phys. Fluids **18**, 672 (1975) 159, 180
20. Brunel, F.: Phys. Rev. Lett. **59**, 52 (1987) 161, 163, 190
21. Brunel, F.: Phys. Fluids **31**, 2714 (1988) 161, 163, 190
22. Landen, O.L., D.Stearns, G., Campbell, E.M.: Phys. Rev. Lett. **63**, 1475 (1989) 161, 162
23. Fedosejevs, R., et al.: Appl. Phys. B **50**, 79 (1990) 161
24. Fedosejevs, R., Ottmann, R., Sigel, R., et al.: Phys. Rev. Lett. **64**, 1250 (1990) 161, 162
25. Bergmann, A., Hüller, S., Mulser, P., Schnabl, H.: Europhys. Lett. **14**, 661 (1991) 162, 168
26. Eidmann, K., et al.: Europhys. Lett. **55**, 334 (2001) 162
27. Godwin, R.P.: Fresnel Absorption, Resonance Absorption, and Bremsstrahlung X-Rays in Laser-Produced Plasmas, Los Alamos Report LA-UR 93-1679 (1993) 163
28. Sauter, F.: Z. Phys. **203**, 488 (1967) 163
29. Forstmann, F., Gerhardts, R.R.: Metal Optics Near the Plasma Frequency, Chaps. 2, 3. Springer, Berlin (1986) 163
30. Manes, K.R., Ruppert, V.C., Auerbach, J.M., Lee, P., Swain, J.E.: Phys. Rev. Lett. **39**, 281 (1977) 163
31. Balmer, J.E., Donaldson, T.P.: Phys. Rev. Lett. **39**, 1084 (1977)
32. Godwin, R.P., Mueller, M.M.: Appl. Opt. **18**, 3555 (1979)
33. Maaswinkel, A.G.M., Eidmann, K., Sigel, R.: Phys. Rev. Lett. **42**, 1625 (1979)
34. Maaswinkel, A.G.M.: Opt. Commun. **33**, 62 (1980) 163
35. Dinger, R., Rohr, K., Weber, H.: Laser & Particle Beams **5**, 691 (1987) 163
36. Adam, J.C., Gourdin Serveniere, A., Laval, G.: Phys. Fluids **2**, 376 (1982) 164
37. Dragila, R.: Phys. Fluids **26**, 1682 (1983)
38. Adam, J.C., Heron, A.: Phys. Fluids **31**, 2602 (1988) 164

39. Mulser, P., Takabe, H., Nima, K.: *Z. Naturforsch.* **37a**, 201 (1982) 165, 183, 184
40. Mulser, P., Schneider, W.: In: McNamara, B. (ed.) *Excitation of Nonlinear Electron Plasma Waves and Particle Acceleration by Laser, Twenty Years of Plasma Physics*, p. 264. World Scientific, Singapore (1985) 166, 173, 174, 181
41. Kull, H.J.: *Phys. Rep.* **206**, 197 (1991) 167
42. Bergmann, A., Schnabl, H.: *Phys. Fluids* **31**, 3266 (1988) 167, 183
43. Bezerides, B., Gitomer, S.J., Forslund, D.W.: *Phys. Rev. Lett.* **44**, 651 (1980) 168, 180
44. Davidson, R.C.: *Methods in Nonlinear Plasma Theory*, Chap. 4. Acad. Press, New York (1972) 168
45. Bergmann, A.: *Nonlinear Resonance Absorption and Wavebreaking*, Dissertation, TH Darmstadt (1990) 168, 180, 181, 187
46. Zakharov, V.E.: *Sov. Phys. JETP* **69**, 334 (1989) 172
47. Büchl, K., Eidmann, K., Mulser, P., Salzmann, H., Sigel, R.: Plasma production with a Nd laser and non-thermal effects. In: Schwarz, H.J., Hora, H. (eds.) *Laser Interaction*, vol. 2, p. 512. Plenum Press, New York (1972) 173
48. Forslund, D.W., Kindel, J.M., Lee, K.: *Phys. Rev. Lett.* **39**, 284 (1977); *Phys. Fluids* **22**, 462 (1979) 173, 180, 181
49. Estabrook, K.G., Krueer, W.L.: *Phys. Rev. Lett.* **40**, 42 (1978) 173, 180, 189
50. Schneider, W.: Elektronenbeschleunigung durch inhomogene Langmuirwellen hoher Amplitude. Electron Acceleration by Inhomogeneous Langmuir Waves of High Amplitude), Dissertation, TH Darmstadt (1984) 173, 174, 175
51. Kruskal, M.: *J. Math. Phys.* **3**, 806 (1962) 174
52. Bogoliubov, N.N., Mitropolsky, Y.A.: *Asymptotic Methods in the Theory of Nonlinear Oscillations*. Gordon and Breach, New York (1962) 174
53. Pocobelli, G.: *Phys. Rev. Lett.* **43**, 1865 (1979) 174
54. Amodt, R.E., Jaeger, E.F.: *Phys. Fluids* **17**, 1386 (1974) 175
55. Estabrook, K.G., Valeo, E.J., Krueer, W.L.: *Phys. Fluids* **18**, 1151 (1975) 180
56. Bezerides, B., Gitomer, S.J.: *Phys. Rev. Lett.* **46**, 593 (1981)
57. Albritton, J.R., Langdon, A.B.: *Phys. Rev. Lett.* **45**, 1794 (1980) 180, 181
58. Krueer, W.L.: *Phys. Fluids* **22**, 1111 (1979) 180
59. Brooks, R.D., Berger, R.G., Pietrzik, Z.A.: Hot electron production by Raman scattering in a preformed underdense plasma. In: Hora, H., Miley, G.H. (eds.) *Laser Interaction*, vol. 6. Plenum Press, New York (1984) 181
60. Brooks, R.D., Pietrzik, Z.A.: *Phys. Fluids* **30**, 3600 (1987)
61. Hauer, A., et al.: Suprathermal electron generation transport and deposition in CO<sub>2</sub> laser irradiated targets. In: Hora, H., Miley, G.H. (eds.) *Laser Interaction*, Vol. 6. Plenum Press, New York (1984)
62. Aithal, S., Pepin, H.: *Phys. Fluids B* **4**, 263 (1992) 181
63. DeGroot, J.S., Mizuno, K., Rogers, J.H., Rasmussen, D., Rambo, P.W., Stone, R.A.: Microwave modelling of moderate laser-plasma interactions. In: Hora, H., Miley, G.H. (eds.) *Laser Interaction*, vol. 7. Plenum Press, New York (1986)
64. Haines, M.G.: The physics of the coronal region. In: Cairns, R.A., Sanderson, J.J. (eds.) *Laser-Plasma Interactions*, p.170, Proc. 20th Scott. Univ. Summer School in Phys. Edinburgh (1980) 181
65. Dawson, J.M.: *Phys. Rev.* **113**, 383 (1959) 182, 185
66. Coffey, T.P.: *Phys. Fluids* **14**, 1402 (1971) 183
67. Bezerides, B., Gitomer, S.J.: *Phys. Fluids* **26**, 1359 (1983) 183
68. Bergmann, A., Mulser, P.: *Phys. Rev. E* **47**, 3585 (1993) 183, 188
69. Bulanov, S.V., Pegoraro, F., Pukhov, A.M., Sakharov, A.S.: *Phys. Rev. Lett.* **78**, 4205 (1997) 183
70. Pukhov, A., Meyer-ter-Vehn, J.: *Phys. Plasmas* **5**, 1880 (1998) 183
71. Ruhl, H.: Collective Super-Intense Laser-Plasma Interaction, Habilitation, TU Darmstadt (2000) 183, 190
72. Mulser, P., Schnabl, H.: *Laser & Particle Beams* **1**, 379 (1983) 189
73. Krueer, W.L., Estabrook, K.: *Phys. Fluids* **28**, 430 (1985) 190
74. Gibbon, P., Bell, A.R.: *Phys. Rev. Lett.* **68**, 1535 (1992) [see vacuum heating] 190
75. Mulser, P., Ruhl, H., Steinmetz, J.: *Laser & Particle Beams* **19**, 23 (2001) 190

# Chapter 5

## The Ponderomotive Force and Nonresonant Effects

A momentum flux is associated with all varieties of plasma waves: electrostatic, electromagnetic, acoustic. As a consequence, a force is transmitted from the wave to a plasma element whenever the momentum flow changes there either in space or in time. As early as 1861 James Clerk Maxwell found out that a light beam of flux density  $I$ , when impinging normally upon a surface of reflectivity  $R$  in vacuo, exerts the pressure

$$p_L = (1 + R) \frac{I}{c} \quad (5.1)$$

This is a global force. In physics in general, and in plasma physics in particular, expressions for the radiation force  $f_p$  on a single charged particle or on a unit volume, i.e. a force density  $\pi$ , are needed. They are secular forces, in contrast to the rapidly changing oscillating force of an electric wave which causes the quiver motion of the electrons and, as far as they are of electric origin, they are given the name ponderomotive force (density). The expressions “light pressure”, “radiation pressure”, or “wave pressure” are also in use. In the following we treat them all as equivalent.  $f_p$  and  $\pi$  originate from the nonlinearity of the momentum equation of the particles.

There are two kinds of ponderomotive forces, one which has its origin in the single particle motion and another one which is caused by collective motions induced in the plasma. As a consequence the first kind leads to a force density  $\pi_0$  which is proportional to the average particle density whereas the second type, indicated by  $\pi_t$ , is proportional to the fluctuation level changes of particle densities. In the treatment given here the most general expression for the force on a single particle in a periodic electric field is deduced from the cycle-averaged relativistic single particle Lagrangian. The collective ponderomotive force density is derived from general momentum conservation in an unmagnetized plasma which enables us to give it a very immediate physical interpretation.

A ponderomotive force arises whenever the radiation or wave field in question changes in space. This force has been recognized as a quantity of central importance in physical phenomena such as the free electron laser [1, 2], particle acceleration [3–5], stabilization of magnetized plasmas [6–8], trapping and cooling of atoms

[9–11], dressed atom model [12], multiphoton ionization [13], and chaotic plasma dynamics [14]. It is of particular relevance to the dynamics and nonlinear optics it induces in laser plasmas. Whereas collisional absorption of laser light and electronic heat diffusion create plasma clouds of smooth density and temperature distributions the ponderomotive force has the tendency to modulate the plasma and to impress a whole variety of structures on it. At the critical points and caustics step- and plateau-like density profile modifications are induced which in turn tend to modify collisional and resonance absorption [15–17]. Inside the plasma density structures appear whenever the electric field amplitude of the laser beam or any strong plasma wave is nonuniform owing to inhomogeneities in the single beam or wave itself, or because the electric field amplitude is periodically modulated by the superposition of different modes [18]. The density structures may be nonresonant; then they appear as the following phenomena: static plasma density modifications, nonresonant self-focusing, filamentation, striation, modulational and oscillating two-stream instabilities. Or they are resonant and are recognized as stimulated Brillouin and Raman scattering or two-plasmon and parametric decay instabilities. Most nonresonant phenomena are treated in this chapter, whereas Chap. 6 is mainly dedicated to the class of resonantly induced ponderomotive effects.

## 5.1 Ponderomotive Force on a Single Particle

There are entire classes of relevant particle trajectories which can be decomposed into two or more motions having distinct time scales. Often there is a fast, nearly periodic component superposed on a smooth orbit of secular character. Prominent examples of this kind are the dynamics of a charged particle gyrating in a magnetic mirror and the oscillatory motion of an electron subject to a nearly periodic hf force. Frequently, one is not interested in all details of the trajectories, but the knowledge of the averaged motion, i.e. its secular component (slow time scale) is of vital interest (e.g. particle acceleration, asymptotic dynamics, transport theory). In a magnetic mirror the secular dynamics is represented by the gyrocenter motion, in the case of a point charge oscillating in an electr(omagnet)ic field the secular component is the oscillation center motion. For an electromagnetic field  $\mathbf{E}(\mathbf{x}, t)$  of frequency  $\omega$  and arbitrary space dependence  $\hat{\mathbf{E}}(\mathbf{x})$ ,

$$\mathbf{E}(\mathbf{x}, t) = \Re \hat{\mathbf{E}}(\mathbf{x}) e^{-i\omega t}, \quad (5.2)$$

it was shown [19–23] that the oscillation center dynamics of a charge  $q$  is governed by the force  $\mathbf{f}_p$ ,

$$\mathbf{f}_p = -\nabla \Phi_p, \quad \Phi_p = \frac{q^2}{4m\omega^2} \hat{\mathbf{E}} \hat{\mathbf{E}}^*. \quad (5.3)$$

The ponderomotive potential  $\Phi_p$  is obtained from a first order perturbation analysis of the Lorentz force (see next section) and is therefore subject to the usual smallness

constraints of certain parameters. In order to obtain some weak generalizations of this expression a variety of different approaches was chosen among which the Hamiltonian description [24–26] and the Lie transform technique [27] appeared to be particularly attractive formalisms. As an alternative, perturbative averaging of a Lagrangian was also used [28]. They are all based on the momentum equation and are characterized by the following limitations: (i) perturbation analysis of momentum, (ii) harmonic fields, and (iii) small ratio of oscillation amplitude  $\hat{\delta}$  to wavelength  $\lambda$ , i.e.  $\hat{\delta}/\lambda \ll 1$ . They all represent local theories, except for one paper which presents an approximate analysis of nonlocal quiver motion [29].

The standard concept of ponderomotive potential  $\Phi_p$  and force  $f_p = -\nabla\Phi_p$  governing the secular component of the oscillatory motion of a free point charge  $q$  in the field of an electric and/or electromagnetic wave is limited to motions  $x(t)$  which can be decomposed into an oscillatory component  $\xi$  that is nearly periodic and a secular component  $x_0$  describing the oscillation center orbit,

$$x(t) = x_0(t) + \xi(t), \quad v(t) = v_0(t) + w(t). \quad (5.4)$$

The total velocity  $v = \dot{x}$  is assumed to be related to an inertial frame of reference and so then is  $v_0 = \dot{x}_0$ , whereas  $w = \dot{\xi}$  refers to the oscillation center frame which, in general, will not be inertial. The decomposition (5.4) is not unique in rigorous mathematical terms, however, the arbitrariness is small as long as the nearly periodic orbit  $\xi(t)$  changes slowly over one spatial cycle  $\lambda$  (generalized “wavelength”). In the opposite case (5.4) becomes meaningless.

In the following we shall show that restrictions (i)–(iii) can be removed by constructing an adiabatic invariant for the secular component of motion. The method we chose here is that of averaging the Lagrangian in time along the fast component of motion  $\xi(t)$ . Adiabaticity is thereby understood in a widely accepted generalized sense [30], not limited to periodic motions. In order, however, to introduce to this subject gradually, first the traditional derivation of  $f_p$  is presented.

### 5.1.1 Conservation of the Cycle-Averaged Energy

The simplest derivation of  $f_p$  is obtained from an energy argument. It has the additional advantage of nonperturbative nature. In the prominent case of a pure electromagnetic wave the Hamiltonian of a charge  $q$  is expressible in terms of a vector potential periodic in time,  $A(x, t)$ , and the canonical momentum  $p = mv + qA$ ,

$$H(p, x, t) = \frac{1}{2m}(p - qA)^2. \quad (5.5)$$

The energy of the particle is not conserved since  $H$  varies rapidly in time. On the other hand, the cycle-averaged oscillation energy  $W$  in a stationary wave is only a function of position when  $v_0$  is held constant. Therefore, when the particle is slowly shifted from a region of high vector potential  $A$  to one of low vector potential, the

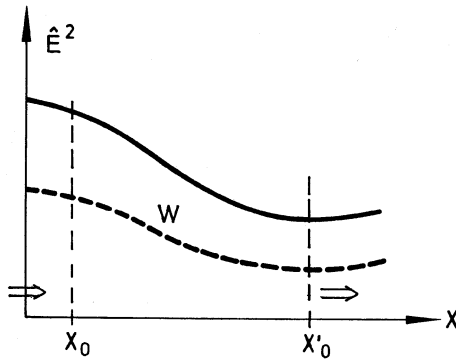


**Fig. 5.1** The time-averaged oscillation energy  $W$  of a free particle (dashed line) in a stationary electromagnetic wave is a unique function of position as long as it undergoes several oscillations per wavelength.  $W$  is identical with the ponderomotive potential  $\Phi_p \sim \hat{E}^2$

question arises where the difference in  $W$  has disappeared (Fig. 5.1). From a quantum point of view one is induced to argue that  $\Delta W$  has been converted into kinetic energy of the oscillation center since a free particle cannot absorb photons and hence  $\Delta W$  cannot be given back to the hf field. We show that classical arguments lead to the same conclusion and, consequently,  $W$  is the ponderomotive potential.

The simplest way to prove this statement is as follows. By injecting  $N$  particles per unit time at a position  $x = x_0$  with the oscillation center velocity  $v_0$ , stationary time-averaged mass and energy flows build up between  $x = x_0$  and  $x = x'_0$ . The position  $x'_0$  is arbitrary, hence

$$Nv_0 = \text{const}, \quad Nv_0 \left( \frac{p_0^2}{2m} + W \right) = \text{const} \quad (5.6)$$

must hold along  $x_0(t)$ , or in particular,

$$H_0(p_0, x_0) = \frac{p_0^2}{2m} + W(x_0, v_0) = \text{const}, \quad (5.7)$$

thus showing that the cycle-averaged quantity

$$\begin{aligned} H_0 &= \frac{1}{\tau} \int_t^{t+\tau} \frac{1}{2m} (\mathbf{p} - q\mathbf{A})^2 dt = \frac{1}{\tau} \int_t^{t+\tau} \frac{1}{2} m(\mathbf{v}_0 + \mathbf{w})^2 dt \\ &= \frac{p_0^2}{2m} + W(x, v_0) \end{aligned}$$

is the Hamiltonian governing the oscillation center motion and

$$\Phi_p = W = \left\langle \frac{1}{2} m \mathbf{w}^2 \right\rangle \quad (5.8)$$

is the ponderomotive potential of a transverse wave. The dependence of  $W$  on  $\mathbf{v}_0$  in (5.7) takes care of the Doppler effect.

A formal, but physically less immediate proof of (5.7) is obtained from dimensional analysis. The quantity  $H_0$  merely depends on  $m$ ,  $\mathbf{v}_0$  and the scalar function  $W(\mathbf{x}, \mathbf{v}_0)$ . From these three variables no quantity with the dimension of time can be constructed. Hence, according to Buckingham's  $\pi$  theorem,  $H_0$  is time-independent and  $H_0 = E = \text{const}$  holds along each trajectory. As a consequence,  $H_0(\mathbf{p}_0, \mathbf{x})$  is the Hamiltonian governing the oscillation center motion, with the desired generalized ponderomotive potential  $\Phi_p = W$ .

The concept adopted here is directly subject to a generalization in different directions:

I. For an arbitrarily strong monochromatic propagating electromagnetic wave

$$W = mc^2 \left\{ \left( 1 + \frac{q^2}{\alpha m^2 c^2 \omega^2} \hat{\mathbf{E}} \hat{\mathbf{E}}^* \right)^{1/2} - 1 \right\}, \quad f_p = -\nabla W, \quad (5.9)$$

holds for the oscillation energies corresponding to plane ( $\alpha = 2$ ) and circular ( $\alpha = 1$ ) polarization [31, 32]. For moderate fields Taylor expansion of this expression leads back to  $\Phi_p$  of (5.3). For a detailed derivation see Sect. 8.2.1.

II. Next a point particle is considered, with an internal degree of freedom that is a harmonic oscillator in dipole approximation,

$$\ddot{\delta} + \omega_0^2 \delta = \frac{q}{\mu} \hat{\mathbf{E}}(\mathbf{x}) e^{-i\omega t}; \quad \mu = m_1 m_2 / (m_1 + m_2). \quad (5.10)$$

The averaged oscillation energy is

$$W = \left\langle \frac{1}{2} \mu \dot{\delta}^2 \right\rangle + E_{\text{pot}} = \frac{q}{4\mu} \frac{\omega^2 + \omega_0^2}{(\omega^2 - \omega_0^2)^2} \hat{\mathbf{E}} \hat{\mathbf{E}}^*.$$

In determining  $\Phi_p$  one has to keep in mind that when the field is switched on the oscillator gains internal energy  $E_{\text{in}}$  also and that the forces producing this energy are internal forces and as such, by definition, cancel each other. Thus  $\Phi_p$  is given by

$$\begin{aligned} \Phi_p &= W - \langle E_{\text{in}} \rangle = W - E_{\text{pot,max}} = W - \frac{q^2}{4\mu} \frac{2\omega_0^2}{(\omega^2 - \omega_0^2)^2} \hat{\mathbf{E}} \hat{\mathbf{E}}^* \\ &= \frac{q^2}{4\mu(\omega^2 - \omega_0^2)} \hat{\mathbf{E}} \hat{\mathbf{E}}^*. \end{aligned} \quad (5.11)$$

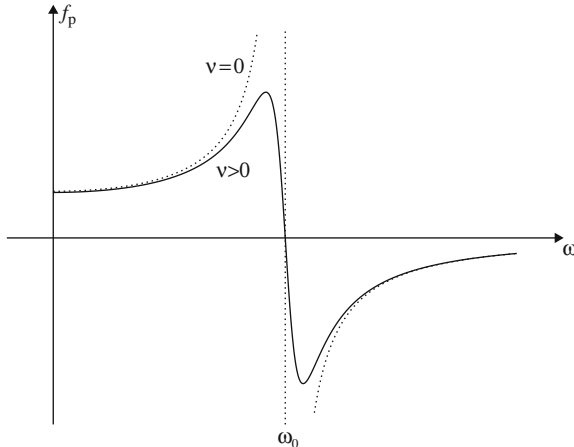


**Fig. 5.2** A harmonic oscillator with eigenfrequency  $\omega_0$  and a charged point particle in a constant perpendicular magnetic field  $B_0$  (cyclotron frequency  $\omega_c$ ) are shifted towards decreasing electric field amplitude when its frequency  $\omega$  exceeds  $\omega_0$  and  $\omega_c$  (special case: free particle with  $\omega_0 = \omega_c = 0$ ); it moves into opposite direction if  $\omega < \omega_0, \omega_c$  holds. At resonance ( $\omega = \omega_0, \omega_c$ )  $f_p$  is zero. Solid curve: damped oscillator, dashed curve: oscillator without damping

The same result is obtained by solving (5.10) up to the first order and determining its secular component. However, the procedure used here is shorter and more general, e.g. a force may result from constant  $\hat{E}$  but changing frequencies  $\omega, \omega_0$ .  $\Phi_p = W - \langle E_{in} \rangle$  also holds for anharmonic  $E$  fields or when the Lorentz force is included. For  $\omega_0 < \omega$  the oscillator behaves like a free particle, i.e.  $f_p$  tries to drive it into a region of decreasing field amplitude. For  $\omega_0 > \omega$  it moves into the opposite direction. By introducing a damping term it is shown that at exact resonance  $f_p$  reduces to zero (Fig. 5.2).  $\Phi_p$  is identical with what in quantum mechanics is called the expectation value of the interaction energy  $E_{int}$ .

It can be shown that (5.11) is correct also for a quantum oscillator [33]. If  $\omega_0$  is properly chosen and an effective oscillator strength is inserted the expression also applies to the radiation force on an atom with negligible degeneracy.  $\Phi_p$  in this case is identical to the level shift  $\Delta E$  of the linear dynamical Stark shift by the electric wave. If degeneracy is present, (5.11) changes accordingly. At first glance one might argue that (5.11) is not useful for a fully ionized plasma in which all electrons are free. However, in the next chapter it will become clear that it is just this expression which enables one to understand the difference between the oscillating two-stream and the parametric decay instability.

III. It is instructive to generalize  $f_p$  to include the case of a charged point particle in a static magnetic field  $\mathbf{B}_0$ . In addition, there exist important applications of this type of situation in magnetically confined plasmas. With  $\mathbf{E}(x, t)$  in the  $x$ -direction and  $\mathbf{B}_0$  parallel to  $z$  one has to set

$$W = \frac{1}{2}m(v_x^2 + v_y^2), \quad \langle V \rangle = \mu B_0.$$

$\mu B_0 = A I B_0$  ( $\mu$  magnetic moment,  $A$  cross section of the closed orbit,  $I$  current) is the “inner” energy of the orbiting particle configuration which has to be subtracted since, by definition, internal forces do not contribute to  $f_p$ . Specializing to  $\mathbf{E} = \mathbf{E}_x \sim e^{-i\omega t}$  yields in analogy to (5.10) and (5.11)

$$\begin{aligned}\ddot{v}_x + \omega_c^2 v_x &= -i\omega \frac{q}{m} E_x, \quad v_y = -i \frac{\omega_c}{\omega} v_x, \quad \omega_c = \frac{q}{m} B; \\ \Phi_p &= W - \langle V \rangle = \frac{q^2}{4m} \frac{\omega^2 + \omega_c^2}{(\omega^2 - \omega_c^2)^2} \hat{\mathbf{E}} \hat{\mathbf{E}}^* - \frac{q^2}{4m} \frac{2\omega_c^2}{(\omega^2 - \omega_c^2)^2} \hat{\mathbf{E}} \hat{\mathbf{E}}^* \\ &= \frac{q^2}{4m(\omega^2 - \omega_c^2)} \hat{\mathbf{E}} \hat{\mathbf{E}}^*,\end{aligned}\tag{5.12}$$

in agreement with results obtained from the momentum equation with weak fields [34]. The cyclotron frequency  $\omega_c$  takes the place of  $\omega_0$ .

In the three cases of a free particle, a harmonic oscillator and a particle in a static magnetic field, considered here, the ponderomotive potential can be written with the help of the dipole moment  $\mathbf{p} = q\delta$  as

$$\Phi_p = E_{int} = \left\langle -\frac{1}{2} \mathbf{p} \cdot \mathbf{E} \right\rangle.$$

If  $\omega_0 > \omega$ ,  $\mathbf{p}$  is parallel to  $\mathbf{E}$  and the oscillator moves into the direction of increasing field; if  $\omega_0 < \omega$ ,  $\mathbf{p}$  is anti-parallel to  $\mathbf{E}$ ; at resonance the phase shift is  $\pi/2$  (Fig. 5.2).

When two or more plane waves are coherently superposed, a variety of spatial structures of  $f_p$  can be produced which may lead to induced striation or vortices. Vortices have been experimentally observed with neutral atoms in two crossed, near resonant standing waves [35].

### 5.1.2 The Standard Perturbative Derivation of the Force

Despite its inherent limitations this procedure may provide an alternative, detailed, physical insight in how the secular force  $f_p$  originates. It starts from the Lorentz equation of a charged particle in a monochromatic electromagnetic field of the form (5.2),

$$m \frac{d\mathbf{v}}{dt} = q(\mathbf{E} + \mathbf{v} \times \mathbf{B}),$$

and makes use of the decomposition (5.4). Under the restriction that the oscillation amplitude  $\hat{\xi}$  is much smaller than the local wavelength  $\lambda(x_0)$ , i.e.  $\hat{\xi} \ll \lambda(x_0)$ , the Lorentz equation may be linearized in  $\hat{\xi}$  and solved separately,

$$m \frac{d\mathbf{v}}{dt} \simeq m \left[ \frac{\partial \mathbf{w}}{\partial t} + (\mathbf{v}_0 \nabla) \mathbf{w} \right] = q [\mathbf{E}(\mathbf{x}_0) + \mathbf{v}_0 \times \mathbf{B}(\mathbf{x}_0)].$$

In general  $\hat{\mathbf{E}}(\mathbf{x})$  is the superposition of a large set of modes,

$$\hat{\mathbf{E}}(\mathbf{x}) = \sum_{\{k\}} \hat{\mathbf{E}}_k e^{ikx}.$$

For a single mode holds

$$\mathbf{w}_k(t) = i \frac{q}{m\omega_k} (\mathbf{E}_k + \mathbf{v}_0 \times \mathbf{B}_k), \quad \omega_k = \omega - \mathbf{v}_0 \cdot \mathbf{k}.$$

The Doppler shift  $\Delta\omega_k = \mathbf{v}_0 \cdot \mathbf{k}$  originates from the convective derivative  $(\mathbf{v}_0 \nabla) \mathbf{w}$ . For nonrelativistic temperatures all  $\Delta\omega_k$  and  $\mathbf{v}_0 \times \mathbf{B}_k$  can be chosen small so that all Fourier components  $\mathbf{w}_k$  superpose to yield

$$\mathbf{w}(t) = i \frac{q}{m\omega} \hat{\mathbf{E}}(\mathbf{x}_0) e^{-i\omega t} = \frac{q}{m} \hat{\mathbf{A}}(\mathbf{x}_0) e^{-i\omega t},$$

$\mathbf{E} = -\partial_t \mathbf{A}$ ,  $\mathbf{A}$  vector potential. In the next order from the Lorentz equation  $\mathbf{v}_0(t)$  is calculated, the time variation of which determines  $f_p$ ,

$$f_p = m \frac{d\mathbf{v}_0}{dt} = q \{ \mathbf{E}(\mathbf{x}_0 + \xi(t)) + \mathbf{w}(t) \times \mathbf{B}(\mathbf{x}_0) \}_0.$$

The bracket contains terms varying with  $2\omega$  and zero frequency. Therefore the subscript “0” has been added to indicate that in determining the secular force  $f_p$  the  $2\omega$ -term has to be suppressed. Taylor expansion of  $\mathbf{E}$  in  $\xi = i\mathbf{w}/\omega$ , using  $\mathbf{B} = \nabla \times \mathbf{A}$ , and observing that physical quantities have to be real leads directly to

$$\begin{aligned} q \{ \mathbf{E} + \mathbf{w} \times \mathbf{B} \}_0 &= -\frac{q^2}{4m} \{ (\hat{\mathbf{A}}^* \nabla) \hat{\mathbf{A}} + \hat{\mathbf{A}}^* \times \nabla \times \hat{\mathbf{A}} + \text{c.c.} \} \\ &= -\frac{q^2}{4m} \nabla (\hat{\mathbf{A}} \hat{\mathbf{A}}^*). \end{aligned}$$

Hence,  $f_p$  is the gradient of a quantity which can be interpreted as a potential  $\Phi_p$ , the ponderomotive potential given by (5.3). In a transverse plane wave  $(\mathbf{w} \nabla) \mathbf{E}$  is zero; if  $\mathbf{E}$  is longitudinal (e.g. an electron plasma wave)  $\mathbf{B}$  is zero and  $f_p$  arises entirely from  $(\mathbf{w} \nabla) \mathbf{E}$ .

Expression (5.3) for  $\Phi_p$  is valid when damping can be ignored. In the presence of a linear damping  $\nu$  according to (2.23) the following expression for  $f_p$  is found straightforwardly in terms of  $\mathbf{E} = \mathbf{E}_r + i\mathbf{E}_i$  [36],

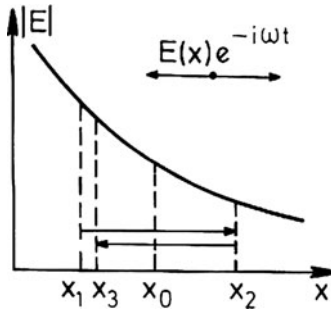


**Fig. 5.3** In an oscillating longitudinal electric field a charged particle experiences a drift in the direction of decreasing wave amplitude. The drift is independent of the sign of charge.  $x_0$  starting point;  $x_1, x_2, x_3$  turning points. In a transverse wave the drift is caused by the Lorentz force

$$f_p = -\frac{q^2}{4m_e\omega^2(1 + \frac{v^2}{\omega^2})} \left\{ \nabla \hat{E} \hat{E}^* + 2\frac{v}{\omega} \left[ \hat{E}_i \times (\nabla \times \hat{E}_r) - \hat{E}_r \times (\nabla \times \hat{E}_i) \right] \right\}, \quad (5.13)$$

$\omega, v = \text{const}$ , and  $\nabla \times f_p$  differs from zero in this case.

In terms of the momentum equation the physical interpretation of the ponderomotive force  $f_p$  is as follows. Let us first assume a pure electrostatic wave in the  $x$ -direction of the form  $\hat{E}(x)e^{-i\omega t}$  with decreasing amplitude  $\hat{E}(x)$  (Fig. 5.3). A free electron is shifted by the  $E$ -field from its original position  $x_0$  to  $x_1$ . From there it is then accelerated to the right until it has passed  $x_0$ . From that moment on the electron is decelerated by the reversed  $E$ -field and is stopped at position  $x_2$ . If  $x'_0$  designates the position in which the field is reversed ( $x'_0 > x_0$ ), the deceleration interval  $x_2 - x'_0$  is larger than that of acceleration since on the right hand side of  $x_0$  the  $E$ -field is weaker and therefore a longer distance is needed to take away the energy gained in the former quarter period of oscillation. On its way back the electron is stopped in the region of higher amplitude; the turning point is shifted from  $x_1$  to  $x_3$  into the direction of decreasing wave amplitude  $\hat{E}(x)$ . In an (inhomogeneous) medium this drift produces, by charge separation, a static  $E$ -field which transmits the force to the ions. Since this consideration is based only on energy and work – there was no need to specify the field direction with respect to the particle speed – it follows that the drift (or force) is independent of the sign of charge: positrons would drift in the same direction. In the case of a plane electromagnetic wave the drift is caused by the  $v \times B$  force which also acts along the direction of propagation.

### 5.1.3 Rigorous Relativistic Treatment

In connection with the development of ultrashort super-intense laser beams a real need for relativistic expressions for  $f_p$ , not bound by the above-mentioned constraints (i)–(iii) arises. As we show in this section the most general result for a free charge  $q$  is obtained again from a cycle-averaging method. However, since such

a procedure does not preserve the canonical character of the Hamiltonian [37] a Lagrangian formulation will be used [14].

The relativistic Lagrangian  $L(\mathbf{x}, \mathbf{v}, t)$ ,  $\mathbf{v} = d\mathbf{x}/dt$ , of a charge  $q$  in an arbitrary electromagnetic field  $\mathbf{E} = -\nabla\Phi - \partial\mathbf{A}/\partial t$  is given by

$$L(\mathbf{x}, \mathbf{v}, t) = -\frac{mc^2}{\gamma} + q\mathbf{v}\mathbf{A} - q\Phi, \quad \gamma = (1 - v^2/c^2)^{-1/2}. \quad (5.14)$$

When an oscillation center exists, the transformation to action-angle variables  $S = S(\mathbf{x}, t)$ ,  $\eta = \eta(\mathbf{x}, t)$ , is possible (e.g.,  $\psi(\mathbf{x}, t) = \int(\mathbf{k} d\mathbf{x} - \omega dt)$  in the case of a traveling monochromatic wave). The action  $S$  and the angle  $\eta$  are both Lorentz invariant. The motion of the particle is governed by Hamilton's principle,

$$\delta S = \delta \int_{\eta_1}^{\eta_2} L(\mathbf{x}(\eta), \mathbf{v}(\eta), t(\eta)) \frac{dt}{d\eta} d\eta = 0. \quad (5.15)$$

From the Lorentz invariance of  $S$  and  $\eta$  it follows that the Lagrangian  $\mathcal{L}(\eta) = L(d\eta/dt)^{-1}$  is invariant with respect to a change of the inertial reference system. Assuming that  $\eta$  is normalized to  $2\pi$  for one full cycle or period of motion, the cycle-averaged Lagrangian  $\mathcal{L}_0$ ,

$$\mathcal{L}_0(\eta) = \frac{1}{2\pi} \int_{\eta}^{\eta+2\pi} \mathcal{L}(\eta') d\eta', \quad (5.16)$$

depending only on the secular (i.e., oscillation center) coordinates  $\mathbf{x}_0$ ,  $\mathbf{v}_0$  through  $\eta$ , is defined. The oscillation center motion is governed by the Lagrange equations of motion,

$$\frac{d}{dt} \frac{\partial \mathcal{L}_0}{\partial \mathbf{v}_0} - \frac{\partial \mathcal{L}_0}{\partial \mathbf{x}_0} = 0, \quad (5.17)$$

with  $L_0 = \mathcal{L}_0 d\eta/dt$ . To demonstrate this assertion we prove the following theorem.

**Theorem 1** *The validity of (5.15) implies*

$$\delta \int_{\eta_i}^{\eta_f} \mathcal{L}_0(\eta) d\eta = o(N^{-1}), \quad (5.18)$$

where  $N = (\eta_f - \eta_i)/2\pi$  is the number of cycles over which  $\mathcal{L}_0$  undergoes an essential change. The symbol  $o(N^{-1})$  means “vanishes at least with order  $1/N$ ”.

*Proof* Let the variation be an arbitrary piecewise continuous function  $\Delta(\eta)$ . The  $n$ th cycle starts at  $\eta = \eta_n$ , where for brevity we use the symbols  $\Delta_n = \Delta(\eta_n)$ ,  $\partial\mathcal{L}_0/\partial\eta_n = (\partial\mathcal{L}_0/\partial\eta)_{\eta=\eta_n}$ . If the same quantities refer to an intermediate point  $\eta \leq \eta_a \leq \eta_n + 2\pi$  we write  $\Delta_a$  and  $\partial\mathcal{L}_0/\partial\eta_a$  and omit the index  $n$  for the interval. To leading order the following holds:

$$\begin{aligned}
\left| \delta \int_{\eta_i}^{\eta_f} \mathcal{L}_0 d\eta \right| &= \left| \int_{\eta_i}^{\eta_f} \delta(\mathcal{L}_0 - \mathcal{L}) d\eta \right| \\
&= \left| \int_{\eta_i}^{\eta_f} [\mathcal{L}_0(\eta + \Delta) - \mathcal{L}(\eta + \Delta)] d\eta - \int_{\eta_i}^{\eta_f} [\mathcal{L}_0(\eta) - \mathcal{L}(\eta)] d\eta \right| \\
&\leq \sum_n \left| \int_{\eta_n}^{\eta_n+2\pi} \mathcal{L}_0(\eta + \Delta) d\eta - 2\pi \mathcal{L}_0(\eta_n + \Delta_n) \right. \\
&\quad \left. - \int_{\eta_n}^{\eta_n+2\pi} \mathcal{L}_0(\eta) d\eta - 2\pi \mathcal{L}_0(\eta_n) \right| \\
&= \sum_n \left| \int_{\eta_n}^{\eta_n+2\pi} \frac{\partial \mathcal{L}_0}{\partial \eta_n} \Delta(\eta) d\eta - 2\pi \frac{\partial \mathcal{L}_0}{\partial \eta_n} \Delta_n \right| \\
&= 2\pi \sum_n \left| \frac{\partial \mathcal{L}_0}{\partial \eta_n} \Delta_n - \frac{\partial \mathcal{L}_0}{\partial \eta_n} \Delta_n \right|.
\end{aligned}$$

In the last step the mean value theorem is used. The function  $\Delta(\eta)$  is arbitrary. Therefore at  $\eta = \eta_n$ ,  $\Delta_n = \Delta_a$  can be chosen without affecting  $\Delta_a$ . With this substitution the leading order gives the result

$$\left| \delta \int_{\eta_i}^{\eta_f} \mathcal{L}_0 d\eta \right| \leq (2\pi)^2 \sum_n \left| \frac{\partial^2 \mathcal{L}_0}{\partial \eta_n^2} \Delta_n \right| \leq (2\pi)^2 N \max \left| \frac{\partial^2 \mathcal{L}_0}{\partial \eta_n^2} \right| \times \max |\Delta_n|.$$

In this last step it is essential that  $\partial \mathcal{L}_0 / \partial \eta$  is a smooth function (in contrast to  $\partial L / \partial \eta$ , which is generally not). Now,  $N = \min(1/2\pi) |\mathcal{L}_{0 \max}| / (\partial \mathcal{L}_0 / \partial \eta_n)$  is chosen; i.e., over  $N$  cycles  $\mathcal{L}_{0 \max}$  changes at most by  $\mathcal{L}_0$ . It follows that

$$\left| \delta \int_{\eta_i}^{\eta_f} \mathcal{L}_0 d\eta \right| \leq \frac{|\mathcal{L}_{0 \max}|}{N} \times \max |\Delta|. \quad (5.19)$$

Performing the variation of this inequality leads to (5.17) with the 0 replaced by a function  $f$  not larger than  $|\mathcal{L}_{0 \max}| \times \max |\Delta| / N^2$ .

In order to understand what inequality (5.19) means let us specialize to a case of the averaged Lagrangian  $\mathcal{L}_0$  not depending explicitly on time. Then the Hamiltonian  $H_0 = \mathbf{p}_0 \mathbf{v}_0 - L_0(\mathbf{x}_0, \mathbf{v}_0)$ , where  $L_0 = -\mathcal{L}_0(\omega - \mathbf{k} \mathbf{v}_0)$ , owing to  $dH_0/dt = \partial H_0 / \partial t = -\partial L_0 / \partial t = 0$ , expresses energy conservation

$$H_0 = E = \text{const.}$$

A straightforward estimate shows that the uncertainty  $f$  in (5.17) leads to an energy uncertainty  $\Delta H_0 / H_0 \lesssim 2\pi/N$ . This means that (5.17) is adiabatically zero and the total cycle-averaged energy is an adiabatic invariant in the rigorous mathematical sense in agreement with Arnold's definition [30]. For  $N \rightarrow \infty$  (5.17) becomes exact. This is the mathematical proof of assertion (5.7) which was established there

by physical arguments. Furthermore, physical arguments were used for expressions (5.11) and (5.12). By making use of (5.15) both expressions follow without using further arguments since nonrelativistically  $L(\mathbf{x}, \mathbf{v}) = 1/2m\mathbf{v}^2 - V(\mathbf{x})$ ,  $V(\mathbf{x})$  potential energy, and  $L(\mathbf{x}, \mathbf{v}) = 1/2m\mathbf{v}^2 - V(\mathbf{x}) + q\mathbf{v}\mathbf{A}$  in the presence of a magnetic field.

The relativistic Hamiltonian of point charge in the electromagnetic field follows from (5.14),

$$H = \mathbf{p}\mathbf{v} - L = \left\{ m^2c^4 + c^2(\mathbf{p} - q\mathbf{A})^2 \right\}^{1/2} + \Phi, \quad (5.20)$$

with the canonical momentum  $\mathbf{p} = \partial L/\partial \mathbf{v} = \gamma m\mathbf{v} + q\mathbf{A}$ . Its numerical value is the total energy  $E = \gamma mc^2 + \Phi$ . Considering a monochromatic wave in vacuum we can set  $\Phi = 0$ . This motion is exactly solvable with the result for the oscillation energy given by (5.9). If the effective mass  $m_{\text{eff}} = \mathcal{L}_0\gamma_0(d\eta/dt)/c^2$  is introduced,  $L_0 = \mathcal{L}_0d\eta/dt$  shows that, in an arbitrary inertial frame in which the oscillation center moves at speed  $\mathbf{v}_0$ ,  $L_0$  and  $H_0$  are those of a free particle with space and time dependent mass  $m_{\text{eff}}$ ,

$$\begin{aligned} L_0(\mathbf{x}_0, \mathbf{v}_0, t) &= -\frac{m_{\text{eff}}c^2}{\gamma_0}, \quad H_0(\mathbf{x}_0, \mathbf{p}_0, t) = \gamma_0 m_{\text{eff}}c^2; \\ \gamma_0 &= \left( 1 - \frac{v_0^2}{c^2} \right)^{-1/2}, \quad p_0 = \gamma_0 m_{\text{eff}} v_0. \end{aligned} \quad (5.21)$$

Expressions (5.21) hold in any electromagnetic field in vacuum in which an oscillation center can be defined. In the special case of (5.9)  $m_{\text{eff}} = (1 + q^2\hat{\mathbf{A}} \cdot \hat{\mathbf{A}}^*/\alpha m^2 c^2)^{1/2} m$ .

In the oscillation center system, i.e., in the inertial frame in which at the instant  $t$   $\mathbf{v}_0(t) = 0$  holds, the ponderomotive force follows from (5.17) and (5.21):

$$\mathbf{f}_{\text{p}}^N \equiv \frac{d\mathbf{p}_0}{d\tau} = \frac{\partial L_0}{\partial \mathbf{x}_0} = -c^2 \nabla m_{\text{eff}}. \quad (5.22)$$

For the meaning of  $f_{\text{p}}^N$  and its transformation to another reference system see Sect. 8.1.

To see the power of the Lagrangian formulation, (5.17), we calculate  $f_{\text{p}}$  in a non-relativistic Langmuir wave of the form  $E(x, t) = \hat{E}(x, t) \sin(kx - \omega t)$  with slowly varying amplitude  $\hat{E}$ . In lowest order the potential is  $\Phi(x, t) = (\hat{E}/k) \cos(kx - \omega t)$  and  $L = mv^2/2 - q\Phi$ . In the frame comoving with  $x_0$  the particle sees the Doppler-shifted frequency  $\Omega = \omega - k\mathbf{v}_0$  (plus higher harmonics that are not essential here). With the periodic excursion  $\xi(t)$  around  $x_0$  the potential is  $\Phi(x, t) \simeq \Phi(x_0, t) + \xi(t)\partial\Phi/\partial x_0$ . From this  $L_0 = mv_0^2/2 - \alpha\hat{E}^2/\Omega^2$ ,  $\alpha = q^2/4m$ , results in lowest order. With this Lagrangian it follows from (5.17) for  $\hat{E} = \hat{E}(x)$  (no explicit time dependence) that

$$f_p = m \frac{dv_0}{dt} = -\alpha \frac{(1 - V_0)(1 - 3V_0)}{\omega^2(1 - V_0)^4 - 6\alpha \hat{E}^2/m v_\varphi^2} \frac{\partial}{\partial x} \hat{E}^2. \quad (5.23)$$

In the last expression  $V_0$  is the oscillation center velocity normalized to the phase velocity  $v_\varphi = \omega/k$ ,  $V_0 = v_0/v_\varphi$ . Equation (5.23) shows that  $f_p$  changes sign when the particle is injected into the Langmuir wave with a velocity  $v_0$  exceeding  $v_\varphi/3$ . In regions where the standard expression for  $f_p$ , (5.3), always exhibits repulsion the more exact treatment can lead to attraction.

Equation (5.23) was also derived in a more formal but physically less transparent manner in [26]. Uphill acceleration in an electron plasma wave of increasing amplitude  $\hat{E}(x)$  is confirmed by the numerical solution of the exact equation of motion (Fig. 5.4). If  $\hat{E}(x)$  grows indefinitely the exact ponderomotive force changes sign again, and the particle stops and is finally reflected; the corresponding path in phase space exhibits a hysteresis. Uphill acceleration, occasionally observed in another context of wave particle interaction [38], is a general ponderomotive phenomenon. It should also be mentioned that for the electrostatic wave considered here uphill acceleration identical with the result of Fig. 5.4 follows from the adiabatic invariant (4.31) for nontrapped particles (see [39] and Chap. 4).

The results can be summarized as follows: (i) When an oscillation center of motion exists, the invariant cycle-averaged Lagrangian describes the ponderomotive motion in arbitrary strong fields. (ii) The ponderomotive force in a monochromatic traveling, locally plane wave of arbitrary strength in any reference system can be expressed analytically. (iii) In a longitudinal wave, uphill acceleration and phase

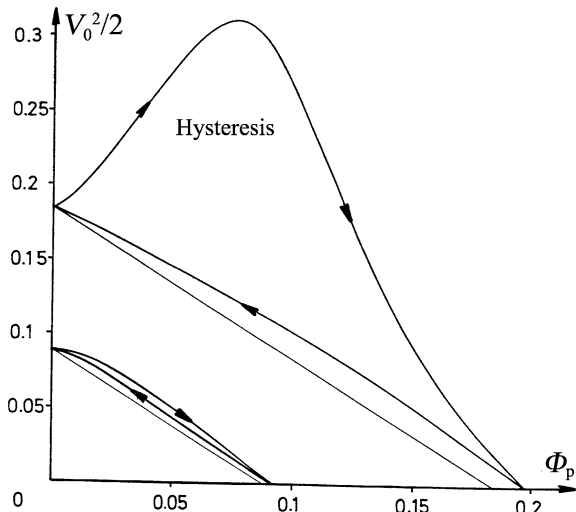


**Fig. 5.4** Normalized kinetic energy  $V_0^2/2$  is shown as a function of  $\Phi_p/m_e v_\varphi^2$  from (5.3) for the linearly increasing field  $2.5 \times 10^{-3} X \sin(X - T)$  and injection velocities  $V_0 = 1/3$  (lower curves) and  $V_0 = 0.43$  (upper curves). The motion shows a pronounced hysteresis in phase space owing to different acceleration in comotion and countermotion

space hysteresis may occur. (iv) The ponderomotive force on particles with internal degrees of freedom and the influence of dissipation (radiation losses, friction) on the ponderomotive force are best understood from conservation of the field-particle interaction energy. A detailed study of the validity of the ponderomotive concept for free electrons in finite laser pulses was presented in [40]. For an extension of ponderomotively induced motion for  $\omega \rightarrow 0$  see Sect. 8.2. Finally we want to point out that at relativistic energies cycle-averaging in the time parameter  $t$  becomes incorrect; rather one has to switch to an angle variable  $\eta$  in order to guarantee a Lorentz-invariant definition of the oscillation center. The problem is similar to the correct definition of the relativistic center of mass discussed in Sect. 8.1.6.

## 5.2 Collective Ponderomotive Force Density

### 5.2.1 Bulk Force

The force density exerted by an electric wave on the bulk of the plasma is proportional to the time averaged electron particle density  $n_0$ . Thus  $\pi$  is given by  $\pi_0$ ,

$$\pi_0 = n_0 f_p, \quad \text{or} \quad \pi_0 = -n_0 \nabla \Phi_p, \quad (5.24)$$

respectively, with  $\Phi_p$  taken from the preceding section. In the weak field approximation of Sect. 5.1.2  $\pi_0$  is given with  $\Phi_p$  from (5.11),

$$\pi_0 = -\frac{\varepsilon_0}{4} \frac{\omega_p^2}{\mu} \nabla \frac{\hat{E} \hat{E}^*}{\omega^2 - \omega_0^2}. \quad (5.25)$$

For free electrons  $\omega_0$  is zero; for free electrons in a constant magnetic field in the above configuration  $\omega_0$  is replaced by  $\omega_c$  and  $\mu = m$ .

### 5.2.2 The Force Originating from Induced Fluctuations

It would be most desirable now to obtain the collective ponderomotive force density  $\pi$ , also from an energy principle or an action integral. Since a sufficiently general derivation of this kind does not seem to exist so far, the following considerations are based on momentum conservation. By definition the ponderomotive force density  $\pi$  is a secular, i.e. low frequency force which originates from a high frequency transverse or longitudinal electric field and applies to the one-fluid model. Thus, when  $\rho_0 = \langle \rho(t) \rangle$  and  $v_0 = \langle v(t) \rangle$  are the density and velocity of a volume element averaged over the high frequency oscillations,  $\pi_0$  is defined by the equation of motion

$$\rho_0 \frac{d\mathbf{v}_0}{dt} = -\nabla(p_e + p_i) + \mathbf{f}_0 + \boldsymbol{\pi}_0 \quad (5.26)$$

where  $p_e$ ,  $p_i$  are the electronic and ionic thermal pressures and  $\mathbf{f}_0$  is any low frequency force (electric and magnetic, gravitational, viscous, frictional, etc.). For the concept of ponderomotive force to apply it is important that the spectra of fast and slow motions in  $\rho\mathbf{v} = \rho_i\mathbf{v}_i + \rho_e\mathbf{v}_e$  are well separated from each other. When including all forces  $\mathbf{f}$ ,  $\mathbf{f} = \mathbf{f}_0 + \mathbf{f}_h$ , where  $\mathbf{f}_h$  originates from the high frequency fields the general momentum conservation equation in the one-fluid model is

$$\frac{\partial}{\partial t}\rho\mathbf{v} + \nabla(\rho\mathbf{v}\mathbf{v} + p\mathbf{I}) = \mathbf{f}.$$

The momentum flow density  $T = \rho\mathbf{v}\mathbf{v} + p\mathbf{I}$ ,  $p = p_e + p_i$ , is a second rank tensor with the components  $T_{kl} = \rho v_k v_l + p \delta_{kl}$ . Hence, by comparison with (5.26)  $\boldsymbol{\pi}_t$  results as follows,

$$\boldsymbol{\pi}_t = \left\langle \frac{\partial}{\partial t}\rho\mathbf{v} + \nabla(\rho\mathbf{v}\mathbf{v} + p\mathbf{I}) - \mathbf{f}_h \right\rangle - \rho_0 \frac{d\mathbf{v}_0}{dt}. \quad (5.27)$$

In the absence of ionic resonances (i.e., no static magnetic fields)

$$\begin{aligned} \rho_i\mathbf{v}_i &= m_i n_{i0} \mathbf{v}_{i0}, & \mathbf{v}_{e0} &= \mathbf{v}_{i0}, \\ \rho_e\mathbf{v}_e &= m_e(n_{e0} + n_{e1} + n_{e2} + \dots)(\mathbf{v}_{e0} + \mathbf{v}_{e1} + \mathbf{v}_{e2} + \dots); \end{aligned} \quad (5.28)$$

holds. The indices 1, 2, etc. indicate the Fourier components of frequencies  $\omega$ ,  $2\omega$ , etc. induced by the high frequency electric or electromagnetic field

$$\mathbf{E}(\mathbf{x}, t) = \hat{\mathbf{E}}(\mathbf{x}, t) e^{-i\omega t}. \quad (5.29)$$

$\hat{\mathbf{E}}(\mathbf{x}, t)$  is the amplitude slowly varying in space and time. Inserting the quantities (5.28) into (5.27) leads to

$$(m_i n_{i0} + m_e n_{e0}) \langle \nabla(\mathbf{v}_{e1}\mathbf{v}_{e1} + \mathbf{v}_{e2}\mathbf{v}_{e2} + \dots) - \mathbf{f}_h \rangle = \boldsymbol{\pi}_0,$$

where the brackets  $\langle \rangle$  contain, in addition, all sums of products  $\mathbf{v}_{ej}\mathbf{v}_{ek}$  with an even number  $l = j + k$  and  $j < k$ . The first nonvanishing term contributing to the collective force  $\boldsymbol{\pi}_t$  originates from  $n_{e1}\mathbf{v}_{e1}$  in  $\langle \partial\rho\mathbf{v}/\partial t \rangle$ . Since this is also the leading term, to lowest order follows

$$\boldsymbol{\pi}_t = \left\langle \frac{\partial}{\partial t}(m_e n_{e1} \mathbf{v}_{e1}) \right\rangle. \quad (5.30)$$

There is no corresponding contribution from the flux term since  $\langle m_e n_{e1} \mathbf{v}_{e1} \mathbf{v}_{e1} \rangle$  is zero. With the help of the electronic equation of motion,

$$\frac{\partial \mathbf{v}_{e1}}{\partial t} = -\frac{e}{m_e} \hat{\mathbf{E}}(\mathbf{x}, t) e^{-i\omega t},$$

for  $\mathbf{v}_{e1}$  and displacement  $\delta_{e1}$  one obtains

$$\begin{aligned} \mathbf{v}_{e1} &= i \frac{e}{m_e \omega} e^{-i\omega t} \left( 1 - \frac{i}{\omega} \frac{\partial}{\partial t} \right) \hat{\mathbf{E}}(\mathbf{x}, t), \\ \delta_{e1} &= \frac{e}{m_e \omega^2} e^{-i\omega t} \left( 1 - \frac{2i}{\omega} \frac{\partial}{\partial t} \right) \hat{\mathbf{E}}(\mathbf{x}, t). \end{aligned} \quad (5.31)$$

The density variation  $n_{e1}$  follows from (3.74):

$$n_{e1} + \nabla n_{e0} \delta_{e1} = 0.$$

With these relations for  $\delta_{e1}$  and  $n_{e1}$ ,  $\boldsymbol{\pi}_t$  can be expressed in terms of the electric field amplitude of the high frequency wave as follows:

$$\boldsymbol{\pi}_t = i \frac{\epsilon_0}{4\omega} \frac{\partial}{\partial t} \left\{ \hat{\mathbf{E}} \left( \nabla \frac{\omega_p^2}{\omega^2} \hat{\mathbf{E}}^* \right) - \hat{\mathbf{E}}^* \left( \nabla \frac{\omega_p^2}{\omega^2} \hat{\mathbf{E}} \right) \right\}. \quad (5.32)$$

As shown in Chap. 6  $\boldsymbol{\pi}_t$  plays a decisive role when an electrostatic fluctuation is modulated by the laser field to resonantly drive another electrostatic mode, as for example in the two-plasmon decay. There is a whole variety of expressions for  $\boldsymbol{\pi}_t$  in the literature differing from each other [41–43] and, when  $\boldsymbol{\pi}_t$  is presented in terms of  $\hat{\mathbf{E}}$  as in (5.32), it is not easy to recognize which of them are correct and which are not. However, the correctness of (5.32) is easily revealed through (5.30), since the latter is accessible to an immediate physical interpretation: Due to the variation of  $\hat{\mathbf{E}}(\mathbf{x}, t)$  in time the secular component of the momentum density  $\langle m_e n_{e1} \mathbf{v}_{e1} \rangle$  induced by the wave changes also. Since, on the other hand the associated momentum flux density term  $\langle m_e n_{e1} \mathbf{v}_{e1} \mathbf{v}_{e1} \rangle$  is zero, the momentum change of a volume element appears as an external force applied to it.

In principle the contributions of  $p_i$ ,  $p_e$  to  $\boldsymbol{\pi}_0$  as well as to  $\boldsymbol{\pi}_t$  have to be considered also. However, by keeping in mind that kinetically  $p_e$  and  $p_i$  are defined each relative to their mean flow velocities  $\mathbf{v}_e(\mathbf{x}, t)$  and  $\mathbf{v}_i(\mathbf{x}, t)$  (and *not* relative to the common center of mass speed  $\mathbf{v} = (\rho_i \mathbf{v}_i + \rho_e \mathbf{v}_e)/(\rho_i + \rho_e)$ ) there is no change in  $p_e$  and  $p_i$  due to the presence of a hf E-field as long as the particle distribution functions  $f_i(\mathbf{x}, \mathbf{u}, t)$ ,  $f_e(\mathbf{x}, \mathbf{u}, t)$  look unchanged in the presence and absence of  $\mathbf{E}$  when both are observed from the systems co-moving with  $\mathbf{v}_e$  and  $\mathbf{v}_i$ . For electrons (and, a fortiori, for ions) this is the case as long as  $v_{e1}^3 \ll \langle u_e \rangle^3$  is fulfilled, since then the electron-ion collision frequency  $\nu_{ei}$  remains essentially unchanged. It must further be pointed out that  $\boldsymbol{\pi}_t$  according to (5.30) or (5.32) is a good approximation only as long as the higher harmonics are weak. For a resonantly excited electron plasma wave close to the breaking limit this may no longer be the case, because all higher harmonics may then become important.

### 5.2.3 Global Momentum Conservation

It may be instructive to cast  $\boldsymbol{\pi}$  into a different form. Let  $\boldsymbol{\kappa}$  be the force density caused by a hf field. With the help of the Poynting vector  $\mathbf{S}$  and Maxwell's stress tensor  $\mathbf{T}$  it is expressed in conservation form as

$$\boldsymbol{\kappa} = -\frac{1}{c^2} \frac{\partial}{\partial t} \mathbf{S} - \nabla \mathbf{T}.$$

$\boldsymbol{\kappa}$  is the sink of electromagnetic momentum and must, therefore, appear as a mechanical force density for the electronic and the ionic fluids according to

$$\boldsymbol{\kappa} = \frac{\partial}{\partial t} (\rho_e \mathbf{v}_e + \rho_i \mathbf{v}_i) + \nabla (\rho_e \mathbf{v}_e \mathbf{v}_e + \rho_i \mathbf{v}_i \mathbf{v}_i + p_e \mathbf{I} + p_i \mathbf{I}),$$

since the momentum of the three fluids, electrons, ions, and photons, must be conserved.  $\boldsymbol{\kappa}$  is rapidly oscillating. Thus, in order to formulate a law of momentum conservation for observable quantities one has to pass to a one-fluid description for  $\rho$  and  $\mathbf{v}$  as used above which after some algebraic manipulations is conveniently expressed as follows,

$$\frac{\partial}{\partial t} \rho \mathbf{v} + \nabla (\rho \mathbf{v} \mathbf{v} + p \mathbf{I}) + \frac{1}{c^2} \frac{\partial}{\partial t} \mathbf{S} + \nabla (\mathbf{T} + \frac{\rho_e \rho_i}{\rho} \mathbf{w} \mathbf{w}) = 0, \quad (5.33)$$

where  $\mathbf{w} = \mathbf{v}_i - \mathbf{v}_e$  [44]. When  $\mathbf{E} = \hat{\mathbf{E}} e^{-i\omega t}$  reduces to zero  $\boldsymbol{\pi}$  vanishes and the last two terms in (5.33) disappear. Hence,  $\boldsymbol{\pi} = \boldsymbol{\pi}_0 + \boldsymbol{\pi}_t$  is to be identified by

$$\boldsymbol{\pi} = - \left( \frac{1}{c^2} \frac{\partial}{\partial t} \mathbf{S} + \nabla \mathbf{T} + \nabla \frac{\rho_e \rho_i}{\rho} \mathbf{w} \mathbf{w} \right), \quad (5.34)$$

which clearly shows that the ponderomotive force  $\boldsymbol{\pi}$  is not the divergence of the Maxwellian stress tensor only;  $\nabla \rho_e \rho_i \mathbf{w} \mathbf{w} / \rho$  is of the same order of magnitude.

The two terms  $\boldsymbol{\pi}_0$  and  $\boldsymbol{\pi}_t$  are qualitatively different: In the absence of dissipation  $\boldsymbol{\pi}_0$  according to (5.24) is a real potential force, or for not too strong fields usually close to it, whereas  $\boldsymbol{\pi}_t$  is not since  $\nabla \times \boldsymbol{\pi}_t \neq 0$ . For instance, the latter appears as a possible source term for magnetic field generation according to [41]

$$\frac{\partial \mathbf{B}_0}{\partial t} = -m_e \frac{\epsilon_0 c^2}{e^2} \nabla \times \left( \frac{1}{n_{i0}} \nabla \times \frac{\partial \mathbf{B}_0}{\partial t} \right) - \frac{1}{e} \nabla \times \frac{\boldsymbol{\pi}_t}{n_{i0}}. \quad (5.35)$$

It is further clear from the derivation presented in this section that  $\boldsymbol{\pi}_0 = -n_{e0} \nabla \Phi_p$  is correct and not  $-\nabla(n_{e0} \Phi_p)$ . A derivation of  $\boldsymbol{\pi}_t$  in the presence of a static magnetic field is given by several authors [8, 45, 46].

### 5.3 Nonresonant Ponderomotive Effects

The ponderomotive force is strongest in regions of high electric wave field gradients. Such large gradients are produced by strong local absorption or by the superposition of waves of equal frequencies but different wave vectors. In the critical region generally both effects contribute to produce large standing amplitude variations.

The radiation pressure  $p_L$  on a plane surface is given by (5.1). In the case of a plasma layer, e.g., an overdense plane target, (5.1) must follow from (5.24). To show this a plasma filling the half space  $x > 0$  with an arbitrary density distribution  $n_e(x)$  is assumed which at some depth becomes overcritical. A plane wave  $\mathbf{E}(\mathbf{x}, t)$  in a homogeneous medium is the superposition of an incident and a reflected wave,

$$\mathbf{E}(\mathbf{x}, t) = \hat{\mathbf{E}}_0 e^{ikx - i\omega t} + \hat{\mathbf{E}}_r e^{-ikx - i\omega t} = \mathbf{E}_0(\mathbf{x}, t) + \mathbf{E}_r(\mathbf{x}, t). \quad (5.36)$$

In the vacuum  $k = k_0 = \omega/c$ . In the plasma such a decomposition does not hold in general. However, for  $\mathbf{k} = k\mathbf{e}_x$  in the whole space  $\mathbf{E}(\mathbf{x}, t)$  obeys the stationary wave equation

$$\frac{\partial^2 \mathbf{E}}{\partial x^2} + k_0^2 \left(1 - \frac{\omega_p^2}{\omega^2}\right) \mathbf{E} = 0 \quad (5.37)$$

The total ponderomotive force per unit area is given by

$$\begin{aligned} p_L &= - \int_{x<0}^{\infty} \frac{\varepsilon_0}{4} \frac{\omega_p^2(x)}{\omega^2} \frac{\partial}{\partial x} \mathbf{E} \mathbf{E}^* dx = - \frac{\varepsilon_0}{4} \int_{x<0}^{\infty} \frac{\partial}{\partial x} \left( \mathbf{E} \mathbf{E}^* + \frac{1}{k_0^2} \frac{\partial \mathbf{E}}{\partial x} \frac{\partial \mathbf{E}}{\partial x} \right) dx \\ &= \frac{\varepsilon_0}{4} [(\mathbf{E}_0 + \mathbf{E}_r)(\mathbf{E}_0^* + \mathbf{E}_r^*) + (\mathbf{E}_0 - \mathbf{E}_r)(\mathbf{E}_0^* - \mathbf{E}_r^*)]_{x<0} \\ &= \frac{\varepsilon_0}{2} (|\mathbf{E}_0|^2 + |\mathbf{E}_r|^2) = (1 + R) \frac{I}{c}, \quad I = \frac{\varepsilon_0}{2} c |\mathbf{E}_0|^2. \end{aligned}$$

The result is obtained by multiplying the wave equation (5.37) by  $\mathbf{E}^{*\prime} = \partial_x \mathbf{E}^*$  and its complex conjugate by  $\mathbf{E}'$ . If in the case of an arbitrary  $\omega_p^2/\omega^2$  is replaced by  $(\eta^2 - 1)/2$  in the wave equation,  $\eta$  refractive index, again (5.1) is recovered, as expected. However, the force density  $\pi$  in a dielectric medium is obtained by such a replacement only in the limit of a dilute medium, as may be seen from (5.25). In dense matter the field polarizing the single molecule differs from the mean field  $\mathbf{E}$  in the medium. Well-known examples for this are the Clausius–Mosotti and Lorentz–Lorenz corrections.

In order to see how a static amplitude modulation acts on a streaming plasma let us consider a partially standing electric wave  $E(x, t)$  of the simplest form (5.36), acting on a stationary isothermal plasma flow parallel to the x-axis. The flow is determined by

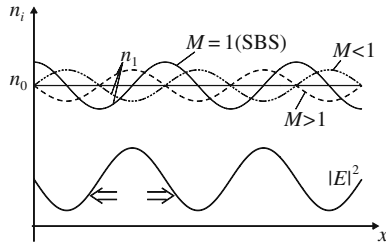


**Fig. 5.5** A homogeneous plasma is periodically modulated by the pressure of a partially standing wave.  $|E|$  electric field amplitude,  $n_0$  average plasma density,  $n_i = n_0 + n_1(x)$  local plasma density,  $M = v/s$  Mach number.  $M > 1$ : maxima of  $n_1$  in phase with maxima of  $|E|^2$ ;  $M < 1$ :  $n_1$  dephased by  $\pi$ ;  $M = 1$ :  $n_1$  dephased by  $\pi/2$  (resonance: stimulated Brillouin scattering, SBS); lower arrows: direction of ponderomotive force

$$\rho v = \rho_0 v_0 = \text{const}, \quad \rho v \frac{\partial v}{\partial x} = -s^2 \frac{\partial \rho}{\partial x} - \frac{\varepsilon_0}{4\rho_c} \rho \frac{\partial}{\partial x} |E_0 + E_r|^2.$$

With the help of the Mach number  $M = v/s$ , for  $\rho \ll \rho_c$  these relations lead to

$$(1 - M^2) \frac{\partial \rho}{\partial x} = \frac{\varepsilon_0}{s^2 \rho_c} \rho k E_0 E_r \sin 2kx \sim -\frac{\partial}{\partial x} |E|^2. \quad (5.38)$$

The solutions of this equation are characterized as follows. If  $M$  is less than unity everywhere a wave field of periodically modulated amplitude produces a stationary density modulation the maxima of which coincide with the minima of  $|E|^2$  and the modulation amplitude increases with increasing Mach number. If the flow is supersonic in the whole region the density modulation is in phase with  $|E|^2$ . At  $M = 1$  the phase shift is  $\pi/2$  (see Fig. 5.5). For a fixed modulation depth of  $|E|$  the density modulation increases monotonically with the flow velocity approaching the sound speed from both sides; it is lowest for the plasma at rest ( $M = M_0 = 0$ ) and tends to zero with  $M \rightarrow \infty$ . At  $M = 1$  the force becomes resonant with the flow: an infinitesimal modulation of  $|E|$ , e.g. infinitesimal reflected wave  $E_r$  is already capable of producing a density modulation, i.e. a sound wave in this case, for which in the linear regime no steady state exists. This situation is treated in detail in Sect. 6.2.

Major nonresonant ponderomotive effects leading to considerable ion density variations are profile steepening at critical density, laser beam self-focusing and filamentation. They are treated in the following sections.

### 5.3.1 Ablation Pressure

Owing to the importance of ablation pressure for applications, it was already treated in Sect. 2.4.3, however, without radiation pressure. The laser beam pressure influences the ablation pressure  $P_a$  in a more complex way than one would assume at

first glance. Already at very low ratios  $p_\pi/p_c$  of ponderomotive pressure  $p_\pi$  at the field maximum to the plasma pressure  $p_c$  at the critical density the radiation pressure leads to plasma flow inhibition at the critical point and to subsequent plasma acceleration around the maximum of  $\hat{E}^2$  (see Fig. 5.6). The phenomenon is known as ponderomotive profile steepening [47, 48]. At vanishing ratio  $p_\pi/p_c$  the ablation pressure scales like  $I_a^{2/3}$ , provided that a steady state builds up in the plasma dynamics and the heat flux  $q_e$  is negligible. As  $p_\pi$  dominates more and more a transition occurs to direct proportionality  $P_a \sim I$ . With radiation pressure included the equations governing the steady state model developed in Sect. 2.4 are now

$$nv = \text{const}, \quad \rho v^2 + p + p_\pi = \text{const},$$

$$I_a - q_r = nv \left\{ \varepsilon + \frac{p + p_\pi}{n} + m_i \frac{v^2}{2} \right\} + P_a v_1, \quad (5.39)$$

$$p_\pi = - \int \frac{Zn}{4n_c} \frac{\partial}{\partial x} (\varepsilon_0 \hat{E}^2) dx, \quad (5.40)$$

$$P_a = \rho v^2 + p + p_\pi, \quad (5.41)$$

$$\left( M + \frac{1}{\gamma M} \right) \frac{1}{s} \frac{\partial s}{\partial x} + \left( M - \frac{1}{\gamma M} \right) \frac{1}{M} \frac{\partial M}{\partial x} + \frac{\varepsilon_0}{4\rho_c s^2 M} \frac{\partial}{\partial x} \hat{E}^2 = 0. \quad (5.42)$$

The term  $P_a v_1$  stands for the work done by the laser to generate the shock wave traveling into the dense material at speed  $v_S$  and matter velocity  $v_1$ . In what follows  $\gamma = 1$  (isothermal situation) is set. We observe that  $\hat{E}^2$  has the typical sharp maxima of a standing wave whereas that of  $s(x > x_c)$  is flat. Therefore, in (5.42) the first term may be dropped since it cannot balance the two following expressions. Hence

$$\left( M - \frac{1}{M} \right) \frac{\partial M}{\partial x} + \frac{\varepsilon_0}{4\rho_c s^2} \frac{\partial}{\partial x} \hat{E}^2 = 0. \quad (5.43)$$

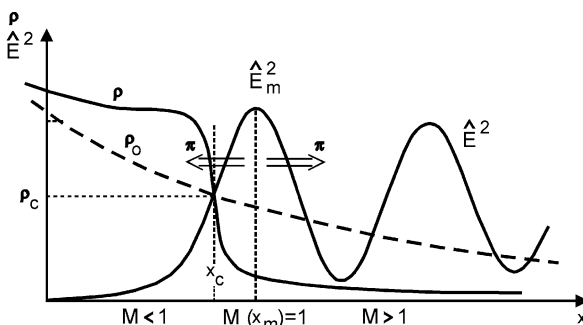


**Fig. 5.6** Ponderomotive density profile steepening in the critical region.  $x_c$  critical point;  $\rho_0$  density distribution under condition  $\pi = 0$ . Transition from the subsonic to supersonic flow occurs at the position  $x_m$  of the first maximum of  $\hat{E}_m^2$

With profile steepening a steady state is reached during a time of the order of  $\tau = \lambda/4s$ , thus  $\tau \lesssim 25$  ps. Under this assumption in the very overdense region  $v$  is subsonic ( $M < 1$ ). In the corona  $v$  is supersonic ( $M > 1$ ). Equation (5.43) states then that the sonic point must coincide with the absolute maximum  $\hat{E}_m^2$  at  $x_m$ . Generally  $\hat{E}_m^2$  coincides with the first local maximum of  $\hat{E}^2$  when counting them in positive  $x$  direction.

In principle  $P_a$  can be evaluated at any point in the coaxial cylinder owing to  $P_a = \text{const}$  throughout the steady state flow region. However, owing to the density dependence of  $p_\pi$  according to (5.40) it is convenient to evaluate  $P_a$  in a maximum or minimum of  $\hat{E}^2$ . We chose here the maximum at  $x = x_m$ . At normal incidence the laser pulse amplitude follows the stationary wave equation

$$\frac{\partial^2}{\partial x^2} \hat{E} + k^2 \left(1 - \frac{Zn}{n_c}\right) \hat{E} = 0; \quad k = \omega/c. \quad (5.44)$$

Multiplying it by  $\hat{E}' = \partial \hat{E} / \partial x$  yields at an arbitrary position

$$p_\pi = \int \frac{Zn}{4n_c} \frac{\partial}{\partial x} \left(\varepsilon_0 \hat{E}^2\right) dx = \frac{\varepsilon_0}{4} \hat{E}^2 + \frac{\varepsilon_0}{4k^2} \hat{E}'^2. \quad (5.45)$$

In the maxima and minima  $\hat{E}'$  vanishes and  $p_\pi$  simplifies. At  $x_m$  holds

$$P_a = 2\rho_m s^2 + \frac{\varepsilon_0}{4} \hat{E}_m^2; \quad \rho_m = \rho_c M_c. \quad (5.46)$$

It is convenient to introduce the normalized quantity  $\mathcal{E}^2 = \varepsilon_0 \hat{E}^2 / 4p_c$ . The critical Mach number  $M_c$  is obtained from integrating (5.43) between  $x_c$  and  $x_m$ ,

$$\mathcal{E}_c^2 = \mathcal{E}_m^2 - \frac{1}{2} \left(M_c^2 - \ln M_c^2 - 1\right). \quad (5.47)$$

This equation together with (5.44) determines  $\mathcal{E}_c$  uniquely if  $\mathcal{E}_m^2$  is assumed to be known. Although it is a simple system, it resisted to all attempts to solve it analytically in explicit form so far. The numerical analysis yields the following best fits

$$\mathcal{E}_m^2 < 1 : M_c \simeq 1 - \sqrt{0.4\mathcal{E}_m^2}; \quad \mathcal{E}_m^2 \geq 1 : M_c \simeq \frac{\mathcal{E}_m^2}{\exp(\mathcal{E}_m^2 + 0.5) - 2}. \quad (5.48)$$

Owing to the action of the radiation pressure  $M_c$  reduces monotonically with increasing  $\mathcal{E}_m$ . At  $\mathcal{E}_m^2 = 1$  the critical Mach number is reduced to  $M_c = 0.38$ .

Now  $\mathcal{E}_m^2$  must be linked to the incident intensity  $I$ . In the following this is done for four relevant cases: normal incidence on a flat target, oblique incidence on a flat target under the angle  $\alpha$  and  $s$ - and  $p$ -polarization, perpendicular incidence on a crater.

### 5.3.1.1 Perpendicular Incidence

Generally at densities below  $\rho_m$  at  $x > x_m$  almost no collisional and collective absorption takes place; the reflection coefficient  $R(x = x_m)$  is close to the overall reflection coefficient  $R$  and  $\rho$  is sufficiently smooth to apply the WKB approximation on  $\hat{E}_m$ ,

$$\mathcal{E}_m^2 = \frac{(1 + \sqrt{R})^2}{(1 - \rho_m/\rho_c)^{1/2}} \frac{p_L}{2p_c}, \quad p_L = \frac{I}{c}. \quad (5.49)$$

In  $p_L$  the vacuum laser intensity  $I$  enters, eventually corrected by the collisional absorption in the corona  $x > x_m$ ;  $p_c$  must be determined from the flux difference  $q_l - q_e - P_a v_1$  defined in (2.145). For  $L_C \simeq \lambda$  and shorter (3.61) will yield more precise values of  $\hat{E}_m$ . The transition to Fresnel's formula for strong profile steepening may be estimated from (3.27) and Table 3.1. For  $\mathcal{E}_m^2 < 1$  this becomes with the help of (5.48)

$$\mathcal{E}_m^2 = 1.2 \left(1 + \sqrt{R}\right)^{8/5} \left(\frac{p_L}{2p_c}\right)^{4/5} \quad (5.50)$$

The radiation pressure-corrected ablation pressure from (5.41) is given by

$$P_a = 2p_c \left(M_c + \frac{\mathcal{E}_m^2}{2}\right) = p_c \left(2M_c + \frac{(1 + \sqrt{R})^2}{2(1 - M_c)^{1/2}} \frac{p_L}{p_c}\right). \quad (5.51)$$

Contrary to what one may expect, for  $\mathcal{E}_m^2 < 1.4$  radiation pressure leads to a reduction of  $P_a/p_c$  since at low ratios  $p_L/p_c$  the stagnation effect of the plasma flow prevails.

In Fig. 5.7  $P_a/p_c$  is plotted as a function of  $\mathcal{E}_m^2$ . The dashed lines are obtained by making use of (5.48) for  $M_c$ . In the interval  $0 \leq \mathcal{E}_m^2 \leq 1.41$  there is a depression of  $P_a$  due to the stagnation effect of  $p_\pi$  on  $M_c$ , with a maximum reduction of 22% at  $\mathcal{E}_m^2$  as low as  $\mathcal{E}_m^2 = 0.35$ . For  $\mathcal{E}_m^2 = 0.15$  the light pressure contributes to  $P_a$  by at most by 10% and can be neglected for  $\mathcal{E}_m^2 \leq 0.15$  and hence (5.46) yields  $P_a \simeq 2p_c M_c$ . In particular, at  $\mathcal{E}_m^2 = 0.15$  follows  $P_a = 1.7 p_c$ . With ns laser pulses generally one moves around such low values of  $\mathcal{E}_m^2$  and it was correct to neglect  $p_\pi$  as an additional term in  $P_a$  of (5.41), as done by all authors so far. However, to neglect its stagnation effect on  $M_c$  would be incorrect. Flow inhibition at  $x_c$  becomes sensitive already at values as low as  $\mathcal{E}_m^2 = 0.02$ , with a 10% reduction of  $P_a$  at temperature  $T$  held fixed. Only from  $\mathcal{E}_m^2 = 0.84$  on the radiation pressure starts dominating the ablative plasma pressure  $2p_c M_c$ .

Stagnation and flow inhibition are synonymous with profile steepening [48, 49]. With the help of (5.43) its scale length  $L$  is given by

$$L = \frac{n}{|\nabla n|} = \frac{M}{|\nabla M|} = \frac{|1 - M^2|}{\nabla \mathcal{E}^2}.$$

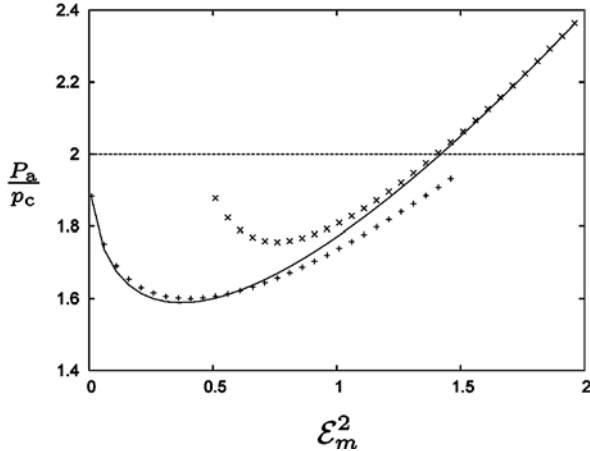


**Fig. 5.7** Normalized ablation pressure  $P_a/p_c$  as a function of  $\mathcal{E}_m^2$

At the critical point it becomes in units of vacuum wavelength  $\lambda$

$$\frac{L}{\lambda} = \frac{1 - M_c^2}{2\lambda \mathcal{E}_c \partial \mathcal{E} / \partial x|_{x=x_c}}. \quad (5.52)$$

Multiplying (5.43) by  $\rho/\rho_c = M_c/M$ , then integrating it from  $x_c$  to  $x_m$  and substituting  $p_{\pi m} - p_c$  from (5.45) yields

$$M_c \left\{ 2 - M_c - \frac{1}{M_c} \right\} + \mathcal{E}_m^2 - \mathcal{E}_c^2 - \frac{1}{k^2} \mathcal{E}'_c^2 = 0.$$

Introducing  $\mathcal{E}_m^2$  and  $\mathcal{E}_c^2$  from (5.47) leads to the desired expression for  $\mathcal{E}'_c$  as a function of  $M_c$ ,

$$\mathcal{E}'_c^2 = \left( 2M_c - \ln M_c - \frac{1}{2} M_c^2 - \frac{3}{2} \right) k^2. \quad (5.53)$$

With this (5.52) becomes

$$\frac{L}{\lambda} = \frac{1 - M_c^2}{2\lambda k \{ \mathcal{E}_m^2 + (1 - M_c^2 + \ln M_c^2)/2 \}^{1/2} \{ 2M_c - \ln M_c - M_c^2/2 - 3/2 \}^{1/2}}. \quad (5.54)$$

The evaluation of this equation proceeds as follows:  $\mathcal{E}_m$  is fixed first. Then the wave equation (5.44) is solved simultaneously with (5.43). In this way  $M_c$  is recovered to be used in (5.54). The result is shown in Fig. 5.8, solid line. If, instead,  $M_c$  is taken from (5.48) and used in (5.54) to determine  $L/\lambda$ , coincidence with the exact result is found (see Fig. 5.8, solid line, dots). For a quick estimate of  $L$  the derivative of  $\mathcal{E}_c^2$  may be approximated by  $\partial \mathcal{E}_c^2 / \partial x \simeq 3k \mathcal{E}_m^2 [1 - 2M_c/(1 + M_c)]^{1/2}/4$ , thus

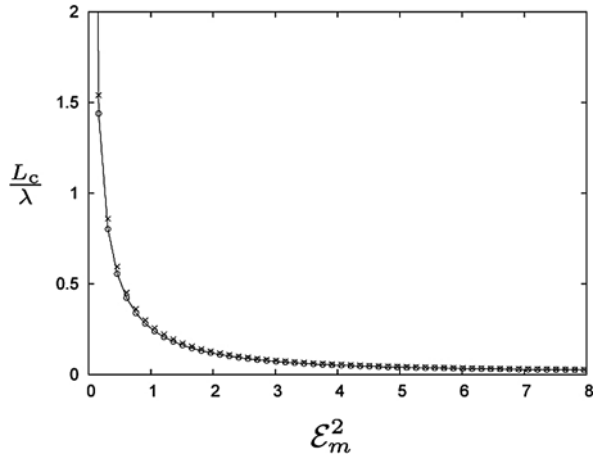


**Fig. 5.8** Scale length at critical point  $L_c/\lambda$  as a function of  $\mathcal{E}_m^2$  from wave equation (solid), from (5.48) and (5.54) (dotted) and from (5.55) (crosses)

$$\frac{L}{\lambda} \simeq \frac{2}{3\pi} (1 - M_c)^{1/2} (1 + M_c)^{3/2} = 0.17 \left( \frac{2}{\mathcal{E}_m} - 0.63 \right)^{3/2}; \quad \mathcal{E}_m^2 < 1. \quad (5.55)$$

As the crosses in Fig. 5.8 show this simple formula is an excellent fit to (5.54).

### 5.3.1.2 Oblique Incidence, s-Polarization

The electric field follows the wave equation

$$\frac{\partial^2}{\partial x^2} \hat{E} + k^2 \left( 1 - \frac{Zn}{n_c} - \sin^2 \alpha \right) \hat{E} = 0.$$

Proceeding in the same way as before one finds at the position  $x_m$

$$p_\pi = \frac{\varepsilon_0}{4} \frac{\hat{E}_m^2}{\cos^2 \alpha}.$$

The density, pressure and Mach number at the vertex,  $\rho_V$ ,  $p_V$ ,  $M_V$ ,

$$\rho_V = \rho_c \cos^2 \alpha, \quad p_V = p_c \cos^2 \alpha, \quad \rho_m = \rho_V M_V,$$

assume the role of the former critical parameters  $\rho_c$ ,  $p_c$  and  $M_c$ . With this step (5.50) transforms into

$$\mathcal{E}_m^2 = \frac{(1 + \sqrt{R})^2}{(1 - \rho_m/\rho_V)^{1/2}} \frac{p_L}{2p_c \cos^2 \alpha} = \frac{(1 + \sqrt{R})^2}{(1 - M_V)^{1/2}} \frac{p_L}{2p_V}, \quad (5.56)$$

i.e., its structure remains invariant. Analogously, in (5.48) and (5.54) for the profile steepening,  $M_c$  is substituted by  $M_V$  and all calculations proceed in the same way as in the case of perpendicular incidence.

### 5.3.1.3 Oblique Incidence, p-Polarization

This is the situation of resonance absorption in a layered medium [50]. At electron temperatures  $T_e \lesssim 10$  keV the electron plasma wave is emitted under the small angle  $\alpha' = \beta \sin \alpha_0$ ,  $\beta = s_e/c$  (see Sect. 3.2.4). In the region  $x_c \leq x \leq x_m$  holds  $|\hat{E}_x| \gg |\hat{E}_y|$  for all angles under which absorption is significant. Therefore  $p_\pi$  and  $\mathcal{E}_m$  can be evaluated by using Piliya's equation (3.70) in the capacitor model approximation, i.e., neglecting  $E_y$ ,  $\beta^2 \sin^2 \alpha_0$ , and setting  $1 - \beta^2$ . The driving term containing  $B$  on the RHS of (3.2.4) is much smaller than  $\hat{E}_{x,m}$  and (5.45) applies again with  $p_{\pi,m} = \varepsilon_0/4\hat{E}_{x,m}^2$ . Then (4.7) yields for  $\mathcal{E}_m^2 = \mathcal{E}_{x,m}^2$

$$\mathcal{E}_m^2 = 1.1(1-R) \left( \frac{kL}{\beta^4} \right)^{1/3} \frac{p_L}{2p_c} \cos \alpha_0. \quad (5.57)$$

Alternatively  $\mathcal{E}_m^2$  can be calculated from the energy flux conservation (3.38) in combination with (3.39),

$$S_{es} = s_e \left( 1 - \frac{\rho}{\rho_c} \right)^{1/2} \frac{\varepsilon_0 \omega^2}{2 \omega_p^2} \hat{E}_m^2 = (1-R)c p_L \cos \alpha_0 \quad (5.58)$$

$$\implies \mathcal{E}_m^2 = \frac{1}{\beta} \frac{1-R}{(1-M_c)^{1/2}} \frac{p_L}{2p_c} \cos \alpha_0. \quad (5.59)$$

With (5.45), (5.46), (5.47), and (5.48) remaining valid the ablation pressure is given by

$$P_a = 2p_c \left( M_c + \frac{\mathcal{E}_m^2}{2} \right) \quad (5.60)$$

and  $L\lambda$  follows from (5.54). For low intensities (5.58) may be correct. It has to be made sure that the resonance width  $d$  from (4.2) does not exceed the density scale length  $L$  of the Stokes equation. The second expression (5.59) is more robust; however, it has also its limitations because  $S_{es}$  is based on linearized equations. On the other hand (4.14) on the limiting intensity  $I_{max}$ , Fig. 4.10 and the considerations on wave breaking in Sect. 4.4.2 may be helpful in the specific case.

### 5.3.1.4 Perpendicular incidence, focused beam

First it has to be made sure which of the absorption mechanisms dominates, collisional or resonance absorption. Such an estimate requires suitable averaging over all angles of incidence  $\alpha_0$  of the beam into the target crater. If resonance prevails (5.60) and

the angle-averaged (5.57) apply. If this is not the case no general recipe can be given here. Rather has there a combination between  $\mathcal{E}_m$  electromagnetic and  $\mathcal{E}_m$  electrostatic to be found. In the intensity regime  $I_a = 10^{12} \sim 10^{16} \text{ Wcm}^{-2} \mu\text{m}^2$  and pulse durations ranging from several ns to ten ps  $p_\pi \ll p_c$  is fulfilled. A similar inequality holds for the compression work going into the shock wave  $P_a v_1$ . With

$$P_a = \rho_0 v_S v_1 = g \rho_0 v_S^2, \quad v_1 = \left( g \frac{P_a}{\rho_0} \right)^{1/2} \quad (5.61)$$

follows

$$\frac{P_a v_1}{I} \leq \frac{P_a v_1}{I_a} \leq 2 \left( M_c \frac{\rho_c}{\rho_0} \right)^{1/2}. \quad (5.62)$$

At short wavelengths in the UV range  $P_a v_1$  must be taken into account. With  $\mathcal{E}_m^2$  as a free parameter  $P_a$  follows from (2.154) by replacing  $\rho_m$  by  $\rho_c M_c$ ,

$$\begin{aligned} P_a &= 2 \frac{(1-R)^{2/3}}{4.65^{2/3}} \rho_c^{1/3} M_c^{1/3} I^{2/3} \\ &= 3.3 \times 10^{-8} (1-R)^{2/3} M_c^{1/3} (\rho_c [\text{g}])^{1/3} \left( I [\text{Wcm}^{-2}] \right)^2 \text{ Mbar}. \end{aligned} \quad (5.63)$$

The critical Mach number  $M_c$  may be taken from (5.48). For plane isothermal heat flow into the corona the corresponding numerical factor is  $3.6 \times 10^{-8}$ .

Formula (5.63) holds for idealized conditions described in the previous analysis. It may be helpful in evaluating the single effects contributing to the ablation pressure in the individual experiment, like heat conduction, different kinds of laser energy absorption, radiation pressure and profile steepening, nonsteady state effects. Within the model presented here the most sensitive aspects are local and nonlocal energy deposition through direct laser light absorption, diffusive heat flow and delocalized preheat by fast electrons. Radiation pressure effects are important for profile steepening and its influence on energy absorption. For  $\mathcal{E}_m^2 \leq 1.4$ ,  $P_a$  is reduced as a consequence of the stagnation effect on the flow at critical density. The dependence of  $P_a$  on the laser intensitiy to the power of 2/3 remains substantially unchanged as long as preheat and lateral heat losses can be ignored. In the experiment a whole variety of power dependences ranging between 0.15 and 2.5 are measured, e.g., 0.3 in [51]. Extensive experimental studies in the intensity range  $10^{13} \sim 10^{15} \text{ Wcm}^{-2}$  and comparison with previous results have been presented by F. Dahmani [52]. The author finds a 2/3 power in  $I_a/\lambda$ , in agreement with (5.63), however, with a numerical factor slightly higher than  $3.3 \times 10^{-8}$ . From thorough acceleration studies of thin low-Z foils at the Asterix III iodine laser ( $\lambda = 1.315 \mu\text{m}$ ) by K. Eidmann *et al.* [53] in the intensity range  $10^{11} - 10^{16} \text{ Wcm}^{-2}$  one extracts  $P_a [\text{Mbar}] = 5.5 \times 10^{-9} (I [\text{Wcm}^{-2}])^{0.65}$ . In another series of experiments with the Asterix III laser at fundamental and third harmonic wavelength ( $\lambda = 0.44 \mu\text{m}$ ) the law  $P_a = 2.8 \times 10^{-8} I_a^{0.6} \lambda^{-0.4}$  was found [54]. In a last example

[55] 12  $\mu\text{m}$  thick gold foils under Nd laser irradiation were analyzed with the result  $P_a = 5.1 \times 10^{-9} I_a^{0.71}$ . For additional comparisons with early experiments consider [56]. In a more recent experiment [57] the authors aimed at achieving 1D conditions without lateral energy losses for  $\lambda = 0.44 \mu\text{m}$  up to intensities  $I_a = 2 \times 10^{14} \text{ Wcm}^{-2}$  on aluminum targets. They found a dependence of  $P_a$  on the target thickness  $d^{-2/15}$  and an overall intensity dependence in “fair agreement with analytical models”, e.g., [58]. In a numerical study by R.G. Evans et al. [59] at Nd wavelength with plane targets and no heat flux limit, and with spherical targets of radius 100  $\mu\text{m}$  and heat flux limit  $f = 0.03$   $P_a = 2.5 \times 10^{-9} I_a^{0.67}$  and  $P_a = 1.9 \times 10^{-10} I_a^{0.767}$ , respectively, was obtained in the interval  $10^{12} - 10^{16} \text{ Wcm}^{-2}$ . To the authors’ knowledge no investigation on the contribution of radiation pressure in this intensity regime is available except [60].

At laser intensities well beyond  $10^{17} \text{ Wcm}^{-2}$  and on fs  $\sim$  ps time scale the light pressure  $p_L$  clearly prevails on plasma pressure. The reason is that  $q_e$  of the fast and medium fast electrons nearly compensates  $I_a$ . To see this we consider heat diffusion in a solid target of  $n_0 = 10^{23} \text{ cm}^{-3}$  for  $I_a = 10^{17} \text{ Wcm}^{-2}$  irradiance at  $t = 1 \text{ ps}$ . From (2.117) a penetration depth  $x_T = 26(f/Z)^{2/9} \mu\text{m}$ ,  $f$  heat flux inhibition factor, and a plasma pressure  $p = n_c k_B T = 2.5 \times 10^{12}(f/Z)^{-2/9}$  [cgs] are calculated. This has to be compared with the radiation pressure  $p_L = I_a/c = 3 \times 10^{13}$  [cgs] which is an order of magnitude higher. In the transition region from  $P_a \sim I_a^{2/3}$  to  $P_a \sim I_a$  around  $I = 10^{17} \text{ Wcm}^{-2}$  accurate values of  $p/p_L$  are accessible only to numerical simulation.

### 5.3.2 Filamentation and Self-Focusing

Filamentary structures in ns beam plasma interactions were reported for the first time by O. Willi and P.T. Rumsby in 1981 [61] to the surprise of the scientific community. At the fundamental, 2nd, and 3rd harmonic Nd laser frequency periodic plasma density perturbations parallel to the incident laser beams had been diagnosed at intensities  $I \simeq 10^{12} - 10^{15} \text{ Wcm}^{-2}$ . In a representative number of shots the spatial periodicity was ranging from 10 to 18  $\mu\text{m}$ . From an expression for the most unstable mode according to [62], the authors obtained 15  $\mu\text{m}$  for  $I = 3 \times 10^{13} \text{ Wcm}^{-2}$  and  $T_e = 500 \text{ eV}$ . In burn-through experiments with flat solid targets the back action of the density modulations onto the intensity profile of the laser could be demonstrated. The plasma flow velocity under different geometries, oblique incidence on flat targets, radial irradiation of spherical targets, had no noticeable influence on the phenomenon of filamentation [63].

Filamentary structures with periodicity orthogonal to the laser beam direction are known to be driven by thermal, ponderomotive, and relativistic effects. The thermal instability [64] arises in the resistive plasma from local collisional overheating by an intensity spike in the laser beam and subsequent plasma expansion. The concomitant increase in the refractive index leads to bending of the rays in the single filament according to (3.12), lateral motion (hosing instability [65]), and to filament self-

focusing in the underdense plasma. In the overdense plasma the thermal instability is driven by jets of fast electrons generating a locally modulated cold return current and a pinching magnetic field owing to spatially unstable current neutralization [66]; see also [67, 68]. A kinetic description with the effect of  $e-e$  and  $e-i$  collisions thoroughly examined is presented in [69, 70]. Although laser beam self-focusing can be viewed as a special case of filamentation consisting of one single filament, or merging of several filaments into one, whole beam self-focusing has been observed only ten years later [71]. In this case the driving force was attributed to the thermal instability.

Ponderomotive filamentation is very simple in principle. Assume a periodically modulated laser beam propagating in  $x$ -direction with a periodic field modulation  $k_{\perp}$  perpendicular to it, say in  $z$ -direction. If the stationary motion of the isothermal plasma is also in  $z$ -direction from (5.26) follows that equilibrium is governed by (5.43). In the subsonic flow ( $M < 1$ ) growth of the modulation occurs when the first term is smaller than the second, ponderomotive term. Above a certain threshold such an imbalance is induced by the lateral expulsion of plasma from regions of high laser intensity and the concomitant increase of the refractive index  $\eta$  along the filament axis. For  $k >$  several  $k_{\perp}$  the ray equation (3.12) applies. It describes bending and compression of the rays towards increasing  $\eta$  which, in turn, reinforces plasma expulsion by increased ponderomotive action. Alternatively, when the plasma density modulation  $n_1[\exp(ik_{\perp}z) + \exp(-ik_{\perp}z)]$  is small compared with the unperturbed density  $n_0$  a linearized ansatz for the laser wave  $\mathbf{E} = \mathbf{E}_0 + \mathbf{E}_1 = \hat{\mathbf{E}}_0 \exp(ikx) + \hat{\mathbf{E}}_1 \exp(ikx + ik_{\perp}z)$  with  $\mathbf{E}_0 \perp k\mathbf{e}_x$  and  $\mathbf{E}_1 \perp (k\mathbf{e}_x + k_{\perp}\mathbf{e}_z)$  is appropriate. Its spatial distribution must fulfill the wave equation (3.7), i.e.,  $\nabla^2 \mathbf{E} + k_0^2[1 - (n_0 + n_1)]\mathbf{E} = 0$ . Ordering according to  $\mathbf{k} = k\mathbf{e}_x$  and  $\mathbf{k}' = k_x\mathbf{e}_x \pm k_{\perp}\mathbf{e}_z$ , and by observing that  $\mathbf{E}_0$  and  $\mathbf{E}_1$  obey the dispersion relation  $k^2 = k_0^2(1 - n_0/n_c)$  yields

$$-k_{\perp}^2 \hat{\mathbf{E}}_1 \exp(ik_{\perp}z) = k_0^2 \frac{n_1}{n_0} \hat{\mathbf{E}}_0^* \exp(ik_{\perp}z), \quad k_0 = \frac{\omega}{c}. \quad (5.64)$$

$\mathbf{E}_1$  is nearly parallel to  $\mathbf{E}_0$  (the sum of both components  $k_x\mathbf{e}_x \pm k_{\perp}\mathbf{e}_z$  is exactly parallel). Maxima and minima of  $E_1$  and  $n_1$  are out of phase by  $\pi$ , in agreement with the prediction from the ray equation. There is an optimum wavelength to be expected for maximum growth of the filamentary instability because the ponderomotive force increases with increasing  $k_{\perp}$ ; when  $k_{\perp}$  becomes of the order of  $k$  or shorter, contrast saturation by diffraction between intensity maxima and minima sets in. Ponderomotive filamentation may be viewed as a special case of Stokes/anti-Stokes stimulated Brillouin forward scattering (see Sect. 6.2.3). The modulations seen in [61, 63] can be interpreted as thermally as well as ponderomotively driven structures. Final clarification is difficult and still missing.

A criterion for whole beam self-focusing is obtained most simply with the aid of a Gaussian laser beam of a radial profile

$$E(x, r) = E_0 e^{-r^2/\sigma^2}, \quad \sigma^2 = \sigma_0^2(1 + x^2/x_0^2), \quad \theta = \frac{\sigma_0}{R} = \frac{2}{k\sigma_0},$$

$$\mathbf{k} = \mathbf{k}_0 \eta, \quad R = x_0 = \frac{k\sigma_0^2}{2}, \quad R_c = \frac{1}{\partial_{xx}\sigma}|_{x=0} = \frac{R^2}{r}; \quad (5.65)$$

$R$  Rayleigh length,  $\theta$  diffraction angle in the homogeneous medium,  $\sigma_0^2$  beam waist (see any volume on optics or diffraction),  $R_c$  curvature radius at  $(x = 0, r)$ . The curvature  $\kappa = 1/R_c$  averaged over  $2R$  results as

$$\bar{\kappa} = \frac{1}{\bar{R}_c} = \frac{1}{2R} \{ \partial_x \sigma(x = 0) + \partial_x \sigma(x = 2R) \} = \frac{r}{\sqrt{5}R^2} \quad \Rightarrow \quad \bar{R}_c \simeq 2 \frac{R^2}{r}.$$

Note, for  $r < \sigma_0$  at  $x = 0$ ,  $\sigma_0$  has to be replaced by  $r$ . It is instructive to observe that the same average curvature  $\bar{R}_c$  is alternatively obtained by elementary means, see Fig. 5.9.

In the ponderomotively driven inhomogeneity of  $\eta$  a ray through  $(x = 0, r)$  undergoes a curvature  $1/R_c$  in the direction opposite to the diffraction that is determined from the ray equation (3.12) with the help of the first Frenet formula and  $\mathbf{k}_0 \nabla \eta = 0$ ,  $\partial_r = \partial_z$  as follows,

$$\frac{d}{ds} \frac{\eta \mathbf{k}_0}{k_0} = \eta \frac{d}{ds} \frac{\mathbf{k}_0}{k_0} = \mathbf{n} \frac{\partial \eta}{\partial r} = -\frac{\mathbf{n}}{2\eta n_c} \frac{\partial n_e}{\partial r};$$

Frenet :  $\frac{\mathbf{n}}{R_c} = \frac{d}{ds} \frac{\mathbf{k}_0}{k_0} \Rightarrow R_c = 2\eta^2 \frac{n_c}{\partial n_e / \partial r}; \quad \mathbf{n} \perp \mathbf{k}_0, \quad \mathbf{n}^2 = 1. \quad (5.66)$

From the equilibrium condition  $\nabla p_e + \pi = 0$  the spatial variation of  $n_e$  and  $R_c$  result as

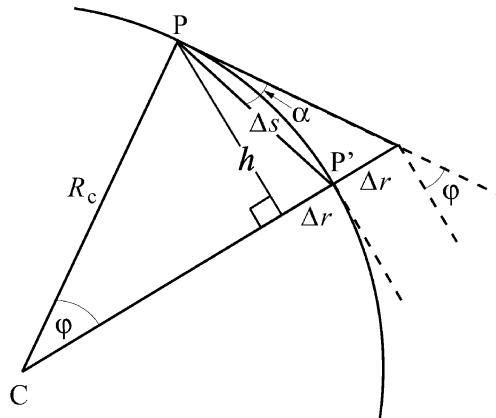


**Fig. 5.9** Determination of the curvature radius  $R_c$  of a Gaussian ray passing through  $PP'$ . Infinitesimal deflection angle  $\alpha = \Delta r / \Delta s = \varphi/2$ ;  $\Delta s = R_c \varphi = 2R$ ,  $R$  Rayleigh length. To first order holds  $2\Delta r R_c = h^2 = \Delta s^2 \Rightarrow R_c = \Delta s^2 / 2\Delta r$ ;  $\Delta r = (\sqrt{5} - 1)r \simeq r \Rightarrow R_c \simeq 2R^2/r$

$$\frac{\partial n_e}{\partial r} = \frac{2r}{\sigma_0^2} \frac{n_e}{p_c} \frac{I(r)}{c}, \quad R_c = \eta^2 \frac{\sigma_0^2 p_c c}{r I(r)} \frac{n_e}{n_e}; \quad (5.67)$$

$p_c$  electron pressure at critical density. The threshold for self-focusing of the limiting ray through  $(x = 0, r)$  is reached when the two curvature radii  $\bar{R}_c$  and  $R_c$  from (5.67) become equal, i.e., when the local intensity  $I(r)$  amounts to

$$I(r) = \frac{2cp_c}{(\sigma_0 k_0)^2} \frac{n_e}{n_e}. \quad (5.68)$$

The higher the intensity  $I(\sigma) = \text{const}$  the higher the fraction of the total beam power  $P = (\pi/2)\sigma_0^2 I_0$  that is focused;  $I_0 = I(r = 0)$ . From  $P$  and (5.68) follows

$$I(r) = \frac{2P}{\pi\sigma_0^2} e^{-2\frac{r^2}{\sigma_0^2}}, \quad P(r) = \pi \frac{c^3 p_c}{\omega_p^2} e^{2\frac{r^2}{\sigma_0^2}}. \quad (5.69)$$

Half power ( $r = 0.6\sigma_0$ ) and 86% power focusing ( $r = \sigma_0$ ) require

$$r = 0.6\sigma_0 : P_{1/2} = 2\pi \frac{c^3 p_c}{\omega_p^2}; \quad r = \sigma_0 : P_{\sigma_0} = \pi \frac{c^3 p_c}{\omega_p^2} e^2, \quad e = 2.718\dots$$

For illustration,  $n_c = 10n_e = 10^{21} \text{ cm}^{-3}$ ,  $T_e = 1 \text{ keV}$ ,  $\sigma_0 = 10\lambda$  (5.69) yields  $I_0 = 4.3 \times 10^{13} \text{ Wcm}^{-2}$  on axis for  $P_{1/2}$  and  $I_0 = 1.6 \times 10^{14} \text{ Wcm}^{-2}$  for  $P_{\sigma_0}$ . The intensity measured by the experimentalist is  $I = P/\pi\sigma_0^2 = I_0/2$ . Relativistic self-focusing is postponed to Chap. 8.

Geometrical optics is based on the concept of light rays and is of limited applicability. Further limitation is imposed by the use of Gaussian beams. In particular, after self-focusing has occurred once, the beam intensity behind will no longer resume a distribution of this type. Ray tracing is useful to show the effect of intensity on beam propagation and to get simple criteria for amplification of deviations from ideality. More recent studies in connection with stimulated Brillouin scattering have elucidated the significance of transient self-focusing for triggering various parametric instabilities and its interplay with them (see Sect. 6.2.3 on SBS). The dynamics of ponderomotive self-focusing shows a whole variety of topological aspects already under the limitation to paraxial geometry in a static ion background [72]. Formation of intensity rings, oscillatory partial beam trapping and focusing on shorter than geometrical distances with non-Gaussian beams have been observed.

### 5.3.3 Modulational Instability

In the oscillation center approximation the ponderomotive force depends on the gradient of the electric field squared and no distinction between transverse or longitudinal polarization with respect to the wave propagation direction results. As

a consequence, the steady state equation of motion (5.43) preserves its structure independently of the angle of the irrotational flow relative to the field propagation direction. Therefore unstable nonresonant pulse propagation is expected also for the case that the  $\mathbf{K}$  vector of the pulse perturbation is parallel to the  $\mathbf{k}$  vector of the wave. This instability is named modulational instability and occurs in electromagnetic as well as electron plasma and ion acoustic modes. Consider an electromagnetic pulse with a narrow frequency spectrum centered around  $(k, \omega)$  propagating in a homogeneous isothermal plasma of density  $n = n_0$  along  $x$ ,  $E(x, t) = \hat{E}(x, t) \exp(i k x - i \omega t)$ . Evaluating the nonresonant ponderomotively induced plasma density  $n$  from (5.43) one is led to  $n = n_0 \exp(-\varepsilon_0 \hat{E}^2 / 4\rho_c s^2)$  for  $M \ll 1$  and to  $n = n_0 / [1 - \varepsilon_0 \hat{E}^2 / (2\rho_c v_0^2)]^{1/2}$  for  $M \gg 1$ . For small differences  $n_1 = n - n_0$  the two expressions become

$$M \gg 1 : \quad n_1 = n_0 \frac{\varepsilon_0 \hat{E}^2}{4\rho_c v_0^2}; \quad M \ll 1 : \quad n_1 = -n_0 \frac{\varepsilon_0 \hat{E}^2}{4\rho_c s^2}. \quad (5.70)$$

With the current density  $j = j_0 + j_1$  from  $n_0$  and  $n_1$  and by observing that  $(k, \omega)$  obey the dispersion relation (3.11) for a smooth, slowly varying amplitude  $\hat{E}$  the wave equation (3.3) reduces straightforwardly to

$$i \frac{\partial}{\partial t} \hat{E} + i \frac{c^2 k}{\omega} \frac{\partial}{\partial x} \hat{E} + \frac{c^2}{2\omega} \frac{\partial^2}{\partial x^2} \hat{E} - \frac{e^2 n_1}{2\varepsilon_0 m} \hat{E} = 0. \quad (5.71)$$

By observing that  $kc^2/\omega = c\eta_0$  is the group velocity  $v_g = \partial\omega/\partial k$  the second term is recognized as the convective part of the total time derivative of  $\hat{E}$ . Transforming to the reference system co-moving with the pulse and substituting  $n_1$  from (5.70), (5.71) assumes the structure of the nonlinear Schrödinger equation

$$i \frac{\partial \Psi}{\partial t} + P \frac{\partial^2 \Psi}{\partial x^2} + Q |\Psi|^2 \Psi = 0, \quad (5.72)$$

with the coefficient  $P = c^2 \omega' / 2\gamma^2 \omega_p^2$  in the comoving frame;  $\gamma$  Lorentz factor. It is a simple model equation used to study mild nonlinear phenomena in many branches of physics. In our context  $\Psi = \hat{E}$ , which without limitation can be assumed as real (for instance, by choosing  $t = t_0$  properly). The correctness of (5.72) after transforming to the relativistic co-moving frame follows from substituting  $\partial_t + v_g \partial_x = \partial_{t'} / \gamma$  according to (8.29) and by observing that  $\partial_{xx} \approx \gamma^2 \partial_{x'x'}$  in the context here. From (8.11) follows  $\omega = \gamma \omega_p^2 / \omega'$ . The plasma frequency is a Lorentz scalar and  $E' = \gamma E$  for  $\mathbf{E} \perp \mathbf{k}$  and  $E' = E$  for the electron plasma wave [see (8.9)]. If the modulation  $n_1$  propagates with  $v_g$  it transforms like  $n'_1 = \gamma n_1$  and the coefficient  $e^2 n_1 / 2\varepsilon_0 m$  in (5.71) is also a Lorentz scalar. If, however,  $n_1$  and  $m$  move at different speed owing to dispersion of  $n_1$ , or the quiver motion in the  $E$ -field becomes relativistic, the situation is more complex and must be treated properly. The complication arises from the nonlinear velocity addition theorem (8.19).

The general solution of (5.72) is accomplished by the inverse scattering method [73]. Here we consider the steady state pump pulse  $E_0 = \hat{E}_0 \exp(iQ\hat{E}_0^2 t)$  that is a solution of (5.72), perturb it by  $E_1 = \hat{E}_1 \exp(+iQ\hat{E}_0^2 t)$  and linearize (5.72) in  $\hat{E} = \hat{E}_0 + \hat{E}_1$ ,

$$i\frac{\partial}{\partial t}\hat{E}_1 + P\frac{\partial^2}{\partial x^2}\hat{E}_1 + Q\hat{E}_0^2[\hat{E}_1 + \hat{E}_1^*] = 0. \quad (5.73)$$

Splitting  $\hat{E}_1$  into real and imaginary part,  $\hat{E}_1 = U + iV$ , yields the system of linear equations

$$\frac{\partial U}{\partial t} + P\frac{\partial^2 V}{\partial x^2} = 0, \quad -\frac{\partial V}{\partial t} + P\frac{\partial^2 U}{\partial x^2} + 2Q\hat{E}_0^2 U = 0 \quad (5.74)$$

that is solved by the ansatz  $\hat{E}_1 = (U_0 + iV_0)\exp[-i(Kx - \Omega t)]$ ,  $U_0, V_0 = \text{const}$ , provided the determinant is zero,  $\Omega^2 + PK^2(2Q\hat{E}_0^2 - PK^2) = 0$ . It shows that modulational growth occurs for  $\Omega = i[PK^2(2Q\hat{E}_0^2 - PK^2)]^{1/2}$  if  $PQ > 0$  and  $\hat{E}_0^2 > PK^2/2Q$ . The unstable  $K$ -interval, growth rate  $\Gamma$ , maximum growth  $\Gamma_{\max}$  and related wave number  $K_m$  are

$$0 \leq K \leq \left(\frac{2Q\hat{E}_0^2}{P}\right)^{1/2}, \quad \Gamma = [PK^2(2Q\hat{E}_0^2 - PK^2)]^{1/2}, \\ \Gamma_{\max} = |Q|\hat{E}_0^2, \quad K_m = \left(\frac{Q}{P}\right)^{1/2}\hat{E}_0. \quad (5.75)$$

$PQ < 0$  yields stability. The coefficient  $P = c^2\omega'/2\gamma^2\omega_p^2$  is positive and hence  $n_1$  must be negative or  $M < 1$  in (5.70).

The electron plasma wave in one dimension exhibits the same structure as the electromagnetic wave, see (3.3), (3.4), (3.7), and the same dispersion with the wave number substituted by  $k = k_e = k_0\eta_0c/s_e$ , see (3.11). Hence, in lowest order (5.71) results again for  $\mathbf{E} \parallel \mathbf{k}$  and (5.75) follows for the modulationally unstable domain of the Langmuir wave. A relativistic treatment of the modulational instability for longitudinal and transverse polarization with account of nonlinear Landau damping is presented in [74]. There is a whole variety of theoretical papers on the ponderomotively driven modulational instability under various conditions [75–80]. By applying a magnetic field in direction of the wave vector the modulational growth  $\Gamma$  is attenuated up to the degree of stabilization [81]. The first direct observation of a modulationally unstable electron plasma wave was accomplished in an electron beam-plasma experiment [82] (authors' claim); the smooth Langmuir pulse evolved into two humps. The initially weak modulation may evolve into a highly nonlinear structure of a finite number of solitons. The existence and stability of such structures in three dimensions is investigated in [83]. The final stage of a pulse after breaking up into solitary humps may be self-contraction with a rate following theoretical

predictions and then a collapse after the onset of other nonlinearities, e.g., electron trapping and acceleration. The collapse of the cavity density  $n$  proceeds under the field trapped in it also after its decoupling from the outer driver [84].

The model equation (5.72) predicts instability only for  $M < 1$ . Modulational instability of  $\hat{E}$  may occur also at  $M > 1$ . To see this one simply has to remember that the plasma density perturbation  $n_1$  is in phase with the humps of the electric wave at  $M > 1$ . For  $K \ll k_0$  (3.26) applies. In the maxima of  $\hat{E}$  the group velocity is lower and hence, under steady state energy flux, wave amplitude, perturbation  $n_1$  and wave pressure are altogether in phase there;  $n_1$  starts growing.

The ion acoustic wave is also modulationally unstable. The derivation of a nonlinear Schrödinger equation of type (5.72) proceeds in a similar way. When  $T_e$  is much higher than  $T_i$  an electric field builds up in the acoustic disturbance according to (2.75). It gives rise to a ponderomotive force acting on the plasma background density and leading to a stabilization or destabilization of it. Detailed analysis shows that at finite angle  $\theta$  between the acoustic wave and the background modulation its amplitude may become unstable. For  $\theta$  exceeding  $\pi/3$  instability extends to the whole  $K$ -domain [85], whereas for  $\theta = 0$  stability is predicted [86].

In the plasma nearly all kinds of waves are subject to the modulational instability. It also occurs in many other branches of physics, e.g., nonlinear crystals and fibers. It is a very versatile phenomenon. An extreme example of electromagnetic pulse modulation by intense laser field ionization may be found in [87].

## References

1. Hopf, F.A., Meyestre, P., Scully, M.O., Louisell, W.H.: Opt. Commun. **18**, 413 (1976) 193
2. Hopf, F.A., Meyestre, P., Scully, M.O., Louisell, W.H.: Phys. Rev. Lett. **37**, 1342 (1976) 193
3. Kupersztych, J.: Phys. Rev. Lett. **54**, 1385 (1985) 193
4. Pukhov, A.: Rep. Prog. Phys. **66**, 47 (2003)
5. Malka, V.: Europhys. News. **35**, No. 2 (2004) 193
6. D'Ippolito, D.A., Myra, J.R.: Phys. Fluids **28**, 1895 (1985) 193
7. Cohen, B.I., Rognlien, Th.D.: Phys. Fluids **28**, 2793 (1985)
8. Similon, Ph.L., Kaufman, A.N., Holm, D.D. (1986): Phys. Fluids **29**, 1900 (1986) 193, 209
9. Phillips, W.D., Prodan, J.V., Metcalf, H.J.: J. Opt. Soc. Am. B **2**, 1751 (1985) 194
10. Raab, E.L., Prentiss, M., Cable, A., Chu, S., Pritchard, D.E.: Phys. Rev. Lett. **59**, 2631 (1977)
11. Diedrich, F., Peik, E., Chen, J.M., Quint, W., Walther, H.: Phys. Rev. Lett. **59**, 2931 (1987) 194
12. Dalibard, J., Cohen-Tanoudji, C.: J. Opt. Soc. Am. B **2**, 1707 (1985) 194
13. Freeman, R.R., Bucksbaum, P.H., Milchberg, H., Darack, S., Schumacher, D., Geusic, M.E.: Phys. Rev. Lett. **59**, 1092 (1987) 194
14. Bauer, D., Mulser, P., Steeb, W.-H.: Phys. Rev. Lett. **75**, 4622 (1995) 194, 202
15. Lee, K., Forslund, D.W., Kindel, J.M., Lindman, E.L.: Phys. Fluids **20**, 51 (1977) 194
16. Max, C.E., McKee, C.F.: Phys. Rev. Lett. **39**, 1336 (1977)
17. Fedosejevs, R., Burgess, M.D.J., Enright, G.D., Richardson, M.C.: Phys. Rev. Lett. **43**, 1664 (1979) 194
18. Hüller, S., Ahedo, E.: Phys. Plasmas **1**, 4061 (1994) 194
19. Landau, L.D., Lifshitz, E.M.: Mechanics, p. 93. Pergamon Press, Oxford (1976) 194
20. Gapunov, A.V., Miller, M.A.: J. Exp. Theor. Phys. **7**, 168 (1958)
21. Boot, H.A.H., Self, S.A., Shersby-Harvie, R.B.R.: J. Electr. Contr. **4**, 434 (1958)
22. Kibble, T.W.B.: Phys. Rev. **150**, 1060 (1966)

23. Hora, H., Pfirsch, D., Schlüter, A.: *Z. Naturforsch.* **22**, 278 (1967) 194
24. Skoric, M.M., ter Haar, D.: *Phys. Fluids* **27**, 2375 (1984) 195
25. Grebogi, G.G., Littlejohn, R.G.: *Phys. Fluids* **27**, 1996 (1984)
26. Weyssow, B., Balescu, R.: *J. Plasma Phys.* **37**, 467 (1987) 195, 205
27. Cary, J.R., Kaufman, A.N.: *Phys. Fluids* **24**, 1238 (1981) 195
28. Kentwell, G.W.: *J. Plasma Phys.* **34**, 289 (1985) 195
29. Hatori, T.: *Phys. Fluids* **28**, 219 (1985) 195
30. Arnold, V.I.: *Dynamical Systems III*, ch. 5 § 2. Springer, Berlin (1988) 195, 203
31. Sarachik, E.S., Schappert, G.T.: *Phys. Rev. D* **1**, 2783 (1970) 197
32. Landau, L.D., Lifshitz, E.M.: *The Classical Theory of Fields*, p. 118. Pergamon Press, Oxford (1980) 197
33. Mulser, P., Uryupin, S., Sauerbrey, R., Wellegehausen, B.: *Phys. Rev. A* **48**, 4547 (1993) 198
34. Sawley, M.L.: *J. Plasma Phys.* **32**, 487 (1984) 199
35. Hemmerich, A., Hänsch, T.W.: *Phys. Rev. Lett.* **68**, 1492 (1992) 199
36. Mulser, P.: In: Cairns, R.A., Sanderson, J.J. (eds.) *Laser–Plasma Interactions*, p. 117. Scottish Universities Summer School in Physics, Edinburgh (1980) 200
37. Balescu, R., R.: *Transport Processes in Plasmas*, vol. 1, Sec. 1.2. North-Holland, Amsterdam (1988) 202
38. Morawetz, K., Jauho, A.P.: *Phys. Rev. E* **50**, 474 (1994) 205
39. Schneider, W.: Elektronenbeschleunigung durch inhomogene Langmuirwellen hoher Amplitude. Electron Acceleration by Inhomogeneous Langmuir Waves of High Amplitude Thesis TH Darmstadt 1984 (in German) 205
40. Quesnel, B., Mora, P.: *Phys. Rev. E* **58**, 3719 (1998) 206
41. Zeidler, A., Schnabl, H., Mulser, P.: *Phys. Fluids* **28**, 372 (1985) 208, 209
42. Lee, N.C., Parks, G.K.: *Phys. Fluids* **26**, 724 (1983)
43. Kentwell, G.W., Jones, D.A.: *Phys. Rep.* **145**, 319 (1987) 208
44. Mulser, P.: *J. Opt. Soc. Am. B* **2**, 1814 (1985) 209
45. Stratham, G., ter Haar, D.: *Plasma Phys.* **25**, 681 (1983) 209
46. Skoric, M.M., Kono, M.: *Phys. Fluids* **31**, 418 (1988) 209
47. Fedosejevs, R., Tomov, L.V., Burnett, N.H., Enright, G.D., Richardson, M.C.: *Phys. Rev. Lett.* **39**, 932 (1977) 212
48. Attwood, D.T., Sweeney, D.W., Auerbach, J.M., Lee, P.H.Y.: *Phys. Rev. Lett.* **40**, 184 (1978) 212, 214
49. Raven, A., Willi, O.: *Phys. Rev. Lett.* **43**, 278 (1979) 214
50. Lindl, J.D., Kaw, P.K.: *Phys. Fluids* **14**, 371 (1971) 217
51. Key, M.H., et al.: *Phys. Fluids* **29**, 2011 (1983); *Phys. Rev. Lett.* **45**, 1801 (1979) 218
52. Dahmani, F.: *J. Appl. Phys.* **74**, 622 (1993); *Phys. Fluids B* **4**, 1585 (1992) 218
53. Eidmann, K., et al.: *Phys. Rev. A* **30**, 2568 (1984) 218
54. Maaswinkel, A.G.M., Eidmann, K., Sigel, R., Witkowski, S.: *Optics Commun.* **51**, 255 (1984) 218
55. Godwal, B.K., Shirsat, T.S., Pant, H.C.: *J. Appl. Phys.* **65**, 4608 (1989) 219
56. Ahlborn, B., Key, M.H., Bell, A.R.: *Phys. Fluids* **25**, 541 (1982) 219
57. Batani, D., et al.: *Phys. Rev. E* **68**, 067403 (2003) 219
58. Mora, P.: *Phys. Fluids* **25**, 1051 (1982) 219
59. Evans, R.G., Bell, A.R., MacGowan, B.J.: *J. Phys. D: Appl. Phys.* **15**, 711 (1982) 219
60. Mulser, P., Hain, S., Cornolti, F.: *Nucl. Instr. Meth. Phys. Res. A* **415**, 165 (1998) 219
61. Willi, O., Rumsby, P.T.: *Opt. Comm.* **37**, 45 (1981) 219, 220
62. Cohen, B.I., Max, C.E.: *Phys. Fluids* **22**, 1115 (1979) 219
63. Willi, O., Rumsby, P.T., Lin, Z.: In: Hora, H., Miley, G.W. (eds.) *Laser Interactions and Related Plasma Phenomena*, vol. 6, p. 633. Plenum, New York (1986) 219, 220
64. Haines, M.G.: *Phys. Rev. Lett.* **47**, 917 (1981) 219
65. Najmudin, Z., et al.: *Phys. Plasmas* **10**, 438 (2003) 219
66. Wei, M.S., et al.: *Phys. Rev. E* **70**, 056412 (2004) 220
67. Hill, J.M., Key, M.H., Hatchett, S.P., Freeman, R.R.: *Phys. Plasmas* **12**, 082304 (2005) 220
68. Deutsch, C., et al.: *Laser and Particle Beams* **26**, 157 (2008) 220
69. Hao, B., Sheng, Z.-M., Zhang, J.: *Phys. Plasmas* **15**, 082112 (2008) 220

70. Hao, B., Sheng, Z.-M., Ren, C., Zhang, J.: Phys. Rev. E **79**, 046409 (2009) 220
71. Afshar-rad, T., et al.: Phys. Rev. Lett. **68**, 942 (1992) 220
72. Cohen, B.I., Lasinski, B.F., Langdon, A.B., Cummings, J.C.: Phys. Fluids B **3**, 766 (1991) 222
73. Zakharov, V.E., Shabat, A.B.: Zh. Eksp. Teor. Fiz. **61**, 118 (1972) 224
74. Pataraya, A., Melikidze, G.: Astrophys. and Space Sci. **68**, 61 (1980) 224
75. Mima, K., Nishikawa, K.: In: Rosenbluth, M.N., Sagdeev, R.Z. (eds.) Handbook of Plasma Physics. North Holland, Amsterdam (1984) (vol. II, Sec. 6.5.4. and refs. therein) 224
76. Vladimirov, S.V., Tsytovich, V.N., Popel, S.I., F.Kh. Kakimov: Modulational Interactions in Plasmas. Kluwer Acad. Publ., Dordrecht (1995)
77. Drake, J., Kaw, P.K., Lee, Y.C., Lin, C.S., Schmidt, G., Rosenbluth, M.: Phys. Fluids **17**, 778 (1974)
78. Shukla, P.K., Baruthram, R., Tsintsadze, L.N.: Phys. Rev. A **35**, 4889 (1987)
79. Tsytovich, V.N., Vladimirov, S.V.: Comm. Plasma Phys. Contr. Fusion **15**, 39 (1992)
80. Vladimirov, S.V., Popel, S.I., Tsytovich, V.N.: Phys. Fluids B **5** (1993) 224
81. Shivamoggi, B.K.: Phys. Rev. A **31**, 1728 (1985) 224
82. Brodskii, Yu.Ya., Litvak, A.G., Nechner, S.I., Slatsker, Ya.Z.: Pis'ma Zh. Eksp. Teor. Fiz. **45**, 176 (1987) 224
83. Laedke, E.W., Spatschek, K.H.: Phys. Rev. A **30**, 3279 (1984) 224
84. Wong, A.Y., Cheung, P.Y.: Phys. Rev. Lett. **52**, 1222 (1984) 225
85. Mishra, M.K., Chhabra, R.S., Sharma, S.R.: Phys. Rev. A **41**, 2176 (1990) 225
86. Shukla, P.K.: Phys. Rev. A **34**, 644 (1986) 225
87. Mulser, P., Cornolti, F., Bauer, D.: Phys. Plasmas **5**, 4466 (1998) 225

# Chapter 6

## Resonant Ponderomotive Effects

Stimulated scattering of an electromagnetic wave from electron density fluctuations induced by acoustic and Langmuir waves plays an important role in laser generated plasmas for understanding its dynamics in detail, fast electron generation and plasma heating, as well as in laser plasma applications. We show that these so-called parametric effects or instabilities, like stimulated Brillouin and Raman scattering, are all resonantly driven by light or wave pressure. In the system co-moving with the electron density disturbance the incident *pump wave* is partially reflected from the inhomogeneities of the refractive index and causes a standing amplitude modulation by superposition of the reflected wave with the pump wave. We show that the phase of the reflected wave with respect to the density modulation is such that the ponderomotive force resulting from the amplitude modulation amplifies the latter which, in turn, leads to increased reflection and finally, by ponderomotive feedback, to exponential growth of the electron density fluctuation and to stimulated scattering of the pump wave. Since in first approximation the longitudinal electric wave obeys a wave equation of the same structure as the transverse electromagnetic wave, and the same is true for the ponderomotive force, both types of waves are subject, damping rates permitting, to the same parametric instabilities. For the physical insight into the dynamics of unstable growth transformation to the reference system co-moving with the refractive index modulation is advantageous because there the modulation is static and the ponderomotive force is secular; for the explicit calculation of growth rates however, the lab frame is generally more appropriate.

### 6.1 Tools

To elaborate the governing equations it may be useful to summarize the necessary main laws and relations derived in the foregoing chapters. In a first approach let us assume a fully ionized ideal plasma of constant density  $n_0$ , temperature  $T_0$  and flow velocity  $v_0$  on which a small static electron density variation  $n_1$ , possibly accompanied by a small temperature variation  $T_1$  is superimposed.

### 6.1.1 Waves, Energy Densities and Wave Pressure

#### 6.1.1.1 Wave Equation

For the purpose of this chapter it is convenient to split the current density  $\mathbf{j} = -en_e(\mathbf{v} - \mathbf{v}_0)$  of (3.3) into the two components

$$\mathbf{j} = \mathbf{j}_0 + \mathbf{j}_1, \quad \mathbf{j}_0 = -en_0(\mathbf{v} - \mathbf{v}_0) = -en_0\mathbf{v}_e, \quad \mathbf{j}_1 = -en_1\mathbf{v}_e.$$

The wave equation for the transverse and parallel field components  $\mathbf{E}_{\perp}(x, \omega)$  and  $\mathbf{E}_{\parallel}(x, \omega)$  in the homogeneous medium ( $n_1 = 0$ ) is obtained from Ohm's law (3.5) in its linearized version,  $\mathbf{j}_0(\omega) = \sigma(\omega)\mathbf{E}(\omega, x, t)$ ,

$$\nabla^2 \mathbf{E}_{\perp,\parallel} - \frac{1}{v_{\varphi}^2} \frac{\partial^2}{\partial t^2} \mathbf{E}_{\perp,\parallel} = 0, \quad \nabla \cdot \mathbf{E}_{\perp} = 0, \quad \nabla \times \mathbf{E}_{\parallel} = 0. \quad (6.1)$$

The individual Fourier components  $\mathbf{E}_{\perp}(\mathbf{k}, \omega)$  and  $\mathbf{E}_{\parallel}(\mathbf{k}, \omega)$  obey the same dispersion relations, i.e., refraction law and ray equation, but propagate with different phase velocities  $v_{\varphi}$ ,

$$\begin{aligned} \mathbf{E}_{\perp}(\mathbf{k}, \omega) : \quad v_{\varphi} &= \frac{c}{\eta}, \quad \eta^2 = 1 - \frac{\omega_p^2}{\omega^2} = 1 - \frac{n_0}{n_c}, \\ \omega^2 &= \omega_p^2 + c^2 k^2, \quad \mathbf{k} = \mathbf{k}_0 \eta, \quad k_0 = \frac{\omega}{c}, \end{aligned} \quad (6.2)$$

$$\begin{aligned} \mathbf{E}_{\parallel}(\mathbf{k}, \omega) : \quad v_{\varphi} &= \frac{s_e}{\eta}, \quad \eta^2 = 1 - \frac{\omega_p^2}{\omega^2} = 1 - \frac{n_0}{n_c}, \\ \omega^2 &= \omega_p^2 + s_e^2 k^2, \quad \mathbf{k} = \mathbf{k}_0 \eta, \quad k_0 = \frac{\omega}{s_e}, \end{aligned} \quad (6.3)$$

$\eta$  refractive index,  $s_e$  electron sound speed. The density perturbation  $n(\mathbf{k}, \omega)$  of the ion acoustic wave obeys

$$\nabla^2 n - \frac{1}{s^2} \frac{\partial^2}{\partial t^2} n = 0; \quad \eta = 1, \quad \omega = sk. \quad (6.4)$$

In general plasmas are inhomogeneous and nonstationary. In the WKB limit in space and time all relations (6.1), (6.2), (6.3), and (6.4) remain valid locally, i.e., for given  $(\mathbf{x}, t)$  dependence. In presence of  $n_1 \neq 0$  in leading order  $n_0$  is to be replaced by  $n_e = n_0 + n_1$  in  $\sigma(\omega)$ ,  $\omega_p$  and  $\eta$ ;  $\mathbf{j}_0 = -en_e\mathbf{v}_{os}$  with  $\mathbf{v}_{os}$  from (2.11). Together with these changes in (2.1), (2.2), and (2.3) the wave equation, complemented by  $\mathbf{j}_1$ , reads now

$$\nabla^2 \mathbf{E}_{\perp,\parallel} - \frac{1}{v_{\varphi}^2} \frac{\partial^2}{\partial t^2} \mathbf{E}_{\perp,\parallel} = -\frac{1}{\epsilon_0 c^2 \beta^2} \frac{\partial en_1 \mathbf{v}_e}{\partial t}, \quad \mathbf{E}_{\perp} : \beta = 1, \quad \mathbf{E}_{\parallel} : \beta = s_e/c. \quad (6.5)$$

As we shall see resonant excitation of a density modulation  $n_1 \ll n_0$  occurs when  $n_1$  represents a plasma eigenmode, that is in our unmagnetized case an ion acoustic or Langmuir mode propagating with its phase velocity  $v_\varphi$ . The current density  $\mathbf{j}_1 = -en_1\mathbf{v}_e$  is parallel to  $\mathbf{E}_{\perp,\parallel}$ .

By changing to a co-moving reference system the perturbation  $n_1$  becomes static. Attention however must be paid to the fact that the wave vector  $\mathbf{k}$  and the frequency  $\omega$  of the pump wave are Doppler-shifted. In the co-moving frame the correctly transformed electric field  $\mathbf{E}'(\mathbf{k}', \omega')$  obeys (6.1) with  $v_\varphi$  depending on  $\angle(\mathbf{k}, \mathbf{v}_{\text{flow}})$ . In the eigenmode system the steady state flow condition  $n_e\mathbf{v} = n_0\mathbf{v}_\varphi$  holds.

### 6.1.1.2 Energy Transport

A summary of Sect. 3.1.3 on the total energy densities of an electromagnetic, electrostatic and ion acoustic wave  $\mathcal{E}_{\text{em}}$ ,  $\mathcal{E}_{\text{es}}$  and  $\mathcal{E}_{\text{a}}$  and their conservation equations reads as follows,

$$\mathcal{E}_{\text{em}} = \mathcal{E}_e + \mathcal{E}_m + \mathcal{E}_{\text{os}} = \frac{1}{2}\varepsilon_0\mathbf{EE}^*; \quad \partial_t\mathcal{E}_{\text{em}} + \nabla\mathbf{v}_g\mathcal{E}_{\text{em}} = 0, \quad v_g = \frac{c^2}{v_\varphi}, \quad (6.6)$$

$$\mathcal{E}_{\text{es}} = \mathcal{E}_e + \mathcal{E}_{\text{os}} + \mathcal{E}_{\text{pot}} = \frac{1}{2}\varepsilon_0\frac{\omega^2}{\omega_p^2}\mathbf{EE}^*; \quad \partial_t\mathcal{E}_{\text{es}} + \nabla\mathbf{v}_g\mathcal{E}_{\text{es}} = 0, \quad v_g = \frac{s_e^2}{v_\varphi}, \quad (6.7)$$

$$\mathcal{E}_{\text{a}} = \mathcal{E}_{\text{i,kin}} + \mathcal{E}_{\text{i,pot}} = n_0 m_i v_{\text{os}}^2; \quad \partial_t\mathcal{E}_{\text{a}} + \nabla\mathbf{v}_g\mathcal{E}_{\text{a}} = 0; \quad v_g = v_\varphi = s. \quad (6.8)$$

The indices os, kin, pot indicate the oscillatory, kinetic and potential particle energy densities;  $\mathcal{E}_e$  and  $\mathcal{E}_m$  are the electric and magnetic contributions. The group velocity  $\mathbf{v}_g = \partial\omega/\partial\mathbf{k}$  is the energy transport velocity of a narrow wave packet. More precisely, as shown in Sect. 3.1.1,  $\mathbf{v}_g$  is the velocity at which a constant  $\mathbf{k}$ -vector propagates. In a stationary plasma the energy flux of frequency  $\omega$  along a ray bundle of cross section  $S(x)$  must be constant,  $v_g\mathcal{E}_{\text{em,es}}S = \text{const}$ ; hence, in one dimension follows the WKB result  $\mathcal{E}_{\text{em,es}}\eta^{1/2} = \text{const}$  in space. Along the way towards the critical density the magnetic energy of  $\mathbf{E}_\perp(\mathbf{k}, \omega)$  and the potential energy of  $\mathbf{E}_\parallel(\mathbf{k}, \omega)$  transform gradually into oscillatory energy of the electrons. At the critical point the magnetic energy reduces to zero.

Imagine an electric wave with a fixed  $\mathbf{k}$ -vector in a homogeneous plasma, for instance a standing wave between two neighboring fixed boundaries, the density of which changes slowly in time. Then

$$E^2\eta = \frac{E^2}{\omega}(\omega^2 - \omega_p^2)^{1/2} = \frac{E^2}{\omega}ck = \text{const} \Rightarrow \frac{E^2}{\omega} = \text{const}; \quad (6.9)$$

thus the action  $E^2/\omega$  is an adiabatic invariant. This is in perfect analogy to the pendulum of slowly varying length where the energy  $\mathcal{E} \sim \omega$ . It shows that under an adiabatic change the photon (plasmon) number density  $N = \mathcal{E}_{\text{em,es}}/\hbar\omega \sim E^2/\omega$  is conserved.

### 6.1.1.3 Ponderomotive Force Density $\pi = \pi_0 + \pi_t$

Assume a pump wave  $\mathbf{E}_1(\mathbf{k}, \omega)$  incident onto a homogeneous plasma in which a much weaker plane wave  $\mathbf{E}_2(\mathbf{k}', \omega)$  is present. The total field  $\mathbf{E} = \mathbf{E}_1 + \mathbf{E}_2$  produces the ponderomotive force density  $\pi_0$  capable of imprinting a regular structure of periodicity  $\mathbf{k} - \mathbf{k}'$ ,

$$\pi_0 = -\frac{\varepsilon_0 \omega_p^2}{4\omega^2} \nabla \mathbf{E} \mathbf{E}^* = -i \frac{\varepsilon_0 \omega_p^2}{4\omega^2} (\mathbf{k} - \mathbf{k}') (\hat{\mathbf{E}}_1 \hat{\mathbf{E}}_2^*) e^{i(\mathbf{k}-\mathbf{k}')\mathbf{x}} + \text{c.c..} \quad (6.10)$$

Thereby weak or moderate damping has been tacitly assumed so that terms  $\nabla|\mathbf{E}_1|^2$  and  $\nabla|\mathbf{E}_2|^2$  are negligible, the latter also owing to  $|\mathbf{E}_2| \ll |\mathbf{E}_1|$ . If one of the waves or both are longitudinal the secular term  $\pi_t = \partial_t \langle m n_1 \mathbf{v}_e \rangle$  has to be added to  $\pi_0$  [see (5.30)]. It plays a role, for instance, in the two plasmon decay. In case  $\mathbf{E}$  is the sum of a transverse and a longitudinal component,  $\mathbf{E} = \mathbf{E}_\perp + \mathbf{E}_\parallel$ , in (6.10) only under the condition  $\mathbf{E} \nabla n_e = 0$  follows  $\nabla \mathbf{E} \mathbf{E}^* = \nabla(\mathbf{E}_\perp \mathbf{E}_\perp^* + \mathbf{E}_\parallel \mathbf{E}_\parallel^*)$ . The general case is more complex.

### 6.1.2 Doppler Shifts

#### 6.1.2.1 Moving Objects and Structures

When transforming from one inertial system  $S$  to another inertial reference system  $S'(\mathbf{v})$  in vacuum wave vectors  $\mathbf{k}$  and frequencies  $\omega$  change, however, the phase  $\phi = \mathbf{k}\mathbf{x} - \omega t$  is a Lorentz scalar, i.e.,

$$\phi = \mathbf{k}\mathbf{x} - \omega t = \mathbf{k}'\mathbf{x}' - \omega't' = \text{const.} \quad (6.11)$$

$\phi$  is not affected by  $S \rightarrow S'(\mathbf{v})$ . As outlined in Sect. 8.1.1 this property implies that  $\mathbf{k}$  and  $\omega$  transform as follows,

$$\mathbf{k}' = \mathbf{k} + \frac{\gamma - 1}{v^2} (\mathbf{v}\mathbf{k})\mathbf{v} - \gamma \omega \frac{\mathbf{v}}{c^2}, \quad \omega' = \gamma(\omega - \mathbf{k}\mathbf{v}). \quad (6.12)$$

If a (partially reflecting) mirror is moving at velocity  $\mathbf{v}$  and it is oriented in such a way that the wave vector of the reflected light is  $\mathbf{k}_r$  in the lab frame, its frequency  $\omega_r$  in the lab frame results shifted to

$$\omega_r = \omega - (\mathbf{k} - \mathbf{k}_r)\mathbf{v} = \omega \left( 1 - \mathbf{k}^0 \frac{\mathbf{v}/c}{1 - \mathbf{k}_r^0 \mathbf{v}/c} \right); \quad \mathbf{k}^0 = \frac{\mathbf{k}}{|\mathbf{k}|}, \quad \mathbf{k}_r^0 = \frac{\mathbf{k}_r}{|\mathbf{k}_r|}. \quad (6.13)$$

This combined Doppler formula follows from (6.12) by observing that  $\omega'$  obeys the equality  $\omega' = \gamma(\omega - \mathbf{k}\mathbf{v}) = \gamma(\omega_r - \mathbf{k}_r\mathbf{v})$ . The orientation of the mirror in vacuum follows from the condition of  $\mathbf{k}'_r$  to be the specularly reflected vector  $\mathbf{k}'$ , i.e.,  $\mathbf{k}'_r \times \mathbf{n}' = \mathbf{k}' \times \mathbf{n}'$ ,  $\mathbf{n}'$  normal vector. In forward direction  $\mathbf{k}_r = \mathbf{k}$  the Doppler shift is zero, in backward direction it is

$$\Delta\omega = 2\omega\beta(1 + \beta), \quad \beta = \frac{v}{c}.$$

Only for  $\beta \ll 1$  the approximation  $k_r = 2k \sin(\vartheta/2)$  is legitimate for the modulus of  $\mathbf{k}_r$ ;  $\vartheta = \angle(\mathbf{k}, \mathbf{k}_r)$ . From the Doppler shift of a signal its velocity  $\mathbf{v}$  can be inferred provided the emitting region is of limited extension. In this case generally, however not necessarily,  $\mathbf{v}$  is the material velocity of the emitting object, e.g., of a moving atom. In the case of a scattering or emitting object extending over several wavelengths interference between the different emitters occurs. To analyze this situation let us consider (3.3). The incident wave  $\mathbf{E}(\mathbf{k}, \omega)$ , transverse or longitudinal, produces a current density  $\mathbf{j} = -en_e(\mathbf{x}, t)\mathbf{v}_{os}$ , with  $\mathbf{v}_{os} = -i(e/m\omega)\mathbf{E} \exp(i\mathbf{k}\mathbf{x} - i\omega t)$ . The scattered field  $\mathbf{E}_s$  obeys also (3.3). Expressing  $n_e(\mathbf{x}, t)$  in Fourier–Laplace components  $n_e(\mathbf{K}, \Omega)$ ,  $\mathbf{E}_s$  and  $\mathbf{j}$  read

$$\begin{aligned} \mathbf{E}_s(\mathbf{x}, t) &= \frac{1}{(2\pi)^2} \int \mathbf{E}(\mathbf{k}_s, \omega_s) e^{i(\mathbf{k}_s \cdot \mathbf{x} - \omega_s t)} d\mathbf{k}_s d\omega_s, \\ \mathbf{j}(\mathbf{x}, t) &= -\frac{1}{(2\pi)^2} \frac{e^2}{m\omega} \mathbf{E} \int \{n_e(\mathbf{K}, \Omega) e^{i[(\mathbf{k} + \mathbf{K}) \cdot \mathbf{x} - (\omega + \Omega)t]} \\ &\quad + n_e^*(\mathbf{K}, \Omega) e^{i[(\mathbf{k} - \mathbf{K}) \cdot \mathbf{x} - (\omega - \Omega)t]}\} d\mathbf{K} d\Omega. \end{aligned}$$

$\{\mathbf{k}_s, \omega_s\}$  represents an orthogonal basis and hence  $\mathbf{E}_s$  and  $\mathbf{j}$  must fulfill the wave equation component-wise. Thus the

Stokes condition:  $\mathbf{k}_s = \mathbf{k} - \mathbf{K}, \quad \omega_s = \omega - \Omega,$   
and (6.14)

anti-Stokes condition:  $\mathbf{k}_s = \mathbf{k} + \mathbf{K}, \quad \omega_s = \omega + \Omega,$

must be fulfilled. In spectroscopy the Stokes and anti-Stokes lines appear with frequencies  $\omega_s = \omega - \Omega$  and  $\omega_s = \omega + \Omega$ , respectively. The fluctuating density mode  $(\mathbf{K}, \Omega)$  propagates at phase velocity  $\mathbf{v}_\varphi = \mathbf{K}^0 \Omega / |\mathbf{K}|$ ,  $\mathbf{K}^0$  unit vector. Hence from  $\Omega = \mathbf{v}_\varphi \cdot \mathbf{K}$  inserted in (6.14) relation (6.13) of the combined Doppler effect,  $\omega_s = \omega - \mathbf{v}_\varphi \cdot (\mathbf{k} - \mathbf{k}_s)$ , is recovered for both, Stokes and anti-Stokes frequencies. Here the relevant velocity responsible for the Doppler shift is the phase velocity  $\mathbf{v}_\varphi$  of the refractive index modulation. Depending on the type of the modulational mode it may represent a material velocity in some cases but in general does not. For example, in a sound wave the oscillatory velocity  $v_{os} = v_\varphi n_1 / n_0$  of the matter is very different from the velocity of the propagation of the density disturbance  $v_\varphi$ . In contrast, an entropy fluctuation in the absence of heat conduction is bound to the material flow because it does not propagate.

### 6.1.2.2 Doppler Effect in the Medium

One may ask how expressions (6.12) look like in matter because  $|\mathbf{v}|$  may exceed  $c$ , for instance when transforming to an electron fluctuation near critical density. To answer this question first we make the formal extension to call  $\omega'$  by definition the

co-moving frequency also in case of  $v > c$ . Formally this is accomplished by setting  $\mathbf{x}' = \mathbf{x} - vt$ ,  $t' = t$ . Now, consider a stationary layered plasma the density  $n(x)$  of which increases smoothly from zero to the constant density  $n_0$  throughout the half space  $x > 0$ . An (infinitely) weak electron plasma wave  $(\mathbf{K}, \Omega)$  is assumed to propagate along the density gradient with phase velocity  $v_{\varphi e}$ . The laser wave  $(\mathbf{k}, \omega)$  with  $\mathbf{k} \parallel \mathbf{K}$  preserves its frequency  $\omega$  throughout the plasma according to (3.15) and its direction. An “observer” moving at  $\mathbf{w} \parallel \mathbf{k}$  in the vacuum, fulfills the condition  $\omega' = \gamma(\omega - \mathbf{k}\mathbf{v}) = \text{const}$  everywhere in the plasma if (and only if)  $\mathbf{v} = \mathbf{w}/\eta$  and  $\gamma = (1 - v^2/c_\varphi^2)^{-1/2} = (1 - w^2/c^2)^{-1/2}$  because of  $\mathbf{k} = \mathbf{k}_0\eta$  and  $c_\varphi = c/\eta$ . Including the transverse Doppler effect,  $\mathbf{v} = \mathbf{v}_\parallel + \mathbf{u}$ ,  $\mathbf{v}_\parallel = \mathbf{w}/\eta$ ,  $\mathbf{u} \perp \mathbf{k}$ , one arrives at (6.12) with  $\gamma = (1 - v_\parallel^2/c_\varphi^2 - u^2/c^2)^{-1/2}$ . The considerations are valid for any homogeneous isotropic medium of refractive index  $\eta$ , hence

$$\omega' = \gamma(\omega - \mathbf{k}\mathbf{v}), \quad \gamma = \left(1 - v_\parallel^2/c_\varphi^2 - \frac{u^2}{c^2}\right)^{-1/2}, \quad \mathbf{v} = \mathbf{u} + \mathbf{v}_\parallel, \quad \mathbf{v}_\parallel = \frac{\mathbf{w}}{\eta}, \quad \mathbf{u} \perp \mathbf{k}.$$

Applied to the electron plasma mode  $(\mathbf{K}, \Omega)$  in the frame moving at its phase velocity  $v_{\varphi e} = \Omega/|\mathbf{K}|$  the mode becomes static,  $(\mathbf{K}, \Omega) \rightarrow (\mathbf{K}', \Omega' = 0)$ . If, for simplicity  $\mathbf{k} \parallel \mathbf{K}$  is assumed the Doppler shifted frequency results as  $\omega' = \gamma(\omega - \mathbf{k}\mathbf{v}_{\varphi e}) = (\omega - k_0 s_e)/(1 - s_e^2/c^2)^{1/2}$ , irrespective of the value of  $\mathbf{v}_{\varphi e}$ . The electron sound velocity never exceeds  $c$ . The general case of oblique incidence is reduced to  $\omega'$  in the vacuum by means of following the light path described by (3.12), or by applying first a Lorentz boost perpendicular to  $\mathbf{K}$  (see Sect. 8.3.2). In the co-moving system of a given mode  $(\mathbf{K}, \Omega)$  holds  $\omega_r' = \omega'$ . This follows already from the combined Doppler formula (6.13) since in deriving it use has been made of this equality. In the homogeneous isotropic medium at rest follows from the translational symmetry perpendicular to  $\mathbf{K}'$  that  $\mathbf{k}'_{r\perp} = \mathbf{k}'_{\perp}$ , i.e., angles of incidence and reflection are equal. However, in presence of flow the fulfillment of the velocity addition theorem (8.19) is incompatible with translational symmetry. It must be kept in mind that only in connection with phases and Doppler shifts  $c$  is substituted by  $c_\varphi = c/\eta$ . No conclusions on dynamics of massive particles should be drawn.

### 6.1.2.3 Transformation of $\pi_0$ to the Lab Frame

In what follows the pump wave and the scattered wave are marked by the indexes 1 and 2; the single Fourier-Laplace mode of the electron density perturbation  $n_1(\mathbf{x}, t)$  is given the index 3, and  $(\mathbf{K}, \Omega) = (\mathbf{k}_3, \omega_3)$ . In the frame co-moving with  $n_1$  according to Sect. 5.1.2 the linearized form of  $\pi_0$  from (6.10) is the secular component of

$$\pi'_0 = -n_0 e \{ (\xi_1 \nabla) \mathbf{E}_2 + (\xi_2 \nabla) \mathbf{E}_1 + \mathbf{w}_1 \times \mathbf{B}_2 + \mathbf{w}_2 \times \mathbf{B}_1 \}_0; \quad (6.15)$$

see Sect. 5.1.2; dashes ('') on the transformed quantities on the RHS of (6.15) are omitted for simplicity. The quantities  $\mathbf{w}_{1,2}$ ,  $\xi_{1,2}$  are the oscillation velocities and the displacements. In the lab frame they oscillate at  $\omega_1$  for the pump and at  $\omega_2$

for the scattered wave. Substitution of  $\mathbf{w}_{1,2} = -ie/2m\omega_{1,2}(\mathbf{E}_{1,2} - \mathbf{E}_{1,2}^*)$ ,  $\xi_{1,2} = e/2m\omega_{1,2}^2(\mathbf{E}_{1,2} + \mathbf{E}_{1,2}^*)$ ,  $\mathbf{B}_{1,2} = -i/2\omega_{1,2}\nabla \times (\mathbf{E}_{1,2} - \mathbf{E}_{1,2}^*)$  yields in the lab frame for  $\omega_3 = \omega_1 - \omega_2$  the resonant ponderomotive component

$$\pi_0 = -\frac{\varepsilon_0\omega_p^2}{2\omega_1\omega_2} \left\{ \nabla(\mathbf{E}_1\mathbf{E}_2^{*c}) + \nabla(\mathbf{E}_2^*\mathbf{E}_1^c) + \frac{\omega_1 - \omega_2}{2} \left[ \frac{(\mathbf{E}_2^*\nabla)\mathbf{E}_1}{\omega_2} - \frac{(\mathbf{E}_1\nabla)\mathbf{E}_2^*}{\omega_1} \right] \right\}. \quad (6.16)$$

(c: field component kept constant). For  $\mathbf{E}_1\nabla n_3 = 0$  the term in the square bracket vanishes; hence

$$\pi_0 = -i\frac{\varepsilon_0\omega_p^2}{2\omega_1\omega_2}(\mathbf{k}_1 - \mathbf{k}_2)(\hat{\mathbf{E}}_1\hat{\mathbf{E}}_2^*)e^{i[(\mathbf{k}_1 - \mathbf{k}_2)\mathbf{x} - (\omega_1 - \omega_2)]}. \quad (6.17)$$

The plasma frequency  $\omega_p$  is Lorentz-invariant [e.g. see (8.15)]. Compared to  $\pi_0 = n_0 f_p$  from (6.10) in the co-moving frame, the new expression (6.17) differs only by the product of the Doppler shifted frequencies  $\omega_1$  and  $\omega_2$  in the denominator and the lab frame representation of the Lorentz-invariant phase  $\phi(\mathbf{K}, \Omega) = \phi(\mathbf{K}, 0)$ . The reader interested in the explicit transformation of the fields  $\mathbf{E}$  and  $\mathbf{B}$  which we do not need here may consult Chap. 8. The field components  $\mathbf{E}_1$ ,  $\mathbf{E}_2$  may stand for two transverse or two longitudinal waves or for a combination of a transverse with a longitudinal wave. In all cases  $\pi_0$  is the same formula (6.17).

#### 6.1.2.4 Thomson Scattering

Spontaneous Thomson scattering is the scattering of light from the free plasma electrons. In the case of hard photons it is preferentially known as Compton scattering. In dense high- $Z$  laser produced plasmas it has proven to represent a powerful tool of plasma diagnostics [1, 2]. Thomson and Compton scattering measurements in the X ray domain have been applied to scan shock compressed solid Be [3]. In order to keep the theory of light scattering and its evaluation as simple as possible the plasma is assumed to be well underdense and locally, i.e., in the active volume, homogeneous and the incident radiation does not alter the plasma properties ( $\hat{v}_{os} \ll v_{th}$ ). The far fields  $\mathbf{E}(\mathbf{x}, t)$  and  $\mathbf{B}(\mathbf{x}, t)$  and the power  $d\mathbf{P}$  irradiated into the solid angle  $d\Omega$  by an electric dipole  $\mathbf{p} = \hat{\mathbf{p}} \exp(-i\omega t')$  at position  $\mathbf{x}'$  and retarded time  $t' = t - |\mathbf{x} - \mathbf{x}'|/c = t - |\mathbf{r}|/c$  are given by

$$\begin{aligned} \mathbf{E}(\mathbf{x}, t) &= \frac{\mathbf{k}^2}{4\pi\varepsilon_0|\mathbf{x} - \mathbf{x}'|} [\mathbf{p} - \mathbf{k}^0(p\mathbf{k}^0)] e^{i\mathbf{k}(\mathbf{x} - \mathbf{x}') - i\omega t'}, \quad \mathbf{B} = \frac{\mathbf{k}}{\omega} \times \mathbf{E}, \\ d\mathbf{P} &= \frac{\omega^4}{8\pi\omega_0 c^3} \hat{\mathbf{p}}^2 \sin^2 \vartheta d\Omega. \end{aligned} \quad (6.18)$$

For a free electron at rest, exposed to the laser field  $\mathbf{E} = \mathbf{E}(\mathbf{x}') \cos \omega t'$  and intensity  $I = \varepsilon_0 c \mathbf{E}^2 / 2$ ,  $\mathbf{p}$  is to be replaced by  $\mathbf{p} = e^2 \mathbf{E} / (m\omega^2)$  and thus the irradiated power  $d\mathbf{P}$  in direction  $d\Omega$  is  $d\mathbf{P} = \sigma_\Omega I d\Omega$ , with the nonrelativistic Thomson differential

scattering cross section  $\sigma_{\Omega} = r_0^2 \sin^2 \vartheta$ , summing up to the total scattering cross section  $\sigma = (8\pi/3)r_0^2 = 0.665$  barn. It is independent of the incident frequency.  $r_0 = e^2/(4\pi\varepsilon_0 mc^2)$  is the “classical electron radius” and  $\vartheta = \angle(\mathbf{E}, d\boldsymbol{\Omega})$ . If the electron moves at nonrelativistic velocity  $\mathbf{v}$  ( $T_e$  up to several keV) in the field with wave vector  $\mathbf{k}$  the power  $d\mathbf{P}(\mathbf{x})$  scattered in the direction of the wave vector  $\mathbf{k}_s$  is still given by  $\sigma_{\Omega} Id\boldsymbol{\Omega}$  but its frequency  $\omega_s$  measured in the lab frame is Doppler shifted according to (6.13) with  $\mathbf{k}_r$  replaced by  $\mathbf{k}_s$ ,

$$\omega_s = \omega - \mathbf{v}(\mathbf{k} - \mathbf{k}_s) = \omega(1 - \mathbf{k}_s^0 \mathbf{v}/c)/(1 - \mathbf{k}_s^0 \mathbf{v}/c). \quad (6.19)$$

In Thomson scattering, or scattering of waves in general, one may encounter two extreme situations. If the scattering centers are uncorrelated the total power  $\mathbf{P}$  scattered from a volume  $\Delta V$  into the unit solid angle per unit frequency is the sum of the single intensities,

$$\begin{aligned} \mathbf{P}(\omega_s) &= \sigma_{\Omega} I \int f(\mathbf{x}, \mathbf{v}) \delta(\boldsymbol{\Omega} - \mathbf{K}\mathbf{v}) d\mathbf{v} d\mathbf{x} = n_e \Delta V I r_0^2 \sin^2 \vartheta F\left(\frac{\boldsymbol{\Omega}}{|\mathbf{K}|}\right), \\ F\left(\frac{\boldsymbol{\Omega}}{|\mathbf{K}|}\right) &= \frac{1}{n_e} \int f(\mathbf{x}, \mathbf{v}_{\perp}) d\mathbf{v}_{\perp}; \mathbf{v}_{\parallel} = \frac{\boldsymbol{\Omega}}{|\mathbf{K}|}, \sigma_{\Omega} = r_0^2 \sin^2 \vartheta. \end{aligned} \quad (6.20)$$

In the case of a Maxwellian  $f(\mathbf{x}, \mathbf{v})$  integration over  $v_{\parallel}$  yields the well-known Doppler broadened line profile centered at  $\omega$ . The explicit calculation with  $f_M$  from (2.28) yields for the full width at half maximum (FWHM)

$$\Delta\omega_s = 4\omega \left( \frac{2k_B T_e}{mc^2} \ln 2 \right)^{1/2} \sin\left(\frac{\vartheta}{2}\right). \quad (6.21)$$

It is a measure of the electron temperature. From the maximum of  $\mathbf{P}$  the electron density can be inferred. On the other hand, from the foregoing considerations on the Stokes and anti-Stokes shifts having their origin in the current density fluctuations  $\{\mathbf{j}(\boldsymbol{\Omega}, \mathbf{K})\} = \delta\mathbf{j}(\mathbf{x}, t)$  it results that the amount of scattered light and its spectrum are an image of the electron and ion density fluctuations  $\delta n_e(\mathbf{x}, t)$ ,  $\delta n_i(\mathbf{x}, t)$ . Thereby the fields  $\mathbf{E}$  and  $\mathbf{B}$  superpose, not the intensities. An ideal plasma of  $n_e = \text{const}$ ,  $n_i = \text{const}$  does not scatter for  $\lambda \gg (n_e)^{-1/3}$ . In the  $(\omega, \mathbf{k})$  picture, or equivalently  $(\boldsymbol{\Omega}, \mathbf{K})$ , the effect of the individual particle motions translates into a pressure contribution in the dispersion equation of the modes in the medium. This allows a qualitative distinction between coherent and incoherent scattering by introducing the scattering parameter  $\alpha = 1/|\mathbf{K}|\lambda_D$ . Thomson scattering is

$$\begin{aligned} \text{coherent if } &\alpha > 1, \\ \text{incoherent if } &\alpha \ll 1. \end{aligned} \quad (6.22)$$

It may be seen as follows. Fluctuations of wavelength  $\lambda = 2\pi/K > 2\pi\lambda_D$  obey a dispersion relation  $\boldsymbol{\Omega} = v_{\varphi} K$ . As explained in Fig. 6.2 light is reflected from all

wave fronts and interferes constructively. In the opposite case,  $\lambda \ll 2\pi\lambda_D$ ,  $K$  and  $\Omega$  are more or less uncorrelated and to a spatially periodic disturbance of periodicity  $K$  corresponds a whole group of frequencies  $\Omega = \pm(\omega - \omega_s)$  by which any interference is washed out. As a result the intensities scattered from the individual electrons add up to the intensity observed in direction  $\mathbf{k}_s$ . Owing to  $K \rightarrow 0$  for  $\mathbf{k}_s$  approaching  $\mathbf{k}$ , scattering into forward direction becomes coherent. In fact, when  $\mathbf{k}$  and  $\mathbf{k}_s$  are collinear,  $\mathbf{k}$  and  $\mathbf{k}_s$  and  $\omega$  and  $\omega_s$  become identical, and thus their phases  $\phi_1$  and  $\phi_2$  are identical also,

$$\begin{aligned}\phi_1 &= \mathbf{k}\mathbf{x}_1 - \omega t_1 + \mathbf{k}_s(\mathbf{x} - \mathbf{x}_1) - \omega_s(t - t_1), \\ \phi_2 &= \mathbf{k}\mathbf{x}_2 - \omega t_2 + \mathbf{k}_s(\mathbf{x} - \mathbf{x}_2) - \omega_s(t - t_2) = \mathbf{k}\mathbf{x} - \omega t = \phi_1.\end{aligned}$$

In practice this means that in a coherent Thomson scattering experiment  $\omega$  must be chosen sufficiently large to fulfill the first of relations (6.22) for scattering angles  $\vartheta$  larger than the aperture cone of the probing light pulse.

Introducing the dynamic form factor or spectral density function  $S(\mathbf{K}, \Omega)$ , defined as

$$\begin{aligned}S(\mathbf{K}, \Omega) &= \lim_{\Delta T, \Delta V \rightarrow \infty} \frac{1}{\Delta T \Delta V} \frac{|\delta n_e(\mathbf{K}, \Omega)|^2}{n_{e0}}, \\ \left[ \frac{\delta n_e(\mathbf{x}, t)}{n_{e0}} \right]^2 &= \frac{1}{2\pi n_{e0}} \int S(\mathbf{K}, \Omega) d\mathbf{K} d\Omega,\end{aligned}\quad (6.23)$$

and expressing it in terms of the dielectric susceptibilities  $\chi_{e,i}(\mathbf{K}, \Omega)$ ,

$$S(\mathbf{K}, \Omega) = \frac{2\pi}{|\mathbf{K}|} \left[ \left| 1 - \frac{\chi_e}{\varepsilon} \right|^2 F_e \left( \frac{\Omega}{|\mathbf{K}|} \right) + Z \left| \frac{\chi_i}{\varepsilon} \right|^2 F_i \left( \frac{\Omega}{|\mathbf{K}|} \right) \right], \quad \varepsilon = 1 + \chi_e + \chi_i, \quad (6.24)$$

with  $\varepsilon$  given by (3.105) plus the analogous integral for the ions ( $\omega_p \rightarrow \omega_{pi}$ ), follows for the scattered power  $P(\omega_s)$  from the unit volume

$$d^2 P / d\Omega d\omega_s = I r_0^2 \sin^2 \vartheta S(\mathbf{K}, \Omega). \quad (6.25)$$

The scattering time interval  $\Delta T$  and the volume  $\Delta V$  have to be chosen large enough so that a Fourier analysis of  $\delta n_{e,i}(x, t)$  makes sense for  $\min |\mathbf{K}|$ ,  $\min \omega$  under consideration. In local thermal equilibrium and  $T_e \approx T_i$  the form factor simplifies to  $S = S_e + S_i$  [4]. With a view on (3.104) the corrections in (6.24) become clear: due to the local polarization of the plasma by the surrounding electrons and ions each bare electron charge is weakened by the susceptibilities  $\chi_{e,i}$ . The asymmetry in the two correction terms expresses the fact that all scattering is due to the electrons only. For details of derivations (6.23), (6.24), and (6.25) the reader may consult Sheffield [5] or, for the essentials, Boyd and Sanderson [6], Chap. 9., and [7]. In the visible and UV spectral region no Compton shift has to be taken into account for the determination of  $\mathbf{k}_s$ ,  $\omega_s$ . In nonideal dense plasmas (warm dense matter)

several corrections have to be introduced (degeneracy, Fermi distribution, quantum effects on collisions), see e.g. [8, 9]. In the hard X-ray scattering domain  $\omega_s$  depends on the Compton shift as well. In dense plasmas the refractive indexes  $\eta$ ,  $\eta_s$  may differ from unity which for the Doppler shift translates into the substitution of  $\mathbf{K}$  by  $\mathbf{K} = \eta\mathbf{k} - \eta_s\mathbf{k}_s$ .

## 6.2 Instabilities Driven by Wave Pressure

High temperature plasmas constitute fluids of almost zero rigidity and undergo therefore a whole variety of deformations induced by the ponderomotive force of combinations of waves of  $\mathbf{k}_s \neq \mathbf{k}$ . If the amplitude modulation exhibits the periodicity of a normal plasma mode, acoustic or electrostatic, it may drive it unstable to high amplitude already at low pump intensity. How this happens in detail is the subject of the following sections.

### 6.2.1 Resonant Ponderomotive Coupling

Consider a static electron density modulation of the form

$$n_e = n_0 + \hat{n}_1(e^{i\mathbf{k}_3\mathbf{x}} + e^{-i\mathbf{k}_3\mathbf{x}}) = n_0 + n_1, \quad n_0 = \text{const} \quad (6.26)$$

with  $\hat{n}_1 \ll n_0$ . When a weak electric pump wave  $\mathbf{E}_1(\mathbf{k}_1, \omega_1)$ , transverse or/and longitudinal, impinges onto the plasma the total field  $\mathbf{E}$  has to obey the stationary wave equation (6.5),

$$\Delta\mathbf{E} + k_0^2 \left( \eta_0^2 - \frac{n_1}{n_c} \right) \mathbf{E} = 0; \quad |\mathbf{k}_0| = \frac{\omega_1}{c} \quad \text{or} \quad |\mathbf{k}_0| = \frac{\omega}{s_e}, \quad \eta_0^2 = 1 - \frac{n_0}{n_c}. \quad (6.27)$$

Since the pump can be taken arbitrarily weak the amplitudes  $\hat{n}_1$  and  $\hat{v}_e$  are nearly constant and  $\partial_t j_1 = -\partial_t e n_1 v_e = 0$  can be set. The general solution of (6.27) is the superposition of a forward wave  $\hat{\mathbf{E}}_1 e^{i\mathbf{k}_1\mathbf{x}-i\omega_1 t}$  and a reflected wave of the same frequency  $\omega_1$ ,  $\hat{\mathbf{E}}_2 e^{i\mathbf{k}_2\mathbf{x}-i\omega_1 t}$ . It is the phase difference  $\Delta\phi$  of  $\mathbf{E}_2$  in relation to  $n_1$  that determines whether  $n_1$  is ponderomotively amplified, attenuated, or merely accelerated or decelerated in its speed of propagation. Owing to the translational symmetry perpendicular to  $\mathbf{k}_3 = \mathbf{k}_1 - \mathbf{k}_2$  all wave vectors can be chosen collinear without limitation of generality. The general case of oblique incidence is obtained from a Lorentz boost. Each density disturbance  $n_1(x)$  sends its reflected signal back to the left contributing to construct the amplitude modulation. If reflection occurs from one single position, as for instance from a mirror,  $\Delta\phi = \pi$  results with the well-known node at its surface. As in the reflecting structure of extension  $\lambda$  the incoming signal of a fixed phase  $\mathbf{E}_1 = \text{const}$  must reach first all points along  $\lambda$  and then send its responses back into the opposite direction; in other words, since the covered distance now divides into two halves, one forward, one backward, the

true phase difference of  $|\mathbf{E}| = |\mathbf{E}_1 + \mathbf{E}_2|$  relative to  $n_1$  is  $\Delta\phi = \pi/2$ , and the ponderomotive force  $\pi_0$  results in phase with the refractive index perturbation by  $n_1$ . It reaches its maxima in the humps of  $n_e$  and its minima in the valleys, as sketched in Fig. 6.1. To see that exactly this configuration leads to indefinite growth of  $\hat{n}_1$  it is sufficient to consider the directions of the ponderomotive force along  $n_1$  in the co-moving system in which holds  $-n_1 v = -n_0 v_\varphi = \text{const}$  on the  $\omega_1$  time scale (the frequently encountered statement of  $\pi_0$  displaying its maxima and minima in the density nodes of  $n_1$  is incorrect). The phase shift  $\Delta\phi = \pi/2$  is the root of the parametric instabilities. An alternative, formal proof of the shift is as follows.

Under the assumption of  $|\mathbf{E}_2| \ll |\hat{\mathbf{E}}_1|$  that is consistent with a small  $\hat{n}_1$  in a medium of limited spatial extension, (6.27) transforms into a wave equation for the reflected wave,

$$\Delta\mathbf{E}_2 + k_2^2 \mathbf{E}_2 = k_0^2 \frac{\hat{n}_1}{n_c} \hat{\mathbf{E}}_1 \left\{ e^{i(k_1+k_3)x} + e^{i(k_1-k_3)x} \right\} e^{-i\omega t}; \quad k_2^2 = k_0^2 \eta_0^2. \quad (6.28)$$

$\mathbf{E}_2$  is excited by the product of the incident wave and the refractive index modulation. In order to represent a propagating wave,  $\mathbf{k}_2 = -\mathbf{k}_1$  must hold. In leading order (6.28) is fulfilled for  $\mathbf{k}_1 - \mathbf{k}_3 = \mathbf{k}_2$ , or  $\mathbf{k}_3 = 2\mathbf{k}_1$ . The term  $e^{i(k_1+k_3)x}$  is nonresonant and causes only a small rapid oscillation in space superposed on the amplitude of  $\mathbf{E}_2$ . With the slowly varying amplitude in space  $\hat{\mathbf{E}}_2 = \hat{\mathbf{E}}_2(x)$  and the matching condition for resonance, (6.28) reduces to

$$2i(\mathbf{k}_2 \nabla) \hat{\mathbf{E}}_2 = -2i(\mathbf{k}_1 \nabla) (-i\Re \hat{\mathbf{E}}_2) = -i(\mathbf{k}_1 \nabla) (\hat{\mathbf{E}}_2 e^{-i\pi/2} + \hat{\mathbf{E}}_2^* e^{i\pi/2}) \\ \Rightarrow \frac{d\Re \hat{\mathbf{E}}_2}{dx} = -k_0 \frac{n_1}{2\eta_0 n_c} \hat{\mathbf{E}}_1, \quad (6.29)$$

since  $\mathbf{E}_2$  has to fulfill its dispersion relation. The second equation follows from the fact that the LHS of the first equation must be real. The reflected wave increases in backward direction  $\mathbf{k}_2/|\mathbf{k}_2|$ . An electron density modulation of amplitude  $\hat{n}_1 = \text{const}$  in space leads to a linear growth of  $\hat{\mathbf{E}}_2$ , hence  $\mathbf{E}_2 = C \hat{\mathbf{E}}_1 e^{-i(2k_1 x + \pi/2)}$ ,  $C = k_0 \hat{n}_1 (\mathbf{x}_0 - \mathbf{x}) / (2\eta_0 n_c)$ ,  $\mathbf{x}_0 - \mathbf{x} > 0$ , and to  $-\nabla |\mathbf{E}_1 + \mathbf{E}_2|^2$  which in leading order is as follows

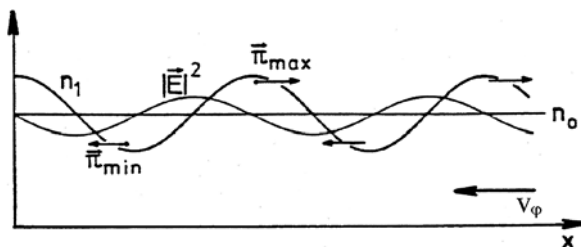


**Fig. 6.1** A static electron density disturbance  $n_1$  in the co-moving frame is resonantly driven by a modulated electric field amplitude  $|\mathbf{E}|$  when the plasma moves at velocity  $-v_\varphi = -\omega_3/k_3$ . The arrows indicate the maxima and minima of the ponderomotive force  $\pi_0$

$$\begin{aligned} -\nabla|E_1 + E_2|^2 &= -\nabla(E_1 E_2^* + E_1^* E_2) \\ &= -C \hat{E}_1^2 \nabla \left\{ e^{i(2k_1 x + \pi/2)} + e^{-i(2k_1 x + \pi/2)} \right\} = 4k_1 \hat{E}_1^2 \cos 2k_1 x. \end{aligned} \quad (6.30)$$

Summarizing, we have shown that an electric wave incident on a static refractive index (= density) perturbation in a medium streaming at phase velocity is reflected in such a way that the ponderomotive force of the total electric field leads to secular amplification of the initial modulation provided the spatial resonance condition

$$k_1 = k_2 + k_3 \quad \Rightarrow \quad k_3 = 2k_1 \quad (6.31)$$

is fulfilled. The comparison of the two arguments for  $\pi_0 \sim n_1$  is an example for the superiority of physical (synthetic) reasoning over formal (analytic) proofs (once a physical picture can be found). A remark is in order here. For simplicity a static density modulation in a plasma at rest has been assumed. In reality  $n_1$  is moving at ion acoustic or Langmuir phase velocity as assumed in Fig. 6.1. Then, in the system of the density modulation  $n_1$  at rest the plasma exhibits a constant flow velocity. A first consequence is that the second of relations (6.31) is only valid for transverse waves  $E_1, E_2$  in the vacuum. However, the first relation is fulfilled at each position and, owing to the Lorentz invariance of the phase  $\phi$  matching holds in all systems of reference. All relations in this section remain valid under oblique incidence of  $E_1(k_1, \omega_1)$  as a consequence of momentum conservation perpendicular to  $k_3$  which in turn is a consequence of translational symmetry along that direction. Under oblique incidence ponderomotive coupling from the superposition of an electromagnetic and a Langmuir wave is also possible, for instance in the two plasmon decay. In conclusion, in any inertial system and in the lab frame in particular, for resonant coupling the matching conditions

$$k_1 = k_2 + k_3, \quad \omega_1 = \omega_2 + \omega_3 \quad (6.32)$$

must be fulfilled. Among the natural plasma fluctuations those modes are selected and driven unstable by a transverse or longitudinal electric wave that fulfill these resonance conditions. The situation is sketched in Fig. 6.2 in the co-moving and in the lab frame. The incident pump wave generates weak reflected signals from all inhomogeneities which interfere constructively to compose  $E_2$ . This latter in turn generates  $\pi_0$  in phase with the electron density disturbance.

For gaining additional insight it may be instructive to formalize also the proof of unstable growth based on Fig. 6.1. To this aim, given two electric waves with  $\omega_1 = \omega_2$  and  $k_1 \neq k_2$ , the density perturbation  $n_1$  they induce is shown to be in phase with  $\pi_0$ . To see this consider (5.43) for nonrelativistic velocities  $v$  and  $v_\varphi$ . By setting  $M = v/v_\varphi$  and replacing  $m_i$  by  $m$  in  $\rho_c$  its validity extends to the electron plasma wave too (the extension to an arbitrary  $v_\varphi$  is guaranteed by the validity of the resonance conditions (6.32) in all systems of reference). At  $M < 1$  the density finds time enough to react to the ponderomotive potential  $\Phi_p$  and to accumulate in the valleys of  $|E|^2$ ; at  $M > 1$  it is retarded by  $\pi$ , i.e.,  $\Phi_p$  is ahead

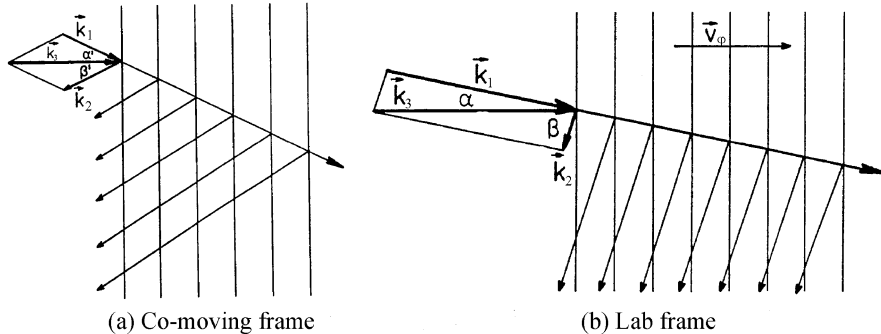


**Fig. 6.2** Induced scattering of an intense pump wave  $\vec{k}_1$  from a refractive index modulation  $\vec{k}_3$ ;  $\vec{k}_2$  scattered wave. (a) Co-moving frame, sketched for slow mode  $\vec{k}_3$ , e.g., Brillouin scattering,  $\alpha' \simeq \beta'$ , (b) lab frame

by  $\pi$  with respect to the “subsonic” case (see Fig. 5.5). At  $M = 1$  no steady state exists. The ponderomotive potential  $\Phi_p$  of the system, as it represents a harmonic oscillator, undergoes a phase shift by  $+\pi/2$  for continuity reasons ( $-\pi/2$  would mean stability and discontinuity in the phase shift), or seen explicitly by observing that in the “sonic” region  $M = 1$  total pressure and kinetic terms balance each other in (5.43). Then, complemented by the partial derivative of  $v$  with respect to time (5.43) reduces to

$$\rho \frac{\partial v}{\partial t} = -v \frac{\partial \rho}{\partial t} = -\pi_0 \quad \Rightarrow \quad \frac{\partial \rho}{\partial t} = \frac{\pi_0}{v_\varphi}, \quad (6.33)$$

i.e., growing  $\rho$  or  $n_l$  happen in phase with the ponderomotive force  $\pi_0$ . This completes our assertion.

For tutorial reasons we may ask ourselves at this point how an electric field does affect a plasma mode  $n_l$  when  $|\vec{E}|^2$ , in contrast to  $\pi_0$ , is modulated *in phase* with the mode. Including  $\pi_0$  in the linearized (2.90) and (2.99), now all quantities taken conveniently in the lab frame, leads to

$$\frac{\partial^2}{\partial t^2} n_l + k_l^2 v_l^2 \left( 1 + \frac{\varepsilon_0 n_0}{2 n_c} \hat{E}_1 \frac{\hat{E}_2}{\hat{n}_l} \right) n_l = 0. \quad (6.34)$$

As the ratio of the amplitudes  $\alpha = |\hat{E}_2|/\hat{n}_l$  is nearly constant, it follows for  $\hat{n}_l/n_0 \ll 1$  that the only effect of  $\pi_0$  on the wave is to increase its phase velocity,

$$v'_l = v_l \left( 1 + \varepsilon_0 \frac{n_0}{2 n_c} |\hat{E}_1| \alpha \right)^{1/2} > v_l,$$

but not its amplitude  $\hat{n}_l$ .

### 6.2.2 Unstable Configurations

The excitation of a mode 2 and a mode 3 by the pump mode 1 can be interpreted as the decay of quanta of type 1 into quanta of type 2 and 3, in symbols  $\omega_1 \rightarrow \omega_2 + \omega_3$ . By assigning the indexes em, es, and a to the different types of modes, electromagnetic, electrostatic, and acoustic, as the carriers of photons  $\hbar\omega_{\text{em}}$ , plasmons  $\hbar\omega_{\text{es}}$ , and phonons  $\hbar\omega_a$ , we conclude from the foregoing section that the following decay instabilities are possible and underlie to the same physical principle:

- |  |   |
|--|---|
| 1. Brillouin instability:              | $\omega_{\text{em}} \rightarrow \omega'_{\text{em}} + \omega_a$   |
| 2. Raman instability:                  | $\omega_{\text{em}} \rightarrow \omega'_{\text{em}} + \omega_{\text{es}}$                                     |
| 3. Two plasmon decay:                  | $\omega_{\text{em}} \rightarrow \omega'_{\text{es}} + \omega_{\text{es}}$                                     |
| 4. Parametric decay instability:       | $\omega_{\text{em}} \rightarrow \omega_{\text{es}} + \omega_a$  |
| 5. Oscillating two-stream instability: | $\omega_{\text{em}} \rightarrow \omega_{\text{es}} + \omega_a, \quad \omega_{\text{es}} > \omega_{\text{em}}$ |
| 6. Langmuir cascade:                   | $\omega_{\text{es}} \rightarrow \omega'_{\text{es}} + \omega_a, \quad \omega'_{\text{es}} \rightarrow \dots$  |
| 7. Two phonon decay of phonon:         | $\omega_a \rightarrow \omega'_a + \omega''_a$   |

Stimulated decay of a phonon into two phonons is possible. In high power-laser plasma interaction it plays at most a secondary role and will not be pursued here. The opposite is true for stimulated Brillouin [10] or Brillouin-Mandelstam [11] scattering (SBS). It consists in the stimulated amplification of an electromagnetic wave scattered off a low frequency ion acoustic mode satisfying the resonance conditions (6.32). In appositely prepared plasmas it can lead to 100% back reflection of the incident laser light [12, 13], in this way preventing the plasma from effective heating. The acoustic mode is a low frequency wave,  $\omega_a \ll \omega_{\text{em}}$ , and hence  $\omega'_{\text{em}} \simeq \omega_{\text{em}}$  and  $|\mathbf{k}_a| \simeq 2|\mathbf{k}_{\text{em}}| \sin(\vartheta/2)$ ,  $\vartheta = \angle(\mathbf{k}_{\text{em}}, \mathbf{k}'_{\text{em}})$ . Owing to the virtual high reflectivity the decay process has been intensively investigated experimentally and theoretically in connection with controlled inertial fusion over more than three decades [14–18]. The repeated decay of a Langmuir wave into another Langmuir wave and an ion acoustic mode (cascading) is called Langmuir decay instability (LDI). It is the electrostatic equivalent to SBS since the underlying coupling physics is the same as for SBS [19, 20]. The process tends to degeneracy by multiple cascading into nearly indistinguishable ion modes. In a limited parameter regime LDI appears to be a secondary instability that can saturate the Langmuir wave generated by the process of stimulated Raman scattering [21, 22].

The stimulated Raman scattering (SRS) in plasma has been investigated for at least four decades [23]. It is the resonant decay of light into an electron plasma wave and a light wave of longer wavelength. The physical mechanism is the same as for Brillouin scattering. Owing to the much higher frequency of the plasma wave the scattered Stokes line undergoes a remarkable red shift, in perfect analogy to the Raman effect in solids from optically active crystal vibrations (optical phonons) producing similar large red shifts. SRS exhibits fast growth rates and high saturation levels in plasmas, at least under ideal conditions [24], and fast electron generation due to particle trapping in the Langmuir wave [4]. The latter is of relevance to indirect drive of inertial fusion pellets [25]. From the inequality  $\omega'_{\text{em}} + \omega_{\text{es}} \geq 2\omega_p$  follows that the instability is limited to the density domain  $n \leq n_c/4$ . At compara-

tively low density and high electron temperature there is another limit due to strong Landau damping of the electron plasma wave for  $k_{es}\lambda_D \gtrsim 0.35$ . On the other hand, kinetic effects induced by SRS show a fast onset which can lead to a strong modification of the electron distribution function and thus to phenomena like nonlinear enhancement of the instability (“inflation regime” [26] and to the excitation of new modes, so called (electron) beam acoustic modes (BAM) [27].

The two plasmon decay (TPD) is excited in the vicinity of  $n_c/4$  because of strong Landau damping outside  $\omega_{es} \simeq \omega_p$ . Like SRS, it is a potential candidate for fast electron generation [28] owing to the high phase velocity of the daughter waves limited only by the finite density scale length due to profile steepening at  $n_c/4$  (compare Fig. 3.6). Langmuir cascading into two electron plasma waves,  $\omega_{es} \rightarrow \omega' + \omega''$  is not possible because the resonance conditions (6.32) cannot be fulfilled in the entire density domain. For the same reason resonant transverse wave cascading into two electromagnetic waves does not occur either.

To give an intuitive physical picture of the TPD is more complex. It is true that also in this case the instability arises from the reflection of the pump wave  $\mathbf{k}_1$  from the Langmuir wave  $\mathbf{k}_2$  ( $\mathbf{k}_3$ ) to result in a ponderomotive force in phase with  $\mathbf{k}_3$  ( $\mathbf{k}_2$ , respectively). However, the geometry for maximum growth is peculiar. Starting from the configuration in the lab frame with the pump  $\mathbf{k}_1$  incident under the arbitrary angle  $\alpha$  onto the plasma mode  $\mathbf{k}_2$  we observe that in good approximation holds

$$\begin{aligned} \omega_2 = \omega_3 = \omega_p = \omega_1/2, \quad \eta_1 = \sqrt{3}/2, \quad c_\varphi = v_{\varphi,1} = \omega_1/k_1, \\ k_1 = k_0\eta_1, \quad k_2 = k_3 \simeq (c/2s_e)k_0 \gg k_1, \quad k_{2,3} = \omega/(2v_{\varphi,2,3}). \end{aligned} \quad (6.35)$$

It follows from  $k_{2,3} \gg k_1$  that the two plasma waves are nearly collinear (see Fig. 6.3). The growth of the two daughter waves  $k_{2,3}$  implies an increase of the momentum densities  $mn_{2,3}v_1$  which, in turn, manifest themselves in a ponderomotive force like an inverse rocket effect. Thus, the ponderomotive force  $\boldsymbol{\pi}_{2,3}$  driving TPD unstable is given by (5.30). It is physically obvious and confirmed by the quantitative analysis in the next section that it acts along  $\mathbf{k}_1$  and exhibits the proportionality

$$\boldsymbol{\pi}_{2,3} \sim \mathbf{k}_1 |\mathbf{E}_1 \mathbf{E}_{2,3}^*|. \quad (6.36)$$

The growth rate  $\gamma$  is proportional to the projection of  $\boldsymbol{\pi}_{2,3}$  in direction  $\mathbf{k}_{2,3}$ , i.e.,  $|\mathbf{k}_1 \mathbf{k}_{2,3}| \sim \cos \alpha$ . On the other hand, the modulus  $|\boldsymbol{\pi}_{2,3}| \sim |\mathbf{E}_1 \mathbf{E}_{2,3}^*| \sim \sin \alpha$ ; hence  $\gamma \sim \sin \alpha \cos \alpha$ , with maximum growth under  $\alpha = \pi/4$ . In linear theory one configuration and its mirror image with respect to  $\mathbf{k}_1$  exhibit identical growth rates  $\gamma$ .

Excitation of TPD under perpendicular incidence,  $\alpha = \pi/2$  is not possible as a consequence of  $\gamma \sim \sin \alpha \cos \alpha$ . If however, one of the modes causing reflection of the pump wave is a low frequency wave,  $\boldsymbol{\pi}_t$  is nearly zero and a symmetric composition of the  $\mathbf{k}$ -diagram can be realized also in the lab frame. This difference in geometry originates from the fact that in presence of a slow (acoustic) mode, e.g.,  $n_3$ , in the co-moving reference system two fast modes  $n_2$  are excited by the laser in

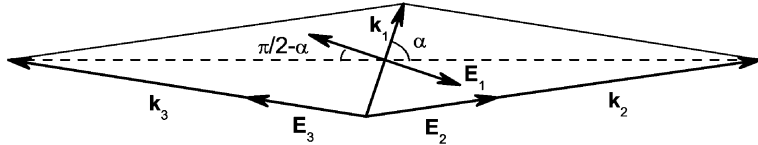


**Fig. 6.3** Stimulated two-plasmon decay;  $k_1 = k_2 - k_3$ ,  $k_1 \ll k_{2,3}$ . Its mirror image with respect to  $k_1$  shows equal growth

opposite directions almost *symmetrically* whereas in the co-moving system of one of two fast modes, as in TPD, the left-right symmetry is destroyed. In the parametric decay (PDI) and the oscillating two stream instability (OTSI) one plasma wave is substituted by an acoustic mode  $(\mathbf{k}_a, \omega_a) = (\mathbf{k}_3, \omega_3)$  and thus (quasi)-symmetry is established with maximum growth occurring at  $\alpha = \pi/2$ . Owing to  $s_e |\mathbf{k}_{es}|$ ,  $\omega_a \ll \omega_p$  the instability is localized in the neighborhood of  $\omega_p \simeq \omega_1$  and  $k_2 \simeq (c/s_e)k_1 \gg k_1$ . Therefore according to (6.32)  $\mathbf{k}_a = \mathbf{k}_3 = \mathbf{k}_2$  and  $\mathbf{k}_1 = 0$  can be set. From  $\pi_t \simeq 0$  the force  $\boldsymbol{\pi} = \boldsymbol{\pi}_0$  that drives the instability now points into  $\mathbf{k}_1 \pm \mathbf{k}_2 \simeq \pm \mathbf{k}_2$  direction and causes maximum growth perpendicularly to  $\mathbf{k}_1$ . With respect to relative phases of the decay products and the ponderomotive forces the considerations from above on SBS, SRS and TPD apply identically, with  $\boldsymbol{\pi}_0$  being in phase with the acoustic density modulation  $n_3$  that leads to an unstable situation again. The PDI has been described first by Silin [29]. It is localized in the underdense plasma region close to  $n_c$ . It was Nishikawa to recognize that it can also work above  $n_c$  when  $\omega_1 < \omega_2$  and  $\omega_3 = \omega_a = 0$  [30]. This is the case of the so-called oscillating two stream instability OTSI. We present the treatment of the two instabilities in terms of wave pressure given by [31].

Consider a spatially uniform laser field  $\mathbf{E}_1 = \hat{\mathbf{E}}_1 e^{-i\omega_1 t}$  impinging orthogonally on a static plasma density modulation  $n_3 = \hat{n}_3 e^{ik_3 x}$ ,  $\mathbf{E}_1 \parallel \mathbf{k}_3$ . It forces the electrons to shift in  $\pm x$ -direction by the amount

$$\delta_1 = \Re \frac{e}{m\omega_1^2} \left( 1 + i \frac{v_{ei}}{\omega_1} \right) \hat{\mathbf{E}}_1 e^{-i\omega_1 t} \quad (6.37)$$

and, in the presence of an ion density modulation  $n_3$ , it gives rise to an induced electric field  $E_d$  obtained from Poisson's equation,

$$\frac{\partial E_d}{\partial x} = -\frac{e}{\epsilon_0} [n_3(x - \delta_1) - n_3(x)] = \frac{e}{\epsilon_0} \delta_1 \frac{\partial n_3}{\partial x} \Rightarrow E_d = \frac{e}{\epsilon_0} \delta_1 n_3. \quad (6.38)$$

The driver excites two symmetric plasmons  $E_2 = \hat{\mathbf{E}}_2 e^{i(\pm k_3 x - \omega_1 t)}$  obeying the harmonic oscillator equation of the displacement  $\delta_2(x)$ ,

$$\frac{\partial^2 \delta_2}{\partial t^2} + \nu \frac{\partial \delta_2}{\partial t} + \omega_2^2 \delta_2 = -\frac{e}{m} (\hat{\mathbf{E}}_1 + \hat{\mathbf{E}}_d) e^{-i\omega_1 t}; \quad \omega_2^2 = \omega_p^2 + s_e^2 k_2^2, \quad k_2 = k_3. \quad (6.39)$$

The derivation is straightforward, with  $E_2$  from (2.93) and  $\delta_2$  from (6.37) after corresponding replacement of the indices. The damping coefficient  $v$  is of Landau or collisional type. The amplitude  $\hat{\delta}_2$  is modulated proportional to  $\hat{n}_3$  and, according to (5.11) gives rise to the ponderomotive force  $\boldsymbol{\pi}_0$ ,

$$\boldsymbol{\pi}_0 = -\frac{\omega_p^2(\omega_1^2 - \omega_2^2)}{(\omega_1^2 - \omega_2^2)^2 + v^2\omega_1^2} \frac{e^2|E_1|^2}{2m(\omega_1^2 + v_{ei}^2)} \nabla n_3; \quad n_3 \text{ real.} \quad (6.40)$$

Only for  $\Delta = \omega_1 - \omega_2 < 0$  the electric force density  $\boldsymbol{\pi}_0$  is in phase with  $n_3$  and thus drives both  $n_2$  and  $n_3$  unstable with the same growth rate  $\gamma > 0$ . The ratio of the amplitudes  $\hat{n}_2/\hat{n}_3$  is determined by (6.38) and (6.39) with the help of (3.74). Formally there is a one to one correspondence of the OTSI with the beam-plasma instability of two counter streaming electron beams. Nishikawa's discovery of the quasi-mode  $\omega_a = 0$  had a major impact on the proper treatment of other parametric instabilities under the influence of a strong driver. If the dephasing ("mismatch") in (6.32) becomes larger than the frequency of one of the modes the contribution of the anti-Stokes component must also be taken into account. Examples will be shown in the following section.

### 6.2.3 Growth Rates

There exist two preferred model situations that greatly facilitate the normal mode analysis of linear instabilities. It seems quite intuitive to describe spatial growth for real frequencies  $\omega$  fixed from outside, and temporal growth for real wave vectors  $\mathbf{k}$  in the infinitely extended homogeneous medium or wave vector  $\mathbf{k}$  fixed by the boundaries of a finite system. In the following temporal growth of the instabilities discussed above  $e^{-i\Omega t} = e^{-i(\omega+i\gamma)t}$  with  $\mathbf{k}$  and  $\omega, \gamma$  all real is determined. Growth happens for  $\gamma > 0$ .

#### 6.2.3.1 Stimulated Brillouin scattering

The transverse pump wave  $\mathbf{E}_1(\mathbf{k}_1, \omega_1)$  impinges onto a homogeneous plasma of density  $n_0$  which is modulated by the ion acoustic mode  $n_3 = \hat{n}_3 e^{i(k_3 x - \omega_3 t)}$ . The polarization of  $\mathbf{E}_1$  is assumed to fulfill  $\mathbf{k}_3 \cdot \mathbf{E}_1 = 0$ . The scattered wave  $\mathbf{E}_2(\mathbf{k}_2, \omega_2)$ ; obeying (6.5); and the density perturbation  $n_3$  follow in leading order the coupled equations with real coefficients:

$$\nabla^2 \mathbf{E}_2 - \frac{1}{c_{\varphi 2}^2} \frac{\partial^2 \mathbf{E}_2}{\partial t^2} = -\frac{1}{\varepsilon_0 c^2} \frac{\partial}{\partial t} (en_3 \mathbf{v}_{os,1}), \quad c_{\varphi 2} = \frac{c}{\eta_2}, \quad (6.41)$$

$$\nabla^2 n_3 - \frac{1}{s^2} \frac{\partial^2 n_3}{\partial t^2} = \frac{1}{m_i s^2} \nabla \boldsymbol{\pi}_0, \quad \boldsymbol{\pi}_0 = -\varepsilon_0 \frac{\omega_p^2}{\omega_1 \omega_2} \nabla (\Re \mathbf{E}_1 \Im \mathbf{E}_2). \quad (6.42)$$

We assume  $|\hat{\mathbf{E}}_1| \gg |\hat{\mathbf{E}}_2|$  and  $\hat{n}_3 \ll n_0$ , and we consider growth in the small signal amplification domain and therefore do not need the coupled equation of  $\mathbf{E}_1$ . To take advantage of the complex Fourier analysis of these two equations in  $(\mathbf{k}, \Omega)$  one of the quantities must be taken real. We choose  $\Re \mathbf{E}_1 = (\mathbf{E}_1 + \mathbf{E}_1^*)/2$  and obtain the netted set of equations

$$(\Omega^2 - v_{\varphi 2}^2 k_2^2) \mathbf{E}_2^{(\Omega)} = \frac{\omega_1 \Omega}{2n_{c1}} \left( \mathbf{E}_1 n_3^{(\Omega-\omega_1)} + \mathbf{E}_1^* n_3^{(\Omega+\omega_1)} \right), \quad (6.43)$$

$$(\Omega^2 - s^2 k^2) n_3^{(\Omega)} = -\frac{\varepsilon_0 k^2}{2m_i} \frac{\omega_p^2}{\omega_1 \omega_2} \left( \mathbf{E}_1 \mathbf{E}_2^{(\Omega-\omega_1)} + \mathbf{E}_1^* \mathbf{E}_2^{(\Omega+\omega_1)} \right). \quad (6.44)$$

On the RHS of (6.44)  $\omega_2 = \omega_1 - \omega_3$  is associated with the Stokes component of  $\mathbf{E}_2$  and  $\omega_2 = \omega_1 + \omega_3$  refers to the anti-Stokes component of  $\mathbf{E}_2$ . We express  $\mathbf{E}_2^{(\Omega-\omega_1)}$  and  $\mathbf{E}_2^{(\Omega+\omega_1)}$  from (6.44) with the help of (6.43),

$$[(\Omega - \omega_1)^2 - v_{\varphi 2}^2 (\mathbf{k} - \mathbf{k}_1)^2] \mathbf{E}_2^{(\Omega-\omega_1)} = -\frac{\omega_1 \omega_2}{2n_{c1}} \mathbf{E}_1^* n_3^{(\Omega)}, \quad (6.45)$$

$$[(\Omega + \omega_1)^2 - v_{\varphi 2}^2 (\mathbf{k} + \mathbf{k}_1)^2] \mathbf{E}_2^{(\Omega+\omega_1)} = \frac{\omega_1 \omega_2}{2n_{c1}} \mathbf{E}_1 n_3^{(\Omega)}, \quad (6.46)$$

and eliminate them from (6.44) to obtain

$$\left[ (\Omega^2 - s^2 k^2) - \frac{\varepsilon_0}{4} \frac{k^2 \omega_p^2}{m_i n_{c1}} \mathbf{E}_1 \mathbf{E}_1^* \left( \frac{1}{D^{(\Omega-\omega_1)}} + \frac{1}{D^{(\Omega+\omega_1)}} \right) \right] n_3^{(\Omega)} = 0. \quad (6.47)$$

The Stokes and anti-Stokes  $\omega_2$  in (6.45) and (6.46) results from setting  $\Omega = \omega_3$  in the RHS terms. The electromagnetic dispersion functions  $(\Omega \pm \omega_1)^2 - v_{\varphi 2}^2 (\mathbf{k} \pm \mathbf{k}_1)^2$  are abbreviated by the symbols  $D^{(\Omega \pm \omega_1)}$ . The infinite chain of equations (6.43) has been cut at  $n_3^{(\Omega \pm \omega_1)}$  because owing to  $|\Omega| \ll \omega_1$  these and all following terms are very small in comparison to the only resonant mode  $n_3^{(\omega)}$ . Furthermore, from (6.32) follows, even in the case of strong mismatch under a strong driver,  $\omega_2 \simeq \omega_1$ ,  $|\mathbf{k}_2| \simeq |\mathbf{k}_1|$ , and hence  $\mathbf{k}_1 \simeq \mathbf{k}_2 + \mathbf{k}_3$  imposes  $k_3 \simeq 2k_1 \sin(\vartheta/2)$ , scattering angle  $\vartheta = \angle(\mathbf{k}_1, \mathbf{k}_2)$ . For backscattering, i.e.,  $\vartheta = \pi$ , this implies  $\mathbf{k} = \mathbf{k}_3 \simeq \mathbf{k}_1 - \mathbf{k}_2 \simeq 2\mathbf{k}_1$ . As the intensity of the pump wave tends to zero the mismatch in (6.30) decreases also to zero. For mild backscattering  $\gamma^2 \ll \omega_3^2 \simeq \omega_a^2$  holds, and from (6.30) follows more precisely  $\mathbf{k}_3 = 2\mathbf{k}_1[1 - \eta_1 s/c]$ . Hence, in (6.47) only the Stokes component  $\mathbf{E}_2^{(\Omega-\omega_1)}$  is resonant; the anti-Stokes term  $D^{(\Omega+\omega_1)}$  can be disregarded. This is the weak coupling limit [24]. The dispersion relation (6.47) shrinks to

$$(2i\gamma\omega_3 - \gamma^2)[(-2i\gamma\omega_1 - 2\omega_1\omega_3) - v_{\varphi 2}^2(k_3^2 - 2\mathbf{k}_1 \cdot \mathbf{k}_3)] = \frac{\varepsilon_0}{4} \frac{k_3^2 \omega_p^2}{m_i n_c} \mathbf{E}_1 \mathbf{E}_1^*. \quad (6.48)$$

With  $\mathbf{k}_3$  from above for backscattering the sum of the real terms in the second bracket yields  $\omega_3^2$  and can be set to zero compared with  $2\gamma\omega_1$ . Hence, one is left with the maximum growth rate for exact backscattering

$$\gamma_{\max} = \frac{1}{2} \frac{\omega_{\text{pi}}}{c(mn_{\text{c}}s)^{1/2}} I^{1/2} = \frac{1}{2^{3/2}} \omega_{\text{pi}} \frac{\eta_1^{1/2} \hat{v}_{\text{os}}}{(cs)^{1/2}}; \quad (6.49)$$

$I = \epsilon_0 c \eta_1 \mathbf{E}_1 \mathbf{E}_1^*/2$ ,  $\omega_{\text{pi}}^2 = (m/m_i) \omega_{\text{pe}}^2$ ,  $\eta_2 \simeq \eta_1$ ,  $\hat{v}_{\text{os}}$  is taken locally. In side scattering ( $\vartheta < \pi/2$ ) the term

$$-2\omega_1\omega_3 - v_{\phi 2}^2(k_3^2 - 2\mathbf{k}_1 \cdot \mathbf{k}_3) = -4\omega_1 k_1 \sin \frac{\vartheta}{2} \left[ s + \frac{c}{\eta_2} \left( \sin \frac{\vartheta}{2} - \cos \frac{\vartheta}{2} \right) \right]$$

is positive and contributes to reduce  $\gamma$ . The reduction is, primarily, a consequence of  $|\mathbf{E}_1 \mathbf{E}_2| = |\mathbf{E}_1| |\mathbf{E}_2| \cos \vartheta$ . A short remark may be in order: In (6.41) the scattered wave  $\mathbf{E}_2$  depends linearly on the pump wave  $\mathbf{E}_1$ . As in side scattering the two vectors are not parallel to each other in general ( $\vartheta \neq 0$ ) additional terms appear in  $\mathbf{k}_3 \mathbf{E}_1 \neq 0$  polarization. The dependence of  $\gamma$  on  $\eta_1$  is due to shrinking of the ion sound wave vector in the plasma,  $\pi_0 \sim \mathbf{k}_3 \sim \mathbf{k}_0 \eta_1$ .

In the so called strong coupling regime [17, 24, 32], i.e., when  $|\Omega|^2 \gg k_3^2 s^2$  holds under the strong driver, in back scattering the approximations

$$\begin{aligned} D^{(\Omega-\omega_1)} &= \Omega^2 - 2\Omega\omega_1 + \omega_1^2 - \omega_{\text{p}}^2 - c^2 k_1^2 (1 - 2\eta_1 s/c)^2 \\ &\simeq -2\Omega\omega_1 + 4\eta_1^2 \omega_1 s k_1 \simeq -2\Omega\omega_1, \quad \Omega^2 - s^2 k^2 \simeq \Omega^2 \end{aligned}$$

are consistent and from (6.47), ignoring the anti-Stokes term, follows  $\Omega$  as the complex cubic root

$$\Omega = \frac{1}{2^{4/3}} \left[ \omega_1 \omega_{\text{pi}}^2 \eta_1^2 \left( \frac{\mathbf{v}_{\text{os}}}{c} \right)^2 \right]^{1/3} (1 + i\sqrt{3}). \quad (6.50)$$

Unstable growth is particularly favored in presence of a strong counter propagating electromagnetic wave, for example, when the incident wave reaches the critical density before sufficient attenuation. In such a case  $\gamma$  may exceed  $\omega_a$  several times. In stationary plasmas with less than critical density a steady state solution of SBS usually establishes. In situations when light is reflected from the critical surface with frequency differing from the red-shifted  $\mathbf{E}_2^{(\Omega-\omega_1)}$  mode SBS becomes non-stationary for a sufficiently high pump wave and the scattered spectrum undergoes strong broadening [33]. Latest in such a situation the scattered anti-Stokes field component  $\mathbf{E}_2^{(\Omega+\omega_1)}$  can no longer be ignored a priori in the dispersion relation term  $1/D^{(\Omega-\omega_1)} + 1/D^{(\Omega+\omega_1)}$  in (6.47) [34].

The anti-Stokes wave is close to resonance for the matching condition

$$\omega_2 = \omega_1 + \omega_3, \quad \mathbf{k}_2 = \mathbf{k}_1 + \mathbf{k}_3. \quad (6.51)$$

It travels into the forward direction as the driver  $\mathbf{E}_1(\omega_1, \mathbf{k}_1)$ . This is most immediately seen in the co-moving frame. Under the influence of the driver  $\mathbf{E}_1$  from each position  $\mathbf{x}$  an elementary electromagnetic disturbance  $\mathbf{E}_2^{(\omega'_1)}$  propagates into opposite directions with strengths the difference of which reduces to zero with flow velocity  $-s$  approaching zero. In the lab frame  $\omega'_1$  becomes the anti-Stokes frequency  $\omega_1 = \gamma(\omega'_1 + \mathbf{k}_2 s) = \omega_1 + \omega_3$  for  $\mathbf{k}_2 \cdot \mathbf{k}_3 \geq 0$ , see (6.12). When  $\mathbf{k}_1$  and  $\mathbf{k}_2$  are approximately collinear,  $|\mathbf{k}_3| \simeq \eta_1 \omega_3 / c \simeq k_0 s / c$  is very small and  $D^{(\Omega+\omega_1)}$  is close to resonant coupling,

$$D^{(\Omega+\omega_1)} = \Omega^2 + 2\Omega\omega_1 + \omega_1^2 - \omega_p^2 - c^2 k_1^2 \left(1 + \frac{2\eta_1 s}{c}\right)^2 \simeq \Omega^2 + 2\Omega\omega_1 - 4\eta_1^2 \omega_1 s k_1.$$

On the other hand, in nearly forward direction the Stokes  $|\mathbf{k}_3|$  can assume arbitrarily small values; anti-Stokes and Stokes frequencies  $\omega_2 = \omega_1 \pm s|\mathbf{k}_3|$  are very close to  $\omega_1$  and with increasing pump wave intensity their bandwidths begin to overlap in a  $|\mathbf{k}_3|$  interval around the dispersion intersection points (see Fig. 6.4). This leads to a redistribution of the energy fluxes and to back reaction onto the  $(\omega_3, \mathbf{k}_3)$  mode that rather to be a free mode will convert into a forced quasi-mode at downshifted frequency  $\omega_a$ . Nishikawas's oscillating two-stream instability with  $\omega_a = 0$  for finite  $|\mathbf{k}_2| = |\mathbf{k}_3|$  is perhaps the most instructive example for the Stokes-anti-Stokes interplay and concomitant frequency shift. The instability results in a long wavelength modulation of the amplitudes  $\hat{n}_3$  and  $|\mathbf{E}| = |\mathbf{E}_1 + \mathbf{E}_2|$ . As a special case of SBS the filamentary instability is obtained from (6.47) by setting  $\mathbf{k}_3 \cdot \mathbf{k}_1 = 0$  and  $\Omega = i\gamma$ . Then,  $D^{(\Omega \pm \omega_1)} = \pm 2i\gamma\omega_1 - c^2 k_3^2$  leads to the equation of growth  $\gamma$ ,

$$(\gamma^2 + s^2 k^2) \frac{1}{4\gamma^2 \omega_1^2 + c^4 k^4} = \frac{\omega_{pi}^2}{8} \left( \frac{\hat{v}_{os}}{c} \right)^2; \quad \mathbf{k} \perp \mathbf{k}_1. \quad (6.52)$$

Here, as throughout the chapter,  $\mathbf{E}_1 \nabla n_3 = 0$  is assumed. As long as the pump wave does not drive plasma resonances, for instance owing to  $\omega_1 > \omega_p$ , polarization effects can be disregarded [34, 35].

Stokes and anti-Stokes electromagnetic components both act to drive the ion acoustic and the electron plasma mode whenever the detuning due to growth exceeds the Stokes shift  $\Delta\omega$ . It is advisable in general, also with other types of unstable modes, to include both components in the analysis and to compare with the result obtained from the resonant Stokes mode alone. After all it must be kept in mind that parametric systems of type (6.43), (6.44) represent a recurrence scheme of an infinite number of equations. For the PDI and OTSI sequences closure and impact of the anti-Stokes component are investigated quantitatively in [36]. The arguments for closure may vary from case to case. So for example numerical studies have shown that ion acoustic harmonics can couple to SBS and lead to reduction of reflectivity, spatial decorrelation and to temporal chaotic plasma dynamics [16].

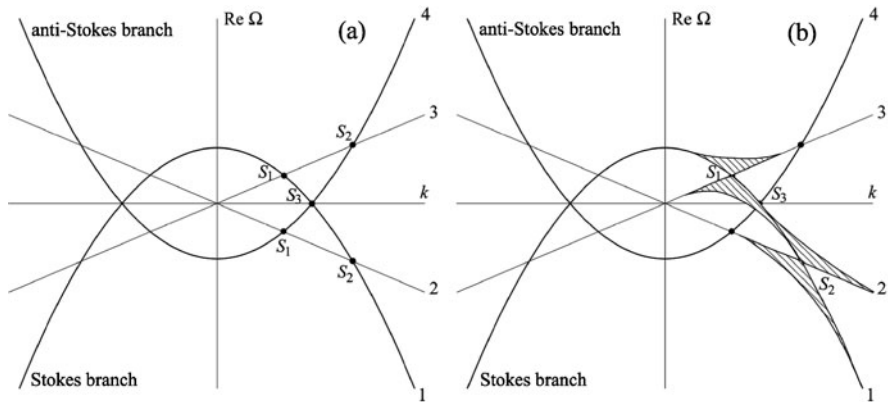


**Fig. 6.4** (a) Brillouin diagram of wave-wave coupling in SBS and PDI. Dispersion diagrams of electromagnetic ( $\omega_{em}$ : 1,4), electrostatic ( $\omega_{es}$ : 1,4) and acoustic ( $\omega_a$ : 2,3) modes. Resonant interaction (coupling) is strongest in the neighborhood of the intersection points  $S_1$ ,  $S_2$ , and  $S_3$ .  $S_1$ ,  $S_3$  unstable, see (6.48) for  $S_1$ , and (6.52) for  $S_3$ . From (6.47) with  $1/D(\Omega - \omega_1) = 0$  follows that  $S_2$  is a stable interaction point in the approximation of (6.48).  $S_2$  is not energy conserving. (b) Excitation of a quasi-mode ( $\omega_3$ ,  $k_3$ ) from overlapping of mismatch zones around  $S_1$  and  $S_2$ . For laser intensity  $I \rightarrow 0$  the graphs delimiting the shadowed regions contract to the intersection points  $S_1$  and  $S_2$

Stimulated Brillouin backscattering contains a relevant practical aspect; it can operate as a phase conjugated plasma mirror. The linear phase conjugation operator “ $*$ ” acts on the spatial part of a plane wave  $A e^{ikx-i\omega t}$  transforming it into its complex conjugate expression,  $(A e^{ikx})^* e^{-i\omega t} = A^* e^{-ikx-i\omega t}$ . This is exactly what happens in Brillouin backscattering. The inversion of the wave vector  $k$  means that a wave on its way back crosses again the same space domain in opposite direction correcting thereby all undesired distortions of the wave front (phase) from its first passage (up to small differences originating from the difference between  $\eta_1$  and  $\eta_2$ ). The distortions of an originally plane wave are eliminated in the phase conjugated reflection. Specular reflection of a beam having for instance the cross section of a question mark produces its mirror image and to primary phase distortions it adds additional distortions on its way back, whereas the back scattered beam reproduces the original shape of the question mark (in laser-plasma interaction first discovered as the *Fragezeicheneffekt* in 1972 [37]).

In long scale length plasmas stimulated Brillouin back and side scattering from a coherent laser beam is an instability that grows rapidly in time to high levels of reflectivity [12, 13]. The acoustic wave has low frequency and, according to (6.8), low energy density  $\mathcal{E}_a$  and does almost no photon energy deposit in the medium, with dramatic consequences for plasma heating in general and inertial confinement fusion and X-ray sources in particular. Therefore much interest has been concentrated in the past three decades on experiments to clarify the saturation level of light reflection  $R$  in long scale length underdense plasmas. In early SBS studies with CO<sub>2</sub> lasers interacting with a smooth plasma [38] and subsequent similar experiments with gas jets [39] showed surprisingly low saturation levels of  $\hat{n}_3/n_0 \simeq 10\text{--}20\%$ ,

corresponding to  $R < 10\%$ . Further drastic reduction of this values of  $R$  from SBS has been achieved by applying average laser beam smoothing through induced spatial incoherence (ISI: broad band laser beam is first divided into many independent beamlets, with mutual time shifts exceeding the coherence time, and then overlapped on the target). With ISI applied to a 2-ns Nd laser beam of peak intensity  $I = 10^{14} \text{ Wcm}^{-2}$  on CH disk targets  $R$  resulted below 1% [40]. These were good news but they resisted for nearly two decades to a satisfactory theoretical explanation. The studies focused on the discrepancy between theoretical expectations and experimental results mostly concentrated on saturation effects of the ion acoustic modes due to steepening and wavebreaking, generation of harmonics, particle trapping and decay into subharmonics of  $\hat{n}_3$ .

In retrospect, however, the low backscatter levels measured in the past have not been analyzed with enough temporal resolution and therefore indicate merely the ratio of back scattered to incident laser energy, generally ignoring transient high backscatter levels that could potentially occur during a fraction of the laser pulse. The ability of combining fluid dynamic and kinetic SBS modeling with laser pulse shaping leads to a more realistic interpretation of the experiments. While often high backscatter levels occur temporarily, in agreement with theory, the average level over a longer time scale, e.g., tens of ps or entire laser pulses, may result moderate or low compared to the incident laser intensity. However, this should not lead to the hasty conclusion that SBS is not of concern under constraints imposed by specific goals, as for example in laser fusion schemes. Independent of all nonlinear effects examined with the attempt to explain saturated SBS levels, laser beam smoothing in plasmas can itself lead to reduction of backscattering: self-focusing of individual laser speckles of spatially smoothed beams (e.g. by random phase plate technique [RPP]) contribute in this way to an additional plasma-induced smoothing as the beam propagates further into the plasma target.

Recently a breakthrough in understanding SBS suppression in long scale length plasmas has been achieved by Hüller et al. [41]. Sophisticated numerical simulations have shown a quite universal behavior applicable to laser beams containing high-intensity hot spots that are subject to self-focusing. Although the growth rate of SBS is higher than the one of self-focusing, SBS starts from a significantly lower noise level. Henceforth it grows primarily in intense self focused hot spots, giving rise to transient high backscatter flashes. Nevertheless, due to subsequent ponderomotive density depletion disruption of the SBS signal takes place [42] and, eventually, backscattering remains on a moderate level averaged over the whole pulse length. It is important to mention that the region behind the self-focusing hot spots does not contribute significantly to SBS due to plasma induced smoothing, see [41]. In this paper the features of SBS were studied for a mono-speckle laser beam at Nd peak intensity  $I = 3 \times 10^{14} \text{ Wcm}^{-2}$  including self-focusing and nonlocal energy transport self consistently. In the linearly rising laser pulse with its maximum at 200 ps SBS starts growing fast as predicted by (6.49) and (6.50) and reaches its maximum of  $R \simeq 10\%$  already at 50 ps and decays after 100 ps so that averaged over the whole pulse of 1 ns  $\langle R \rangle \simeq 1\text{--}1.5\%$  results with nonlocal transport included, and  $\langle R \rangle \simeq 4\%$  without. The results are in excellent

agreement with the concomitant experiment. On the other hand, when self-focusing was suppressed in the simulation, maximum values of  $R = 50\%$  were reached in coincidence with the maximum of the laser pulse at 200 ps. The conclusion is twofold: (1) self-focusing, i.e., local intensity concentration, is responsible for the fast growth; (2) the sudden disruption of SBS after a short time is triggered by an effect localized in spots of high laser intensity. The simulations allow the identification of (2) with the resonant filament instability [43, 44]. Due to the ponderomotive force a density well forms along a filament which is capable of supporting electromagnetic eigenmodes like a waveguide. When the threshold intensity for self-focusing is reached they grow rapidly unstable and lead to lateral bending of the filament and eventually to its complete breakup. After some time it forms again and disrupts. The process leads to increased lateral scattering of the laser beam and to correlation length reduction to 10–15 μm in laser plasma interaction regions of mm-scale. Very good agreement between experiment and the large scale simulations and the identification of the resonant filament instability as the effect responsible for low level SBS reflectivity may lead to the conclusion that herewith the two decades old problem of Brillouin anomaly in high power laser interaction is solved, or very close to its solution. It should be stressed that the outlined scenario appears quite universal with beams containing hot spots at power densities above the self-focusing threshold [45].

### 6.2.3.2 Stimulated Raman Scattering

In (6.42) the low frequency plasma mode  $n_3$  from SBS is replaced by the high frequency Langmuir wave. As for the rest the underlying physics is identical the governing equations are

$$\nabla^2 \mathbf{E}_2 - \frac{1}{v_{\varphi 2}^2} \frac{\partial^2 \mathbf{E}_2}{\partial t^2} = -\frac{1}{\varepsilon_0 c^2} \frac{\partial}{\partial t} (e n_3 \mathbf{v}_{os,1}), \quad c_{\varphi 2} = \frac{c}{\eta_2}, \quad (6.53)$$

$$\nabla^2 n_3 - \frac{1}{v_{\varphi 3}^2} \frac{\partial^2 n_3}{\partial t^2} = \frac{1}{ms_e^2} \nabla \pi_0, \quad \pi_0 = -\varepsilon_0 \frac{\omega_p^2}{\omega_1 \omega_2} \nabla (\Re \mathbf{E}_1 \Im \mathbf{E}_2). \quad (6.54)$$

Limiting ourselves again to the small signal amplification the Fourier analysis reproduces equations (6.43), (6.44), (6.45), and (6.46), with  $s$  and  $m_i$  replaced by  $v_{\varphi 3}$  from (6.3) and  $m$ , and the corresponding dispersion equation

$$(\Omega^2 - v_{\varphi 3}^2 k^2) - \frac{\varepsilon_0}{4} \frac{k^2 \omega_p^2}{mn_{c1}} \mathbf{E}_1 \mathbf{E}_1^* \left( \frac{1}{D^{(\Omega-\omega_1)}} + \frac{1}{D^{(\Omega+\omega_1)}} \right) = 0. \quad (6.55)$$

For a moderately strong driver the matching conditions (6.32) are well satisfied. The scattered frequency and wave number range from  $(\omega_2, k_2) = (\omega_1, k_1)$  to  $(\omega_1/2, 0)$ . Since  $\omega_3$  is close to  $\omega_p$ , for the Stokes component follows from  $\omega_2 \simeq \omega_1 - \omega_p$  that in back or side scattering the anti-Stokes frequency  $\omega_{2a} \simeq \omega_1 + \omega_p$  is nonresonant almost everywhere and  $1/D^{(\Omega+\omega_1)}$  can be neglected. The dispersion relation

reduces to

$$\begin{aligned} & (\omega_3^2 + 2i\omega_3\gamma - \omega_p^2 s_e^2 k_3^2)[(\omega_3 - \omega_1)^2 + 2i\gamma(\omega_3 - \omega_1) - \omega_p^2 - c^2(k_3 - k_1)^2] \\ &= \frac{\varepsilon_0}{4} \frac{k_3^2 \omega_p^2}{mn_{c1}} \mathbf{E}_1 \mathbf{E}_1^*. \end{aligned} \quad (6.56)$$

Maximum growth occurs close to resonance of  $\omega_2$  and  $\omega_3$ ; hence

$$2i\gamma_{\max}\omega_3[2i\gamma_{\max}(\omega_3 - \omega_1)] = \frac{\varepsilon_0}{4} \frac{k_3^2 \omega_p^2}{mn_{c1}} \mathbf{E}_1 \mathbf{E}_1^*. \quad (6.57)$$

$$\Rightarrow \gamma_{\max} = \frac{k_3}{4} \left[ \omega_p^2 (\omega_2 \omega_3) \frac{e^2}{m^2 \omega_1^2} \mathbf{E}_1 \mathbf{E}_1^* \right]^{1/2} = \frac{k_3}{4} \hat{v}_{os} \left[ \frac{\omega_p^2}{\omega_2 \omega_3} \right]^{1/2}. \quad (6.58)$$

For exact back scattering follows from (6.32) and (2.92)  $k_2 = k_0(1 - 2\omega_p/\omega_1)^{1/2}$ ,  $k_3 = |k_3| = k_1 + k_2$ . The comparison of  $\gamma_{\max}$  for SRS and SBS for  $s \simeq 10^{-3}c$  and  $m/m_i \simeq 10^{-4}$  shows that they are of the same order of magnitude. SRS into exact forward direction is also possible. Its relevance lies in the possibility of exciting an electron plasma wave of particularly high phase velocity in the low density plasma of  $\omega_p \ll \omega_1$ , e.g., hohlraum plasma in indirect inertial fusion drive, and subsequent preheat by trapped fast electrons [46–49]. In regions of low plasma density  $\omega_3 \simeq \omega_p$ ,  $\eta_1 = \eta \simeq 1$ , and in forward direction the matching condition implies for the anti-Stokes and Stokes lines  $k_3 = |\mathbf{k}_1 - \mathbf{k}_2| = (\omega_1 \pm \omega_p)/c \simeq \omega_1/c$ . The dispersion functions  $D^{(\Omega \pm \omega_1)} = D^{(\omega_3 \pm i\gamma \pm \omega_1)}$  simplify to

$$\begin{aligned} D^{(\Omega - \omega_1)} &= 2i\gamma(\omega_p - \omega_1) \simeq -2i\gamma\omega_1, \quad D^{(\Omega + \omega_1)} = 2i\gamma(\omega_p + \omega_1) \simeq +2i\gamma\omega_1, \\ D^{(\Omega - \omega_1)} + D^{(\Omega + \omega_1)} &= 4i\gamma\omega_p, \quad D^{(\Omega - \omega_1)} D^{(\Omega + \omega_1)} = 4\gamma^2 \omega_1^2. \end{aligned}$$

Both terms are nearly resonant and must be used in (6.55) to yield the growth rate

$$\gamma = \frac{1}{2^{3/2}} \frac{\omega_p^2}{\omega_1} \frac{\hat{v}_{os}}{c}. \quad (6.59)$$

### 6.2.3.3 Two Plasmon Decay

Short inspection of (6.53) and (6.54) shows that the equations governing the two plasmon decay are obtained by replacing  $\mathbf{E}_{\perp 2}$  by  $\mathbf{E}_{\parallel 2}$  of a second plasma wave or associated electron density perturbation  $n_2$ ,

$$\nabla^2 n_2 - \frac{1}{v_{\varphi 2}^2} \frac{\partial^2 n_2}{\partial t^2} = \frac{1}{mv_{\varphi 2}^2} \nabla \boldsymbol{\pi}_2, \quad \nabla^2 n_3 - \frac{1}{v_{\varphi 3}^2} \frac{\partial^2 n_3}{\partial t^2} = \frac{1}{mv_{\varphi 3}^2} \nabla \boldsymbol{\pi}_3. \quad (6.60)$$

The wave pressure term now is given by the resonant terms of  $\boldsymbol{\pi} = \boldsymbol{\pi}_0 + \boldsymbol{\pi}_t$ , i.e.,

$$\boldsymbol{\pi}_{2,3} = (\boldsymbol{\pi}_0 + \boldsymbol{\pi}_t)_{2,3} = -n_0 m \nabla(\mathbf{v}_1 \mathbf{v}_{2,3}) + m \frac{\partial n_{2,3} \mathbf{v}_1}{\partial t}, \quad (6.61)$$

with  $\mathbf{v}_1 = (\mathbf{v}_{os} + \mathbf{v}_{os}^*)$  induced by the laser. We substitute  $\mathbf{v}_{2,3}$  by  $n_{2,3}$  with the help of (2.92), Fourier-analyze (6.60) and keep only the resonant terms to obtain

$$\begin{aligned} (-\Omega^2 + \omega_2^2)n_2^{(\Omega)} &= -(\mathbf{k} - \mathbf{k}_1) \frac{\mathbf{v}_{os}}{2} \left[ \frac{k^2(\Omega - \omega_1)}{(\mathbf{k} - \mathbf{k}_1)^2} + \Omega \right] n_3^{(\Omega - \omega_1)}, \\ [-(\Omega - \omega_1)^2 + (\omega_2 - \omega_1)^2]n_3^{(\Omega - \omega_1)} &= -\frac{\mathbf{k}\mathbf{v}_{os}^*}{2} \left[ (\mathbf{k} - \mathbf{k}_1)^2 \frac{\Omega}{k^2} + (\Omega - \omega_1) \right] n_2^{(\Omega)}. \end{aligned}$$

Elimination of  $n_3^{(\Omega - \omega_1)}$  and approximating  $\omega_2 = \omega_3 = \omega_p = \omega_1/2$ , yields the dispersion equation

$$(\Omega^2 - \omega_2^2)[(\Omega - \omega_1)^2 - (\omega_2 - \omega_1)^2] - \frac{1}{4}(\mathbf{k} - \mathbf{k}_1)\hat{\mathbf{v}}_{os}(\mathbf{k}\hat{\mathbf{v}}_{os}^*)\omega_p^2 \frac{[(\mathbf{k} - \mathbf{k}_1)^2 - k^2]^2}{k^2(\mathbf{k} - \mathbf{k}_1)^2}. \quad (6.62)$$

Setting  $\Omega = \omega_p + i\gamma$  and  $\mathbf{k} - \mathbf{k}_1 \simeq \mathbf{k}$  determines the growth rate  $\gamma$ ,

$$\gamma = \mathbf{k}\hat{\mathbf{v}}_{os} \left| \frac{(\mathbf{k} - \mathbf{k}_1)^2 - k^2}{k|\mathbf{k} - \mathbf{k}_1|} \right|. \quad (6.63)$$

With the angle between the pump  $\mathbf{k}_1$  and  $\mathbf{k} = \mathbf{k}_2$  of  $n_2$ ,  $\alpha = \angle(\mathbf{k}_1, \mathbf{k}_2)$ , and  $(\mathbf{k} - \mathbf{k}_1)^2 - k^2 = -2\mathbf{k}_1\mathbf{k} + k_1^2 \simeq -2\mathbf{k}_1\mathbf{k}$  the growth  $\gamma$  results proportional to  $|\mathbf{k}_2\hat{\mathbf{v}}_{os}||\mathbf{k}_1\mathbf{k}| \sim \sin \alpha \cos \alpha$ , in agreement with the elementary reasoning. For  $\alpha = \pi/4$  it assumes its maximum value,

$$\gamma = \frac{\omega_1}{4\sqrt{2}} \frac{\hat{\mathbf{v}}_{os}}{c}. \quad (6.64)$$

From experiments with multiple overlapping laser beams in spherical and planar geometry it is concluded that the TPD instability is the main source of superthermal electron generation in the plasma corona with nonvanishing density scale length at  $n_c$ . The experiments show that the total overlapped intensity governs their scaling rather than the number of overlapped beams [50]. Theoretical investigations and concomitant numerical simulations confirm once more the production of hot electrons and show the transition of the SRS to the TPD when increasing the plasma density scale lengths [51]. An additional important feature is the emission of  $3/2 \omega_1$  radiation as a consequence of the current density component  $\mathbf{j}_{3\omega/2} = -en_{e,\omega/2}\mathbf{v}_{os}$  in the wave equation of the driver  $\mathbf{E}_1$ .

#### 6.2.3.4 Oscillating Two-Stream Instability

The growth rate  $\gamma$  of the OTSI is easily found with the help of  $\boldsymbol{\pi}_0$  from (6.40). Combining it with the ion momentum equation and particle conservation after linearization leads to

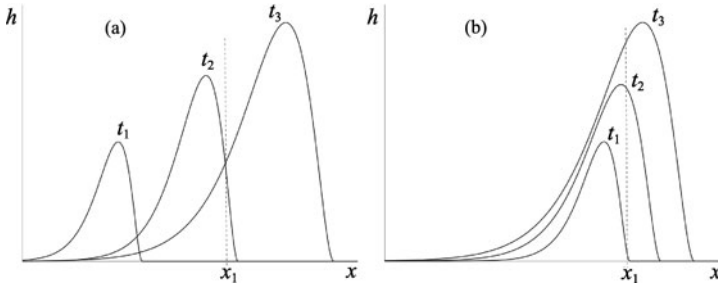


**Fig. 6.5** Convective (a) and absolute instability (b). The convectively unstable quantity  $h(x)$  grows in time up to a maximum and then decays at an arbitrary position  $x_1$ . The absolutely unstable quantity  $h(x)$  shows indefinite growth in time at any position  $x_1$

$$\frac{\partial^2}{\partial t^2} n_3 = - \left( \frac{\pi_0}{mn_0} + s^2 \right) k_3^2 n_3. \quad (6.65)$$

The interesting unstable domain for  $\omega_1$  is close to  $\omega_2 \simeq \omega_p$ . For  $v_{ei} \ll \omega_1$  and  $\omega_1^2 - \omega_2^2 = 2\omega\Delta$  follows

$$\frac{\gamma^2}{k_3^2} = - \frac{\Delta}{\Delta^2 + v^2/4} \frac{m}{m_i} \frac{\hat{v}_1^2}{4} - s^2. \quad (6.66)$$

Since  $n_3$  is quasi-static and not propagating the instability is absolute and, typical for it, even in the absence of any dissipation, exhibits a finite threshold for the pump intensity. The reason is obvious: growth can start when the ponderomotive force ( $\sim |\mathbf{E}_1|^2 n_3$ ) prevails on the thermal plasma pressure gradient ( $\sim s^2 n_3$ ).

For practical purposes it may be convenient to distinguish between convective and absolute instabilities. The difference is illustrated by Fig. 6.5. A convectively unstable pulse grows and then decays at each arbitrary position of interest (a); an absolutely unstable quantity grows indefinitely in time everywhere (b). The distinction is dictated by experimental requirements. If the group velocity of the pulse maximum in 6.5a is high enough the pulse may decay very quickly before growing to a dangerous height. The distinction between convective and absolute is not covariant; it depends on the relative motion of the system of reference.

### 6.2.3.5 Parametric Decay Instability

In contrast, the PDI is the resonant decay of a photon into a plasmon and a propagating phonon. An observer co-moving with  $n_3$  at speed  $s > 0$  sees a static modulation to which the former analysis applies, with the difference however that the plasmons emanating from  $n_3$  are Doppler-shifted by  $\Delta\omega_2 = \pm\omega_3$  whereas  $\omega_1$ , apart from an insignificant transverse shift from time dilation, is not. Introducing  $\omega_{\pm} = \omega_2 \pm \omega_3$ ,  $d_t = \partial_t - s\partial_x$  momentum conservation and (6.40) combine to

$$\frac{d^2}{dt^2}n_3 = -\left\{\left[\frac{\omega_1^2-\omega_+^2}{(\omega_1^2-\omega_+^2)^2+v^2\omega_1^2} + \frac{\omega_1^2-\omega_-^2}{(\omega_1^2-\omega_-^2)^2+v^2\omega_1^2}\right]e^{-i\pi/2}\right. \\ \left.\times \frac{e^2\omega_p^2|E_1|^2}{4mm_i(\omega^2+v^2)}\right\}k_3^2n_3 \quad (6.67)$$

This is in agreement with the somewhat lengthy treatments [29, 30, 52]. The phase change by  $\Delta\varphi = -\pi/2$  comes from (5.43) at resonance, as extensively discussed in Sect. 6.2.1. In the denominator there appears the factor 4 now instead of 2 in (6.40) since, pictorially spoken, half the electrons have anti-Stokes eigenfrequency  $\omega_+$  and the other half are resonant at the Stokes frequency  $\omega_-$  owing to the flow  $v = -s$ . The growth rate just above threshold follows from  $d_t^2 = (\partial_t - s\partial_x)^2 \simeq -(2i\gamma\omega_3 + s^2k_3^2)$ ,

$$\gamma = -\left\{\frac{\Delta_+}{\Delta_+^2 + v^2/4} + \frac{\Delta_-}{\Delta_-^2 + v^2/4}\right\}\frac{m\omega}{m_i\omega_3}\frac{\hat{v}_1}{16}; \quad \Delta_{\pm} = \omega_+ - \omega_{\pm}. \quad (6.68)$$

For vanishingly small damping it reduces to

$$\gamma = -\left\{\frac{1}{\Delta_+} + \frac{1}{\Delta_-}\right\}\frac{m\omega}{m_i\omega_3}\frac{\hat{v}_1^2}{16}, \quad (6.69)$$

thus indicating that at low driver intensity the PDI is convective. Both terms in the bracket are negative for  $\omega_1 - \omega_- = \Delta + \omega_3 < 0$ . Growth also occurs with  $0 > \Delta > -\omega_3$ . At exact resonance  $\Delta = 0$  neither the OTSI nor the PDI can grow.

### 6.2.3.6 Impact of Dissipation and Inhomogeneities

At resonance an undamped harmonic oscillator  $\delta(t)$  is excited to arbitrarily high amplitude by an arbitrarily weak driver  $E_d$ ; the onset of growth starts at threshold zero. In presence of linear damping  $v\delta$  growth can start when  $-e\overline{E_d\delta} > mv\delta^2$  is fulfilled. Applied to the parametric three wave process with dispersion equation of type (6.47) this reads in the weak coupling limit at optimum matching, consistent with weak damping  $v_{2,3} \ll \omega_{2,3}$ ,

$$v_2\delta_2^2 < C_2E_1^*\delta_3\delta_2, \quad v_3\delta_3^2 < C_3E_1\delta_2\delta_3 \Rightarrow v_2v_3 < C|E_1|^2, \quad (6.70)$$

$C = C_2C_3 = \text{const. } |E_{\text{th}}|^2 = v_2v_3/C = \gamma_{\text{th}}^2$  is the threshold pump intensity in presence of dissipation. By intuition  $|E_{\text{th}}|^2$  follows from the undamped growth rate

$$\gamma = \gamma_{\text{th}} = \sqrt{v_2v_3}; \quad C = \frac{v_2v_3}{|E_{\text{th}}|^2}. \quad (6.71)$$

Alternatively, inserting the damping terms  $iv_3\omega_3$  and  $iv_2(\omega_3 - \omega_1)$  in (6.46), (6.47), at exact resonance (6.70) becomes

$$(2\gamma + v_2)(2\gamma + v_3) - C|E_1|^2 = 0.$$

The solution for growth is

$$\gamma = -\frac{v_2 + v_3}{4} + \frac{1}{2} \left\{ \frac{(v_2 + v_3)^2}{4} - (v_2 v_3 - C|E_1|^2) \right\}^{1/2},$$

with (6.71) for  $\gamma = 0$  at the threshold. Hence, in presence of weak linear dissipation the growth is given by

$$\gamma = -\frac{v_2 + v_3}{4} + \frac{1}{2} \left\{ \frac{(v_2 - v_3)^2}{4} + C|E_1|^2 \right\}^{1/2}. \quad (6.72)$$

If instead of  $v$  the coefficient for kinetic energy damping  $v_E$  is introduced  $v_E = v/2$  has to be kept in mind. Damping may be either of collisional nature or of linear Landau type. Perhaps less intuitive, if one of the  $v_{2,3}$  vanishes  $|E_{\text{th}}|$  is again zero.

As a rule laser interaction creates inhomogeneous plasmas. In a region of validity of the optical WKB approximation the phase mismatch  $\psi(\mathbf{x})$  of the wave vectors is given by  $\psi = \int (\mathbf{k}_1 - \mathbf{k}_2 - \mathbf{k}_3) d\mathbf{x}$ . It is independent of the path of integration from  $\mathbf{x}_0$  to  $\mathbf{x}$ . Let us assume that at position  $\mathbf{x}_0$  there is perfect matching. Spatial growth will stop when  $\psi = \pi$  is reached. Owing to  $\nabla \times \mathbf{k}_{1,2,3} = 0$  holds  $(d\mathbf{x} \nabla) \boldsymbol{\kappa} = \nabla(d\mathbf{x} \boldsymbol{\kappa}) = \boldsymbol{\kappa}' \boldsymbol{\kappa}^0 d\mathbf{x}$ , with  $\boldsymbol{\kappa} = \mathbf{k}_1 - \mathbf{k}_2 - \mathbf{k}_3$  and  $\boldsymbol{\kappa}' = \nabla |\boldsymbol{\kappa}|$  pointing along  $\boldsymbol{\kappa}$ . Under gentle electron density variation Taylor expansion in  $\mathbf{x}_0$  along  $\boldsymbol{\kappa}$  yields  $\psi = \int_{\mathbf{x}_0}(\boldsymbol{\kappa}) d\mathbf{x} = \boldsymbol{\kappa}'(\mathbf{x}_0)(x - x_0)^2/2$ . Thus the amplification length is  $x - x_0 = \sqrt{2\pi/\kappa'}$ . At threshold the energy fed into the unstable modes 2, 3 in the intervals  $\Delta_{2,3} = (x - x_0)/\cos \alpha_{2,3}$ ,  $\alpha_{2,3} = \angle(\boldsymbol{\kappa}, \mathbf{k}_{2,3})$ , is convectively carried out of the interaction region,  $v_{g2,3} E_{2,3} = v_{2,3} \Delta_{2,3} E_{2,3}$ . The damping coefficients inserted in (6.71) yield

$$\frac{C|E_1|^2}{v_2 v_3} = 2\pi C|E_{\text{th}}|^2 \frac{\cos \alpha_2 \cos \alpha_3}{|\boldsymbol{\kappa}' v_{g2} v_{g3}|} = 1. \quad (6.73)$$

This is the celebrated Piliya–Rosenbluth criterion for  $|E_{\text{th}}|$  in the inhomogeneous plasma [53, 54]. As the emphasis in this chapter is primarily on the basic physical effects driving the plasma unstable and on the basic wave dynamics the influence of inhomogeneities on the individual growth rates is not pursued further. An extensive introduction to parametric instabilities in inhomogeneous plasmas may be found in [55] and a list of thresholds and linear growth rates may be found in [56].

### 6.3 Parametric Amplification of Pulses

The foregoing section was devoted to the basic mechanisms of resonant three wave interactions in the homogeneous plasma in situations where the constant amplitude approximation is justified. It represents the purest, i.e. the most idealized, case of

wave-wave coupling by the wave pressure. To give this theory “a touch of reality” ([6], Sect. 10.3) in the following the coupled three wave equations for slowly varying amplitudes are formulated. At the same time such an extension will exhaust the limits of the Hamiltonian description of wave dynamics in terms of action angle variables and preserve the number of quasi-particles introduced in Sect. 3.1.1, and finally, it will yield additional insight by revealing the perfect symmetry between the three coupled waves.

### 6.3.1 Slowly Varying Amplitudes

The waves considered in this subsection exhibit the more general structure  $A(\mathbf{x}, t) = \hat{A}(\mathbf{x}, t) \exp[i\Phi(\mathbf{x}, t)]$  with amplitudes  $\hat{A}(\mathbf{x}, t)$  slowly varying in space according to the WKB approximation, and wave vectors  $\mathbf{k}$  and frequencies  $\omega$  defined by  $\mathbf{k} = \nabla\Phi$ ,  $\omega = -\partial_t\Phi$ . We begin with the laser pump wave  $\mathbf{E}_1$  by expanding (6.5) up to first order,

$$\begin{aligned} (-c_{\varphi 1}^2 \mathbf{k}_1^2 + \omega_1^2) e^{i\Phi_1} \hat{\mathbf{E}}_1 + 2i[c^2(\mathbf{k}\nabla)\hat{\mathbf{E}}_1 + \omega\partial_t\mathbf{E}_1]e^{i\Phi_1} &= \frac{e^2\omega_1}{2\varepsilon_0 m\omega_2} e^{i(\Phi_2+\Phi_3)} \hat{\mathbf{E}}_2 \hat{n}_3 \\ &= \frac{-ie\omega_1}{2m\omega_2} e^{i(\Phi_2+\Phi_3)} \hat{\mathbf{E}}_2 (\mathbf{k}_3 \hat{\mathbf{E}}_3); \quad \mathbf{E}_3 = i \frac{e}{\varepsilon_0} \mathbf{k}_3 n_3. \end{aligned} \quad (6.74)$$

Note that  $c$  in the second term is the light speed in vacuum. The first term vanishes by definition. Recalling  $c_g c_\varphi = c^2$  one is led to

$$(\mathbf{c}_g \nabla) \hat{\mathbf{E}}_1 + \partial_t \hat{\mathbf{E}}_1 = -\frac{1}{4} \frac{ek_3\omega_1}{m\omega_1\omega_2} \hat{\mathbf{E}}_2 \hat{\mathbf{E}}_3 e^{i(\Phi_2+\Phi_3-\Phi_1)}. \quad (6.75)$$

We chose the stimulated Raman effect as the most illustrative example in the context here. The scattered transverse wave  $\mathbf{E}_2$  is subject to the same procedure as  $\mathbf{E}_1$ ; it reads

$$(\mathbf{c}_g \nabla) \hat{\mathbf{E}}_2 + \partial_t \hat{\mathbf{E}}_2 = \frac{1}{4} \frac{ek_3\omega_2}{m\omega_1\omega_2} \hat{\mathbf{E}}_1 \hat{\mathbf{E}}_3^* e^{-i(\Phi_2+\Phi_3-\Phi_1)}. \quad (6.76)$$

Only the  $\hat{n}_3$  and  $\hat{\mathbf{E}}_3^*$  components fulfill the resonance condition. Equation (6.54) is a consequence of (6.5) because only the velocity component of  $\mathbf{v}_e$  parallel to  $\mathbf{E}_3$  and  $\mathbf{k}_3$  contributes. Analogously to (6.74) with  $v_g v_\varphi = s_e^2$  we obtain

$$(\mathbf{c}_g \nabla) \hat{\mathbf{E}}_3 + \partial_t \hat{\mathbf{E}}_3 = \frac{1}{4} \frac{ek_3\omega_p^2}{m\omega_1\omega_2\omega_3} \hat{\mathbf{E}}_1 \hat{\mathbf{E}}_2^* e^{-i(\Phi_2+\Phi_3-\Phi_1)}. \quad (6.77)$$

Introducing the symbol  $d_i = \partial_t + (\mathbf{v}_g \nabla)$  for the total, i.e., convective, derivative, multiplying  $\mathbf{E}_i$  by its cc  $\mathbf{E}_i^*$  in the last three equations above and setting  $\Delta\Phi = \Phi_2 + \Phi_3 - \Phi_1$  for the dephasing (“mismatch”) of the modes and  $C = \varepsilon_0 e k_3 / 8 m \omega_1 \omega_2$ ,

(6.75), (6.76), and (6.77) read

$$\frac{1}{\omega_1} d_1 \left( \frac{\varepsilon_0}{2} \hat{\mathbf{E}}_1 \hat{\mathbf{E}}_1^* \right) = -C \left( \hat{\mathbf{E}}_1^* \hat{\mathbf{E}}_2 \hat{\mathbf{E}}_3 e^{i\Delta\Phi} + \hat{\mathbf{E}}_1 \hat{\mathbf{E}}_2^* \hat{\mathbf{E}}_3^* e^{-i\Delta\Phi} \right), \quad (6.78)$$

$$\frac{1}{\omega_2} d_2 \left( \frac{\varepsilon_0}{2} \hat{\mathbf{E}}_2 \hat{\mathbf{E}}_2^* \right) = C \left( \hat{\mathbf{E}}_1^* \hat{\mathbf{E}}_2 \hat{\mathbf{E}}_3 e^{i\Delta\Phi} + \hat{\mathbf{E}}_1 \hat{\mathbf{E}}_2^* \hat{\mathbf{E}}_3^* e^{-i\Delta\Phi} \right), \quad (6.79)$$

$$\frac{\omega_3}{\omega_p^2} d_3 \left( \frac{\varepsilon_0}{2} \hat{\mathbf{E}}_3 \hat{\mathbf{E}}_3^* \right) = C \left( \hat{\mathbf{E}}_1^* \hat{\mathbf{E}}_2 \hat{\mathbf{E}}_3 e^{i\Delta\Phi} + \hat{\mathbf{E}}_1 \hat{\mathbf{E}}_2^* \hat{\mathbf{E}}_3^* e^{-i\Delta\Phi} \right), \quad (6.80)$$

The expressions on the LHS of (6.78), (6.79), and (6.80) represent the convective derivatives of the energy densities  $\varepsilon_i$  divided by their frequencies  $\omega_i$ ,  $i = 1, 2, 3$ . Throughout the chapter we have used the electric fields  $\mathbf{E}_i$  with frequencies  $\omega_i = \text{const}$  for convenience. In the case of slight inhomogeneities in space and time the  $\omega_i$  and  $\mathbf{k}_i$  both are subject to slow (secular) changes that have to be taken into account in deriving the energy conservation relations. In Sect. 3.2.1 it has been shown that in the absence of source terms the Hamiltonian concept leads to the conservation of  $\varepsilon_0 \mathbf{E}_i \mathbf{E}_i^* / 2\omega_i$  for transverse waves [see (3.19)] rather than of the energy densities  $\varepsilon_0 \mathbf{E}_i \mathbf{E}_i^* / 2$ . That means that when identifying the quiver velocity with the vector potential,  $\mathbf{v}_{\text{os}} = -e\mathbf{A}/m$ , instead of (2.11) and keeping the derivatives of the amplitudes one arrives at the correct expressions  $d_i(\varepsilon_0 \mathbf{E}_i \mathbf{E}_i^* / 2\omega_i)$ . For the longitudinal modes the same follows from the assertion that dispersion relations of identical structure lead to analogous conservation relations, proved in Sect. 3.1.3, (3.48)ff.

Introducing  $K = ek_3\omega_p/(8m^2\omega_1\omega_2\omega_3)^{1/2}$ ,  $a_{1,2} = (\varepsilon_0/2\omega_{1,2})^{1/2} \mathbf{E}_{1,2}$ , and  $a_3 = (\varepsilon_0\omega_3/2\omega_p^2)^{1/2} \mathbf{E}_3$ , (6.78), (6.79), and (6.80) transform into

$$\begin{aligned} d_1 |a_1|^2 &= -K(a_1^* a_2 a_3 + \text{cc}), \\ d_1 |a_2|^2 &= +K(a_1^* a_2 a_3 + \text{cc}), \\ d_1 |a_3|^2 &= +K(a_1^* a_2 a_3 + \text{cc}), \end{aligned} \quad (6.81)$$

These relations show the perfect equivalence of coupling of mode  $i$  by the two modes  $j$  and  $k$ . It is straightforward to show it also for the acoustic mode. So far it has been evident from (6.54) and (6.60) that the longitudinal modes couple ponderomotively to transverse modes. The symmetry of (6.81) reveals the identical nature of coupling due to wave pressure for all modes. However, the coupling coefficients for  $\mathbf{E}_\perp$  differ from those for  $\mathbf{E}_\parallel$ . When two modes drive a velocity field  $\mathbf{v}$  with  $\text{div } \mathbf{v} = 0$  the resulting unstable mode is an electromagnetic plane wave.

### 6.3.2 Quasi-Particle Conservation and Manley–Rowe Relations

According to (3.19) the LHS of (6.78), (6.79), and (6.80) are the total derivatives of the quasi-particle densities  $f_{1,2,3}$ . As the creation and annihilation rates on the RHS are identical the classical so-called Manley–Rowe relations hold [57–59],

$$-\frac{df_1}{dt} = \frac{df_2}{dt} = \frac{df_3}{dt}. \quad (6.82)$$

These relations yield the justification for characterizing the parametric instabilities in Sect. 6.2.2 in terms of particle decay processes. The extension of the operator  $d/dt$  to linear damping and diffusion is very easy in the framework of classical theory. It may be surprising at first glance that for the expectation values a quantum concept holds exactly with the same range of validity in a purely classical field. Only for counting the real number of quasi-particles additional information not available in classical physics is needed. This new element is Planck's constant  $\hbar$ . The surprise vanishes after some simple reflections on what classical and quantum theory have in common in the homogeneous and isotropic environment. Free particles can be represented by plane waves and as such they are characterized by the parameters  $\mathbf{k}$  (momentum) and  $\omega$  (energy); furthermore, the complex exponentials  $e^{i\phi}$  are eigenstates of the operators  $\partial_{\mathbf{k}}$  and  $\partial_t$  of the wave operator  $\nabla^2 - \partial_{v_e}^2 t$ . Finally, the steady state wave equation  $\nabla^2 \mathbf{E} + k_0^2 \eta^2 \mathbf{E} = 0$  is identical with the Schrödinger equation if the identifications  $k_0^2 = 2mE/\hbar^2$  and  $\eta^2 = 1 - V/E$  with potential and total energies  $V$  and  $E$  are made. When (6.82) is integrated over a finite volume  $V$  fixed in space the balance reads

$$\frac{d}{dt} \int_V (f_2 + f_3 - f_1) dV + \int_{\Sigma(V)} (f_2 v_{g2} + f_3 v_{g3} - f_1 v_{g1}) d\Sigma = 0. \quad (6.83)$$

This is the conservation of quasi-particles in its standard form; the total loss through the surface  $\Sigma(V)$  equals their production in the volume. As seen from (6.78), (6.79), and (6.80) the production rates depend on the dephasing angle  $\Delta\Phi$ . If in the inhomogeneous plasma matching is perfect in one position in space it will, depending on the dispersion relations, deteriorate in its neighborhood and may eventually stop unstable growth.

### 6.3.3 Light Scattering at Relativistic Intensities

Stimulated Raman and Brillouin scattering from a pump wave in the relativistic regime, typically  $I \geq 10^{18} \text{ W/cm}^2$ , have been investigated analytically and semi-analytically by several authors, as for example [60–63]. By taking self-focusing, ponderomotive nonlinearities and pump depletion into account the latter author finds that reflection of the backscattered Brillouin wave at normalized incident intensity in circular polarization  $a^2 = (e\hat{E}/mc\omega)^2 = 4.0$  does not exceed 15%. When considering the effect of Landau damping on Raman forward and backward scattering in a moderately relativistic regime one should be aware that the Landau damping coefficients for plasma parameters relevant to controlled thermonuclear fusion have to be revisited; they may be by several orders of magnitude lower than the nonrelativistic values [64]. A new and remarkable variant under several aspects of stimulated forward Raman scattering is reported in [65]: The Raman radiation is downshifted by

half the plasma frequency; the growth is not exponential but of explosive type, i.e., it diverges after a finite time. Also, interestingly, a quasi-static electric field moving along with the laser pulse is found.

A first impression of unstable growth at high laser intensities may still be gained from the linear formulas of growth from Sect. 6.2.3, now taken for circular polarization for simplicity, by substituting

$$\left(\frac{\hat{v}_{os}}{c}\right)^2 \rightarrow \frac{\hat{a}^2}{1 + \hat{a}^2}, m \rightarrow \frac{m}{(1 + \hat{a}^2)^{1/2}}; \hat{a} = \frac{e\hat{E}}{mc\omega}. \quad (6.84)$$

For its motivation see Sect. 8.2.1. The inverse growth rates for SRS, OTSI and filamentation at  $I = 10^{18} \text{ W/cm}^2$  are 2, 5, 26, 136 fs for Nd and 1.5, 4, 15, 117 fs for KrF. At  $I = 10^{20} \text{ W/cm}^2$  they shorten to 13, 1.2, 11, 36 fs for Nd and 0.3, 0.6, 4, 18 fs for KrF, hence ranging from sub-fs to  $\sim 100$  fs. Growth is fastest for SRS and is expected to saturate quickly. To get insight into the dynamics of SRS growth and its saturation level, recurrence must be made to numerical simulations. In the following the results obtained by S. Hain [66] in a plasma of  $Z = 1$  and  $T_e = 1 \text{ keV}$  are summarized.

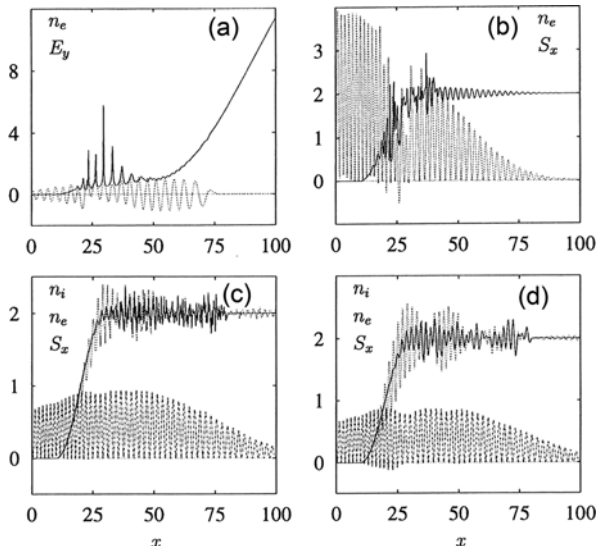


**Fig. 6.6** 1D2V fluid simulation of stimulated Raman scattering (SBS) at  $\lambda_{Nd}$ . Electron and ion densities  $n_e, n_i$  (solid and dotted, resp.), critical density  $n_c = 4 \times 10^{21} \text{ cm}^{-3}$ , electric field  $E_y$  in units of  $3 \times 10^{10} \text{ Vcm}^{-1}$ , Poynting flux  $S_x$  in units of  $2.5 \times 10^{18} \text{ Wcm}^{-2}$  (lower graphs, dotted), space coordinate  $x$  in units  $\lambda_{Nd}/\pi$ . **(a)**: Incident intensity from left  $I = 3.5 \times 10^{17}$ ; electron plasma wave strongly nonlinear, regular (solid), electric field  $E_y$  (dotted); laser beam trapping around  $n_c/4$ , negligible reflection  $R$ . **(b)**:  $I = 1.4 \times 10^{18}$ , electron plasma wave broken; strong trapping around  $n_c/4$ , relativistically increased by factor 1.5 – 1.6;  $R = 10\%$ . **(c)**: SRS from stochastic ion density profile, static (solid),  $\langle k \rangle > 2k_{\text{Laser}}$ ,  $I = 3.5 \times 10^{17}$ ,  $n_e$  (dotted),  $R = \text{few \%}$ . **(d)**: SRS from stochastic ion density profile (solid),  $\langle k \rangle = 2k_{\text{Laser}}$ , strong light trapping around rel.  $n_c/4$  with subsequent detrapping;  $R = 10\%$

First simulations from a 1D2V two-fluid model with a linearly polarized Nd laser beam in the intensity range of  $10^{18} \text{ Wcm}^{-2}$  are presented with parameters given in Fig. 6.6. Maxwell's equations together with the relativistic electron fluid equations of motion

$$\partial_t n_e + \nabla n_e v_e = 0, \quad \frac{d\gamma \mathbf{v}_e}{dt} = \frac{1}{m} \nabla p_e - e(\mathbf{E} + \mathbf{v}_e \times \mathbf{B}) \quad (6.85)$$

are solved. Typical results of Raman backward scattering from flat and perturbed ion background are presented in Fig. 6.6 First the instability builds up with a growth rate similar to (6.59) corrected by (6.84). At sub-relativistic intensity in (a) the electron mode shows the spiky structure well-known from Fig. 4.6 which then goes over into the broken structure of (b). As maximum growth occurs around  $n_c/4$  the reflected wave manifests itself as a standing wave of wavelength of the extension of the active plasma volume, best seen in (a) from the low frequency modulation of  $E_y$ . In (b) strong trapping of incident light at  $n_c/4$  up to 50% is observed with following detrapping into forward direction. The saturated reflection level does not

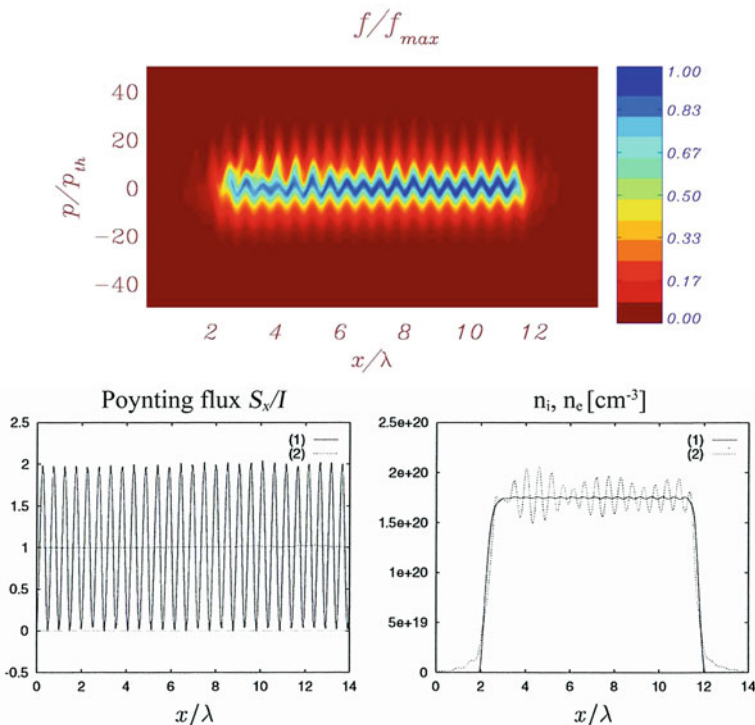


**Fig. 6.7** SRS: Linearly polarized Ti:Sa laser pulse of  $I = 10^{18} \text{ Wcm}^{-2}$  impinges onto  $10\lambda$  thick  $n_c/10$  plasma from LHS. Electron distribution function  $f(x, p_x)$ ,  $p_{th} = (k_B T_e)^{1/2}$ , Poynting flux  $S_x(t)$  (1: solid) and cycle-averaged  $S_x$  (2: dotted) and  $n_i$  (1: solid),  $n_e$  (2: dotted) after 40 laser cycles. Electron wave is perfectly regular; almost no back reflection.  $\hat{E}_x \approx 0.02 \hat{E}_1$ (pump)

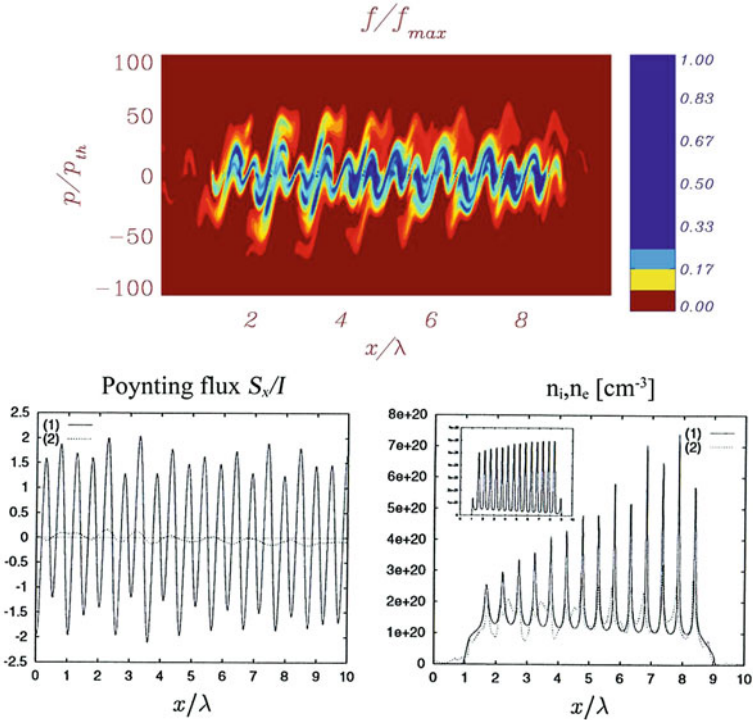


**Fig. 6.8** SRS: Linearly polarized standing pump pulse. Parameters and symbols as in Fig. 6.7. Electron density becomes chaotic when the two pump beams start overlapping. The ponderomotively driven ion density profile remains regular; amplitudes are reduced due to electron chaos, compare inset on ion density profile from hydrodynamic simulation. Back reflection level remains very low despite  $\hat{E}_x \approx 0.2\hat{E}_1$

exceed 10%. Backscattering from a stochastic ion background becomes significant ( $\sim 10\%$ ) only from a Brillouin-matched spatial modulation of  $2k_{\text{Laser}}$ . In the fluid dynamic simulation local wavebreaking must be bridged somehow artificially each time over the instant of breaking.

Alternatively SRS is simulated kinetically by solving the Vlasov equation. This is a 3D problem. However, if only for the thermal  $v_x$  velocity component  $T_e \neq 0$  is assumed and the laser field is approximated by a plane wave  $E_y = -\partial_t A_y$ , owing to the canonical momentum conservation  $mv_y = eA_y$  collinear scattering is reducible to a 1D1V problem for the electron distribution function  $f(x, p_x, p_y, t) = f(x, p_x, t)\delta(p_y - eA_y)$ . Including the Lorentz force component (ponderomotive term) the relativistic Vlasov equation (8.39) reads

$$\frac{\partial f}{\partial t} + \frac{p_x}{\gamma m} \frac{\partial f}{\partial x} - e(E_x + \frac{e}{2\gamma m} \partial_x A_y^2) \frac{\partial f}{\partial p_y} = 0. \quad (6.86)$$

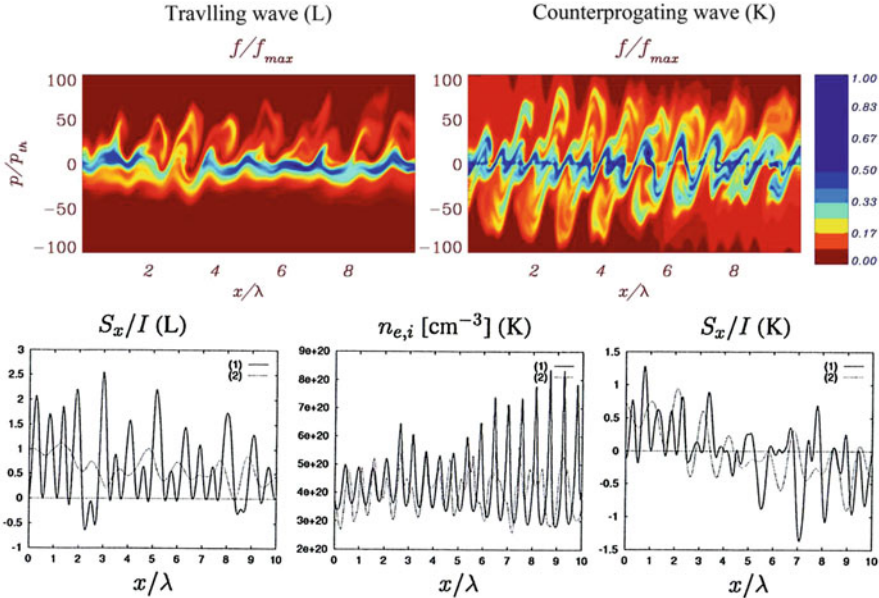


**Fig. 6.9** SRS after 40 cycles from a linearly polarized traveling pump pulse (L),  $I = 10^{18} \text{ Wcm}^{-2}$ , and two counter-propagating pulses (K) in  $n_c/4$  plasma, same intensity  $10^{18} \text{ Wcm}^{-2}$  both directions. Symbols and rest of parameters as in Fig. 6.7. In both cases, L and K, the electron plasma wave breaks and stabilizes back scattering; the ion density remains regular.  $\hat{E}_x \approx 0.2\hat{E}_1$  (L) and  $\hat{E}_x \approx 0.3\hat{E}_1$  (K). In the scattered low-frequency wave  $\hat{E}_2$  trapping of  $\hat{E}_1$  occurs up to 50% in intensity

In circular polarization  $A_y$ ,  $E_y$  are to be substituted by  $A_\perp = (A_y^2 + A_z^2)^{1/2}$ ,  $E_\perp = -\partial_t A_\perp$ . The ion dynamics is calculated in the nonrelativistic fluid approach with an ion temperature  $T_i = 100 \text{ eV}$ . For the electrons a “one-dimensional” temperature  $T_e = 1 \text{ keV}$  is chosen. Simulations are made in linear and circular polarization with a Ti:Sa beam of constant  $10^{18} \text{ Wcm}^{-2}$  and rise time 30 fs that is impinging on  $\sim 10$  wavelengths thick targets of constant densities  $n_e = n_i = n_c/10$  and  $n_c/4$ . The results after different numbers of light periods are presented in Figs. 6.7, 6.8, and 6.9. We start with SRS from a beam in linear polarization propagating through  $n_c/10$  density. In Fig. 6.7  $f(x, p_x)/f_{\max}$ , normalized Poynting flux  $S_x$  and  $n_i$  (1: solid) and  $n_e$  are shown after 40 laser cycles. The electron distribution function and  $n_e$ ,  $n_i$  are perfectly regular and saturate at a very low level,  $\hat{E}_x \approx 0.02\hat{E}_1$ . The modulation in  $\hat{E}_x$  originates from the Raman anti-Stokes component. A completely different picture of the electron dynamics is obtained from two counter-propagating pump beams (standing wave, e.g. total reflection from critical point) after 40 cycles (Fig. 6.8). When the two beams overlap the electrons start moving chaotically and back reflection saturates, under a low level again as inferred from the cycle-averaged Poynting flux  $S_x$  (dotted line). The ions behave perfectly regular. Stronger Raman back scattering and increased chaotic dynamics is to be expected from  $n_c/4$  density.

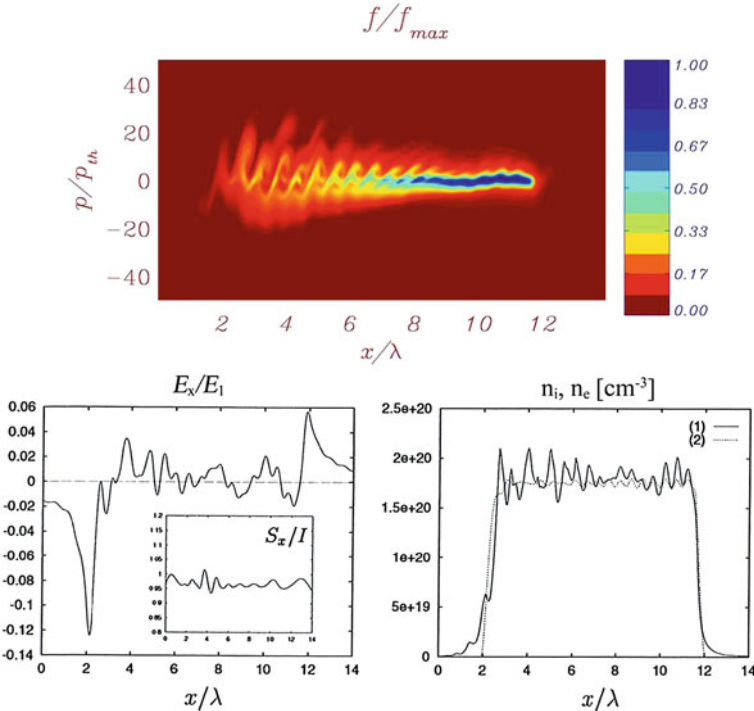


**Fig. 6.10** SRS after 40 cycles from a linearly polarized traveling pump pulse in  $n_c/10$  plasma density,  $I = 10^{18} \text{ Wcm}^{-2}$ . Symbols and parameters as in Fig. 6.7. Owing to breaking of  $n_e$ , see  $f(x, p_x)$  and  $E_x \approx 0.02 \hat{E}_1$ , reflection saturates at 2–5%, see Poynting flux  $S_x/I$  in the inset

The latter is true as Fig. 6.9 shows, however,  $S_x/I(L)$  indicates that back reflection remains low in this case again.

SRS of a circularly polarized traveling pump wave of  $I = 10^{18} \text{ Wcm}^{-2}$  from an  $n_c/10$  plasma is presented in Fig. 6.10 after 40 cycles. The time for the instability to grow is 4 cycles only. At early times regular structures in  $n_i$  and  $n_e$  similar to those in Fig. 6.6 build up, however following onset of breaking destroys them (lower right picture) and stabilizes back reflection at 2–5%, see  $S_x/I$  in the inset of lower left picture of  $E_x$ . It has been a general observation through all simulations that circular polarization shows the tendency towards higher degree of chaotic dynamics and at the same time towards increased back reflection. With increasing background plasma density the difference tends to vanish. For the parameters of Fig. 6.9 there is almost no difference between linear and circular polarization. It can be concluded that at relativistic intensities SRS saturates, mainly owing to breaking, at an insignificant low level, in qualitative agreement with hydro simulations where the latter overestimate scattering for obvious reasons. In the context here it may be interesting to note that in a very early paper [67] it has been stated on pure physical grounds that at relativistic intensities parametric instabilities are not important, in agreement with the simulations presented here.

## References

1. Glenzer, S.H., Rozmus, W., McGowan, B.J., et al.: Phys. Rev. Lett. **82**, 97 (1999) 235
2. Glenzer, S.H., Redmer, R.: Rev. Mod. Phys. **81**, 1625 (2009) 235
3. Lee, K.J., Neumayer, P., Castor, J., et al.: Phys. Rev. Lett. **102**, 115001 (2009) 235
4. Baldis, H.A., Campbell, E.M., Krueer, W.L.: In: Rosenbluth, M.N., Sagdeev, R.Z. (eds.) Laser–Plasma Interactions, Handbook of Plasma Physics, vol. 3, pp. 383–396. North-Holland, Amsterdam (1991) 237, 242
5. John Sheffield: Plasma Scattering of Electromagnetic Radiation, Acad. Press. New York (1975) 237
6. Boyd, T.J.M., Sanderson, J.J.: The Physics of Plasmas, Cambridge Univ. Press. Cambridge (2003) 237, 257
7. Chihara, J.: J. Phys.: Metal Physics **17**, 295 (1987); J. Phys.: Condensed Matter **12**, 231 (2000) 237
8. Fortmann, C., Redmer, R., Reinholtz, H., Röpke, G., Wierling, A., Rozmuws, W.: High Energy Density Physics **2**, 57 (2006) 238
9. Fortmann, C., Thiele, R., Fäustlin, R.R., Bornath, Th., et al.: High Energy Density Physics **5**, 208 (2009) 238
10. Brillouin, L.: La theorie des solides er les quanta (1928), and Wave propagation in periodic structures (1940). Experimental verification of the effect by Gross in 1930 (Léon Brillouin predicted the effect in 1922) 242
11. Landsberg, G., Mandelstam, L.: Eine neue Erscheinung bei der Lichtstreuung in Metallen. A new phenomenon in the light scattering from metals), Die Naturwissenschaften **16**, 557 (1928) 242
12. Handke, J., Rizvi, S.A.H., Kronast, B.: Appl. Phys. **25**, 109 (1981) 242, 249
13. Gellert, B., Kronast, B.: Appl. Phys. B **32**, 175 (1983) 242, 249
14. Baldis, H., et al.: Phys. Fluids B **5**, 3319 (1993) 242
15. Kline, J.L., J. Phys.: Conf. Ser. **112**, 022042 (2008)
16. Hüller, S., Masson-Laborde, P.E., Pesme, D., Casanova, M., Detering, F., Maximov, A.: Phys. Plasmas **13**, 022703 (2006) 248
17. Pesme, D. In: Dautray, R., Watteau, J.P. (eds.) La fusion thermonucléaire inertiel par laser (1993) 247
18. Johnston, T.W., et al.: Plasma Phys. Contr. Fusion **27**, 473 (1985) 242
19. Kadomtsev, B.B.: Plasma Turbulence. Acad. Press, New York (1965) 242
20. Davidson, R.C., Goldman, R.: Phys. Rev. Lett. **21**, 1671 (1968) 242
21. Depierreux, S., et al.: Phys. Rev. Lett. **84**, 2869 (2000) 242
22. Fouquet, Th., Pesme, D.: Phys. Rev. Lett. **100**, 055006 (2008) 242
23. Goldman, M.V., DuBois, D.F.: Phys. Fluids **8**, 1404 (1965) 242
24. Forslund, D.W., Kindel, J.M., Lindman, E.L.: Phys. Fluids **18**, 1002 (1975) 242, 246, 247
25. Strozzi, D.J.: Vlasov simulations of kinetic enhancement of Raman backscatter in laser fusion plasmas. Massachusetts Institute of Technology, Thesis (2006) 242
26. Vu, H.X., DuBois, D.F., Bezzerezides, B.: Phys. Plasmas **14**, 012702 (2007) 243
27. Yin, L., Daughton, W., Albright, B.J., et al.: Phys. Plasmas **13**, 072701 (2006) 243
28. Baldis, H.A., Campbell, E.M., Krueer, W.L.: In: Rosenbluth, M.N., Sagdeev, R.Z. (eds.) Laser–Plasma Interactions, Handbook of Plasma Physics, vol. 3, pp. 397–408. North-Holland, Amsterdam (1991) 243
29. Silin, V.P.: Sov. Phys. JETP **21**, 1127 (1965) 244, 255
30. Nishikawa, K.: J. Phys. Soc. Japan **24**, 1152 (1968) 244, 255
31. Mulser, P., Giulietti, A.: Europhys. Lett. **12**, 335 (1990) 244
32. Krueer, W.L.: The Physics of Laser Plasma Interactions, p. 91. Addison-Wesley Publ., Redwood City, CA. (1988) 247
33. Hüller, S., Mulser, P., Rubenchik, A.M.: Phys. Fluids B **3**, 3339 (1991) 247
34. Drake, J.F., Kaw, P.K., Lee, Y.C., Schmidt, G., Liu, C.S., Rosenbluth, M.N.: Phys. Fluids **17**, 778 (1974) 247, 248
35. Berger, R.L., et al.: Phys. Fluids B **5**, 2243 (1993) 248

36. Cassedy, E.S., Mulser, P.: Phys. Rev. A **10**, 2349 (1974) 248
37. Eidmann, K., Sigel, R.: In: Schwarz, H.J., Hora, H. (eds.) *Laser Interaction and Related Plasma Phenomena*, vol. 3B, p. 667. Plenum, New York (1974) 249
38. Clayton, C.E., Joshi, C., Chen, F.F.: Phys. Rev. Lett. **51**, 1656 (1983) 249
39. Bernard, J.E., Meyer, J.: Phys. Fluids **29**, 2313 (1986) 249
40. Mostovych, A.M., et al.: Phys. Rev. Lett. **59**, 1193 (1987) 250
41. Hüller, S., Masson, P.E.-Laborde, Pesme, D., Labaune, C., Bandulet, H.: J. Phys.: Conf. Series **112**, 022031 (2008) 250
42. Tikhonchuk, V.T., Hüller, S., Ph. Mounaix: Phys. Plasmas **4**, 4369 (1997) 250
43. Pesme, D., Rozmus, W., Tikhonchuk, V.T., Maximov, A., Ourdev, I., Still, C.H.: Phys. Rev. Lett. **84**, 278 (2000) 251
44. Michel, P., Labaune, C.: Phys. Fluids **10**, 3545 (2003) 251
45. Masson-Laborde, P.E., Hüller, S., Pesme, D., Casanova, M., Loiseau, P.: J. Phys. IV France **133**, 247 (2006) 251
46. Drake, R.P., Turner, R.E., Lasinski, B.F., et al.: Phys. Rev. Lett. **40**, 3219 (1989) 252
47. Strozzi, D.J., Shoucri, M.M., Bers, A., Williams, E.A., Langdon, A.B.: J. Plasma Phys. **72**, 1299 (2006)
48. Ze, F., et al.: Comm. Plasma Phys. Contr. Fusion **10**, 33 (1986)
49. Mourenas, D., Divol, L., Casanova, M., Rousseaux, C.: Phys. Plasmas **8**, 557 (2001) 252
50. Stoeckl, C., Baldis, H., et al.: Phys. Rev. Lett. **90**, 235002 (2003) 253
51. Sheng, Z.-M., Li, Y.T., Zhang, J., Veisz, L.: IEEE Transactions on Plasma Sci. **33**, 486 (2005) 253
52. Sanmartin, J.R.: Phys. Fluids **13**, 1533 (1970) 255
53. Piliya, A.D.: *Phenomena in Ionized Gases*, p. 287. Proc. 11th Int. Conf., Oxford (1971) 256
54. Rosenbluth, M.N.: Phys. Rev. Lett. **29**, 565 (1972) 256
55. Liu, C.S.: In: Simon, A., Thompson, W.B. (eds.) *Advances in Plasma Physics*, vol. 6, pp.121–177. John Wiley & Sons, New York (1976) 256
56. Babonneau, D.: *Instabilités Paramétriques en Plasma Inhomogène*, Centre d'Etudes de Limeil B.P.no 27, Note C.E.A. no 1749 (June 26 1974) 256
57. Manley, J.M., Rowe, H.E.: Proc. Inst. Radio Engrs. **44**, 904 (1956) 258
58. Brown, J.: Electron. Lett. **1**, 23 (1965)
59. Brizard, A.J., Kaufman, A.N.: Phys. Rev. Lett. **74**, 4567 (1995) 258
60. Salimullah, M., Hassan, M.H.A.: Phys. Rev. A **41**, 6963 (1990) 259
61. Guerin, S., Laval, G., Mora, P., Adam, J.C., Heron, A.: Phys. Plasmas **2**, 2807 (1995)
62. Mahmoud, S.T., Sharma, R.P.: Phys. Plasmas **8**, 3419 (2001)
63. Mahmoud, S.T.: Phys. Scr. **76**, 259 (2007) 259
64. Bers, A., Shkarowski, I.P., Shoucri, M.: Phys. Plasmas **16**, 022104 (2009) 259
65. Shvets, G., Fish, N.J., Rax, J.M.: Phys. Plasmas **3**, 1109 (1996) 259
66. Steffen Hain: *Ausbreitung intensiver Laserstrahlung in Materie. Propagation of intense laser radiation in matter*, PhD thesis, Tech. Univ. Darmstadt; GCAVerlag, Herdecke (1999), pp. 50–62, in German 260
67. Kaw, P., Dawson, J.: Phys. Fluids **13**, 472 (1970) 264

# Chapter 7

## Intense Laser–Atom Interaction

In this chapter we shall introduce the fundamental effects that occur when intense laser light interacts with isolated atoms, that is, ionization by the laser field, laser-assisted recombination (i.e., harmonic generation), and laser-assisted collisional ionization (nonsequential ionization). The focus of this chapter is on a self-contained but concise account of these most fundamental effects and the common theory behind them. Readers interested in more details on particular subjects (or subjects not covered at all in this chapter) may find the following (incomplete) list of reviews and monographs useful: [1–4] (general), [5] (tunneling ionization), [6] (intense-field S-matrix theory), [7] (few-cycle laser pulses), [8, 9] (above-threshold ionization), [10] (harmonic generation), [11] (stabilization), [12] (multiple ionization), [13–15] (attosecond physics), [16] (“double-slit in time”), [17] (two-electron atoms in laser fields), [18] (Floquet method and beyond), [19, 20] (relativistic laser–atom interaction), [21, 22] (time-dependent density functional theory), [23–25] (molecules in intense laser fields), and [24–27] (laser–cluster interaction).

### 7.1 Atomic Units

We use atomic units (a.u.) in this chapter, not only because they greatly simplify actual calculations but also give a feeling for whether an entity has to be considered large or small on the atomic scale. For instance, the laser frequency of 800 nm laser light is  $\omega = 0.057$  a.u., telling us immediately that the laser period is large compared to the period of an electron on, e.g., the first Bohr orbit in a hydrogen atom.

We will introduce the atomic units in a somewhat formal way. For beginners, the use of atomic units is sometimes confusing because dimensional checks are not possible in a straightforward way once  $\hbar$ ,  $m_e$ ,  $e$  have been set “equal to unity”. Another practical problem for beginners is to convert the result of a calculation performed using atomic units back to SI units. If one sticks to SI units and the result of a calculation is, say, 42, one knows that the result is dimensionless. If in atomic units the result is 42 it could be as well  $42 \hbar$ ,  $42 e$ ,  $42 m_e$ ,  $42 \cdot 4\pi \varepsilon_0$ ,  $42 \hbar m_e/e$ , .... A good example is the expression for the nonrelativistic eigenenergies of hydrogen-like ions, which in atomic units is simply given by

$$\mathcal{E}_n = -\frac{Z^2}{2n^2}, \quad n = 0, 1, 2, \dots \quad (\text{atomic units}) \quad (7.1)$$

where  $Z$  is the nuclear charge, and  $n$  is the principal quantum number. The right-hand side appears to be dimensionless. Hence, without knowing that the left-hand side is an energy, there would be no way back to SI units. If one performs the entire calculation (i.e., the solution of the Schrödinger equation) in SI units, one obtains

$$\mathcal{E}_n = -\frac{Z^2}{2n^2} \frac{m_e e^4}{\hbar^2 (4\pi \varepsilon_0)^2}, \quad n = 0, 1, 2, \dots \quad (\text{SI units}). \quad (7.2)$$

Even without knowing the left-hand side we can recover from the right-hand side alone that the result is an energy, provided we know the SI units of  $\hbar$ ,  $m_e$ ,  $e$ , and  $\varepsilon_0$ . This seeming asymmetry between the unit systems arise from the fact that “setting  $\hbar$ ,  $m_e$ ,  $e$ , and  $4\pi \varepsilon_0$  equal to unity” is more than a change of units. It is like setting kg, m, s, and C to unity. However, if one knows what the dimension of the final result is, the conversion from atomic units back to SI units is unique.

As in Sect. 2.2.3, let us denote mass, length, time, and charge by M, L, T, and C, respectively. In atomic units we wish to use the action  $\hbar$ , the electron mass  $m_e$ , the modulus of the electron charge  $e$ , and  $4\pi$  times the permittivity of vacuum,  $4\pi \varepsilon_0$ , as the basic units. The relation between both system of units is established by (“[...]” meaning “units of [...]”, see also Sect. 2.2.3)

$$[\hbar] = M^{a_{11}} L^{a_{12}} T^{a_{13}} C^{a_{14}}, \quad (7.3)$$

$$[m_e] = M^{a_{21}} L^{a_{22}} T^{a_{23}} C^{a_{24}}, \quad (7.4)$$

$$[e] = M^{a_{31}} L^{a_{32}} T^{a_{33}} C^{a_{34}}, \quad (7.5)$$

$$[4\pi \varepsilon_0] = M^{a_{41}} L^{a_{42}} T^{a_{43}} C^{a_{44}}. \quad (7.6)$$

The exponents  $a_{41}, \dots, a_{44}$ , for instance, are determined by noticing that in SI units the dimension of  $\varepsilon_0$  is Coulomb per Volt and meter. Volt is a derived unit,  $V = ML^2/(CT^2)$ , and hence

$$[4\pi \varepsilon_0] = M^{-1} L^{-3} T^2 C^2. \quad (7.7)$$

Similarly, the remainder of the dimensional matrix is easily calculated and reads

$$A = \begin{pmatrix} a_{11} & a_{12} & a_{13} & a_{14} \\ a_{21} & a_{22} & a_{23} & a_{24} \\ a_{31} & a_{32} & a_{33} & a_{34} \\ a_{41} & a_{42} & a_{43} & a_{44} \end{pmatrix} = \begin{pmatrix} 1 & 2 & -1 & 0 \\ 1 & 0 & 0 & 0 \\ 0 & 0 & 0 & 1 \\ -1 & -3 & 2 & 2 \end{pmatrix}. \quad (7.8)$$

The SI values of one atomic mass, length, time, and charge unit, denoted by  $\mathcal{M}$ ,  $\mathcal{L}$ ,  $\mathcal{T}$ , and  $\mathcal{C}$ , respectively, are needed for the transformation back to SI units. Mass and charge are trivial:  $\mathcal{M} = m_e$ ,  $\mathcal{C} = e$ . Let us calculate the value of the atomic length unit:

$$\mathcal{L} = \hbar^{b_{21}} m_e^{b_{22}} e^{b_{23}} (4\pi \varepsilon_0)^{b_{24}}. \quad (7.9)$$

Plugging in (7.3), (7.4), (7.5), and (7.6) and using the values for the  $a_{ij}$  in (7.8) lead to

$$\mathcal{L} = M^{b_{21}+b_{22}-b_{24}} L^{2b_{21}-3b_{24}} T^{-b_{21}+2b_{24}} C^{b_{23}+2b_{24}}, \quad (7.10)$$

giving us four equations for the four  $b_{2j}$ . Since  $\mathcal{L}$  is a length,  $2b_{21} - 3b_{24} = 1$ , and the exponents of mass, time, and charge must be zero. One finds  $b_{21} = 2$ ,  $b_{22} = -1$ ,  $b_{23} = -2$ ,  $b_{24} = 1$  so that

$$\mathcal{L} = \frac{\hbar^2 4\pi \varepsilon_0}{m_e e^2} = 0.5292 \cdot 10^{-10} \text{m}, \quad (7.11)$$

which is the Bohr radius  $a_0$ . The corresponding calculation for  $\mathcal{T}$  is left as an exercise. The inverse dimensional matrix is

$$\mathcal{M} = \hbar^{b_{11}} m_e^{b_{12}} e^{b_{13}} (4\pi \varepsilon_0)^{b_{14}}, \quad (7.12)$$

$$\mathcal{L} = \hbar^{b_{21}} m_e^{b_{22}} e^{b_{23}} (4\pi \varepsilon_0)^{b_{24}}, \quad (7.13)$$

$$\mathcal{T} = \hbar^{b_{31}} m_e^{b_{32}} e^{b_{33}} (4\pi \varepsilon_0)^{b_{34}}, \quad (7.14)$$

$$\mathcal{C} = \hbar^{b_{41}} m_e^{b_{42}} e^{b_{43}} (4\pi \varepsilon_0)^{b_{44}} \quad (7.15)$$

with

$$B = \begin{pmatrix} b_{11} & b_{12} & b_{13} & b_{14} \\ b_{21} & b_{22} & b_{23} & b_{24} \\ b_{31} & b_{32} & b_{33} & b_{34} \\ b_{41} & b_{42} & b_{43} & b_{44} \end{pmatrix} = \begin{pmatrix} 0 & 1 & 0 & 0 \\ 2 & -1 & -2 & 1 \\ 3 & -1 & -4 & 2 \\ 0 & 0 & 1 & 0 \end{pmatrix}. \quad (7.16)$$

It is readily checked that  $A \cdot B = B \cdot A = 1$ .

We conclude this section by giving the explicit expressions and values for frequently occurring entities in laser-atom interaction in Table 7.1. In the entry for the velocity the fine structure constant

$$\alpha = \frac{e^2}{\hbar 4\pi \varepsilon_0 c} = \frac{1}{137.04} \quad (7.17)$$

appears. The value of the light velocity in vacuum in atomic units equals the inverse fine structure constant. Note that with  $\hbar$ ,  $e$ ,  $m_e$ , and  $\varepsilon_0$  alone it is not possible to construct a dimensionless entity (as it is impossible with kg, m, s, and C). One needs a fifth building brick, which is  $c$  in the case of the fine structure constant. A useful and frequently used formula to convert the field strength  $E$  in atomic units to a laser intensity  $I$  in the commonly used  $\text{Wcm}^{-2}$  is

$$(I \text{ in } \text{Wcm}^{-2}) = 3.51 \cdot 10^{16} \times (E^2 \text{ in a.u.}). \quad (7.18)$$

**Table 7.1** One atomic unit of frequently occurring entities expressed in SI units

One atomic unit of		Value
Mass	$m_e$	$9.1094 \cdot 10^{-31} \text{ kg}$
Length	$\frac{\hbar^2 4\pi \varepsilon_0}{e^2 m_e} = a_0$	$0.5292 \cdot 10^{-10} \text{ m}$
Time	$\frac{\hbar^3 (4\pi \varepsilon_0)^2}{m_e e^4}$	$2.4189 \cdot 10^{-17} \text{ s}$
Charge	$e$	$1.6022 \cdot 10^{-19} \text{ C}$
Action	$\hbar$	$1.0546 \cdot 10^{-34} \text{ J}$
Permittivity	$4\pi \varepsilon_0$	$4\pi \cdot 8.8542 \cdot 10^{-12} \text{ CV}^{-1} \text{ m}^{-1}$
Energy	$\frac{m_e e^4}{\hbar^2 (4\pi \varepsilon_0)^2}$	$4.3598 \cdot 10^{-19} \text{ J} = 27.21 \text{ eV}$
Velocity	$\frac{e^2}{\hbar 4\pi \varepsilon_0}$	$2.1877 \cdot 10^6 \text{ ms}^{-1} = \alpha c$
El. field	$\frac{m_e^2 e^5}{\hbar^4 (4\pi \varepsilon_0)^3}$	$5.1422 \cdot 10^{11} \text{ V m}^{-1}$
Magn. flux density	$\frac{m_e^2 e^5}{\hbar^3 (4\pi \varepsilon_0)^2}$	$2.3505 \cdot 10^5 \text{ T}$
Laser intensity	$\frac{e^{12} m_e^4}{8\pi \alpha \hbar^9 (4\pi \varepsilon_0)^6}$	$3.5095 \cdot 10^{20} \text{ W m}^{-2}$

## 7.2 Atoms in Strong Static Electric Fields

Although we assume the external electric field to be static in this section, the following analysis is useful for atoms in laser fields too, as will become clear below. The Hamiltonian governing an electron moving in a Coulomb potential  $-Z/r$  and a static electric field  $\mathbf{E} = E \mathbf{e}_z$  reads

$$\hat{H} = \frac{\hat{\mathbf{p}}^2}{2} + V_{\text{eff}}, \quad V_{\text{eff}} = -\frac{Z}{r} + E z. \quad (7.19)$$

The effective potential  $V_{\text{eff}}$  describes a tilted Coulomb potential (see Fig. 7.1). A perturbative treatment of the problem can be found in almost all quantum mechanics or atomic physics text books (Stark effect, see, e.g., [28–30]). In first order (linear Stark effect) the degeneracy with respect to the angular quantum number  $\ell$  is removed while the degeneracy in the magnetic quantum number  $m$  is maintained. The non-degenerate ground state is only affected in second order (quadratic Stark effect). It is down-shifted in energy since the potential widens in the presence of the field. In the case of the hydrogen atom ( $Z = 1$ ) this down-shift is given by  $\Delta E = -9E^2/4$ .

Let us first point out that, strictly speaking, there exist no discrete, bound states anymore even for the tiniest electric field. This is because even a very small field gives rise to a potential barrier (see Fig. 7.1) through which the initially bound electron may tunnel. The electric field couples all bound states to the continuum and thus all discrete states become resonances with a finite line width. Mathematically speaking, the Hamiltonian (7.19) has only a continuous spectrum, and the eigenfunctions are no longer square-integrable. However, since the barrier for small fields is far out, the probability for tunneling is extremely low (note that the

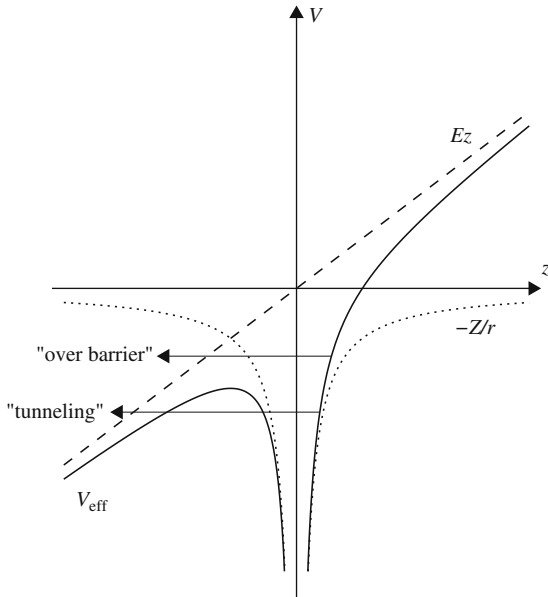


**Fig. 7.1** Effective potential  $V_{\text{eff}}$  in field direction. The unperturbed Coulomb potential and the field potential are also shown separately. Depending on the initial (and possibly Stark-shifted) state, the electron may either escape via tunneling or classically via “over-barrier” ionization

tunneling probability decreases exponentially with the distance to be tunneled, as will be shown in Sect. 7.2.2) and the states are “quasi-discrete”.

A strong increase in the ionization probability is expected when the electron can even escape classically, that is, when the distance to be tunneled shrinks to zero. In a crude approximation (which, in fact, is wrong for hydrogen-like ions, as will be discussed in the subsequent section) this so-called “critical field”  $E_{\text{crit}}$  may be estimated as follows: neglecting the Stark effect, classical over-barrier ionization sets in when the barrier maximum coincides with the energy level of the electron. The position of the barrier is (for  $E > 0$ ) located at

$$z_{\text{barr}} = -\sqrt{\frac{Z}{E}} \quad (7.20)$$

and the energy at the barrier maximum is

$$V_{\text{barr}} = -2\sqrt{ZE}. \quad (7.21)$$

Hence, if we restrict ourselves to the ground state of hydrogen-like ions, we require that

$$\mathcal{E} = -\frac{Z^2}{2} \stackrel{!}{=} -2\sqrt{ZE_{\text{crit}}} \quad (7.22)$$

so that

$$E_{\text{crit}} = \frac{Z^3}{16}. \quad (7.23)$$

Because of the strong  $Z$ -dependence of the critical field even with the most intense lasers available today it is not possible to fully strip heavy elements. For hydrogen-like ions (7.23) even underestimates the critical field by more than a factor of two, as will be shown now.

### 7.2.1 Separation of the Schrödinger Equation

The Schrödinger equation with the Hamiltonian (7.19) separates in parabolic coordinates  $(\xi, \eta, \varphi)$  (see, e.g., [28–30]),

$$\xi = r + z, \quad \eta = r - z, \quad r = \frac{1}{2}(\xi + \eta), \quad z = \frac{1}{2}(\xi - \eta), \quad 0 \leq \xi, \eta. \quad (7.24)$$

Here,  $r$  is the radial coordinate, and  $\varphi$  is the azimuthal angle (as in spherical, polar or cylindrical coordinates). Cuts of contours of constant  $\xi$  and  $\eta$  in the  $xz$ -plane are shown in Fig. 7.2. The Hamiltonian in parabolic coordinates reads

$$\hat{H} = -\frac{2}{\xi + \eta} [\partial_\xi(\xi \partial_\xi) + \partial_\eta(\eta \partial_\eta)] - \frac{1}{2\xi\eta} \partial_\varphi^2 - \frac{2Z}{\xi + \eta} + E \frac{\xi - \eta}{2}. \quad (7.25)$$

Plugging the ansatz

$$\Psi = f_1(\xi) f_2(\eta) e^{im\varphi} \quad (7.26)$$

into the Schrödinger equation  $\mathcal{E}\Psi = \hat{H}\Psi$  and multiplying by  $(\xi + \eta)/2$  leads to an equation that can be decoupled into

$$\frac{d}{d\xi} \left( \xi \frac{df_1}{d\xi} \right) + \left( \frac{\mathcal{E}}{2}\xi - \frac{m^2}{4\xi} - \frac{E}{4}\xi^2 \right) f_1 + Z_1 f_1 = 0, \quad (7.27)$$

$$\frac{d}{d\eta} \left( \eta \frac{df_2}{d\eta} \right) + \left( \frac{\mathcal{E}}{2}\eta - \frac{m^2}{4\eta} + \frac{E}{4}\eta^2 \right) f_2 + Z_2 f_2 = 0 \quad (7.28)$$

where  $Z_1, Z_2$  are separation constants fulfilling

$$Z_1 + Z_2 = Z. \quad (7.29)$$

Division by  $2\xi$  and  $2\eta$ , respectively, yields the two Schrödinger equations

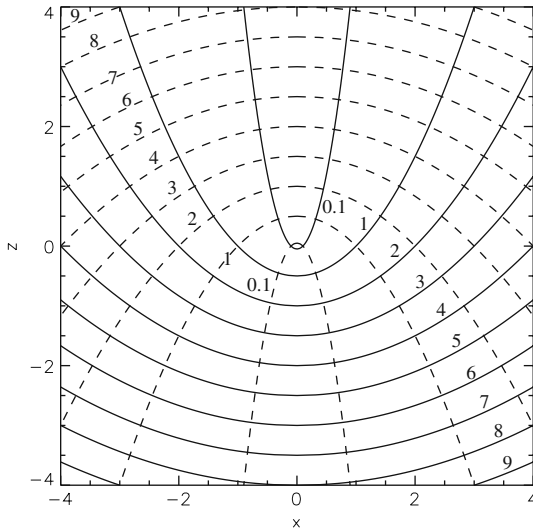


**Fig. 7.2** Illustration of parabolic coordinates. Cuts of contours  $\xi = \text{const}$  (dashed, values given next to the lines) and  $\eta = \text{const}$  (solid) in the  $xz$ -plane (azimuthal symmetry with respect to the  $z$ -axis)

$$\left[ -\frac{1}{2} \left( \frac{d^2}{d\xi^2} + \frac{1}{\xi} \frac{d}{d\xi} - \frac{m^2}{4\xi^2} \right) - \frac{Z_1}{2\xi} + \frac{E}{8}\xi \right] f_1 = \frac{\mathcal{E}}{4} f_1, \quad (7.30)$$

$$\left[ -\frac{1}{2} \left( \frac{d^2}{d\eta^2} + \frac{1}{\eta} \frac{d}{d\eta} - \frac{m^2}{4\eta^2} \right) - \frac{Z_2}{2\eta} - \frac{E}{8}\eta \right] f_2 = \frac{\mathcal{E}}{4} f_2 \quad (7.31)$$

which have the same shape as two Schrödinger equations in cylindrical coordinates for the potentials

$$V_\xi = -\frac{Z_1}{2\xi} + \frac{E}{8}\xi, \quad V_\eta = -\frac{Z_2}{2\eta} - \frac{E}{8}\eta. \quad (7.32)$$

Both potentials have a Coulombic part and a linear contribution, like  $V_{\text{eff}}$  in (7.19). However, because  $\xi, \eta \geq 0$ , the potential  $V_\xi$  has only bound states (we assume without loss of generality  $E > 0$ ). The potential  $V_\eta$  instead displays a barrier. Hence, in parabolic coordinates ionization happens with respect to the  $\eta$  coordinate while the electron remains confined in  $\xi$ . The consequences of this in Cartesian coordinates can be understood with the help of Fig. 7.2: confinement to a region  $\xi < \xi_{\max}$  implies preferred electron emission towards negative  $z$  with a lateral spread that can be estimated by the confining contour  $\xi_{\max}$ . The potentials  $V_\xi$  and  $V_\eta$  are called “uphill” and “downhill potential,” respectively. They are illustrated in Fig. 7.3. Given an energy  $\mathcal{E}$  one finds a sequence of  $Z_1$  for which the solution of the Schrödinger equation in  $\xi$ , (7.30), leads to normalizable bound states. This sequence can be labeled by the number of nodes in  $f_1$  for  $\xi > 0$ ,  $n_1 = 0, 1, 2, \dots$  (note that  $Z_1 < 0$  is also possible). The second equation (7.31) has to be solved for

$Z_2 = Z - Z_1$  and the same energy  $\mathcal{E}$ . This is possible because the corresponding Hamiltonian  $\hat{H}_\eta$  [i.e., the square bracket in (7.31)] has a continuous spectrum and is neither bound from below nor from above.

In the field-free case  $E = 0$  the two Schrödinger equations (7.30) and (7.31) are identical, and the relation between the “usual” principal quantum number  $n$  and the parabolic quantum numbers  $n_1, n_2$  is given by

$$n_i + \frac{|m| + 1}{2} = n \frac{Z_i}{Z}, \quad n_1 + n_2 + |m| + 1 = n, \quad i = 1, 2. \quad (7.33)$$

Instead of working directly with the parabolic coordinates  $\xi$  and  $\eta$ , one can perform an additional, simple coordinate transformation

$$u = \sqrt{2\xi}, \quad v = \sqrt{2\eta} \quad (7.34)$$

which, after multiplication of the new Schrödinger equation by  $(u^2 + v^2)/4$ , and with the ansatz  $\Psi = \Phi_u(u)\Phi_v(v)e^{im\varphi}$  yields

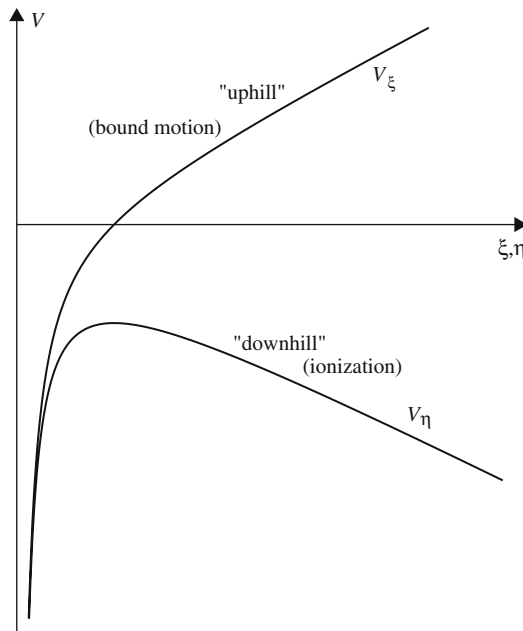


**Fig. 7.3** Illustration of the potentials  $V_\xi$  and  $V_\eta$  (7.32). The “uphill potential”  $V_\xi$  (for  $E > 0$ ) supports only bound states while the “downhill potential”  $V_\eta$  displays a barrier through which the electron may tunnel

$$\left[ -\frac{1}{2} \left( \frac{1}{u} \partial_u (u \partial_u) - \frac{m^2}{u^2} \right) + \frac{1}{2} \Omega^2 u^2 - \frac{1}{4} g u^4 \right] \Phi_u = Z_1 \Phi_u, \quad (7.35)$$

$$\left[ -\frac{1}{2} \left( \frac{1}{v} \partial_v (v \partial_v) - \frac{m^2}{v^2} \right) + \frac{1}{2} \Omega^2 v^2 + \frac{1}{4} g v^4 \right] \Phi_v = Z_2 \Phi_v, \quad (7.36)$$

where, again,  $Z = Z_1 + Z_2$  is used, and  $\Omega$  and  $g$  are defined as

$$\frac{1}{2} \Omega^2 = -\frac{\mathcal{E}}{4}, \quad \mathcal{E} \leq 0, \quad g = -\frac{E}{4}. \quad (7.37)$$

The Schrödinger equations (7.35) and (7.36) have the shape of two-dimensional oscillators (with radial coordinates  $u$  and  $v$ , respectively) of frequency  $\Omega$  and with a quartic perturbation that is proportional to the electric field. In the field-free case, the Coulomb problem is mapped to two two-dimensional oscillators where, however, the energy assumes the role of the oscillator frequency, and the nuclear charge (splitted into  $Z_1$  and  $Z_2$ ) assumes the role of the energy. The transformation to the coordinates  $(u, v, \varphi)$  corresponds to the Kustaanheimo–Stiefel transformation [31].

Let us now evaluate an improved critical field for the case of hydrogen-like ions [32]. As mentioned above, formula (7.23) underestimates the critical field by more than a factor of two.

In the unperturbed case ( $g = 0$ ) and for  $m = 0$  (groundstate) the solutions to (7.35) and (7.36) are Gaussians. We therefore use

$$\Phi_u(u) = \sqrt{\frac{a_u}{\pi}} e^{-a_u u^2/2} \quad (7.38)$$

(and analogous for  $v$ ) as trial functions with parameters  $a_u$  and  $a_v$ . Denoting the square bracket in (7.35) as  $\hat{H}_u$  the “energy” reads

$$Z_1(g) = 2\pi \int_0^\infty du u \Phi_u^* \hat{H}_u \Phi_u = \frac{1}{a_u} \left( \frac{\Omega^2}{2} - \frac{a_u^2}{2} \right) + a_u - \frac{g}{2a_u^2}. \quad (7.39)$$

Minimizing this energy yields up to first order in  $g$

$$a_u = \Omega \left( 1 - \frac{g}{2\Omega^3} \right), \quad a_v = \Omega \left( 1 + \frac{g}{2\Omega^3} \right). \quad (7.40)$$

The oscillator “energies” are

$$Z_1(g) = \Omega \left( 1 - \frac{g}{2\Omega^3} \right), \quad Z_2(g) = \Omega \left( 1 + \frac{g}{2\Omega^3} \right). \quad (7.41)$$

Note that this is consistent with the fact that the linear Stark effect vanishes for the ground state since

$$Z_1(g) + Z_2(g) = 2\Omega \quad (7.42)$$

is independent of the field  $g$ . Since  $Z_1 + Z_2 = Z$  we have  $Z = 2\Omega$  which is [see (7.37)] equivalent to  $\mathcal{E} = -Z^2/2$ , as it should for the ground states of hydrogen-like ions.

In physical coordinates the variationally determined wave function for, e.g., hydrogen ( $Z = 1$ ) reads

$$\Psi_H(\mathbf{r}) = \frac{1 - 4E^2}{\sqrt{\pi}} e^{-r} e^{-2E \cdot \mathbf{r}}, \quad (7.43)$$

i.e., the unperturbed wave function is multiplied by a “deformation factor”.

If  $E > 0$  we have  $g < 0$  and vice versa. Let us assume  $g > 0$  so that the  $u$ -oscillator displays a barrier while the  $v$ -oscillator does not. The barrier is located at  $u_{\text{barr}} = \Omega/\sqrt{g}$  and the energy at the barrier maximum is  $\Omega^2 u_{\text{barr}}^2/2 - gu_{\text{barr}}^4/4 = \Omega^4/(4g)$ . At the critical field strength the energy of the  $u$ -state coincides with the barrier-energy, giving us

$$Z_1(g) = \Omega - \frac{g}{2\Omega^2} = \frac{\Omega^4}{4g} \quad \Rightarrow \quad g_{\text{crit}} = \Omega^3(1 - 2^{-1/2}) \simeq 0.3\Omega^3 \quad (7.44)$$

which translates [using (7.37)] to [32]

$$E_{\text{crit}}^{\text{H-like}} = (\sqrt{2} - 1) \mathcal{E}^{3/2}. \quad (7.45)$$

In the case of atomic hydrogen one obtains  $E_{\text{crit}}^{\text{H-like}} = 0.147$  instead of the 0.0625 predicted by (7.23). The new value is in agreement with [33]. The wrong prediction of (7.23) is due to the erroneous assumption that the electron motion in  $z$ -direction and in lateral direction are independent. Instead, the problem separates in parabolic coordinates. However, since the “exceptional” symmetry of hydrogen-like ions is broken in many-electron atoms, simple over-barrier estimates [such as those above leading to (7.23)] are useful and sufficiently accurate for many practical applications. Of particular interest is the “appearance intensity”  $I_{\text{app},Z}$  for a charge state  $Z$  of an atom with ionization potential  $\mathcal{E}_{\text{ip},Z}$ . Here, “appearance intensity” should be understood as the intensity where a certain charge state  $Z$  is becoming abundant. This is the case once the electron may escape classically from the binding potential. The derivation is thus analogous to (7.20), (7.21), (7.22), and (7.23), leading to

$$I_{\text{app},Z} = \frac{\mathcal{E}_{\text{ip},Z}^4}{16Z^2}. \quad (7.46)$$

Comparison of the appearance intensities predicted by (7.46) for the experiments reported in, e.g., [34, 35] yields good agreement, and the scaling is confirmed by a Thomas–Fermi treatment [36].

### 7.2.2 Tunneling Ionization

Going one step beyond a classical over-barrier analysis amounts to take tunneling into account. This can be done in a semi-classical way. Let us consider the tunneling of the electron in atomic hydrogen through the barrier of the “downhill potential” in Fig. 7.3 [28]. We assume that the electron is initially in the 1s ground state. The Schrödinger equation (7.31) for  $m = 0$ ,  $Z_2 = 1/2$ ,  $\mathcal{E} = -1/2$  reads

$$\left[ -\frac{1}{2} \left( \frac{d^2}{d\eta^2} + \frac{1}{\eta} \frac{d}{d\eta} \right) - \frac{1}{4\eta} - \frac{E}{8} \eta \right] f_2(\eta) = -\frac{1}{8} f_2(\eta). \quad (7.47)$$

Substituting  $\chi(\eta) = \sqrt{\eta} f_2(\eta)$  yields

$$\frac{d^2\chi}{d\eta^2} + \left( -\frac{1}{4} + \frac{1}{2\eta} + \frac{1}{4\eta^2} + \frac{1}{4} E \eta \right) \chi = 0. \quad (7.48)$$

Comparison with

$$-\frac{1}{2} \frac{d^2\chi}{d\eta^2} + V(\eta)\chi = \epsilon\chi \quad (7.49)$$

shows that we effectively deal with one-dimensional motion of an electron in the potential

$$V(\eta) = -\frac{1}{2} \left( \frac{1}{2\eta} + \frac{1}{4\eta^2} + \frac{1}{4} E \eta \right) \quad (7.50)$$

with total energy  $\epsilon = -1/8$ . The potential  $V(\eta)$  is of the form depicted in Fig. 7.4. We now match at a position  $\eta_0$  inside the barrier,

$$1 \ll \eta_0 \ll 1/E \quad (7.51)$$

the “left” quasi-classical wave function

$$\chi_{\text{left}}(\eta) = -\frac{iC}{\sqrt{|p|}} \exp \left( \left| \int_{\eta_0}^{\eta} p(\eta') d\eta' \right| \right) \quad (7.52)$$

with the “right” quasi-classical outgoing wave function

$$\chi_{\text{right}}(\eta) = \frac{C}{\sqrt{p}} \exp \left( i \int_{\eta_0}^{\eta} p(\eta') d\eta' + i\pi/4 \right) \quad (7.53)$$

where

$$p(\eta) = \sqrt{2[\epsilon - V(\eta)]} = \sqrt{-\frac{1}{4} + \frac{1}{2\eta} + \frac{1}{4\eta^2} + \frac{1}{4} E \eta}. \quad (7.54)$$

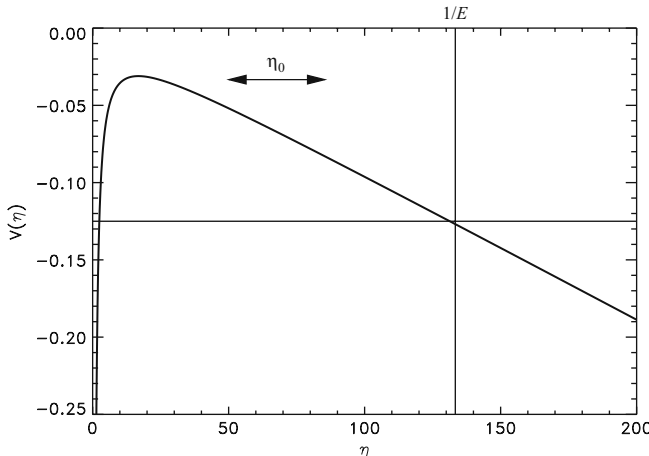


**Fig. 7.4** Plot of the potential  $V(\eta)$  (7.50) for  $E = 0.0075$ . The tunnel “exit”  $\eta_1$  for sufficiently low fields  $E$  is in good approximation given by  $\eta_1 \simeq 1/E$ . The matching point  $\eta_0$  is located inside the barrier where  $1 \ll \eta_0 \ll 1/E$  holds

The semi-classical approximation breaks down at the classical turning point  $\eta_1 \simeq 1/E$  since  $p(\eta_1) = 0$ . In general, semi-classical wave functions are accurate as long as the de Broglie wave length  $2\pi\hbar/p$  is small compared to the length scale characterizing changes in the potential (i.e., the potential should be sufficiently “flat”). For vanishing momentum  $p$  the de Broglie wave length is infinite so that the semi-classical approximation necessarily breaks down. However, for the calculation of the probability flux out of the potential the disagreement between the semi-classical wave function and the exact wave function in a narrow region around the classical turning point  $\eta_1$  plays no role.

For the determination of the normalization constant  $C$  we set the left wave function at position  $\eta_0$  equal to the unperturbed wave function so that

$$-\frac{iC}{\sqrt{|p_0|}} = \sqrt{\eta_0} \frac{1}{\sqrt{\pi}} e^{-(\xi+\eta_0)/2} \quad (7.55)$$

with  $p_0 = p(\eta_0)$ . The “uphill” coordinate  $\xi$  appears as a parameter here which will be integrated out later on; in other words: the wave function is assumed to retain its ground state shape with respect to  $\xi$  (i.e., the Stark effect is neglected). We obtain for the right wave function

$$\chi_{\text{right}}(\eta, \xi) = i \sqrt{\frac{\eta_0 |p_0|}{\pi p(\eta)}} e^{-(\xi+\eta_0)/2} \exp \left( i \int_{\eta_0}^{\eta} p(\eta') d\eta' + i\pi/4 \right) \quad (7.56)$$

so that

$$|\chi_{\text{right}}(\eta, \xi)|^2 = \frac{\eta_0 |p_0|}{\pi p(\eta)} \exp \left( -\xi - \eta_0 + 2\Re \left[ i \int_{\eta_0}^{\eta} p(\eta') d\eta' \right] \right) \quad (7.57)$$

where  $\Re$  denotes the real part. Because of (7.51) we can expand  $p(\eta)$  in  $\varepsilon = 1/\eta$ ,

$$p(\eta) = \begin{cases} \frac{1}{2} \left( \sqrt{E\eta - 1} + \frac{1}{\eta\sqrt{E\eta - 1}} + \dots \right) & \text{outside barrier, } \eta > \eta_1 \\ \frac{1}{2} \left( i\sqrt{1 - E\eta} + \frac{1}{i\eta\sqrt{1 - E\eta}} + \dots \right) & \text{inside barrier, } \eta < \eta_1 \end{cases}. \quad (7.58)$$

Since  $E\eta_0 \ll 1$ , it is sufficient to take  $|p_0| = 1/2$ . In order to keep the leading terms dependent on  $E$  in the prefactor as well as in the exponent, we set in the denominator of the prefactor in (7.57)  $p(\eta) = (\sqrt{E\eta - 1})/2$ . In the exponent we integrate inside the barrier and have to keep both terms in the expansion (7.58). We thus obtain

$$|\chi_{\text{right}}(\eta, \xi)|^2 = \frac{\eta_0}{\pi\sqrt{E\eta - 1}} e^{-(\xi + \eta_0)} \times \exp \left( - \int_{\eta_0}^{\eta_1} \left[ \sqrt{E\eta - 1} - \frac{1}{\eta\sqrt{E\eta - 1}} \right] d\eta \right). \quad (7.59)$$

The integral can be solved. Using  $\eta_1 \simeq 1/E$  and  $\eta_0 E \ll 1$  we obtain for the probability density outside the barrier

$$|\chi_{\text{right}}(\eta, \xi)|^2 = \frac{4e^{-\xi}}{\pi E\sqrt{E\eta - 1}} e^{-2/(3E)}. \quad (7.60)$$

The total probability current through a plane perpendicular to the  $z$ -axis is

$$\Gamma = \int_0^\infty |f_1(\xi) f_2(\eta)|^2 v_z 2\pi\rho d\rho \quad (7.61)$$

where  $f_1(\xi)$ ,  $f_2(\eta)$  are the wave functions introduced in (7.26),  $v_z$  is the velocity in  $z$ -direction and  $\rho$  is the radial cylindrical coordinate. The  $\xi$ -dependent part  $|f_1|^2$  is included in  $|\chi_{\text{right}}(\eta, \xi)|^2$  so that

$$\Gamma = \int_0^\infty \frac{|\chi_{\text{right}}(\eta, \xi)|^2}{\eta} v_z 2\pi\rho d\rho. \quad (7.62)$$

With  $z = (\xi - \eta)/2 \simeq -\eta/2$  for small  $\xi$  and large  $\eta$ , we estimate for  $v_z$

$$-\frac{1}{2} = \frac{1}{2}v_z^2 + Ez \simeq \frac{1}{2}v_z^2 - \frac{1}{2}E\eta \quad \Rightarrow \quad v_z \simeq \sqrt{E\eta - 1} \quad (7.63)$$

so that

$$\Gamma = \int_0^\infty \frac{|\chi_{\text{right}}(\eta, \xi)|^2}{\eta} \sqrt{E\eta - 1} 2\pi\rho d\rho. \quad (7.64)$$

Finally, with

$$\rho = \sqrt{\xi\eta} \quad \Rightarrow \quad d\rho = d\sqrt{\xi\eta} = \frac{1}{2} \frac{\eta}{\sqrt{\xi\eta}} d\xi + \frac{1}{2} \frac{\xi}{\sqrt{\xi\eta}} d\eta \simeq \frac{1}{2} \sqrt{\frac{\eta}{\xi}} d\xi \quad (7.65)$$

(where the last step again follows from  $\eta \gg \xi$ ) we arrive at

$$\Gamma = \int_0^\infty \frac{|\chi_{\text{right}}(\eta, \xi)|^2}{\eta} \sqrt{E\eta - 1} 2\pi \sqrt{\xi\eta} \frac{1}{2} \sqrt{\frac{\eta}{\xi}} d\xi = \int_0^\infty \frac{4}{E} e^{-2/(3E)} e^{-\xi} d\xi$$

so that

$$\Gamma = \frac{4}{E} e^{-2/(3E)}. \quad (7.66)$$

This is the Landau-rate for tunneling ionization of atomic hydrogen from the ground state [28]. The Landau-rate is exact in the limit of low field strengths  $E$  while it overestimates ionization as the over-barrier field strength is approached. Figure 7.5 shows the rate  $\Gamma$  vs the field strength  $E$ .

It is desirable to extend the above calculation to laser fields, to more complex atoms, and to higher field strengths. All directions have been pursued, and there exists a vast amount of literature on tunneling ionization (see [5] for a review). Undeservedly, the most commonly cited tunneling formula is the so-called “ADK-rate” [37] while full credit should go to the authors of [38–41] instead (see also Sect. 13.13 in [5]). Introducing the characteristic momentum  $\kappa$ , the reduced field strength  $F$ , the effective principal quantum number  $n^*$ , and the Keldysh parameter  $\gamma$  [42] (derived below in Sect. 7.3),

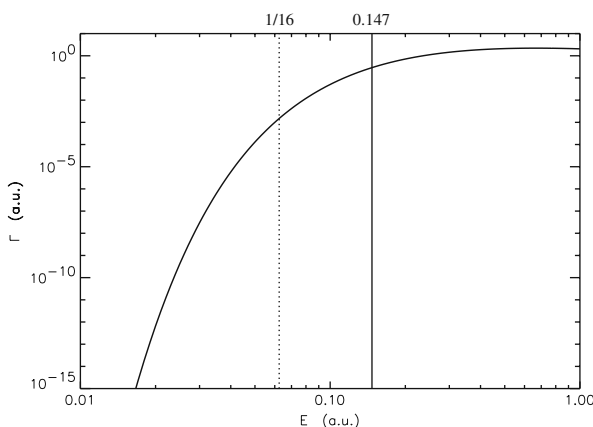


**Fig. 7.5** The Landau-rate (7.66) vs field strength  $E$ . The vertical lines indicate the (here wrong) over-barrier field strength (7.23) ( $1/16$ , dashed) and the correct (7.45)  $0.147$  (solid), respectively

$$\kappa = \sqrt{2\mathcal{E}_{ip}}, \quad F = E/\kappa^3, \quad n^* = Z/\kappa, \quad \gamma = \frac{\kappa\omega}{E}, \quad (7.67)$$

with  $\omega$  the laser frequency, the so-called “PPT-rate” [39] for initial states of vanishing angular momentum  $\ell$  and for a linearly polarized laser field reads

$$\Gamma = \kappa^2 C_\kappa^2 \sqrt{\frac{3F}{\pi}} 2^{2n^*} F^{1-2n^*} \exp\left[-\frac{2}{3F}\left(1 - \frac{\gamma^2}{10}\right)\right], \quad (7.68)$$

where

$$C_\kappa^2 = \frac{2^{2n^*-2}}{n^*(n^*)!(n^*-1)!}. \quad (7.69)$$

The factor  $\sqrt{3F/\pi}$  arises from the averaging over one laser cycle. This factor is absent for circular polarization, for which also the correction term  $\gamma^2/10$  should be replaced by  $\gamma^2/15$ . A rate formula for  $\ell > 0$  has also been derived (see the review [5] or the original articles [38–41]). However, since  $\ell$  and  $m$  are no “good quantum numbers” for many-electron atoms or ions, the question arises which values to take in actual calculations and whether in multiple ionization the electrons have time to configure in the “new” ionic ground state before the next ionization event occurs [35, 43].

### 7.3 Atoms in Strong Laser Fields

There are at least three different energy scales (and the related time scales) in the physics of atoms in strong laser fields: (i) the ionization potential  $\mathcal{E}_{ip} = |\mathcal{E}|$ , (ii) the photon energy  $\omega$ , and (iii) the ponderomotive energy  $U_p$ . The pulse duration may introduce an additional laser-related time-scale while the energy spectrum of the atom, through typical transitions, could introduce an additional species-related time-scale. If one ignores the two latter parameters, the atomic species enter through  $\mathcal{E}_{ip}$  only.

In case  $\omega > \mathcal{E}_{ip} \gg U_p$  or  $\mathcal{E}_{ip} > \omega \gg U_p$  perturbation theory in lowest non-vanishing order (LOPT) can be applied. In contrast, when with the increasing laser intensity the regime  $\mathcal{E}_{ip} > U_p > \omega$  is reached, non-perturbative effects such as above-threshold ionization (ATI) and channel-closings take place. This regime is commonly referred to as (nonperturbative) multiphoton ionization (MPI). Finally, increasing the intensity further (or decreasing the photon energy) one arrives at  $U_p > \mathcal{E}_{ip} > \omega$ . Translated into the time-domain this implies that both the inner-atomic time-scale and the ionization dynamics are fast with respect to a laser period. If this is the case, a quasi static field ionization picture may be applied where, at the instant of ionization  $t'$ , the electron moves in an effective potential which is the sum of the Coulomb (or effective core) potential and the instantaneous potential of the laser, as depicted in Fig. 7.1. If the field reaches the critical field estimated above, the

electron may escape classically over the barrier [over-barrier or barrier suppression ionization (OBI) and (BSI), respectively], as already discussed in Sect. 7.2.1. Below the critical field strength the electron can escape via tunneling through the barrier (tunneling ionization, cf. Sect. 7.2.2).

The Keldysh parameter  $\gamma$  [42] introduced in (7.67) above can be interpreted as the ratio of the “tunneling time” and the laser period. In semi-classical WKB theory the time to tunnel through a static Coulomb barrier is

$$T_{\text{tunnel}} \simeq \int_0^{z_{\text{exit}}} \frac{dz}{|p(z)|} = \int_0^{\kappa^2/2E} \frac{dz}{\sqrt{\kappa^2 - 2Ez}} = \frac{\kappa}{E} \quad (7.70)$$

so that

$$\gamma = \omega T_{\text{tunnel}} = \frac{\omega \kappa}{E} = \sqrt{\frac{\mathcal{E}_{\text{ip}}}{2U_p}}. \quad (7.71)$$

Hence, the Keldysh parameter indicates whether the tunneling process is fast on the inneratomic time scale ( $\gamma < 1$ , tunneling ionization) or the laser field reverses sign before the tunneling is completed ( $\gamma > 1$ , MPI). Besides  $\gamma < 1$  also  $\mathcal{E}_{\text{ip}}/\omega \gg 1$  must be satisfied (i.e., very many photons are involved in the tunneling process) to render the semi-classical tunneling approach applicable. Moreover, for higher and higher field amplitude (and thus decreasing  $\gamma$ ) one sooner or later enters the BSI regime. Extrapolating tunneling rate formulas to the BSI usually overestimates the ionization rate. By increasing the field strength or decreasing the laser frequency one also approaches the relativistic regime where  $U_p \simeq mc^2$  or greater. However, just because the laser driven *free* electron dynamics is relativistic does not mean that relativistic corrections are already important for the *tunneling* dynamics. Relativistic and QED corrections to the binding energy  $\mathcal{E}$  because of a high nuclear charge  $Z$  have to be taken into account, of course.

Numerous strong laser-atom experiments operate around  $\gamma \simeq 1$  or at  $\gamma > 1$  and are thus not in the tunneling domain. Taking, for instance, the case of atomic hydrogen in an 800 nm and  $10^{14} \text{ W/cm}^2$  laser pulse one finds  $\gamma \simeq 1.1$ . This is a typical value for ATI measurements.

What are the differences between the ionization dynamics in the MPI and in the tunneling domain? Since in the tunneling regime the process is fast compared to a laser period, significant ionization occurs during a single half laser cycle, predominantly around the electric field maximum because the barrier is lowest then. Furthermore, in tunneling ionization the quiver amplitude  $E/\omega^2$  of the freed electron in the laser field is large compared to the atomic dimension, unlike in MPI. This has consequences for the rescattering dynamics that is responsible for various effects, such as the ATI plateau, high-harmonic generation, and nonsequential ionization, as will be discussed below.

### 7.3.1 Floquet Theory and Dressed States

If the laser pulse duration is long, i.e., if the pulse contains many laser cycles, we may in good approximation consider it infinitely long. As a consequence the Hamiltonian is periodic,

$$\hat{H}(t + T) = \hat{H}(t), \quad T = \frac{2\pi}{\omega}, \quad (7.72)$$

and the time-dependent Schrödinger equation (TDSE) is a partial differential equation with periodic coefficients. This type of problem has been studied by Floquet more than 120 years ago [44]. The Floquet theorem ensures that the TDSE

$$\hat{\mathcal{H}}(t)|\Psi(t)\rangle = 0, \quad \hat{\mathcal{H}}(t) = \hat{H}(t) - i\frac{d}{dt} \quad (7.73)$$

has solutions of the form

$$|\Psi(t)\rangle = e^{-i\epsilon t}|\Phi(t)\rangle, \quad |\Phi(t+T)\rangle = |\Phi(t)\rangle, \quad (7.74)$$

i.e., the wave function  $|\Phi(t)\rangle$  is periodic (while  $|\Psi(t)\rangle$  itself is not). The Bloch theorem used in solid state physics to treat particle motion in periodic potentials is the Floquet theorem applied to spatially periodic systems. Inserting (7.74) into (7.73) leads to the eigenvalue equation

$$\hat{\mathcal{H}}(t)|\Phi(t)\rangle = \epsilon|\Phi(t)\rangle. \quad (7.75)$$

$\epsilon$  is called quasi-energy or Floquet-energy. Note that if  $\epsilon$  and  $|\Phi(t)\rangle$  solve (7.75), then also

$$\epsilon' = \epsilon + m\omega, \quad |\Phi(t)\rangle' = e^{im\omega t}|\Phi(t)\rangle, \quad m \in \mathbb{Z} \quad (7.76)$$

do. Let  $|\alpha\rangle$  be the solution of the unperturbed problem, i.e.,  $\hat{H}(t) = \hat{H}_0 + \hat{W}(t)$  and

$$\hat{H}_0|\alpha\rangle = \mathcal{E}_\alpha^0|\alpha\rangle. \quad (7.77)$$

Because of the periodicity of  $|\Phi(t)\rangle$  we can Fourier-expand

$$|\Psi(t)\rangle = e^{-i\epsilon t}|\Phi(t)\rangle = e^{-i\epsilon t} \sum_{n=-\infty}^{\infty} \sum_{\alpha} \Phi_{\alpha}^{(n)}|\alpha\rangle e^{-in\omega t} \quad (7.78)$$

where the expansion coefficients  $\Phi_{\alpha}^{(n)}$  are time-independent. Inserting (7.78) into (7.73) gives

$$\sum_{n\alpha} [\hat{H}(t) - \epsilon - n\omega] \Phi_{\alpha}^{(n)} |\alpha\rangle e^{-in\omega t} = 0. \quad (7.79)$$

Multiplying from the left with  $\langle\beta|$ ,  $e^{im\omega t}$ , and integrating  $T^{-1} \int_0^T dt$  yields

$$\sum_{n\alpha} [\langle\beta|\hat{H}^{(m-n)}|\alpha\rangle - (\epsilon + m\omega)\delta_{nm}\delta_{\alpha\beta}] \Phi_{\alpha}^{(n)} = 0 \quad (7.80)$$

with the time-independent Hamiltonian

$$\hat{H}^{(m-n)} = \frac{1}{T} \int_0^T \hat{H}(t) e^{i(m-n)\omega t} dt. \quad (7.81)$$

Introducing the Floquet state

$$|\alpha n\rangle = |\alpha\rangle \otimes |n\rangle, \quad \langle t|n\rangle = e^{in\omega t} \quad (7.82)$$

we can recast (7.80) into

$$\sum_{n\alpha} [\langle\beta m|\hat{H}_F|\alpha n\rangle - \epsilon \langle\beta m|\alpha n\rangle] \Phi_{\alpha}^{(n)} = 0 \quad (7.83)$$

where  $\hat{H}_F$  is the Floquet-Hamiltonian whose matrix elements read

$$\langle\beta m|\hat{H}_F|\alpha n\rangle = \langle\beta|\hat{H}^{(m-n)}|\alpha\rangle - m\omega\delta_{mn}\delta_{\alpha\beta}. \quad (7.84)$$

Hence, we obtain the eigenvalue equation

$$\sum_{n\alpha} \langle\beta m|\hat{H}_F|\alpha n\rangle \Phi_{\alpha}^{(n)} = \epsilon \Phi_{\beta}^{(m)} \quad (7.85)$$

or, in matrix notation,

$$H_F \Phi = \epsilon \Phi. \quad (7.86)$$

Here,  $H_F$  and  $\Phi$  are an infinite matrix and an infinite vector, respectively. In practice, the size of the system has to be truncated, of course. Numerical solutions of the time-dependent Schrödinger equation following the Floquet approach have been pursued by several groups (see, e.g., [3, 18] for reviews and [45] for a Floquet-solver). The Floquet method is not applicable to atoms interacting with few-cycle laser pulses because the assumption  $\hat{W}(t+T) \simeq \hat{W}(t)$  is not valid in this case.

We illustrate the Floquet approach by applying it to a laser-driven two-level system where the Hamiltonian in dipole approximation reads

$$\hat{H}(t) = \underbrace{\omega_a |a\rangle\langle a| + \omega_b |b\rangle\langle b|}_{\hat{H}_0} - q \underbrace{\hat{E} z \cos \omega t}_{-\hat{W}(t)}, \quad \omega_a > \omega_b. \quad (7.87)$$

We thus have

$$\hat{H}^{(n)} = \frac{1}{T} \int_0^T dt \hat{H}(t) e^{in\omega t} = \hat{H}_0 \delta_{n0} - \frac{q \hat{E} z}{2} (\delta_{n,-1} + \delta_{n,1}), \quad (7.88)$$

i.e., a tridiagonal Hamiltonian in the “photon subspace”. For (7.84) we obtain

$$\langle \beta m | \hat{H}_F | \alpha n \rangle = \left( \langle \beta | \hat{H}_0 | \alpha \rangle - m\omega \delta_{\alpha\beta} \right) \delta_{nm} - \frac{1}{2} q \hat{E} \langle \beta | z | \alpha \rangle (\delta_{m,n-1} + \delta_{m,n+1}) \quad (7.89)$$

so that (using  $\langle \beta | \hat{H}_0 | \alpha \rangle = \omega_\alpha \delta_{\alpha\beta}$ ) (7.85) reads

$$\sum_{n,\alpha} \left[ (\omega_\alpha - m\omega) \delta_{\alpha\beta} \delta_{mn} - \frac{q \hat{E}}{2} \langle \beta | z | \alpha \rangle (\delta_{m,n-1} + \delta_{m,n+1}) \right] \Phi_\alpha^{(n)} = \epsilon \Phi_\beta^{(m)}.$$

Defining

$$A = -\frac{1}{2} q \hat{E} \langle a | z | b \rangle = -\frac{1}{2} \Omega_R e^{-i\varphi}, \quad \mathcal{E}_\alpha^{(m)} = \omega_\alpha - m\omega, \quad (7.90)$$

where  $\Omega_R$  is the Rabi-frequency, the corresponding matrix equation has the structure

$$\begin{pmatrix} \mathcal{E}_a^{(-1)} & & A & \\ & \mathcal{E}_b^{(-1)} & A^* & \\ \hline & A & \mathcal{E}_a^{(0)} & \\ \hline A^* & & \mathcal{E}_b^{(0)} & A \\ \hline & & A & \mathcal{E}_a^{(1)} \\ \hline & & A^* & \mathcal{E}_b^{(1)} \end{pmatrix} \begin{pmatrix} \Phi_a^{(-1)} \\ \Phi_b^{(-1)} \\ \Phi_a^{(0)} \\ \Phi_b^{(0)} \\ \Phi_a^{(1)} \\ \Phi_b^{(1)} \end{pmatrix} = \epsilon \begin{pmatrix} \Phi_a^{(-1)} \\ \Phi_b^{(-1)} \\ \Phi_a^{(0)} \\ \Phi_b^{(0)} \\ \Phi_a^{(1)} \\ \Phi_b^{(1)} \end{pmatrix} \quad (7.91)$$

around  $m = 0$ . We now restrict ourselves to “energy-conserving” transitions between Floquet states  $|\alpha n\rangle$  and  $|\beta m\rangle$  where  $\mathcal{E}_\alpha^{(n)} = \mathcal{E}_\beta^{(m)}$  holds. This is equivalent to the application of the rotating wave approximation (RWA) (see any volume on quantum optics, e.g., [46]). Hence,  $\mathcal{E}_a^{(n)} = \omega_a - n\omega \stackrel{!}{=} \omega_b - m\omega = \mathcal{E}_b^{(m)}$  so that

$$\mathcal{E}_a^{(n)} - \mathcal{E}_b^{(m)} = \Delta = \underbrace{\omega_a - \omega_b}_{\omega_{ab}} - \underbrace{(n - m)\omega}_{\stackrel{!}{=} 1}$$

where  $\Delta$  is the detuning, and we are only interested in one-photon transitions between  $|a\rangle$  and  $|b\rangle$  (so that  $n - m = 1$ ). Equation (7.91) now reduces to the  $2 \times 2$  equation

$$\begin{pmatrix} \mathcal{E}_b^{(n-1)} & A^* \\ A & \mathcal{E}_a^{(n)} \end{pmatrix} \begin{pmatrix} \Phi_b^{(n-1)} \\ \Phi_a^{(n)} \end{pmatrix} = \epsilon \begin{pmatrix} \Phi_b^{(n-1)} \\ \Phi_a^{(n)} \end{pmatrix}. \quad (7.92)$$

The eigenvalues are

$$\epsilon_{1,2}^{(n)} = \frac{1}{2}(\omega_a + \omega_b) + \omega \left( \frac{1}{2} - n \right) \pm \frac{1}{2}\sqrt{\Omega_R^2 + \Delta^2}. \quad (7.93)$$

The first term is the energy half way between  $|b\rangle$  and  $|a\rangle$ , the second term is the energy of the “photon field”, and the third term gives rise to two levels, separated by the frequency  $\Omega = \sqrt{\Omega_R^2 + \Delta^2}$ . Figure 7.6 illustrates the situation for vanishing detuning  $\Delta = 0$ . The energy levels (7.93) are called field-dressed states.

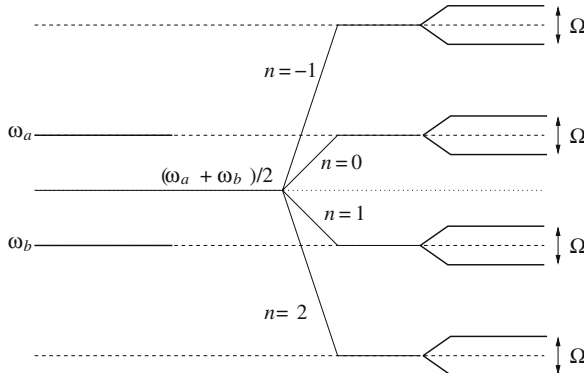


**Fig. 7.6** Illustration of (7.93) for  $\Delta = 0$ . The coupling of the two unperturbed levels  $b$  and  $a$  to the laser field gives rise to an infinite manifold of pairs of field-dressed levels (labelled by  $n$ ). Because of (7.76) all the different  $ns$  are equivalent. The field-dressed levels are separated by the energy  $\Omega = \sqrt{\Omega_R^2 + \Delta^2}$  (which equals  $\Omega_R$  for the vanishing detuning considered here)

Let us finally calculate the field-dressed states for our two-state problem in RWA and vanishing detuning. Because of (7.76) we are free to choose, say,  $n = 1$ . We also can, without loss of generality, set  $\omega_b = 0$ . Vanishing detuning  $\Delta = 0$  then implies  $\omega_a = \omega$ . Moreover we assume  $A$  to be real. Then

$$\epsilon_{1,2} = \pm \frac{1}{2}\Omega_R, \quad (7.94)$$

and the eigenvalue problem reduces to

$$\begin{pmatrix} 0 & A \\ A & 0 \end{pmatrix} \begin{pmatrix} \Phi_b^{(0)} \\ \Phi_a^{(1)} \end{pmatrix} = \epsilon_{1,2} \begin{pmatrix} \Phi_b^{(0)} \\ \Phi_a^{(1)} \end{pmatrix}. \quad (7.95)$$

The matrix

$$\mathbf{M} = \frac{1}{\sqrt{2}} \begin{pmatrix} -1 & 1 \\ 1 & 1 \end{pmatrix} = \mathbf{M}^{-1} \quad (7.96)$$

diagonalizes (7.95). The two eigenvectors correspond to the field-dressed or Floquet states

$$|\Psi^+\rangle = \frac{1}{\sqrt{2}} (|a\rangle + |b\rangle), \quad |\Psi^-\rangle = \frac{1}{\sqrt{2}} (|a\rangle - |b\rangle). \quad (7.97)$$

If the system is, e.g., at time  $t = 0$  in state  $|a\rangle$ , we have to choose a *superposition* of field-dressed states to fulfill the initial conditions:

$$|\Psi(t)\rangle = \frac{1}{\sqrt{2}} (|\Psi^+(t)\rangle + |\Psi^-(t)\rangle). \quad (7.98)$$

Here, according (7.78)

$$|\Psi^+(t)\rangle = e^{-i\epsilon_1 t} \left[ e^{-i\omega t} |a\rangle + |b\rangle \right], \quad (7.99)$$

$$|\Psi^-(t)\rangle = e^{-i\epsilon_2 t} \left[ e^{-i\omega t} |a\rangle - |b\rangle \right]. \quad (7.100)$$

Calculating the populations  $|a(t)|^2 = |\langle a|\Psi(t)\rangle|^2$  or  $|b(t)|^2 = |\langle b|\Psi(t)\rangle|^2$ , one obtains the well-known Rabi-oscillations of frequency  $\Omega$ .

### 7.3.2 Non-Hermitian Floquet Theory

As long as we are dealing only with discrete states the quasi-energies  $\epsilon$  are real. If, on the other hand, we allow for transitions into the continuum, e.g., via (multiphoton) ionization, the quasi-energies become complex,

$$\epsilon = \epsilon_0 + \Delta\epsilon - i\frac{\Gamma}{2}. \quad (7.101)$$

Here,  $\epsilon_0$  is the unperturbed energy,  $\Delta\epsilon$  is the AC Stark shift, and  $\Gamma$  is the ionization rate. One may wonder why a Hermitian Floquet Hamiltonian should yield complex eigenvalues. The reason for complex quasi-energies lies in the boundary conditions. Decaying dressed bound states or dressed resonances must fulfill the so-called Siegert boundary conditions [47]. Instead of explicitly taking these boundary conditions into account one may apply the complex dilation (also called complex scaling) method (see, e.g., [18, 48–50]).

Figure 7.7 shows the ionization rate of atomic hydrogen H(1s) for  $\lambda = 1064$  nm laser light as a function of the laser intensity, calculated by Potvliege and Shakeshaft [51] using the non-Hermitian Floquet method. At this wavelength at least 12 photons

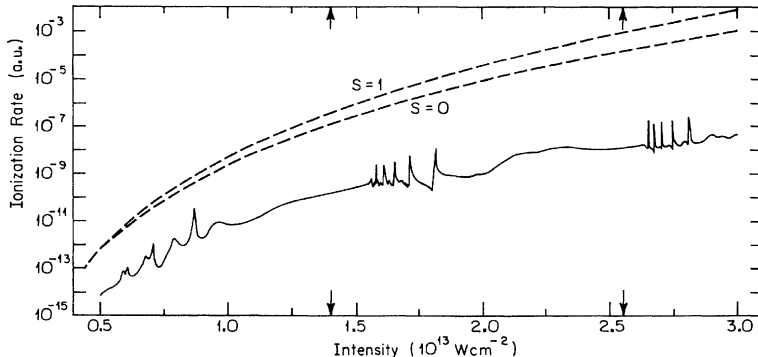


**Fig. 7.7** Ionization rate vs laser intensity for H(1s) irradiated by linearly polarized light of wavelength  $\lambda = 1064 \text{ nm}$ . Dashed curves are partial rates for  $(12 + S)$ -photon ionization obtained within LOPT. The arrows indicate the intensities at which the real part of the 1s Floquet eigenvalue crosses the 13- and 14-photon ionization thresholds (from [51])

must be absorbed by the electron in order to escape. The LOPT results for  $S$  excess photon-ionization (i.e.,  $(12 + S)$ -photon ionization) are included in Fig. 7.7. They by far overestimate the ionization rate. The exact Floquet-result displays interesting structures. As the AC Stark up-shift of the continuum (which is given by the ponderomotive potential  $U_p$ ) increases, the minimum number of photons required for ionization increases from 12 to 13 (first arrow) and to 14 (second arrow). After these thresholds are passed because of the increasing laser intensity, structures appear, indicating a strong enhancement of the ionization rate at certain laser intensities. This is due to Rydberg states that are brought into  $(12 + S)$ -photon resonance with the ground state via the AC Stark effect (Freeman resonances) [52].

### 7.3.3 Stabilization

The coupling  $\hat{W}(t)$  to the laser field reads in dipole approximation and velocity gauge

$$\hat{W}(t) = \hat{\mathbf{p}} \cdot \mathbf{A}(t) + \frac{1}{2} \mathbf{A}^2(t) \quad (7.102)$$

with  $\mathbf{A}(t)$  the vector potential. The transformation of the wave function

$$|\Psi(t)\rangle = e^{-\frac{i}{2} \int_{-\infty}^t A^2(t') dt'} e^{-i\alpha(t) \cdot \hat{\mathbf{p}}} |\Psi_{\text{PF}}(t)\rangle \quad (7.103)$$

removes the  $\mathbf{A}^2$ -term and transforms to the system of an electron oscillating with an excursion

$$\alpha(t) = \int_{-\infty}^t \mathbf{A}(t') dt' \quad (7.104)$$

in the laser field [Pauli–Fierz (PF) or Kramers–Henneberger transformation] [53–55]. In this system the nuclear potential appears to oscillate. The TDSE then reads

$$i\frac{d}{dt}|\Psi_{\text{PF}}(t)\rangle = \left(\frac{\hat{\mathbf{p}}^2}{2} + V[\mathbf{r} + \boldsymbol{\alpha}(t)]\right)|\Psi_{\text{PF}}(t)\rangle. \quad (7.105)$$

The PF Hamiltonian

$$\hat{H}_{\text{PF}}(t) = \frac{\hat{\mathbf{p}}^2}{2} + V[\mathbf{r} + \boldsymbol{\alpha}(t)] \quad (7.106)$$

is for an infinitely long laser pulse periodic as well so that we may apply the Floquet theorem. Introducing the time-averaged potential

$$V_{\text{PF}}(\hat{\boldsymbol{\alpha}}, \mathbf{r}) = \frac{1}{T} \int_0^T V[\mathbf{r} + \boldsymbol{\alpha}(t)] dt, \quad \hat{\boldsymbol{\alpha}} = \max |\boldsymbol{\alpha}(t)|, \quad (7.107)$$

which is the zero-frequency contribution in the Fourier-expansion of the potential [see (7.81)], (7.80) can be written as

$$-(\epsilon + m\omega)\Phi_{\beta}^{(m)} + \sum_{\alpha} \langle \beta | \frac{\hat{\mathbf{p}}^2}{2} + V_{\text{PF}}(\hat{\boldsymbol{\alpha}}, \mathbf{r}) | \alpha \rangle \Phi_{\alpha}^{(m)} + \sum_{\substack{\alpha n \\ n \neq m}} \langle \beta | V^{(m-n)} | \alpha \rangle \Phi_{\alpha}^{(n)} = 0. \quad (7.108)$$

If the laser frequency is large compared to the relevant inner-atomic transitions, we may neglect the third term so that we are left with an equation diagonal in the photon index, which corresponds to the solution of the time-independent Schrödinger equation

$$\epsilon |\Psi_{\text{PF}}\rangle = \left(\frac{\hat{\mathbf{p}}^2}{2} + V_{\text{PF}}(\hat{\boldsymbol{\alpha}}, \mathbf{r})\right) |\Psi_{\text{PF}}\rangle. \quad (7.109)$$

If it is possible to transfer the entire electron population to the bound states of  $V_{\text{PF}}(\hat{\boldsymbol{\alpha}}, \mathbf{r})$  there will be no ionization whatsoever. For intense fields where  $\hat{\boldsymbol{\alpha}} \gg 1$  the potential  $V_{\text{PF}}(\hat{\boldsymbol{\alpha}}, \mathbf{r})$  looks very different from the unperturbed nuclear potential since it has a double-well structure with the minima close to the classical turning points  $\pm \hat{\boldsymbol{\alpha}}$ . If electronic probability density is trapped in this potential the ionization rate decreases despite increasing laser field strength. This has indeed been observed in numerical simulations and is called adiabatic stabilization (see [11] for a review). The stabilization effect survives also for a “real” laser pulse with an up- and a down-ramp (dynamic stabilization).

Figure 7.8 illustrates stabilization of a one-dimensional model atom employing a soft-core binding potential  $V(x) = -(x^2 + \varepsilon)^{-1/2}$  with  $\varepsilon = 1.9$  (leading to a binding energy of  $-0.5$ ). The full TDSE was solved. The laser pulse of frequency

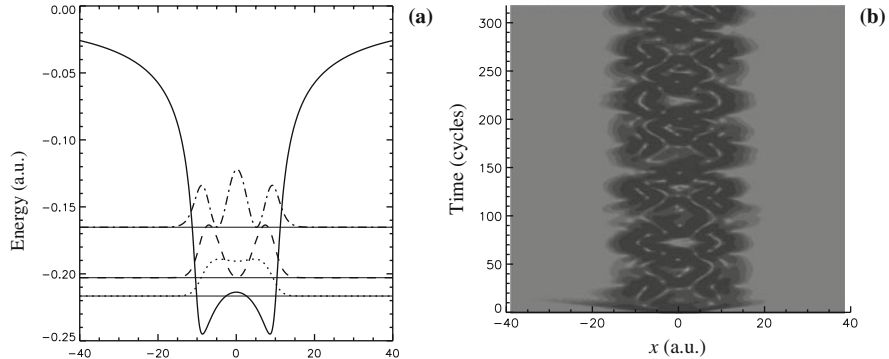


**Fig. 7.8** Dynamic stabilization in a one-dimensional model atom. The cycle-averaged ionic potential in a reference frame where a freely oscillating electron is at rest is depicted in (a) (solid line). The three lowest energy levels in this “dressed” potential and the corresponding probability densities are also plotted. In (b) a shadowgraph of the probability density, obtained from the full solution of the time-dependent Schrödinger equation, is shown. The probability density remains trapped in the effective potential. Low-frequency Rabi-flopplings are responsible for the oscillatory pattern. Note that the time scale of these oscillations is small compared to the laser period

$\omega = 2.5$  was ramped over 10 cycles up to  $\hat{E} = 62.5$  and thereafter held constant. The excursion of a free electron in this field is  $\alpha(t) = 10 \sin \omega t$ . The cycle-averaged potential, its three lowest levels and the corresponding probability densities are indicated in Fig. 7.8a. The potential has the above mentioned double-well shape with the minima close to the classical turning points  $\pm\hat{\alpha}$ . In Fig. 7.8b a shadowgraph of the probability density obtained from the TDSE solution in the PF frame is shown. The probability density remains confined between the two turning points. Only during the up-ramping of the pulse some density escapes. Obviously, not only a single dressed state is occupied since the probability density distribution oscillates in time. Note that the time-scale of this dynamics is slow compared to the laser period. The splitting of the probability density due to the double-well character of the PF potential is called “dichotomy” [56]. In circularly polarized multi-color laser field configurations more complex structures were observed [57].

Figure 7.9 shows the lifetime (i.e., the inverse ionization rate) of atomic H in circularly laser pulses of various frequencies and intensities as predicted by the high-frequency Floquet theory [58]. With increasing laser intensity the lifetime first decreases (i.e., ionization increases). This is the expected behavior from LOPT. Then, however, the lifetime passes through a minimum (the “death valley” [11, 59]) before it increases again (i.e., ionization is reduced).

So far, adiabatic stabilization with the electron starting from the ground state was observed in numerical simulations only. This is because there are no sufficiently strong lasers available yet at short wavelengths. The photon energy  $\omega$  has to exceed the ionization potential, and the laser intensity must be strong enough in order to lead to the two minima in the time-averaged potential. Since the elongation  $\alpha$  is inversely proportional to  $\omega^2$ , the laser intensity necessary for adiabatic stabilization

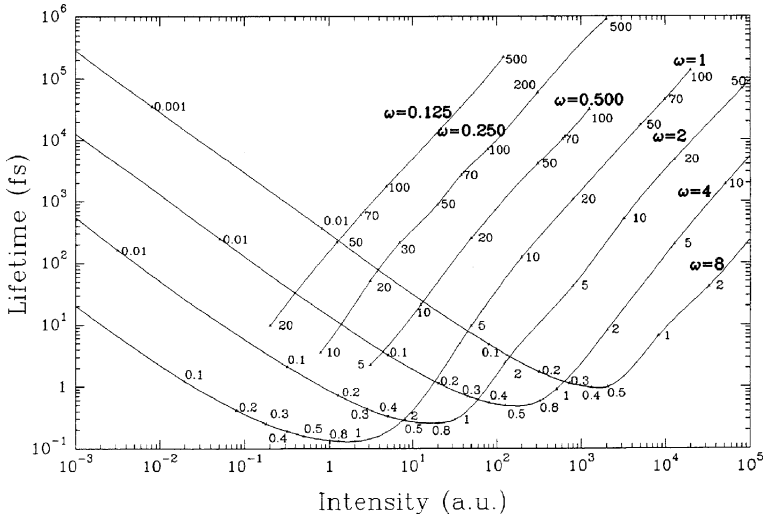


**Fig. 7.9** Lifetime of the H atom in the ground state according to the high-frequency Floquet theory, vs intensity, at various laser frequencies  $\omega$ ; circular polarization. Numbers adjacent to points on the curves are the corresponding values of  $\hat{\alpha}$ . The descending branches of the curves correspond to LOPT, the ascending ones to adiabatic stabilization (the latter can be “trusted” as the laser frequency increases beyond the ionization potential 0.5). From [59]

increases with  $\omega$ . Because  $\omega > \mathcal{E}_{\text{ip}}$  it is thus desirable to reduce  $\mathcal{E}_{\text{ip}}$  so that already available laser sources can be used. In fact, the stabilization of Rydberg atoms was already demonstrated [60].

There are (at least) three effects which counteract against adiabatic stabilization. Firstly, there is the so-called “death-valley” effect [59]: an atom experiences during the rising edge of a strong laser pulse field intensities in which violent ionization occurs and hence no more electrons are left to be stabilized once the optimal stabilization condition is reached. Secondly, in more complex atoms or ions inner electrons might be excited or removed by few photon processes induced by the incident high frequency radiation. Then the question arises whether an outer electron can stabilize although there are electron holes in the lower lying shells [61]. Thirdly, at high frequencies and high intensities the dipole approximation breaks down, and the magnetic  $\mathbf{v} \times \mathbf{B}$ -force pushes the electron into the propagation direction, thus enhancing ionization [62, 63]. These three effects will probably make the experimental verification of stabilization of atoms starting from the ground state a formidable task. Even the new short-wavelength free electron laser sources under construction worldwide are of too low intensity, let alone that they do not deliver long flat-top pulses, which would be ideal to observe dynamic stabilization. However, there is no doubt that sooner or later such light sources will be available so that a new and interesting kind of “meta-matter” will be produced: pseudo atoms with charge clouds extending over tens or more atomic units and artificial molecules of tunable internuclear separations.

### 7.3.4 Strong Field Approximation

The strong field approximation (SFA), also known as “Keldysh–Faisal–Reiss” (KFR)-theory [42, 64, 65], and its extensions are the theoretical workhorse in strong field laser–atom and laser–molecule interaction and often gives insight into the mechanisms behind strong field effects. As the laser field is far from being a small perturbation, “conventional” perturbation theory in the number of photons involved is not applicable [66]. The SFA does neither consider the laser field being small compared to the binding forces nor does it assume the contrary at all times during the interaction. Instead, in the SFA the binding potential is considered dominant until ionization whereas the laser field takes over after ionization. The SFA has been applied to ionization, harmonic generation, and nonsequential ionization. The beauty of the SFA lies, besides in its predictive power, in the possibility to interpret its equations in intuitively accessible terms, as will be shown below in Sect. 7.3.5. However, there are limits as well, to be discussed in the last part of this section.

Let the initial state be an electronic eigenstate of the field-free Hamiltonian. The electron may at time  $t_i$  be in the ground state  $|\Psi_0\rangle = |\Psi_0(t_i)\rangle$  of energy  $\mathcal{E}_0 < 0$ , for instance, and the laser field is not yet switched on. Now let us consider the picture-independent bound-free transition matrix element

$$M_p(t) = \langle \Psi_p | \hat{U}(t, t_i) | \Psi_0 \rangle \quad (7.110)$$

for a transition from the initial state  $|\Psi_0\rangle$  to the target state  $|\Psi_p\rangle = |\Psi_p(t_i)\rangle$ , which is a continuum state of asymptotic momentum  $p$ .  $\hat{U}(t, t_i)$  is the (picture-independent) time evolution operator. The probability to find the electron at time  $t$  in the scattering state  $|\Psi_p\rangle$  is  $w(t) = |M_p(t)|^2$ . The time-evolution operator  $\hat{U}(t, t') = \hat{U}^\dagger(t', t)$  fulfills

$$i \frac{d}{dt} \hat{U}(t, t') = \hat{H}(t) \hat{U}(t, t') \quad (7.111)$$

in any picture [67]. The TDSE in the Schrödinger picture reads

$$i \frac{d}{dt} |\Psi(t)\rangle = \hat{H}(t) |\Psi(t)\rangle, \quad \hat{H}(t) = \frac{1}{2} [\hat{\mathbf{p}} + \mathbf{A}(t)]^2 + \hat{V}(\mathbf{r}) \quad (7.112)$$

where  $\mathbf{A}(t)$  is the vector potential describing the laser field (in dipole approximation). The minimum coupling Hamiltonian  $\hat{H}(t)$  can be splitted in various ways:

$$i \frac{d}{dt} |\Psi(t)\rangle = [\hat{H}_0 + \hat{W}(t)] |\Psi(t)\rangle = [\hat{H}^{(V)}(t) + \hat{V}(\mathbf{r})] |\Psi(t)\rangle, \quad (7.113)$$

with

$$\hat{H}_0 = \frac{\hat{\mathbf{p}}^2}{2} + \hat{V}(\mathbf{r}), \quad \hat{H}^{(V)}(t) = \frac{\hat{\mathbf{p}}^2}{2} + \hat{W}(t), \quad (7.114)$$

and  $\hat{W}(t)$  the interaction with the laser field,

$$\hat{W}(t) = \hat{\mathbf{p}} \cdot \mathbf{A}(t) + \frac{1}{2} \mathbf{A}^2(t) \quad (\text{velocity gauge}). \quad (7.115)$$

The gauge transformation of the potentials (both scalar potential  $\phi$  and vector potential  $\mathbf{A}$ ) and the wave function  $|\Psi(t)\rangle$ ,

$$\mathbf{A}' = \mathbf{A} + \nabla\chi(\mathbf{r}, t), \quad \phi' = \phi - \frac{\partial\chi(\mathbf{r}, t)}{\partial t}, \quad |\Psi'(t)\rangle = e^{-i\chi(\mathbf{r}, t)}|\Psi(t)\rangle$$

where  $\chi(\mathbf{r}, t)$  is an arbitrary differential scalar function, leaves the electric and the magnetic field unchanged:

$$\mathbf{E} = -\partial_t \mathbf{A} - \nabla\phi = \mathbf{E}', \quad \mathbf{B} = \nabla \times \mathbf{A} = \mathbf{B}'. \quad (7.116)$$

This gauge invariance offers the possibility to choose a gauge that suits best, e.g., as far as computational simplicity is concerned. Observables are not affected by gauge transformations while the interpretation of the underlying physics may change (e.g., there is no potential barrier in velocity gauge to tunnel through). Moreover, approximations may destroy the gauge invariance (see below).

The transformation to the so-called length gauge (also known as the Göppert–Mayer gauge [68]) is achieved by choosing

$$\chi(\mathbf{r}, t) = -\mathbf{A}(t) \cdot \mathbf{r}. \quad (7.117)$$

Because of  $\nabla\chi = -\mathbf{A}$  the vector potential is “transformed away” while  $\phi' = -\partial_t\chi = -\mathbf{E} \cdot \mathbf{r}$ . The Hamiltonian in length gauge reads

$$\hat{H}'(t) = \frac{\hat{\mathbf{p}}^2}{2} + \hat{V}(\mathbf{r}) - \phi'(\mathbf{r}, t) = \frac{\hat{\mathbf{p}}^2}{2} + \hat{V}(\mathbf{r}) + \mathbf{E}(t) \cdot \hat{\mathbf{r}} \quad (7.118)$$

(one could also absorb  $\hat{V}(\mathbf{r})$  in  $\phi$  and  $\phi'$ ). Note that the transformation of the wave function

$$|\Psi'(t)\rangle = e^{i\hat{\mathbf{r}} \cdot \mathbf{A}(t)}|\Psi(t)\rangle \quad (7.119)$$

can be interpreted as a translation in momentum space. In fact, while in velocity gauge the quiver momentum is effectively subtracted from the kinetic momentum, leading to a canonical momentum different from the kinetic momentum, in length gauge kinetic and canonical momentum are equal.

From (7.118) we infer

$$\hat{W}'(t) = \mathbf{E}(t) \cdot \hat{\mathbf{r}} \quad (\text{length gauge}) \quad (7.120)$$

with  $\mathbf{E}(t) = -\partial_t \mathbf{A}(t)$ .

$\hat{H}_0$  describes the unperturbed atom and seemingly does not depend on the gauge chosen, i.e.,  $\hat{H}_0 = \hat{H}'_0$ . However, one should bear in mind that the momentum  $\hat{\mathbf{p}}$  in  $\hat{H}_0$  is not the kinetic momentum (which, in atomic units, equals the velocity) while in  $\hat{H}'_0$  (length gauge) it is.

The Gordon–Volkov–Hamiltonian  $\hat{H}^{(V)}(t)$  governs the free motion of the electron in the laser field [69, 70]. The Gordon–Volkov state  $|\Psi_p^{(V)}\rangle$  fulfills in the Schrödinger picture and velocity gauge

$$\mathrm{i}\frac{d}{dt}|\Psi_p^{(V)}(t)\rangle = \hat{H}^{(V)}(t)|\Psi_p^{(V)}(t)\rangle = \frac{1}{2}[\hat{\mathbf{p}} + \mathbf{A}(t)]^2|\Psi_p^{(V)}(t)\rangle. \quad (7.121)$$

Thanks to the dipole approximation the Gordon–Volkov–Hamiltonian is diagonal in momentum space. The solution of (7.121), i.e., the Gordon–Volkov-state, is thus readily written down:

$$|\Psi_p^{(V)}(t, t_i)\rangle = e^{-iS_p(t, t_i)}|\mathbf{p}\rangle, \quad S_p(t, t_i) = \frac{1}{2} \int_{t_i}^t dt' [\mathbf{p} + \mathbf{A}(t')]^2 \quad (7.122)$$

where  $|\mathbf{p}\rangle$  are momentum eigenstates,  $\langle \mathbf{r} | \mathbf{p} \rangle = e^{i\mathbf{p} \cdot \mathbf{r}} / (2\pi)^{3/2}$ . Note that the lower integration limit  $t_i$  affects the overall phase of the Gordon–Volkov solution only. As mentioned above, the transition to the length gauge corresponds to a translation in momentum space. It is thus easy to check that in length gauge one has

$$|\Psi_p^{(V)'}(t, t_i)\rangle = e^{-iS_p(t, t_i)}|\mathbf{p} + \mathbf{A}(t)\rangle \quad (\text{length gauge}) \quad (7.123)$$

with the same action  $S_p(t, t_i)$  as in (7.122).

Let us now continue to derive the SFA transition matrix element. As the time evolution operator  $\hat{U}(t, t')$  satisfies (7.111),

$$\mathrm{i}\frac{d}{dt}\hat{U}(t, t') = [\hat{H}_0 + \hat{W}(t)]\hat{U}(t, t'), \quad (7.124)$$

the integral equations

$$\begin{aligned} \hat{U}(t, t') &= \hat{U}_0(t, t') - \mathrm{i} \int_{t'}^t dt'' \hat{U}(t, t'') \hat{W}(t'') \hat{U}_0(t'', t'), \\ &= \hat{U}_0(t, t') - \mathrm{i} \int_{t'}^t dt'' \hat{U}_0(t, t'') \hat{W}(t'') \hat{U}(t'', t'), \end{aligned} \quad (7.125)$$

are fulfilled [71]. Here,  $\hat{U}_0(t, t')$  is the evolution operator corresponding to the TDSE with  $\hat{H}_0$  only. Inserting (7.125) in the matrix element (7.110) leads to

$$M_p(t) = -i \int_{t_i}^t dt' \langle \Psi_p | \hat{U}(t, t') \hat{W}(t') | \Psi_0(t') \rangle \quad (7.126)$$

where use of  $\langle \Psi_p | \hat{U}_0(t, t_i) | \Psi_0 \rangle = \langle \Psi_p | \Psi_0(t) \rangle = 0$  was made because  $|\Psi_p\rangle$  is a scattering state orthogonal to  $|\Psi_0(t)\rangle = e^{-i\mathcal{E}_0(t-t_i)}|\Psi_0\rangle$ , and  $\hat{U}_0(t', t_i)|\Psi_0\rangle = |\Psi_0(t')\rangle$ . Since the propagator  $\hat{U}(t, t')$  also satisfies the integral equations

$$\begin{aligned} \hat{U}(t, t') &= \hat{U}^{(V)}(t, t') - i \int_{t'}^t dt'' \hat{U}^{(V)}(t, t'') \hat{V} \hat{U}(t'', t'), \\ &= \hat{U}^{(V)}(t, t') - i \int_{t'}^t dt'' \hat{U}(t, t'') \hat{V} \hat{U}^{(V)}(t'', t'), \end{aligned} \quad (7.127)$$

where  $\hat{U}^{(V)}(t, t')$  is the evolution operator corresponding to the TDSE (7.121), one obtains, upon inserting (7.127) in (7.126),

$$\begin{aligned} M_p(t) &= -i \left[ \int_{t_i}^t dt' \langle \Psi_p | \hat{U}^{(V)}(t, t') \hat{W}(t') | \Psi_0(t') \rangle \right. \\ &\quad \left. - i \int_{t_i}^t dt'' \int_{t''}^t dt' \langle \Psi_p | \hat{U}^{(V)}(t, t') \hat{V} \hat{U}(t', t'') \hat{W}(t'') | \Psi_0(t'') \rangle \right]. \end{aligned} \quad (7.128)$$

Using  $\int_{t_i}^t dt'' \int_{t''}^t dt' = \int_{t_i}^t dt' \int_{t_i}^t dt'' \Theta(t' - t'') = \int_{t_i}^t dt' \int_{t_i}^{t'} dt''$  expression (7.128) may be recast in the form

$$\begin{aligned} M_p(t) &= -i \int_{t_i}^t dt' \langle \Psi_p | \hat{U}^{(V)}(t, t') \left[ \hat{W}(t') | \Psi_0(t') \rangle \right. \\ &\quad \left. - i \int_{t_i}^{t'} dt'' \hat{V} \hat{U}(t', t'') \hat{W}(t'') | \Psi_0(t'') \rangle \right]. \end{aligned} \quad (7.129)$$

Equation (7.129) is still exact and gauge invariant. Whatever is missed in the first term of (7.129) is included in the second term where the full but unknown time evolution operator  $\hat{U}(t', t'')$  appears. Neglecting the second term, replacing the final state  $|\Psi_p\rangle$  by a plane wave  $|\mathbf{p}\rangle$ , and making use of the expansion of the Gordon–Volkov-propagator into Gordon–Volkov waves

$$\hat{U}^{(V)}(t, t') = \int d^3k |\Psi_k^{(V)}(t, t_i)\rangle \langle \Psi_k^{(V)}(t', t_i)|, \quad (7.130)$$

( $t_i$  is arbitrary since it cancels) we obtain the SFA or so-called Keldysh-amplitude

$$M_p^{(\text{SFA})}(t) = -i \int_{t_i}^t dt' \langle \Psi_p^{(V)}(t', t) | \hat{W}(t') | \Psi_0(t') \rangle. \quad (7.131)$$

The SFA transition amplitude integrates over all ionization times  $t'$  where the transition from the bound state  $|\Psi_0(t')\rangle$  to the Gordon-Volkov state  $|\Psi_p^{(V)}(t', t)\rangle$ , mediated by the interaction with the laser field  $\hat{W}(t')$ , may take place. Unfortunately, the replacement of the final state by a plane wave destroys the gauge invariance, and under certain circumstances SFA results can be very different in different gauges [72–74].

In velocity gauge, where  $\hat{W}(t) = \hat{\mathbf{p}} \cdot \mathbf{A}(t) + A^2(t)/2$  is diagonal in momentum representation, the Keldysh amplitude (7.131) becomes

$$M_p^{(\text{SFA})}(t) = -i \int_{t_i}^t dt' e^{iS_p(t', t)} \left[ \mathbf{p} \cdot \mathbf{A}(t') + \frac{1}{2} A^2(t') \right] \langle \mathbf{p} | \Psi_0 \rangle e^{-iE_0(t' - t_i)} \quad (7.132)$$

with  $E_0$  the initial energy. Multiplying this matrix element by the overall phase factor  $\exp[iS_p(t, t_i)]$  and splitting  $\mathbf{p} \cdot \mathbf{A}(t') + A^2(t')/2$  in the form  $[\mathbf{p} + \mathbf{A}(t')]^2/2 - E_0 - p^2/2 + E_0$  leads – upon integration by parts—to

$$\begin{aligned} M_p^{(\text{SFA})}'(t) &= -\Psi_0(\mathbf{p}) e^{iS_p, E_0(t', t_i)} \Big|_{t_i}^t \\ &\quad + i\Psi_0(\mathbf{p}) \left( \frac{\mathbf{p}^2}{2} - E_0 \right) \int_{t_i}^t e^{iS_p, E_0(t', t_i)} dt' \end{aligned} \quad (7.133)$$

with the classical action

$$S_{p, E_0}(t, t_i) = \int_{t_i}^t \left[ \frac{\mathbf{p}^2}{2} - E_0 + \hat{W}(t') \right] dt' \quad (7.134)$$

and  $\Psi_0(\mathbf{p}) = \langle \mathbf{p} | \Psi_0 \rangle$  the Fourier-transformed initial state wave function

$$\Psi_0(\mathbf{p}) = \frac{1}{(2\pi)^{3/2}} \int d^3r e^{-i\mathbf{p} \cdot \mathbf{r}} \Psi_0(\mathbf{r}). \quad (7.135)$$

The first term in (7.133) vanishes when the asymptotic rate

$$\Gamma_p = \lim_{T \rightarrow \infty} \frac{|M_p|^2}{T}, \quad M_p = \lim_{\substack{t_i \rightarrow -\infty \\ t \rightarrow \infty}} M_p(t) \quad (7.136)$$

is calculated. In this way we recover Reiss' result [65]

$$M_p^{(\text{SFA})}' = i\Psi_0(\mathbf{p}) \left( \frac{\mathbf{p}^2}{2} - E_0 \right) \int_{-\infty}^{\infty} e^{iS_p, E_0(t, -\infty)} dt. \quad (7.137)$$

### 7.3.4.1 Circular Polarization and Long Pulses

In this case one may write the vector potential in dipole approximation as

$$\mathbf{A}(t) = \frac{1}{2} \hat{A} [\boldsymbol{\epsilon} \exp(i\omega t) + \boldsymbol{\epsilon}^* \exp(-i\omega t)] \quad (7.138)$$

where the polarization vectors  $\boldsymbol{\epsilon}, \boldsymbol{\epsilon}^*$  fulfill  $\boldsymbol{\epsilon}^2 = \boldsymbol{\epsilon}^{*2} = 0$  and  $\boldsymbol{\epsilon} \cdot \boldsymbol{\epsilon}^* = 1$ , e.g.,  $\boldsymbol{\epsilon} = (\mathbf{e}_x + i\mathbf{e}_y)/\sqrt{2}$ . The factor 1/2 is introduced in order to obtain  $U_p = \hat{A}^2/4$ , as in the linearly polarized case. With

$$[\mathbf{p} + \mathbf{A}(t)]^2 = \mathbf{p}^2 + \frac{1}{2} \hat{A}^2 + 2\hat{A}|\mathbf{p} \cdot \boldsymbol{\epsilon}| \cos(\omega t - \varphi), \quad (7.139)$$

where  $\mathbf{p} \cdot \boldsymbol{\epsilon} = |\mathbf{p} \cdot \boldsymbol{\epsilon}| \exp(-i\varphi)$ , the action (7.134) reads

$$S_{\mathbf{p}, \mathcal{E}_0}(t, -\infty) = \left( \frac{\mathbf{p}^2}{2} - \mathcal{E}_0 + U_p \right) t + \frac{\hat{A}}{\omega} |\mathbf{p} \cdot \boldsymbol{\epsilon}| \sin(\omega t - \varphi) \quad (7.140)$$

where we neglected contributions from  $t_i = -\infty$  since they just affect the irrelevant, overall phase of the SFA transition matrix element

$$\begin{aligned} M_{\mathbf{p}, \text{circ.}}^{(\text{SFA})}' &= 2\pi i \Psi_0(\mathbf{p}) \sum_{n=-\infty}^{\infty} (n\omega - U_p) \exp(in\varphi) \\ &\times J_n \left( \frac{-\hat{A}|\mathbf{p} \cdot \boldsymbol{\epsilon}|}{\omega} \right) \delta(p^2/2 - \mathcal{E}_0 + U_p - n\omega). \end{aligned} \quad (7.141)$$

$J_n(\zeta)$  are Bessel functions obeying

$$\exp[-i\zeta \sin(\omega t - \varphi)] = \sum_{n=-\infty}^{\infty} J_n(\zeta) \exp[-in(\omega t - \varphi)]. \quad (7.142)$$

The time integration in (7.137) leads to the energy-conserving  $\delta$ -function. Employing (7.136) and using

$$\delta(\Omega) = \frac{1}{2\pi} \lim_{T \rightarrow \infty} \int_{-T/2}^{T/2} \exp(i\Omega t) dt = \lim_{T \rightarrow \infty} \frac{T}{2\pi} \quad \text{for } \Omega = 0 \quad (7.143)$$

(and zero otherwise) to evaluate the square of the  $\delta$ -function one obtains the ionization rate

$$\Gamma_{\mathbf{p}, \text{circ.}}^{(\text{SFA})} = 2\pi |\Psi_0(\mathbf{p})|^2 \sum_{n=-\infty}^{\infty} (n\omega - U_p)^2 J_n^2 \left( \frac{-\hat{A}|\mathbf{p} \cdot \boldsymbol{\epsilon}|}{\omega} \right) \delta(p^2/2 - \mathcal{E}_0 + U_p - n\omega). \quad (7.144)$$

$\Gamma_{\mathbf{p}, \text{circ.}}^{(\text{SFA})}$  has the dimension of a density in momentum space per time. To evaluate the total rate  $\Gamma$  the partial rate  $\Gamma_{\mathbf{p}}$  has to be integrated over all final momenta  $\mathbf{p}$ ,

$$\Gamma = \int d^3 p \Gamma_{\mathbf{p}} = \int dp d\Omega p^2 \Gamma_{\mathbf{p}} = \int d\Omega \frac{d\Gamma}{d\Omega} \quad (7.145)$$

where  $d\Omega = \sin \vartheta d\vartheta d\varphi$  is the solid angle element. The final rate for ionization with the electron ejected into the solid angle  $d\Omega$  is given by

$$\frac{d\Gamma_{\text{circ.}}^{(\text{SFA})}}{d\Omega} = 2\pi \sqrt{8\omega^5} \sum_{n=n_{\min}}^{\infty} (n - U_p/\omega)^2 \frac{p_n}{\sqrt{2\omega}} |\Psi_0(p_n)|^2 J_n^2 \left( \frac{-\hat{A} p_n \sin \vartheta}{\sqrt{2\omega}} \right), \quad (7.146)$$

with

$$p_n = \sqrt{2(n\omega - U_p + \mathcal{E}_0)}. \quad (7.147)$$

The sum in (7.146) runs over all  $n$  which yield real  $p_n$  and starts with the minimum number of absorbed photons  $n_{\min}$ , which depends not only on  $\mathcal{E}_0$  but also on  $U_p$  – an utterly nonperturbative, nonlinear effect!

### 7.3.4.2 Channel-Closing in Above-Threshold Ionization

The increase of  $n_{\min}$  with increasing  $U_p$  is the channel-closing phenomenon (see, e.g., [75, 76]). This is illustrated in Fig. 7.10. We expect peaks in the photoelectron spectra at the positions

$$\mathcal{E}_n = \frac{1}{2} p_n^2 = n\omega - (U_p + \mathcal{E}_{\text{ip}}), \quad n \geq n_{\min} \quad (7.148)$$

where  $\mathcal{E}_{\text{ip}} = |\mathcal{E}_0|$  is the ionization potential and  $U_p + \mathcal{E}_{\text{ip}}$  is the “effective” ionization potential due to the AC Stark shift of the continuum threshold with respect to the ground state level. Due to the fact that peaks  $n > n_{\min}$  are present – even with higher probability than  $n = n_{\min}$  – the name above-threshold ionization (ATI) has been coined for this strong field ionization phenomenon, which was first observed by Agostini et al. [77]. The peak positions in strong field photoelectron spectra according (7.148) are well confirmed by ab initio solutions of the TDSE in dipole approximation. However, in actual measurements the positions of the peaks depend on the laser pulse duration. In short-pulse experiments the released electrons have no time to leave the focus before the laser pulse is over. In long pulses, instead, the electron has time to leave the focus and, in so doing, gains back the energy  $U_p$ . As a consequence the  $U_p$ -term in (7.148) is canceled and the peak positions in the long-pulse regime are determined by

$$\mathcal{E}_n^{(\text{long pulse})} = \frac{1}{2} p_n^2 = n\omega - \mathcal{E}_{\text{ip}}, \quad n \geq n_{\min} \quad (7.149)$$

with  $n_{\min}$ , however, still to be calculated with  $U_p$  (since before leaving the laser focus, ionization has to occur in the first place).

In Fig. 7.10a the  $U_p$ -shift of the continuum threshold is small, and the channel  $n = 5$  is responsible for the first peak in the photoelectron spectrum. At higher laser intensity, in Fig. 7.10b, the channels  $n = 5$  and  $n = 6$  are closed since 6 photons are not sufficient to overcome the effective ionization potential  $\mathcal{E}_{ip} + U_p$ . In the long pulse regime peaks corresponding to a certain channel are always at the same positions in the energy spectrum whereas in the short pulse regime the peaks move with  $U_p$ . As a consequence, focal averaging reduces the contrast in the short pulse regime whereas it has less of an effect in the long pulse regime because of the automatic cancellation of  $U_p$  at the position of electron-emission.

In Fig. 7.11 we show the example of an experimental long-pulse spectrum where lower order peaks are indeed suppressed due to channel-closings.

### 7.3.4.3 Linear Polarization and Long Pulses

We assume a laser field of the form

$$\mathbf{A}(t) = \hat{A}\boldsymbol{\epsilon} \cos(\omega t), \quad \boldsymbol{\epsilon}^2 = 1. \quad (7.150)$$

The action (7.134) reads in this case

$$S_{\mathbf{p},\mathcal{E}_0}(t, -\infty) = \left( \frac{\mathbf{p}^2}{2} - \mathcal{E}_0 + U_p \right) t - \frac{\hat{A}}{\omega} \mathbf{p} \cdot \boldsymbol{\epsilon} \sin(\omega t) + \frac{\hat{A}^2}{8\omega} \sin(2\omega t).$$

Proceeding as in the circular field-case one arrives at [65]

$$\begin{aligned} M_{\mathbf{p},\text{lin.}}^{(\text{SFA})}' &= 2\pi i \Psi_0(\mathbf{p}) \sum_{n=-\infty}^{\infty} (n\omega - U_p) \tilde{J}_n \left( \frac{-\hat{A}\mathbf{p} \cdot \boldsymbol{\epsilon}}{\omega}, -\frac{U_p}{2\omega} \right) \delta(p^2/2 - \mathcal{E}_0 + U_p - n\omega), \\ \Gamma_{\mathbf{p},\text{lin.}}^{(\text{SFA})} &= 2\pi |\Psi_0(\mathbf{p})|^2 \sum_{n=-\infty}^{\infty} (n\omega - U_p)^2 \tilde{J}_n^2 \left( \frac{-\hat{A}\mathbf{p} \cdot \boldsymbol{\epsilon}}{\omega}, -\frac{U_p}{2\omega} \right) \delta(p^2/2 - \mathcal{E}_0 + U_p - n\omega), \\ \frac{d\Gamma_{\text{lin.}}^{(\text{SFA})}}{d\Omega} &= 2\pi \sqrt{8\omega^5} \sum_{n=-\infty}^{\infty} (n - U_p/\omega)^2 \frac{p_n}{\sqrt{2m\omega}} |\Psi_0(p_n)|^2 \tilde{J}_n^2 \left( \frac{-\hat{A}\mathbf{p} \cdot \boldsymbol{\epsilon}}{\omega}, -\frac{U_p}{2\omega} \right). \end{aligned}$$

$\tilde{J}_n$  is the generalized Bessel function of integer order  $n$  defined by

$$\tilde{J}_n(u, v) = \frac{1}{2\pi} \int_{-\pi}^{\pi} d\theta \exp[i(u \sin \theta + v \sin(2\theta) - n\theta)].$$

The relation to the ordinary Bessel functions is

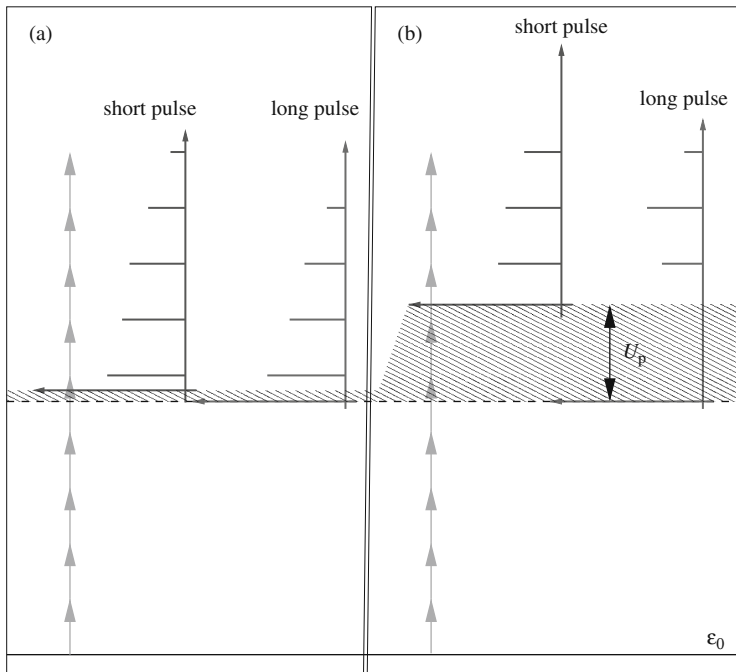


**Fig. 7.10** Channel-closing in the short and long pulse regime. In (a) the laser intensity is small so that the  $U_p$ -shift of the continuum threshold is less than a photon energy. In (b) the channels  $n = 5$  and  $n = 6$  are closed due to the pronounced AC Stark shift of the continuum. The photoelectron spectra look different in the short and long pulse regime since the released electrons gain  $U_p$  in the latter case upon leaving the laser focus

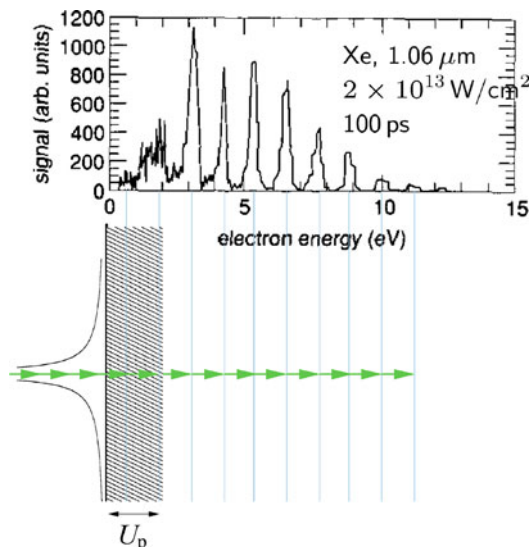


**Fig. 7.11** Channel-closing in the long-pulse regime. The experimental spectrum was taken from [78]. The two channels in the shaded area are closed

$$\tilde{J}_n(u, v) = \sum_{k=-\infty}^{\infty} J_{n-2k}(u) J_k(v)$$

and

$$\sum_{n=-\infty}^{\infty} \exp(in\theta) \tilde{J}_n(u, v) = \exp[iu \sin \theta + iv \sin(2\theta)].$$

Further properties of the generalized Bessel functions may be found in the appendix B of the original SFA paper by Reiss [65]. In the same article it is also demonstrated how the typical exponential behavior  $\sim \exp[-2(2\mathcal{E}_{\text{ip}})^{3/2}/(3E)]$  arises in the case of tunneling ionization [see (7.66)] through the asymptotic behavior of the generalized Bessel functions  $\tilde{J}_n$ .

### 7.3.5 Few-Cycle Above-Threshold Ionization

In few-cycle pulses the pulse envelope  $\hat{A}(t)$  varies on a time scale comparable to the period  $T = 2\pi/\omega$  determined by the carrier frequency  $\omega$ . Moreover, the carrier envelope phase  $\phi$ , governing the shift of the carrier wave with respect to the envelope, affects many observables. Hence, instead of (7.150) we write

$$A(t) = \hat{A}(t)\epsilon \sin(\omega t + \phi) \quad (7.151)$$

with  $\hat{A}(t)$  a  $\sin^2$  or a Gaussian envelope, for instance.

In the case of few-cycle pulses it would be very cumbersome to deal with Bessel functions, as we did above for constant (or slowly varying)  $\hat{A}$ . Instead, we start off with the still exact matrix element (7.129) and replace once again the final state by a plane wave and the full propagator  $\hat{U}(t', t)$  by  $\hat{U}^{(\text{V})}(t', t)$ . In that way we obtain the extended SFA transition matrix element

$$M_p^{(\text{SFA})}(t) = M_p^{(\text{SFA,dir})}(t) + M_p^{(\text{SFA,rec})}(t), \quad (7.152)$$

$$M_p^{(\text{SFA,dir})}(t) = M_p^{(\text{SFA})}(t) = -i \int_{t_i}^t dt' \langle \Psi_p^{(\text{V})}(t', t) | \hat{W}(t') | \Psi_0(t') \rangle, \quad (7.153)$$

$$\begin{aligned} M_p^{(\text{SFA,rec})}(t) \\ = - \int_{t_i}^t \int_{t_i}^{t'} dt'' \langle \Psi_p^{(\text{V})}(t', t) | \hat{V} \hat{U}^{(\text{V})}(t', t'') \hat{W}(t'') | \Psi_0(t'') \rangle. \end{aligned} \quad (7.154)$$

In what follows we set  $t_i = 0$ , and we assume that

$$A(0) = A(T_p) = \mathbf{0} \quad (7.155)$$

where  $T_p$  is the laser pulse duration. Note that the integral over the electric field of a realistic laser pulse must vanish (see, e.g., appendix A in [9]), so that  $A(0) = A(T_p)$ , and (7.155) does not pose a loss of generality. It is left as an exercise to the reader that relabeling the integration variables, multiplication by an overall phase factor and making use of the fact that ionization can only happen while the laser is on, (7.153) and (7.154) can be recast in length gauge in the form

$$M_p^{(\text{SFA,dir})'} = -i \int_0^{T_p} dt_{\text{ion}} \langle \mathbf{p} + \mathbf{A}(t_{\text{ion}}) | \mathbf{r} \cdot \mathbf{E}(t_{\text{ion}}) | \Psi_0 \rangle e^{iS_{\mathbf{p},\mathcal{E}_0}(t_{\text{ion}})}, \quad (7.156)$$

where

$$S_{\mathbf{p},\mathcal{E}_0}(t) = \int_0^t dt' \left( \frac{1}{2} [\mathbf{p} + \mathbf{A}(t')]^2 - \mathcal{E}_0 \right), \quad S_{\mathbf{p}}(t) = \frac{1}{2} \int_0^t dt' [\mathbf{p} + \mathbf{A}(t')]^2.$$

$t_{\text{ion}}$  can be interpreted as the ionization time. Analogously, the rescattering matrix element can be written for  $t \rightarrow \infty$  in the form

$$M_p^{(\text{SFA,esc})'} = - \int_0^{T_p} dt_{\text{ion}} \int_{t_{\text{ion}}}^{\infty} dt_{\text{resc}} \int d^3 k e^{iS_{\mathbf{p}}(t_{\text{resc}})} \langle \mathbf{p} + \mathbf{A}(t_{\text{resc}}) | \hat{V} | \mathbf{k} + \mathbf{A}(t_{\text{resc}}) \rangle \\ \times e^{-iS_{\mathbf{k}}(t_{\text{resc}})} \langle \mathbf{k} + \mathbf{A}(t_{\text{ion}}) | \mathbf{r} \cdot \mathbf{E}(t_{\text{ion}}) | \Psi_0 \rangle e^{iS_{\mathbf{k},\mathcal{E}_0}(t_{\text{ion}})} \quad (7.157)$$

with  $t_{\text{resc}}$  the rescattering time or, introducing the new variables  $t = t_{\text{resc}}$ ,  $\tau = t_{\text{resc}} - t_{\text{ion}}$ ,

$$M_p^{(\text{SFA,esc})'} = - \int_0^{\infty} dt e^{iS_{\mathbf{p},\mathcal{E}_0}(t)} \int_0^t d\tau \int d^3 k V_{\mathbf{p}-\mathbf{k}} e^{-iS_{\mathbf{k},\mathcal{E}_0}(t,\tau)} \\ \times \langle \mathbf{k} + \mathbf{A}(t-\tau) | \mathbf{r} \cdot \mathbf{E}(t-\tau) | \Psi_0 \rangle \quad (7.158)$$

where

$$S_{\mathbf{k},\mathcal{E}_0}(t, t-\tau) = \int_{t-\tau}^t dt' \left( \frac{1}{2} [\mathbf{k} + \mathbf{A}(t')]^2 - \mathcal{E}_0 \right) \quad (7.159)$$

and  $V_{\mathbf{p}-\mathbf{k}} = \langle \mathbf{p} | \hat{V} | \mathbf{k} \rangle$ . The time  $\tau$  is the time the electron spends in the continuum between ionization and rescattering. The infinite upper limit in the integration over the rescattering time in (7.157) can be restricted to  $T_p$  since rescattering after the laser is off will not lead to energy absorption. As a consequence, the final energy will be within a region strongly dominated by the more probable direct ionization process.

The integration over the intermediate momentum  $\mathbf{k}$  can be approximated seeking the momentum  $\mathbf{k}_s(t, \tau)$  contributing most to the  $\mathbf{k}$ -integration:

$$\nabla_{\mathbf{k}} S_{\mathbf{k}, \mathcal{E}_0}(t, t - \tau) \stackrel{!}{=} \mathbf{0} \quad \Rightarrow \quad \mathbf{k}_s(t, \tau) = -\frac{\alpha(t) - \alpha(t - \tau)}{\tau} \quad (7.160)$$

with  $\alpha(t)$  the excursion as in (7.104). Hence,

$$M_p^{(\text{SFA, resc})'} = - \int_0^{T_p} dt e^{iS_{p, \mathcal{E}_0}(t)} \int_0^t d\tau \left( \frac{2\pi}{i\tau} \right)^{3/2} V_{p-\mathbf{k}_s(t, \tau)} e^{-iS_{s, \mathcal{E}_0}(t, t - \tau)} \times \langle \mathbf{k}_s(t, \tau) + \mathbf{A}(t - \tau) | \mathbf{r} \cdot \mathbf{E}(t - \tau) | \Psi_0 \rangle \quad (7.161)$$

where the stationary action  $S_{s, \mathcal{E}_0}(t, t - \tau)$  is given by

$$S_{s, \mathcal{E}_0}(t, t - \tau) = S_{\mathbf{k}_s(t, \tau), \mathcal{E}_0}(t, t - \tau) \quad (7.162)$$

and the factor  $[2\pi/(i\tau)]^{3/2}$  arises from the saddle-point integration (see, e.g., [79]). In actual numerical evaluations the denominator  $i\tau$  is regularized by adding a real, positive  $\epsilon$ . The results are independent of  $\epsilon$  as long as it is not too small but much smaller than a laser period.

In the case of a hydrogen-like atom the matrix element needed in (7.161) reads

$$\langle \mathbf{k} | \mathbf{r} \cdot \mathbf{E}(t) | \Psi_0 \rangle = -i2^{7/2} (2\mathcal{E}_{\text{ip}})^{5/4} \frac{\mathbf{k} \cdot \mathbf{E}(t)}{\pi(k^2 + 2\mathcal{E}_{\text{ip}})^3}. \quad (7.163)$$

For rescattering at potentials of the form

$$V(r) = -\left(b + \frac{a}{r}\right) e^{-\lambda r} \quad (7.164)$$

the matrix element  $V_{p-k}$  is given by

$$V_{p-k} = -\frac{2b\lambda + aC}{2\pi^2 C^2}, \quad C = (\mathbf{p} - \mathbf{k})^2 + \lambda^2. \quad (7.165)$$

In few-cycle laser pulses the concept of an ionization rate is not useful since the latter would be time-dependent and sensitive to all details of the pulse (duration, shape, carrier-envelope phase, peak field strength). In experiments one measures the differential ionization probability  $w_p$ , which is the probability to find an electron of final energy  $\mathcal{E}_p = p^2/2$  emitted in a certain direction corresponding to the solid angle element  $d\Omega_p$ . The probability  $w_p$  is related to the transition matrix element  $M_p$  through

$$w_p \underbrace{d\mathcal{E}_p}_{p dp} d\Omega_p = |M_p|^2 d^3 p = |M_p|^2 p^2 dp d\Omega_p \quad (7.166)$$

so that

$$w_p = p |M_p|^2. \quad (7.167)$$

### 7.3.6 Simple Man’s Theory

The remaining time integral(s) in (7.156) and (7.161) can be either solved numerically or approximately by using (modifications of) the saddle-point method with respect to time (see [8] and Appendix B in [9]). We do not want to go into the details but only emphasize here that the SFA transition matrix element can be approximated by a sum over the stationary contributions,

$$M_p^{(\text{SFA})} = \sum_s a_{s,p} e^{iS_{s,p}}. \quad (7.168)$$

As it turns out the saddle-point equations define quantum orbits [80, 81] that are close to the classical orbits of the so-called simple man’s theory, but complex. In the following we will use simple man’s theory to derive the cut-off laws for the photoelectron spectra.

If an electron is set free at time  $t_{\text{ion}}$  and from thereon does not interact with the ionic potential anymore, its momentum and position at times  $t > t_{\text{ion}}$  are given by

$$\mathbf{p}(t) = - \int_{t_{\text{ion}}}^t dt' \mathbf{E}(t') = \mathbf{A}(t) - \mathbf{A}(t_{\text{ion}}), \quad (7.169)$$

$$\begin{aligned} \mathbf{r}(t) &= \int_{t_{\text{ion}}}^t dt' \mathbf{A}(t') - \mathbf{A}(t_{\text{ion}})(t - t_{\text{ion}}) \\ &= \boldsymbol{\alpha}(t) - \boldsymbol{\alpha}(t_{\text{ion}}) - \mathbf{A}(t_{\text{ion}})(t - t_{\text{ion}}) \end{aligned} \quad (7.170)$$

with the excursion  $\boldsymbol{\alpha}(t)$  as defined in (7.104). If the vector potential fulfills (7.155) the momentum at the end of the pulse is determined by the value of the vector potential at the time of ionization,  $\mathbf{p}(T_p) = -\mathbf{A}(t_{\text{ion}})$ , so that the final energy is

$$\mathcal{E}_{\text{dir},p}(t_{\text{ion}}) = \frac{1}{2} A^2(t_{\text{ion}}) \leq 2U_p \quad (7.171)$$

because the ponderomotive potential is  $U_p = \hat{A}^2/4$ . The fact that the direct electrons are classically restricted to energies up to  $2U_p$  is one of the celebrated cut-off laws in strong field physics.

Let us now allow for one rescattering event, i.e., at the time  $t_{\text{resc}}$  the electron returns to the origin (where the ion is located),

$$\epsilon \stackrel{!}{>} |\mathbf{r}(t_{\text{resc}})| = |\boldsymbol{\alpha}(t_{\text{resc}}) - \boldsymbol{\alpha}(t_{\text{ion}}) - \mathbf{A}(t_{\text{ion}})\tau| \quad (7.172)$$

where  $\epsilon$  is a distance small compared to the Bohr radius. Let us assume the extreme case of 180° back-reflection where the electron changes the sign of its momentum so that immediately after the scattering event

$$\mathbf{p}(t_{\text{resc}+}) = -[\mathbf{A}(t_{\text{resc}}) - \mathbf{A}(t_{\text{ion}})]. \quad (7.173)$$

At later times we have

$$\begin{aligned} \mathbf{p}(t > t_{\text{resc}}) &= - \int_{t_{\text{resc}}}^t dt' \mathbf{E}(t') - [\mathbf{A}(t_{\text{resc}}) - \mathbf{A}(t_{\text{ion}})] \\ &= \mathbf{A}(t) - 2\mathbf{A}(t_{\text{resc}}) + \mathbf{A}(t_{\text{ion}}) \end{aligned} \quad (7.174)$$

so that  $\mathbf{p}_{\text{resc}}(T_p) = -2\mathbf{A}(t_{\text{resc}}) + \mathbf{A}(t_{\text{ion}})$  and

$$\mathcal{E}_{\text{resc},p}(t_{\text{resc}}, t_{\text{ion}}) = \frac{1}{2}[\mathbf{A}(t_{\text{ion}}) - 2\mathbf{A}(t_{\text{resc}})]^2 \leq 10U_p. \quad (7.175)$$

Because of the condition (7.172) the  $10U_p$  cut-off law for the rescattered electrons is not so obvious. However, it can be readily checked numerically by plotting  $\mathcal{E}_{\text{resc},p}(t_{\text{resc}}, t_{\text{ion}})$  vs all possible  $t_{\text{resc}}, t_{\text{ion}}$  (where  $t_{\text{resc}} > t_{\text{ion}}$ ) and then indicating those pairs of  $t_{\text{ion}}, t_{\text{resc}}$  that fulfill (7.172). The result is shown in Fig. 7.12.

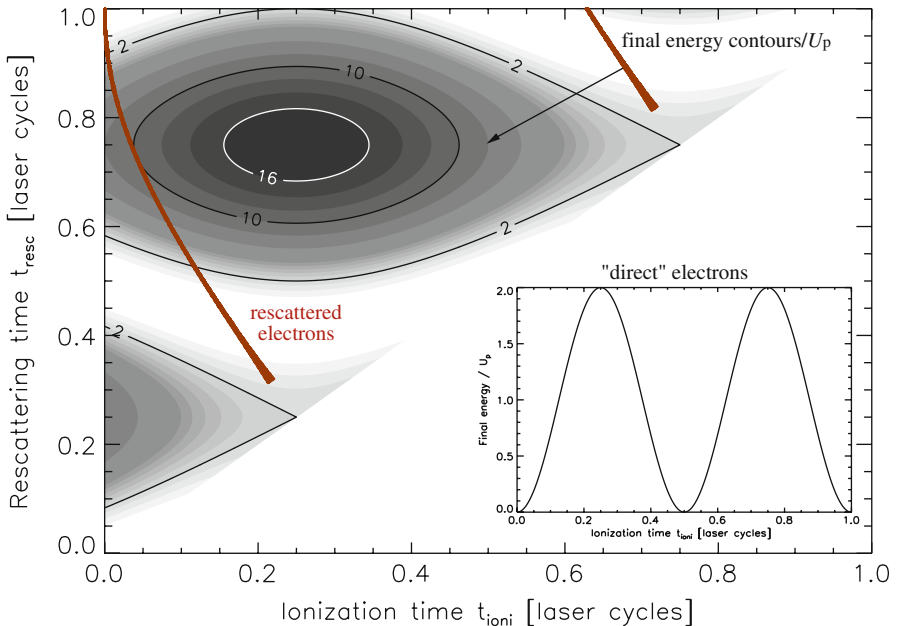


**Fig. 7.12** Final photoelectron energy  $\mathcal{E}_{\text{resc},p}$  vs ionization time  $t_{\text{ion}}$  and rescattering time  $t_{\text{resc}} > t_{\text{ion}}$  (black: high value of  $\mathcal{E}_{\text{resc},p}$ , white: small value of  $\mathcal{E}_{\text{resc},p}$ , contours 2, 10 and  $16U_p$  labeled explicitly). The branch labeled “rescattered electrons” indicates times  $t_{\text{ion}}$  and  $t_{\text{resc}}$  where (7.172) is fulfilled (for an  $\epsilon \ll 1$ ). The highest energy those rescattered electrons can have is  $10U_p$  (see branch touching the  $10U_p$ -contour). The inset shows the final energy (7.171) of the “direct” electrons vs the ionization time. The highest energy there is  $2U_p$

### 7.3.6.1 How Good Is the Strong Field Approximation?

In order to answer this question we compare the results of an ab initio TDSE solution with the corresponding SFA predictions. Apart from the dipole approximation (which is well applicable here) the TDSE result is exact. Comparisons with TDSE results serve as a much more demanding testing ground for approximate theories such as the SFA than comparison with experiments, because of focal averaging effects present in experiments, the uncertainties in laser intensity, pulse duration, and shape, the limited resolution in energy, and the limited dynamic range in the yields.

In Fig. 7.13 the results for an  $n = 4$ -cycle pulse of the form  $\mathbf{E}(t) = \hat{E} \mathbf{e}_z \sin^2[\omega t/(2n)] \cos(\omega t + \phi)$  for  $0 < t < n2\pi/\omega$ ,  $\omega = 0.056$ ,  $\hat{E} = 0.0834$ ,  $\phi = 0$  are shown. The agreement between TDSE and SFA results improve with increasing photoelectron energy. A possible explanation for that might be that slow electrons spend more time in the vicinity of the atomic potential where Coulomb corrections are expected to be important. As can be seen in Fig. 7.13, the transition regime between the cut-off for the direct electrons at  $\mathcal{E} = 2U_p = 1.1$  up to energies where rescattered electrons start to take over at  $\mathcal{E} \approx 2.5$  is quite smooth in the TDSE spectra whereas pronounced interference patterns are visible in the SFA results. Moreover, at very low energies the positions of the local maxima disagree. It has been shown that the agreement at lower energies improves if the binding potential is made short-range by cutting it at certain distances. This is expected since the crucial assumption in SFA is that the electron is not affected by the ionic potential anymore once ionization has occurred [9, 82]. This assumption is well justified for short-range potentials but less so for long range Coulombic ones as, e.g., in the H(1s) case.

A lot of effort has been devoted to the development of Coulomb-corrections, taking into account the effect of the Coulomb-potential on the outgoing electron, e.g. in [83–86]. However, only a few of them are able to reproduce the striking features seen in experimental and numerical ab initio spectra, which are in strong disagreement with the plain SFA, such as rotated angular distributions [87], fan-like structures in momentum distributions at low energies [85], and the recently observed “low energy feature” at long wavelengths [88]. The pronounced interference pattern showing a spiky, downward-pointing structure in the rescattering plateau in Fig. 7.13 between energies  $\approx 3$  and  $6$  a.u. instead is remarkably well reproduced using the extended SFA taking into account (7.158) without further Coulomb-correction.

### 7.3.7 Interference Effects

The spiky structure in Fig. 7.13 is due to quantum interference. For a fixed final momentum  $\mathbf{p}$  the sum (7.168) is a sum over all quantum orbits that end up with the same momentum at the detector. It turns out that, most of the time, there are two dominating contributions per cycle. Depending on their phase-difference those may interfere constructively (local maxima in Fig. 7.13) or destructively (downward-

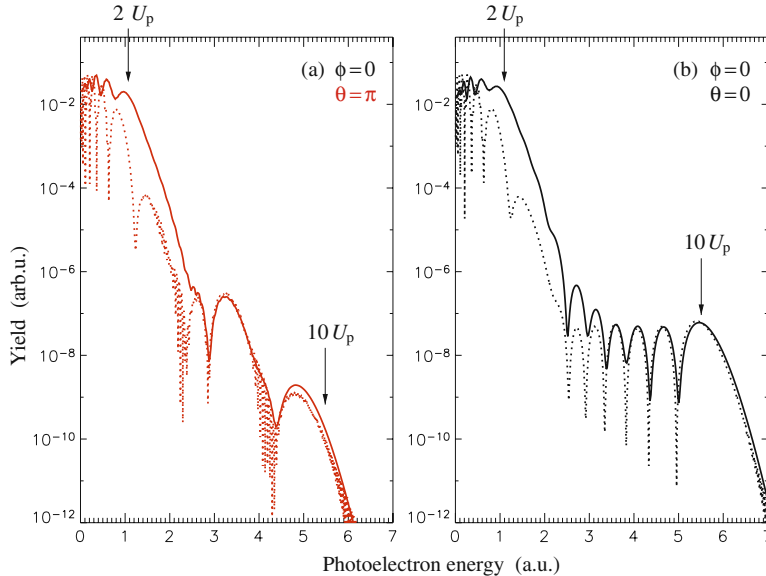


**Fig. 7.13** Photoelectron spectra of the H(1s) electron after irradiation with a 4-cycle laser pulse ( $\omega = 0.056$ ,  $\phi = 0$ ,  $\hat{E} = 0.0834$ ). The TDSE and SFA results are drawn solid and dashed, respectively. Panel **(a)** shows the “left-going” electrons (i.e., opposite to the laser polarization  $e_z$ ), panel **(b)** the “right-going” electrons (in  $e_z$ -direction). The spectra were adjusted vertically by multiplication with a single factor in such a way that agreement is best in the cut-off region for the right-going electrons. The spectra were not shifted in energy

pointing spikes in Fig. 7.13). The corresponding two trajectories of simple man’s theory can be readily calculated. As an example we show the final energy vs the ionization time for a “flat-top” pulse in Fig. 7.14. In the lower panel of Fig. 7.14 the course of the electric field is indicated. Let us focus on the time  $t = 0.5$  cycles where the electric field has a maximum and ionization is therefore most likely. The upper panel shows that a “direct” electron emitted at that time will have vanishing final energy. In order for a direct, classical electron to have the maximum energy  $2U_p$  it has to be emitted at times where the electric field is zero (which is unlikely in the tunneling and over-barrier regime). However, if an electron is emitted around the maximum of the electric field and rescatters once, its final energy may be close to  $10U_p$ . It is clearly seen that two emission times very close to each other lead to the same final energy (as indicated in the upper panel). These are the two trajectories that interfere. Exactly at the cut-off  $10U_p$  those two solutions merge to a single one. The “travel times”  $t_{\text{esc}} - t_{\text{ion}}$  between rescattering and ionization are color-coded from black ( $t_{\text{esc}} - t_{\text{ion}} = 0$ ) to yellow ( $t_{\text{esc}} - t_{\text{ion}} = 2$  cycles).

In very short pulses the situation is more complex than in the regular, flat-top pulse case. Since the ionization probability is strongly weighted with the modulus of the electric field, only a few “time-windows” may remain “open”, thus affecting the number of interfering quantum orbits for a given  $p$ . The interference pattern is

then very sensitive to the details of the few-cycle pulse, e.g., to the carrier-envelope phase. Because of the “time-windows” that are opened and closed depending on the parameters of the few-cycle pulse, one may view the setup as a “double slit experiment in time” [89], a detailed analysis of which is given in [16]. There are two dominating quantum trajectories contributing to a given final momentum in the case of linear polarization. One of them goes directly to the detector while the other one starts in the “wrong” direction but turns around within a fraction of a laser half period. It thus sweeps over the nucleus on the way towards the detector. The two quantum orbits correspond to the reference wave and the object wave in a holography experiment. Hence, the interference pattern in the momentum spectra may be viewed as a hologram of the binding potential [90, 91].

### 7.3.8 High-Order Harmonic Generation

When an intense laser pulse of frequency  $\omega_1$  impinges on any kind of target, in general harmonics of  $\omega_1$  are emitted. A typical signature of the emission spectrum in the case of strongly driven atoms, molecules or clusters is that the harmonic yield does not simply roll-off exponentially with increasing harmonic order. Instead, a plateau is observed. This is a prerequisite for high-order harmonic generation (HOHG)

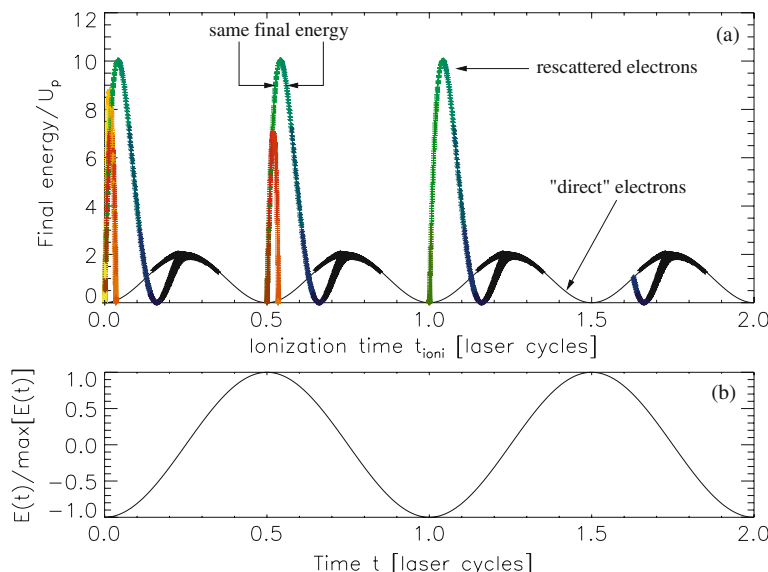


**Fig. 7.14** (a) Final energy of direct electrons (black line) vs the ionization time. If rescattering is allowed, higher energies may occur. The color coding for the rescattered electrons indicates the time spent in the continuum between ionization and rescattering (the lighter the color the longer the time). The cut-off energies for the direct and the rescattered electrons are 2 and  $10U_p$ , respectively. Panel (b) shows the course of the laser field. Ionization is improbable for small  $|E(t)|$

being of practical relevance as an efficient short wavelength source. As targets for HOHG one may think of single atoms, dilute gases of atoms, molecules, clusters, crystals, or the surface of a solid (which is rapidly transformed into a plasma by the laser). In fact, for all those targets HOHG has been observed experimentally. Even a strongly driven two-level system displays nonperturbative HOHG [92, 93]. The mechanism generating the harmonics and its efficiency, of course, vary with the target-type. In the case of atoms the so-called “three-step model” explains the basic mechanism in the spirit of simple man’s theory: an electron is freed by the laser at a certain time  $t'$ , subsequently it oscillates in the laser field, and eventually recombines with its parent ion upon emitting a photon of frequency

$$\omega = n \omega_1, \quad n \geq 1. \quad (7.176)$$

This process is illustrated in Fig. 7.15. If the energy of the returning electron is  $\mathcal{E}$ , the energy of the emitted photon is  $\omega = \mathcal{E} + |\mathcal{E}_f|$  where  $\mathcal{E}_f$  is the energy of the level which is finally occupied by the electron, for example, the groundstate.

From this simple considerations we conclude that the maximum photon energy one can expect is  $\omega_{\max} = \mathcal{E}_{\max} + |\mathcal{E}_f|$ . Using (7.169) we obtain at the recombination time  $t_{\text{rec}}$  for the return energy  $\mathcal{E}_{\text{ret}}$

$$\mathcal{E}_{\text{ret}} = \frac{1}{2} p^2(t_{\text{rec}}) = \frac{1}{2} [\mathbf{A}(t_{\text{rec}}) - \mathbf{A}(t_{\text{ion}})]^2 \quad (7.177)$$

where we have to impose [see (7.172)]

$$|\mathbf{r}(t_{\text{rec}})| = |\boldsymbol{\alpha}(t_{\text{rec}}) - \boldsymbol{\alpha}(t_{\text{ion}}) - \mathbf{A}(t_{\text{ion}})(t_{\text{rec}} - t_{\text{ion}})| \stackrel{!}{<} \epsilon. \quad (7.178)$$

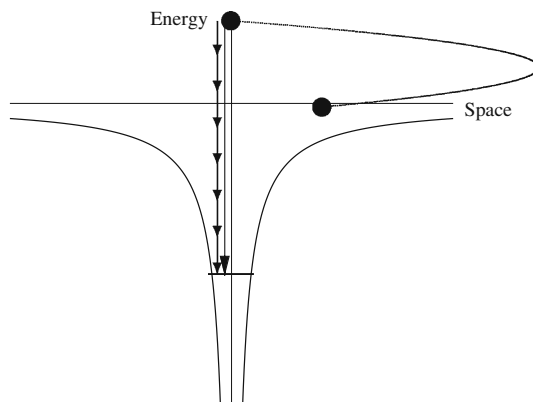


**Fig. 7.15** Illustration of the three-step model for high harmonic generation. An electron is (i) released, (ii) accelerated in the laser field, and (iii) driven back to the ion. There it may recombine upon emitting a single photon which corresponds to a multiple of the photon energy of the incident laser light

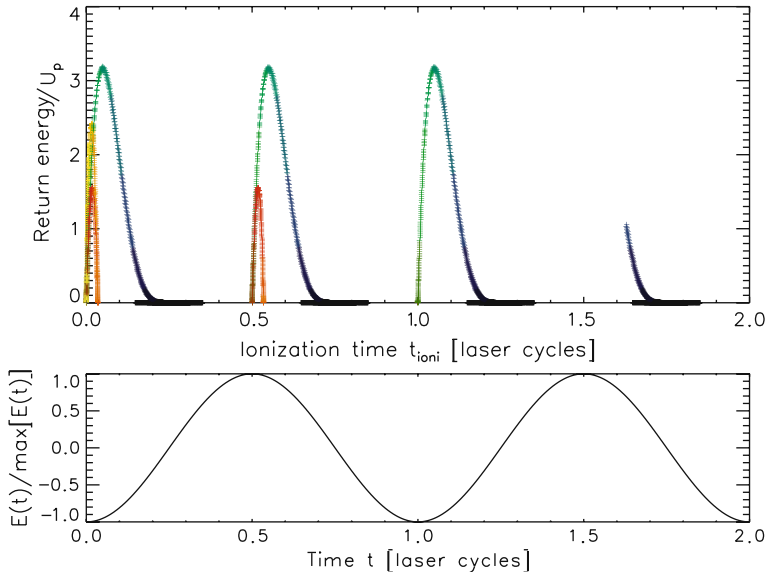


**Fig. 7.16** Return energy as a function of the ionization time. The color coding indicates the time between ionization and recombination (the longer this time the lighter the color). The maximum return energy is  $\simeq 3.17U_p$ . The course of the laser field is shown in the lower panel

Figure 7.16 shows the possible return energies fulfilling (7.177) and (7.178). We infer that the maximum return energy is around  $\simeq 3.2$ . Closer inspection shows that the number is 3.17 so that the cut-off law reads

$$\omega_{\max} = 3.17U_p + |\mathcal{E}_f|. \quad (7.179)$$

This celebrated  $\approx 3U_p$  cut-off rule was first established empirically [94] and explained soon after within simple man's theory [95, 96].

Lewenstein and co-workers [97] showed that, more precisely, it reads  $\omega_{\max} = 3.17U_p + 1.32|\mathcal{E}_f|$ .

From simple man's theory one expects that harmonic generation should be much less efficient in elliptically polarized laser fields since, classically, the freed electron never comes back to its parent ion so that recombination can be considered unlikely. This indeed was confirmed experimentally (see [10], and references therein).

Harmonic generation in atoms, molecules and clusters has huge practical relevance as an efficient source of intense XUV radiation. This is because (i) the ponderomotive scaling of the cut-off allows to achieve high values of  $\mathcal{E}_{\max}$  and thus high harmonic orders  $n$ , and (ii), fortunately, the strength of the harmonics does not decay exponentially with the order  $n$  but displays, after a decrease over the first few harmonics, an overall plateau (at least on the logarithmic scale) up to the cut-off energy  $3.17U_p + |\mathcal{E}_f|$ , allowing relatively high intensities at short wavelengths. In

fact, high-order harmonics below  $\lambda = 4.4$  nm, the so-called water-window (between the K-edges of carbon and oxygen) have been observed experimentally [98, 99]. The intensity of the emitted radiation in the plateau region is about  $10^{-6}$  of the incident laser intensity which is typically  $10^{15}\text{--}10^{18}\text{ Wcm}^{-2}$  in rare gas experiments. Therefore, the intensity of the high-order harmonics is sufficient for various kinds of applications, such as interferometry, for dense plasma diagnostics, holography, high-contrast microscopy of biological materials, and attosecond spectroscopy or metrology. Attosecond pulses are generated via harmonic generation. If the incoming pulse is already short (i.e., consists only of a few cycles) the harmonic emission is restricted to a narrow time window similar to the “double slit in time”-experiment mentioned above. As a consequence, the harmonic pulse has a duration that is short compared to the laser period of the incoming pulse (usually a few hundred attoseconds). If the incoming laser pulse is longer, one can construct attosecond pulse trains by selecting a few phase-locked harmonics. Attosecond pulses that are generated via harmonic generation have been used to probe the ionizing laser field itself [100] as well as fast atomic processes such as Auger decay [101].

For calculating the rate of harmonic emission one may follow the same route as in the SFA treatment of ionization. Harmonic generation and ATI are complementary to each other: while in harmonic generation the electron comes back to the ion and eventually recombines, upon emitting radiation, in high-order ATI it rescatters upon which it may gain additional energy. In harmonic generation one observes a plateau reaching up to photon energies  $3.17 U_p + |\mathcal{E}_f|$ . In ATI a plateau is observed as well – this time with respect to the kinetic energy of the photo electrons – extending up to  $10 U_p$  (for one rescattering event).

In classical electrodynamics, the total radiated power by a dipole of charge  $q$  is given by Larmor’s formula

$$P = \frac{2q^2}{3c^3} |\ddot{\mathbf{r}}|^2. \quad (7.180)$$

Thus, in a semiclassical approach, it appears reasonable to replace the acceleration by its quantum mechanical expectation value and making use of Ehrenfest’s theorem. One obtains (in length gauge)

$$P = \frac{2q^2}{3c^3} \left| \frac{d^2}{dt^2} \langle \hat{\mathbf{r}} \rangle \right|^2 = \frac{2q^2}{3c^3} \left| \frac{1}{m} \left\langle -\frac{\partial \hat{H}}{\partial \hat{\mathbf{r}}} \right\rangle \right|^2. \quad (7.181)$$

The last expression on the right-hand side is particularly suited for the numerical evaluation of the harmonic spectra. In order to simplify even further we write the dipole as a Fourier-transform,

$$\mathbf{d}(t) = q \langle \hat{\mathbf{r}} \rangle = \frac{1}{\sqrt{2\pi}} \int_{-\infty}^{\infty} d\omega \exp(i\omega t) \mathbf{d}(\omega). \quad (7.182)$$

The total emitted energy then is

$$\mathcal{E}_{\text{rad}} = \int_{-\infty}^{\infty} dt P = \frac{2}{3c^3} \int_{-\infty}^{\infty} d\omega \omega^4 |\mathbf{d}(\omega)|^2, \quad (7.183)$$

and we infer that the yield radiated into a spectral interval  $[\omega, \omega + d\omega]$  is

$$\epsilon_{\text{rad}, \omega} d\omega \sim \omega^4 |\mathbf{d}(\omega)|^2 d\omega. \quad (7.184)$$

A full quantum mechanical treatment reveals that calculating the harmonic spectrum emitted by a single atom from the square of the dipole expectation value is actually incorrect [92, 102]. Since the expectation value of the number of photons in a mode  $\omega, \mathbf{k}$  (with creation and annihilation operators  $\hat{a}^\dagger, \hat{a}$ , respectively) at time  $t$  is [103]

$$\begin{aligned} \langle \hat{a}^\dagger(t) \hat{a}(t) \rangle &= \langle \hat{a}^\dagger(t_i) \hat{a}(t_i) \rangle + 2C \Re \int_{t_i}^t dt' \langle \hat{\mathbf{r}}(t') \hat{a}(t_i) \rangle \exp(-i\omega t') \\ &\quad + C^2 \int_{t_i}^t dt' \int_{t_i}^t dt'' \langle \hat{\mathbf{r}}(t'') \hat{\mathbf{r}}(t') \rangle \exp[i\omega(t' - t'')], \end{aligned} \quad (7.185)$$

where  $C$  is a coupling constant, one sees that if the mode under consideration is not excited at the initial time  $t = t_i$ , as it is the case here, only the third term survives. This term accounts for spontaneous emission and scattering. Hence, the harmonic spectrum of a single atom should be calculated from the two-time dipole-dipole correlation function  $\langle \hat{\mathbf{r}}(t'') \hat{\mathbf{r}}(t') \rangle$  instead of the Fourier-transformed one-time dipole. However, if one considers a sample of  $N$  atoms

$$\langle \hat{a}^\dagger(t) \hat{a}(t) \rangle = C^2 \sum_{k=1}^N \sum_{j=1}^N \int_{t_i}^t dt' \int_{t_i}^t dt'' \langle \hat{\mathbf{r}}_k(t'') \hat{\mathbf{r}}_j(t') \rangle \exp[i\omega(t' - t'')] \quad (7.186)$$

results and, by assuming that all these atoms are uncorrelated, that is  $\langle \hat{\mathbf{r}}_k(t'') \hat{\mathbf{r}}_j(t') \rangle \simeq \langle \hat{\mathbf{r}}_k(t'') \rangle \langle \hat{\mathbf{r}}_j(t') \rangle$ , one arrives at

$$\langle \hat{a}^\dagger(t) \hat{a}(t) \rangle \approx C^2 \left| \sum_{k=1}^N \int_{t_i}^t dt' \langle \hat{\mathbf{r}}_k(t') \rangle \exp(i\omega t') \right|^2 \quad (7.187)$$

if  $N \gg 1$  is assumed so that the self-interaction terms  $\sim \langle \hat{\mathbf{r}}_k(t'') \rangle \langle \hat{\mathbf{r}}_k(t') \rangle$  contribute negligibly. Moreover, if all atoms “see” the same field one obtains simply the absolute square of  $N$  times the single dipole expectation value. Therefore, calculating the harmonic spectra from the Fourier-transformed dipole, although not correct in the single atom response case, is a reasonable method when comparison with HOHG experiments in dilute gas targets is made. Hence, for the study of macroscopic

propagation effects the dipole expectation value may be inserted as a source into Maxwell's equations.

### 7.3.9 Strong Field Approximation for High-Order Harmonic Generation: the Lewenstein Model

The dipole expectation value of a single atom with one active electron ( $q = -1$ ) is

$$\begin{aligned} \mathbf{d}(t) &= -\langle \Psi(t) | \hat{\mathbf{r}} | \Psi(t) \rangle \\ &= -\langle \Psi_0(t_i) | \hat{U}(t_i, t) \hat{\mathbf{r}} \hat{U}(t, t_i) | \Psi_0(t_i) \rangle, \end{aligned} \quad (7.188)$$

where we assumed again that at the initial time  $t_i$  the electron starts in the state  $|\Psi_0(t_i)\rangle =: |\Psi_0\rangle$ . Using (7.125) we obtain

$$\begin{aligned} \mathbf{d}(t) &= -\langle \Psi_0(t) | \hat{\mathbf{r}} | \Psi_0(t) \rangle \\ &\quad -i \int_{t_i}^t dt' \langle \Psi_0(t') | \hat{W}(t') \hat{U}(t', t) \hat{\mathbf{r}} | \Psi_0(t) \rangle \\ &\quad +i \int_{t_i}^t dt' \langle \Psi_0(t) | \hat{\mathbf{r}} \hat{U}(t, t') \hat{W}(t') | \Psi_0(t') \rangle \\ &\quad - \int_{t_i}^t dt' \int_{t_i}^t dt'' \langle \Psi_0(t') | \hat{W}(t') \hat{U}(t', t) \hat{\mathbf{r}} \hat{U}(t, t'') \hat{W}(t'') | \Psi_0(t'') \rangle. \end{aligned} \quad (7.189)$$

The first term vanishes for a spherically symmetric binding potential. The second and third term are complex conjugates of each other and describe ionization ( $\hat{W}$ ), propagation ( $\hat{U}$ ), and recombination ( $\hat{\mathbf{r}}$ ) (i.e., the emission of harmonic radiation) in different time-ordering. The last term involves one additional interaction with the laser field. We will neglect it here (see [104]). As in the SFA for ionization we replace the full time evolution operator  $\hat{U}$  by  $\hat{U}^{(V)}$ ,

$$\mathbf{d}^{(L)}(t) = -i \int_{t_i}^t dt' \langle \Psi_0(t') | \hat{W}(t') \hat{U}^{(V)}(t', t) \hat{\mathbf{r}} | \Psi_0(t) \rangle + \text{c.c.}, \quad (7.190)$$

recovering the Lewenstein-result [97]. In length gauge  $[\hat{W}(t) = \mathbf{E}(t) \cdot \hat{\mathbf{r}}]$  we obtain (suppressing the “+c.c.”)

$$\mathbf{d}^{(L)}(t) = -i \int_{t_i}^t dt' \int d^3 p \langle \Psi_0(t') | \mathbf{E}(t') \cdot \hat{\mathbf{r}} | \mathbf{p} + \mathbf{A}(t') \rangle \langle \mathbf{p} + \mathbf{A}(t) | \hat{\mathbf{r}} | \Psi_0(t) \rangle e^{-iS_p(t', t)} \quad (7.191)$$

where we used (7.123) and  $\hat{U}^{(V)}(t', t) | \mathbf{p} + \mathbf{A}(t) \rangle = e^{-iS_p(t', t)} | \mathbf{p} + \mathbf{A}(t') \rangle$ . With

$$S_{\mathbf{p}, \mathcal{E}_0}(t, t') = \int_{t'}^t dt'' \left( \frac{1}{2} [\mathbf{p} + \mathbf{A}(t'')]^2 - \mathcal{E}_0 \right) \quad (7.192)$$

we can write (7.191) as

$$\mathbf{d}^{(L)}(t) = -i \int_{t_i}^t dt' \int d^3 p \langle \Psi_0 | \mathbf{E}(t') \cdot \hat{\mathbf{r}} | \mathbf{p} + \mathbf{A}(t') \rangle \langle \mathbf{p} + \mathbf{A}(t) | \hat{\mathbf{r}} | \Psi_0 \rangle e^{-iS_{\mathbf{p},\mathcal{E}_0}(t',t)}. \quad (7.193)$$

Introducing the dipole matrix element

$$\boldsymbol{\mu}(\mathbf{p}) = \langle \mathbf{p} | \hat{\mathbf{r}} | \Psi_0 \rangle = i \nabla_{\mathbf{p}} \langle \mathbf{p} | \Psi_0 \rangle = \frac{1}{(2\pi)^{3/2}} \int d^3 r e^{-i\mathbf{p} \cdot \mathbf{r}} \mathbf{r} \Psi_0(\mathbf{r}) \quad (7.194)$$

we have

$$\mathbf{d}^{(L)}(t) = i \int_{t_i}^t dt' \int d^3 p e^{-iS_{\mathbf{p},\mathcal{E}_0}(t,t')} \boldsymbol{\mu}^*[\mathbf{p} + \mathbf{A}(t)] \mathbf{E}^*(t') \cdot \boldsymbol{\mu}[\mathbf{p} + \mathbf{A}(t')] + \text{c.c.}$$

The integration over momentum can be approximated using the stationary phase method again, i.e.,

$$\nabla_{\mathbf{p}} S_{\mathbf{p},\mathcal{E}_0}(t, t') \stackrel{!}{=} 0. \quad (7.195)$$

For a linearly polarized laser pulse with a slowly varying envelope we have

$$\mathbf{E}(t) = \hat{E} \mathbf{e}_z \cos \omega t, \quad \mathbf{A}(t) = -\frac{\hat{E}}{\omega} \mathbf{e}_z \sin \omega t, \quad (7.196)$$

so that

$$\boldsymbol{\alpha}(t) - \boldsymbol{\alpha}(t') = \int_{t'}^t dt'' \mathbf{A}(t'') = \frac{\hat{E}}{\omega^2} \mathbf{e}_z (\cos \omega t - \cos \omega t') \quad (7.197)$$

and

$$\frac{\partial S_{\mathbf{p},\mathcal{E}_0}(t, t')}{\partial p_z} = p_z(t - t') + \frac{\hat{E}}{\omega^2} (\cos \omega t - \cos \omega t') \stackrel{!}{=} 0 \quad (7.198)$$

$$\Rightarrow p_{z,s}(t, \tau) = -\frac{\hat{E} [\cos \omega t - \cos \omega(t - \tau)]}{\omega^2 \tau}, \quad \tau = t - t'. \quad (7.199)$$

The transverse stationary momentum vanishes,  $p_{x,s} = p_{y,s} = 0$ . Plugging  $\mathbf{p}_s$  into (7.192) and integrating yield the stationary action

$$S_s(t, \tau) = (U_p - \mathcal{E}_0)\tau - 2U_p \frac{1 - \cos \omega \tau}{\omega^2 \tau} - U_p \frac{C(\tau)}{\omega} \cos[(2t - \tau)\omega] \quad (7.200)$$

with

$$C(\tau) = \sin \omega \tau - \frac{4}{\omega \tau} \sin^2 \frac{\omega \tau}{2}. \quad (7.201)$$

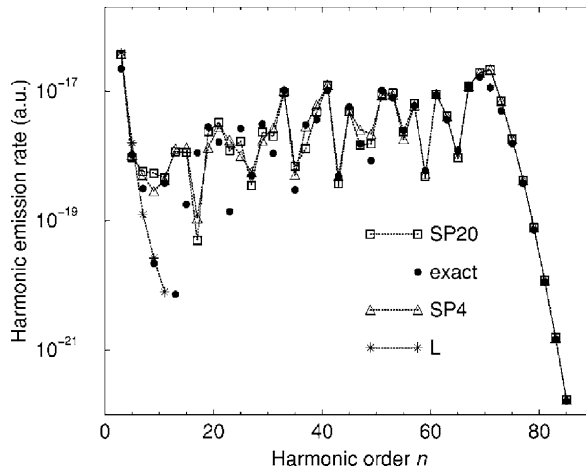


**Fig. 7.17** Harmonic spectrum obtained using the SFA (Lewenstein model) for H(1s),  $2 \times 10^{14} \text{ Wcm}^{-2}$ , and photon energy 1.17 eV. The time integral in (7.202) was calculated either directly (labeled “exact”) or applying the saddle-point approximation. The expected cut-off at harmonic order  $n = 72.3$  is confirmed (from [105])

In the original Lewenstein-paper [97] it is shown that the cut-off law  $3.17U_p + \mathcal{E}_{ip}$  can be derived from the function  $C(\tau)$ . Setting  $t_i = 0$ , the final result for the SFA dipole after saddle-point integration reads

$$\begin{aligned} d^{(L)}(t) = i \int_0^t d\tau & \left( \frac{2\pi}{i\tau} \right)^{3/2} \mu_z^* [p_{z,s}(t, \tau) + A(t)] \\ & \times \mu_z [p_{z,s}(t, \tau) + A(t - \tau)] \hat{E} \cos[\omega(t - \tau)] e^{-iS_s(t, \tau)} + \text{c.c.} \end{aligned} \quad (7.202)$$

from which, via Fourier-transformation, the harmonic spectra  $\epsilon_{rad, \omega}$  (7.184) can be calculated. Figure 7.17 shows an example for a harmonic spectrum calculated using the Lewenstein model.

### 7.3.10 Harmonic Generation Selection Rules

As the name “harmonics” suggests, the emission of laser-driven targets mainly occurs at multiples of the fundamental, incoming laser frequency  $\omega_1$ , that is  $\omega = n\omega_1$  with  $n$  the harmonic order. In the case of atoms in a linearly polarized laser field, for instance, only odd harmonics are emitted, i.e.,  $n = 1, 3, 5, \dots$ . One could think that this “quantized” emission is a quantum effect. However, this is not the case. Pure classical simulations also show harmonic generation and not just continuous spectra. The selection rules governing which harmonic orders  $n$  are allowed and which are forbidden are determined by the symmetry of the combined system target + laser field, i.e., the symmetry of the field-dressed target, also called dynamical

symmetry. We shall now employ the Floquet theory introduced in Sect. 7.3.1 to derive the selection rules for harmonic emission for a few exemplary systems.

Let  $\hat{H}(t)$  be the Hamiltonian of an electron in a linearly polarized monochromatic laser field  $E \cos(\omega_1 t) \mathbf{e}_z$  of amplitude  $E$  and an ionic potential  $\hat{V}(\hat{\mathbf{r}})$ ,

$$\hat{H}(t) = \frac{\hat{p}^2}{2} + \hat{V}(\hat{\mathbf{r}}) + E\hat{z} \cos \omega_1 t. \quad (7.203)$$

The Schrödinger equation reads  $i\frac{d}{dt}|\Psi(t)\rangle = \hat{H}(t)|\Psi(t)\rangle$ , and since the Hamiltonian is periodic in time,

$$\hat{H}(t + 2\pi/\omega_1) = \hat{H}(t), \quad (7.204)$$

from the Floquet theorem (cf. Sect. 7.3.1)

$$|\Psi(t)\rangle = e^{-ie\epsilon t}|\Phi(t)\rangle, \quad |\Phi(t + 2\pi/\omega_1)\rangle = |\Phi(t)\rangle \quad (7.205)$$

follows, and  $|\Phi(t)\rangle$  fulfills the Schrödinger equation

$$\hat{\mathcal{H}}(t)|\Phi(t)\rangle = \epsilon|\Phi(t)\rangle, \quad \hat{\mathcal{H}}(t) = \hat{H}(t) - i\frac{d}{dt} \quad (7.206)$$

which looks like a stationary Schrödinger equation in an extended Hilbert space [106] with the time as an additional dimension and  $\epsilon$  a quasi-energy. The scalar product in this extended Hilbert space reads

$$\langle\langle\Phi|\Phi'\rangle\rangle := \frac{\omega_1}{2\pi} \int_0^{2\pi/\omega_1} dt \langle\Phi(t)|\Phi'(t)\rangle. \quad (7.207)$$

For the derivation of the harmonic generation selection rules we consider an infinitely long laser pulse and assume that the system is well described by a single, nondegenerate Floquet state. The only nonvanishing dipole expectation value is in field-direction and then reads

$$d(t) = -\langle\Psi(t)|\hat{z}|\Psi(t)\rangle = -\langle\Phi(t)|\hat{z}|\Phi(t)\rangle. \quad (7.208)$$

We define the dipole strength of the harmonic  $n$  as

$$|d(n)|^2 = \left| \frac{\omega_1}{2\pi} \int_0^{2\pi/\omega_1} dt \exp(-in\omega_1 t) d(t) \right|^2 = \left| \langle\langle\Phi|\exp(-in\omega_1 t)\hat{z}|\Phi\rangle\rangle \right|^2, \quad (7.209)$$

which is proportional to the absolute square of the Fourier-transformed dipole. The squared, extended Hilbert space matrix element on the right-hand side of (7.209)

may be also interpreted as the probability for a transition from a Floquet state to itself, generated by the operator  $\exp(-in\omega_1 t) \hat{z}$ , accompanied by the emission of radiation of frequency  $n\omega_1$ .

The Floquet–Hamiltonian  $\hat{\mathcal{H}}(t)$  is invariant under space inversion plus a translation in time by  $\pi/\omega_1$ ,

$$\hat{P}_{\text{inv}} = (\mathbf{r} \rightarrow -\mathbf{r}, t \rightarrow t + \pi/\omega_1) \quad (7.210)$$

so that  $\hat{P}_{\text{inv}}|\Phi\rangle = \sigma|\Phi\rangle$ , and  $\sigma$  is a phase, i.e.,  $|\sigma|^2 = 1$ . Inserting the unity  $\hat{P}_{\text{inv}}^{-1}\hat{P}_{\text{inv}}$  in the matrix element in (7.209) twice yields

$$\begin{aligned} \langle\langle\Phi|\exp(-in\omega_1 t)\hat{z}|\Phi\rangle\rangle &= \underbrace{\langle\langle\Phi|\hat{P}_{\text{inv}}^{-1}\hat{P}_{\text{inv}}\exp(-in\omega_1 t)\hat{z}\hat{P}_{\text{inv}}^{-1}\hat{P}_{\text{inv}}|\Phi\rangle\rangle}_{\langle\langle\Phi|\sigma^*\rangle\rangle} \\ &= \langle\langle\Phi|\hat{P}_{\text{inv}}\exp(-in\omega_1 t)\hat{z}\hat{P}_{\text{inv}}^{-1}|\Phi\rangle\rangle = -\exp(-in\pi)\langle\langle\Phi|\exp(-in\omega_1 t)\hat{z}|\Phi\rangle\rangle. \end{aligned}$$

It follows that  $n$  must be odd in order to fulfill

$$-\exp(-in\pi) = 1. \quad (7.211)$$

Hence, only odd harmonics are emitted in the case of linearly polarized laser pulses impinging on spherically symmetric systems such as atoms.

In the case of monochromatic circularly polarized laser light (with the electric field vector in the  $xy$ -plane) the Floquet–Hamiltonian may be written (using the cylindrical coordinates  $\rho$  and  $\varphi$ ) as

$$\hat{\mathcal{H}}(t) = \hat{H}_{\text{kin}} + \hat{V}(\hat{\mathbf{r}}) + \frac{E}{\sqrt{2}}\rho \cos(\varphi - \omega_1 t) - i\frac{d}{dt}. \quad (7.212)$$

This expression is invariant under the continuous symmetry operation

$$\hat{P}_{\text{rot}} = (\varphi \rightarrow \varphi + \theta, t \rightarrow t - \theta/\omega_1) \quad (7.213)$$

with  $\theta$  an arbitrary real number. We thus have

$$\begin{aligned} &\langle\langle\Phi|\exp(-in\omega_1 t)\rho\exp(\mp i\varphi)|\Phi\rangle\rangle \\ &= \exp(in\theta \mp i\theta)\langle\langle\Phi|\exp(-in\omega_1 t)\rho\exp(\mp i\varphi)|\Phi\rangle\rangle \end{aligned}$$

where  $\rho\exp(\mp i\varphi)$  is the dipole operator for circularly polarized light (with the same helicity (−) and the opposite helicity (+) as the incident pulse, respectively). Hence, for all  $\theta$

$$\exp[i\theta(n \mp 1)] = 1 \quad (7.214)$$

must hold, which cannot be fulfilled for any  $n > 1$  so that no harmonics are emitted. However, circularly polarized harmonics may be emitted if bichromatic incident laser light is used [107–109]. With the two lasers polarized in opposite directions and frequencies  $\omega_1$  and  $m\omega_1$ , respectively, the interaction Hamiltonian reads

$$\hat{W}(t) = \frac{E_1}{\sqrt{2}}\rho \cos(\varphi - \omega_1 t) + \frac{E_2}{\sqrt{2}}\rho \cos(\varphi + m\omega_1 t). \quad (7.215)$$

$E_1$  and  $E_2$  are the electric field amplitudes of the first and second laser, respectively. The symmetry operation under which the Floquet–Hamiltonian is invariant now reads

$$\hat{P}_{\text{rot}}^{(m+1)} = \left( \varphi \rightarrow \varphi + \frac{2\pi}{m+1}, t \rightarrow t - \frac{2\pi}{\omega_1(m+1)} \right). \quad (7.216)$$

In the same manner as in the two previous examples one arrives at the condition

$$1 = \exp\left(i2\pi \frac{n \mp 1}{m+1}\right). \quad (7.217)$$

Hence, harmonics of order

$$n = k(m+1) \pm 1, \quad k = 1, 2, 3, \dots \quad (7.218)$$

are expected. The harmonics with  $n = k(m+1) + 1$  have the same polarization as the incident laser, whereas those with  $n = k(m+1) - 1$  are oppositely polarized. With increasing  $m$  more and more low order harmonics are suppressed.

The same selection rule (7.218) is obtained for a target having an  $M$ -fold discrete rotational symmetry axis parallel to the laser propagation direction [110]. An example for such a target is the benzene molecule with  $M = 6$ . The Floquet–Hamiltonian in this case may be written as

$$\hat{\mathcal{H}}(t) = \hat{H}_{\text{kin}} + \hat{V}(\rho, \varphi, z) + \frac{E}{\sqrt{2}}\rho \cos(\varphi - \omega_1 t) - i\frac{d}{dt}. \quad (7.219)$$

Owing to the discrete rotational symmetry  $C_M$  of  $\hat{V}(\rho, \varphi, z)$  the symmetry operation of interest now is

$$\hat{P}_{\text{rot}}^{(M)} = \left( \varphi \rightarrow \varphi + \frac{2\pi}{M}, t \rightarrow t - \frac{2\pi}{\omega_1 M} \right), \quad (7.220)$$

from which the selection rule

$$n = kM \pm 1, \quad k = 1, 2, 3, \dots \quad (7.221)$$

follows, which is indeed of the same form as in the bichromatic, atomic case (7.218). Note that (7.219) is only a single active electron-Hamiltonian but sufficient for the purposes here because the electron-electron interaction term is invariant under the operation (7.220) anyway.

For deducing these selection rules one assumes that the incident laser pulse is infinitely long. This is required for (7.204) to be true. In finite laser pulses the simple selection rules above may be violated and one has to consider not only a single Floquet states but superpositions of them [111, 112].

## 7.4 Strong Laser–Atom Interaction Beyond the Single Active Electron

Since the early eighties sufficiently intense lasers were available to produce noncollisional multiple ionization of atoms [113]. A sequential viewpoint where at a certain intensity of the laser pulse envelope the currently outermost electron is released, leaving the remaining core essentially in the ground state, was successful in explaining most of the experimentally observed results [17]. Signatures of double-electron excitation were observed but simultaneous two-electron ejection was not detected. The situation changed when in 1992 Fittinghoff et al. [114] observed nonsequential double-ionization (NSDI) of helium at 614 nm in 120 fs laser pulses. This phenomenon will be discussed in more detail in Sect. 7.4.1.

The theoretical treatment of correlated multi-electron systems is a formidable task already in the stationary case. The direct solution of the Schrödinger equation is prohibitive because of the so-called “exponential wall” [115]: the dimension of the configuration space scales with the number of particles  $N$  so that the computational cost of the representation of the  $N$ -body wave function scales exponentially. Matters get worse for nonperturbative, time-dependent problems where the wave function must be propagated in time. In full dimensionality, the simulation of helium in strong laser fields is currently at the limit of feasibility [116].

A technique which allows to calculate nonperturbatively single (or, recently, also double) ionization but taking into account excitation of the other electrons is the  $R$ -matrix Floquet theory [117–119]. This method is a combination of the powerful and in the electron-atom collisions-community well-known  $R$ -matrix method [120, 121] and Floquet theory. Alternative methods for the study of ionization in two active electron systems are the complex scaling technique used in [48–50], and the state-specific approach [122, 123]. However, none of these methods so far reproduced, e.g., nonsequential double ionization. On the other hand, low-dimensional model systems [124–133] where the degrees of freedom of the two or more electrons is restricted, are rather inaccurate on a quantitative level but helped to identify, e.g., the nonsequential ionization mechanism and, moreover, serve as important test cases for approximative approaches [61, 124, 127, 128, 134–136].

Methods such as time-dependent Hartree-Fock (TDHF) and simple versions of time-dependent density functional theory (TDDFT) fail miserably in describing

laser-driven correlated electron dynamics [129, 137, 138]. This triggered strong interest in the multi-configurational TDHF (MCTDHF) approach [139–141] and in the improvement of TDDFT [134–136]. MCTDHF becomes exact if a sufficient number of configurations is taken into account but is very demanding computationally. TDDFT, on the other hand, is also – in principle – exact and numerically rather inexpensive as long as “standard” exchange-correlation functionals (such as the local density approximation, for instance) are used as an approximation. However, these standard functionals do not reproduce correlated strong-field phenomena such as NSDI or resonant interactions so that further improvements of the method are required [134–136].

### 7.4.1 Nonsequential Ionization

As already mentioned in the introduction of this chapter Fittinghoff et al. [114] found a signature of nonsequential ionization (NSDI) in the He ion yields after the interaction with a 614 nm, 120 fs laser pulses. A refined measurement at 780 nm with 160 fs pulses was presented by Walker et al. [142]. The main result is shown in Fig. 7.18. One sees that below  $10^{15} \text{ Wcm}^{-2}$  the measured  $\text{He}^{2+}$  yield is many orders of magnitude greater than expected from a sequential “single active electron” (SAE) ionization scenario. The latter is sketched by the solid curves in the plot. At around  $10^{15} \text{ Wcm}^{-2}$  the  $\text{He}^{2+}$  curve changes slope and tends to merge with the theoretical SAE prediction, forming the so-called NSDI “knee”. This happens when the previous charge state saturates, indicating that the NSDI emission of the second electron is correlated with the dynamics of the first electron. The experimental ion yields continue to increase even after saturation because of the focal expansion  $\sim I^{3/2}$  [143]. Obviously, the increased  $\text{He}^{2+}$  yield originates from the interaction of the two electrons in the laser field. NSDI was also observed in other rare gases and higher charge states [34, 144, 145], and in  $\text{In}^+$  [146].

Two possible mechanisms responsible for NSDI were suggested. Corkum proposed a rescattering scenario [96] where the electron released first is driven back to the ionic core by the laser and dislodges the second electron by a collision. Fittinghoff et al. [114] suggested a “shake-off” of the second electron due to the sudden loss of screening when the first electron is removed. Another mechanism one may think of is collective tunneling. However, the amplitude for such a process is too low for explaining NSDI [147, 148].

The measurement of strongly driven multi-particle dynamics received a new twist with the invention of the so-called reaction microscope (see Ref. [149] for a review): cold target recoil ion momentum spectroscopy (COLTRIMS) and electron momentum spectroscopy provide correlated momentum spectra containing much more information than just the total ion yields. For recent experiments using the new technique see, e.g., [150–159].

In sequential ionization the momentum distribution of the ion is centered at zero. Note that the ion momentum equals the sum of the electron momenta because the

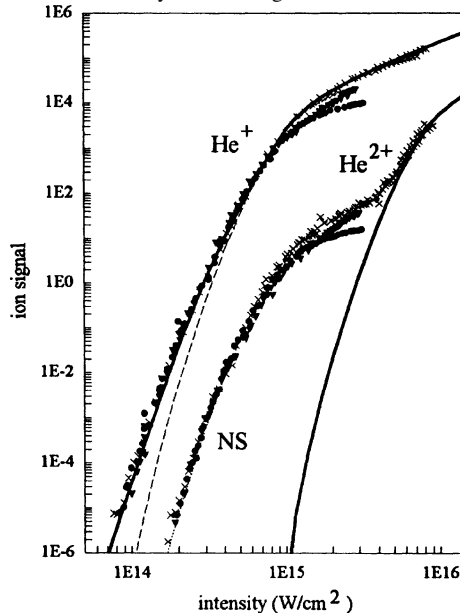


**Fig. 7.18** Experimental ion yields for  $\text{He}^+$  and  $\text{He}^{2+}$  after the interaction with a 160 fs 780 nm laser pulse. The solid lines are the theoretically expected yields when a sequential, single active electron ionization scenario is assumed. It is seen that below  $10^{15} \text{ Wcm}^{-2}$  the measured  $\text{He}^{2+}$  yield is many orders of magnitude greater before it merges with the theoretical prediction. The deviation from the sequential rate (*solid curve*) is the so-called nonsequential ionization (NSDI) “knee”. From [142]

photon momentum can be neglected for laser wavelengths  $\simeq 800 \text{ nm}$ . In NSDI instead, the momentum distribution shows a clear double-peaked structure, as shown in Fig. 7.19. This is an indication that NSDI is not a pure “shake-off” effect because an isotropic momentum distribution is expected for the second electron in this case. Experimentally obtained differential momentum spectra show that the two electrons escape finally in almost the same direction [152, 153]. This is in contrast to double ionization with energetic photons where the two electrons are emitted “back to back” in opposite directions due to their mutual Coulomb repulsion. At low frequencies the electric field of the laser prevails, thus forcing the electrons to move in the same direction.

Theoretically, NSDI was successfully analyzed by solving the TDSE of low-dimensional two-electron model atoms [128–130, 133], by classical simulations [160–163], and simplified quantum models based on distinguishable electrons (i.e., an “inner” and an “outer” one) [164–166]. As in the case of high-order ATI and HOHG, the SFA treatment gives the deepest physical insight into the NSDI process, especially when interpreted in terms of quantum trajectories. The standard, single active electron SFA needs to be extended in order to allow for (laser field-dressed) collisional ionization by the rescattered electron [6, 157, 167–179]. Starting point is the still exact expression for the transition matrix element (7.129), but now formu-

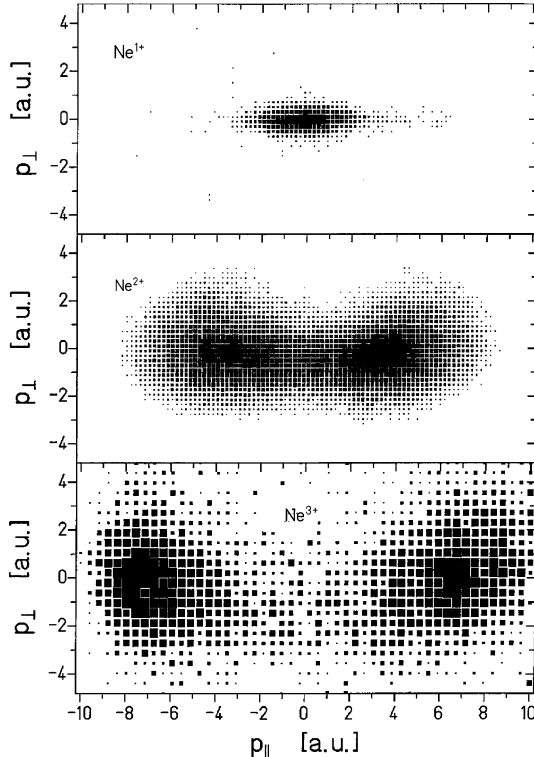


**Fig. 7.19** Momentum distributions of  $\text{Ne}^{n+}$  ions at  $1.3 \text{ PWcm}^{-2}$  ( $\text{Ne}^+$ ,  $\text{Ne}^{2+}$ ) and  $1.5 \text{ PWcm}^{-2}$  ( $\text{Ne}^{3+}$ ) after a 30 fs 795 nm laser pulse obtained with the COLTRIMS method.  $p_{\parallel}$  is the momentum parallel to the laser polarization,  $p_{\perp}$  perpendicular to it. The distribution for  $\text{Ne}^{2+}$  and  $\text{Ne}^{3+}$  shows a minimum at  $p_{\parallel}$ , indicating that NSDI is not a (pure) shake-off effect but relies on Coulomb interaction of the electrons. From [150]

lated for two electrons. In terms of Feynman diagrams, this matrix element contains all graphs with arbitrary large numbers of vertices. Without having a physical picture of the NSDI process in mind it is hard to extract the leading diagram describing the NSDI process. However, if rescattering of one of the electrons is crucial for NSDI, it is clear that the NSDI process is contained in the second term of (7.129). We assume that initial and final state correlations are unimportant. Moreover, we approximate the final states by plane waves, so that the matrix element of interest reads

$$M_{\mathbf{p}_1 \mathbf{p}_2} = - \int_{t_i}^t dt' \int_{t_i}^{t'} dt'' \langle \mathbf{p}_1 + \mathbf{A}(t') | \langle \mathbf{p}_2 + \mathbf{A}(t') | \hat{V} \hat{U}(t', t'') \hat{W}(t'') \\ \times |\Psi_{01}\rangle |\Psi_{02}\rangle \exp \left( -i(\mathcal{E}_{01} + \mathcal{E}_{02})t'' - i \sum_{i=1}^2 S_{\mathbf{p}_i}(t, t') \right)$$

with  $\mathcal{E}_{0i}$  the initial energies of the two electrons  $i = 1, 2$ . Here, we suppress an explicit antisymmetrization of the initial and final two-electron states as the tran-

sition matrix element with proper symmetry can easily be constructed a posteriori. The NSDI matrix element is obtained by selecting only a particular of the very many processes implicitly contained in the sequence of operators  $\hat{V}\hat{U}(t', t'')\hat{W}(t'')$ , namely  $\hat{V}_{12}\{[\hat{U}_1^{(V)}(t', t'')\hat{W}_1(t'')] \otimes \hat{U}_{02}(t', t'')\}$ . Here,  $\hat{U}_{02}$  is the field-free time evolution operator  $\hat{U}_0$  acting on electron 2,  $\hat{U}_1^{(V)}$ ,  $\hat{W}_1(t'')$  act on electron 1, and  $\hat{V}_{12}$  governs the interaction between the two electrons (i.e., the collision). In length gauge we obtain

$$M_{\mathbf{p}_1 \mathbf{p}_2}^{\text{NSDI}} = - \int_{t_i}^t dt' \int_{t_i}^{t'} dt'' \langle \mathbf{p}_1 + \mathbf{A}(t') | \langle \mathbf{p}_2 + \mathbf{A}(t') | \hat{V}_{12} \hat{U}_1^{(V)}(t', t'') \hat{W}_1(t'') \\ \times |\Psi_{01}\rangle |\Psi_{02}\rangle \exp \left( -i\mathcal{E}_{01}t'' - i\mathcal{E}_{02}t' - i \sum_{i=1}^2 S_{\mathbf{p}_i}(t, t') \right).$$

The interpretation is that at time  $t''$  electron 1 is ionized by the field ( $\hat{W}_1(t'')$ ) and propagates thereafter in the vacuum until time  $t'$  ( $\hat{U}_1^{(V)}(t', t)$ ). Electron 2 meanwhile remains in its bound state ( $\hat{U}_{02}(t', t'')$ ), which simply becomes  $\exp[-i\mathcal{E}_{02}(t' - t'')]$  when applied to  $|\Psi_{02}\rangle$ ). At time  $t'$  the first electron returns to its parent ion and interacts via  $\hat{V}_{12}$  with the second electron. The latter may be dislodged due to this interaction. NSDI thus may be viewed as laser-driven collisional ionization. In reality, the second electron may be excited instead of immediately ejected. It then may be freed later by the laser pulse, leading also to double ionization. This process was coined RESI (recollision-induced excitation followed by subsequent field ionization) [156]. Whether NSDI or RESI are dominant in an actual experiment is target-dependent and can be distinguished because both processes lead to different momentum spectra, as will become clear below. The SFA devised here does not include excited states so that RESI is not covered. Using (7.130) in length gauge for  $\hat{U}_1^{(V)}(t', t'')$  yields

$$M_{\mathbf{p}_1 \mathbf{p}_2}^{\text{NSDI}} = - \int_{t_i}^t dt' \int_{t_i}^{t'} dt'' \int d^3 k_1 \langle \mathbf{p}_1 + \mathbf{A}(t') | \langle \mathbf{p}_2 + \mathbf{A}(t') | \hat{V}_{12} | \mathbf{k}_1 + \mathbf{A}(t') \rangle \\ \times \langle \mathbf{k}_1 + \mathbf{A}(t'') | \mathbf{r}_1 \cdot \mathbf{E}(t'') | \Psi_{01}\rangle |\Psi_{02}\rangle \\ \times \exp \left( -i\mathcal{E}_{01}t'' - i\mathcal{E}_{02}t' - iS_{\mathbf{k}_1}(t', t'') - i \sum_{i=1}^2 S_{\mathbf{p}_i}(t, t') \right).$$

Introducing the form factor

$$V_{\mathbf{p}_i \mathbf{k}_1}(t') = \langle \mathbf{p}_1 + \mathbf{A}(t') | \langle \mathbf{p}_2 + \mathbf{A}(t') | \hat{V}_{12} | \mathbf{k}_1 + \mathbf{A}(t') \rangle | \Psi_{02}\rangle, \quad (7.222)$$

the matrix element

$$W_{\mathbf{k}_1}(t'') = \langle \mathbf{k}_1 + \mathbf{A}(t'') | \mathbf{r}_1 \cdot \mathbf{E}(t'') | \Psi_{01}\rangle, \quad (7.223)$$

and the total action

$$S_{\mathbf{p}_i \mathbf{k}_1}(t, t', t'') = \mathcal{E}_{01} t'' + \mathcal{E}_{02} t' + S_{\mathbf{k}_1}(t', t'') + \sum_{i=1}^2 S_{\mathbf{p}_i}(t, t') \quad (7.224)$$

the NSDI matrix element reads

$$M_{\mathbf{p}_1 \mathbf{p}_2}^{\text{NSDI}} = - \int_{t_1}^t dt' \int_{t_1}^{t'} dt'' \int d^3 k_1 V_{\mathbf{p}_i \mathbf{k}_1}(t') W_{\mathbf{k}_1}(t'') \exp[-i S_{\mathbf{p}_i \mathbf{k}_1}(t, t', t'')]. \quad (7.225)$$

Upon integration by parts and neglecting boundary terms (cf. [71]) the matrix element

$$M_{\mathbf{p}_1 \mathbf{p}_2}^{\text{NSDI}'} = - \int_{t_1}^t dt' \int_{t_1}^{t'} dt'' \int d^3 k_1 V_{\mathbf{p}_i \mathbf{k}_1}(t') V_{\mathbf{k}_1}(t'') \exp[-i S_{\mathbf{p}_i \mathbf{k}_1}(t, t', t'')] \quad (7.226)$$

is obtained, where

$$V_{\mathbf{k}_1}(t'') = \langle \mathbf{k}_1 + \mathbf{A}(t'') | \hat{V}_1 | \Psi_{01} \rangle. \quad (7.227)$$

The matrix element (7.226) is widely used in the literature (see, e.g., [178]). Assuming a monochromatic laser field and a contact-type interaction  $\hat{V}_{12} \sim \delta(\mathbf{r}_1 - \mathbf{r}_2)\delta(\mathbf{r}_2)$ , all of the integrals in (7.226) apart from a single, remaining time integral can be solved. For few-cycle pulses the two time integrals remain to be evaluated numerically. This is nontrivial because of the highly oscillatory nature of the integrand. Alternatively, the saddle-point method (or refined versions of it) may be applied (see, e.g., [178]). Figure 7.20 shows results for correlated momentum spectra

$$P(p_{1\parallel}, p_{2\parallel}) = \int d^2 p_{1\perp} \int d^2 p_{2\perp} \left| M_{\mathbf{p}_1 \mathbf{p}_2}^{\text{NSDI}'} \right|^2, \quad (7.228)$$

calculated for neon in a 4-cycle, linearly polarized laser pulse of the form  $\mathbf{A}(t) = A_0 \mathbf{e}_z \exp[-4(\omega t - \pi n)^2 / (\pi n)^2] \sin[\omega t + \phi]$ . The actual values of all the parameters are given in the figure caption. The momenta  $p_{i\parallel}$  and  $p_{i\perp}$  are parallel and perpendicular to the laser polarization direction, respectively. The typical diagonal “double blob” structure in the  $p_{1\parallel}, p_{2\parallel}$ -plane is observed, indicating that the electrons are preferentially emitted in the same direction. In the case of phase-stabilized few-cycle laser pulses, the structure sensitively depends on the carrier-envelope phase  $\phi$ , as was also demonstrated experimentally [180]. Integrating  $P(p_{1\parallel}, p_{2\parallel})$  for fixed sum momenta  $p_{\parallel} = p_{1\parallel} + p_{2\parallel}$  (i.e., perpendicular to the diagonal  $p_{1\parallel} = p_{2\parallel}$  in the plots in Fig. 7.20) a double-hump structure is obtained in the NSDI regime. In the case of few-cycle pulses the weights of the two humps depend sensitively on the carrier-envelope or absolute phase  $\phi$ . Because of momentum conservation the double-hump in the electron sum momenta is reflected in the measured ion recoil

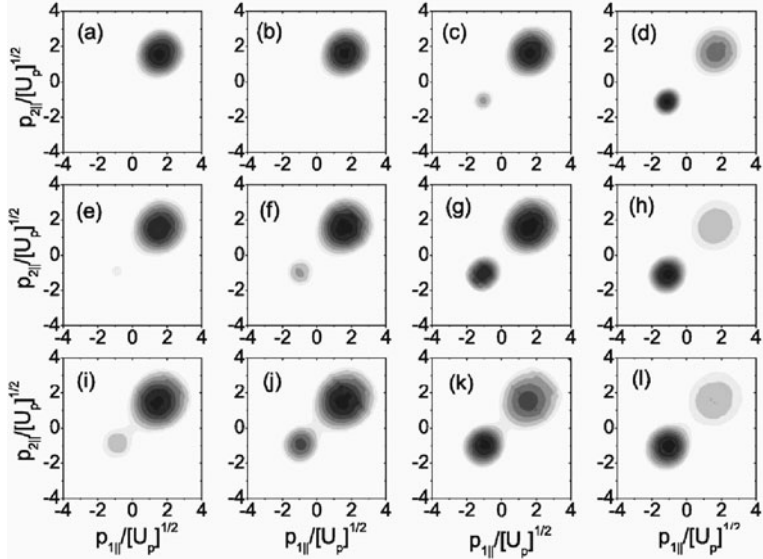


**Fig. 7.20** Differential electron momentum distributions computed for neon ( $\mathcal{E}_{01} = -0.79$  and  $\mathcal{E}_{02} = -1.51$  a.u.) subject to a four-cycle pulse of frequency  $\omega = 0.057$  (Ti:Sapphire,  $\lambda \simeq 800$  nm) and various intensities and absolute phases. The upper, middle and lower panels correspond to  $I = 4 \cdot 10^{14}$  Wcm $^{-2}$  ( $U_p = 0.879$ ),  $I = 5.5 \cdot 10^{14}$  Wcm $^{-2}$  ( $U_p = 1.2$ ), and  $I = 8 \cdot 10^{14}$  Wcm $^{-2}$  ( $U_p = 1.758$ ), respectively. The absolute phases are given as follows: Panels (a), (e), and (i):  $\phi = 0.87\pi$ ; panels (b), (f), and (j):  $\phi = 0.9\pi$ ; panels (c), (g), and (k):  $\phi = \pi$ ; and panels (d), (h), and (l):  $\phi = 1.1\pi$ . Taken from [178]

momentum spectra (the momentum of the near infrared photons involved can be neglected).

As already demonstrated for ATI and HOHG, cut-offs in intense laser-atom interaction can always be explained by means of classical electron trajectories. The same holds true for the maximum electron sum momentum in NSDI. The link between classical trajectories and the SFA is formally established by the stationary phase approach already used in (7.160) and (7.195). To that end we seek those values of  $\mathbf{k} = \mathbf{k}_1, t'$ , and  $t''$  such that  $S = S_{p_i k}(t, t', t'')$  is stationary. The conditions  $\partial_{t'} S = 0$ ,  $\partial_{t''} S = 0$ , and  $\nabla_{\mathbf{k}} S = \mathbf{0}$  give

$$\sum_{i=1}^2 [\mathbf{p}_i + \mathbf{A}(t')]^2 = 2\mathcal{E}_{02} + [\mathbf{k} + \mathbf{A}(t')]^2, \quad (7.229)$$

$$[\mathbf{k} + \mathbf{A}(t'')]^2 = 2\mathcal{E}_{01}, \quad (7.230)$$

$$\int_{t''}^{t'} dt [\mathbf{k} + \mathbf{A}(t)] = 0, \quad (7.231)$$

respectively. Equations (7.229) and (7.230) ensure energy conservation at the rescattering time  $t'$  and the emission time  $t''$  of the first electron. Equation (7.231) restricts

the first electron's intermediate momentum such that rescattering occurs. Since  $\mathcal{E}_{01} < 0$ , (7.230) has only solutions for complex times  $t''$  ( $\mathbf{k}$  is kept real). The classical trajectories of simple man's theory are obtained for vanishing  $\mathcal{E}_{01}$ . Equation (7.230) then implies  $\mathbf{k} = -\mathbf{A}(t'')$ . Together with (7.231) we have

$$-\mathbf{A}(t'')(t' - t'') + \boldsymbol{\alpha}(t') - \boldsymbol{\alpha}(t'') = 0.$$

Comparison with (7.170) shows that this expression is indeed equivalent to  $\mathbf{r}_1(t') = 0$  when electron 1 was emitted at time  $t''$ . If the second electron is dislodged with vanishing initial momentum at a time  $t'$  when the electric field of the laser vanishes, its kinetic energy will assume the maximum value  $2U_p$  so that  $|p_{2\parallel}| = 2\sqrt{U_p}$  is expected. This crude estimate is well confirmed by virtue of Fig. 7.20. If  $n$  electrons are involved in the multiple ionization process and all acquire this maximum momentum (in the same direction), the ultimate classical cut-off for the ion recoil momentum is  $2n\sqrt{U_p}$ . Recoil ion spectra of neon confirm this estimate [156]. However, if the returning electron is likely to excite but not to directly free the second electron (i.e., the above mentioned RESI occurs), the delayed ionization occurs at high electric field values so that the drift momentum of the second electron will be much lower than  $2\sqrt{U_p}$ . Whether collisional ionization or collisional excitation prevails strongly depends on the target.

## References

- Burnett, K., Reed, V.C., Knight, P.L.: J. Phys. B: At. Mol. Opt. Phys. **26**, 561 (1993) 267
- Protopapas, M., Keitel, C.H., Knight, P.L.: Rep. Prog. Phys. **60**, 389 (1997)
- Joachain, C.J., Dörr, M., Kylstra, N.J.: Adv. At. Mol. Opt. Phys. **42**, 225 (2000) 284
- Brabec, Th. (ed.): Strong Field Laser Physics. Springer, New York (2008) 267
- Popov, V.S.: Physics Uspekhi **47**, 855 (2004) 267, 280, 281
- Becker, A., Faisal, F.H.M.: J. Phys. B: At. Mol. Opt. Phys. **38**, R1 (2005) 267, 321
- Brabec, T., Krausz, F.: Rev. Mod. Phys. **72**, 545 (2000) 267
- Becker, W., et al.: Adv. At. Mol. Opt. Phys. **48**, 35 (2002) 267, 304
- Milošević, D.B., Paulus, G.G., Bauer, D., Becker, W.: J. Phys. B: At. Mol. Opt. Phys. **39**, R203 (2006) 267, 302, 304, 306
- Salières, P., L'Huillier, A., Antoine, P., Lewenstein, M.: Adv. At. Mol. Opt. Phys. **4**, 83 (1999) 267, 310
- Mihai Gavrila: J. Phys. B: At. Mol. Opt. Phys. **35**, R147 (2002) 267, 289, 290
- Becker, A., Dörner, R., Moshammer, R.: J. Phys. B: At. Mol. Opt. Phys. **38**, S753 (2005) 267
- Agostini, P., DiMauro, L.F.: Rep. Prog. Phys. **67**, 1563 (2004); corrigendum in **67**, 1563 (2004) 267
- Scrinzi, A., Ivanov, M.Yu., Kienberger, R., Villeneuve, D.M.: J. Phys. B: At. Mol. Opt. Phys. **39**, R1 (2006)
- Krausz, F., Ivanov, M.: Rev. Mod. Phys. **81**, 163 (2009) 267
- Paulus, G.G., Bauer, D.: Time in Quantum Mechanics II, Lecture Notes in Physics, p. 303. Springer, Berlin Heidelberg (2010) 267, 308
- Lambropoulos, P., Maragakis, P., Zhang, J.: Phys. Rep. **305**, 203 (1998) 267, 319
- Chu, S.-I., Telnov, D.A.: Phys. Rep. **390**, 1 (2004) 267, 284, 287
- Keitel, C.H.: Contemp. Phys. **42**, 353 (2001) 267
- Salamin, Y.I., Hu, S.H., Hatsagortsyan, K.Z., Keitel, C.H.: Phys. Rep. **427**, 41 (2006) 267
- Marques, M.A.L., Gross, E.K.U.: Annu. Rev. Phys. Chem. **55**, 427 (2004) 267

22. Marques, M.A.L., Ullrich, C.A., Nogueira, F., Rubio, A., Burke, K., Gross, E.K.U. (eds.): Time-Dependent Density Functional Theory. Springer, Berlin (2006) 267
23. Bandrauk, A.D. (ed.): Molecules in Laser Fields. Marcel Dekker, New York (1993) 267
24. Posthumus, J. (ed.): Molecules and Clusters in Intense Laser Fields. Cambridge University Press, Cambridge (2001) 267
25. Lein, M.: *J. Phys. B: At. Mol. Opt. Phys.* **40**, R135 (2007) 267
26. Saalmann, U., Siedschlag, Ch., Rost, J.M.: *J. Phys. B: At. Mol. Opt. Phys.* **39**, R39 (2006)
27. Fennel, Th., Meiwas-Broer, K.-H., Tiggesbäumker, J., Reinhard, P.-G., Dinh, P.M., Suraud, E.: preprint arXiv:0904.2706 (to be published in *Rev. Mod. Phys.*) 267
28. Landau, L.D., Lifshitz, E.M.: Volume 3 of Course of Theoretical Physics: Quantum Mechanics. Pergamon, Oxford (1965) 270, 272, 277, 280
29. Friedrich, H.: Theoretical Atomic Physics. Springer, Berlin (1998)
30. Bransden, B.H., Joachain, C.J.: Physics of Atoms and Molecules. Prentice Hall, Harlow (2003) 270, 272
31. Kustaanheimo, P., Stiefel, E.: *J. Reine Angew. Mathematik* **218**, 204 (1965) 275
32. Bauer, D.: *Phys. Rev. A* **55**, 2180 (1997) 275, 276
33. Shakeshaft, R., Potvliege, R.M., Dörr, M., Cooke, W.E.: *Phys. Rev. A* **42**, 1656 (1990) 276
34. Larochelle, S., Talebpour, A., Chin, S.L.: *J. Phys. B* **31**, 1201 (1998) 276, 320
35. Gubbini, E., Eichmann, U., Kalashnikov, M., Sandner, W.: *Phys. Rev. Lett.* **94**, 053602 (2005) 276, 281
36. Pittrelli, D., Bauer, D., Macchi, A., Cornolti, F.: *J. Phys. B: At. Mol. Opt. Phys.* **33**, 829 (2000) 276
37. Ammosov, M.V., Delone, N.B., Krainov, V.P.: *Sov. Phys. JETP* **64**, 1191 (1986) 280
38. Nikishov, A.I., Ritus, V.I.: *Zh. Eksp. Teor. Fiz.* **50**, 255 (1966) [Sov. Phys. JETP] **23**, 162 (1966)] 280, 281
39. Perelomov, A.M., Popov, V.S., Terent, M.V.'ev: *Zh. Eksp. Teor. Fiz.* **50** 1393; **51** 309 (1966) [Sov. Phys. JETP] **23**, 924 (1966); **24**, 207 (1967)] 281
40. Perelomov, A.M., Popov, V.S.: *Zh. Eksp. Teor. Fiz.* **52**, 514 (1967) [Sov. Phys. JETP] **25**, 482 (1967)]
41. Nikishov, A.I., Ritus, V.I.: *Zh. Eksp. Teor. Fiz.* **52**, 223 (1967) [Sov. Phys. JETP] **25**, 145 (1967) 280, 281
42. Keldysh, L.V.: *Eksp. Teor. Fiz.* **47**, 1945 (1964) [Sov. Phys. JETP] **20**, 1307 (1965)] 280, 282, 292
43. Taïeb, R., Véniard, V., Maquet, A.: *Phys. Rev. Lett.* **87**, 053002 (2001) 281
44. Floquet, G.: *Ann. Ecol. Norm. Sup.* **12**, 47 (1883) 283
45. Potvliege, R.M.: *Comput. Phys. Comm.* **114**, 42 (1998) 284
46. Scully, M.O., Zubairy, M.S.: Quantum Optics. Cambridge University Press, Cambridge (1997) 285
47. Siegert, A.J.F.: *Phys. Rev.* **56**, 750 (1939) 287
48. Armin Scrinzi and Bernard Piraux: *Phys. Rev. A* **58**, 1310 (1998) 287, 319
49. Scrinzi, A., Geissler, M., Brabec, T.: *Phys. Rev. Lett.* **83**, 706 (1999)
50. Scrinzi, A.: *Phys. Rev. A* **61**, 041402(R) (2000) 287, 319
51. Potvliege, R.M., Robin Shakeshaft: *Phys. Rev. A* **40**, 3061 (1989) 287, 288
52. Freeman, R.R., Bucksbaum, P.H., Milchberg, H., Darack, S., Schumacher, D., Geusic, M.E.: *Phys. Rev. Lett.* **59**, 1092 (1987) 288
53. Pauli, W., Fierz, M.: *Nuovo Cimento* **15**, 167 (1938) 289
54. Kramers, H.A.: Collected Scientific Papers. North-Holland, Amsterdam (1956)
55. Henneberger, W.C.: *Phys. Rev. Lett.* **21**, 538 (1968) 289
56. Pont, M., Walet, N.R., Gavrila, M., McCurdy, C.W.: *Phys. Rev. Lett.* **61**, 939 (1988) 290
57. Bauer, D., Ceccherini, F.: *Phys. Rev. A* **66**, 053411 (2002) 290
58. Pont, M., Gavrila, M.: *Phys. Rev. Lett.* **65**, 2362 (1990) 290
59. Lambropoulos, P.: *Phys. Rev. Lett.* **55**, 2141 (1985) 290, 291
60. de Boer, M.P., Hoogenraad, J.H., Vrijen, R.B., Noordam, L.D., Muller, H.G.: *Phys. Rev. Lett.* **71**, 3263 (1993) 291
61. Bauer, D., Ceccherini, F.: *Phys. Rev. A* **60**, 2301 (1999) 291, 319
62. Gaier, L.N., Keitel, C.H.: *Phys. Rev. A* **65**, 023406 (2002) 291
63. Staudt, A., Keitel, C.H.: *Phys. Rev. A* **73**, 043412 (2006) 291

64. Faisal, F.H.M.: *J. Phys. B: Atom. Molec. Phys.* **6**, L89 (1973) 292
65. Reiss, H.R.: *Phys. Rev. A* **22**, 1786 (1980) 292, 296, 299, 301
66. Faisal, F.H.M.: *Theory of Multiphoton Processes*. Plenum Press, New York (1987) 292
67. Fick, E.: *Einführung in die Grundlagen der Quantentheorie*. Aula-Verlag, Wiesbaden (1988) 292
68. Göppert-Mayer, M.: *Ann. Phys.* **9**, 273 (1931) 293
69. Gordon, W.: *Z. Phys.* **40**, 117 (1926) 294
70. Volkov, D.V.: *Z. Phys.* **94**, 250 (1935) 294
71. Lohr, A., Kleber, M., Kopold, R., Becker, W.: *Phys. Rev. A* **55**, R4003 (1997) 294, 324
72. Bauer, D., Milošević, D.B., Becker, W.: *Phys. Rev. A* **72**, 023415 (2005) 296
73. Becker, W., Chen, J., Chen, S.G., Milošević, D.B.: *Phys. Rev. A* **76**, 033403 (2007)
74. Bergues, B., Ansari, Z., Hanstorp, D., Kiyani, I.Yu.: *Phys. Rev. A* **75**, 063415 (2007); see also Comment by Reiss, H.R.: *Phys. Rev. A* **77**, 067401 (2008) 296
75. Paulus, G.G., Grasbon, F., Walther, H. H., Kopold, R., Becker, W.: *Phys. Rev. A* **64**, 021401 (2001) 298
76. Kopold, R., Becker, W., Kleber, M., Paulus, G.G.: *J. Phys. B: At. Mol. Opt. Phys.* **35**, 217 (2002) 298
77. Agostini, P., Fabre, F., Mainfray, G., Petite, G., Rahman, N.: *Phys. Rev. Lett.* **42**, 1127 (1979) 298
78. Freeman, R.R., Bucksbaum, P.H.: *J. Phys. B: At. Mol. Opt. Phys.* **24**, 325 (1991) 300
79. Bleistein, N., Handelsmann, R.A.: *Asymptotic Expansions of Integrals*. Dover Publications, New York (1986) 303
80. Salhières, P., et al.: *Science* **292**, 902 (2001) 304
81. Milošević, D.B., Bauer, D., Becker, W.: *J. Mod. Opt.* **53**, 125 (2006) 304
82. Bauer, D., Milošević, D.B., Becker, W.: *J. Mod. Opt.* **53**, 135 (2006) 306
83. Faisal, F.H.M., Schlegel, G.: *J. Phys. B* **38**, L223 (2005); *J. Mod. Opt.* **53**, 207 (2006) 306
84. Smirnova, O., Spanner, M., Ivanov, M.: *Phys. Rev. A* **77**, 033407 (2008)
85. Arbó, D.G., et al.: *Phys. Rev. A* **77**, 013401 (2008) 306
86. Popruzhenko, S.V., Bauer, D.: *J. Mod. Opt.* **55**, 2573 (2008) 306
87. Popruzhenko, S.V., Paulus, G.G., Bauer, D.: *Phys. Rev. A* **77**, 053409 (2008) 306
88. Blaga, C.I., et al.: *Nature Physics* **5**, 335 (2009) 306
89. Lindner, F., et al.: *Phys. Rev. Lett.* **95**, 040401 (2005) 308
90. Arbó, D.G., Persson, E., Burgdörfer, J.: *Phys. Rev. A* **74**, 063407 (2006) 308
91. Gopal, R., et al.: *Phys. Rev. Lett.* **103**, 053001 (2009) 308
92. Sundaram, B., Milonni, P.W.: *Phys. Rev. Lett.* **41**, 6571 (1990) 309, 312
93. Di Piazza, A., Fiordilino, E., Mittleman, M.H.: *J. Phys. B: At. Mol. Opt. Phys.* **34**, 3655 (2001) 309
94. Krause, J.L., Schafer, K.J., Kulander, K.C.: *Phys. Rev. Lett.* **68**, 3535 (1992) 310
95. Kulander, K.C., Schafer, K.J., Krause, J.L.: In: Piraux, B., et al. (eds.) *Super-Intense Laser–Atom Physics*, NATO ASI series B, vol. 316, p. 95. Plenum Press, New York (1993) 310
96. Corkum, P.B.: *Phys. Rev. Lett.* **71**, 1994 (1993) 310, 320
97. Lewenstein, M., Balcou, Ph., Ivanov, M.Yu., L’Huillier, A., Corkum, P.B.: *Phys. Rev. A* **49**, 2117 (1994) 310, 313, 315
98. Spielmann, Ch., et al.: *Science* **278**, 661 (1997) 311
99. Chang, Z., Rundquist, A., Wang, H., Murnane, M., Kapteyn, H.: *Phys. Rev. Lett.* **79**, 2967 (1997) 311
100. Goulielmakis, E., et al.: *Science* **305**, 1267 (2004) 311
101. Drescher, M., et al.: *Nature* **419**, 803 (2002) 311
102. Eberly, J.H., Fedorov, M.V.: *Phys. Rev. A* **45**, 4706 (1992) 312
103. Knight, P.L., Milonni, P.W.: *Phys. Rep.* **66**, 21 (1980) 312
104. Becker, W., Lohr, A., Kleber, M., Lewenstein, M.: *Phys. Rev. A* **56**, 645 (1997) 313
105. Milošević, D.B., Becker, W.: *Phys. Rev. A* **66**, 063417 (2002) 315
106. Sambe, H.: *Phys. Rev. A* **7**, 2203 (1973) 316
107. Eichmann, H., Egbert, A., Nolte, S., Momma, C., Wellegehausen, B., Becker, W., Long, S., McIver, J.K.: *Phys. Rev. A* **51**, R3414 (1995) 318

108. Becker, W., Chichkov, B.N., Wellegehausen, B.: Phys. Rev. A **60**, 1721 (1999)
109. Milosevic, D.B., Becker, W., Kopold, R.: Phys. Rev. A **61**, 063403 (2000) 318
110. Averbukh, V., Alon, O.E., Moiseyev, N.: Phys. Rev. A **60**, 2585 (1999) 318
111. Ceccherini, F., Bauer, D.: Phys. Rev. A **64**, 033423 (2001) 319
112. Ceccherini, F., Bauer, D., Cornolti, F.: J. Phys. B: At. Mol. Opt. Phys. **34**, 5017 (2001) 319
113. Luk, T.S., Pummer, H., Boyer, K., Shakidi, M., Egger, H., Rhodes, C.K.: Phys. Rev. Lett. **51**, 110 (1983) 319
114. Fittinghoff, D.N., Bolton, P.R., Chang, B., Kulander, K.C.: Phys. Rev. Lett. **69**, 2642 (1992) 319, 320
115. Kohn, W.: Rev. Mod. Phys. **71**, 1253 (1999) 319
116. Smyth, E.S., Parker, J.S., Taylor, K.T.: Comput. Phys. Comm. **114**, 1 (1998) 319
117. Burke, P.G., Francken, P., Joachain, C.J.: Europhys. Lett. **13**, 617 (1990) 319
118. Burke, P.G., Francken, P., Joachain, C.J.: J. Phys. B: At. Mol. Opt. Phys. **24**, 761 (1991)
119. Feng, L., van der Hart, H.W.: J. Phys. B: At. Mol. Opt. Phys. **36**, L1 (2003) 319
120. Wigner, E.P.: Phys. Rev. **70**, 15 (1946) 319
121. Burke, P.G., Robb, W.D.: Adv. At. Mol. Opt. Phys. **11**, 143 (1975) 319
122. Themelis, S.I., Mercouris, T., Nicolaides, C.A.: Phys. Rev. A **61**, 024101 (2000) 319
123. Mercouris, T., Themelis, S.I., Nicolaides, C.A.: Phys. Rev. A **61**, 013407 (2000) 319
124. Pindzola, M.S., Griffin, D.C., Bottcher, C.: Phys. Rev. Lett. **66**, 2305 (1991) 319
125. Grobe, R., Eberly, J.H.: Phys. Rev. Lett. **68**(2), 905 (1992)
126. Haan, S.L., Grobe, R., Eberly, J.H.: Phys. Rev. A **50**, 378 (1994)
127. Pindzola, M.S., Robicheaux, F., Gavras, P.: Phys. Rev. A **55**, 1307 (1997) 319
128. Bauer, D.: Phys. Rev. A **56**, 3028 (1997) 319, 321
129. Lappas, D.G., van Leeuwen, R.: J. Phys. B: At. Mol. Opt. Phys. **31**, L249 (1998) 320
130. Lein, M., Gross, E.K.U., Engel, V.: Phys. Rev. Lett. **85**, 4707 (2000) 321
131. Roso, L., et al.: Laser Phys. **15**, 1393 (2005)
132. Ruiz, C., Plaja, L., Roso, L.: Phys. Rev. Lett. **94**, 063002 (2005)
133. Ruiz, C., Plaja, L., Roso, L., Becker, A.: Phys. Rev. Lett. **96**, 053001 (2006) 319, 321
134. Lein, M., Kümmel, S.: Phys. Rev. Lett. **94**, 143003 (2005) 319, 320
135. Wilken, F., Bauer, D.: Phys. Rev. Lett. **97**, 203001 (2006)
136. Ruggenthaler, M., Bauer, D.: Phys. Rev. Lett. **102**, 233001 (2009) 319, 320
137. Petersilka, M., Gross, E.K.U.: Laser Physics **9**, 105 (1999) 320
138. Bauer, D., Ceccherini, F.: Optics Express **8**, 377 (2001) 320
139. Zanghellini, J., Kitzler, M., Brabec, T., Scrinzi, A.: J. Phys. B: At. Mol. Opt. Phys. **37**, 763 (2004) 320
140. Kitzler, M., et al.: Phys. Rev. A **70**, 041401 (2004)
141. Caillat, J., et al.: Phys. Rev. A **71**, 012712 (2005) 320
142. Walker, B., Sheehy, B., DiMauro, L.F., Agostini, P., Schafer, K.J., Kulander, K.C.: Phys. Rev. Lett. **73**, 1227 (1994) 320, 321
143. Cervenan, M.R., Isenor, N.R.: Opt. Comm. **13**, 175 (1975) 320
144. Talebpour, A., Chien, C.-Y., Liang, Y., Larochelle, S., Chin, S.L.: J. Phys. B **30**, 1721 (1997) 320
145. Maeda, H., Dammasch, M., Eichmann, U.: Phys. Rev. A **62**, 035402 (2000) 320
146. Maeda, H., Dammasch, M., Eichmann, U.: Phys. Rev. A **63**, 025401 (2001) 320
147. Zon, B.: J. Exp. Theor. Phys. **89**, 219 (1999) 320
148. Eichmann, U., Dörr, M., Maeda, H., Becker, W., Sandner, W.: Phys. Rev. Lett. **84**, 3550 (2000) 320
149. Ullrich, J., et al.: Rep. Prog. Phys. **66**, 1463 (2003) 320
150. Moshammer, R., et al.: Phys. Rev. Lett. **84**, 447 (2000) 320, 322
151. Weber, Th., et al.: Phys. Rev. Lett. **84**, 443 (2000)
152. Weber, Th., et al.: Nature **404**, 658 (2000) 321
153. Dörner, R., Giessen, H., Moshammer, R., Rottke, H.: Phys. Bl. **57**, 49 (2001) (in German) 321
154. Moshammer, R., et al.: J. Phys. B: At. Mol. Opt. Phys. **36**, L113 (2003)
155. Weckenbrock, M., et al.: Phys. Rev. Lett. **92**, 213002 (2004)
156. Rudenko, A., et al.: Phys. Rev. Lett. **93**, 253001 (2004) 323, 326
157. Liu, X., et al.: Phys. Rev. Lett. **93**, 263001 (2004) 321

158. Böttcher, M., et al.: *J. Phys. B: At. Mol. Opt. Phys.* **38**, L389 (2005)
159. Zrost, K., et al.: *J. Phys. B: At. Mol. Opt. Phys.* **39**, S371 (2006) 320
160. Fu, L.-B., Liu, J., Chen, S.-G.: *Phys. Rev. A* **65**, 021406(R) (2002) 321
161. Haan, S.L., Wheeler, P.S., Panfili, R., Eberly, J.H.: *Phys. Rev. A* **66**, 061402(R) (2002)
162. Panfili, R., Haan, S.L., Eberly, J.H.: *Phys. Rev. Lett.* **89**, 113001 (2002)
163. Ho, P.J., Panfili, R., Haan, S.L., Eberly, J.H.: *Phys. Rev. Lett.* **94**, 093002 (2005) 321
164. Watson, J.B., Sanpera, A., Lappas, D.G., Knight, P.L., Burnett, K.: *Phys. Rev. Lett.* **78**, 1884 (1997) 321
165. Tolley, A.J.: *J. Phys. B: At. Mol. Opt. Phys.* **32**, 3449 (1999)
166. Prager, J., Keitel, C.H.: *J. Phys. B: At. Mol. Opt. Phys.* **35**, L167 (2002) 321
167. Becker, A., Faisal, F.H.M.: *Phys. Rev. A* **50**, 3256 (1994) 321
168. Becker, A., Faisal, F.H.M.: *J. Phys. B: At. Mol. Opt. Phys.* **29**, L197 (1996)
169. Becker, A., Faisal, F.H.M.: *Phys. Rev. Lett.* **84**, 3546 (2000)
170. Becker, A., Faisal, F.H.M.: *Phys. Rev. Lett.* **89**, 193003 (2002)
171. Kopold, R., Becker, W., Rottke, H., Sandner, W.: *Phys. Rev. Lett.* **85**, 3781 (2000)
172. Heinrich, A., Lewenstein, M., Sanpera, A.: *J. Phys. B* **37**, 2087 (2004)
173. Goreslavskii, S.P., Popruzhenko, S.V., Kopold, R., Becker, W.: *Phys. Rev. A* **64**, 053402 (2002)
174. Popruzhenko, S.V., Korneev, Ph.A., Goreslavskii, S.P., Becker, W.: *Phys. Rev. Lett.* **89**, 023001 (2002)
175. Figueira de Morisson Faria, C., Becker, W.: *Laser Phys.* **13**, 1196 (2003)
176. Figueira de Morisson Faria, C., Liu, X., Becker, W., Schomerus, H.: *Phys. Rev. A* **69**, 021402(R) (2004)
177. Figueira de Morisson Faria, C., Schomerus, H., Liu, X., Becker, W.: *Phys. Rev. A* **69**, 043405 (2004)
178. Figueira de Morisson Faria, C., Liu, X., Sanpera, A., Lewenstein, M.: *Phys. Rev. A* **70**, 043406 (2004) 324, 325
179. Figueira de Morisson Faria, C., Lewenstein, M.: *J. Phys. B: At. Mol. Opt. Phys.* **38**, 3251 (2005) 321
180. Liu, X., Figueira de Morisson Faria, C.: *Phys. Rev. Lett.* **92**, 133006 (2004) 324

# Chapter 8

## Relativistic Laser–Plasma Interaction

### 8.1 Essential Relativity

#### 8.1.1 Four Vectors

Sporadically, relativistic energies have been considered already in the foregoing chapters. As the laser flux density in the near infrared and visible long wavelength regime exceeds  $I \simeq 10^{18} \text{ Wcm}^{-2}$ , the electron quiver energy assumes relativistic values. A brief presentation of basic relativity may be useful here.

Empty space is homogeneous and isotropic. As a consequence the transformation from a system of reference  $S$  to one  $S'$  moving at constant velocity  $\mathbf{v}$  relative to  $S$  must be linear. If the existence of states or characterizable configurations is postulated, the linear transformations from  $S$  to  $S'$  must form a group. If no limiting (maximum) speed exist the only possible transformation satisfying the requirements above is Galilean,

$$\mathbf{x}' = \mathbf{x} - \mathbf{v}t, \quad t' = t. \quad (8.1)$$

We recall that a reference system is called inertial if Newton's law of motion holds,

$$\frac{d\mathbf{p}}{dt} = \mathbf{f}(\mathbf{x}, \mathbf{v}). \quad (8.2)$$

A force  $f$  explicitly depending on time would violate Galilean relativity [1]. From (8.1) follows that the class of inertial reference systems  $S'(\mathbf{v})$  comprises all systems  $S'$  moving at constant speed relative to each other. An example is the class of free falling elevators, each starting at its individual velocity  $\mathbf{v}_0$  at the instant  $t$ .

Einstein recognized that Maxwell's equations put a finite limit  $c$  on every velocity  $v = |\mathbf{v}|$  reachable in  $S$ . His argument is very simple. Imagine an observer following a light front from behind at  $v$  slightly greater than  $c$ , slowing down to  $c$  when he has caught up with the front and then accelerating slowly away. Along such a travel he observes a finite, quasistatic electric field behind the light front and zero field ahead. In other words, he sees field lines ending in empty space. This is in contradiction with Maxwell's equation  $\nabla \mathbf{E} = \rho_{\text{el}}/\epsilon_0$ , which implies that static field lines must

end in a charge or extend to infinity. With a limiting speed  $c \geq v$  the only transformation from  $S$  to  $S'$  obeying linearity, homogeneity and isotropy of empty space, and forming a group is of Lorentzian type [2]

$$\mathbf{x}' = \mathbf{x} + \frac{\gamma - 1}{v^2}(\mathbf{v}\mathbf{x})\mathbf{v} - \gamma \mathbf{v}t, \quad t' = \gamma \left( t - \frac{\mathbf{v}\mathbf{x}}{c^2} \right) \quad (8.3)$$

with  $\gamma = (1 - v^2/c^2)^{-1/2}$ . The inverse transformation  $(\mathbf{x}', t') \rightarrow (\mathbf{x}, t)$  must show the same structure with the relative velocity  $\mathbf{v}'$  of  $S$  with respect to  $S'$ . From the principle that all  $S$  are equivalent to each other follows  $\mathbf{v}' = -\mathbf{v}$ , a property which was taken for granted by Einstein and followers and was proven only half a century later [3]. Thus

$$\mathbf{x} = \mathbf{x}' + \frac{\gamma - 1}{v^2}(\mathbf{v}\mathbf{x}')\mathbf{v} + \gamma \mathbf{v}t', \quad t = \gamma \left( t' + \frac{\mathbf{v}\mathbf{x}'}{c^2} \right). \quad (8.4)$$

From either (8.3) or (8.4) one deduces the invariant

$$\mathbf{x}'^2 - c^2 t'^2 = \mathbf{x}^2 - c^2 t^2. \quad (8.5)$$

With the pseudo-Euclidean metric  $g_{\alpha\beta} = \delta_{\alpha\beta}$  for  $\alpha, \beta = 1, 2, 3$  and  $g_{4\beta} = -\delta_{4\beta}$  with  $\beta = 1, 2, 3, 4$ , the invariant is recognized as the scalar product of the four vector  $X = (\mathbf{x}, ct) = (x^1, x^2, x^3, x^4)$ ,

$$X^2 = XX = g_{\alpha\beta}x^\alpha x^\beta = \mathbf{x}^2 - c^2 t^2 = s^2. \quad (8.6)$$

The quantity  $s$  is the length of the four vector  $X$ . Its invariance under a Lorentz transformation tells that a reference system change from  $S$  to  $S'(\mathbf{v})$  in four space is a rotation by a certain angle. In (8.6) summation over the repeatedly appearing indices  $\alpha$  and  $\beta$  is understood (summation convention). Greek indices are reserved to four quantities and run from  $\alpha, \beta, \dots = 1$  to 4 while latin indices are used to indicate the spatial components  $i, j, \dots = 1, 2, 3$  of the corresponding four quantities. Bold italic letters designate vectors in the physical space  $\mathbb{R}^3$ .

Imagine now a mass point moving according to  $\mathbf{x} = \mathbf{v}t$  in  $S$ . Then, owing to  $s' = s = \text{const}$  in any inertial frame, in the comoving system  $S'(\mathbf{v})$  holds  $X' = (\mathbf{0}, ct')$  and

$$-c^2 t'^2 = v^2 t^2 - c^2 t^2 \quad \Rightarrow \quad t' = \left( 1 - \frac{v^2}{c^2} \right)^{1/2} t = \frac{t}{\gamma}.$$

The time  $t'$  in the system comoving with the particle is called the proper time  $\tau$ . In differential form (8.6) reads

$$ds^2 = d\mathbf{x}^2 - c^2 dt^2 = -c^2 d\tau^2 \quad \Rightarrow \quad d\tau = \frac{dt}{\gamma}. \quad (8.7)$$

The last of these relations is the formula for time dilation (e.g., of the lifetime of a moving, excited atom). Conversely, it can be shown that from the invariance of  $ds$  alone follows the Lorentz transformation (8.3). The proof of this assertion and all the formulas in this section can be found in [4], Chap. 3 or, better, can be derived as an exercise by the reader himself on the basis of the principles mentioned in the text here (homogeneity and isotropy, existence of states, relativity principle).

Another important consequence of (8.5) or (8.7) is the length contraction of moving scales. Suppose the scale, moving or at rest, in  $S$  is  $d\mathbf{x}$ . If its length in  $S'(\mathbf{v})$  is to be measured it must be kept in mind that the end points of  $d\mathbf{x}'$  have to be fixed at the same time  $t'$ . Hence,  $dt' = 0$  and from (8.7) and (8.3) follows

$$d\mathbf{x}'^2 = d\mathbf{x}^2 - c^2 dt^2, \quad 0 = dt' = \gamma \left( dt - \frac{\mathbf{v} d\mathbf{x}}{c^2} \right).$$

Elimination of  $dt$ , with  $\mathbf{v}_{\parallel}$  the component of  $\mathbf{v}$  parallel to  $d\mathbf{x}$ , yields

$$d\mathbf{x}'^2 = d\mathbf{x}^2 \left( 1 - \frac{\mathbf{v}_{\parallel}^2}{c^2} \right) \quad \Rightarrow \quad |d\mathbf{x}'| = \frac{|d\mathbf{x}|}{\gamma_{\parallel}} \quad (8.8)$$

with  $\gamma_{\parallel} = (1 - \mathbf{v}_{\parallel}^2/c^2)^{-1/2}$ . The scale of length  $dx = |d\mathbf{x}|$  measured in  $S$  appears contracted by the factor  $\gamma_{\parallel}^{-1}$  to an observer measuring its length  $dx' = |d\mathbf{x}'|$  in  $S'(\mathbf{v})$ . The same result is directly obtained from (8.4) by setting  $t' = 0$  where  $t'$  is now the difference in time at which the end points  $\mathbf{x}'_1 = 0$  and  $\mathbf{x}'_2 = \mathbf{x}'$  are fixed. With  $\mathbf{v} \parallel \mathbf{x}$  (8.4) yields  $x = \gamma x'$ , hence  $x' = x/\gamma$ . In order to decide whether to use (8.3) or (8.4) it must be known in which system,  $S$  or  $S'$ , simultaneity of events is required. The Lorentz contraction cannot be “seen.” Formulas (8.8) refer to distances between simultaneous events  $(\mathbf{x}(P_1), t)$ ,  $(\mathbf{x}(P_2), t)$  in spacetime. Observations relate to simultaneous arrivals of light signals (originating from  $P_1$  and  $P_2$ ) in the observer’s eye.

A first useful application of (8.7) and (8.8) is encountered in the transformation of the electromagnetic field from  $S$  to  $S'(\mathbf{v})$ . Assume an electric field  $\mathbf{E}$  and a magnetic field  $\mathbf{B}$  in  $S$ . Imagine an equivalent  $\mathbf{E}$ -field in a given point, generated by a capacitor at rest in  $S$ . An observer at rest in  $S'(\mathbf{v})$  sees an invariant surface charge density  $\sigma$  when  $\mathbf{v}$  is perpendicular to the plates, hence the field component parallel to  $\mathbf{v}$  remains unaltered,  $\mathbf{E}'_{\parallel} = \mathbf{E}_{\parallel}$ . However, when the plates are parallel to  $\mathbf{v}$  the charge density  $\sigma$  is increased by  $\gamma$  as a consequence of the length contraction (8.8). Thus  $\mathbf{E}'_{\perp} = \gamma \mathbf{E}_{\perp}$ . By applying Faraday’s law to a rectangular infinitesimal loop with one segment  $d\mathbf{l}$  moving at velocity  $\mathbf{v}$  one deduces that along the segment the electric field  $\mathbf{v} \times \mathbf{B}$  is induced (see any volume on classical electrodynamics). However, one must be aware that this result is obtained in Galilean relativity (8.1), i.e., from the magnetic flux derivative  $d\Phi/dt$  in  $S$ . This is inconsistent because  $d\Phi/dt'$  in  $S'(\mathbf{v})$  must be calculated. According to (8.7) holds  $d\Phi/dt' = \gamma d\Phi/dt$  and hence  $\gamma \mathbf{v} \times \mathbf{B}$  is the electric field induced by  $\mathbf{B}$  in the moving segment  $d\mathbf{l}$ . Thus the field  $\mathbf{E}'$  acting on a point charge at rest in  $S'(\mathbf{v})$  is given by

$$\mathbf{E}'_{\parallel} = \mathbf{E}_{\parallel}, \quad \mathbf{E}'_{\perp} = \gamma(\mathbf{E}_{\perp} + \mathbf{v} \times \mathbf{B}). \quad (8.9)$$

The magnetic field generated by an infinitely long coil does not change when the coil moves with velocity  $\mathbf{v} \parallel \mathbf{B}$  because cross section and magnetic field flux (number of field lines) remain unchanged. To find the transformation law of  $\mathbf{B}_{\perp}$  the inverse transformation  $\mathbf{E}'_{\perp} \rightarrow \mathbf{E}_{\perp} = \gamma(\mathbf{E}'_{\perp} - \mathbf{v} \times \mathbf{B}')$  can be used to calculate  $\mathbf{v} \times \mathbf{E}_{\perp}$  with the help of (8.9),

$$\begin{aligned} \frac{1}{\gamma^2} \mathbf{v} \times \mathbf{E}_{\perp} &= \frac{1}{\gamma} \mathbf{v} \times (\mathbf{E}'_{\perp} - \mathbf{v} \times \mathbf{B}'_{\perp}) = \mathbf{v} \times (\mathbf{E}_{\perp} + \mathbf{v} \times \mathbf{B}_{\perp}) - \frac{1}{\gamma} \mathbf{v} \times (\mathbf{v} \times \mathbf{B}'_{\perp}) \\ &= \mathbf{v} \times \mathbf{E}_{\perp} - v^2 \mathbf{B}_{\perp} + \frac{1}{\gamma} v^2 \mathbf{B}'_{\perp}. \end{aligned}$$

Thus  $\mathbf{B}$  transforms according to

$$\mathbf{B}'_{\parallel} = \mathbf{B}_{\parallel}, \quad \mathbf{B}'_{\perp} = \gamma \left( \mathbf{B}_{\perp} - \frac{1}{c^2} \mathbf{v} \times \mathbf{E} \right). \quad (8.10)$$

The second equation in (8.10) is directly deduced from (8.9) by making use of the analogy of  $\nabla \times \mathbf{B} = \partial_t \mathbf{E}/c^2$  with  $\nabla \times \mathbf{E} = -\partial_t \mathbf{B}$ . From (8.9) and (8.10) one deduces  $\mathbf{E}'^2 - c^2 \mathbf{B}'^2 = \mathbf{E}^2 - c^2 \mathbf{B}^2$ , and  $\mathbf{E}' \mathbf{B}' = \mathbf{E} \mathbf{B}$ , i.e., the two expressions are Lorentz scalars. The second relation says that  $\mathbf{E} \perp \mathbf{B}$  is an invariant property with respect to a Lorentz transformation; for example the  $\mathbf{k}$  vector of a plane electromagnetic wave may change direction, however  $\mathbf{k}$ ,  $\mathbf{E}$ ,  $\mathbf{B}$  remain mutually orthogonal.

Any quantity  $Y$ , which transforms like a position vector  $X = (x, y, z, ct) = (x^1, x^2, x^3, x^4)$  is called a four vector. The following easily provable criterion is very useful. If the scalar product  $ZY = g_{\alpha\beta} z^{\alpha} y^{\beta}$  of a four vector  $Z$  with a four quantity  $Y$  remains unchanged under an arbitrary Lorentz transformation (8.3),  $Y$  is a four vector, and vice versa, i.e., the scalar product of two four vectors  $Z$  and  $Y$  is Lorentz invariant. Using this criterion, the correct transformation laws of frequency  $\omega$  and wave vector  $\mathbf{k}$  of a light wave in vacuum is found. The phases  $\phi = \mathbf{k}\mathbf{x} - \omega t$  in  $S$  and  $\phi' = \mathbf{k}'\mathbf{x}' - \omega't'$  in  $S'$  must be equal because they count the number of maxima, for example, which reach the observers in  $S$  and  $S'$ . Hence,  $K = (\mathbf{k}, \omega/c)$  is a four vector and transforms as

$$\mathbf{k}' = \mathbf{k} + \frac{\gamma - 1}{v^2} (\mathbf{v}\mathbf{k})\mathbf{v} - \gamma \frac{\mathbf{v}}{c^2} \omega, \quad \omega' = \gamma(\omega - \mathbf{k}\mathbf{v}). \quad (8.11)$$

It is evident that the following quantities with proper time  $\tau$  and rest mass  $m$  are four vectors:

$$\begin{aligned} \text{four velocity} \quad V &= dX/d\tau = \gamma(\mathbf{v}, c), \quad V^2 = \gamma^2(v^2 - c^2) = -c^2, \\ \text{four momentum} \quad P &= mV = (\mathbf{p}, \gamma mc), \quad \mathbf{p} = \gamma m\mathbf{v}, \quad P^2 = -m^2c^2, \\ \text{four acceleration} \quad A &= dV/d\tau, \quad VA = \frac{1}{2} dV^2/d\tau = 0 \quad \Rightarrow \quad A \perp V, \\ &\quad A^2 = \mathbf{a}^2, \quad \mathbf{a} = d\mathbf{v}/dt. \end{aligned}$$

A special criterion for a four quantity  $Y$  to be a four vector is that its square  $Y^2 = g_{\alpha\beta}y^\alpha y^\beta$  is invariant against a Lorentz transformation. From the knowledge  $V^2 = -c^2$ ,  $P^2 = -m^2c^2$ ,  $A^2 = \mathbf{a}^2$  alone follows that  $V$ ,  $P$ ,  $A$  are four vectors. At first glance it may surprise that  $V$ ,  $P$ ,  $A$  are constructed with the help of the position vector  $X$  in  $S$  and the proper time  $\tau$  related to the comoving frame  $S'(\mathbf{v})$ . However, from (8.7) follows that  $d\tau$  is proportional to  $ds$ , which, as an invariant, may be evaluated in  $S$  as well.

If a four quantity  $F = F(x, \mathbf{v})$  is related to the change of the four momentum  $P$  by

$$\frac{dP}{d\tau} = F, \quad (8.12)$$

$F$  is called a four force or Minkowski force. If its spatial components are indicated by  $\mathbf{f} = (f^1, f^2, f^3)$ , it follows

$$\frac{d\mathbf{p}}{d\tau} = \mathbf{f} \Leftrightarrow \frac{d\mathbf{p}}{dt} = \mathbf{f}_E, \quad \mathbf{f}_E = \mathbf{f}/\gamma. \quad (8.13)$$

For obvious reasons  $\mathbf{f}_E$  is given the name Einstein force. It is the relativistically correct three force describing the momentum change in an arbitrary inertial reference frame. In a reference frame  $S'$  comoving with the point particle,  $d\mathbf{p}/dt$  reduces to  $m d\mathbf{v}/dt$ , and  $\mathbf{f}_E$  becomes equal to  $\mathbf{f}$ , which we give the index N,  $\mathbf{f} = \mathbf{f}_N$ , and call  $\mathbf{f}_N$  a Newton force,

$$m \frac{d\mathbf{v}}{dt} = \mathbf{f}_N. \quad (8.14)$$

In general it is correct only in the comoving inertial frame.

As an application of (8.13) we show that the plasma frequency  $\omega_p$  is a Lorentz invariant. For the infinitesimal displacement  $\xi$  (weak field!) in the electric field direction holds in an arbitrary reference system  $S(\mathbf{v}_0)$

$$\begin{aligned} \frac{d\mathbf{p}}{dt} &= \frac{d}{dt}\gamma(\mathbf{v})m\mathbf{v} = \gamma(\mathbf{v}_0)m\frac{d\mathbf{v}}{dt} = \gamma(\mathbf{v}_0)m\frac{d^2\xi}{dt^2} = -e\mathbf{E}; \quad \mathbf{E} = \frac{e}{\epsilon_0}n_e\xi \\ \Rightarrow \frac{d^2\xi}{dt^2} &= -\frac{e^2n_e}{\epsilon_0 m}\xi = -\frac{e^2n_0}{\epsilon_0 m}\xi = -\omega_p^2(n_0)\xi. \end{aligned} \quad (8.15)$$

The last step follows from  $n_e(\mathbf{v}_0) = \gamma(\mathbf{v}_0)n_0$  as a consequence of the Lorentz contraction of  $\xi = \xi'/\gamma(\mathbf{v}_0)$ . Note  $n_e\xi = n_0\xi'$ .

Owing to  $dp^4/dt = dp^4/d\tau = 0$  in the comoving frame  $S'$ , the Minkowski force is  $\mathbf{F} = (\mathbf{f}_N, 0)$ , and hence in an arbitrary reference system  $S(\mathbf{w})$  the four force  $\mathbf{F} = (\mathbf{f}, f^4)$  is given through

$$\mathbf{f} = \mathbf{f}_N + \frac{\gamma - 1}{w^2}(\mathbf{w}\mathbf{f}_N)\mathbf{w}, \quad f^4 = -\gamma \frac{\mathbf{w}}{c} \mathbf{f}_N = -\frac{\mathbf{w}}{c} \mathbf{f}. \quad (8.16)$$

Note that if the particle has a velocity  $\mathbf{v}$  in  $S$ , owing to  $\mathbf{v} = -\mathbf{w}$  one has  $f^4 = \gamma \mathbf{v} f_N/c$ . This relation follows also from  $F \perp P$ . In fact,  $dP^2/d\tau = 2PF = 2\gamma m(\mathbf{v}f - cf^4) = 0$ . With the help of (8.16) the Einstein force on a point charge  $q$  is found. By definition of the electric field, in the rest frame  $S'$  of the charge  $f_N = q\mathbf{E}' = q[\mathbf{E}_\parallel + \gamma(\mathbf{E}_\perp + \mathbf{v} \times \mathbf{B})]$  holds [see (8.9)]. In a frame  $S$  moving at  $-\mathbf{v}$  relative to  $S'$  the transformation law (8.16) requires  $F = q[\mathbf{E}_\parallel + \gamma(\mathbf{E}_\perp + \mathbf{v} \times \mathbf{B}) + (\gamma - 1)\mathbf{E}_\parallel, \gamma \mathbf{v} \mathbf{E}]$ . Hence,  $f_E = q(\mathbf{E} + \mathbf{v} \times \mathbf{B})$ , and the correct relativistic equation of motion in three-space reads

$$\frac{d}{dt}(\gamma m \mathbf{v}) = q(\mathbf{E} + \mathbf{v} \times \mathbf{B}). \quad (8.17)$$

Sometimes the difference between the orbits from (8.13) and (8.17) and the corresponding nonrelativistic equation of motion is attributed to the “relativistic mass increase”. Except special cases this is not a good concept because the “mass increase” depends on the particular motion (e.g. “longitudinal” mass  $m_\parallel$  differing from “transverse” mass  $m_\perp$ ) and may obscure the real origin of (8.13) and (8.17) that is the Minkowski metric of space time.

### 8.1.2 Momentum and Kinetic Energy

Integrating (8.12) from  $\tau = 0$  to  $\tau > 0$  with the point particle initially at rest yields with the help of (8.13)

$$\begin{aligned} P(t) - P(0) &= \left( \int_0^\tau f d\tau, \frac{1}{c} \int_0^\tau f \mathbf{v} d\tau \right) = \left( \int_0^t f_E dt, \frac{1}{c} \int_0^t f_E dx \right) \\ &= (\mathbf{p}, \gamma mc - mc). \end{aligned}$$

It shows that the kinetic energy of the particle is  $E_{\text{kin}} = \gamma mc^2 - mc^2 = E - E_0$  because  $\int_0^t f_E dx$  is the work done by the Einstein force. Hence

$$E = E_0 + E_{\text{kin}} = \gamma mc^2 \quad \Leftrightarrow \quad E^2 = m^2 c^4 + p^2 c^2. \quad (8.18)$$

The second relation is nothing but  $P^2 = -m^2 c^2 = -E_0^2/c^2$ .

Sometimes formulas relating the velocity  $\mathbf{u}$  and the four momentum  $P$  measured in  $S$  to the corresponding quantities  $\mathbf{u}'$  and  $P'$  measured in  $S'(\mathbf{v})$  are useful. According to (8.4) holds for  $dx = \mathbf{u} dt$  and  $dx' = \mathbf{u}' dt'$

$$\mathbf{u} dt = \left( \mathbf{u}' + \frac{\gamma - 1}{v^2} (\mathbf{v} \mathbf{u}') \mathbf{v} + \gamma \mathbf{v} \right) dt', \quad dt = \gamma \left( 1 + \frac{\mathbf{v} \mathbf{u}'}{c^2} \right) dt', \quad \gamma = \gamma(v).$$

Elimination of  $dt'$  leads to the so-called relativistic velocity addition theorem  $\mathbf{v}$  and  $\mathbf{u}'$ ,

$$\mathbf{u} = \frac{\mathbf{u}' + \mathbf{v}[\gamma(1 + \mathbf{u}'\mathbf{v}/v^2) - \mathbf{u}'\mathbf{v}/v^2]}{\gamma(1 + \mathbf{u}'\mathbf{v}/c^2)}. \quad (8.19)$$

If  $u' < c$ ,  $v < c$  is fulfilled  $u < c$  follows because (8.19) implies  $(c^2 - u^2)/c^2 = (c^2 - u'^2)(c^2 - v^2)/(c^2 + \mathbf{u}'\mathbf{v})$ . The inverse transformation for  $\mathbf{u}'$  is obtained from (8.19) by interchanging  $\mathbf{u}$  and  $\mathbf{u}'$  and substituting  $\mathbf{v}$  by  $-\mathbf{v}$ . The analogous formula for  $P$  and  $P'$  is accordingly

$$P = (\mathbf{p}, \gamma mc) = \left( \frac{\mathbf{p}'/\gamma' + \mathbf{v}[\gamma(m + \mathbf{p}'\mathbf{v}/(\gamma'v^2)) - \mathbf{p}'\mathbf{v}/(\gamma'v^2)]}{1 + \mathbf{p}'\mathbf{v}/(\gamma'c^2)}, \gamma mc \right) \quad (8.20)$$

with  $\gamma' = \gamma(u')$ .

The Lagrangian of a particle of rest mass  $m$  moving in a time-independent potential  $V = V(\mathbf{x})$  is

$$L(\mathbf{x}, \mathbf{v}) = T - V = -\frac{m}{\gamma}c^2 - V \quad (8.21)$$

because it obeys the equation of motion

$$\frac{d}{dt} \frac{\partial L}{\partial \mathbf{v}} - \frac{\partial L}{\partial \mathbf{x}} = \frac{d}{dt}(\gamma m \mathbf{v}) + \nabla V = 0,$$

if the force is correctly given by  $-\nabla V$ . Keeping in mind that it should be an Einstein force  $f_E$ , the weakness of a noncovariant Lagrangian (8.21), i.e., a Lagrangian not expressed in four quantities, appears. For instance, when going from  $S$  to  $S'(\mathbf{v})$ , the potential may assume the wrong time dependence. If (8.21) is acceptable the Hamiltonian is given by

$$H(\mathbf{p}, \mathbf{x}) = \frac{\partial L}{\partial \mathbf{v}} \mathbf{v} - L = (m^2 c^4 + p^2 c^2)^{1/2} + V(\mathbf{x}), \quad (8.22)$$

and the canonical equations of motion

$$\frac{d}{dt} \mathbf{p} = -\frac{\partial H}{\partial \mathbf{x}}, \quad \frac{d\mathbf{x}}{dt} = \frac{\partial H}{\partial \mathbf{p}} \quad (8.23)$$

yield the equation of motion above and the connection between  $\mathbf{v}$  and  $\mathbf{p}$  for a point particle, respectively.

### 8.1.3 Scalars, Contravariant and Covariant Quantities

In the basis  $\{\mathbf{e}_i\}$  the vector  $\mathbf{x}$  is the unique linear combination  $\mathbf{x} = x^i \mathbf{e}_i$ , with  $x^i$  the contravariant components (Fig. 8.1). The same vector can also be expressed uniquely by its covariant components  $x_i$ , which are the projections of  $\mathbf{x}$  onto the

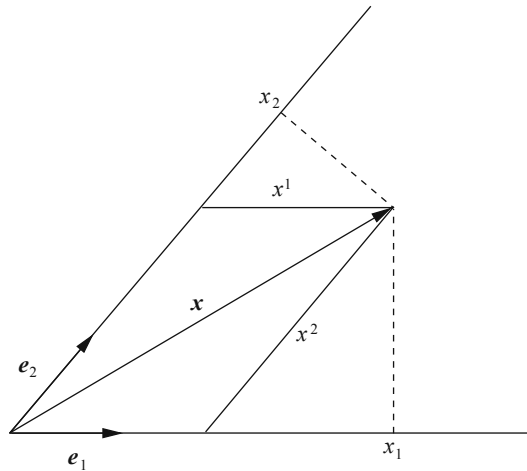


**Fig. 8.1** Contravariant components  $x^1, x^2$  and covariant components (projections)  $x_1$  and  $x_2$

vectors  $\mathbf{e}_i$ ,  $x_i = \mathbf{x} \cdot \mathbf{e}_i$ . With the help of the Euclidean metric  $g_{ik} = \mathbf{e}_i \cdot \mathbf{e}_k = g_{ki}$  and the inverse matrix  $(g^{ik}) = (g_{ik})^{-1}$ , the transformation from one set of components to the other is accomplished by

$$x_i = g_{ik} x^k, \quad x^i = g^{ik} x_k. \quad (8.24)$$

The use of the two types of coordinates allows a compact representation of the scalar product,

$$\begin{aligned} \mathbf{x} \cdot \mathbf{y} &= (x^i \mathbf{e}_i) \cdot \mathbf{y} = x^i (\mathbf{e}_i \cdot \mathbf{y}) = x^i y_i = g_{ik} x^i x^k, \\ ds^2 &= d\mathbf{x} \cdot d\mathbf{x} = g_{ik} dx^i dx^k. \end{aligned} \quad (8.25)$$

The metric of special relativity for a Cartesian coordinate system in  $\mathbb{R}^4$  is given by the  $g_{\alpha\beta}$  of (8.6). It is identical with its inverse matrix,  $g^{\alpha\beta} = g_{\alpha\beta}$ .

A scalar quantity, or Lorentz scalar, is by definition a quantity which is invariant under a general Lorentz transformation. The rest mass  $m$  of a particle and its charge  $q$  are Lorentz scalars, but the density of particles  $n$ , of charge  $\rho_{\text{el}} = nq$  and of mass  $\rho$  are not. In fact, from (8.8) and (8.18) follows in  $S'(\mathbf{v})$

$$n = \gamma n_0, \quad \rho_{\text{el}} = \gamma \rho_{\text{el},0}, \quad \rho = \gamma^2 \rho_0, \quad \gamma = (1 - v^2/c^2)^{-1/2}. \quad (8.26)$$

The index “0” refers to the rest frame  $S$ .

Any four quantity  $Y$ , which transforms like the position vector  $X$ , is a four vector, e.g.,  $V, P, A, K = (\mathbf{k}, \omega/c)$ . For  $Y$  this is the case if  $XY = x^\alpha y_\alpha = f$  with an arbitrary  $X$  is a Lorentz scalar. Any four quantity  $T^{\alpha\beta}$ , which transforms like the product  $x^\alpha x^\beta$ , is a four (or Lorentz) contravariant tensor of second rank, etc. In particular, any null four quantity is a four tensor. The four gradient  $\partial_\alpha$ ,

$$\text{grad}_\alpha = \partial_\alpha = \left( \frac{\partial}{\partial x^1}, \frac{\partial}{\partial x^2}, \frac{\partial}{\partial x^3}, \frac{\partial}{\partial x^4} \right) \quad (8.27)$$

when applied to a scalar  $f$  generates a four vector since

$$df = \frac{\partial f}{\partial x^\alpha} dx^\alpha = \text{grad}_\alpha f dX$$

is invariant under a Lorentz transformation, and  $dX$  is a four vector. According to the criterion above  $\text{grad}_\alpha f = \partial_\alpha f$  is a covariant four vector. Analogously,  $\text{grad}^\alpha f = \partial^\alpha f = \partial f / \partial x_\alpha$  is a contravariant four vector. Further, it is evident that  $\text{grad}_\alpha Y = \partial_\alpha y^\beta$  generates a mixed tensor of second rank  $T_\alpha^\beta$ . The four divergence of a four vector  $V = v^\alpha$ , a four tensor  $T = T^{\alpha\beta}$ , etc.,

$$\text{div } V = \partial_\alpha v^\alpha = \frac{\partial}{\partial x^\alpha} v^\alpha, \quad \text{div } T = \partial_\alpha T^{\alpha\beta} = \frac{\partial}{\partial x^\alpha} T^{\alpha\beta}$$

generates a Lorentz scalar, a four vector, etc.. It is left as an exercise to the reader that the converse is also true.

In practical applications one is frequently faced with the problem of how the partial derivatives  $\partial_t$  and  $\partial_x$  of an entity  $F(x, t)$  transform to  $\partial_{t'}$  and  $\partial_{x'}$  operating on  $F'(x', t')$  in a system  $S'$  moving with velocity  $v$  along  $x$ . To this aim let us assume  $x = g(x', t')$ ,  $t = h(x', t')$ . Equating the total differentials  $dF$  and  $dF'$ ,

$$\begin{aligned} dF &= \partial_{t'} F' dt' + \partial_{x'} F' dx' = \partial_t F dt + \partial_x F dx \\ &= \partial_t F(h_{t'} dt' + h_{x'} dx') + \partial_x F(g_{t'} dt' + g_{x'} dx'), \end{aligned}$$

$g_{t'} = \partial_{t'} g$ , etc., leads to

$$\partial_{t'} F' = \partial_t F h_{t'} + \partial_x F g_{t'}, \quad \partial_{x'} F' = \partial_t F h_{x'} + \partial_x F g_{x'}. \quad (8.28)$$

In the special case of  $g = \gamma(x' + vt')$ ,  $h = \gamma(t' + vx'/c^2)$  results

$$\begin{aligned} \partial_{t'} F' &= \gamma(\partial_t F + v \partial_x F), \quad \partial_{x'} F' = \gamma \left( \frac{v}{c^2} \partial_t F + \partial_x F \right); \\ \partial_t F &= \gamma(\partial_{t'} F' - v \partial_{x'} F'), \quad \partial_x F = \gamma \left( -\frac{v}{c^2} \partial_{t'} F' + \partial_{x'} F' \right). \end{aligned} \quad (8.29)$$

They show the symmetry required by the relativity principle, i.e., the inverse transformation follows from interchanging  $F$  and  $F'$  and substituting  $v$  by  $-v$ . In Galileian relativity  $x = x' + vt'$ ,  $t = t'$  and  $\partial_{t'} F' = \partial_t F + v \partial_x F$ ,  $\partial_x F = \partial_{x'} F'$ .

### 8.1.4 Ideal Fluid Dynamics

In the reference system  $S$  in which an ideal fluid (isotropic pressure, no dissipation) is locally at rest, according to (2.54) and (2.77,  $\boldsymbol{\pi} = 0$ ) holds

$$\partial_t n_0 + \partial_i n_0 v^i = 0, \quad \partial_t \rho_0 v^i + \partial_j (\rho_0 v^i v^j + p \delta^{ij}) = 0. \quad (8.30)$$

The quantities  $J_n = n_0 V = n_0 \gamma(\mathbf{v}, c) = j_n^\alpha$ ,  $n_0$  particle density, and  $T = \rho_0 v^\alpha v^\beta$  are the four vectors of particle flow density and the momentum flow density tensor, respectively. Since their divergence  $\text{div } J_n$  and  $\text{div } T$  are a Lorentz scalar and a Lorentz vector, respectively, and since in the system locally at rest they reduce to (8.30) for a fluid in the absence of pressure ( $p = 0$ ), relativistic particle and momentum conservation for a pressure-free fluid read

$$\partial_\alpha j_n^\alpha = 0, \quad \partial_\alpha T^{\alpha\beta} = 0. \quad (8.31)$$

Thus,  $\text{div } T^{\alpha 4} = \partial_\alpha \rho_0 v^\alpha v^4 = c \partial_i n_0 m \gamma^2 v^i + c \partial_t n_0 m \gamma^2 = 0$  (note  $V = v^\alpha = (\gamma v^i, v^4)$ ,  $v^4 = \gamma c t$  in our convention). Hence, the familiar nonrelativistic equations of particle and mass conservation,

$$\frac{\partial}{\partial t} n + \nabla n \mathbf{v} = 0, \quad \frac{\partial}{\partial t} \rho + \nabla \rho \mathbf{v} = 0, \quad n = \gamma n_0, \quad \rho = \gamma m n \quad (8.32)$$

are also relativistically correct. However, at relativistic energies certain particles may transform into others.

In perfect analogy follows in the absence of pressure that

$$\frac{\partial}{\partial t} \rho v^i + \frac{\partial}{\partial x^j} \rho v^i v^j = 0, \quad \frac{\partial}{\partial t} \rho c^2 + \frac{\partial}{\partial x^i} \rho c^2 v^i = 0 \quad (8.33)$$

hold for all energies. They are identical with their nonrelativistic expressions. The quantity  $\rho c^2$  is the internal energy density (see Sect. 8.1.6). If  $p \neq 0$  the four tensor  $\rho_0 v^\alpha v^\beta$  must be completed by a four tensor  $S^{\alpha\beta}$  in such a way as to yield  $\partial_i S^{ij} = \partial_i p \delta^{ij}$ ,  $i, j = 1, 2, 3$ . This is accomplished by setting

$$T^{\alpha\beta} = \rho_0 v^\alpha v^\beta + S^{\alpha\beta} = \left( \rho_0 + \frac{p}{c^2} \right) v^\alpha v^\beta + p g^{\alpha\beta}. \quad (8.34)$$

$T^{\alpha\beta}$  is clearly a tensor, and hence  $\partial_\alpha T^{\alpha\beta}$  is a four vector  $F$ , which for vanishing velocity  $\mathbf{v}$  must reduce to zero (see (2.77),  $\boldsymbol{\pi} = 0$ ). Therefore  $F = 0$  must hold in any inertial frame, i.e.,  $\partial_\alpha T^{\alpha\beta} = 0$  are the relativistic conservation equations of energy (mass) and momentum. In  $(x, t)$  representation they read

$$\partial_t \left( \rho c^2 + \gamma^2 p \frac{v^2}{c^2} \right) + \nabla(\rho c^2 + \gamma^2 p) \mathbf{v} = 0, \quad (8.35)$$

$$\partial_t \left( \rho + \gamma^2 \frac{p}{c^2} \right) \mathbf{v} + \nabla \left\{ \left( \rho + \gamma^2 \frac{p}{c^2} \right) \mathbf{v} \mathbf{v} + p \mathbf{I} \right\} = 0, \quad \mathbf{I} = (\delta^{ij}). \quad (8.36)$$

In contrast to (2.77) and (2.79) in the relativistic formulation the pressure seems to contribute to the internal energy density  $\rho c^2$  and to the momentum density  $\rho \mathbf{v}$ . However, this would be an erroneous interpretation because the internal energy is defined in the rest frame of the fluid where the pressure term in (8.35) reduces to zero. On the other hand, its presence in the time derivatives of the relativistic conservation equations is understandable from the spatial derivatives of the corresponding expressions in (8.35) and (8.36). In fact,  $\nabla(\gamma^2 p \mathbf{v})$  in (8.35) stands for the work a volume element spends to remove the neighboring fluid element undergoing a spatial change of the field quantities and inducing a corresponding temporal variation through the interconnecting space and time coordinates in a Lorentz transformation. With the help of (8.35) momentum conservation (8.36) can be cast into the Eulerian form just in the same way as in Chap. 2,

$$\left( \rho + \gamma^2 \frac{p}{c^2} \right) \left( \frac{\partial \mathbf{v}}{\partial t} + (\mathbf{v} \nabla) \mathbf{v} \right) = - \left( \nabla p + \mathbf{v} \frac{\partial p}{\partial t} \right). \quad (8.37)$$

### 8.1.5 Kinetic Theory

Multifluid equations may be derived from a relativistic kinetic equation among which the simplest is the collisionless Boltzmann or Vlasov equation. It is obtained as follows. If  $f(X, \mathbf{p}) = f(x^\alpha, p^i)$  is the one-particle distribution function in the 6-dimensional phase space  $(x, \mathbf{p})$  at time  $t$ , the number  $\mathcal{N}(t)$  of noninteracting (i.e., collisionless) particles of one species (electrons, ions of charge  $Z$ , etc.) contained in the one-particle phase space volume element  $\Delta\Gamma(t) = \Delta x \Delta \mathbf{p}$  is given by

$$\mathcal{N}(t) = f(x, \mathbf{p}, t) \Delta\Gamma(t),$$

with  $\Delta\Gamma(t)$  centered around the trajectory  $(x(t), \mathbf{p}(t))$ . The motion of the individual particles is described by the relativistic Hamiltonian  $H(x^i, p^i, t)$  and its canonical equations

$$\frac{dx^i}{dt} = \frac{\partial H}{\partial p^i}, \quad \frac{dp^i}{dt} = -\frac{\partial H}{\partial x^i}, \quad i = 1, 2, 3. \quad (8.38)$$

The trajectories contained in  $\Delta\Gamma(t)$  differ only by their initial conditions  $x_0^i, p_0^i$  at  $t = t_0$  and the Einstein force  $\mathbf{f}_E$  varying from point to point. First we show that the measure of the volume element  $\Delta\Gamma$  is conserved in time (relativistic Liouville theorem). In fact, its  $i$ th projection in Cartesian coordinates is at time  $t + dt$

$$\begin{aligned}
\Delta\Gamma_i(t+dt) &= \Delta x^i(t+dt) \Delta p^i(t+dt) \\
&= \left[ \Delta x^i(t) + \frac{d\Delta x^i}{dt} dt \right] \left[ \Delta p^i(t) + \frac{d\Delta p^i}{dt} dt \right] \\
&= \left\{ \Delta x^i(t) + \left[ \frac{\partial H(x^i + \Delta x^i)}{\partial p^i} - \frac{\partial H(x^i)}{\partial p^i} \right] dt \right\} \\
&\quad \times \left\{ \Delta p^i(t) - \left[ \frac{\partial H(p^i + \Delta p^i)}{\partial x^i} - \frac{\partial H(p^i)}{\partial x^i} \right] dt \right\} \\
&= \left[ \Delta x^i(t) + \frac{\partial^2 H}{\partial x^i \partial p^i} \Delta x^i dt \right] \left[ \Delta p^i(t) - \frac{\partial^2 H}{\partial p^i \partial x^i} \Delta p^i dt \right] \\
&= \Delta x^i(t) \Delta p^i(t) \left[ 1 - \left( \frac{\partial^2 H}{\partial x^i \partial p^i} \right)^2 (dt)^2 \right].
\end{aligned}$$

Thus  $d(\Delta\Gamma_i)/dt = 0$  and hence  $d(\Delta\Gamma)/dt = 0$ . We have chosen this elementary proof because it shows that the only condition for the validity of Liouville's theorem in any finite-dimensional space is the existence of a correct relativistic Hamiltonian. Alternatively, if the validity of Liouville's theorem is taken for granted in the nonrelativistic domain, by transforming to the system comoving with  $\Delta\Gamma$  one is reduced again to the nonrelativistic case of  $d\Delta\Gamma(\mathbf{v} = 0)/d\tau = d(\Delta\mathbf{x}_0 \Delta\mathbf{p}_0)/d\tau = 0$ , and hence in  $S(\mathbf{v})$  holds  $\Delta\Gamma(\mathbf{v}) = (\Delta\mathbf{x}_0/\gamma)(\gamma \Delta\mathbf{p}_0) = \Delta\Gamma(\mathbf{v} = 0)$  and  $d\Delta\Gamma(\mathbf{v})/dt = (1/\gamma)d\Delta(\mathbf{v} = 0)/d\tau = 0$ . From its definition it is clear that  $\mathcal{N}(t)$  is a Lorentz scalar and as such it is conserved,

$$\frac{d\mathcal{N}}{dt} = \frac{df}{dt} \Delta\Gamma + f \frac{d(\Delta\Gamma)}{dt} = \frac{df}{dt} \Delta\Gamma = 0 \quad \Rightarrow \quad \frac{df}{dt} = 0,$$

or, written in explicit form, the Vlasov equation reads

$$\frac{\partial f}{\partial t} + \frac{\partial H}{\partial \mathbf{p}} \frac{\partial f}{\partial \mathbf{x}} - \frac{\partial H}{\partial \mathbf{x}} \frac{\partial f}{\partial \mathbf{p}} = 0 \quad \Leftrightarrow \quad \frac{\partial f}{\partial t} + \{H, f\} = 0. \quad (8.39)$$

$\mathbf{p}$  is the canonical momentum which may differ from the mechanical momentum  $\mathbf{p}_m = \gamma m \mathbf{v}$ . It may be convenient to formulate the Vlasov equation in terms of  $\mathbf{x}$  and  $\mathbf{p}_m$  instead of  $\mathbf{x}$  and  $\mathbf{p}$ . For this purpose we observe that Liouville's theorem remains valid if a new momentum is defined by  $\mathbf{p}' = \mathbf{p} + \mathbf{G}(\mathbf{x}, t)$  because the Jacobian remains unaltered,

$$\frac{\partial(\mathbf{x}, \mathbf{p}')}{\partial(\mathbf{x}, \mathbf{p})} = \frac{\partial(\mathbf{x}, \mathbf{p})}{\partial(\mathbf{x}, \mathbf{p})} = 1.$$

If  $\mathbf{G} = -q\mathbf{A}(\mathbf{x}, t)$  is set, with  $\mathbf{A}(\mathbf{x}, t)$  the vector potential, (8.39) transforms into

$$\frac{\partial f}{\partial t} + \frac{\mathbf{p}_m}{\gamma m} \frac{\partial f}{\partial \mathbf{x}} + f_E \frac{\partial f}{\partial \mathbf{p}_m} = 0, \quad (8.40)$$

where  $f = f(\mathbf{x}, \mathbf{p}_m, t)$ . In the case of charged particles one has  $f_E = q(\mathbf{E} + \mathbf{v} \times \mathbf{B})$ . The one-particle distribution function  $f = \mathcal{N}/(\Delta\Gamma)$  is a Lorentz scalar. The three-form (8.39) is clearly Lorentz invariant since no use of a special reference system has been made in any step of its derivation.

From (8.39) or (8.40) conservation equations, e.g., for momentum and energy densities and their fluxes, can be obtained in the form of moment equations by multiplying it with  $t^{\alpha_1\alpha_2\cdots\alpha_s} = p^{\alpha_1} p^{\alpha_2} \cdots p^{\alpha_s}$  and integrating over the momentum space  $\mathbb{R}_p^3$ , just in the same way as in the nonrelativistic case (see end of Sect. 2.2.1). In order to preserve the four-character of  $t^{\alpha_1\alpha_2\cdots\alpha_s}$  one has to integrate over an invariant volume element in momentum subspace, i.e.,  $d\mathbf{p}/\gamma$  or  $d\mathbf{p}/p^4$ ,  $p^4 = \gamma mc$ . The integrals

$$T^{\alpha_1\alpha_2\cdots\alpha_s} = \int p^{\alpha_1} p^{\alpha_2} \cdots p^{\alpha_s} f(X, \mathbf{p}) \frac{d\mathbf{p}}{\gamma(\mathbf{p})mc} \quad (8.41)$$

clearly define a contravariant four tensor  $T$  of rank  $s$  because any finite sum over the four tensor  $t^{\alpha_1\alpha_2\cdots\alpha_s}$  and hence also the limiting sum, i.e., the integral over the invariant volumes  $d\mathbf{p}/(\gamma mc)$ , are tensors of the same kind. The link with the fluid equations is established by introducing kinetic expressions for particle and charge density, internal energy, pressure, etc. and their fluxes. To this aim the global dynamics has to be split up into an inner component and a macroscopic outer flow component. In other words, the relativistic concept of the center of momentum has to be introduced.

### 8.1.6 Center of Momentum and Mass Frame of Noninteracting Particles

In analogy to the nonrelativistic limit we define for particles of nonvanishing rest mass  $m_i$

$$P = \sum_{i=1}^N m_i V_i = \sum_{i=1}^N m_i \gamma_i (\mathbf{v}_i, c) = M V = M \gamma(v) (\mathbf{v}, c) \quad (8.42)$$

with  $\gamma_i = \gamma(v_i)$ . This definition implies  $\gamma(v)M = \sum_i m_i \gamma_i$ , which is compatible with the definition of the center of mass position four vector

$$\tilde{X} = \frac{1}{\gamma(v)M} \sum_{i=1}^N m_i \gamma_i X_i \quad \Leftrightarrow \quad \tilde{\mathbf{x}} = \frac{1}{\gamma(v)M} \sum_{i=1}^N m_i \gamma_i \mathbf{x}_i \quad (8.43)$$

as long as no forces act on the particles. Then

$$\frac{d\tilde{\mathbf{x}}}{dt} = \frac{1}{\gamma(v)M} \sum_{i=1}^N m_i \gamma_i \mathbf{v}_i, \quad (8.44)$$

in agreement with the center of momentum velocity  $\mathbf{v}$  obtained from (8.42). The point  $\tilde{\mathbf{x}}(t)$  defined by (8.43) may vary from one reference system  $S$  to another  $S'$ . If, for instance, it coincides with the position  $\mathbf{x}_j(t)$  of a particle at time  $t$ ,  $\tilde{\mathbf{x}}(t) = \mathbf{x}_j(t)$ , this may no longer be true when changing to another inertial frame  $S'$ , i.e.,  $\tilde{\mathbf{x}}'(t') \neq \mathbf{x}'_j(t')$  owing to the weighting factors  $\gamma_i$  having changed. In other words, due to the presence of the  $\gamma_i$ ,  $\tilde{\mathbf{X}}$  is not a Lorentzian four vector, in contrast to  $\mathbf{P}$  from (8.42). To illustrate this the reader may imagine two point masses  $m_1 = m_2 = m$  moving at speed close to  $c$  against each other. An observer comoving with mass  $m_1$  sees the center of mass close to  $m_2$ , an observer comoving with  $m_2$  sees it close to  $m_1$ .

It is evident that a reference system  $S_c$  exists in which  $V = (0, c)$  in (8.42). Then

$$\begin{aligned} M_c &= \sum_{i=1}^N m_i \gamma_{ic}, & P = M_c U &= \gamma(\mathbf{u}) M_c(\mathbf{u}, c), \\ \mathbf{x}_c &= \frac{1}{M_c} \sum_{i=1}^N m_i \gamma_{ic} \mathbf{x}_i, & \gamma_{ic} &= \gamma_i(v_{ic}). \end{aligned} \quad (8.45)$$

By  $\mathbf{x}_c$  the center of mass in the rest frame is defined.  $X_c = (\mathbf{x}_c, ct)$  is a Lorentz vector, and with  $\mathbf{x}_c(t) = \mathbf{x}_j(t)$  also  $\mathbf{x}'_c(t') = \mathbf{x}'_j(t')$  holds. An additional advantage of the special choice of the definition (8.45) is that  $M_c c^2$  can be given the simple interpretation of the total internal energy in the case of noninteracting particles. The kinetic energy of the system of  $N$  point masses in the rest frame then reads  $(M_c - \sum_i m_i)c^2$ . Owing to  $c^4(\sum m_i \gamma_i)^2 = M_c^2 c^4 + c^2 \mathbf{p}_c^2$ ,  $\mathbf{p}_c = M_c \gamma_c \mathbf{v}_c$ , the internal energy  $M_c c^2$  is the minimum kinetic energy which the system can assume under a Lorentz transformation. If the center of mass is defined according to (8.43) no such interpretation exists for  $M$ . The only valid statement is that according to (8.44), besides  $\mathbf{x}_c$ , all centers of mass  $\tilde{\mathbf{x}}$  are also at rest in the center of momentum system.

For the interested reader a proof of the existence of  $S_c$  with  $V = (0, c)$  is given. A four vector  $Y = (y, y^4)$  is time-like if  $Y^2 = y^2 - (y^4)^2 < 0$  and space-like if  $Y^2 > 0$ . By choosing a reference system  $S(\mathbf{v}_t)$  with  $\gamma_t \mathbf{v}_t = cy/y^4$  the time-like  $Y$  reduces to  $Y = (0, y_0^4)$  in  $S(\mathbf{v}_t)$  whereas, when setting  $\mathbf{v}_s = cy^4 \mathbf{y}/y^2$  a space-like  $Y$  becomes  $Y = (y_0, 0)$  in  $S(\mathbf{v}_s)$ .  $V_i$  and  $P_i = m V_i$  are time-like. Hence,  $P = P_1 + P_2 = (0, P_1^4) + (P_2, P_2^4)$  is also time-like owing to  $P^2 = -P_1^2 + \mathbf{p}^2 - (P_2^4)^2 - 2P_1^4 P_2^4 < 0$  and  $P_1^4, P_2^4 > 0$ . Assertion  $V = (0, c)$  follows by induction on  $P$  and from  $V = P/M_c$ ,  $M_c$  from (8.45).

### 8.1.7 Moment Equations

In (8.41) the Lorentz invariant volume element in momentum space was introduced to preserve the four tensor character of  $t^{\alpha_1 \alpha_2 \dots \alpha_s}$  under integration. It is shown now that such a choice is stringent on physical grounds and is helpful in interpreting the various moment terms. In Sect. 8.1.5 the distribution function  $f(\mathbf{x}, \mathbf{p}, t)$  was defined

with the help of the co-moving 6D phase space volume element  $d\Gamma_0 = d\mathbf{x}_0 d\mathbf{p}_0$ , indicated here by the index “<sub>0</sub>”.  $d\Gamma = d\mathbf{x} d\mathbf{p}$  is also a Lorentz scalar and as such invariant in any inertial frame, e.g., in the lab frame  $S$ , and hence for the particle number  $d\mathcal{N}$  holds

$$d\mathcal{N} = f \, d\mathbf{x} \, d\mathbf{p} = f_0 \, d\mathbf{x}_0 \, d\mathbf{p}_0. \quad (8.46)$$

By definition the particle number density of momentum  $\mathbf{p}$  in  $S$  in the co-moving frame is  $dn_0 = d\mathcal{N}/d\mathbf{x}_0 = f_0 d\mathbf{p}_0$ . When calculating the particle density  $n(\mathbf{x}, t)$  in  $S$  one has to bear in mind that for each momentum  $\mathbf{p}$  the corresponding  $d\mathbf{x}_0$  has to be chosen such that owing to the Lorentz length contraction it assumes the size  $d\mathbf{x}$  in  $S$ , i.e.,  $d\mathbf{x}_0 = \gamma d\mathbf{x}$ . Thus from (8.46) follows

$$d\mathcal{N} = d\mathbf{x} \, f \, d\mathbf{p} = \gamma \, d\mathbf{x} \, f_0 \frac{d\mathbf{p}}{\gamma} \quad \Rightarrow \quad n_0(\mathbf{x}, t) = \int f \frac{d\mathbf{p}}{\gamma}, \quad (8.47)$$

in agreement with  $d\mathbf{p}_0 = d\mathbf{p}/\gamma$ ,  $d\Gamma = d\Gamma_0$ , and  $f = f_0$ . From (8.41) with  $p^\alpha = p^4$  results  $n(\mathbf{x}, t) = j_n^4/c$  which shows that  $n(\mathbf{x}, t)c = \gamma(\mathbf{u})n_0(\mathbf{x}, t)c$  is the fourth component of the particle current density. Furthermore,  $c \int \mathbf{p} f \, d\mathbf{p}/p^4 = \int \mathbf{v} f \, d\mathbf{p} = \mathbf{j}_n$ . With a view onto (8.42) it shows that the flow velocity  $\mathbf{u}$  is defined by  $\mathbf{u} = \mathbf{j}_n/n$ . In conclusion the following definitions are introduced:

$$\begin{aligned} J_n &= c \int P f \frac{d\mathbf{p}}{p^4} = n(\mathbf{u}, c) = n_0 U, & U &= \gamma(\mathbf{u})(\mathbf{u}, c), \\ n &= \int f \, d\mathbf{p}, & \mathbf{u} &= \frac{1}{n} \int \mathbf{v} f \, d\mathbf{p}, & n &= \gamma(\mathbf{u})n_0, \\ \varepsilon &= c \int (p^4)^2 \frac{d\mathbf{p}}{p^4} = mc^2 \int \gamma(\mathbf{p}) f \, d\mathbf{p} = \varepsilon_{\text{in}} + \varepsilon_{\text{kin}}. \end{aligned} \quad (8.48)$$

The internal energy density  $\varepsilon_{\text{in}}$  is the energy density in the center of momentum system (8.45) with  $\mathbf{u} = 0$ . For clarity the average velocities of the ensemble here and whenever it appears useful is given the symbol  $U$  and  $\mathbf{u}$  to better distinguish it from the individual particle velocities  $V$  and  $\mathbf{v}$ . Note that the averaging procedure for particle density  $n(\mathbf{x}, t)$  and mean flow velocity  $\mathbf{u}(\mathbf{x}, t)$  in the relativistic and nonrelativistic case are identical [compare (2.82)]. In this context formula (8.41) for the moments was justified by the argument that in determining the total number of particles at the time instant  $t$  lying in the interval  $dx^i$  around  $x^i$  each group when moving at momentum  $p^i$  contracts by  $\gamma$  in space. Since, on the other hand  $dx^i \, dp^i$  is Lorentz invariant the shrinking  $dx^i$  has to be compensated by choosing its size in momentum space as  $dp^i/\gamma$ . The averaging procedure (8.41) can be justified on purely formal grounds: If a quantity under consideration coincides with its nonrelativistic expression in the rest frame (like  $n$  and  $j^\alpha$ ) it is relativistically correct in any frame  $S(\mathbf{v})$  because (8.41) generates four quantities out of four quantities.

Decomposition into intrinsic and dynamic components by means of the center of momentum concept (8.45) (Eckart's decomposition [5, 6]) is appropriate for

particles of finite rest mass. In contrast to the nonrelativistic case no simple addition theorem exists for the individual velocity three vectors [see (8.19)]. Decomposition is therefore done in four space. To this aim the individual particle momentum  $P = (\mathbf{p}, p^4)$  is represented as the sum of a vector parallel to the mean flow four velocity  $U$  and a vector  $W = (\mathbf{w}, w^4)$  perpendicular to it,

$$p^\alpha = m(gu^\alpha + w^\alpha), \quad UW = u_\beta w^\beta = 0 \quad (8.49)$$

so that  $w^4 = u_i w^i / u^4$ . In the center of momentum system follows from (8.42)  $\mathbf{w}_i = \gamma_{ic} \mathbf{v}_{ic}$  and  $w_i^4 = 0$ .  $W$  is a space-like vector. From  $P^2 = m^2(gU + W)^2$ ,  $U^2 = -c^2$ , and  $P^2 = -m^2 c^2$  the coefficient  $g = -UP/(mc^2)$  is obtained as  $g = (1 + W^2/c^2)^{1/2}$ . The average  $\langle W \rangle$  is a measure of the internal energy per particle in units of the rest energy  $mc^2$ . In passing from  $\mathbf{p}$  to  $\mathbf{w}$  in (8.41)

$$\frac{d\mathbf{p}}{p^4} = \frac{m^2}{g} \frac{d\mathbf{w}}{u^4} \quad (8.50)$$

has to be used. The general validity of this relation can be verified by a lengthy explicit calculation of the Jacobian  $|\partial(\mathbf{p})/\partial(\mathbf{w})|$ . Alternatively it follows directly in the center of mass system ( $w^4 = 0$ ) and hence in any inertial frame because  $d\mathbf{p}/p^4$  is an invariant measure. The decomposition (8.49) yields for the particle current density  $J = j^\alpha$  and the energy-stress tensor  $T = T^{\alpha\beta}$

$$j^\alpha = n_0 u^\alpha, \quad (8.51)$$

$$T^{\alpha\beta} = (\rho_0 + \epsilon/c^2)u^\alpha u^\beta + P^{\alpha\beta} + (u^\alpha q^\beta + u^\beta q^\alpha), \quad (8.52)$$

where, with  $h(X, \mathbf{w}) = m^3 c f(X, \mathbf{p})$ , the single terms are given by

$$\begin{aligned} \rho_0 &= m \int h \frac{d\mathbf{w}}{u^4}, \quad \epsilon = mc^2 \int (g - 1)h \frac{d\mathbf{w}}{u^4}, \quad P^{\alpha\beta} = m \int w^\alpha w^\beta h \frac{d\mathbf{w}}{gu^4}, \\ q^\alpha &= mc^2 \int (g - 1)w^\alpha h \frac{d\mathbf{w}}{gu^4}. \end{aligned} \quad (8.53)$$

In the local rest frame ( $u^4 = c, w^4 = 0$ ) the mass density  $\rho_0$ , the internal energy  $\epsilon$ , and the corresponding three vectors and three tensors read with  $h' = h/c$

$$\begin{aligned} \rho_0 &= m \int h' d\mathbf{w}, \quad \epsilon = mc^2 \int \left[ \left( 1 + \frac{\mathbf{w}^2}{c^2} \right)^{1/2} - 1 \right] h' d\mathbf{w}, \\ P^{ik} &= m \int \frac{w^i w^k}{(1 + \mathbf{w}^2/c^2)^{1/2}} h' d\mathbf{w}, \\ q^i &= mc^2 \int \left[ 1 - \frac{1}{(1 + \mathbf{w}^2/c^2)^{1/2}} \right] w^i h' d\mathbf{w}. \end{aligned} \quad (8.54)$$

The quantity  $q^i$  represents the local heat flow density. In the nonrelativistic limit  $q^i$  and the remaining quantities in (8.54) reduce to (2.82), (2.83), (2.84), and (2.85) after interchanging  $\mathbf{v}$  for flow with  $\mathbf{u}$  for the single particle there. The total energy density in the rest frame is  $\rho_0 c^2 + \epsilon = T^{\alpha\beta} u_\alpha u_\beta$ . It is also possible to identify  $U$  with the energy transport velocity and  $J = J_m$  with  $\rho_0 u + R$ ,

$$u^\alpha = (\rho_0 + \epsilon/c^2) u^\alpha u^\beta u_\beta = T^{\alpha\beta} u_\beta, \quad R^\alpha = mc^2 \int w^\alpha h \frac{d\mathbf{w}}{gu^4} \quad (8.55)$$

in which case  $q^\alpha = 0$  and  $R^\alpha \neq 0$  holds (see Landau and Lifshitz [7]). With this decomposition the heat flux is hidden in  $J$ . Such a choice may be advantageous in case of massless particles, e.g., photons.

The conservation laws (equations of motion) are obtained from the zeroth order and first order moments of  $P = p^\alpha$ ,

$$\begin{aligned} \text{0th order: } & \int f(X, p) d\mathbf{p} = \int p^4 f(X, p) \frac{d\mathbf{p}}{p^4}, \\ \text{1st order: } & \int p^\alpha f(X, p) d\mathbf{p} = \int p^\alpha p^4 f(X, p) \frac{d\mathbf{p}}{p^4}. \end{aligned}$$

Folding the Vlasov equation (8.40) with  $p^4$  by the invariant measure  $d\mathbf{p}/p^4$ ,

$$\int p^4 [\partial_t f + \mathbf{v} \partial_{\mathbf{x}} f + q(\mathbf{E} + \mathbf{v} \times \mathbf{B}) \partial_{\mathbf{p}} f] \frac{d\mathbf{p}}{p^4} = 0, \quad (8.56)$$

partial integration of the third term and comparison with (8.48) leads to the particle number or charge conservation  $\partial_\alpha j_n^\alpha = 0$  from (8.31):

$$\begin{aligned} 0 &= \int \partial_t f d\mathbf{p} + \int \mathbf{v} \partial_{\mathbf{x}} f d\mathbf{p} + q \int (\mathbf{E} + \mathbf{v} \times \mathbf{B}) \partial_{\mathbf{p}} f d\mathbf{p} \\ &= \partial_t \int f d\mathbf{p} + \partial_{\mathbf{x}} \int \mathbf{v} f d\mathbf{p} + q \sum \int [(E + v \times B)^j f]_{p^j=-\infty}^{p^j=+\infty} dp^k dp^l \\ &= \partial_t n(\mathbf{x}, t) + \nabla[n(\mathbf{x}, t) \mathbf{u}(\mathbf{x}, t)] = \partial_\alpha j_n^\alpha. \end{aligned}$$

The third term vanishes owing to  $f(p^i = \pm\infty) = 0$  and  $\partial_{p^i} v_{j \neq i} = 0$ . Momentum and energy conservation are obtained in the same way by folding (8.40) with  $t^{\alpha 4} = p^\alpha p^4$  as the divergence of  $T^{\alpha i}$  and  $T^{\alpha 4}$ ,

$$\partial_\alpha T^{\alpha i} = n q (\mathbf{E} + \mathbf{u} \times \mathbf{B})^i, \quad \partial_\alpha T^{\alpha 4} = n q \mathbf{u} \cdot \mathbf{E}, \quad (8.57)$$

with  $T^{\alpha i}$ ,  $T^{\alpha 4}$  given by (8.52). Thereby use has been made of

$$\int (\mathbf{E} + \mathbf{v} \times \mathbf{B})^j p^i \frac{\partial f}{\partial p^j} d\mathbf{p} = \delta_{ij} \left\{ \int |\varepsilon_{jkl}| (\mathbf{E} + \mathbf{v} \times \mathbf{B})^j p^i f|_{p^j=-\infty}^{p^j=+\infty} dp^k dp^l - \int (\mathbf{E} + \mathbf{v} \times \mathbf{B})^j f d\mathbf{p} \right\}, \quad (k < l) \quad (8.58)$$

and (8.17) for the fourth component of the Lorentz force.

For a gas of weakly interacting particles in local thermal equilibrium all thermodynamic properties (specific heat, pressure, etc.) are obtained from Maxwell's velocity distribution. From the canonical distribution for (distinguishable) particles the relativistic Maxwell distribution function is obtained by expressing the energy according (8.18) with  $\mathbf{p}$  taken in the local center of mass system,

$$f_M(\mathbf{x}, \mathbf{p}, t) = n_0(\mathbf{x}, t) \mathcal{N} \exp \left[ - \left( E_0^2 + \mathbf{p}^2 c^2 \right)^{1/2} / (k_B T) \right]. \quad (8.59)$$

$\mathcal{N}$  normalizes the exponential to unity,  $n_0$  is the local particle density in the local rest frame and  $t$  is a time variation which is slow on the microscopic time scale. With  $f$  strictly Maxwellian (8.54) yields  $q^i = 0$ .

### 8.1.8 Covariant Electrodynamics

By introducing a vector potential  $\mathbf{A}$  whose curl yields the magnetic field,  $\nabla \times \mathbf{A} = \mathbf{B}$ , the induction law in differential form can be written as  $\nabla \times \mathbf{E} + \dot{\mathbf{B}} = \nabla \times (\mathbf{E} + \dot{\mathbf{A}}) = 0$ . The general solution of this equation is  $\mathbf{E} + \dot{\mathbf{A}} = -\nabla \Phi$  where  $\Phi$  is an arbitrary scalar function of  $\mathbf{x}$  and  $t$ . Hence,

$$\mathbf{E} = -\dot{\mathbf{A}} - \nabla \Phi, \quad \mathbf{B} = \nabla \times \mathbf{A}. \quad (8.60)$$

By defining the four quantity

$$\mathbf{A} = (c\mathbf{A}, \Phi) = (A^1, A^2, A^3, A^4 = \Phi) \quad (8.61)$$

and supposing for the moment that  $A$  is a four vector, the quantity

$$\frac{F_{\alpha\beta}}{c} = \partial_\alpha A_\beta - \partial_\beta A_\alpha \quad (8.62)$$

is a covariant, antisymmetric four tensor (see Sect. 8.1.3). Equation (8.60) is linked to  $F_{\alpha\beta}$  by

$$\begin{aligned} cB_x &= \partial_2 A_3 - \partial_3 A_2 = F_{23}/c, & E_x &= \partial_1 A_4 - \partial_4 A_1 = F_{14}/c, \\ cB_y &= \partial_3 A_1 - \partial_1 A_3 = F_{31}/c, & E_y &= \partial_2 A_4 - \partial_4 A_2 = F_{24}/c, \\ cB_z &= \partial_1 A_2 - \partial_2 A_1 = F_{12}/c, & E_z &= \partial_3 A_4 - \partial_4 A_3 = F_{34}/c. \end{aligned} \quad (8.63)$$

Hence

$$F_{\alpha\beta} = c \begin{pmatrix} 0 & cB_z & -cB_y & E_x \\ -cB_z & 0 & cB_x & E_y \\ cB_y & -cB_x & 0 & E_z \\ -E_x & -E_y & -E_z & 0 \end{pmatrix}, \quad F^{\alpha\beta} = c \begin{pmatrix} 0 & cB_z & -cB_y & -E_x \\ -cB_z & 0 & cB_x & -E_y \\ cB_y & -cB_x & 0 & -E_z \\ E_x & E_y & E_z & 0 \end{pmatrix}.$$

In a general Euclidean metric  $g$  holds  $F^{\alpha\beta} = g^{\alpha\gamma} g^{\beta\delta} F_{\gamma\delta}$ . According to (8.26) and (8.31) the four current density is given by

$$J = \rho_{\text{el},0} V, \quad \partial_\alpha j^\alpha = 0. \quad (8.64)$$

The four current is divergence-free, i.e., the electric charge is conserved. It can be shown that with (8.64) the total charge  $Q$  is both conserved and a Lorentz-scalar (see [2], Sect. 6). The first pair of Maxwell equations

$$\varepsilon_0 c^2 \nabla \times \mathbf{B} - \varepsilon_0 \dot{\mathbf{E}} = \mathbf{j}, \quad \nabla \mathbf{E} = \frac{\rho_{\text{el}}}{\varepsilon_0} \quad (8.65)$$

reads in terms of  $F^{\alpha\beta}$

$$\partial_\alpha F^{\alpha\beta} = -\frac{j^\beta}{\varepsilon_0} \Leftrightarrow \text{div } \mathbf{F} = -\frac{J}{\varepsilon_0}. \quad (8.66)$$

Since  $J$  is a four vector  $F^{\alpha\beta}$  is a four tensor, and consequently  $A$  from (8.61) is a four vector potential.

By comparing the remaining pair of Maxwell equations

$$\nabla \times \mathbf{E} + \dot{\mathbf{B}} = \mu_0 c \mathbf{j}_{\text{mag}}, \quad \nabla \mathbf{B} = \mu_0 c^3 \rho_{\text{mag}}, \quad J_{\text{mag}} = (\mathbf{j}_{\text{mag}}, c\rho_{\text{mag}}) = 0$$

with (8.65) the corresponding field tensor

$$F'^{\alpha\beta} = c \begin{pmatrix} 0 & E_z & -E_y & cB_x \\ -E_z & 0 & E_x & cB_y \\ E_y & -E_x & 0 & cB_z \\ -cB_x & -cB_y & -cB_z & 0 \end{pmatrix} \quad (8.67)$$

satisfying

$$\text{div } \mathbf{F}' = 0 \Leftrightarrow \partial_\alpha F'^{\alpha\beta} = 0 \quad (8.68)$$

is obtained.

There are the two simple, nontrivial Lorentz scalars

$$F_{\alpha\beta} F^{\alpha\beta} = 2c^2(c^2 \mathbf{B}^2 - \mathbf{E}^2), \quad \frac{1}{8c^2} \varepsilon_{\alpha\beta\gamma\delta} F^{\alpha\beta} F^{\gamma\delta} = \mathbf{E} \cdot \mathbf{B} \quad (8.69)$$

where  $\epsilon_{\alpha\beta\gamma\delta}$  is the totally antisymmetric Levi–Civita tensor. The invariance of  $\mathbf{EB}$  against a Lorentz transformation also follows explicitly using (8.9) and (8.10),

$$\begin{aligned}\mathbf{E}'\mathbf{B}' &= \mathbf{E}'_{\parallel}\mathbf{B}'_{\parallel} + \mathbf{E}'_{\perp}\mathbf{B}'_{\perp} = \mathbf{E}_{\parallel}\mathbf{B}_{\parallel} + \gamma_2 \left[ \mathbf{E}_{\perp}\mathbf{B}_{\perp} - \frac{1}{c^2}(\mathbf{v} \times \mathbf{B})(\mathbf{v} \times \mathbf{E}) \right] \\ &= \mathbf{E}_{\parallel}\mathbf{B}_{\parallel} + \mathbf{E}_{\perp}\mathbf{B}_{\perp} = \mathbf{EB},\end{aligned}$$

or from the transformation law of the electromagnetic field tensors  $F$  and  $F'$ . In fact, the Lorentz transformations (8.3) and (8.4) are linear and hence can be written in the form

$$x'^{\beta} = \Lambda_{\alpha}^{\beta}x^{\alpha}, \quad x^{\alpha} = \Lambda_{\beta}^{\alpha}x'^{\beta}, \quad \Lambda_{\beta}^{\gamma}\Lambda_{\alpha}^{\beta} = \delta_{\alpha}^{\gamma} \Leftrightarrow (\Lambda_{\alpha}^{\beta}) = (\Lambda_{\alpha}^{\beta})^{-1} \quad (8.70)$$

to obtain  $F'^{\alpha\beta}$ . It is more convenient to associate the dash ' with the indices, i.e., to write  $x^{\beta'}$  for  $x'^{\beta}$  and  $F^{\alpha'\beta'}$  for  $F'^{\alpha\beta}$ . Hence  $F^{\alpha'\beta'} = \Lambda_{\alpha}^{\alpha'}\Lambda_{\beta}^{\beta'}F^{\alpha\beta}$ . From this equality formulas (8.9) and (8.10) are found again. The matrix  $\Lambda$  describes a so-called Lorentz boost.

The already familiar div-operator  $\partial_{\alpha}$  and the d'Alembertian  $\square$ ,

$$\square = \partial_{\alpha}^{\alpha} = g^{\alpha\beta}\frac{\partial}{\partial x^{\alpha}}\frac{\partial}{\partial x^{\beta}} = \nabla^2 - \frac{1}{c^2}\frac{\partial^2}{\partial t^2} \quad (8.71)$$

are Lorentz covariant and invariant operators, respectively. The invariance of the d'Alembertian is evident owing to the scalar product  $\square = \partial_{\alpha}\partial^{\alpha}$ . To show the covariance of the four divergence consider  $\partial_{\alpha}T^{\alpha\beta}$  where  $T^{\alpha\beta}$  is an arbitrary four tensor. For  $x^{\alpha'} = \Lambda_{\alpha}^{\alpha'}x^{\alpha}$ ,  $T^{\alpha'\beta} = \Lambda_{\kappa}^{\alpha'}T^{\kappa\beta}$

$$\partial_{\alpha'}T^{\alpha'\beta} = \frac{\partial x^{\alpha}}{\partial x^{\alpha'}}\partial_{\alpha}\Lambda_{\kappa}^{\alpha'}T^{\kappa\beta} = \Lambda_{\alpha'}^{\alpha}\Lambda_{\kappa}^{\alpha'}\partial_{\alpha}T^{\kappa\beta} = \delta_{\kappa}^{\alpha}\partial_{\alpha}T^{\kappa\beta} = \partial_{\alpha}T^{\alpha\beta}$$

holds, demonstrating the proper transformation behavior of  $\partial_{\alpha}$  as a four vector. Moreover, if  $\partial_{\alpha}T^{\alpha\beta} = t^{\beta}$  with  $t^{\beta}$  a four vector,  $T^{\alpha\beta}$  is a four tensor (and vice versa). Use of this criterion was made above after (8.66) for the electromagnetic field tensor.

The four vector potential leading to a given field configuration  $F^{\alpha\beta}$  is not unique. One may add the gradient  $\nabla\Psi$  of an arbitrary scalar function  $\Psi(\mathbf{x}, t)$  to  $\mathbf{A}$  and  $-\dot{\Psi}$  to  $\Phi$  without affecting the fields  $\mathbf{E}$  and  $\mathbf{B}$  (gauge transformation).  $\Psi$  can be chosen such that

$$\partial_{\alpha}A^{\alpha} = \nabla c\mathbf{A} + \frac{\partial}{\partial ct}\Phi = 0 \quad (\text{Lorentz gauge}), \quad (8.72)$$

leading to the two separate, inhomogeneous wave equations

$$\Delta A - \frac{1}{c^2} \frac{\partial^2}{\partial t^2} A = -\frac{\mathbf{j}}{\varepsilon_0 c^2}, \quad \Delta \Phi - \frac{1}{c^2} \frac{\partial^2}{\partial t^2} \Phi = -\frac{\rho_{\text{el}}}{\varepsilon_0} \quad (8.73)$$

or in covariant form

$$\square A = -\frac{J}{\varepsilon_0 c}. \quad (8.74)$$

The well-known particular solutions of these equations are given in terms of retarded integrals of  $\mathbf{j}$  and  $\rho_{\text{el}}$ . In the special case of a moving point charge the so-called Liénard-Wiechert potentials read

$$\mathbf{A}(\mathbf{x}, t) = \frac{q}{4\pi\varepsilon_0 c^2} \frac{\mathbf{v}(t')}{R - \mathbf{R}\mathbf{v}(t')/c}, \quad \Phi(\mathbf{x}, t) = \frac{q}{4\pi\varepsilon_0} \frac{1}{R - \mathbf{R}\mathbf{v}(t')/c}, \quad (8.75)$$

where  $t' = t - R/c$ . The vector  $\mathbf{R} = \mathbf{x} - \mathbf{x}_0(t')$  has its origin at the retarded position  $\mathbf{x}_0(t')$  of the particle moving with velocity  $\mathbf{v}(t')$  and points to the point of observation  $\mathbf{x}$ .

## 8.2 Particle Acceleration in an Intense Laser Field

The principle of particle acceleration by a wave, either electromagnetic or electrostatic (or both) is simple and is illustrated by Fig. 8.2 where a point particle is injected into potentials. In (a) the mass point acquires kinetic energy corresponding to its height,  $\Delta E_{\text{kin}} = mgh$ . It gains, however, more energy if the previously fixed structure is moving to the right, as indicated in (b). This is because now the force perpendicular to the slope also does work upon accelerating the particle in  $x$  direction. In the intense electromagnetic wave an electron is first accelerated by the ponderomotive force in the propagation direction (if the transverse gradient of  $E^2$  is weak). In the relativistic regime, direct acceleration by  $\mathbf{E}' = \mathbf{v} \times \mathbf{B}$  sets in preferentially into forward direction over arbitrarily long distances, in principle (c). This is a consequence of the strong frequency Doppler down shift at  $v_x \approx c$ . To avoid misinterpretations, in the lab frame all acceleration work is done by the  $\mathbf{E}$ -field of the laser beam, the Lorentz force, perpendicular to  $\mathbf{v}$ , merely provides for bending the orbit into forward direction. From the engineering point of view the main problem consists in (i) trapping the particle, (ii) guiding the intense wave over a long distance and, perhaps most difficult, (iii) extracting the particle in the right moment before it starts to be decelerated and to lose energy again.

The covariant equation of motion reads

$$m \frac{dV}{d\tau} = \frac{q}{c^2} FV \quad \Leftrightarrow \quad m \frac{dv_\alpha}{d\tau} = \frac{q}{c^2} F_{\alpha\beta} v^\beta, \quad (8.76)$$

which is identical with

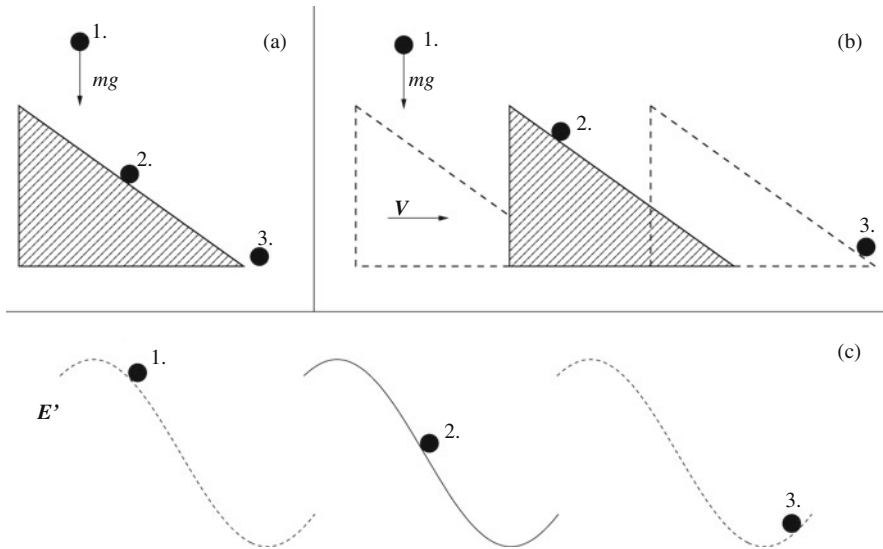


**Fig. 8.2** The principle of particle acceleration in a finite potential structure. (a) Fixed slope, (b) moving slope, (c) electron trapped in a traveling wave

$$\frac{d}{dt}m\gamma v = q(E + v \times B), \quad \frac{d}{dt}m\gamma c^2 = qvE. \quad (8.77)$$

The nonrelativistic Hamiltonian for a point charge in an electromagnetic field is accomplished by the passage from the mechanical momentum  $\mathbf{p}_m = m\gamma\mathbf{v}$  to its canonical counterpart  $\mathbf{p} = \mathbf{p}_m + q\mathbf{A}$ . The Hamiltonian as the sum of kinetic and potential energy  $E = \mathbf{p}_m^2/(2m) + V$  then is  $H = (\mathbf{p} - q\mathbf{A})^2/(2m) + q\Phi$ . According to (8.18) the relativistic energy is  $E = [m^2c^4 + \mathbf{p}_m^2c^2]^{1/2} + V = m\gamma c^2 + V$ . Correspondingly, the relativistic Hamiltonian is set as

$$\begin{aligned} H &= [m^2c^4 + (\mathbf{p} - q\mathbf{A})^2c^2]^{1/2} + q\Phi \\ &= mc^2 \left[ 1 + \left( \frac{\mathbf{p}}{mc} - \mathbf{a} \right)^2 \right]^{1/2} + q\Phi, \end{aligned} \quad (8.78)$$

with

$$\mathbf{a} = \frac{q\mathbf{A}}{mc}.$$

The correctness of the relativistic Hamiltonian (8.78) follows from the canonical equations

$$\begin{aligned}\dot{\mathbf{x}} &= \frac{\partial H}{\partial \mathbf{p}} = \frac{\mathbf{p} - q\mathbf{A}}{m \left[ 1 + (\mathbf{p}/(mc) - \mathbf{a})^2 \right]^{1/2}} = \frac{m\gamma \mathbf{v}}{m\gamma} = \mathbf{v}, \\ \dot{\mathbf{p}} &= -\frac{\partial H}{\partial \mathbf{x}} = -\frac{1}{2m\gamma} \frac{\partial}{\partial \mathbf{x}} (\mathbf{p} - q\mathbf{A})^2 \\ &= q\mathbf{v} \times \mathbf{B} + q(\mathbf{v}\nabla)\mathbf{A} - q\nabla\Phi =: \mathbf{C},\end{aligned}\quad (8.79)$$

and

$$\dot{\mathbf{p}} = \frac{d}{dt} m\gamma \mathbf{v} + q \left[ \frac{\partial \mathbf{A}}{\partial t} + (\mathbf{v}\nabla)\mathbf{A} \right] \stackrel{!}{=} \mathbf{C},$$

leading to the correct equation of motion (8.77). The identity  $\nabla\mathbf{b}^2 = 2[\mathbf{b} \times (\nabla \times \mathbf{b}) + (\mathbf{b}\nabla)\mathbf{b}]$  was used to arrive at expression (8.79).

### 8.2.1 Particle Acceleration in Vacuum

In order to explore the limits of particle acceleration by laser pulses the idealized situation of a plane, linearly polarized electromagnetic wave propagating in  $x$ -direction and acting on a point charge of rest mass  $m$  and charge  $q$  is considered. Let the wave be described by the vector potential  $\mathbf{A}$  and  $\Phi = 0$  (Coulomb gauge),

$$\mathbf{A} = \mathbf{e}_\perp A(\xi), \quad \xi = x - ct, \quad \mathbf{e}_\perp \mathbf{e}_x = 0, \quad \mathbf{e}_\perp^2 = 1. \quad (8.80)$$

The equations of motion with  $\mathbf{e}_\perp = \mathbf{e}_y$  are

$$\dot{p}_y = -\frac{\partial H}{\partial y} = 0, \quad \dot{p}_x = -\frac{\partial H}{\partial x} = \frac{q}{m\gamma} (p_y - qA) \frac{dA}{d\xi}. \quad (8.81)$$

The first equation implies the conservation of the transverse canonical momentum

$$p_y = \gamma mv_y + qA = p_0 = \text{const.} \quad (8.82)$$

From (8.81) and (8.82) follows

$$v_y(\xi) = \frac{p_0}{m\gamma} - \frac{q}{m\gamma} A(\xi), \quad \frac{d}{dt} \gamma mv_x = \frac{q}{m\gamma} (p_0 - qA) \frac{dA}{d\xi}. \quad (8.83)$$

By  $d/dt = (d\xi/dt)d/d\xi = (v_x - c)d/d\xi$  the first of the two equations transforms into

$$\frac{dy}{d\xi} = \frac{p_0}{m\gamma(v_x - c)} - \frac{q}{m\gamma(v_x - c)} A(\xi). \quad (8.84)$$

Energy and momentum conservation require

$$\frac{d}{dt}m\gamma c^2 = qE_y v_y, \quad \frac{d}{dt}m\gamma v_x = qv_y B_z$$

so that

$$\frac{d}{dt}m\gamma(v_x - c) = qv_y \left( \frac{1}{c} \frac{\partial A}{\partial t} + \frac{\partial A}{\partial x} \right) = 0 \Rightarrow m\gamma(v_x - c) = \text{const.} \quad (8.85)$$

Starting with  $v_x = 0$ ,  $x = 0$ , and  $y = 0$  at  $t = 0$  yields

$$y(\xi) = \frac{q}{mc\gamma_0} \int_0^\xi A(\xi') d\xi' - \frac{p_0}{mc\gamma_0} \xi, \quad \gamma_0 = \gamma(v_0), \quad v_0 = v_y(t = 0). \quad (8.86)$$

By integration under the initial conditions  $v_x(t = 0) = 0$ ,  $v_0 = v_y(t = 0)$ ,  $\gamma_0 = \gamma(v_0)$  the second equation of (8.83) becomes

$$\gamma m v_x = \frac{q^2}{2\gamma_0 mc} [A^2(\xi) - A^2(\xi = 0)] - \frac{q}{\gamma_0 mc} p_0 [A(\xi) - A(\xi = 0)]. \quad (8.87)$$

Integrating once more  $v_x = dx/dt$  of this expression in  $t$  under the initial conditions above one arrives at

$$\begin{aligned} x(\xi) = & - \left( \frac{q}{mc\gamma_0} \right)^2 \frac{1}{2} \left[ \int_0^\xi A^2(\xi') d\xi' - A^2(\xi = 0)\xi \right] \\ & + \frac{q}{(mc\gamma_0)^2} p_0 \left[ \int_0^\xi A(\xi') d\xi' - A(\xi = 0)\xi \right]. \end{aligned} \quad (8.88)$$

The energy of the point charge follows from  $\mathcal{E}^2 = m^2 c^4 + c^2 m^2 \gamma^2 (v_x^2 + v_y^2)$ . By substituting the formulas above for  $v_x$ ,  $v_y$  this results in a lengthy expression. It shrinks to a compact size for the initial conditions  $v_x(0) = v_y(0) = A(0) = 0$ ,

$$\mathcal{E} = mc^2 \left[ 1 + \frac{1}{2} \left( \frac{qA}{mc} \right)^2 \right]. \quad (8.89)$$

Finally,  $t(\xi)$  is recovered from  $\xi = x - ct$ ,

$$t = \frac{1}{c}(x - \xi) = -\frac{\xi}{c} + \frac{x(\xi)}{c}, \quad (8.90)$$

with  $x(\xi)$  according to (8.88). The trajectory of the particle is completely determined by the (8.86), (8.88) as a function of  $\xi$ . Owing to  $x < ct$  follows  $\xi < 0$  for increasing  $t$  and hence, a positive or negative charge initially at rest at  $x = \xi = 0$  is pushed into the direction of the propagating wave, i.e., in positive  $x$ -direction here.

For an arbitrary plane wave holds:

- (i) After the pulse has left the particle behind,  $v_x$ ,  $v_y$ , and the energy  $\mathcal{E}$  of the point charge return to their initial values before the arrival of the pulse. In particular, no net energy gain (acceleration) is possible in an interaction over a whole number of cycles. This result for a plane wave in vacuum is a special case of the Lawson–Woodward theorem which states that the net energy gain of a relativistic electron interacting with a continuous electromagnetic field in vacuum is zero [8]. In the photon picture this is a familiar statement: A free charge cannot absorb or emit real photons. The only net effect is a shift in position by  $\Delta x$  according to (8.88) or (8.94).
- (ii) During the laser pulse, maximum acceleration of a charge initially at rest is

$$\Delta\mathcal{E} = \frac{1}{2}\hat{a}^2 mc^2. \quad (8.91)$$

Its lateral angular spread in a pulse of  $A(\xi = 0) = 0$  is

$$\tan \alpha = \left| \frac{v_y}{v_x} \right| = \frac{2}{\hat{a}}. \quad (8.92)$$

The monochromatic plane wave with slowly varying amplitude  $\hat{A}(\varphi)$

$$\mathbf{A}(\mathbf{x}, t) = e_y \hat{A}(\varphi) \sin \varphi, \quad \varphi = kx - \omega t, \quad \omega = ck \quad (8.93)$$

is of particular interest. With the charge initially ( $t = 0$ ) at rest at  $\mathbf{x} = 0$  follows

$$\begin{aligned} \gamma \frac{v_x}{c} &= \frac{1}{2}\hat{a}^2 \sin^2 \varphi, & \gamma \frac{v_y}{c} &= -\hat{a} \sin \varphi, & \frac{v_z}{c} &= 0, & \hat{a} &= \frac{a\hat{A}}{mc}, \\ x &= -\frac{1}{4k}\hat{a}^2 \left( \varphi - \frac{1}{2} \sin(2\varphi) \right), & y &= -\frac{1}{k}\hat{a} \cos \varphi, & z &= 0 & (8.94) \\ t &= \frac{1}{\omega}(kx - \varphi), & \mathcal{E} &= mc^2 \left( 1 + \frac{1}{2}\hat{a}^2 \sin^2 \varphi \right). \end{aligned}$$

In an intense laser field ( $\hat{a} \gg 1$ ) a free charge is mainly accelerated in forward direction under the angle  $\alpha = 2/\hat{a}$ . It should be noted that the Lawson–Woodward theorem can be violated in the presence of additional  $\mathbf{E}$  and  $\mathbf{B}$  fields or in fields of finite extension.

The reference frame in which the oscillation center is at rest deserves special attention. The vector potential in this frame may be assumed as

$$\mathbf{A}(\varphi) = e_y \hat{A}(\varphi) \cos \varphi, \quad \varphi = k(x - ct).$$

From (8.83) and (8.86), (8.87), and (8.88) follows

$$\begin{aligned}\frac{v_y}{c} &= -\frac{\hat{a}}{\gamma(\varphi)} \cos \varphi, & y &= \frac{1}{k} \frac{\hat{a}}{\gamma_0} \sin \varphi, \\ \frac{v_x}{c} &= \frac{\hat{a}^2}{4\gamma_0\gamma(\varphi)} \cos(2\varphi), & x &= -\frac{\hat{a}^2}{8\gamma_0^2 k} \sin(2\varphi).\end{aligned}\quad (8.95)$$

Equation (8.95) describe a figure-8 trajectory. The constant  $\gamma_0$  is conveniently determined with the help of (8.85) for  $\varphi = \pi/4$  since  $v_x(\pi/4) = 0$  and  $v_0 = v_y(\pi/4) = -2^{-1/2}\hat{a}c/\gamma_0$ . Hence,

$$\gamma_0 = \left(1 - \frac{v_0^2}{c^2}\right)^{-1/2} = \left(1 + \frac{\hat{a}^2}{2}\right)^{1/2}. \quad (8.96)$$

The ratio of the excursion amplitudes is given by  $\hat{x}/\hat{y} = \hat{a}/(8\gamma_0)$ . For  $I \rightarrow 0$  it behaves proportional to  $I^{1/2}$  while for  $I \rightarrow \infty$  it saturates at  $\hat{x}/\hat{y} = 2^{-1/2}/4 = 0.1768$  (i.e., the figure-8 never becomes fat).

The mean oscillatory energy  $W$  in the reference frame of the oscillation center may be regarded as an internal energy,  $W = mc^2(\bar{\gamma} - 1)$ . From the considerations on how to define an invariant center of mass it becomes clear that averaging has to be done over the invariant phase  $\varphi = k(x - ct)$  which differs from averaging over time. By observing

$$\gamma d\varphi = \gamma \frac{d\varphi}{dt} dt = \gamma k(v_x - c) dt = -\gamma_0 d(\omega t) \quad (8.97)$$

the invariant oscillation energy results as

$$W = mc^2 \left[ \left(1 + \frac{\hat{a}^2}{2}\right)^{1/2} - 1 \right]. \quad (8.98)$$

This is the elementary proof of (2.17) and the justification for identifying this average with the ponderomotive potential  $\Phi_p$  in (2.22). For an alternative derivation from the Hamilton–Jacobi theory the reader may consult [9].

For a circularly polarized laser field  $\hat{a}^2/2$  has to be replaced by  $\hat{a}^2$ . If the light pulse is not monochromatic but of the form (8.80) the averaging is meaningful if there exists a tangential reference frame in which the particle orbit is almost closed. If in this reference frame the averaged particle mass is  $\gamma_{oc}m$ , its four momentum in the lab frame L is  $P = \gamma_{oc}mV$ . Owing to  $c^2 P^2 = \gamma_{oc}^2 m^2 c^4$  the energy  $W$  averaged in  $\xi$  over one period in the lab frame is correctly given by

$$W = mc^2 \left[ \left(1 + \overline{a^2(\xi)}\right)^{1/2} - 1 \right] = \gamma_L \gamma_{oc} mc^2 \quad (8.99)$$

with  $\gamma_L = \gamma(v_{oc})$  the Lorentz factor of the oscillation center velocity in L.

With a monochromatic wave in the oscillation center frame the velocities  $v_{y \text{ max}}$  and  $v_{x \text{ max}}$  are reached at, e.g.,  $\varphi = 0$  and  $\varphi = \pi/2$ , respectively. For  $\hat{a} \rightarrow \infty$ ,  $v_{y \text{ max}}$  approaches  $c$ , as expected, whereas for  $v_{x \text{ max}}$  from (8.85) and (8.95)

$$\frac{v_{x \text{ max}}}{c} = \frac{\hat{a}^2}{4(1 + 3\hat{a}^2/8)}, \quad (8.100)$$

results with the high intensity limit  $v_{x \text{ max}} \rightarrow 2c/3$ .

To get a feeling for how efficient particle acceleration by laser in vacuum is, the energy and other relevant parameters for free electrons and protons in a Ti:Sa laser beam of intensities between  $I = 10^{18}$  and  $10^{24} \text{ Wcm}^{-2}$  are shown in Table 8.1. The front of the laser pulse is assumed to pass  $x = 0$  at  $t = 0$  and then to increase adiabatically to the steady state intensities given in the Table. Electron (index  $e$ ) and proton (index  $p$ ) are at rest at  $t = 0$ . Maximum energy  $\mathcal{E}_{\text{free}}$  is gained during a quarter cycle ( $\Delta\varphi = \pi/2$ ). If instead a pulse of the form  $\hat{A}_y \cos \varphi$  is used with an amplitude extremely rapidly rising from  $\hat{A}_y(t = 0) = 0$  to its constant full value, according to (8.89) follows the same maximum energy  $mc^2 \hat{a}^2/2$  if now acceleration occurs over half a period  $\Delta\varphi = \pi$ , i.e.,  $T' = \pi/\omega'$  in the co-moving frame. In the lab frame this “half period”  $T$  can be very long.

For comparison, the formulas relevant for Table 8.1 are listed below:

free particle acceleration	quiver motion in oscillation center frame
$A_y = \hat{A}_y(\varphi) \sin \varphi, \quad \varphi = k(x - ct)$	$A_y = \hat{A}_y(\varphi) \cos \varphi, \quad \varphi = k(x - ct)$
$\gamma \frac{v_x}{c} = \frac{1}{2} \hat{a}^2, \quad \gamma \frac{v_y}{c} = -\hat{a}$	$\hat{x} = -\frac{1}{8k} \frac{\hat{a}^2}{\gamma_0}, \quad \hat{y} = \frac{1}{k} \frac{\hat{a}}{\gamma_0}$
$\Delta x = \frac{1}{4k} \hat{a}^2 \frac{\pi}{2}$	$\gamma_0 = \gamma_{\text{oc}} = \left(1 + \frac{1}{2} \hat{a}^2\right)^{1/2}$
$\gamma_{\text{free}} = 1 + \frac{1}{2} \hat{a}^2$	$W = mc^2 \left[ \left(1 + \frac{\hat{a}^2}{2}\right)^{1/2} - 1 \right]$
$\mathcal{E}_{\text{free}} = \frac{1}{2} mc^2 \hat{a}^2$	(8.101)

For electrons the amplitude ratio  $\hat{x}/\hat{y}$  of the quiver motion saturates already at  $I = 10^{20} \text{ Wcm}^{-2}$ . From  $I = 10^{22} \text{ Wcm}^{-2}$  on proton acceleration  $\mathcal{E}_{\text{free}}$  and quiver energy  $W$  are no longer negligible. It is further seen from Table 8.1 that in direct

**Table 8.1** Maximum achievable acceleration  $\mathcal{E}_{\text{free}}$  of electrons and protons in a fourth cycle of a plane Ti:Sa laser pulse (row 5) and corresponding quiver energy  $W$  (row 8) in the oscillation center frame.  $I$  laser intensity,  $\hat{a}$  normalized vector potential amplitude,  $v_y/v_x$  ratio of velocities in field and pulse direction,  $\gamma_{\text{free}}$ ,  $\gamma_{\text{oc}}$  Lorentz factors,  $\Delta x/\lambda$  acceleration distance during a fourth cycle  $\Delta\varphi = \pi/2$  in units of Ti:Sa wavelength ( $\lambda = 800 \text{ nm}$ ) during a fourth cycle,  $\hat{x}/\hat{y}$  ratio of oscillation amplitudes. First column for a given intensity gives the values for electrons, second column (where listed) the values for protons

$I [\text{Wcm}^{-2}]$	$10^{18}$	$10^{20}$	$10^{22}$	$10^{24}$	
$\hat{a}_e, \hat{a}_p$	0.69	6.87	68.67	$3.7 \times 10^{-2}$	686.7
$v_y/v_x$	2.91	0.3	0.03	53.5	$2.9 \times 10^{-3}$
$\gamma_{\text{free}} - 1$	0.24	23.6	$2.36 \times 10^3$	$7 \times 10^{-4}$	$2.36 \times 10^5$
$\mathcal{E}_{\text{free}}$	120.5 keV	12.0 MeV	1.2 GeV	656 keV	120 GeV
$\Delta x/\lambda$	0.03	2.95	295	$8.7 \times 10^{-5}$	$2.95 \times 10^4$
$\gamma_{\text{oc}} - 1$	0.16	3.96	47.6	$3.5 \times 10^{-4}$	484.6
$W$	81.8 keV	2.02 MeV	24.3 MeV	292 keV	247.6 MeV
$\hat{x}/\hat{y}$	0.0740	0.1730	0.1766	$4.6 \times 10^{-3}$	0.1767
					0.045

acceleration by  $I = 10^{22} \text{ Wcm}^{-2}$  the electrons become “heavier” than the protons (1.2 GeV vs. 0.94 GeV). Comparing the two Lorentz factors,  $\gamma_{\text{free}}$  vs.  $\gamma_{\text{oc}}$ , it becomes evident that, in order to get maximum energy gain from the laser field, free particles gain higher energies than particles whose oscillation center is held fixed by reaction forces as is the case in overdense targets. For this reason highest electron energies are observed in tenuous plasmas. Although formulas (8.87) and (8.89) are valid for plane traveling waves only they represent a useful generalization of the ponderomotive concept. When the laser pulse starts sweeping over a slow particle it is ponderomotively accelerated into the direction of the light pulse. With decreasing frequency in the particle frame  $\Phi_p$  increases faster than the intensity of the pulse. Finally, at sufficiently high laser field strength the particle is trapped in the wave and, from then on it gains energy by direct acceleration in the longitudinal field component  $\mathbf{E}' = \gamma \mathbf{v}_y \times \mathbf{B}_z$  thereby maintaining its velocity  $\mathbf{v}$  perpendicular to the total Lorentz force. .

In order to set the accelerated particles free one could think of cutting a plane pulse abruptly, latest at its maximum. However, a quick view to (8.87) shows that this does not help because a rapid change of  $A_y(x, t)$  produces an enormous magnetic field  $B_z = \partial_x A_y$  which reduces  $v_x$  to zero. Nevertheless the plane wave concept is very useful as it shows what the maximum possible acceleration is. With conventional accelerators not much higher energies per unit length than the “standard”  $s = 100 \text{ MeV/m}$  can be reached. It is interesting to note that in the plane monochromatic laser pulse high multiples of  $s$  are achieved, to be precise, according to (8.91)

$$\frac{\mathcal{E}_{\text{free,max}}}{\Delta x} = \frac{\hat{a}^2/2}{\pi \hat{a}^2/8k} mc^2 = \frac{8mc^2}{\lambda}, \quad (8.102)$$

or, for electrons and Ti:Sa,  $\mathcal{E}_{\text{free,max}}/\Delta x = 5 \times 10^4 \text{ s}$ , independently of  $\hat{a}$ . To make the concept of laser acceleration feasible one could think of producing realistic

intense 3D pulses of suitable length. In this case in  $\mathbf{B} = \nabla \times \mathbf{A} = e_z (\partial_x A_y - \partial_y A_x)$  the intense component  $\partial_x A_y$  may be partially neutralized by  $\partial_y A_x$ . Such studies with realistic shock-like laser pulses can be found in the published literature [10]. The pulses used were formed with a steep rise of the field strength inside a half wavelength, with additional minor oscillations which did not disturb anymore the motion of the electron. With  $\hat{a} = 10$  for electrons  $\mathcal{E}_{\text{free}} \cong 30 mc^2$  was calculated. For comparison, an idealized box-like half a wavelength long 1D pulse would yield  $\mathcal{E}_{\text{free}} = 200 mc^2$  [11].

One complication is to inject the electrons into the intense laser field. In order to study this problem the electromagnetic field of a realistic beam of finite width was considered. The Maxwell equations were solved numerically in the paraxial approximation using the angular spectrum method. The idea is to let the electron enter sideways into the laser beam [12]. In most cases this processes leads to a reflection of the electron by the laser beam. Under certain incident angles the electron is captured, and a very moderate acceleration occurs in the periphery of the laser beam. A first proof of principle of particle acceleration by lasers in vacuum was given by focusing a 300 fs Nd laser pulse into the tenuous plasma cloud expanding from a plastic target [13]. At an intensity of about  $10^{19} \text{ Wcm}^{-2}$  typically  $10^5$  electrons could be accelerated into the MeV kinetic energy domain. Large spreads in angle and energy ( $\Delta E$  is almost 100%) are characteristic features of this kind of direct acceleration. By replacing the extended tenuous plasma cloud by a very thin foil of thickness much less than a wavelength it is possible to reduce considerably the energy spread of the accelerated electron bunch in long pulses. To reduce also the angular spread clusters of diameters up to a few tens of nm have to be used and placed into the beam focus in a reproducible way. Analytical studies of 3D solutions for electromagnetic waves, correct even for sub-cycle pulses, and related PIC simulations have shown the possibility of generating coherent ultracold electron beams from very thin foils [14]. The first experimental observation of laser-driven electron acceleration by a single Gaussian laser beam in a semi-infinite vacuum is reported in [15]. The longitudinal field strengths measured are similar to those in conventional accelerators.

### 8.2.2 Wakefield and Bubble Acceleration

Instead of basing acceleration solely on the laser field the use of the high-intensity longitudinal electric field of a plasma wave offers several advantages: (1) intensity increase of the laser pulse by self-focusing and its guiding over longer distances than the geometric focal length, (2) tunability of the excited plasma wave length through careful choice of the plasma density, (3) electrostatic field increase by resonance effects, and (4) ponderomotive self-trapping of electron bunches by self-modulation and backward and forward Raman instability. As a result a much higher number of particles is accelerated, typically of the order of  $10^9$  electrons. On the other hand, the extraction of the particles after successful acceleration is in general a more complex enterprise.

In the laser wake field accelerator (LWFA, [16]) a highly intense laser pulse is focused into an underdense plasma of  $n_e$  ranging typically from some  $10^{18}$  to several  $10^{19}$  electrons per cc. Resonant ponderomotive excitation of an electron plasma wave occurs when the (cold) plasma wavelength  $\lambda_p = 2\pi c_g/\omega_p$ ,  $c_g = \eta c \cong c$  group velocity of the laser pulse, is twice the laser pulse length. When the laser pulse power  $P$  is close to or above the relativistic self-focusing threshold,  $P > 17(\omega/\omega_p)^2$  GW, no such matching condition is necessary because the laser beam amplitude undergoes self-modulation at the plasma frequency by the Raman forward and side scattering instability [17]. This effect resonantly enhances the creation of wake fields by ponderomotively expelling locally the electrons and subsequent overshooting in their return flow. LWFA in the self-modulated regime has been demonstrated in several experiments [18]. Theoretical investigations on self-focusing dynamics and stability are presented in [19]. In the wake fields up to several  $10^{11} \text{ Vm}^{-1}$  could be generated. The spectra of electrons from such fields may vary from purely Maxwellian to genuine spike structures depending in first order on the ratio of laser pulse length to the wavelength  $\lambda_p$  of the excited electron plasma wave. However, next the laser intensity is most important because it determines the regime of operation (e.g., self-modulation).

From a good accelerator device monoenergetic, low divergence beams are expected. A break-through in this respect has been achieved by A. Pukhov with the discovery of the so-called bubble acceleration regime [20]. It consists in a short laser pulse of length  $l = N\lambda = 2\pi c/\omega$  satisfying the inequality  $l \lesssim \lambda_p/2$  and an intensity such as to generate an electron wake which breaks completely after the first oscillation. The laser pulse expels the electrons ponderomotively outward from the region of highest intensity  $\hat{a}^2$ , in forward and lateral direction in much the same way as an electric charge does in the equilibrium plasma (see Fig. 8.3). In the subsequent restoring motion, owing to weak damping, an electron plasma wave develops with wave fronts that move faster on the axis (higher electron density) than on the

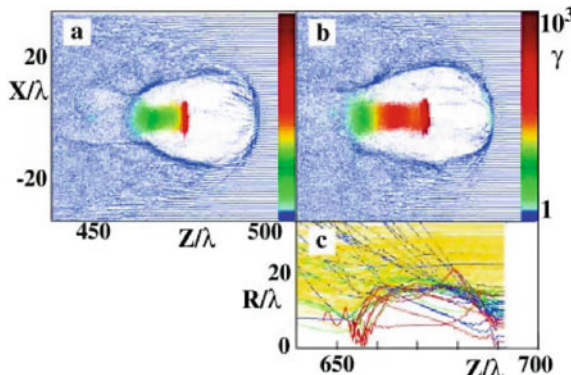


**Fig. 8.3** Solitary laser-plasma cavity produced by a 12J, 33 fs laser pulse in a plasma of density  $n_e = 10^{19} \text{ cm}^{-3}$  [20]. (a)  $ct/\lambda = 500$ , (b)  $ct/\lambda = 700$ , (c) electron trajectories in the frame moving together with the laser pulse

flanks of the laser pulse. As a consequence, transverse (geometrical) wave breaking may set in downstream after a few oscillations. This has been simulated in 3D PIC with a 20 mJ,  $\hat{a} = 1.7$  laser pulse of 6.6 fs length propagating through a uniform plasma of  $n_e = 3.5 \times 10^{19} \text{ cm}^{-3}$ . Most significant,  $10^9$  electrons, preferentially along the axis in front of the trailing electron wave crest, with acceleration up to 50 MeV were observed. The conversion of laser energy into fast electrons amounted to surprising 15%. Their energy spectrum had a plateau-like shape with an abundance of population in the neighborhood of the cutoff. The angular divergence was  $\pm 1^\circ$ .

A second computer run was performed with a 12 J,  $\hat{a} = 10$ , 33 fs long pulse in the same background plasma as before. At such intensity the ponderomotive expulsion is so violent that a nearly evacuated region of the shape of a bubble is created with no following wave crest owing to destructive self-interaction of the electron wake (Fig. 8.3). From the rear side of this solitary bubble an axial high-density bunch of trapped electrons grows out and gains energy in running down the quasistatic potential hill. As a consequence, successively a quasi-monochromatic (20% energy spread) unidirectional ( $\pm 2^\circ$  angular spread) electron beam of  $\mathcal{E}_{\text{free}} \simeq 350 \text{ MeV}$  builds up after  $N = 750$  cycles (Fig. 8.4). Starting from the relations  $N \simeq \lambda_p/\lambda \sim n_e^{-1/2}$ ,  $\mathcal{E}_{\text{wavebreaking}}/\hat{a} \sim (\lambda_p/\lambda)/\hat{a} = \text{const}$  [21] the following scaling for laser irradiance  $I\lambda^2$ , laser power  $P$ , pulse energy  $\mathcal{E}_L$  and maximum electron energy  $\mathcal{E}_{\text{free,max}}$  on the number of laser cycles  $N$  is given in [20]:

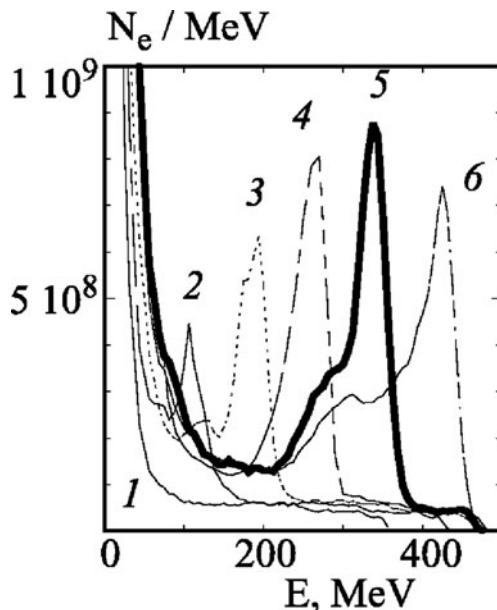


**Fig. 8.4** Time evolution of the spectra of accelerated electrons for the same parameters as in Fig. 8.3. (1)  $ct/\lambda = 350$ , (2)  $ct/\lambda = 450$ , (3)  $ct/\lambda = 550$ , (4)  $ct/\lambda = 650$ , (5)  $ct/\lambda = 750$ , (6)  $ct/\lambda = 850$

$$\begin{aligned} I\lambda^2 &\sim \hat{a}^2 \sim N, & P &\sim I\lambda^2, \\ \frac{\lambda_p^2}{\lambda^2} &\sim N^3, \mathcal{E}_L \sim PN \sim N^4, & \mathcal{E}_{\text{free,max}} &= e E_{\text{max}} L_d \sim N^{5/2} \end{aligned} \quad (8.103)$$

$L_d$  is the “dephasing length”, i.e., the distance an electron covers during its acceleration in the electrostatic field  $E_{\text{max}}$ .  $L_d$  plays an important role because, in order not to lose part of its energy gained along  $L_d$ , the electron must be extracted after the dephasing time  $\tau_d = L_d/c$ . Finally, it has been found that most efficient acceleration is achieved when the parameters laser pulse length and gas (plasma) density are chosen such that acceleration is entirely by the plasma wave and not by the combined action of the laser and the wake field. For completeness it must be mentioned that wake field acceleration driven by short duration intense electron beams in the bubble regime should work in an analogous manner [22].

Recently successful generation of relativistic quasi-monochromatic, highly collimated electron beams has been demonstrated in three experiments. Two of them were run in the resonant mode acceleration [23, 24], the third was operated with pulses longer than  $2\lambda_p$  in a plasma channel in the self-modulated LWFA mode [25]. The experiments yield surprising results and represent more than one step forward in the development of table-top accelerators for significant applications, as for example generation of fs X-rays and coherent TH and infrared radiation. The main parameters and achievements are summarized in Table 8.2. The technique of LWFA with self-guided laser beams in capillary tubes has made rapid progress since then and electron bunches of 1 GeV and beyond have been produced over lengths of the order of 3 cm [26].

### 8.2.2.1 Generation of Intense Ion Beams

The fast electrons produced at the front of a solid target by anharmonic resonance (see Sect. 8.3.3) lead, after crossing the target, to the formation of a hot electron

**Table 8.2** Experiments by Mangles et al. [23], Faure et al. [24] and Geddes et al. [25]. Ti:Sa laser energy  $\mathcal{E}_L$ , pulse duration  $\tau$ , intensity  $I$ , background electron density  $n_e$ , electron energy at peak maximum  $\mathcal{E}_{\text{free}}$ , energy spread  $\Delta\mathcal{E}$ , angular spread  $\alpha$ , number of electrons in the bunch  $N_e$ ,  $N_s$  multiple of acceleration standards  $s = 100 \text{ MeV m}^{-1}$ , acceleration efficiency  $\eta_a = N_e \mathcal{E}_{\text{free}} / \mathcal{E}_L$

Exp.	[23]	[24]	[25]
$\mathcal{E}_L$ [J]	0.5	1.0	0.5
$\tau$ [fs]	40	30	55
$I$ [ $\text{W cm}^{-2}$ ]	$2.5 \times 10^{18}$	$\cong 10^{19*}$	$1.1 \times 10^{19}$
$n_e$ [ $\text{cm}^{-3}$ ]	$2 \times 10^{19}$	$6 \times 10^{18}$	$1.9 \times 10^{19}$
$\mathcal{E}_{\text{free}} \pm \Delta\mathcal{E}$ [MeV]	$70 \pm 3$ %	$170 \pm 11$ %	$86 \pm 2$ %
$\alpha$	$\pm 2.5^\circ$	$\pm 0.3^\circ$	$\pm 1.7^\circ$
$N_e$	$1.4 \times 10^8$	$3 \times 10^9$	$2 \times 10^9$
$N_s$	$1.3 \times 10^3$	570	430
$\eta_a$ [%]	0.3	8.1	5.5

\* Estimated

cloud at the back side and to corresponding space charge fields of  $1 - 10 \text{ MeV}/\mu\text{m}$ . Protons and ions are accelerated from the surface to high energies (“target normal sheath acceleration”, TNSA mechanism) [27–30]. At super-high laser intensities of circularly polarized light ( $\sim 10^{22} \text{ W/cm}^2$ ) direct ponderomotive acceleration of ions starts competing with the TNSA mechanism [31–33].

### 8.3 Collisionless Absorption in Overdense Matter and Clusters

In this Section the interaction of ultrashort laser pulses of high irradiance  $I\lambda \gtrsim 10^{16} \text{ Wcm}^{-2}\mu\text{m}^2$  with overdense plasmas, i.e., with solid and liquid targets is studied. The target surface is ionized in a few cycles of the light wave by field ionization and collisions. Under steady state conditions all phenomena of absorption of intense laser light in extended media are described by the cycle-averaged Poynting theorem,

$$\overline{\nabla S} = -\overline{j E}, \quad (8.104)$$

with  $I = |\overline{S}|$ . In terms of this relation the absorption by the free electrons in the plasma is due to deviations of their phase from  $\pi/2$  between  $j$  and  $E$ . By introducing a phenomenological collision frequency  $\nu$  in a generalized Drude model the right hand side term becomes for a harmonic field  $E = \hat{E}(x) \exp(-i\omega t)$

$$\overline{j E} = \frac{1}{2} \epsilon_0 \omega_p^2 \frac{\nu}{\omega^2 + \nu^2} \hat{E} \hat{E}^*. \quad (8.105)$$

The current density is the sum of three terms,

$$j = j_b + j_i + j_e, \quad (8.106)$$

where  $j_b$  is the polarization current of the bound electrons,  $j_i$  is the current density generated by the electrons escaping from atoms undergoing ionization, and  $j_e$  is the contribution by the free electrons. On the basis of kinetic considerations moment equations can be derived which result in nonstandard fluid equations [34]. With  $W_i$  the ionization rate,  $n_b$  the density of the bound electrons, and  $\mathcal{E}_i + \langle \mathcal{E}_j \rangle$  the sum of ionization energy  $\mathcal{E}_i$  and average ejection or above-threshold ionization energy  $\langle \mathcal{E}_j \rangle$ , the ionization current density reads (neglecting the influence of  $B$ )

$$j_i = n_b W_i \frac{\mathcal{E}_i + \langle \mathcal{E}_j \rangle}{E^2} E. \quad (8.107)$$

As a rule, under the action of a strong laser field both classical as well as quantum calculations lead to an average ejection energy [35]

$$\langle \mathcal{E}_j \rangle \cong \frac{1}{2} \mathcal{E}_i. \quad (8.108)$$

Neglecting  $j_b$  as a small quantity and keeping in mind that the power going into kinetic and heating energy is represented by  $j_e E - v_i n_e m u_e^2$  with  $u_e$  the electron fluid velocity, in the Drude model (see (2.23)) the ionization energy balance reads as  $v_i n_e m u_e^2 = n_b W_i (\mathcal{E}_i + \langle \mathcal{E}_j \rangle)$ . Hence,

$$v_i = \frac{n_b}{n_e} W_i \frac{\mathcal{E}_i + \langle \mathcal{E}_j \rangle}{m u_e^2}, \quad (8.109)$$

and  $v$  from (8.105) is the sum  $v = v_i + v_{ei} + v_{en}$  where  $v_{en}$  is the collision frequency of the free electrons with the neutral atoms and molecules. The “ionization frequency”  $v_i$  induces the necessary dephasing of  $j_e$  with respect to its free motion to account for the amount of energy spent in field ionization. When  $u_e$  is close to changing sign,  $v_i$  has a tendency to become singular. Therefore in numerical simulations direct use of  $j_i$  from (8.105) in  $\bar{j} \bar{E}$  is the better choice than  $v_i$  in combination with the right hand side of (8.105) although the two expressions are equivalent.

From (8.105) an estimate of the efficiency of “collisional” absorption is obtained by setting  $I = \varepsilon_0 c \hat{E} \hat{E}^*$  and  $\bar{j} \bar{E} = -dI/dx$ . The absorption length  $L_\alpha = 1/\alpha$ ,  $\alpha$  absorption coefficient in the sense of Beer’s law, becomes

$$L_\alpha^{-1} = \frac{n_e}{n_c} \frac{v}{c(1 + v^2/\omega^2)}. \quad (8.110)$$

In using this expression one has to keep in mind that for large values of  $n_e/n_c$  generally almost all incident radiation is reflected unless  $v^2/\omega^2 \gtrsim n_e/n_c$ . After the very initial phase of irradiation ( $I \gtrsim 10^{17} \text{ W cm}^{-2}$ )  $v_{ei}$  prevails on  $v_i$ . Then, a typical electron density may be of the order of  $n_e = 10^{23} \text{ cm}^{-3}$ . With  $n_e/n_c \cong 60$ ,  $T_e = 1 \text{ keV}$  follows  $v_{ei}/\omega_{Ti:Sa} \cong 0.05$  and  $L_\alpha \cong 0.07 \lambda_{Ti:Sa}$ . This has to be compared with the skin length  $\lambda_s = c/\omega_p = 0.02 \lambda_{Ti:Sa} \ll L_\alpha$ . Furthermore, the condition for strong reflection,  $R = (\eta - 1)^2/(\eta + 1)^2 \cong 0.6$ , is fulfilled owing to  $n_e \gg n_c$  and  $\eta^2 \cong n_e/n_c$ . Thus, latest from  $T_e = 1 \text{ keV} \times Z^2$  on collisional absorption is ineffective. It has indeed been shown clearly in experiments that the laser plasma interaction assumes a universal behavior at high laser irradiances which is predominantly determined by collective interactions [36].

### 8.3.1 Computer Simulations of Collisionless Laser–Target Interaction

The interaction at relativistic intensities, i.e., when the oscillatory electron energy is determined by (8.98) and no longer by  $mc^2 \hat{a}^2/4$ , is highly nonlinear even in the simplest geometry and is therefore a domain of computer simulations. The procedures used so far are based on particle-in-cell (PIC) [37, 38], Vlasov [39], and molecular dynamics (MD) methods [40, 41]. PIC codes are, in principle, collisionless and

suitable to describe collective interactions with reasonable computing effort in three space dimensions and three dimensions in momentum/velocity space (3D3V). PIC is flexible, bound to a mesh and relatively noisy. Entropy conservation is not so well fulfilled. Relativistic Vlasov codes solve the Vlasov equation (8.40) in combination with Maxwell's equations plus the momentum equation (8.17). At present, time economy is possible only in 2D3V. As a compensation Vlasov codes are nearly free of noise. MD codes can handle collective and collisional interactions, altogether mesh-free, with great precision. The effort in describing the collective interaction is greatly reduced by making use of a tree hierarchy [42, 41].

The treatment of relativistic interaction of an obliquely incident plane wave on a half space filled with a fully ionized plasma is feasible in p-polarization by a 1D2V Vlasov code [39]. Since it offers a detailed and very accurate picture of the collisionless interaction a summary of the main aspects of interaction obtained from Vlasov runs is presented in what follows.

A fully ionized target is assumed with the ions forming an immobile overdense background which is separated from the vacuum by a small plane transition layer of relative thickness  $L/\lambda \ll 1$ ,  $\lambda$  being the vacuum wavelength. The laser pulse is represented by a plane p-polarized wave incident under the angle  $\alpha$ . The size of the simulation box needed depends on the intensity and the scale length. Four vacuum wavelengths in the  $x$ -direction and  $50mv_{\text{th}}$  ( $v_{\text{th}}$  is the thermal velocity) in momentum space proved to be sufficient to conserve energy and particle number.

First, collective absorption of a plane wave under normal incidence is studied. The ion density  $n_i$ , normalized to the critical density  $n_c$ , is taken as large as  $n_i = 25$ . The electrons start from a Maxwellian distribution of initial temperature  $T_e = 10 \text{ keV}$  and a local equilibrium particle density  $n_e(x)$  corresponding to the ambipolar field produced by  $T_e$ . In order to simulate the pure case of a solid target with a step-like transition from the vacuum  $n_e = 0$  to  $n_e = 25$  the transition layer was chosen as small as  $L/\lambda = 0.023$ . The laser beam is switched on over half an oscillation period. Four cycles later all physical quantities have turned into a steady

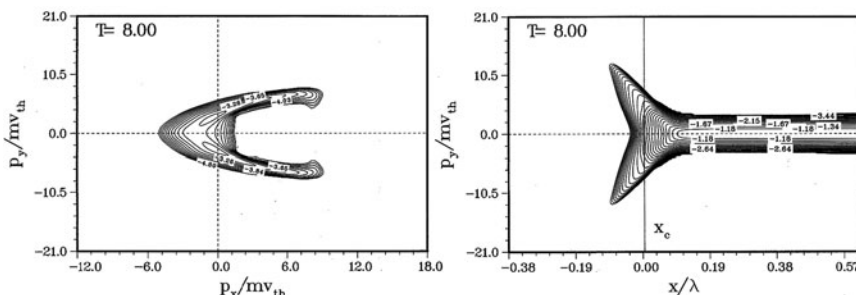


**Fig. 8.5** Contour line plot of the cycle-averaged electron distribution function centered at  $T = 8$  cycles in a logarithmic scale [39] (a):  $f_e(x, p_x, p_y, t)$  at critical density. (b):  $g_e(x, p_y, t)$ ,  $x_c$  position of the critical density (“critical point”); the conservation of the canonical momentum is evident. The parameters are  $I\lambda^2 = 10^{18} \text{ Wcm}^{-2}\mu\text{m}^2$ ,  $n/n_c = 25$ ,  $T_e = 10 \text{ keV}$ ,  $L/\lambda = 0.023$ , and  $\theta = 0^\circ$

state. Figure 8.5(a) shows the contour lines of the cycle-averaged electron distribution function  $f_e(x, p_x, p_y, t)$  at critical density  $x = x_c$ . The perfect symmetry of  $f_e$  with respect to  $p_y = 0$  suggests fast electron generation twice a cycle. Due to the conservation of the transverse canonical momentum the force on the electrons is of second order in  $A_y$  and oscillates with twice the frequency of the laser field. Hence, it produces jets twice per cycle as was first described by Kruer and Estabrook [43]. By simple reasoning their maximum energy  $E_{\max}$  was obtained,

$$E_{\max} = mc^2 \left\{ \left[ 1 + \frac{v_{\text{th}}^2}{c^2} \left( \frac{p_x}{mv_{\text{th}}} \right)_{\max}^2 \right]^{1/2} - 1 \right\} \simeq 310 \text{ keV}; \quad (8.111)$$

it equals four times the mean vacuum oscillation energy ( $v_{\text{th}} = \sqrt{k_B T_e / m}$ ). A similar expression was obtained by Wilks [44]. Since  $A_y$  vanishes in the overdense plasma the electron distribution function  $g_e(x, p_y, t) = \int dp_x f_e(x, p_x, p_y, t)$  must retain its original shape there owing to canonical momentum conservation (8.82) in  $y$ -direction [see Fig. 8.5(b)]. For the parameters of Fig. 8.5 the formation of electron jets results in an absorption of 13.6%. The generation of fast particles is best seen from the time-resolved distribution function  $g_e(x, p_x, t) = \int dp_y f_e(x, p_x, p_y, t)$ . It is particularly pronounced for low  $n_e/n_c$  values (see Fig. 8.6 for  $n_e/n_c = 2$ ).

The case of oblique incidence is studied in the boosted frame in which the transverse canonical momentum  $p_y - eA_y(x, t)$  is again conserved (see next Section). Figure 8.7 shows that for an angle of incidence of  $\theta = 45^\circ$  particle jets of two different peak velocities exist. The energy of the fastest particles now exceeds the energy of those generated at normal incidence. The force on the electrons is now of first order in  $A_y$ . Thus, it oscillates with the laser frequency and produces electron

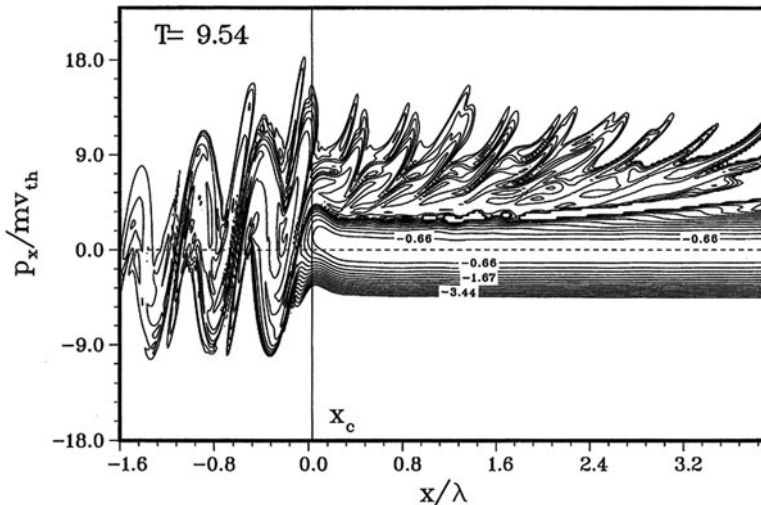


**Fig. 8.6** Contour line plot of the electron distribution function  $g_e(x, p_x, t)$  in a logarithmic scale at  $T = 9.54$  cycles [39]. The parameters are  $I\lambda^2 = 10^{18} \text{ Wcm}^{-2}\mu\text{m}^2$ ,  $n_e/n_c = 2$ ,  $T_e = 10 \text{ keV}$ ,  $L/\lambda = 0.15$ , and  $\theta = 0^\circ$ ;  $x_c$  is critical point

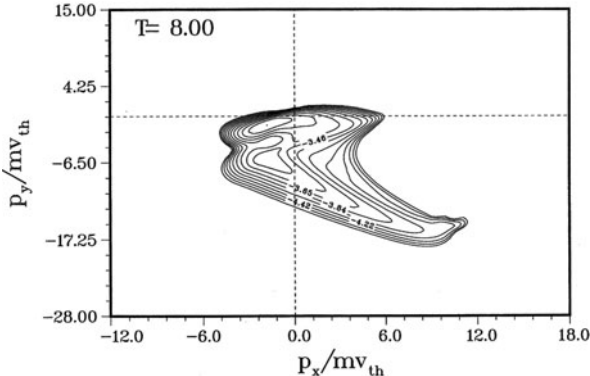


**Fig. 8.7** Contour line plot of the cycle-averaged electron distribution function  $f_e(x, p_x, p_y, t)$ , centered at  $T = 8$  cycles, in the boosted frame at critical density in a logarithmic scale [39]. The parameters are  $I\lambda^2 = 10^{18} \text{ Wcm}^{-2}\mu\text{m}^2$ ,  $n_e/n_c = 25$ ,  $T_e = 10 \text{ keV}$ ,  $L/\lambda = 0.023$ , and  $\theta = 45^\circ$

jets only once per cycle. This is the reason for the asymmetry of  $f_e(x, p_x, p_y, t)$  in Fig. 8.7. For the maximum energy (8.111) one obtains  $\mathcal{E}_{\max} \simeq 485 \text{ keV}$  which is now six times the mean vacuum oscillation energy. The time-resolved distribution function  $g_e(x, p_x, t) = \int dp_y f_e(x, p_x, p_y, t)$  for  $n_e/n_c = 2$  is shown in Fig. 8.8. The isocontours in Figs. 8.5 – 8.8 are labeled according to  $\ln[f_e(\mathbf{p})/f_e(\mathbf{p} = 0)] = -\mathbf{p}^2/2mk_B T_e$  and  $\ln[g_e(p_{x,y})/g_e(p_{x,y} = 0)] = -p_{x,y}^2/2mk_B T_e$ ;  $T_e$  initial temperature. Note, in the absence of collisions, as here, the electron orbits do not cross the isodensity contour lines.

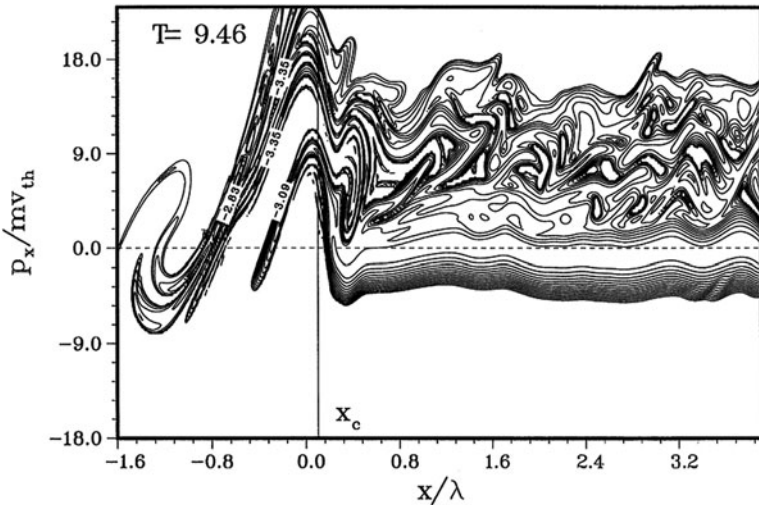


**Fig. 8.8** Contour line plot of the electron distribution function  $g_e(x, p_x, t)$  in the boosted frame in a logarithmic scale at  $T = 9.54$  cycles [39]. The parameters are  $I\lambda^2 = 10^{18} \text{ Wcm}^{-2}\mu\text{m}^2$ ,  $n/n_c = 2$ ,  $T_e = 10 \text{ keV}$ ,  $L/\lambda = 0.15$ , and  $\theta = 45^\circ$ . The position of  $n_c$  is indicated by  $x_c$ . The return current ( $p_x < 0$  at  $x > 0$ ) is only slightly disturbed (see lower contours for  $p_x < 0$ )

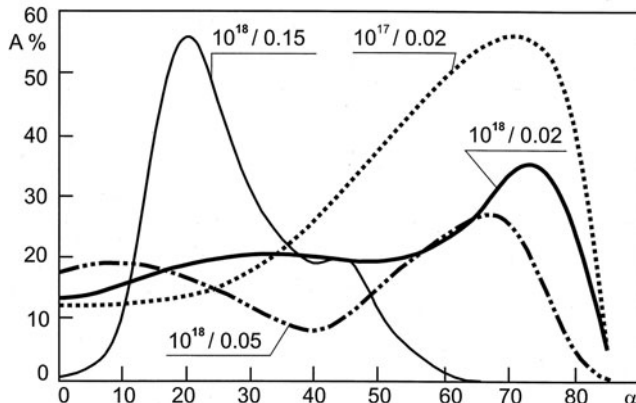


**Fig. 8.9** Vlasov simulation of collective absorption  $A$  in a plane target as a function of the angle of incidence  $\alpha$ . The parameters indicate the irradiance in  $\text{Wcm}^{-2}\mu\text{m}^2$  and the ion density profile length  $L$  in units of wavelength  $\lambda$ . The plasma is 25 times overcritical, except thin solid line for  $10^{18}/0.15$  where  $n_e/n_c = 2$ . With  $L$  fixed  $A$  decreases with increasing irradiance;  $A$  is very sensitive to  $L$

Of particular interest is the cycle-averaged overall absorption coefficient  $A$  versus angle of incidence, given here for different parameters: irradiance, density, profile length (Fig. 8.9). It shows important aspects not observed in earlier PIC simulations: (i) for short scale lengths the maximum absorption occurs around  $\alpha = 70^\circ$ ; (ii) for high irradiances substructures (secondary maximum and local minimum) are present; (iii) the degree of absorption correlates with the magnitude of a secular (dc) magnetic field generated on the target surface. For  $I\lambda^2 = 10^{17} \text{ Wcm}^{-2}\mu\text{m}^2$  and  $L/\lambda = 0.02$  the magnetic field  $B_z$  is small ( $B_z \leq 8 \text{ MG}$ ). The corresponding absorption profile has a simple shape with only one maximum ( $A_{\max} \simeq 56\%$ ). For  $I\lambda^2 = 10^{18} \text{ Wcm}^{-2}\mu\text{m}^2$  and  $L/\lambda = 0.02$  (bold solid curves)  $B_z$  reaches up to 33 MG. The associated peak absorption decreases by almost a factor of two compared to the case where  $B_z \max = 8 \text{ MG}$ . In addition, the absorption profile shows a pronounced plateau. Furthermore, by increasing the scale length to  $L/\lambda = 0.05$  the secular magnetic field more than doubles ( $B_z \max \simeq 85 \text{ MG}$ ), thus lowering the overall absorption below the former values and depressing the former plateau to a pronounced minimum at  $\alpha \simeq 45^\circ$ . The origin of the dc  $\mathbf{B}$ -field is to be attributed to light pressure. The electron density is ponderomotively steepened and hence in the largely overdense plasma ( $n_e = 25 n_c$ ) a charge double layer is generated, positive ( $n_e < n_i$ ) at the vacuum boundary and negative ( $n_e > n_i$ ) inside. In the system boosted at a speed  $c \sin \alpha$  the charge imbalance gives rise to a narrow current double layer which, according to Ampère's law leads to a well localized dc magnetic field. In the slightly overdense plasma  $n_e \simeq 2 n_c$  substructures appear in the charge double layer, with the consequence of substructures in  $\mathbf{B}$ . For  $I\lambda^2 = 10^{18} \text{ Wcm}^{-2}\mu\text{m}^2$ ,  $L/\lambda = 0.15$ , and  $n/n_c = 2$  one observes the familiar scaling of the peak of resonance absorption with a scale length according to

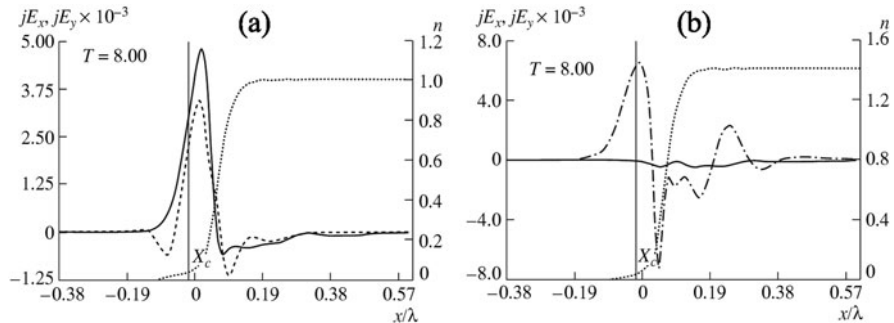


**Fig. 8.10** 1D2V Vlasov results of  $\overline{j_x E_x}$  (solid) and  $\overline{j_y E_y}$  (dotted or dotted-dashed) at  $10^{18} \text{ Wcm}^{-2} \mu\text{m}^2$  as a function of position  $x$  for an angle of incidence  $\alpha = 45^\circ$  in the lab and in the boosted frame. Plasma (dotted line) is 25 times overcritical; critical density is located at  $x_c = 0$ .  $\overline{j_x E_x} = 0$  in the boosted frame is well fulfilled

$(2\pi L/\lambda)^{2/3} \sin^2 \alpha \approx 0.5$  (Sect. 4.1). The distribution of the absorbed power (8.104) at  $T = 8$  laser periods in space is presented in Fig. 8.10 from the view of the lab frame and the boosted frame. In the latter case  $\overline{j_x E_x}$  is nearly zero. Under which conditions this holds is discussed in the next Section. The electrons (dotted line) are pushed into the target by the light pressure.

Plane geometry with translational symmetry as considered here is convenient for studying basic aspects of the interaction. A more realistic picture is obtained by passing to 2D3V simulations. In 2D corrugated targets can be described. Owing to the high light pressure the nonuniformity of the incident laser beam creates a crater-like structure resembling the interaction of long pulses with solid targets (see Chap. 2). As will be seen deviations from plane geometry will add additional topological possibilities to the interaction dynamics. It would be desirable to perform Vlasov calculations also in 2D. However, at present they are too time-consuming in general, and hence, in more complex cases, use of PIC simulations has to be made in the following analysis of 2D effects. Part of these simulations are performed with mobile ions. For them, surface corrugation is dynamically generated in the course of the simulations. Other simulations are parametric, i.e., the corrugation is imposed in the first place [45].

In 2D simulations all fields depend on the spatial variables  $x$  and  $y$ . The Vlasov distribution functions for the ions and electrons also depend on two momentum coordinates  $p_x$  and  $p_y$ . A  $350 \times 128 \times 51 \times 51$  grid for the electrons and a  $350 \times 128 \times 41 \times 41$  grid for the ions is used. In all Vlasov simulations presented now the initial temperatures are 1 keV for ions and 10 keV for electrons. The laser wavelength is 1  $\mu\text{m}$ . For the PIC simulations a  $1500 \times 1028$  spatial grid for the electrons and ions is used. The quasi-particle numbers for electrons and ions are  $1.5 \times 10^7$  each. The initial electron and ion temperatures are zero. However, a resolution corresponding to the thermal Debye length at 10 keV is taken. The wavelength is 1  $\mu\text{m}$ . For both simulation methods the intensities are kept constant after a rise time of two optical cycles.

First a thin target is considered, i.e., a preformed plasma layer with an imposed deformation characterized by the longitudinal position of the peak density  $x(y) = \delta \exp[-(y - y_0)^2/\gamma^2]$ , where  $\delta$  is the deformation depth as indicated in Fig. 8.11 and  $\gamma$  is the deformation width. The beam diameter is  $5 \mu\text{m}$  at full-width half maximum and  $\gamma = 3.8 \mu\text{m}$ . The laser beam is normally incident, and its axis coincides with  $y_0$ . The thickness of the plasma layer is  $d = 0.2 \mu\text{m}$ , and the ion mass is  $m_i = 8.0 \times 10^{-27} \text{ kg}$ . The absorption of the laser energy as a function of time is presented in Fig. 8.11b for three different values of  $\delta$  showing a monotonous increase with the deformation depth. For  $\delta = 2 \mu\text{m}$ , absorption saturates close to 80%, much larger than what is obtained for planar targets ( $\delta = 0$ ). The plot of Fig. 8.11c shows that absorption weakly increases with intensity above  $\approx 10^{18} \text{ Wcm}^{-2}\mu\text{m}^2$ . The plot of Fig. 8.11d shows that absorption decreases for higher densities but is still high ( $\sim 45\%$ ) and has a similar temporal behavior as in 1D. Hence, absorption tends to become a unique function of deformation.

The increase of absorption when a crater is formed suggests the following interpretation. At oblique incidence the laser beam drives a dc electric surface current towards the center of the crater in approximate radial direction. When arrived there, in order to form a closed loop, it is either turned around behind to form its own return current, or continues flowing radially outwards underneath the direct surface current coming from the opposite direction. In other words, two closed loops are formed of the extensions of the beam radius, or one closed loop of an 8-like structure of twice the extension before builds up. In both cases additional energy is stored in the target in contrast to the case of a laser beam interacting with a plane surface. High

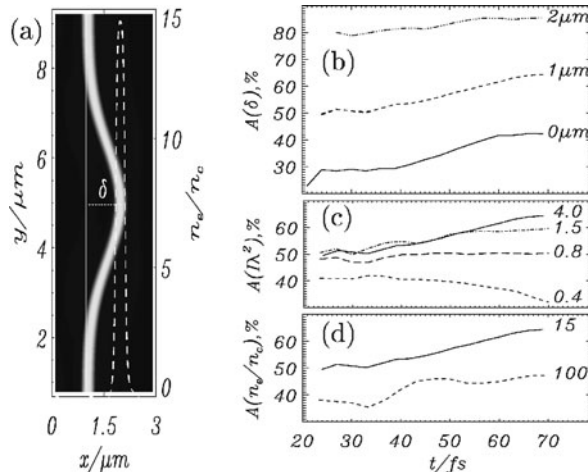


**Fig. 8.11** Vlasov simulation results for a deformed target [45]. (a) Electron density  $n_e$  (normalized to  $n_c$ ) for  $\delta = 1 \mu\text{m}$  at  $t = 0 \text{ fs}$ . The thick solid line shows the density along  $y = 5 \mu\text{m}$ . (b)–(d) Absorption  $A$  vs time (b) as a function of  $\delta$  for  $I\lambda^2 = 4.0 \times 10^{18} \text{ Wcm}^{-2}\mu\text{m}^2$  and  $n_e/n_c = 15.0$ , (c) as a function of  $I\lambda^2$  in units of  $10^{18} \text{ Wcm}^{-2}\mu\text{m}^2$  for  $\delta = 1 \mu\text{m}$  and  $n_e/n_c = 15.0$ , and (d) as a function of  $n_e/n_c$  for  $I\lambda^2 = 4.0 \times 10^{18} \text{ Wcm}^{-2}\mu\text{m}^2$  and  $\delta = 1 \mu\text{m}$

collisionless absorption up to 70% and beyond is well confirmed by experiments [46, 47].

### 8.3.2 Search for Collisionless Absorption

#### 8.3.2.1 Lorentz Boost

In plane geometry with all physical quantities depending only on  $x$  it is sufficient to consider the case of normal incidence. In fact, by applying a Lorentz boost of velocity

$$\mathbf{v}_0 = c \mathbf{e}_y \frac{(\mathbf{k} \mathbf{e}_y)}{|\mathbf{k}|}, \quad v_0 = c \sin \alpha, \quad \alpha = \angle(\mathbf{k}, \mathbf{e}_x) \quad (8.112)$$

along  $\mathbf{e}_y$ , in the reference system  $S'(v_0)$  according to (8.11) the wavevector  $\mathbf{k}$  transforms into [48]

$$\mathbf{k}' = \mathbf{k} - \frac{\mathbf{v}_0}{v_0^2} (\mathbf{v}_0 \mathbf{k}), \quad |\mathbf{k}'| = k \cos \alpha = |\mathbf{k}'_x|. \quad (8.113)$$

From (8.9), (8.10), and (8.11) and (8.32) and  $\gamma_0 = (1 - \sin^2 \alpha)^{-1/2} = \cos \alpha$  follows for the incident wave

in p-polarization:

$$E'_y = E_y = \frac{|\mathbf{E}|}{\gamma_0}, \quad E'_x = 0, \quad B'_x = B'_y = 0, \quad B'_z = \frac{|\mathbf{B}|}{c \gamma_0} \quad (8.114)$$

in s-polarization:

$$E'_x = E'_y = 0, \quad E'_z = \frac{E_z}{\gamma_0}, \quad B'_y = B_y = \frac{|\mathbf{B}|}{\gamma_0}, \quad B'_x = 0. \quad (8.115)$$

Owing to

$$\omega' = \frac{\omega}{\gamma_0}, \quad A = -i \frac{\mathbf{E}}{\omega}, \quad A' = -i \frac{\mathbf{E}'}{\omega'}, \quad I = \frac{1}{2} \epsilon_0 c |\mathbf{E}|^2, \quad I' = \frac{1}{2} \epsilon_0 c |\mathbf{E}'|^2 \quad (8.116)$$

it follows that

$$\begin{aligned} \text{p-polarization: } A'_y &= \gamma_0 A_y, & I' &= \frac{I}{\gamma^2} = I \cos^2 \alpha \\ \text{s-polarization: } A'_z &= A_z, \end{aligned} \quad (8.117)$$

The transformation  $I \rightarrow I'$  is most immediate in the photon picture, since  $I' = n' c \hbar \omega' = (n/\gamma) c \hbar (\omega/\gamma) = I/\gamma^2$  with the photon number density  $n' = n/\gamma$

owing to Lorentz contraction along  $y$ . The reduction of oblique incidence to normal incidence is of great advantage in analytic theory as well as for simulations. In the case of p-polarization it enables one to reduce an originally 2D2V problem to 1D2V. In PIC such a Lorentz boost was used for the first time in [37] and in Vlasov simulations in [39]. The term “Lorentz” in conjunction with “boost” may induce one to think that it is a relativistic transformation. The truth is that a boost in itself, i.e.  $\mathbf{k} \rightarrow \mathbf{k}_\perp = \mathbf{k}'$ , is of pure kinetic nature. Relativity comes into play only when one claims that  $\mathbf{E}' \perp \mathbf{k}_\perp$ . It seems that exactly this fact, i.e.  $\nabla \mathbf{E}' = 0$  in the vacuum, induced Einstein to postulate the existence of a finite maximum velocity. For  $v > c$  follows  $\nabla \mathbf{E}' \neq 0$  at  $X = (x, ct)$  appropriately chosen.

By a Lorentz boost of the foregoing kind an increase in symmetry is gained which may enable one to try further conclusions as shown in the following. In full generality, in plane geometry perpendicular incidence of the infinitely extended laser beam may be considered. The interaction with the fully ionized plasma filling the half space  $x \geq 0$  is governed by the Maxwell and the Lorentz equation,

$$-\varepsilon_0 c^2 \frac{\partial}{\partial x} B_z = \varepsilon_0 \frac{\partial}{\partial t} E_y + j_y, \quad (8.118)$$

$$0 = \varepsilon_0 \frac{\partial}{\partial t} E_x + j_x, \quad (8.119)$$

$$\frac{\partial E_x}{\partial x} = \frac{e}{\varepsilon_0} (n_0 - n_e), \quad E_x = -\frac{\partial}{\partial x} \Phi, \quad (8.120)$$

$$\gamma m v_y = e A_y - m \gamma(v_0) v_0, \quad v_0 = c \sin \alpha, \quad (8.121)$$

$$\frac{d}{dt} \gamma m v_x = e \frac{\partial}{\partial x} \Phi - e v_y \frac{\partial A_y}{\partial x}. \quad (8.122)$$

For simplicity, the ion charge number is assumed to be unity. Equation (8.122) implies vanishing electron temperature  $T_e$ . From (8.118) and (8.119) follows

$$j_x E_x = \frac{\varepsilon_0}{2} \frac{\partial}{\partial t} E_x^2 \quad (8.123)$$

$$j_y E_y = \varepsilon_0 \left( c^2 \frac{\partial A_y}{\partial t} \frac{\partial^2 A_y}{\partial x^2} - \frac{1}{2} \frac{\partial}{\partial t} E_y^2 \right) \quad (8.124)$$

Under the following reasonable assumptions, supported by PIC and Vlasov simulations,

1. a steady state is reached,
2.  $E_x, E_y$  are periodic in time with finite but arbitrary period  $\tau$

holds

$$\overline{j_x E_x} = \frac{\varepsilon_0}{2} \frac{1}{\tau} \int_{-\tau/2}^{\tau/2} \frac{\partial}{\partial t} E_x^2 dt = 0, \quad (8.125)$$

$$\overline{j_y E_y} = \varepsilon_0 c^2 \frac{1}{\tau} \int_{-\tau/2}^{\tau/2} \frac{\partial A_y}{\partial t} \frac{\partial^2 A_y}{\partial x^2} dt. \quad (8.126)$$

The first of these relations is of general validity and may serve as a test in numerical calculations. In the boosted frame its validity can be deduced alternatively from the following argument,

$$\overline{\mathbf{j}E} = \overline{j_x E_x} + \overline{j_y E_y} = j_y E_{\text{Laser}}, \quad E_y = E_{\text{Laser}} \Rightarrow \overline{j_x E_x} = 0, \quad (8.127)$$

because in  $y$ -direction the only field is that of the laser and along  $x$  there is no external driver. Equation (8.127) also states that all absorption is accomplished by the  $E$ -field in  $y$ -direction. In fact, in the absence of  $E_{\text{Laser}}$  there is no net absorption. It is remarkable that under the assumptions (1) and (2) above a quite general field for the overdense evanescent region of the structure

$$A_y = A(t) e^{ikx}, \quad k = k(x), \quad (8.128)$$

where  $k(x)$  is an arbitrary complex function of  $x$ , does not lead to any absorption owing to  $-\int k^2 \partial_t A^2(t) dt = 0$  over an entire cycle  $\tau$ . This is in contrast to Fig. 8.10. Hence, absorption is made possible only by breaking the symmetry of a nonpropagating evanescent wave  $A_y = f(t)g(x)$ , which may be surprising at first glance.

On the basis of (8.125) one could be tempted to exclude the possibility of any absorption and heating or acceleration by claiming that no net work is done by the Lorentz force  $\mathbf{j} \times \mathbf{B}$  along  $x$ . However, this is not a stringent conclusion because it is model-dependent. It is true, of course, that all work is done by the laser field  $E_y$  (or  $A_y$ ) but it is difficult, if not impossible, to determine analytically the phase shift between  $E_y$  and  $j_y$  to obtain the correct absorption. An alternative procedure therefore is to split  $E_x$  into the sum of a driving and an induced field,  $E_x = E_d + E_{\text{in}}$ , with  $E_d = v_y B_z$  (p-polarization), and  $E_x = -\partial_x \Phi$ , from (8.120). In this model the effect of the laser is represented by  $E_d$ , the absorbed power results from  $\overline{j_x E_d} > 0$  and may be used to determine the actual phase shift between  $j_y$  and  $E_y$ . The model shows that the electrons are not free because of the presence of the space charge field  $E_{\text{in}}$ . It will be shown in detail in the following that it is exactly  $E_{\text{in}}$  which makes the absorption of a photon by a “free” electron possible. The Brunel effect [49] was the first attempt to explain collisionless absorption by means of  $E_{\text{in}}$ . We shall come back to the underlying physics of Brunel’s model later.

### 8.3.2.2 Historical Routes to Irreversibility

At the latest when a solid target is heated up to an electron temperature  $T_e \simeq 10^3 Z^2$  eV,  $Z$  ion charge, collisional absorption becomes negligibly small. Subsequent heating and generation of fast electrons in the multi keV/several MeV range shows that the main absorption process occurs during this second phase, as proved by a variety of experiments with laser intensities  $I \gtrsim 10^{18}$  Wcm $^{-2}$  during the last two decades. Efficient collisionless absorption is also well confirmed by computer simulations [37–39]. However, neither the experiment, nor the numerical simulations tell which are the underlying physical mechanisms leading to irreversible energy gain by the electrons in the absence of collisions with the ions. Thus, they need interpretation. Good absorption, typically 50%, is measured and calculated for very short sub-ps pulses during the irradiation by which almost no hydrodynamic motion has set in. Here, linear resonance effects cannot be invoked because the plasma frequency  $\omega_p$  is by an order of magnitude higher at least than the laser frequency  $\omega$ . Instead however, owing to the small penetration depth of the laser pulse which equals approximately the classical skin layer thickness  $\lambda_s = c/\omega_p$ ,  $c$  vacuum light speed, an electron can cross this layer in a fraction of the laser cycle time and pick up irreversibly energy from the laser field. For the first time a nonresonant collisionless absorption mechanism based on such considerations was proposed in 1977 for a sharp-edged slightly overdense plasma ( $\omega_p > \omega$ ) already before the invention of the chirped pulse amplification (CPA) technique in 1985 (“sheath layer absorption” [50]). For intense fs pulses and arbitrarily overdense plasma layers this adiabaticity-breaking finite transit time mechanism was used in 1989 to calculate absorption coefficients of the order of 3–10% at normal incidence [51]. As soon as the interaction with the laser field is shorter than  $\simeq \tau/3$ ,  $\tau = 2\pi/\omega$ , it is collision-like and, consequently the refractive index  $\eta$  can be cast into the Drude form

$$\eta^2 = 1 - \frac{n_e}{n_c} X + i \frac{n_e}{n_c} Y, \quad (\text{Drude}) \quad (8.129)$$

with  $X, Y > 0$ ,  $X < 1$ ,  $n_e$  electron density,  $n_c$  critical (= cut off) density. For a finite collision frequency  $\nu$ ,  $X$  and  $Y$  assume the well-known form  $X = \omega^2/(\omega^2 + \nu^2)$ ,  $Y = \nu X/\omega$ . In both papers [50, 51] the magnetic field  $\mathbf{B}$  of the laser beam is neglected. This is incorrect because owing to the high gradients in the narrow skin layer  $c\mathbf{B}$  becomes much larger than the electric field  $\mathbf{E}$  and, in general, must be included, also in a linearized treatment. Such a self-consistent calculation of the effect in a highly overdense plasma slab ( $\omega_p^2 \gg \omega^2$ ) has been performed in linear approximation [52]. For a Maxwellian electron distribution the authors find that including the  $\mathbf{B}$ -field leads to identical absorption coefficients as without magnetic field, hence justifying a posteriori the assumptions made in the two foregoing references [50, 51]. In the analytical treatments it is standard to assume that the electrons are reflected instantaneously at the vacuum-target interface. In a more recent paper arguments are presented for diffuse reflection of a fraction  $p$  of electrons as to be closer to reality [53]. Increased absorption as well as enhanced heat diffusion are

found as soon as  $p$  exceeds the value 0.15. Collisionless absorption under oblique incidence is also treated analytically as well as numerically [54]. In all cases [50–54] the analysis is performed under the assumption that the thermal pressure exceeds the ponderomotive pressure, or that the latter is absent.

Looking through the enormous amount of theoretical papers that have appeared since the invention of the CPA technique in 1985 on ultrashort intense light pulse interaction with dense matter including clusters three aspects emerge,

- I. a quantitative analysis of the interaction (absorption, fast electron spectra) is not accessible to an analytical treatment but has to rely on computer simulations;
- II. (too) many collisionless absorption mechanisms have been proposed which are not well separated from each other:  $j \times \mathbf{B}$  heating [43], Brunel effect [49], vacuum heating [55], sheath layer inverse bremsstrahlung [50], anomalous skin layer absorption [52, 54], stochastic heating [56, 57], relativistic ponderomotive heating, both longitudinal [58] as well as transverse [59], absorption and acceleration by wavebreaking, “laser dephasing heating” [60], linear and nonlinear Landau damping [61, 62], and excitation of surface plasmons [63];
- III. the underlying physical principles of the collisionless absorption phenomenon has not been elaborated with sufficient clarity and a clear ordering of the mechanisms under II according to their strength is still missing.

The excitation of surface plasmons needs very peculiar conditions for efficient coupling [64]. Perhaps being very sensitive to distortions of the solid target surface under the action of the laser and to the coupling conditions in general it has never been observed so far in experiments with flat noncorrugated targets. Landau damping is a very universal concept; probably all kinds of collisionless interaction may be reducible to it. However, its success in a quantitative analysis depends on the specific scenario on which the calculation is based. In the collisionless regime a “free” plasma electron only couples to an external field, e.g., that of a laser, and to the collective  $\mathbf{E}$  and  $\mathbf{B}$  fields generated by the hot plasma. In such an extended environment the electrons undergo only adiabatic, i.e., reversible, changes as soon as the impinging light pulse contains more than two oscillations. In order to make absorption possible the adiabaticity must be broken. This is accomplished either by disturbances, microscopic (“collisions”) or macroscopic (“field fluctuations”), that are shorter than  $\simeq \tau/3$  (with  $\tau = 2\pi/\omega$  oscillation period in the frame comoving with the particle), or by resonances. In the absence of electron-ion collisions the only marked collisional events are represented by the interactions with the steep gradients of the macroscopic fields. If the crossing time is short enough skin layer absorption as discussed in [50–54] is expected to occur, however only as long as the discontinuity of transition is not washed out.

There seems to be a kind of agreement that high degrees of collisionless absorption are mainly due to  $j \times \mathbf{B}$  heating, Brunel effect, or vacuum heating, or a combination of them. It is therefore important to concentrate briefly on each of them.

### 8.3.2.3 $j \times B$ Heating

The majority of researchers in the field seem to favor the so-called “ $j \times B$  heating” [43]. In PIC simulations “electrons are accelerated and then beamed into the plasma by the oscillating ponderomotive force” resulting in up to 17% at  $I\lambda = 10^{18} \text{ Wcm}^{-2}\mu\text{m}^2$  under normal incidence. Since  $j \times B$  is a reversible force for free electrons, the question arises where does “beaming”, i.e., irreversibility come from. The value of their work consists in having recognized first the significance of the motion perpendicular to the target surface for absorption and having done in this way the first step towards understanding collisionless absorption. As we shall see what has to be done is to associate a physical effect with “beaming” which produces it.

### 8.3.2.4 Brunel Effect

Two years later the “Brunel effect” was considered as to give rise to “beaming” with the concomitant annihilation of photons [49]. Consider a harmonic electrostatic field  $\mathbf{E}$  (or electromagnetic wave of infinite wavelength under angle of incidence  $\alpha$ ) with the normal to an infinitely overdense plasma of collisionless electrons neutralized by fixed ions of density  $n_0 \gg n_c$ . Under the assumption of a steady state the surface layer of electrons is pulled out into the vacuum by the full field strength and then, approximately half a cycle later pushed back into the target. If no massive target were there, in the following half cycle the electrons would be slowed down to rest. However, since the electric field is completely screened according to Poisson’s law after the thickness  $\lambda_{es} = \varepsilon_0 |\mathbf{E}| \cos \beta / n_0 Ze$ , the evanescent field in the extremely thin skin layer can no longer hold them back from their free motion through the solid. In each full cycle the number  $N_e = Z n_0 \lambda_{es}$  of “free” electrons is pushed into the target with an average energy  $1.57 \text{ W}$  per electron,  $W$  given by (8.99). The numerical factor is obtained from a simple transcendental equation and is correct (the authors of the book found 1.61) under the assumption (i) that  $N_e$  is the correct number of electrons per bunch and unit area and that (ii) the electron layers do not overtake each other. The argument in favor of assumption (ii) is that the layer behind the forefront layer is already partially screened by the latter, the third layer is screened by two layers in front of it, etc., up to the last layer seeing no field at all at depth  $\lambda_{es}$ . The model leads to an absorbed energy  $\mathcal{A}I$  per cycle and unit area and fixed angle  $\alpha = \pi/2 - \beta$  of laser beam incidence,

$$\mathcal{A}I \frac{2\pi}{\omega} = 1.6 N_e \omega \sim I^{1/2} \frac{I}{\omega^2} \quad \Rightarrow \quad \mathcal{A} \sim (I\lambda^2)^{1/2}. \quad (8.130)$$

Such a dependence of  $\mathcal{A}$  is neither observed in simulations nor in experiments. In addition somewhere beyond  $I_{Nd} = 10^{18} \text{ Wcm}^{-2}$   $\mathcal{A}$  starts exceeding unity. The oversimplified skin layer thickness  $\lambda_{es}$  originates from the omission of the magnetic field of the wave through  $\mathbf{k} = 0$  (i.e.,  $\lambda = \infty$ ). However, despite the fact that hypothesis (ii) does not hold owing to resonance where the Jacobian (2.56) becomes singular and layers do overtake each other and mix up (wavebreaking; the author of [49] is aware of it; see also Fig. 8.8), the Brunel effect offers, on the

qualitative level, a correct physical scenario into irreversibility: The “free” electrons are not free; rather they are subject to the additional space charge field which acts on them, like a uniform gravitational field, providing for the necessary phase shift of  $j$  with respect to the driving  $E$ -field. The main shortcoming of the model: resonances are suppressed and are excluded mathematically by forbidden crossing of adjacent layers.

### 8.3.2.5 Vacuum Heating

“Vacuum heating”, originally coined for a well-defined phenomenon in 1992 [37], has become subsequently one of the most mysterious and most popular expressions in the context of collisionless absorption. It has been invented to address the fact that at higher laser intensities a low-density, hot electron cloud forms in the vacuum which, as PIC simulations show, contains a certain amount of particles not entering the target with the periodicity of the laser frequency. The contribution to absorption of these electrons circulating in the vacuum has never been investigated separately, presumably because of the lack of a clear definition of the phenomenon. Some authors seem to attribute collisionless absorption entirely to vacuum heating [65, 66], others consider a combination of  $j \times B$  heating [43] and vacuum heating responsible for absorption [67]. However, one must be aware that none of these concepts explains any physics of absorption, i.e., they do not show any well defined route into irreversibility in physical terms. The situation does not change when vacuum heating is interpreted as a consequence of unspecified wavebreaking [68] because there are numerous different scenarios (e.g., of fluid dynamics [69], kinetic [70], resonant (Sect. 8.3.3), geometric type [71]) leading to the vague and not well understood phenomenon of wavebreaking.

To shed more light on the phenomenon test particle simulations under perpendicular and oblique incidence of intense laser beams have been performed [72]. They reveal some important aspects of the electron dynamics in the vacuum. So, for instance, electrons entering the vacuum from the target acquire energies which depend strongly on the phase the laser wave exhibits at the instant of crossing the interface. In addition, in contrast to a general belief, the moderately energetic electrons are not reflected in the narrow neighborhood of the interface but an appreciable fraction turns around before reaching the interface. This fact together with the skin layer thickness oscillating with the periodicity of the laser frequency  $\omega$  ( $2\omega$  for perpendicular incidence) tells us that the standard static treatment of the anomalous skin effect and the absorption connected with it have to be handled with caution. The extension  $L$  of the plasma cloud into the vacuum is determined by the light pressure competing with space charge effects. In [72]  $L \simeq \lambda/3$  is found ( $\lambda$  laser wavelength) whereas the Debye length was about three times longer. Finally, as the collective electrostatic field within the plasma cloud is rather smooth, except perhaps around the critical point, the circulating electrons in the cloud experience almost no collisional or stochastic “vacuum heating”. Both terms  $j \times B$  heating and vacuum heating do not address well-defined physical effects, nor are they selfexplaining.

### 8.3.3 Collisionless Absorption by Anharmonic Resonance

Any model of collisionless absorption in strongly overdense plasmas must be able to explain the salient features of simulations, first of all,

- (1) how adiabaticity of dynamics is broken or, equivalently, irreversibility, i.e., conversion and/or heating is accomplished. Under periodic excitations by a laser field this is equivalent to indicate a physical effect causing a finite phase shift  $\phi$  in  $\mathbf{j}$ . Under steady state conditions the absorbed power density averaged over a full laser cycle  $T = 2\pi/\omega$  results from Poynting's theorem as

$$\overline{\mathbf{j} \cdot \mathbf{E}} \sim \overline{\sin(\omega t + \phi) \cos \omega t} = \frac{1}{2} \sin \phi. \quad (8.131)$$

If, in the absence of collisions  $\phi = 0$ , zero absorption follows unless a dynamic process guaranteeing  $\phi \neq 0$  is found. However,  $\phi \neq 0$  is not all. Further requirements are

- (2) capability of high conversion ( $\geq 70\text{--}80\%$ );
- (3) instantaneous (i.e., on fs time scale) generation of fast electrons exceeding many times their mean quiver energy  $W$  for the Maxwellian tail;
- (4) delay-less absorption at any ratio of target electron density to critical density  $n_{e0}/n_c > 1$ ;
- (5) polarization dependence of heating: strong heating in linear p-polarization, almost no heating in circular polarization under normal incidence.

Property (3), although observed in all PIC simulations has never been commented in the literature so far. Under the assumption that collisionless absorption is accomplished by one single physical effect it follows from property (3) that it can only be resonance in the collective plasma potential, for no other physical effect is known capable of exciting to nearly arbitrary high energies during a few laser cycles and undergoing a phase shift at resonance. Property (4) requires that the resonance is anharmonic because only then the eigenfrequency  $\omega_0$  can shift, through its amplitude dependence, from the harmonic plasma frequency down to the exciting laser frequency  $\omega$  and below. A final argument in favor of resonance is that anharmonic resonance may be viewed as an extension of the universally accepted principle that a single point charge cannot absorb a photon unless it resonates in an outer potential or it undergoes a collision in a microscopic or macroscopic field.

Collisionless absorption of long ps and fs pulses is, in leading order, by linear resonance at  $\omega = \omega_p$ . It is therefore quite natural to speculate whether such a resonant conversion is the leading absorption mechanism also in ultrashort pulses on highly overdense targets (solids, liquids, and clusters) before appreciable rarefaction has set in. For more than two decades resonance absorption at  $\omega_p \gg \omega$  has been categorically excluded by the scientific community. The insight that this statement is incorrect, because limited to the harmonic oscillator only, is the key to the solution of collisionless absorption [73]. This is shown in the following subsection.

### 8.3.3.1 Irreversible Energy Gain by Linear and Nonlinear Oscillators

A nonlinear oscillator is governed by an equation of the type

$$\ddot{\xi} + f(\xi) = \mathbf{D}(t), \quad (8.132)$$

where  $f(\xi)$  is any sufficiently smooth restoring force, and  $\mathbf{D}(t)$  is an external driver. The linear oscillator is described by  $f(\xi) = \omega_0^2 \xi$  with constant eigenfrequency  $\omega_0$  at all excitation amplitudes. Under the action of a harmonic driver  $\mathbf{D}(t) = \hat{\mathbf{D}}(t) \cos \omega t$ ,  $\omega \neq \omega_0$ , (8.132) behaves adiabatically as soon as  $\hat{\mathbf{D}}(t)$  is an envelope of several cycles  $T = 2\pi/\omega$  long, whereas it continues to oscillate indefinitely (net energy absorption) if  $\hat{\mathbf{D}}(t)$  is  $\delta$ -peak like [74].

To gain insight into the behavior of (8.132) it is advisable, following [74], to reconsider first collisional and adiabatic excitation of the linear oscillator with both, constant and with time-varying eigenfrequency  $\omega_0$ . The one-dimensional oscillator

$$\ddot{\xi} + \omega_0^2 \xi = \hat{\mathbf{D}}(t) \cos \omega t \quad (8.133)$$

under the initial condition  $\xi(-\infty) = \dot{\xi}(-\infty) = 0$ ,  $\hat{\mathbf{D}}(-\infty) = 0$  evolves in time according to

$$\begin{aligned} \xi(t) &= \frac{\sin \omega_0 t}{\omega_0} \int_{-\infty}^t \hat{\mathbf{D}}(t') \cos \omega_0 t' \cos \omega t' dt' \\ &\quad - \frac{\cos \omega_0 t}{\omega_0} \int_{-\infty}^t \hat{\mathbf{D}}(t') \sin \omega_0 t' \cos \omega t' dt'. \end{aligned} \quad (8.134)$$

For  $\hat{\mathbf{D}}(t) = \omega_0 \xi_0 \delta(t)$  the ballistic solution  $\xi(t > 0) = \xi_0 \sin \omega_0 t$  results. The general solution can be cast into the form

$$\begin{aligned} \xi(t) &= \frac{\sin \omega_0 t}{2\omega_0} \int_{-\infty}^t \hat{\mathbf{D}}(t')[\cos \omega_1 t' + \cos \omega_2 t'] dt' \\ &\quad - \frac{\cos \omega_0 t}{2\omega_0} \int_{-\infty}^t \hat{\mathbf{D}}(t')[\sin \omega_1 t' + \sin \omega_2 t'] dt'. \end{aligned} \quad (8.135)$$

where  $\omega_1 = \omega_0 + \omega$  and  $\omega_2 = \omega_0 - \omega$ . For laser interaction with solid density matter  $\omega \ll \omega_0$  can be chosen. With a rectangular excitation amplitude  $\hat{\mathbf{D}}(t) = \omega_0^2 x_0$ , centered around  $t = 0$  and  $\Delta t = 2t_0$  long,

$$\xi(t \geq t_0) = 2\xi_0 \sin \omega_0 t_0 \sin \omega_0 t \quad (8.136)$$

results.

Maximum irreversible energy gain is achieved with exciting pulses of length  $\Delta t \approx \pi/\omega_0 = 2T_0 \ll T = 2\pi/\omega$ . Alternatively, if  $\hat{\mathbf{D}}(t)$  is a smooth function of halfwidth  $\Delta t/2 = t_0 \gtrsim T$  integration by parts of (8.135) with suitable test functions

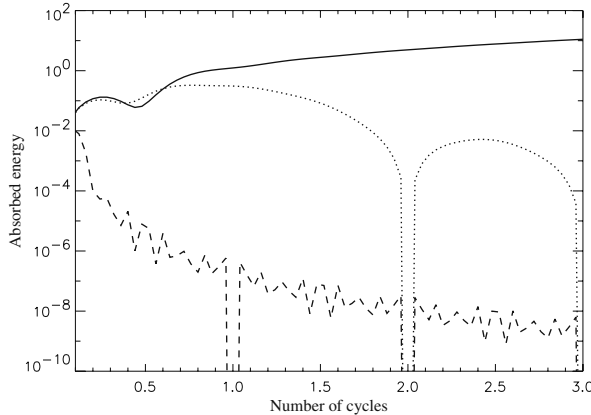


**Fig. 8.12** Ballistic vs adiabatic excitation of the linear oscillator (8.133). Absorbed energy in units of  $(D_0/\omega)^2$  from a  $\sin^2$ -pulse,  $n$  cycles long; dashed:  $\omega_0 = 10\omega$ , dotted:  $\omega_0 = 2\omega$ . Maximum irreversible energy gain is achieved with pulses of length  $0.1T = T_0$  for  $\omega_0 = 10\omega$  and  $0.7T = 1.4T_0$  for  $\omega_0 = 2\omega$  (ballistic excitation). The higher the detuning  $q$ ,  $\omega_0 = q\omega$ , the faster drops the energy gain with increasing pulse duration (adiabatic behavior). For comparison the energy absorption at resonance  $q = 1$  is also shown (*solid*)

$\hat{D}(t)$  shows that the irreversible energy gain  $e_a(t = \infty)$  compared to the maximum oscillatory energy  $e_{\max}$  during the pulse is much less than unity. In Fig. 8.12 the transition of  $e_a(t > t_0)$  from ballistic to adiabatic excitation of (8.133) is shown at  $\omega_0 = \omega$  (solid),  $\omega_0 = 2\omega$  (dotted), and  $\omega_0 = 10\omega$  (dashed) as a function of the number of exciting  $\omega$ -cycles  $n$  for  $\hat{D}(t) = D_0 \sin^2[\omega t/(2n)]$  in the interval  $0 < \omega t/(2n) < \pi$  and zero outside. It is seen that far from resonance ballistic excitation with finite irreversible gain  $e_a(t \rightarrow \infty)$  is achieved with very short pulses only. To save 1% of the maximum  $e_a(t \rightarrow \infty)$ , reached with pulses of length  $0.1T = T_0$  for  $\omega_0 = 10\omega$  and  $0.7T = 1.4T_0$  for  $\omega_0 = 2\omega$ , the exciting pulse length must not exceed  $0.2T$  and  $1.9T$ , respectively. For comparison the energy gain at resonance  $\omega_0 = \omega$  is also plotted. It resembles the quadratic time dependence of the energy gain at constant amplitude.

Next we consider the linear oscillator with time varying eigenfrequency  $\omega_0(t)$  from Sect. 4.4.1,

$$\ddot{\xi} + \omega_0^2(t)\xi = \hat{D} \cos \omega t, \quad \omega_0(t) = \omega e^{-\alpha t}, \quad \alpha > 0. \quad (8.137)$$

It is a model for linear as well as nonlinear resonance absorption, and wave-breaking with nanosecond laser pulses. The driver is adiabatically switched on at  $t = -\infty$  and held constant in the interval of interest. The eigenfrequency varies from  $\omega_0(-\infty) = \infty$  to  $\omega_0(+\infty) = 0$ . Highest excitation is expected for  $\alpha \ll \omega$ , i.e., when the oscillator remains close to resonance  $\omega_0(t = 0) = \omega$  for a time as long as possible. Under  $\alpha \ll \omega$  the functions  $\sin \phi$  and  $\cos \phi$ , with

$$\phi = \int_0^t \omega_0(t') dt' = \frac{\omega}{\alpha} (1 - e^{-\alpha t}), \quad \dot{\phi} = -\alpha \omega_0 \gg -\omega_0^2, \quad (8.138)$$

represent two independent solutions of the homogeneous oscillator equation (8.137) to a satisfactory approximation. Hence the desired solution of (8.137) with  $\xi(-\infty) = \dot{\xi}(-\infty) = 0$  is

$$\xi(t) \approx \hat{D} \left\{ \sin \phi(t) \int_{-\infty}^t \frac{\cos \phi(t')}{\omega_0(t')} \cos \omega t' dt' - \cos \phi(t) \int_{-\infty}^t \frac{\sin \phi(t')}{\omega_0(t')} \cos \omega t' dt' \right\}. \quad (8.139)$$

This expression becomes an exact solution if on the RHS of (8.137) the term

$$y(t) = \ddot{\phi} \hat{D} \left\{ \cos \phi(t) \int_{-\infty}^t \frac{\cos \phi(t')}{\omega_0(t')} \cos \omega t' dt' + \sin \phi(t) \int_{-\infty}^t \frac{\sin \phi(t')}{\omega_0(t')} \cos \omega t' dt' \right\} \quad (8.140)$$

is added. The amplitude  $\hat{\xi}(t)$  of  $\xi(t)$  is expected to grow appreciably only in a narrow interval  $\Delta \omega_0$  around the resonant point  $t = 0$ . Therefore, under the integral (and only there)  $\omega_0(t)$  and  $\phi(t)$  can be expanded to lowest order,

$$\omega_0(t) = \omega e^{-\alpha t} \approx \omega(1 - \alpha t), \quad \phi(t) \approx \omega(t - \alpha t^2/2). \quad (8.141)$$

By observing that  $\cos \phi \cos \omega t = [\cos(\phi + \omega t) + \cos(\phi - \omega t)]/2$ ,  $\sin \phi \cos \omega t = [\sin(\phi + \omega t) + \sin(\phi - \omega t)]/2$  the terms containing  $\cos(\phi + \omega t)$  and  $\sin(\phi + \omega t)$  can be omitted since they merely lead to fast low-amplitude modulations, whereas the two terms containing  $\phi - \omega t$  exhibit a stationary phase around  $\omega_0 = \omega$ . This is analogous to the rotating wave approximation in the magnetic and optical Bloch models. Further,  $\omega_0(t)$  can be taken out of the integrals. Then  $\xi(t)$  from (8.139) reads in the resonance region

$$\xi(t) \approx \frac{\hat{D}}{2\omega} \left\{ \sin \phi(t) \int_{-\infty}^t \cos \frac{\alpha}{2} \omega t'^2 dt' + \cos \phi(t) \int_{-\infty}^t \sin \frac{\alpha}{2} \omega t'^2 dt' \right\}. \quad (8.142)$$

By the substitution  $t = [\pi/(\alpha\omega)]^{1/2}\eta$  it transforms into

$$\xi(\eta) \approx \frac{\pi^{1/2} \hat{D}}{2\alpha^{1/2} \omega^{3/2}} \left\{ \left[ \frac{1}{2} + C(\eta) \right] \sin \phi(\eta) + \left[ \frac{1}{2} + S(\eta) \right] \cos \phi(\eta) \right\}, \quad (8.143)$$

with the Fresnel integrals [75]

$$C(\eta) = \int_0^\eta \cos \frac{\pi}{2} \eta'^2 d\eta', \quad S(\eta) = \int_0^\eta \sin \frac{\pi}{2} \eta'^2 d\eta'. \quad (8.144)$$

For  $\eta \rightarrow \infty$  they behave as

$$C(\eta) = \frac{1}{2} + \frac{1}{\pi\eta} \sin \frac{\pi}{2}\eta^2 + O(\eta^{-2}), \quad S(\eta) = \frac{1}{2} - \frac{1}{\pi\eta} \cos \frac{\pi}{2}\eta^2 + O(\eta^{-2}).$$

Solution (8.143) can be expressed in terms of amplitude and phase,

$$\begin{aligned} \xi(\eta) &\approx \hat{\xi}(\eta) \sin[\phi(\eta) + \psi(\eta)], \\ \hat{\xi}(\eta) &= \frac{\pi^{1/2} \hat{D}}{2\alpha^{1/2} \omega^{3/2}} \left\{ \left[ \frac{1}{2} + C(\eta) \right]^2 + \left[ \frac{1}{2} + S(\eta) \right]^2 \right\}^{1/2}, \\ \psi(\eta) &= \arctan \left( \frac{S(\eta) + 1/2}{C(\eta) + 1/2} \right) + \psi_0. \end{aligned} \quad (8.145)$$

The plot of  $I(\eta) = C(\eta) + iS(\eta)$  in the complex plane yields the familiar Cornu spiral, Fig. 4.19, well known from diffraction theory in classical optics. The path  $s$  along the spiral from the origin to a point  $P = C(\eta) + iS(\eta)$  is the parameter  $\eta$  itself,  $s(\eta) = \eta$ , the amplitude  $A(\eta) = \{[1/2 + C(\eta)]^2 + [1/2 + S(\eta)]^2\}^{1/2}$ , to be identified with  $|w|$  in Fig. 4.19, is the length of the arrow pointing from  $O' = -(1/2 + i/2)$  to  $P = C(\eta) + iS(\eta)$ . The resonance width and the factor of amplitude growth are conveniently defined by the change of phase  $\psi(\eta)$  (in Fig. 4.19 indicated by  $\delta$ ) from  $\psi_0 - \pi/2$  to  $\psi_0 + \pi/2$  and  $S(\eta) = C(\eta)$ . This is the case for  $\eta = \eta_r = 1.27$  and  $\eta = -\eta_r$ , respectively. According to (8.143) the resonance interval and frequency halfwidth are

$$\omega + \Delta\omega_0 \geq \omega_0 \geq \omega - \Delta\omega_0, \quad \frac{\Delta\omega_0}{\omega} = \left( \frac{\pi\alpha}{\omega} \right)^{1/2} \eta. \quad (8.146)$$

The resonance interval  $2\Delta\omega_0$  increases as  $\alpha^{1/2}$  and covers the number of oscillations

$$N = \frac{2t_r}{2\pi/\omega} = \left( \frac{\omega}{\pi\alpha} \right)^{1/2} \eta_r. \quad (8.147)$$

For  $\alpha = \omega/100$  and  $\alpha = \omega/10$  results  $N = 7.2$  and  $N = 2.3$ . The associated resonance halfwidths are  $\Delta\omega_0/\omega = 0.23$  and  $\Delta\omega_0/\omega = 0.7$ . In general the quantities  $\xi(t)$  and  $y(t)/\ddot{\phi}$  from (8.139) and (8.140) are of the same magnitude. Therefore  $\xi(t)$  is expected to be a good approximation if  $(\alpha/\omega)^{1/2} \ll 1$  is fulfilled. The same restriction follows also from (8.146) for the validity of expansion (8.141). From the numerical examples above for  $\Delta\omega_0/\omega$  one sees that with  $\alpha/\omega = 10^{-2}$  the two quantities  $\exp(-\alpha t_r)$  and  $(1 - \alpha t_r)$  differ very little from each other at the border of resonance (3%) whereas for  $\alpha/\omega = 10^{-1}$  the difference is 33%. Nevertheless the Fresnel integrals yield very satisfactory results also in this case.

For determining the factor of resonant growth of  $\xi(t)$  and the amount of energy absorbed by the oscillator we observe that outside the resonance width any adiabatic variation of  $\omega_0(t) \neq \omega$  under an adiabatically varying driver  $\hat{D}(t)$  may influence the shape of the two spirals of Fig. 4.19 but has no effect on the resonance segment

in between ( $|\eta| < \eta_r$ ). Hence, the growth of  $\xi(t)$  for  $\omega_0(t) = \omega \exp(-\alpha t_r)$  is (nearly) the same as for  $\omega_0(t)$  from (8.141), provided  $\alpha/\omega \leq 0.3$ . After the driver is switched off adiabatically  $\xi(t \rightarrow \infty)$  points to the center of the upper spiral at  $C(\infty) = S(\infty) = 1/2$ . This position also indicates the final energy  $e_a(\infty)$  irreversibly gained by the oscillator after crossing the resonance point if its frequency is kept at  $\omega_0(t_r) = \omega_f = \text{const}$ . Equation (8.145) yields the following quantities for resonant and asymptotic amplitude increase  $\kappa_r$ ,  $\kappa_\infty$ , and stored energy  $e_a(\infty)$ ,

$$\begin{aligned}\kappa_r &= \frac{\hat{\xi}(\eta_r)}{\hat{\xi}(-\eta_r)} = 7.0, & \kappa_\infty &= \frac{\hat{\xi}(\infty)}{\hat{\xi}(-\eta_r)} = 6.0, \\ e_a(\infty) &= \frac{1}{2}\omega^2\hat{\xi}^2(\infty) = \frac{\pi\hat{D}^2(\eta=0)}{4\alpha\omega}.\end{aligned}\quad (8.148)$$

For  $\omega_0(t > t_r) \rightarrow 0$  the final energy depends on how rapidly the parabolic potential flattens: if the number of turning points is infinite  $e_a(\infty)$  is zero, if it is finite the particle escapes with finite kinetic energy. We conclude by observing that if the oscillator is switched off adiabatically before  $-t_r$  it returns to its starting position  $C = S = -1/2$ ; if it is adiabatically switched off after  $+t_r$  and  $\omega_0(t_r) = \omega_f$  is kept constant it has made the irreversible transition from the center of the lower spiral to the center of the upper spiral in Fig. 4.19. A linear oscillator can gain irreversible energy (absorption) under ballistic (collisional) excitation or, adiabatically, by crossing a resonance.

An undamped nonlinear oscillator may exhibit properties differing in many respects from its linear counterpart. For our purpose here its most important difference is the dependence of the eigenperiod  $T_0$  on the excitation level, i.e., on the amplitude. In the case of the very general nonlinear oscillator (8.132) in 1D its eigenperiod  $T_0$  is given by  $\int dt = \int d\xi/v$ ,  $v$  particle velocity, or

$$T_0 = \oint \frac{d\xi}{\left\{ \left( \frac{2}{m} \right) [V_0 - V(\xi)] \right\}^{1/2}}, \quad V_0 = \max V(\xi). \quad (8.149)$$

$V(\xi)$  is the potential associated with the restoring force  $f(\xi)$  so that  $f(\xi) = -\partial_\xi V(\xi)$ . If the graph of  $V(\xi)$  stays inside the parabola  $\omega_0^2\xi^2/2$  the eigenperiod decreases with the amplitude; if however it widens compared to the parabola its eigenperiod increases with increasing level of excitation. This latter case is of particular interest because Coulomb systems exhibit such a characteristics owing to the  $1/r$ -dependence of the Coulomb potential at large charge separation and, in concomitance, at a fixed driver period the nonlinear system may enter into resonance when excited to high amplitude. This property opens the new possibility to couple appreciable amounts of energy by adiabatic excitation into such systems originally out of resonance. Since even the shortest laser pulse contains several oscillations ballistic excitation is not possible, in a locally plane wave not even in principle,

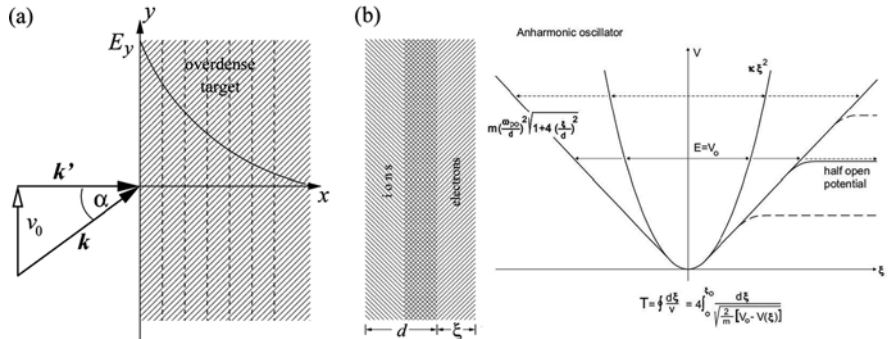


**Fig. 8.13** (a) Oblique incidence of parallel laser beam of wave vector  $\mathbf{k}'$  in the lab frame and  $\mathbf{k}' \parallel \mathbf{x}$  in the system boosted by  $v_0 = c \sin \alpha$ . The overdense target is cut into layers of thickness  $d$ . (b) Large electron displacement  $\xi$  in plasma layer (LHS) and harmonic (*parabola*) and anharmonic closed (*solid*) and half-open potentials (*solid, dashed*). In wider potentials than harmonic the frequency decreases with increasing  $\xi$

regardless of how short the electromagnetic pulse is. Energy coupling into a system originally out of resonance is illustrated in the following for a cold plasma.

A plane, fully ionized target is assumed to fill the half space  $x > 0$ . A plane wave  $\mathbf{E}(\mathbf{x}, t) = \mathbf{E}_0 \exp[i(\mathbf{k} \cdot \mathbf{x} - \omega t)]$  in p-polarization in  $y$ -direction, wave vector  $\mathbf{k}$  and frequency  $\omega$ , is incident from  $-\infty$  under an angle  $\alpha$  onto the plasma surface (Fig. 8.13a). After applying a Lorentz boost  $v_0 = c \sin \alpha$  the wave impinges normally. The target is thought to be cut into a sufficient number of thin parallel layers, each of which is exposed to a driving force  $F$  acting along  $x$  of magnitude  $e v_0 B$  and frequency  $\omega$ , and an additional component originating from the Lorentz force of the oscillatory motion along  $y$  of frequency  $2\omega$  ( $e$  electron charge,  $B$  magnetic field of the laser). With the electron displacement  $\xi$  in  $x$ -direction and immobile ions of density  $n_0$  (corresponding to  $\omega_{p0}$ ) the motion of a single layer (Fig. 8.13b) in the nonrelativistic limit is determined by

$$\frac{d^2\xi}{dt^2} + \omega_{p0}^2 \left(1 - \frac{|\xi|}{2d}\right) \xi = D, \quad |\xi| \leq d, \quad (8.150)$$

$$\frac{d^2\xi}{dt^2} + \omega_{p0}^2 \left(\frac{d}{2|\xi|}\right) \xi = D, \quad |\xi| \geq d. \quad (8.151)$$

The free plasma oscillator ( $D = 0$ ) oscillates at  $\omega_{p0}$  if the displacement is small. For a fixed energy  $V_0 = \epsilon$  at high excitation and  $\omega_{p0} \gg \omega$ ,  $T_0$  according to (8.149) is given by  $T_0 = 8(\omega_{p0}^2 d)^{-1/2} \xi_0^{1/2}$ . The eigenfrequency  $\omega_0 = 2\pi/T_0 = (\pi/4)(\omega_{p0}^2 d)^{1/2} \xi_0^{-1/2}$  decreases with increasing oscillation amplitude  $\xi_0$ , in contrast to the linear harmonic oscillator, and approaches zero for  $\xi \rightarrow \infty$ . (An exact mechanical analogy is represented by an elastic sphere bouncing on an elastic horizontal glass plate under the influence of gravity, and its mirror image:  $\omega_0 \rightarrow \infty$  for  $\xi_0 \rightarrow 0$  and  $\omega_0 \rightarrow 0$  for  $\xi_0 \rightarrow \infty$ ). Under a weak driver  $D$  and  $\omega_{p0} > \omega$ ,

$\xi$  oscillates in phase with  $D$ ; under a strong driver  $\xi$  becomes large and, owing to  $\omega_0 \rightarrow 0$ , it oscillates similarly to a free particle, i.e. dephased by  $\pi$  with respect to  $D$ . Principal resonance [76] occurs at  $\omega_0 = \omega$  with  $\xi_0 = \xi_r = (\pi\omega_{p0}/4\omega)^{1/2}$ . The transition from nonresonant to resonant state at  $\omega_0 = \omega$  is irreversible, i.e., resonance breaks adiabaticity. In the neighborhood of resonance the product  $(d\xi/dt)D \sim jE$  changes from  $-\sin\omega t \times \cos\omega t$  into  $\cos^2\omega t$ , with nonvanishing cycle average. This is illustrated by a numerical example now.

The two equations of motion above for  $|\xi| \leq d$  and  $|\xi| \geq d$  convert into a single dimensionless equation for the potential  $V = m(\omega_{p0}d/2)^2(1 + \zeta^2)^{1/2}$ ,

$$\frac{d^2\zeta}{d\tau^2} + \frac{\partial(1 + \zeta^2)^{1/2}}{\partial\zeta} = D(\tau), \quad (8.152)$$

where  $\zeta = 2\xi/d$ ,  $m$  electron mass,  $\tau = \omega_{p0}t$  and  $D \rightarrow 2D/(\omega_{p0}^2d)$ . With  $D = D_0 \sin^2[\omega\tau/(2K)] \cos\omega\tau$ ,  $\sin^2$  for  $f(t)$ ,  $K$  number of periods, the results of Fig. 8.14 are obtained numerically. At  $D_0 = 0.921$  the layer remains below resonance, the energy gain  $\varepsilon$  after the pulse is over is negligible (a). Increasing the driver by only  $\Delta D_0 = 0.002$ , resonance takes place. Much energy, i.e., 43 times more than in (a), is stored now in the oscillator [see the horizontal orbits in (b)]. Under the assumption that resonance lasts half a laser cycle, i.e., when the driver amplitude  $E_0 = m\omega_{p0}^2d/(4e)$ , with  $d = 0.1 - 0.2$  nm and  $\omega_{p0} = 2 \times 10^{16}$  s<sup>-1</sup>,

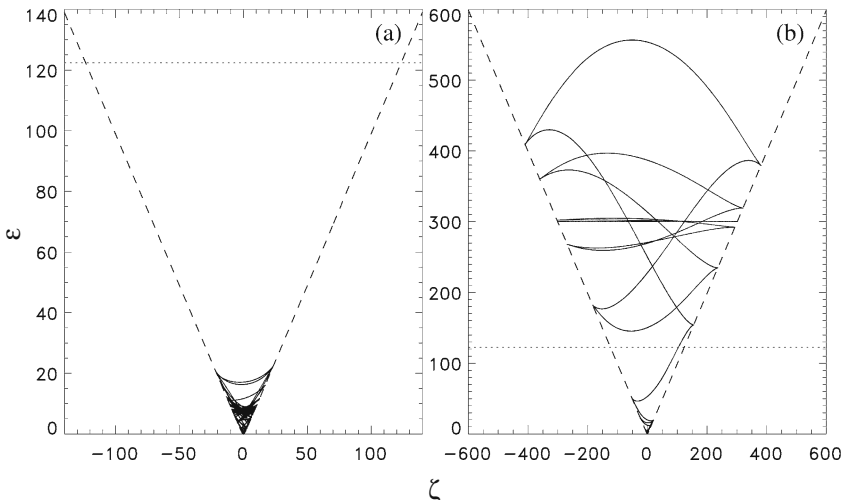


**Fig. 8.14** Excitation  $\varepsilon(\zeta) = \dot{\zeta}^2/2 + V(\zeta)$  of the oscillator from (8.152) by the driver  $D(\tau) = \hat{D} \sin^2[\omega\tau/(2N\omega_{p0})] \cos\omega\tau/\omega_{p0}$ ,  $\omega/\omega_{p0} = 0.1$ ,  $N = 20$ , (a) below resonance ( $\hat{D} = 0.921$ ), (b) above resonance ( $\hat{D} = 0.923$ ) with an 43 times higher final energy gain  $\varepsilon_f$  than in (a) although the driver strength is changed only by 0.2%. The potential and the resonant energy level are indicated dashed and dotted, respectively. Note the different scales in a, b

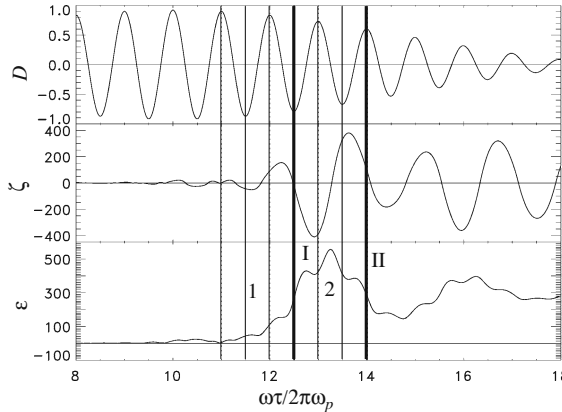


**Fig. 8.15** Driver  $D(\tau)$ , excursion  $\zeta(\tau)$  and absorbed energy  $\varepsilon(\tau)$  vs time (in driver cycles) for the case in Fig. 8.14. Each time resonance is crossed  $\zeta$  undergoes a phase shift by  $\pi$ . Bold lines I, II indicate instants of phase lag  $\zeta \pm \pi/2$  between  $D$  and  $\zeta$ , i.e., maximum energy gain and loss (points of stationary phase); modulations in  $\varepsilon$  originate from the  $\omega + \omega_0$  spectral component

primary resonance of a single isolated layer happens at the laser intensity as low as  $I = 10^{15} \text{ Wcm}^{-2}$ .

Figure 8.15 is of particular relevance. It shows the driving field  $D(\tau)$ , the displacement  $\zeta(\tau)$ , and the energy gained  $\varepsilon(\tau)$ . At position 1 the oscillator is entering resonance ( $\varepsilon$  starts increasing,  $\omega_0 > \omega$ ),  $D$  and  $\zeta$  are in phase; at 2 it is leaving resonance ( $\varepsilon$  starts decreasing,  $\omega_0 < \omega$ ),  $D$  and  $\zeta$  are dephased by  $\pi$ . Positions I and II (points of stationary phase) indicate maximum energy gain and maximum energy loss,  $D$  and  $\zeta$  are dephased by  $\pm\pi/2$ . Thus, the resonance signature is preserved in a rapid transition. The phenomenon repeats in the second maximum of  $\varepsilon$ , etc. Resonance, i.e.,  $\omega_0$  becoming equal to  $\omega$ , is intimately connected with the phase shift by  $\pi$  owing to the different reaction of the oscillator to the driver under a strong restoring force ( $\omega_0 \gg \omega$ ) and a weak one of a nearly free particle. The absorption term (8.131)  $jE \sim \dot{\xi}D$  at resonance transits from  $\sim \sin \tau \times \cos \tau$  to  $\sim \cos^2 \tau$ . This guarantees energy transfer from the driver to the oscillator. Further illustration of the phase shift at resonance for different parameters are found in [74], Fig. 5. The time-dependence of  $\omega_0$  from (8.137) in (8.152) is accomplished through the amplitude  $\zeta_0$ ,  $\omega_0 = \omega_0(\zeta_0[D(t)])$ .

### 8.3.3.2 Anharmonic Resonance Absorption in Cold and Warm Plasma

The extension of the dynamics from one layer of electrons and ions to  $N$  layers is accomplished by considering all attractive forces of the fixed ion layers (index  $l$ ) on all electron layers (index  $k$ ) and all repulsive forces between the electron layers (indices  $k, k'$ ). This results into the nonseparable (nonintegrable, chaotic), yet elementary Hamiltonian

$$H = \sum_{k=1}^N \left( \frac{p_k^2}{2} + \frac{1}{2} \sum_{k' \neq k}^N V_{kk'} + \sum_{l=1}^N V_{kl} - D(\tau) \zeta_k \right) \quad (8.153)$$

with  $p_k = d\zeta_k/d\tau$ , and the potentials with the structure of  $V$  from (2),  $V_{kk'} = -[1 + (\zeta_k - \zeta_{k'})^2]^{1/2}$  and  $V_{kl} = [1 + (\zeta_k - \zeta_{0l})^2]^{1/2}$ ,  $\zeta_k = 2x_k/d$ ,  $\zeta_{0l} = 2a_l/d$ ,  $a_l$  position of the  $l$ th ion layer. When one of the layers is driven into resonance it starts moving oppositely to the coherently moving nonresonant layers, thereby crossing one or several adjacent oscillators. Incidentally, this is a new scenario of very effective breaking of flow (special case: breaking of wave) not described in the literature so far. As a representative case we study the dynamics of a 100 times overdense target, subdivided into layers of  $d = 0.125$  nm each, on which  $I = 3.5 \times 10^{18}$  Wcm $^{-2}$  at  $\lambda = 800$  nm and is impinging with  $f(t)$  increasing from zero to unity within 2 laser periods  $T$  and then remaining constant. The intensity of  $D$  on the  $k$ th electron layer is calculated at each time instant by determining the screening due to all layers lying in front of it according to the exponential decay  $\exp(-k\eta_i d)$ , with  $\eta_i$  the imaginary refractive index. The typical scenario is as follows: After being pulled out into the vacuum and oscillating there for some time (“vacuum heating”: no heating!) the layers are pushed back in a disruption-like manner into the target (formation of jets; Fig. 8.16 and Figs. 8.6, 8.7, and 8.8). Layers leaving from the back of the target are replaced by new layers with zero momentum (cold return current). First indication of resonance: More than half of the layers have gained

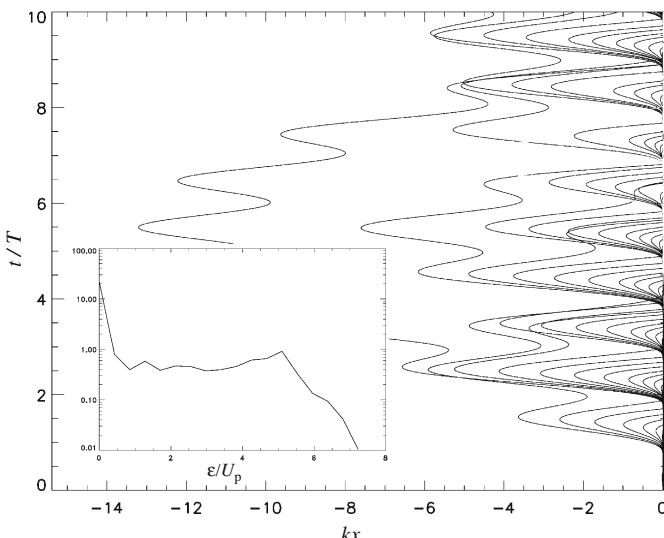


**Fig. 8.16** Time history of the electron layers during the first 10 laser periods  $T$  under the action of a pulse as described in the text, with  $f(t) = \text{const}$  for  $t \geq 2T$ : displacements  $\zeta_k(t)$  in dimensionless units  $kx$ ,  $k$  wave number. No detectable “vacuum heating”. Inset: energy spectrum of 2700 layers at  $t/T = 100$ ,  $W = U_p$  quiver energy

energies exceeding their quiver energy  $W$ . The energy spectrum shows a plateau between  $1W$  and the cut off at  $6W$  (see inset in Fig. 8.16). In other runs with more realistic driver field and the magnetic field included similar energy spectra were obtained with plateaus extending up to  $20W$ . To show the occurrence of resonance explicitly the phase of each layer with respect to the driving laser field is investigated. A typical example with  $N = 120$  is shown in Fig. 8.17 for layer #32, LHS trajectory and driver field (a), middle absorbed energy (b), RHS phase  $\varphi$  of velocity  $v \sim \sin(\omega t + \varphi)$  with respect to the driver  $E \sim \cos \omega t$  (c): over  $T/2$  there is a continuous and smooth transition of  $\varphi$  through  $-\pi/2$  at  $t/T = 2.8$  (I) with a simultaneous strong increase in the absorbed energy (b) and the excursion (a), with following disruption of the layer at  $t/T = 3.6$ . The change of  $\varphi$  is clearly seen also in (a). Another resonance of the same kind is found at  $t/T = 8.8$  (II). Other two passages of  $\varphi$  through  $-\pi/2$  at  $t/T = 5.7$  (1) and  $8.1$  (2) show rapid fluctuations and hence almost no energy gain [see (b)] and no disruption [see (a)]. Transitions of this latter kind are morphologically clearly distinguishable from the former case, and for none of the 120 layers they are able to accelerate them across the target. In the cold plasma model we find that all layers (no exception) get their energy from resonance and keep it in the underdense region. Only after undergoing resonance

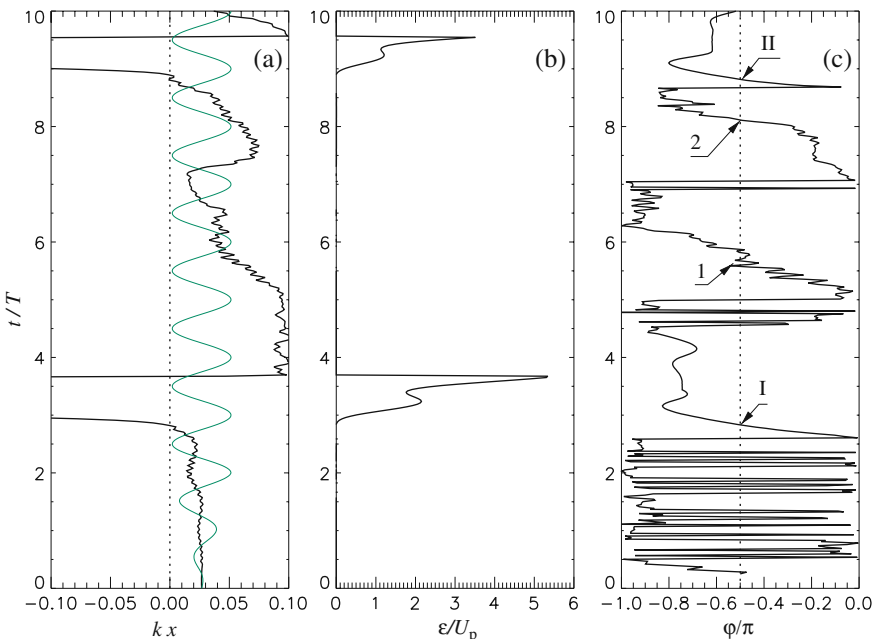


**Fig. 8.17** Resonance dynamics of layer #32 as a function of laser periods. Position  $kx$  (a),  $k$  wave number, absorbed energy  $\epsilon$  (b) and phase  $\varphi$  between velocity  $v$  and driving laser field from Fig. 8.16 (mapped into the interval  $[-\pi, 0]$ ) (c);  $\epsilon$  in units of quiver energy  $U_p$ . Passages through  $-\pi/2$  are indicated by I, II, and 1 and 2 (see text). After resonance at  $3.5$  laser periods the layer is pushed back into the target with high velocity (“disruption”). After crossing the opposite target surface the layer is substituted by a new layer. Note  $E \sim -D$

each time the layers disrupt, in the present case in chaotic order 6, 5, 4, 3, 2, 15, 17, 16, 9, 11, 10, 8, 12, 24, 31, 34, 28, 32, 14, 30, 1, 33, 45, 26, 36, 27, etc.; layer 113 disrupts before front layer 0. This is one of the fundamental differences in the dynamics in comparison to [49]. It may be interesting in this context to compare with an earlier PIC simulation of a cold plasma from [77]. They also show the resonance character of absorption (although not properly understood when the article was written). The question at which intensity resonance sets in is difficult to answer and is reserved to further investigations. Simulations with 2, 10 and 20 layers show a decrease and a broadening of its threshold, in agreement with analytical estimates. The advantage of the model lies in its Hamiltonian structure. In combination with simplified and oversimplified drivers it offers much flexibility and considerable help in interpreting PIC simulations. So, for example, property (5) is easily explained: in circular polarization the electron motion is entirely transverse and no resonance is excited in  $x$ -direction. The simplest driver considered here reproduces already all properties (1)–(5) Figures 8.16 and 8.17 show no detectable “vacuum heating”. As this is of stochastic heating type by fluctuating fields it generates Brownian-like orbits.

Resonance, i.e., energy gain during about half an oscillation implies a phase shift  $\varphi_l(t)$  for the individual electron or electron layer. All  $\varphi_l$  at a given position and time  $(\mathbf{x}, t)$  sum up to a non vanishing  $\phi(t)$  value once at least one electron (charge  $e$ , amplitude  $\mathbf{v}_{0l}$ ) is resonant,

$$\begin{aligned} \mathbf{j}(\mathbf{x}, t) &= -e \sum_l \delta(\mathbf{x} - \mathbf{x}_l(t)) \mathbf{v}_{0l} \sin(\omega t + \varphi_l) \\ &= -en_e \mathbf{v}_0 \sin(\omega t + \phi). \end{aligned} \quad (8.154)$$

With respect to resonance variations of  $D$  had no qualitative consequences. For quantitative results recurrence must be made to PIC, Vlasov, or molecular dynamics. Anharmonic resonance constitutes a very efficient scenario leading to breaking of regular dynamics of a fluid (special case: wavebreaking). Once a fluid layer undergoes resonance it may move opposite to the adjacent fluid layer and thus destroy the continuous mapping (2.57). We give it the name “resonant (wave) breaking”.

In order to reveal the dominant role in warm, i.e., realistic plasma, a  $10^6$  particles PIC simulation with the PSC code [78] in its collisionless mode under  $45^\circ$  irradiation is performed. In the boosted frame a Gaussian Nd laser beam of  $I = 10^{17}$   $\text{Wcm}^{-2}$  and halfwidth of 26 fs acts on a plane 80 times overcritical  $7.3 \mu\text{m}$  thick target. In some sense 1D is the most severe case because it limits the number of absorption channels; for example storage of energy in induced ring currents and concomitant magnetic fields decaying later [45] are excluded. On the other hand the absorption values of 70–80% have been achieved in PIC simulations in 1D and measured in 1D [37, 38, 79]. Requirement (3) is proven if we succeed in showing that in 1D simulations almost all absorption is due to resonance. To reveal resonance single particle orbits must be followed. It is achieved by embedding a sufficient

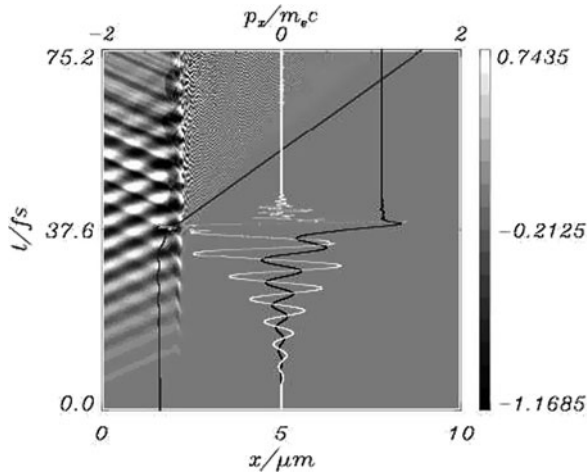


**Fig. 8.18** 1D3V PIC simulation of a Nd laser beam interacting with a thick overdense target with mobile ions in the boosted frame (parameters see text). Regular shadow structure: laser field, LHS black trajectory: displacement  $x(t)$  of test electron #4, RHS black trajectory: corresponding momentum  $p_x$  in units of  $m_e c$ , white line: total electric field at position  $x(t)$ . Resonance (strong momentum increase and phase shift  $\varphi(t)$ ) and disruption are impressive. In all tests: no disruption without preceding resonance. Resonances look all very similar to each other (see following Figure)

number of test electrons, here 200, at equal distance from each other in the target and following momentum  $p_x(t)$  and space coordinate  $x(t)$ , during 15 laser periods  $T_{Nd} = 5$  fs.

The outcome of the statistics is overwhelming: all test electrons interacting with the laser field are resonantly accelerated and either escape in a disruption-like manner into the target interior or move out into the vacuum from where they are driven back by the space charge. In Fig. 8.18 the time history of a typical test electron is depicted. The electron enters the laser field (shadowed interference pattern), interacts resonantly (see the evolution of momentum normalized to  $mc$ ) and escapes into the target an instant later with 15.3 times  $W$ . Resonance is ensured by the high energy gain [property (2)], the total  $E$ -field deviating only slightly from sinusoidal behavior (white line), and the phase shift in the last half electron oscillation: last maxima of the two lines exactly coincide, the former are dephased by  $\pi/2$ , as they should at  $\omega_p/\omega > 1$ . The shadowed fine structure right of the laser field is due to plasmons. All orbits entering the laser field undergo resonance and look very similar to each other, see Fig. 8.19 with other resonant layers. Properties (1)–(4) are herewith proven once more. One could object that only the contribution of  $\overline{j \cdot E}$  in  $x$  direction has been considered. However, owing to the conservation of the canonical momentum in  $y$  direction in 1D at normal incidence,  $p_y + e\Re(E/i\omega) = \text{const}$ ,  $j_y E_y$  leads only to the change of  $p_x$  described above. The simulation analysis tells also important details on the heating mechanism: The fast electrons are generated first by resonance; they excite “solitary”, i.e., non-Bohm–Gross plasmons in the

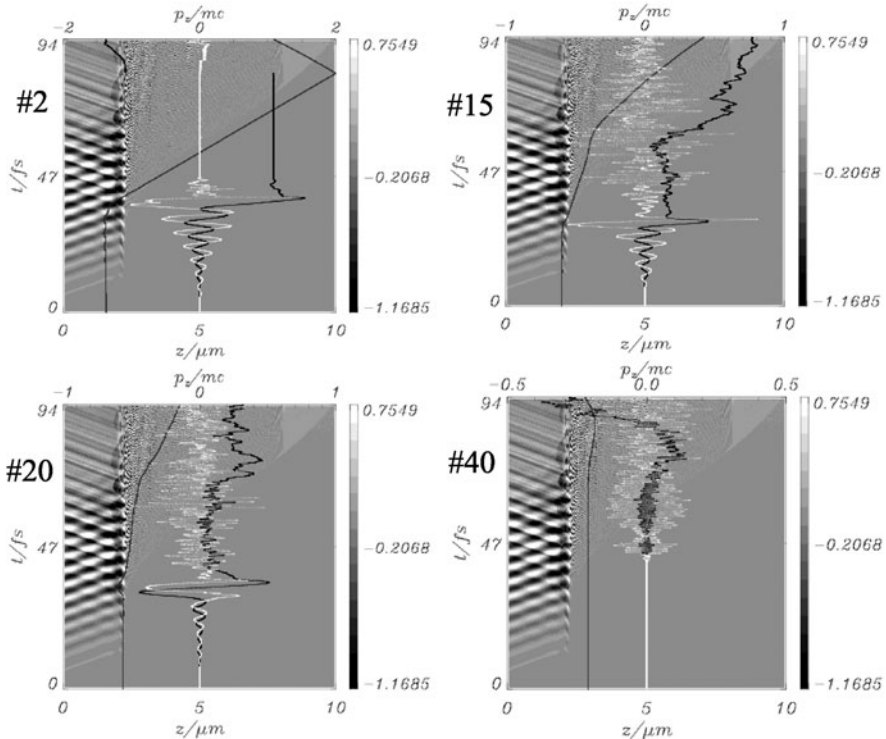


**Fig. 8.19** A selection of other 3 resonant layers, #2, #15, #20. Parameters as in Fig. 8.18. Layer #40 never “sees” the laser field. It is heated by interacting with the fluctuating electrostatic field in the target interior

dense interior which, in turn, heat cold electrons by a mechanism resembling Landau damping. The simulations have also revealed that the electron spectrum is subject to continuous metamorphosis in time, an aspect which may play an important role in fast ignition.

The mechanism of anharmonic resonance is also active in the collisionless absorption in clusters during the early interaction phase when ion expansion is negligible [80, 81].

Anharmonic resonance has already found its first experimental verification in the few laser cycle absorption experiment by Cerchez et al. [79]. After various estimates and cross checks the conclusion is that this represents the most promising candidate for the measured absorption. It should be stressed that the mechanism is active also in long fs or ps pulses when profile steepening is so strong that no linear resonance can take place. The main practical relevance of resonance may be seen in the possibility to tailor the electron spectrum for various applications (electron and ion acceleration, fast ignition, etc.) by designing targets properly, for instance by choosing carefully their thickness, structure and shape.

## 8.4 Some Relativity of Relevance in Practice

*There are no limits; horizons only*

Gerard A. Mourou

DPG Spring Meeting Düsseldorf 2007

### 8.4.1 Overview

At high intensities electromagnetic waves behave strongly nonlinear, at a degree which goes far beyond the familiar nonlinear optics. The origin of the drastically increased nonlinearity lies in the self-generated sudden variation of the local electron density due to field ionization (i), the ponderomotive (or wave pressure) effects (ii) and, at relativistic intensities, the coupling of transverse and longitudinal fields already in the homogeneous plasma (iii). Whereas in standard nonlinear optics the number of wave crests of a pulse is invariant, as a consequence of (i) it can vary: after transition or reflection e.g. five crests become six or seven crests [34]. Ponderomotive effects (ii) lead to a large number of instabilities, formation of irregular structures, solitons, cavitons, wavebreaking, and chaos. In addition, due to (iii) all effects may even become stronger. So far, transverse and longitudinal wave propagation at relativistic intensities has been studied extensively only with waves of constant phase velocity in plasmas of constant density [82–84], and recently stationary quasiperiodic solutions have also been presented [85]. Under the influence of (ii) the plasma medium is expected to become heavily deformed and even self-quenching of the electromagnetic mode may occur. As extreme intensities are to be expected in the near future ( $I > 10^{23} \text{ Wcm}^{-2}$ ) hot dense matter at solid and above solid density may be produced by relativistic overcritical light penetration. The study of intense wave propagation in dense matter is of vital importance, in itself as well as for applications (equation of state, fast ignition [86], astrophysics). The beauty in this context is that a great portion of related experiments can already be performed, by analogy, at nonrelativistic and close to relativistic intensities in sub- and super-critical foams and porous media with standard fs laser pulses. With increasing light intensity laser-based nuclear physics will become a reality [87]. In analogy to atomic systems excitation, stimulated de-excitation and triggering of single decay processes may be controlled by laser. Already with the next generation of photon flux densities ( $> 10^{23}$ , perhaps  $\gg 10^{23} \text{ Wcm}^{-2}$ ) the direct excitation of nuclear levels and the triggered decay of isomeric nuclei can be studied, provided the photon energy is high enough (order of keVs, free electron laser systems, [88]). Alternatively, the aim may be reached by the coherent superposition of extremely high order harmonics generated from solid targets [89]. Such pulses will be used also to study the nuclear Stark effect and fine tuning of nuclear levels for various applications and diagnostics. All kinds of vacuum nonlinearities have their origin in the separation (slang: “creation”) of electron-positron or more massive pairs by a corresponding energy supply. The critical field for the lightest pair production is  $E = 1.3 \times 10^{18} \text{ V/m}$ , corresponding to the laser intensity  $I = 2.3 \times 10^{29} \text{ Wcm}^{-2}$ .

Their existence becomes noticeable already through their virtual appearance at much lower energies (and fortunately, after all “there are no limits” of  $I$  to make them real). Nonperturbative vacuum nonlinearities manifest themselves in a variety of processes and effects of the quantum vacuum exposed to superintense photon fields: generation of harmonics, photon splitting, light by light scattering, vacuum polarization [90]. Two favored candidates, accessible to the most intense available fs laser installations, are the merging of two photons in the laser field interacting with TeV protons and the dramatic increase of electron bremsstrahlung from a nucleus in the intense radiation field by many orders of magnitude.

### ***8.4.2 Critical Density Increase for Fast Ignition***

Currently high power lasers emit in the infrared (Nd YAG, Ti:Sa), or in the near UV if for convenience a KrF system can be used. This means that the emitted laser beams cannot penetrate matter of solid density with electron densities of typically  $10^{23}$ – $10^{24}$  cm $^{-3}$ . On the other hand it is of extreme interest to heat such dense, and even denser, plasmas uniformly and isochorically for studies of equations of state, bright X ray sources, generation of high harmonics and for fast ignition of inertial fusion pellets [91, 92]. In the latter case, with a laser beam emitting in the soft X ray range several problems of radiation-pellet coupling of traditional lasers would be eliminated. It is a fortune that at intensities at which the electrons gyrate relativistically in a circularly polarized beam an increase of the critical electron density is obtained owing to the electronic current decrease (“relativistic mass increase”) by the relativistic Lorentz factor  $\gamma = (1 - v^2/c^2)^{-1/2}$ ,  $v$  gyrovelocity,  $c$  speed of light in vacuum [93]. In linear polarization “anomalous penetration” was found by means of numerical studies in [94], i.e., considerably weaker penetration than corresponding to their formula for  $n_c$ . This and analogous results indicate that the general problem of relativistic penetration needs further investigations. At low, nonrelativistic laser intensities the fully ionized plasma can be treated as a monofluid for electromagnetic wave propagation in the homogeneous medium with an invariant plasma frequency. At high laser intensities one is faced with a different situation: on the fast time scale the ions can still be treated as immobile objects while the electrons move at relativistic velocity. Thus, in any reference system one has to deal with a two-fluid model and the problem has to be faced what the implications of the transition from a monofluid to a two-fluid model are. In addition, the question arises whether the concept of a critical density remains still valid when at relativistic intensities highly nonlinear density structures and cavitons may form [95, 96]. Both problems, the existence of a critical density and its correct relativistic increase in a highly overdense plasma, are to be clarified “experimentally”, i.e., by particle-in-cell (PIC) simulations owing to the high nonlinearities involved, and fitted by analytical expressions.

#### ***8.4.2.1 Relativistic Critical Density Increase***

Under the assumption of an invariant electron density an intense circularly polarized electromagnetic wave can penetrate considerably deeper into a fully ionized plasma

owing to the already mentioned relativistic electron current decrease by the Lorentz factor  $\gamma$ ,

$$\begin{aligned} \gamma &= (1 + \hat{\mathbf{a}}^2)^{1/2}, \quad \hat{\mathbf{a}} = \frac{e\hat{\mathbf{A}}}{mc}, \quad \mathbf{A} = -\frac{i}{\omega}\mathbf{E}, \\ (\mathbf{A}, \mathbf{E})(\mathbf{x}, t) &= (\hat{\mathbf{A}}, \hat{\mathbf{E}})(\mathbf{x}, t) \exp(-i\omega t); \end{aligned} \quad (8.155)$$

$\mathbf{A}$ ,  $\hat{\mathbf{A}}$ ,  $\mathbf{E}$ ,  $\hat{\mathbf{E}}$  vector potential and electric field with associated amplitudes [93]. The refractive index is  $\eta = (1 - n_e/\gamma n_c)^{1/2}$ , thus showing that the relativistic critical density for circular polarization is  $n_{\text{cr}} = \gamma n_c$ . By analogy, in linear polarization the true  $\gamma$  factor is expected to be  $\gamma = (1 + \hat{\mathbf{a}}^2/2)^{1/2}$  of a single electron in the vacuum. The departure from this value will depend on the electron density variation  $dn_e/dt = -n_e \nabla \mathbf{v}$  induced by the Lorentz force in propagation direction. The available time for restoring quasineutrality, i.e.,  $\nabla \mathbf{v} = 0$ , is only half a laser cycle  $\pi/\omega$ . In a tenuous plasma ( $\omega_p \ll \omega$ ) perturbation theory yields  $n_{\text{cr}} = (1 + 3\hat{\mathbf{a}}^2/8)^{1/2} n_c$ , with  $3/8 < 1/2$  for this reason [83, 82]. The dispersion of propagating plane waves of arbitrary strength and linear polarization in a constant plasma density under Lorentzian gauge is governed by the set of equations

$$\begin{aligned} \square \mathbf{A} &= -\frac{J}{\varepsilon_0 c^2}, \quad \partial_\alpha A^\alpha = 0, \quad \mathbf{A} = (\mathbf{A}, \phi/c), \quad \mathbf{J} = (\mathbf{j}, c\rho_e), \\ \rho_e &= e(n_{i0} - n_e) = \varepsilon_0 \left( \frac{v_\varphi^2}{c^2} - 1 \right) \frac{\partial^2 \phi}{\partial x^2}, \quad \frac{\partial \phi}{\partial x} = \frac{c^2}{v_\varphi} \frac{\partial A_x}{\partial x}, \\ j_y &= -\frac{e^2 n_{e0}}{\gamma m} A_y + \varepsilon_0 \left[ e v_\varphi \left( 1 - \frac{c^2}{v_\varphi^2} \right) \frac{\partial^2 A_x}{\partial x^2} \right] \frac{A_y}{\gamma m}. \end{aligned} \quad (8.156)$$

$\phi$  is the scalar potential and  $v_\varphi$  the constant phase velocity. The second of these relations is the Lorentz gauge. The current density  $j_y$  follows from the canonical momentum conservation  $\gamma m v_y = e A_y$  for a cold electron fluid initially at rest. In circular polarization the second term (square bracket) in  $j_y$  vanishes owing to  $A_x = \phi/c = 0$ . The dispersion of waves described by (8.156) has been extensively studied and discussed recently also close to cut-offs and it has been found that the majority of electromagnetic modes exhibits the typical eight-like electron motion as in the tenuous plasma [82]. Besides, a purely electrostatic mode with circular electron motion in the plane of incidence is also possible, in accordance with the fact that the  $\mathbf{B}$ -field of an electromagnetic wave near cut-off behaves like  $\hat{\mathbf{B}}\eta \rightarrow 0$ . Unfortunately, light coupling to high density matter, which is the typical fast ignition-relevant situation, is accompanied by plasma density profile steepening, partial reflection and extremely nonuniform electron fluid expansion [89] and recession during one cycle, with a concomitant laser frequency Doppler shift in the frame of co-moving critical layer. Owing to such complexity and, eventually, due to caviton formation [96, 97], a reliable determination of the critical density increase is accessible only to particle-in-cell (PIC) or similar simulation procedures

(e.g. Vlasov). Here the 3D PSC PIC code [78] is used to give the promised “experimental” answer.

### 8.4.2.2 Quasiperiodic and Chaotic Electron Orbits

In the critical region the phenomena addressed above lead to a strongly fluctuating potential  $\phi$  which in combination with the laser field may transform the regular 8-shape electron motion into quasiperiodic and chaotic orbits with unknown Lorentz factor  $\gamma_p$ . To illustrate the situation a time-independent typical self generated potential  $\phi = mc^2\hat{a}[1 + \kappa^2(x/\lambda)^2]^{1/2}$  with the free parameter  $\kappa$  and the laser wavelength  $\lambda$  is used. The beam propagates in  $x$ -direction. The laser field strength is held fixed at  $\hat{a} = 1$  and  $\kappa$  is varied (see Fig. 8.20). The first picture, obtained with  $\kappa = 6.2$ , shows a stable configuration of the electron orbiting around a vacuum-like 8-shape trajectory. Only a slight asymmetry in diagonal direction is observable. At  $\kappa = 6.5$  the electron manages it to escape from the stable configuration after several turns in the direction  $y$  of the laser field, and eventually it comes back again (picture at RHS). By a further increase of  $\kappa$  by only 8% to  $\kappa = 7.0$  a very complex orbit results (3rd picture). By plotting the time history of the transverse motion ( $[y, t]$ -plot in 4th picure) it becomes clear that during the registered 100 laser cycles the electron

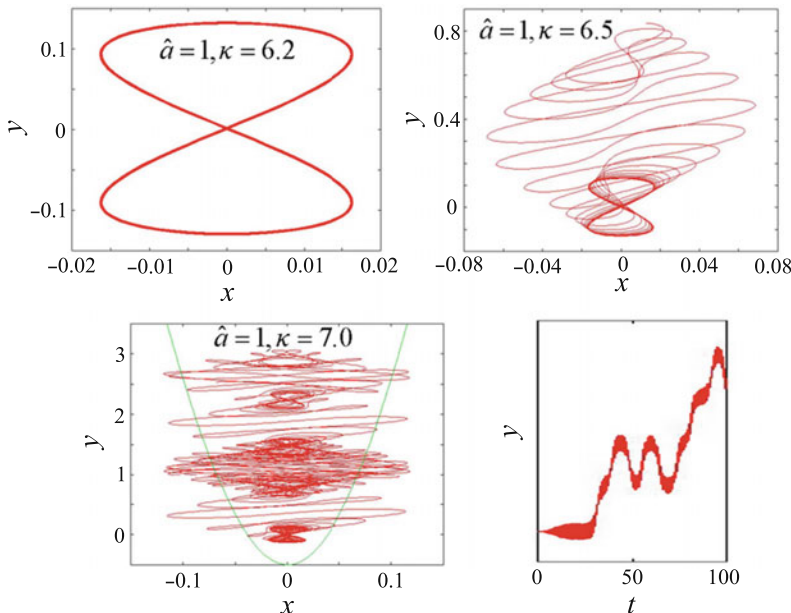


**Fig. 8.20** Evolution towards chaotic dynamics of the electron motion in presence of an electrostatic potential  $\phi = mc^2\hat{a}(1 + \kappa^2x^2)^{1/2}$ . The motion is very sensitive to variations of the free parameter  $\kappa$  around  $\kappa \simeq 7.0$ . Note the close resemblance to chaotic ponderomotive motion in a standing wave, Fig. 2 in [98]

crosses 9 attractors. In a sense, the trajectory is a repeated composition of orbits from the 2nd picture. The contribution of such orbits to the relativistic increase of the critical density is not known. Additionally, due to inherent stochasticity anharmonic resonance is accompanied by a heating effect.

#### 8.4.2.3 “Experimental” $\gamma$ Factor

In the rest frame of an electron fluid element the bare electron mass  $m$  turns into the “dressed” thermal mass  $m_{\text{th}} = \gamma_{\text{th}} m$ , with  $\gamma_{\text{th}}$  to be determined kinetically. The electron becomes “heavier” by  $\gamma_{\text{th}}$ , thus acting in favor of a high  $\gamma$  value.  $\gamma_p$  originating from orbit deformations as presented in Fig. 8.20 can act in both directions and has not been studied so far. As the  $\gamma$  values associated with these various effects interact in a complex nonlinear manner with the effect of the relativistic increase of the bare electron mass, the correct value of the resulting  $\gamma$  actually is determined in the most reliable manner by analyzing 1D PIC runs at a sequence of laser intensities. Furthermore, only such an “experimental” procedure can reveal to what extent the existence of a critical density and a well defined critical point are secure or whether they have to be given up owing to irregular density fluctuations and aperiodic recessions at extreme laser intensities.

A fully ionized target of 100 times critical density with heavy ions (to suppress hole boring, of no interest in the context) is exposed to linearly polarized laser irradiance of  $I\lambda^2 = 10^s \text{ Wcm}^{-2}\mu\text{m}^2$ ,  $s = 18-22$ , under perpendicular and p-45° incidence and, when the interaction has become stationary, all field quantities are averaged over two laser cycles [99]. A typical result for  $I\lambda^2 = 5 \times 10^{21} \text{ Wcm}^{-2}\mu\text{m}^2$  under 45° on target is presented in Fig. 8.21 for  $t = 80$  fs. In contrast to strongly fluctuating pictures taken at single time instants, after sufficiently averaging quiescent shapes in all field quantities are obtained. Hence, a first result is that

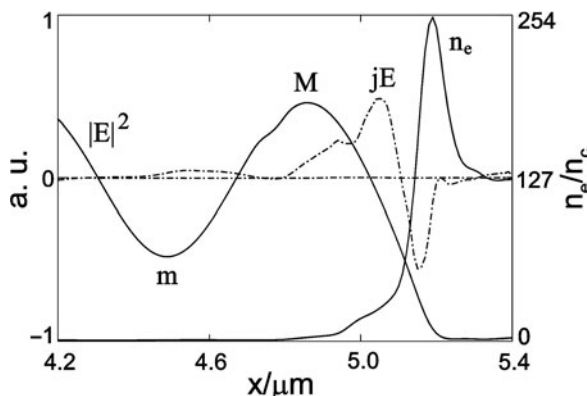


**Fig. 8.21** Cycle-averaged distributions in space ( $x$  coordinate) of the field amplitude squared  $|E|^2$  with closest maximum  $M$  and minimum  $m$ , absorption  $jE$  and electron density  $n_e$  after 80 fs of irradiance  $I\lambda^2 = 5 \times 10^{21} \text{ Wcm}^{-2}\mu\text{m}^2$ . Critical density in the lab frame is  $n_c = n_0/100$ . Angle of incidence  $\alpha = 45^\circ$

the concept of a cycle-averaged, not instantaneous, critical density makes sense. It is to be expected at the point of zero curvature of the evanescent branch of  $|E|^2$  occurring close to half the maximum. In nearly all cases this position coincides with the maximum of absorption  $jE$ , a fact which is of great help in the analysis. Thus the density at this point is taken as the (“experimental”) relativistic critical density  $n_{cr}$  and its relativistic increase  $\gamma = n_{cr}/n_c$ , respectively. The values obtained at the 5 intensities are indicated by the first two columns for perpendicular and  $45^\circ$  laser incidence in Fig. 8.22. For laser intensities  $I \geq 10^{20} \text{ Wcm}^{-2}$  higher  $\gamma$  values result at oblique incidence than at normal irradiation. The hump in  $|E|^2$  between  $x = 4.6$  and  $x = 5.0$  is due to the superposition of higher harmonics [89]. For supporting the numerical results and perhaps gaining some physical insight, in the absence of any knowledge on  $\gamma_{th}$ , we start from the assumption of regular vacuum-like 8-shape orbits and determine a “theoretical”  $\gamma$  factor from the formula

$$\gamma = \left[ 1 + (1+r)^2 \frac{\hat{a}^2}{2} \right]^{1/2}, \quad (8.157)$$

with  $r\hat{a}$  the reflected normalized wave amplitude. Note that this expression is invariant with respect to a rotation by an angle of incidence  $\alpha$ . This can be recognized by transforming to the boosted reference system in which both quantities  $\hat{E}$  and  $\omega$  are multiplied by  $\cos \alpha$  and  $\hat{A}$  is their ratio [see (8.155)]. The magnitude of  $r$  is obtained from  $\max |E|^2 = M$  and  $\min |E|^2 = m$  closest to the cut-off according to

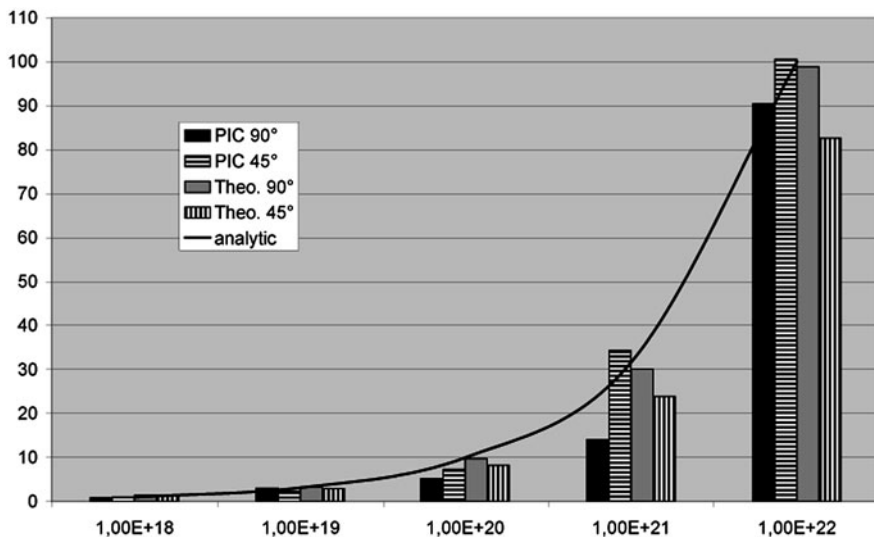


**Fig. 8.22** Relativistic critical density increase, cycle averaged, in the intensity range  $I = 10^{18} - 10^{22} \text{ Wcm}^{-2}$ . Black and gray columns: normal incidence, dashed columns:  $45^\circ$  incidence. Solid line: (8.159), “analytic”

$$r = \frac{(\sqrt{M} - \sqrt{m})^2}{M - m}. \quad (8.158)$$

The  $\gamma$  factors resulting from (8.158) are visualized in Fig. 8.22 by columns 3 and 4 for normal and  $45^\circ$  incidence, respectively (“theoretical”). All values, theoretical and experimental, are taken at  $t = 80$  fs. Although at some intensities, in particular at  $I\lambda^2 = 10^{21} \text{ Wcm}^{-2}\mu\text{m}^2$ , the  $\gamma$  values for  $90^\circ$  and  $45^\circ$  from PIC differ considerably from each other, and so does  $\gamma$  obtained by means of (8.157) for  $90^\circ$  and  $45^\circ$  at all intensities  $I\lambda^2 \geq 10^{20} \text{ Wcm}^{-2}\mu\text{m}^2$ , in first approximation the results look like as if produced by the relativistic mass increase only and almost no relativistic influence stemming from changes of  $n_e$  and from chaotic orbits. The latter are revealed by test particle injection in the PSC simulations and following their motion. The impression of dominating mass increase is reinforced if a fit to the averages of each of the five quadruplets is done. For this it was found

$$\gamma = \left( 1 + I\lambda^2 [\text{Wcm}^{-2}\mu\text{m}^2] / 10^{18} \right)^{1/2}, \quad (8.159)$$

see black solid line. The weak relativistic contribution from  $n_e$  to  $\gamma$  has a qualitative explanation, *a posteriori*. By the radiation pressure strong electron density profile steepening sets in over a scale length which is a small fraction of the laser wavelength  $\lambda$  only. As a consequence the laser wave acts mostly on a low density shelf with  $n_e \ll n_{\text{cr}}$  and, in the evanescent region, on  $n_e \gg n_{\text{cr}}$  (see Fig. 8.21). For  $n_e \ll n_{\text{cr}}$ ,  $\gamma$  is close to the vacuum value ( $3/8$  instead of  $1/2$ ). At  $n_e \simeq n_0$  charge neutralization is up to 20 times faster than  $2\pi/\omega$ . It can be concluded that up to the intensities considered an average critical density makes sense and its approximate relativistic increase is given by a simple formula which reflects essentially the vacuum-like 8-shape motion of the electrons.

#### 8.4.2.4 Implications for Fast Ignition by Laser

The advantages of fast pellet ignition with powerful lasers for inertial confinement fusion are well known: Decoupling of compression from ignition phase, less requirements on pulse shaping of the main compression pulse, lowering of symmetry constraints on peak compression, explicitly shown in [100]. Extensive computer studies with flux limited Spitzer heat transport have shown that a typical ignition energy is 70 kJ and, by optimizing the process, 50 kJ at a laser intensity not lower than  $I = 10^{20} \text{ Wcm}^{-2}$  may represent the minimum energy and intensity requirements [101]. Under the condition that such an amount of energy is deposited in fast electrons the density of the deposition zone has not to be less than  $4\text{--}5 \text{ gcm}^{-3}$  DT; below  $1 \text{ gcm}^{-3}$  in no run a burn wave evolved. As the laser energy cannot be deposited beyond the critical density in standard coronal ignition the flux of the energetic electrons has to travel a long distance up to the compressed core thereby undergoing sensitive diffusive attenuation. For comparison, simulations in [100] with the heat flux limiter turned off show that the energy needed for the pure ignition process

(the “free ignition energy”) is typically 15 kJ, in agreement with simpler models of direct energy deposition in the most favorable region [102, 103]. Originally hole boring was intended as to reducing noticeably the distance between the laser deposition region and the compressed core. Unfortunately hole boring has proven to be not efficient enough for this purpose [104]. Cone guided fast ignition is more advantageous to bring the two regions closer together and, in addition, to provide for better coupling of the laser beam [91]. However, also in this scheme there is the constraint on laser energy conversion into kinetic energy of the electrons not beyond the critical density. Inspired by [91] and [105] we consider a model in which the hot electrons basically propagate ballistically through the critical and intermediate densities and interact collisionally in the compressed pellet core. The minimum flux density of hot electrons  $q_0 = 10^{21} \text{ Wcm}^{-2}$  is estimated to be sufficient when generated by the 3rd harmonic of Nd laser frequency  $\omega = 1.78 \times 10^{15} \text{ s}^{-1}$ . Assuming  $R = 0.5$  for the laser follow  $\gamma = 6.7$  and  $n_{\text{cr}} = 6.7 \times 10^{22} \text{ cm}^{-3}$ , the latter exceeding solid DT density  $n_{\text{DT}} = 5 \times 10^{22} \text{ cm}^{-3}$ . In order to transport the absorbed flux density  $q_0$  with electron velocity  $u$  for the mean energy  $\langle E \rangle$  of the hot electrons must hold

$$n_{\text{cr}} \langle E \rangle u = q_0, \quad u = c \left( 1 - \frac{1}{\gamma} \right)^{1/2}, \quad \gamma = 1 + \frac{\langle E \rangle}{mc^2}. \quad (8.160)$$

From (8.160) the mean energy results as low as  $\langle E \rangle = 0.37 \text{ MeV}$ . An upper limit for  $\langle E \rangle$  is obtained by making the very reasonable assumption that it may not be much higher than the mean oscillatory electron energy which in the specific case with  $\hat{a} = 4.3$  is  $E_{\text{os}} = 1.1 \text{ MeV}$ , i.e., consistency is guaranteed. If already in the critical and medium density domain strong thermalization occurs a diffusive model applies. In [101] it was found on the basis of [100] that the minimum required flux density has to be close to  $q_0 = 10^{21} \text{ Wcm}^{-2}$  because most of the energy supplied is diffusively spread all over the compressed pellet and there in particular all over its low density corona. In addition the deposition density should not be inferior to  $\rho_{\text{dep}} = (4-5) \text{ gcm}^{-3}$  DT; below  $\rho_{\text{dep}} = 1 \text{ gcm}^{-3}$  no ignition was possible [100]. With this value for  $n_{\text{dep}} = 5 \times 10^{22} \text{ cm}^{-3}$  and a safety factor  $s = (4-5)$  the condition  $n_{\text{cr}} = n_{\text{dep}}s = \gamma(\lambda)n_c(\lambda)$  together with  $I(\lambda) = 2q_0$  for  $R = 0.5$  must be fulfilled. For Nd holds  $n_c(\lambda) = n_{c\text{Nd}}\lambda_{\text{Nd}}^2/\lambda^2$ . Hence, from (8.159) is recovered

$$\begin{aligned} \frac{\lambda}{\lambda_{\text{Nd}}} &= \frac{n_{c\text{Nd}}}{n_{\text{dep}}s} \left( \frac{2q_0}{10^{18}} \right)^{1/2} = \frac{0.9}{s} \quad \Rightarrow \quad \omega = 1.1s\omega_{\text{Nd}}; \\ \gamma(\lambda) &= \left( \frac{2q_0}{10^{18}} \right)^{1/2} \frac{\lambda}{\lambda_{\text{Nd}}} = \frac{40}{s}. \end{aligned} \quad (8.161)$$

At  $I = 2 \times 10^{21} \text{ Wcm}^{-2}$  the maximum wavelength for achieving ignition is close to  $\lambda_{\text{Nd}}$  if  $s = 1$  is set. For the fundamental of the Ti:Sa laser the condition is fulfilled. It is obvious that the consistency condition (8.160) is fulfilled with a large safety factor. As  $\langle E \rangle = 0.95 \text{ MeV}$  and  $u = 0.87c$  consistency is secured easily also for  $s = 5$ , i.e., the fifth harmonic of  $\omega_{\text{Nd}}$  because of  $E_{\text{os}} = 3.5 \text{ MeV} > \langle E \rangle$ . It can be

concluded that at high laser intensities the relativistic increase of the critical density is favorable to achieve uniform heating of condensed matter and to facilitate energy coupling in fast ignition provided the production of fast electrons can be contained within reasonable limits.

### 8.4.3 Relativistic Self-Focusing

Whole laser beam self-focusing is considered in a tenuous underdense plasma under the idealized condition of uniform electron density  $n_e = n_0$ . Provided it can be assumed that the change of the refractive index is essentially by the relativistic electron mass increase only the refractive index  $\eta = (1 - n_0/\gamma n_c)^{1/2}$ ,  $\gamma = (1 + \hat{a}^2/2)^{1/2}$ , is higher in regions of high beam intensity, for example along the beam axis or at the center of a filament, and the phase velocity is lower. As a consequence, local self focusing and eventual beam or filament collapse occur. A threshold of self focusing as given by [106] is most easily derived for the Gaussian beam of Sect. 5.3.2. Under the condition of  $n_0 \ll n_c$ ,  $\hat{a}^2 \ll 1$ , from (5.66) and  $\hat{a}^2 = 2e^2 I(r)/\varepsilon_0 c^3 m^2 \omega^2$

$$\frac{\partial}{\partial r} \frac{n_e}{\gamma n_c} = \frac{n_e}{n_c} \frac{r}{\sigma_0^2} \hat{a}^2, \quad R_c = \eta^2 \frac{n_c}{n_e} \frac{\varepsilon_0 c^3 m^2 \omega^2}{e^2 r I(r)} \sigma_0^2;$$

Self-focusing will occur when equality of  $R_c$  with  $\bar{R}_c = 2R^2/r$  for a Gaussian ray is reached, i.e., at local intensity  $I(r)$  and power  $P(r)$

$$I(r) = 2 \frac{\varepsilon_0 m^2 c^5}{e^2 \sigma_0^2} \frac{n_c}{n_e},$$

$$P(r) = \int_0^\infty I(r) e^{\frac{2}{\sigma_0^2}(r^2 - r'^2)} 2\pi r' dr' = \pi \frac{\varepsilon_0 m^2 c^5}{e^2} \frac{n_c}{n_e} e^{\frac{2r^2}{\sigma_0^2}}. \quad (8.162)$$

The total beam power is  $P = \pi \sigma_0^2 I(r=0)/2$ , hence the intensity measured by the experimentalist is  $I = P/\pi \sigma_0^2 = I(r=0)/2$ . The power required for half beam self-focusing  $P_{1/2}$  and for 86% beam focusing  $P_{\sigma_0}$  result from (8.162) as

$$P_{1/2} = 2\pi \frac{\varepsilon_0 m^2 c^5}{e^2} \frac{n_c}{n_e} = 4.2 \frac{n_c}{n_e} \text{ GW};$$

$$P_{\sigma_0} = e^2 \pi \frac{\varepsilon_0 m^2 c^5}{e^2} \frac{n_c}{n_e} = 15.5 \frac{n_c}{n_e} \text{ GW}. \quad (8.163)$$

Frequently  $P_{\sigma_0} = 17n_c/n_e$  GW for “whole beam” focusing is given in the literature as a result of averaged quantities used for this estimate. This and (8.163) are gross criteria, see comments made on ponderomotive self-focusing, (5.69); they apply here also. A far more detailed picture is gained by a linearized wave dynamic treatment of an initially Gaussian beam. Light and density nonuniformities along the

axis lead to variations in the focusing strength  $1/R_c$  that may give rise to unstable growth of hot spots, transverse and longitudinal coupling of modes and beam self-compression already in the weakly relativistic regime [107].

## References

1. Arnold, V.I.: Mathematical Methods of Classical Mechanics, p. 8. Springer, New York (1978) 331
2. Weinberg, S.: Gravitation and Cosmology, Chap. 2. John Wiley & Sons, New York (1972) 332, 349
3. Berzi, V., Gorini, V.: Math. Phys. **10**, 1518 (1969) 332
4. Rindler, W.: Essential Relativity, Chaps. 2–6. Springer, New York (1979) 333
5. Eckart, C.: Phys. Rev. **58**, 919 (1940) 345
6. Hain, S., Mulser, P., Cornolti, F., Opower, H.: Las. Part. Beams **17**, 245 (1999); Hain, S.: Propagation of Intense Laser Radiation in Matter PhD-thesis, TU Darmstadt (in German), Chap. 1.2. GCA-Verlag, Herdecke (1999) 345
7. Landau, L.D., Lifshitz, E.M.: Fluid Mechanics, Chap. XV. Pergamon, Oxford (1959) 347
8. Lawson, J.D.: IEEE Trans. Nucl. Sci. NS-26, 4217 (1979) 355
9. Landau, L.D., Lifshitz, E.M.: The Classical Theory of Fields. Pergamon, Oxford (1975), § 47, Problem 2 356
10. Wang, J.X., Scheid, W., Hoelss, M., Ho, Y.K.: Phys. Lett. A **275**, 323 (2000) 359
11. Häuser, Th., Scheid, W., Hora, H.: Phys. Lett. A **186**, 189 (1994) 359
12. Wang, P.X., Ho, Y.K., et al.: J. Appl. Phys. **91**, 856 (2002) 359
13. Malka, G., Lefebre, E., Michel, J.L.: Phys. Rev. Lett. **78**, 3314 (1997); Phys. Rev. Lett. **80**, 1352 (1998) 359
14. Rau, B., Tajima, T., Hojo, H.: Phys. Rev. Lett. **78**, 3310 (1997); Kim, K.-J., et al.: Phys. Rev. Lett. **84**, 3210 (2000); Rau, B., Tajima, T., Hojo, H.: Phys. Rev. Lett. **84**, 3211 (2000) 359
15. Plettner, T., Byer, R.L., Colby, E., et al.: Phys. Rev. Lett. **95**, 134801 (2005); Phys. Rev. ST Accel. Beams **8**, 121301 (2005) 359
16. Tajima, T., Dawson, J.: Phys. Rev. Lett. **43**, 267 (1979) 360
17. Sprangle, P., et al.: Phys. Rev. Lett. **69**, 2200 (1992); Antonsen, M., Mora, P.: Phys. Rev. Lett. **69**, 2204 (1992) 360
18. Modena, A., et al.: Nature **377**, 606 (1995); Ting, A., et al.: Phys. Plasmas **4**, 1889 (1997); Santala, M.I.K., et al.: Phys. Rev. Lett. **86**, 1227 (2001); Malka, V., et al.: Phys. Plasmas **8**, 2605 (2001); Giulietti, D., et al.: Phys. Plasmas **9**, 3655 (2002) 360
19. Reitsma, A.J.W., et al.: Phys. Rev. Lett. **88**, 014802 (2002); Schröder, C.B., et al.: Phys. Rev. Lett. **82**, 1177 (1999) 360
20. Pukhov, A., Meyer-ter-Vehn, J.: Appl. Phys. B **74**, 355 (2002) 360, 361
21. Bulanov, S.V., Pegoraro, F., Pukhov, A., Sakharov, A.S.: Phys. Rev. Lett. **78**, 4205 (1997) 361
22. Rosenzweig, J.B., et al.: Phys. Rev. A **44**, R6189 (1991) 362
23. Mangles, S.P.D., et al.: Nature **431**, 535 (2004) 362
24. Faure, J., et al.: Nature **431**, 541 (2004) 362
25. Geddes, C.G.R., et al.: Nature **431**, 538 (2004) 362
26. Leemans, W.P., et al.: Nature Phys. **2**, 696 (2006) 362
27. Clark, E.L., et al.: Phys. Rev. Lett. **84**, 670 (2000) 363
28. Snavely, R.A., et al.: Phys. Rev. Lett. **85**, 2945 (2000)
29. Roth, M., et al.: Phys. Rev. Lett. **86**, 436 (2001)
30. Wilks, S.C., et al.: Phys. Plasmas **8**, 542 (2001) 363
31. Yan, X.Q., et al.: Phys. Rev. Lett. **100**, 135003 (2008) 363
32. Yan, X.Q., Chen, M., Sheng, Z.M., Chen, J.E.: Phys. Plasmas **16**, 044501 (2009)
33. Schlegel, T., Naumova, N., Tikhonchuk, V., et al.: Phys. Plasmas **16**, 083103 (2009) 363
34. Mulser, P., Cornolti, F., Bauer, D.: Phys. Plasmas **5**, 4466 (1998) 363, 392
35. Bauer, D.: Phys. Rev. A **55**, 2180 (1997) 363

36. Price, D.F., More, R.M., et al.: Phys. Rev. Lett. **75**, 252 (1995) 364
37. Gibbon, P., Bell, A.R.: Phys. Rev. Lett. **68**, 1535 (1992); Gibbon, P.: Phys. Rev. Lett. **73**, 664 (1994) 364, 372, 374, 377, 389
38. Wilks, S.C., Krueer, W.L., Tabak, M., Langdon, A.B.: Phys. Rev. Lett. **69**, 1383 (1992); Denavit, J.: Phys. Rev. Lett. **69**, 3052 (1992) 364, 389
39. Ruhl, H., Mulser, P.: Phys. Lett. A **205**, 388 (1995) 364, 365, 366, 367, 372, 374
40. Hockney, R.W., Hockney, R.W., Eastwood, J.W.: Computer Simulation Using Particles. IOP, Bristol (1988) 364
41. Gibbon, P., Pfalzner, S.: Many-body Tree Methods in Physics. Cambridge University Press, Cambridge (2005) 364, 365
42. Pfalzner, S., Gibbon, P.: Comp. Phys. Comm. **79**, 24 (1994) 365
43. Krueer, W.L., Estabrook, K.: Phys. Fluids **28**, 431 (1985) 366, 375, 376, 377
44. Wilks, S.C.: Phys. Fluids B **5**, 2603 (1993) 366
45. Ruhl, H., Macchi, A., Mulser, P., Cornolti, F., Hain, S.: Phys. Rev. Lett. **82**, 2095 (1999) 369, 370, 389
46. Sauerbrey, R., et al.: Phys. Plasmas **1**, 1635 (1994) 371
47. Feurer, T., et al.: Phys. Rev. E **56**, 4608 (1997) 371
48. Boudier, A.: Phys. Fluids **26**, 1804 (1983) 371
49. Brunel, F.: Phys. Rev. Lett. **59**, 52 (1987) 373, 375, 376, 389
50. Catto, P.J., More, R.M.: Phys. Fluids **20**, 704 (1977) 374, 375
51. Mulser, P., Pfalzner, S., Cornolti, F.: In: Velarde, G., et al. (eds.) Laser Interaction with Matter, p. 142. World Scientific, Singapore (1989) 374
52. Brian Yang, T.-Y., Krueer, W.L., More, R.M., Bruce Langdon, A.: Phys. Plasmas **2**, 3146 (1995) 374, 375
53. Ferrante, G., Zarcone, M., Uryupin, S.A.: Phys. Plasmas **9**, 4560 (2002) 374
54. Brian Yang, T.-Y., Krueer, W.L., Bruce Langdon, A., Johnston, T.W.: Phys. Plasmas **3**, 2702 (1996) 375
55. Umstadter, D., J. Phys. D: Appl. Phys. **36**, R151 (2003) 375
56. Rastunkov, V.S., Krainov, V.P., Laser Physics **15**, 262 (2005) 375
57. Sentoku, Y., Bychenkov, V.Y., Flippo, K., Maksimchuk, A., Mima, K., Mourou, G., Sheng, Z.M., Umstadter, D.: Appl. Phys. B **74**, 207 (2002) 375
58. Sofronov, A.V., Krainov, V.P.: J. Phys. B: At. Mol. Opt. Phys. **37**, L329 (2004) 375
59. Pukhov, A.: Rep. Progr. Phys. **66**, 47 (2003) 375
60. Jungreuthmayer, C., Geissler, M., Zanghellini, J., Brabec, T.: Phys. Rev. Lett. **92**, 133401 (2004) 375
61. Zaretsky, D.F., Korneev, Ph.A., Popruzhenko, S.V., Becker, W., J. Phys. B: At. Mol. Opt. Phys. **37**, 4817 (2004) 375
62. Korneev, Ph.A., Popruzhenko, S.V., Zaretsky, D.F., Becker, W.: Laser Physics Lett. **2**, 452 (2005) 375
63. Macchi, A., Cornolti, F., Pegoraro, F., Liseikina, T.V., Ruhl, H., Vshivkov, V.A.: Phys. Rev. Lett. **87**, 205004 (2001); Macchi, A., Cornolti, F., Pegoraro, F.: Phys. Plasmas **9**, 1704 (2002) 375
64. Kahaly, S., Yadav, S.K., Wang, W.M., Sengupta, S., Sheng, Z.M., Das, A., Kaw, P.K., Ravindra Kumar, G.: Phys. Rev. Lett. **101**, 145001 (2008) 375
65. Chen, L.M., Zhang, J., Dong, Q.L., Teng, H., Liang, T.J., Zhao, L.Z.: Wei, Z.Y., Phys. Plasmas **8**, 2925 (2001) 377
66. Dong, Q.L., Zhang, J., Teng, H.: Phys. Rev. E **64**, 026411 (2001) 377
67. Kato, S.: J. Plasma Fusion Res. Series **6**, 658 (2004) 377
68. Hong-bo Cai: Phys. Plasmas **13**, 063108 (2006) 377
69. Mulser, P., Schnabl, H.: Laser and Particle Beams **1**, 379 (1983) 377
70. Bergmann, A., Mulser, P.: Phys. Rev. E **47**, 3585 (1993) 377
71. Pukhov, A., Meyer-ter-Vehn, J.: Phys. Plasmas **5**, 1880 (1998) 377
72. Bauer, D., Mulser, P.: Phys. Plasmas **14**, 023301 (2007) 377
73. Mulser, P., Bauer, D., Ruhl, H.: Phys. Rev. Lett. **101**, 225002 (2008) 378
74. Bauer, D., Mulser, P.: J. Phys. Conf. Series **11**, 169 (2005) 379, 386
75. Born, M., Wolf, E.: Principles of Optics, p. 480. Cambridge University Press, Cambridge (1988) 381

76. Nayfeh, A.H., Mook, D.T.: Nonlinear Oscillations, Chap. 4. John Wiley & Sons, New York (1979) 385
77. Mulser, P., Ruhl, H., Steinmetz, J.: Laser and Particle Beams **19**, 23 (2001), Figs. 1 and 3 389
78. Ruhl, H.: In Bonitz, M., Sempke, D. (eds.) Introduction to Computational Methods in Many Particle Body Physics. Rinton Press, Paramus, New Jersey (2006) 389, 395
79. Cerchez, M., et al.: Phys. Rev. Lett. **100**, 245001 (2008) 389, 391
80. Mulser, P., Kanapathipillai, M., Hoffmann, D.H.H.: Phys. Rev. Lett. **95**, 103401 (2005) 391
81. Kundu, M., Bauer, D.: Phys. Rev. Lett. **96**, 123401 (2006) 391
82. Pesch, T.C., Kull, H.-J.: Phys. Plasmas **14**, 083103 (2007) 392, 394
83. Kaw, P., Dawson, J.: Phys. Fluids **13**, 472 (1970) 394
84. McKinstrie, C.J., Forslund, D.W.: Phys. Fluids **30**, 904 (1987) 392
85. Pesch, T.C., Kull, H.-J.: In: Mulser, P. (ed.) Quasiperiodic Waves in Relativistic Plasmas, ILIAS Prog. Rep. **3**, GSI Darmstadt (2008) 392
86. Tabak, M., et al.: Phys. Plasmas **1**, 1626 (1994) 392
87. Schwörer, H., Magill, L., Beleites, B. (eds.): Lasers and Nuclei. Springer, Heidelberg (2006) 392
88. Pálffy, A., Evers, J., Keitel, C.H.: Phys. Rev. Lett. **99**, 172502 (2008) 392
89. Baeva, T.: High Harmonic Generation from Relativistic Plasmas. VDM Verlag Dr. Müller, Saarbrücken (2008) 392, 394, 397
90. Müller, C., Di Piazza, A., Shahbaz, A., Bürvenich, T., Evers, J., Hatsagortsyan, K., Keitel, C.H.: Laser Physics **18**, 175 (2008) 393
91. Kodama, R., et al.: Nature **412**, 798 (2001); Kodama, R., et al., Nature **418**, 933 (2002) 393, 399
92. Atzeni, S., et al.: J. Phys.: Conference Series **112**, 022062 (2008) 393
93. Akhiezer, A.I., Polovin, R.V.: Sov. Phys. JETP **3**, 696 (1956) 393, 394
94. Sakagami, H., Mima, K.: Phys. Rev. E **54**, 1870 (1996) 393
95. Lontano, M., Passoni, M., Bulanov, S.V.: Phys. Plasmas **10**, 639 (2003) 393
96. Sircombe, N.J., Arber, T.D., Dendy, R.O.: Phys. Plasmas **12**, 012303 (2005) 393, 394
97. Weber, S., Lontano, M., Passoni, M., et al.: Phys. Plasmas **12**, 112107 (2005) 394
98. Bauer, D., et al.: Phys. Rev. Lett. **75**, 4622 (1995) 395
99. Mulser, P., Ruhl, H., Schneider, R., Batani, D.: J. Phys. Conf. Ser. **112**, 022074 (2008) 396
100. Hain, S., Mulser, P.: Phys. Rev. Lett. **86**, 015 (2001) (The calculated 10 kJ apply to the free ignition energy; total energy supplied to the corona amounts to 50–70 kJ) 398, 399
101. Mulser, P., Bauer, D.: Laser & Particle Beams **22**, 5 (2004) 398, 399
102. Atzeni, S.: Phys. Plasmas **6**, 3316 (1999) 399
103. Atzeni, S., Temporal, M., Honrubia, J.J.: Nucl. Fusion **42**, L1 (2002) 399
104. Mulser, P., Schneider, R.: Laser & Particle Beams **22**, 157 (2004) 399
105. Sentoku, Y., Chrisman, B., Kemp, A., Cowan, T.E.: Hot electron energy coupling in cone-guided fast ignition, Paper Tu07.6 at IFSA **2007**, Kobe, Sept. 9–14, 2007 399
106. Sprangle, P., Tang, C.M., Esarey, E.: IEEE Transactions on Plasma Science **15**, 145 (1987) 400
107. Karle, Ch., Spatscheck, K.H.: Phys. Plasmas **15**, 123103 (2008) 401

# Index

## A

- Ablation, 70, 74, 76, 77, 81
  - pressure, 74, 82, 211, 214
- Ablative
  - laser intensity, 78
- Above-threshold ionization, 281, 298
  - few-cycle, 301
- Absolute
  - instability, 254
- Absorption
  - anharmonic resonance, 386
  - anomalous skin layer, 375
  - coefficient, 15, 102
  - coherent collisional, 146
  - collisional, 91, 118, 148
    - in special density profiles, 113
  - collisionless, 91, 363
    - by anharmonic resonance, 378
  - inverse bremsstrahlung, 146
  - linear resonance, 154
  - nonlinear resonance, 164
  - resonance, 42, 152
- Acceleration
  - bubble, 359
  - electron, 173, 181
  - of particles, 351, 353
    - in a Langmuir wave, 178
  - wakefield, 359
- Action, 294, 296
  - stationary, 303
- Adiabatic
  - compression, 55, 57
  - stabilization, 289
- ADK
  - ionization rate, 280
- Airy function, 108, 109
- Amplification
  - parametric
    - of pulses, 256

## Amplitude

- Keldysh, 295
- Anharmonic resonance
  - absorption, 378
    - in cold plasma, 386
    - in warm plasma, 386

## Anomalous heating, 29

- Anomalous skin layer
  - absorption, 375

## Anti-Stokes

- component, 263
- line, 233, 246, 247

## Appearance intensity, 276

- Approximation
  - eikonal, 93
  - optical, 92
  - strong field, 292, 306
  - WKB, 92, 98

## ATI, 281, 298

- few-cycle, 301

## Atomic units, 267, 270

## Attosecond pulses, 311

## B

### Backscattering

- stimulated Brillouin, 249

### Ballistic model, 91, 134

### Barkas effect, 150

### Barrier suppression ionization, 282

### Beer's law, 102

- Bernoulli
  - equation, 80, 83

### Bessel functions, 130, 140, 297

- generalized, 299

- modified, 122

### Bichromatic

- laser light, 318

### Blast wave, 47

- Bohm-Gross
  - dispersion relation, 38
- Bohr radius, 10
- Boltzmann equation, 142
- Bounce frequency, 41, 172
- Boundary conditions
  - Siebert, 287
- Breaking
  - resonant, 190
  - threshold, 189
- Bremsstrahlung
  - inverse, 146
- Brillouin
  - diagram, 249
  - instability, 242
  - Mandelstam scattering, 242
  - scattering, 242, 245, 259
- Brunel effect, 376
- BSI, 282
- Bubble
  - acceleration, 359
- Buckingham
  - $\pi$ -theorem, 44, 45
  
- C**
- Canonical
  - equations, 337
  - Hamilton's equations, 96
  - momentum, 342
    - conservation, 365
- Canonical momentum
  - conservation, 262
- Carrier envelope phase, 301
- Center
  - of mass, 343
  - of momentum, 343
- Channel-closing, 281, 298
- Chaos, 262
- Chaotic
  - attractor, 187
  - electron orbits, 395
- Circular polarization, 10, 263
  - ionization in, 297
- Cluster, 19, 145, 363
- Coherent, 236
- Cold
  - wavebreaking, 183
- Collective
  - fields, 5
  - interaction, 91
  - ponderomotive force, 206
  - tunneling, 320
  
- Collision
  - frequency, 13, 21, 120, 127, 138
  - electron-electron, 22
  - electron-ion, 135, 139
- Collisional
  - absorption, 90, 91, 118
  - ionization
    - laser-driven, 323
- Collisional absorption
  - in special density profiles, 113
- Collisionless
  - absorption, 363
    - by anharmonic resonance, 378
    - shock, 57
- Collisions
  - overlapping, 126
  - simultaneous, 119
- COLTRIMS, 320
- Complex
  - dilation, 287
  - scaling, 287, 319
- Compression, 63
  - adiabatic, 55, 57
  - ratio, 55
  - wave, 57
- Conservation
  - canonical momentum, 353, 365
  - equation, 36
  - quasi-particle, 258
  - relativistic
    - of momentum, 340
    - of particles, 340
- Continuity equation, 26
- Continuous symmetry, 317
- Contraction
  - Lorentz, 333
- Contravariant, 337
  - components, 337
  - coordinates, 337
- Convective
  - instability, 254
- Coordinates
  - Eulerian, 25
  - Lagrangian, 26
  - parabolic, 272
- Cornu spiral, 184, 185, 382
- Coulomb
  - correction, 306
  - cross section, 21
  - focusing, 144
  - logarithm, 124, 127, 135–137, 139
    - double, 133
    - generalized, 145

- potential  
tilted, 270
- Covariant, 337  
components, 337  
coordinates, 337  
electrodynamics, 348
- Criterion  
Piliya-Rosenbluth, 256
- Critical  
field, 271, 275, 276  
runaway field, 31  
Mach number, 213, 215
- Critical density, 5, 39, 95, 396  
increase, 393  
relativistic, 393
- Cross section  
Coulomb, 21
- Current  
density, 92
- Curvature radius, 221
- Cut-off, 39  
 $10U_p$ , 305  
 $2U_p$ , 304  
in electron-ion collisions, 136  
for HOHG, 310
- Cut-off law  
for photoelectron spectra, 304
- D**
- Death valley, 290
- De Broglie  
wavelength, 22
- Debye  
length, 17, 18, 121, 125  
potential, 18, 136
- Decay  
instabilities, 242  
processes, 259
- Decomposition  
Eckart's, 345  
Landau's, 347
- Dense matter, 6
- Density  
critical, 39  
energy, 231  
photon, 97  
flux, 97  
ponderomotive, 232  
profile  
reflection-free, 112
- Density functional theory  
time-dependent, 319
- Density profile  
modifications, 194
- Dephasing, 257
- Detrapping, 261
- Detuning, 285
- Diagram  
Brillouin, 249
- Dichotomy, 290
- Dielectric  
function, 130  
model, 91, 132, 143
- Dimensional  
analysis, 45  
matrix, 45, 268
- Dimensionless  
variables, 45
- Dipole  
Fourier-transformed, 311
- Dipole-dipole correlation function, 312
- Direct electron, 307
- Dispersion  
relation, 94  
Bohm-Gross, 38
- Distribution  
Maxwellian, 348, 365
- Distribution function  
non-Maxwellian, 143  
one-particle, 35, 341  
two-particle, 36
- Doppler-broadened  
line profile, 236
- Doppler broadening, 236
- Doppler effect, 232  
in the medium, 233
- Double slit  
in time, 308
- Downhill potential, 273
- Dressed states, 283
- Drude form  
of refractive index, 374
- Drude model, 142, 143
- Dusty plasma, 146
- Dynamic  
stabilization, 289
- Dynamic form factor, 237
- E**
- Eckart's decomposition, 345
- Effective  
potential, 271
- Ehrenfest theorem, 311
- Eigenvalue  
equation, 284

- Eikonal
  - approximation, 93, 96, 97, 100, 106
- Einstein
  - coefficients, 148
  - force, 335
- Electric field
  - amplitude
    - maximum, 111, 158
  - static
    - atoms in, 270
- Electrodynamics
  - covariant, 348
- Electromagnetic
  - field tensor, 350
- Electron
  - acceleration, 181
  - beam instability, 40
  - direct, 307
  - plasma wave, 37, 38
    - high amplitude, 165
    - nonlinear, 167
  - sound velocity, 39
  - temperature, 24
- Electron beam
  - quasi-monochromatic, 361
- Electron distribution function, 263
- Electron orbits
  - chaotic, 395
- Electron trapping, 181
- Electrostatic wave, 38
- Energy
  - balance, 32
  - conservation, 101
  - density, 231
    - thermal, 24
  - electric, 101
    - kinetic, 101
    - magnetic, 101
  - emitted in HOHG, 312
  - equations, 27
  - Floquet, 283
  - flux, 101, 231
  - internal, 345
  - loss, 16
  - oscillation, 358
  - quasi, 283, 287
  - quiver, 358
  - transport, 231
- Epstein profile, 177
- Epstein transition layer, 99
- Equation
  - Bernoulli, 80, 83
  - Boltzmann, 142
- canonical, 337
- conservation, 36
- eigenvalue, 284
- Hamilton-Jacobi, 96
- harmonic oscillator, 184
- relativistic Vlasov, 262
- Schrödinger
  - nonlinear, 223
  - time-dependent, 283
- Stokes, 107
- Vlasov, 36, 262
- Eulerian
  - coordinates, 25
  - picture, 25
- Exceptional symmetry
  - of H-like ions, 276
- Expansion
  - Fourier, 289
- Explosive instability, 260
- Exponential wall, 319
- F**
- Fast ignition, 393
- Fermat's principle, 94
- Fermi energy, 18
- Few-cycle
  - ATI, 301
- Field
  - critical, 271, 275, 276
- Field ionization, 13
- Field operator, 9
- Field-dressed
  - state, 286, 287
- Filamentation, 219
- Fine structure constant, 269
- Floquet
  - energy, 283
  - Hamiltonian, 284, 317
  - state, 287, 316
  - theorem, 283, 316
  - theory, 283, 316
    - high-frequency, 290
    - non-Hermitian, 287
    - $R$ -matrix, 319
- Fluid dynamics
  - ideal, 340
- Fluid models, 24
- Flux
  - energy, 231
- Focal
  - averaging, 299, 306
  - expansion, 320
- Fock state, 8

- Focusing  
self-, 251
- Force  
density, 27  
Lorentz, 199, 262, 348  
ponderomotive, 12, 204  
radiation, 193
- Form factor  
dynamic, 237
- Four vector, 331
- Fourier  
expansion, 283, 289
- Fragezeicheneffekt, 249
- Freeman resonance, 288
- Frequency  
bounce, 172  
collision, 120, 127, 138  
electron-ion, 135, 139  
Rabi, 285
- Fresnel formula, 160
- G**
- Galilean relativity, 333
- Gauge  
Göppert-Mayer, 293  
invariance, 293  
length, 293  
transformation, 293  
velocity, 293
- Gaussian  
laser beam, 220  
super, 144
- Gay-Lussac  
experiment, 34
- Generation  
hot electron, 172  
magnetic field, 209
- Geometrical  
wavebreaking, 183
- Giant ions, 145
- Glauber state, 8
- Göppert-Mayer gauge, 293
- Gordon-Volkov-Hamiltonian, 294
- Gordon-Volkov state, 294
- Group velocity, 39, 96
- Growth rate, 47, 245, 260
- H**
- Hamiltonian, 337  
Gordon, 294  
of a free electron, 10  
relativistic, 352  
Volkov, 294
- Hamilton-Jacobi equation, 96
- Hamilton's canonical equations, 96
- Harmonic generation, 267
- Harmonic oscillator, 184
- Harmonic oscillator model, 91
- Hartree-Fock  
time-dependent, 319  
multi-configurational, 320
- Heat  
conduction  
electronic, 29  
current density  
anomalous, 182  
flow, 49  
flux  
inhibition, 62, 77  
flux density  
anomalous, 181  
wave, 50, 52, 59, 62
- Heating  
anomalous, 29  
Brunel, 376  
 $j \times B$ , 376  
stochastic, 375  
vacuum, 377
- High harmonic  
selection rules, 315
- High-frequency  
Floquet theory, 290
- High-order  
ATI, 311  
harmonic generation, 308
- Hilbert space  
extended, 316
- HOHG, 308
- Hologram  
of binding potential, 308
- Hot electron  
generation, 172
- Hugoniot  
equation of state, 55
- Huntley's addition, 50
- Hydrodynamic  
wavebreaking, 183, 184
- Hysteresis  
ponderomotive, 205
- I**
- Ideal fluid dynamics, 340
- Incoherent, 236
- Index  
refractive, 93
- Induced scattering, 241

- Instability
  - absolute, 254
  - Brillouin, 242
  - convective, 254
  - electron beam, 40
  - explosive, 260
  - Langmuir cascade, 242
  - modulational, 222
  - oscillating two-stream, 242, 253
  - parametric decay, 242, 254
  - Raman, 242
  - Rayleigh-Taylor, 47
  - resonant filament, 251
  - two phonon decay, 242
  - two plasmon decay, 240, 242, 252
- Intensity
  - appearance, 276
- Interaction
  - collective, 91
- Interference
  - in photoelectron spectra, 306
  - quantum, 306
- Internal energy, 345
- Inversion
  - spatial, 317
- Ion
  - acoustic wave, 42
  - beam, 362
    - stopping, 149
  - giant, 145
  - plasma frequency, 43
  - separation, 68
  - sound velocity, 43
  - temperature, 24
- Ion momentum
  - distribution, 322
- Ionization, 267
  - above-threshold, 281, 298
  - barrier suppression, 282
  - collisional, 13
  - energy, 16
  - field, 13
  - frequency, 16
  - multiphoton, 23, 281
  - multiple, 319
  - nonsequential, 23, 267, 319, 320
  - over barrier, 282
  - probability
    - differential, 303
  - rate, 287, 297
    - ADK, 280
    - Landau, 280
    - PPT, 281
- time, 296, 302
- tunneling, 277, 282
- Irreversibility, 374
- J**
  - Jacobian, 26, 342, 346
- K**
  - Keldysh
    - parameter, 280, 282
  - Keldysh amplitude, 295
  - Keldysh-Faisal-Reiss theory (KFR), 292
  - Kinetic theory, 341
    - wavebreaking, 186
  - Kirchhoff's law, 147
  - Knee
    - NSDI, 320
  - Kramers-Henneberger transformation, 289
  - Kustaanheimo-Stiefel transformation, 275
- L**
  - Lagrange
    - equation, 105, 337
  - Lagrangian, 105, 106, 337
    - coordinates, 26
    - phase-averaged, 106
    - picture, 25
    - WKB approximation, 106
  - Landau
    - damping, 37, 39, 259
    - ionization rate, 280
    - parameter, 21
  - Landau's decomposition, 347
  - Langmuir
    - cascade, 242
    - wave, 38, 95, 178
  - Larmor formula, 146, 311
  - Laser
    - beam
      - Gaussian, 220
    - fields
      - atoms in, 281
    - high power, 6
    - intensity
      - ablative, 78
    - light
      - bichromatic, 318
  - Laser-atom
    - interaction, 267
  - Laser-driven
    - collisional ionization, 323
  - Laser-plasma
    - dynamics, 58
    - relativistic, 331

- Law  
Beer's, 102  
Kirchhoff's, 147  
Ohm's, 92
- Least action principle, 105
- Length gauge, 293
- Lewenstein model, 313
- Liénard-Wiechert  
potentials, 351
- Light scattering  
at relativistic intensities, 259
- Light trapping, 261
- Line  
anti-Stokes, 233, 246, 247  
Stokes, 233, 246
- Linear  
resonance  
absorption, 154
- Linear polarization  
ionization in, 299
- Liouville  
theorem, 36, 97  
relativistic, 341
- Local density  
approximation, 320
- Logarithm  
Coulomb, 124, 127, 135–137, 139  
generalized, 145  
double, 141
- Long-pulse  
photoelectron spectrum, 299
- LOPT, 281
- Lorentz  
boost, 350, 371  
contraction, 333  
force, 9, 199, 262, 348  
gauge, 350  
scalar, 349  
transformation, 333
- Lotz formula, 16
- M**
- Mach number, 55, 211  
critical, 75, 213, 215
- Magnetic field  
generation, 209
- Manley-Rowe relations, 258
- Matching condition, 247
- Matrix  
dimensional, 268
- Maxwellian  
distribution, 348, 365  
electron distribution, 15
- Mechanical momentum, 342
- Medium  
layered, 95  
stratified, 95
- Minkowski force, 335
- Mode  
quasi, 248
- Model  
ballistic, 91, 134  
dielectric, 91  
Drude, 142, 143  
harmonic oscillator, 91  
Lewenstein, 313
- Modulational instability, 222
- Moment equations, 343, 344
- Moments  
first-order, 347  
zeroth order, 347
- Momentum  
canonical, 342  
density, 32  
density flux, 32  
distribution  
of ions, 322  
equations, 27  
flux density tensor, 32  
loss, 134  
mechanical, 342
- MPI, 281
- Multicomponent plasma, 67
- Multi-configurational  
Hartree-Fock  
time-dependent, 320
- Multiphoton ionization, 281
- Multiphoton processes, 5
- Multiple ionization, 319
- N**
- Newton  
force, 335
- Non-Hermitian  
Floquet theory, 287
- Nonlinear  
Schrödinger equation, 223
- Non-Maxwellian  
distribution function, 143
- Nonresonant  
ponderomotive effects, 210
- Nonsequential  
ionization, 267, 319, 320
- NSDI, 320  
knee, 320

- O**
- OBI, 282
  - Ohm's law, 92, 101
  - One-fluid model
    - description, 31
    - model, 24
  - One-particle distribution function, 35, 341
  - Operator
    - phase conjugation, 249
    - time evolution, 292
  - Optical approximation, 92
  - Orbits, 35
  - Oscillating two-stream instability, 242, 253
  - Oscillation
    - center, 194, 202, 355, 356
    - frame, 195
    - orbit, 195
    - energy, 10, 197, 356, 358
  - Oscillator model, 120, 125
  - Over barrier ionization, 282
  - Overdense matter, 363
- P**
- Parabolic coordinates, 272
  - Parabolic quantum numbers, 274
  - Parameter Keldysh, 280, 282
  - Parametric amplification of pulses, 256
  - Parametric decay, 242, 254
  - Particle acceleration
    - by Langmuir wave, 178
    - in laser field, 351
    - in vacuum, 353
    - trapping, 42, 187, 189
  - Particle-in-cell method, 62, 80, 376, 389
  - Pauli-Fierz transformation, 289
  - Perturbation quartic, 275
  - Perturbation theory lowest order, 281
  - Phase velocity, 39, 117
  - Phase conjugated plasma mirror, 249
  - Phase conjugation operator, 249
  - Photon density, 97
  - flux, 97
  - subspace, 285
  - Photon number, 8
  - Photon number state, 8
  - PIC simulation, 62, 80, 376, 389
  - Piliya-Rosenbluth criterion, 256
  - Piliya's equation, 115
  - Plane wave, 7
  - Plasma breakdown, 15
  - degenerate, 18
  - echoe, 42
  - formation, 5
  - frequency, 38, 92
  - ion, 43
  - fully ionized, 24
  - heating, 13
  - mirror
  - phase conjugated, 249
  - multicomponent, 67
  - production, 60
  - rarefied, 35
  - wave
    - electron, 37, 38
  - Point explosion, 47
  - Poisson distribution, 8
  - Polarization circular, 10
    - ionization in, 297
  - linear
    - ionization in, 299
  - Ponderomotive coupling
    - resonant, 238
  - effects nonresonant, 210
    - resonant, 228
  - force, 12, 193
    - collective, 193, 206
    - density, 232
    - harmonic oscillator, 198
    - magnetized plasma, 193
    - relativistic, 201
    - on single particle, 194
  - hysteresis, 205
  - potential, 12, 199
  - resonant component, 235
  - scaling, 310

Potential  
Coulomb  
    tilted, 270  
Debye, 18, 136  
downhill, 273  
effective, 271  
Liénard-Wiechert, 351  
ponderomotive, 12  
scalar, 293  
uphill, 273  
vector, 293  
Poynting  
    theorem, 101  
    vector, 7  
PPT  
    ionization rate, 281  
Pressure  
    ablation, 74, 211, 214  
    electron, 20  
    radiation, 214  
Principle  
    least action, 105  
Probability  
    current, 279  
    flux, 278  
Profile steepening, 214  
Propagation  
    laser light, 91, 95  
Propagator  
    Gordon-Volkov, 295  
Proper time, 334  
Pseudo-Euclidean metric, 332

**Q**  
Quantum holography, 308  
Quantum numbers  
    good, 281  
    parabolic, 274  
Quartic perturbation, 275  
Quasi  
    classical  
        wave function, 277  
    energy, 283, 287  
    mode, 248  
    monochromatic  
        electron beam, 361  
    neutrality, 16  
    particle  
        conservation, 258  
Quiver  
    energy, 358

**R**  
Rabi  
    frequency, 285  
    oscillations, 287  
Radiation  
    field, 8  
    force, 193  
    pressure, 214  
    temperature, 31  
    transport, 97  
Raman instability, 242  
Raman scattering, 242, 251,  
    259  
    backward, 261  
Rankine-Hugoniot relations, 54  
Rarefaction  
    isothermal, 81  
Rate  
    ADK, 280  
    growth, 47, 245, 260  
    ionization, 287, 297  
    Landau, 280  
    partial, 298  
    PPT, 281  
Ray  
    equation, 93, 95  
    tracing, 96  
Rayleigh length, 221  
Rayleigh-Taylor instability, 47  
Raytracing, 95  
Reaction microscope, 320  
Recollision-induced  
    excitation, 323  
    ionization, 323  
Recombination, 267  
Reflection  
    coefficient, 100, 110, 113  
Reflection-free  
    density profiles, 112  
Refractive  
    index, 93, 102  
        Drude form, 374  
Relations  
    Rankine-Hugoniot, 54  
Relativistic  
    conservation  
        of momentum, 340  
        of particles, 340  
    critical density  
        increase, 393  
    Hamiltonian, 352  
    laser-plasma, 331  
    self-focusing, 400

- velocity addition, 336
- Vlasov equation, 262
- Rescattering, 304
  - scenario, 320
  - time, 302
- Resonance
  - absorption, 42, 152
  - linear, 154
  - nonlinear, 164
  - Freeman, 288
- Resonant
  - breaking, 190
  - coupling, 98, 156
  - filament instability, 251
  - interaction, 320
  - ponderomotive
    - component, 235
  - ponderomotive coupling, 238
  - ponderomotive effects, 228
  - wavebreaking, 183
- Rotating wave approximation, 285
- Rotational
  - symmetry, 318
- Runaway field, 31
  
- S**
- Saddle-point
  - integration, 303
  - method, 304
- Scalar, 337
  - potential, 293
- Scattering
  - Brillouin, 242, 245
  - Brillouin-Mandelstam, 242
  - induced, 241
  - Raman, 242, 251
  - Thomson, 235
- Schneider's spoons, 180
- Schrödinger
  - equation
    - nonlinear, 223
    - separation, 272
- Screening, 17, 18, 121, 125
- Screening length, 18
- Selection rules
  - high harmonic, 315
- Self-focusing, 219, 251
  - relativistic, 400
- Self-similar
  - solution, 46
- Separation
  - Schrödinger equation, 272
- Separatrix, 41, 175
- SFA, 292, 306
  - transition amplitude, 296
  - transition matrix element, 294
- Shake-off, 320
- Shock
  - collisionless, 57
  - strong, 55
  - velocity, 54
  - wave, 54, 64
- Short-range
  - potential, 306
- Siebert boundary conditions, 287
- Similarity, 44, 69
  - solutions, 44, 46
- Simple man's theory, 304, 309, 310
- Simulation
  - PIC, 62, 80, 376, 389
  - Vlasov, 179, 262, 368, 370
- Small angle deflection, 22
- Solutions
  - self-similar, 46
  - similarity, 44, 46
- Sound velocity
  - adiabatic, 48
  - electron, 39
  - ion, 43
- Space
  - inversion, 317
- Spectral density function, 237
- Stabilization, 288
  - adiabatic, 289
  - dynamic, 289
- Stark
  - effect, 270
  - linear, 275
  - shift, 12
  - AC, 287, 298
- State
  - field-dressed
    - superposition, 287
  - Floquet, 287
  - Gordon-Volkov, 294
  - Volkov, 294
- Stationary
  - action, 303
  - momentum, 302
- Steady state wave equation, 259
- Stimulated Brillouin backscattering, 249
- Stimulated Raman
  - effect, 257, 259
- Stochastic heating, 375

- Stokes  
equation, 107  
homogeneous, 107, 111, 117  
inhomogeneous, 115  
line, 233, 246
- Stopping  
ion beam, 149
- Strong field approximation, 292, 306
- Strong shock, 55
- Strong trapping, 261
- Super-Gaussian, 144
- Superposition  
of field-dressed states, 287  
of Floquet states, 287, 319
- Surface plasmons  
excitation of, 375
- Symmetry  
continuous, 317  
rotational, 318
- T**
- TDSE, 283
- Temperature  
electron, 24  
ion, 24  
radiation, 31
- Theorem  
Buckingham  $\pi$ , 44
- Theory  
kinetic, 341
- Thermal  
energy density, 24  
speed, 13
- Thermalization  
time, 22
- Thomas-Fermi, 276
- Thomson differential  
scattering cross section, 236
- Thomson scattering, 235, 236  
coherent, 236  
incoherent, 236
- Three-step model, 309
- Threshold  
breaking, 189
- Tilted  
Coulomb potential, 270
- Time-dependent  
density functional theory, 319  
Hartree-Fock, 319  
multi-configuration, 320  
Schrödinger equation, 283
- Time dilation, 333
- Time evolution  
operator, 292
- Time window, 307
- Topological aspects, 33
- Transformation  
gauge, 293  
Kramers-Henneberger, 289  
Kustaanheimo-Stiefel, 275  
Lorentz, 333  
Pauli-Fierz, 289
- Transition  
matrix element  
SFA, 294
- Transition layer  
Epstein, 99
- Translation  
in momentum space, 293  
in time, 317
- Transport  
of energy, 231
- Trapping  
in laser beam, 260  
of electrons, 181, 187, 189  
of electrons in a wave, 177, 179
- Tunneling, 282  
collective, 320  
ionization, 277, 282
- Two phonon decay, 242
- Two plasmon decay, 240, 242, 243, 252
- Two-fluid model, 24
- Two-level system, 284
- Two-particle distribution function, 36
- U**
- Units  
atomic, 267, 270
- Uphill potential, 273
- V**
- Vacuum heating, 377
- Variables  
dimensionless, 45
- Vector  
four, 331
- Vector potential, 10, 293
- Velocity  
addition theorem, 336  
electron sound, 39  
gauge, 293  
group, 39, 96  
phase, 39, 117
- Viscosity  
ion, 29
- Viscous effects, 28

**Vlasov**

- equation, 36, 262, 342
- simulation, 179, 262, 368, 370

Volkov-state, 294

**W****Wakefield**

acceleration, 359

**Warm**

wavebreaking, 182

**Wave**

blast, 47

breaking, 42

compression, 57

electron plasma

- high amplitude, 165

- nonlinear, 167

electrostatic, 38

equation, 92, 93

ion acoustic, 42

Langmuir, 38, 178

nonlinear heat, 50

rarefaction

- adiabatic, 48

- isothermal, 48

- shock, 54, 64

**Wave function**

- quasi-classical, 277

**Wavebreaking**, 182, 184, 262

- cold, 183

- geometrical, 183

- hydrodynamic, 183, 184

- kinetic theory, 186

- resonant, 183, 389

- warm, 182

**WKB**

- approximation, 92, 98, 106, 109

- theory, 282

**X****XUV radiation**

- from HOHG, 310